Synthesis, Characterization, and Applications of Ruthenium(II) Complexes Bearing 1,1-Dithiolate Ligands

Mohammed ZAIN ALDIN

A Thesis submitted for the degree of Doctor of Science
under the supervision of Professor Lionel Delaude

Laboratory of Organometallic Chemistry and Homogeneous Catalysis
Department of Chemistry, Faculty of Sciences, University of Liege
Academic Year 2024–2025

Table of contents

Chapter I Supporting Information (SI)

This chapter contains the supporting information of research papers already published and further experimental details of the studies described in this doctoral thesis:

1. Synthesis, characterization, and catalytic evaluation of ruthenium–diphosphine complexes bearing xanthate ligands.
   M. Zain Aldin, A. Maho, G. Zaragoza, A. Demonceau, and L. Delaude, *Dalton Transactions*, **2018**, *47*, 13926-13938. DOI: 10.1039/C8DT02838A.

2. Synthesis of Ruthenium–dithiocarbamate chelates bearing diphosphine ligands and their use as latent initiators for atom transfer radical additions.
   M. Zain Aldin, G. Zaragoza, and L. Delaude, *Journal of Organometallic Chemistry*, **2021**, *950*, 121993. DOI: 10.1016/j.jorganchem.2021.121993.

3. Synthesis, Characterization, and Biological Activity of Water-Soluble, Dual Anionic and Cationic Ruthenium–Arene Complexes Bearing Imidazol(in)ium-2-dithiocarboxylate Ligands.
   M. Zain Aldin, G. Zaragoza, W. Deschamps, J.-C.D. Tomani, J. Souopgui, and L. Delaude, *Inorganic Chemistry*, **2021**, *60*, 16769-16781. DOI: 10.1021/acs.inorgchem.1c02648.

4. Synthesis, characterization, and biological activity of cationic ruthenium–arene complexes with sulfur ligands.
   M. Zain Aldin, G. Zaragoza, E. Choquenet, G. Blampain, G. Berger, and L. Delaude, *Journal of Biological Inorganic Chemistry*, **2024**, *29*, 441–454. DOI: 10.1007/s00775-024-02052-2.

I.1. Supporting Information (SI) for Chapter V: Synthesis, characterization, and catalytic evaluation of ruthenium–diphosphine complexes bearing xanthate ligands

Electronic Supporting Information (ESI) for:

Synthesis, characterization, and catalytic evaluation of ruthenium–diphosphine complexes bearing xanthate ligands

Mohammed Zain Aldin,[a] Anthony Maho,[b] Guillermo Zaragoza,[c] Albert Demonceau,[a] and Lionel Delaude*[a]

[a]*Laboratory of Organometallic Chemistry and Homogeneous Catalysis, Institut de chimie (B6a), Allée du six Août 13, Quartier Agora, Université de Liège, 4000 Liège, Belgium*

[b]*GreenMAT, Institut de Chimie (B6a), Allée du six Août 13, Quartier Agora, Université de Liège, 4000 Liège, Belgium*

[c]*Unidade de Difracción de Raios X, Edificio CACTUS, Universidade de Santiago de Compostela, Campus Vida, 15782 Santiago de Compostela, Spain*

Table of content

Part 1 – NMR spectra

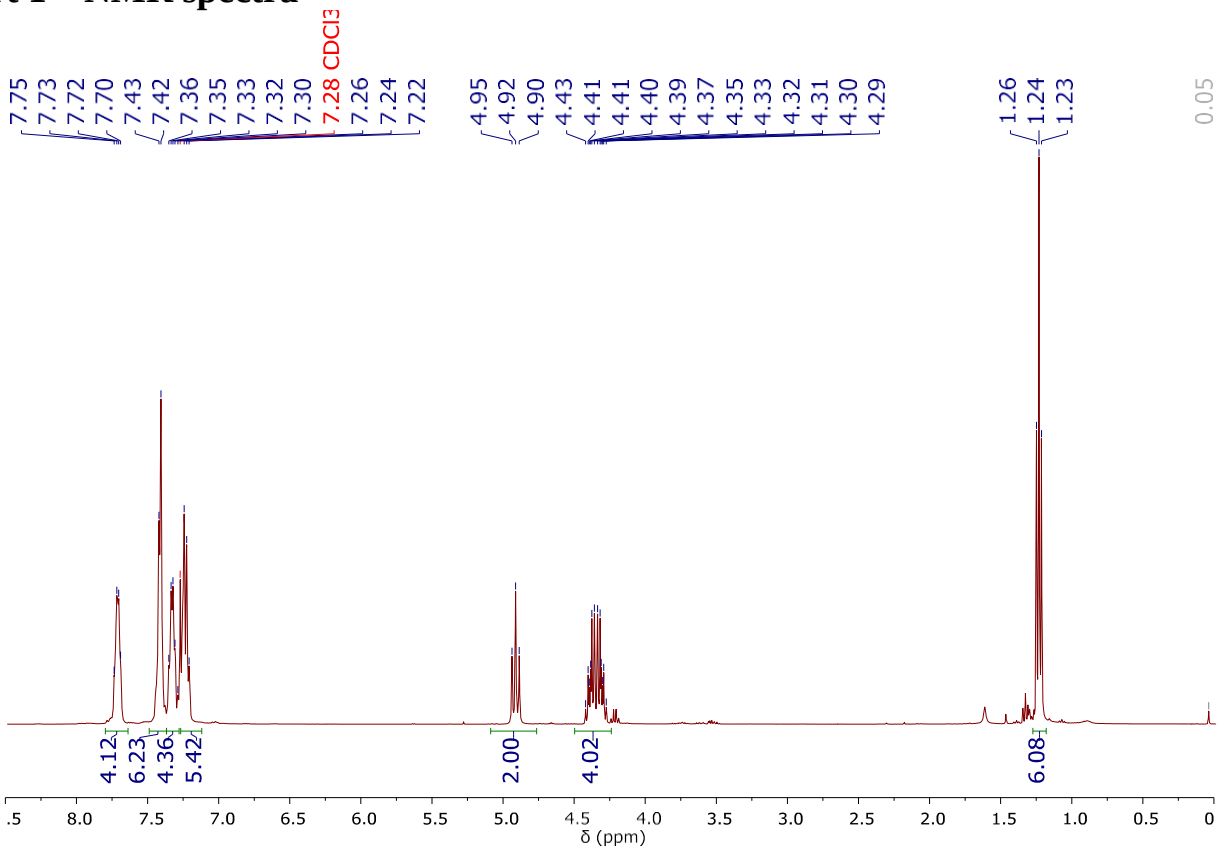

Fig. S1. ^{1}H NMR spectrum (400 MHz, $CDCl_3$, 298 K) of [Ru(S_2COEt)$_2$(dppm)] (**1**)

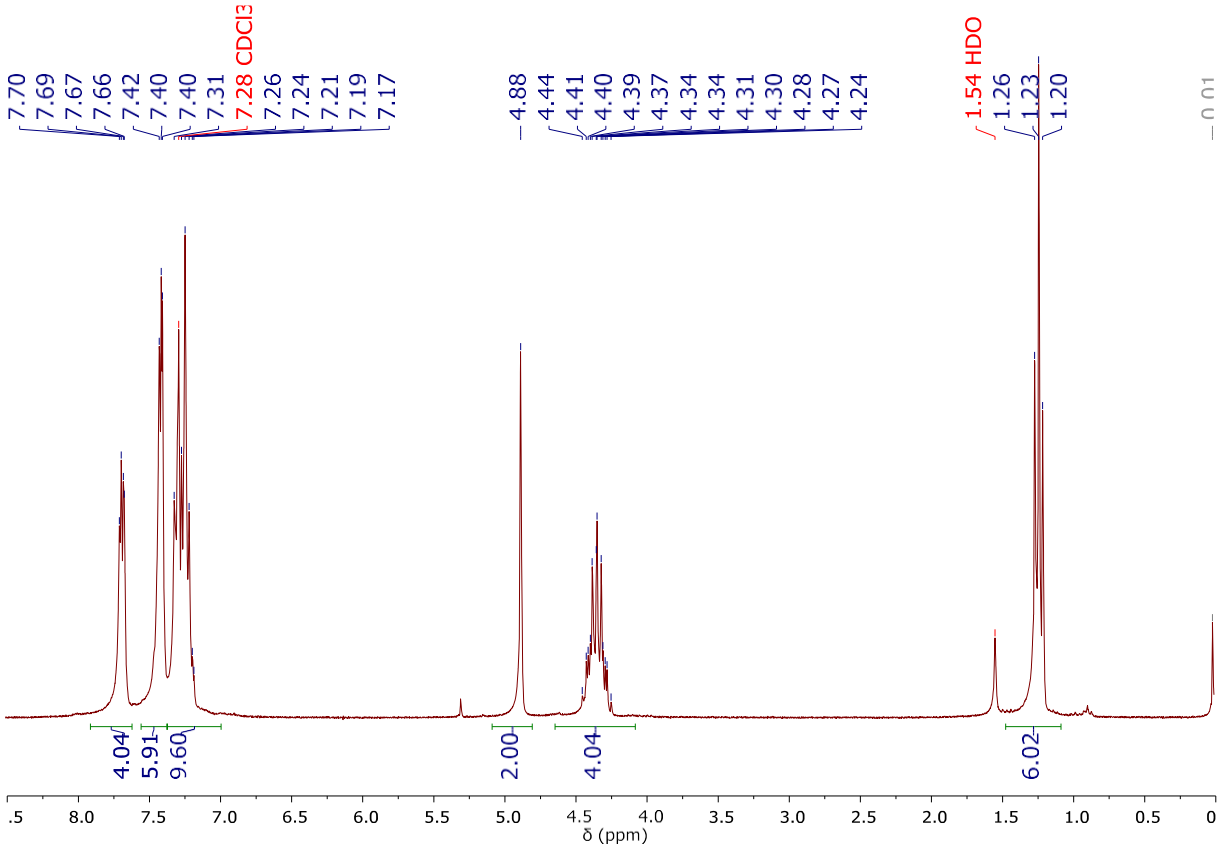

Fig. S2. ^{1}H{^{31}P} NMR spectrum (250 MHz, $CDCl_3$, 298 K) of [Ru(S_2COEt)$_2$(dppm)] (**1**)

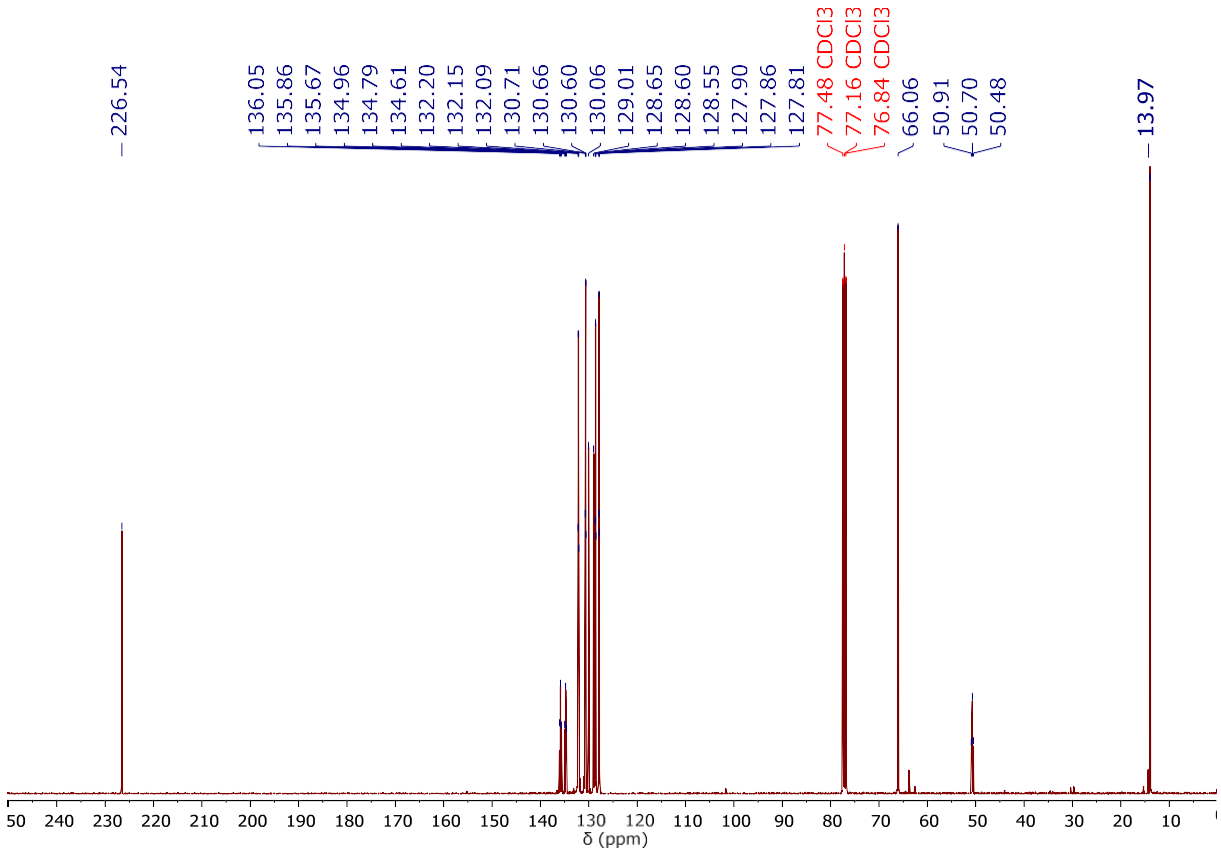

Fig. S3. $^{13}C\{^{1}H\}$ NMR spectrum (101 MHz, $CDCl_3$, 298 K) of $[Ru(S_2COEt)_2(dppm)]$ (**1**)

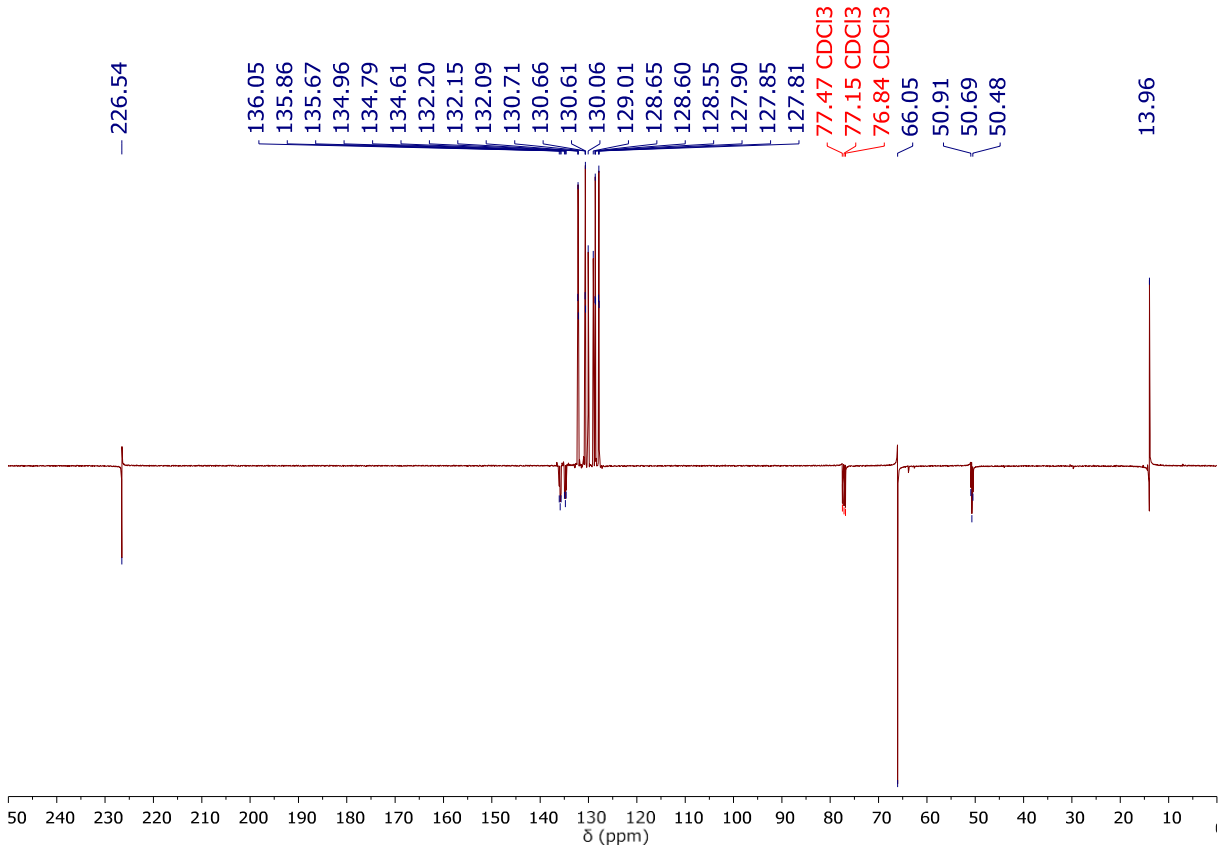

Fig. S4. $^{13}C\{^{1}H\}$ APT NMR spectrum (101 MHz, $CDCl_3$, 298 K) of $[Ru(S_2COEt)_2(dppm)]$ (**1**)

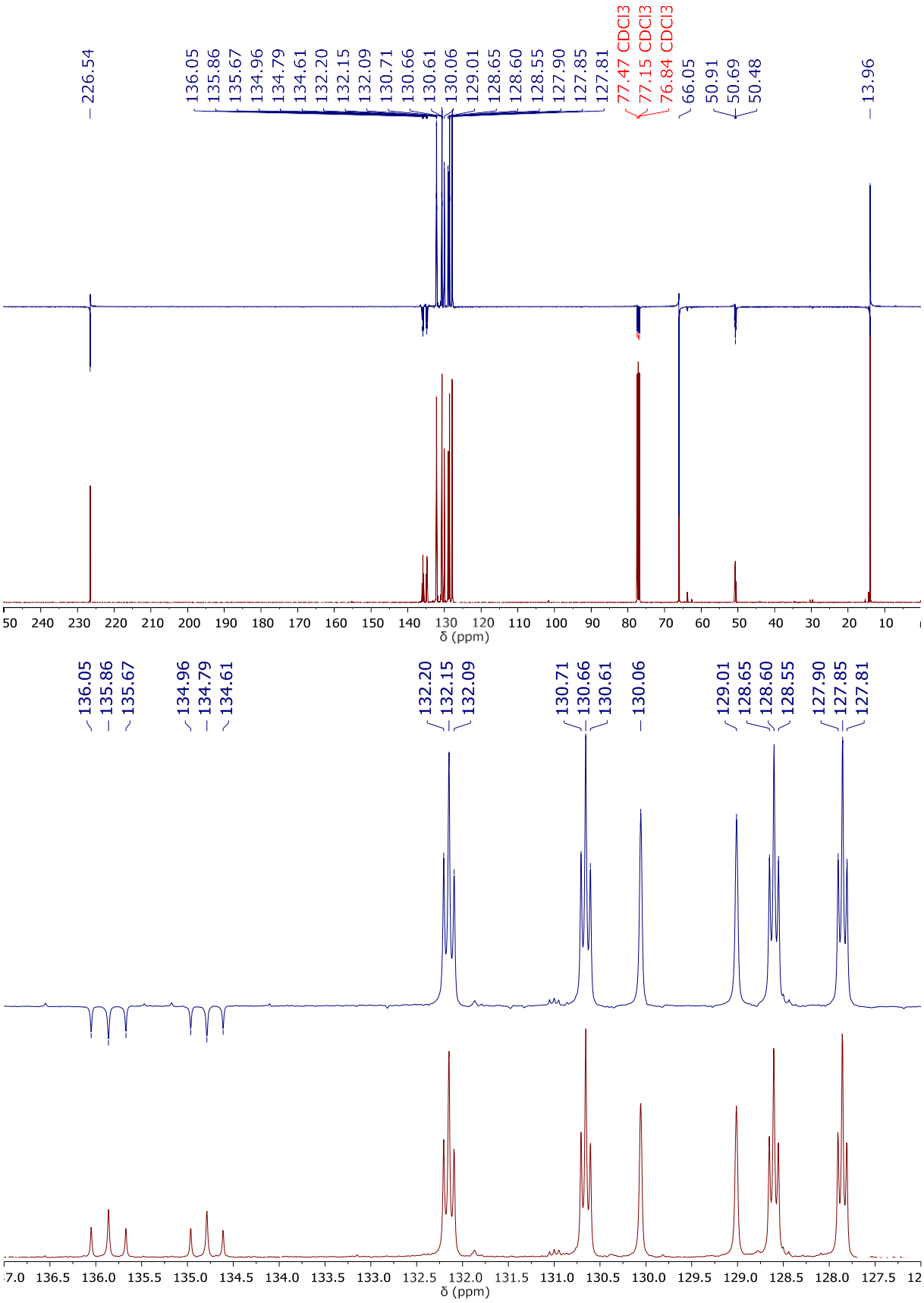

Fig. S5. ^{13}C CPD and APT NMR spectra (101 MHz, $CDCl_3$, 298 K) of [Ru($S_2COEt)_2$(dppm)] (**1**)

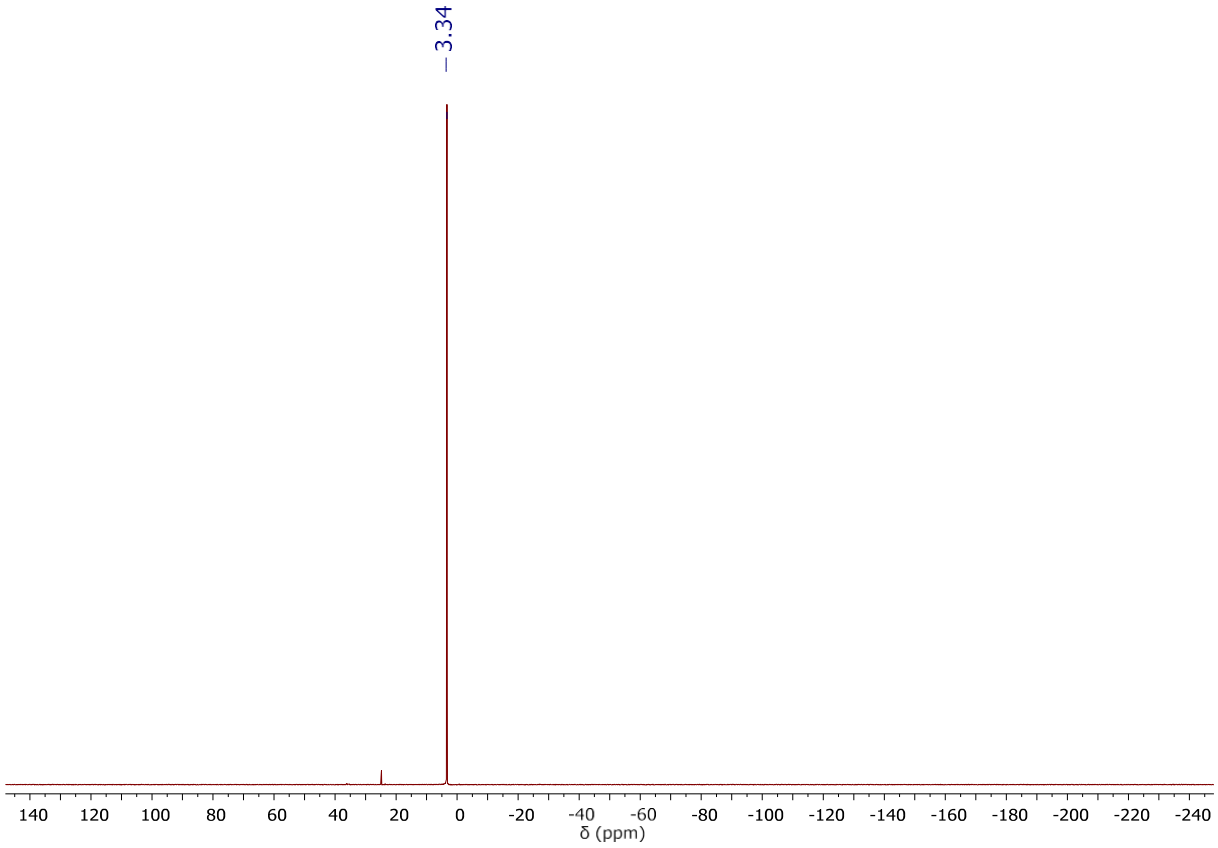

Fig. S6. ^{31}P NMR spectrum (162 MHz, $CDCl_3$, 298 K) of [Ru($S_2COEt)_2$(dppm)] (**1**)

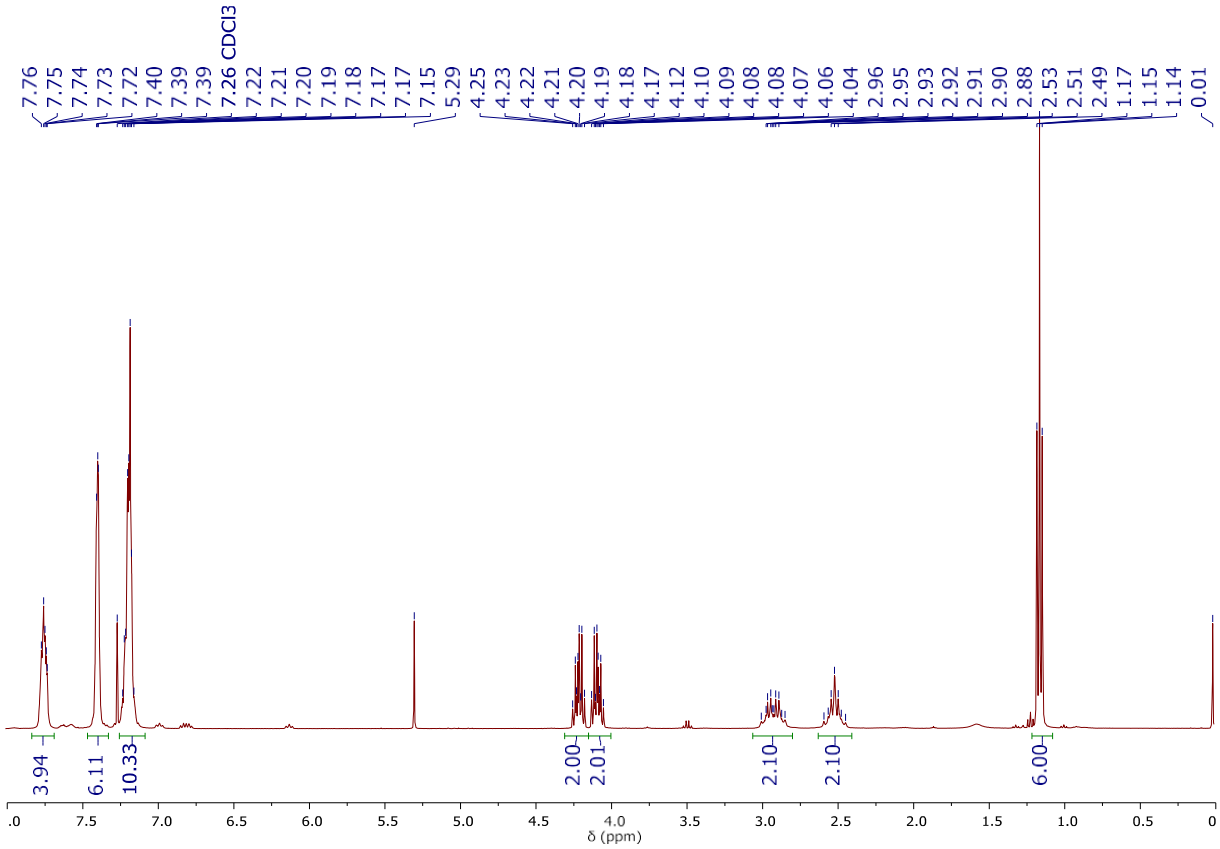

Fig. S7. ^{1}H NMR spectrum (400 MHz, $CDCl_3$, 298 K) of [Ru($S_2COEt)_2$(dppe)] (**2**)

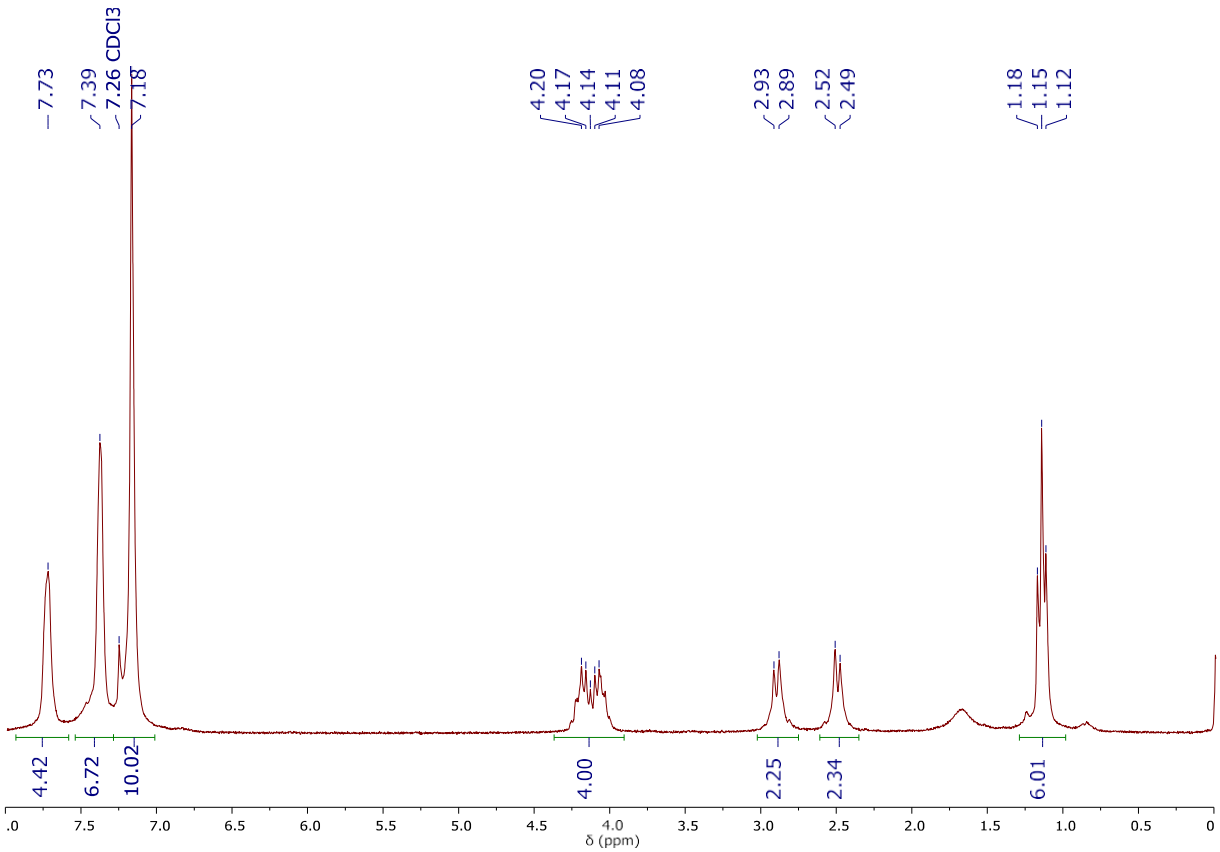

Fig. S8. $^{1}H\{^{31}P\}$ NMR spectrum (250 MHz, $CDCl_3$, 298 K) of $[Ru(S_2COEt)_2(dppe)]$ (**2**)

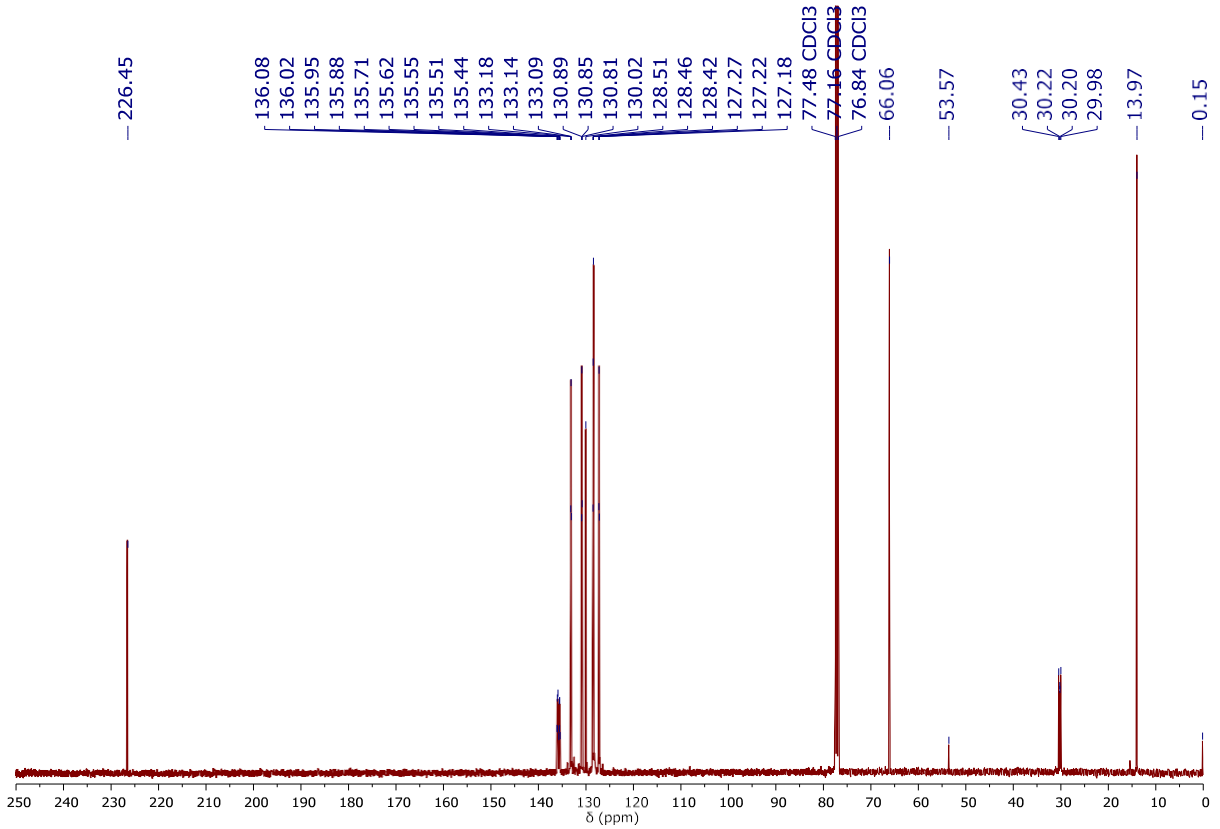

Fig. S9. $^{13}C\{^{1}H\}$ NMR spectrum (101 MHz, $CDCl_3$, 298 K) of $[Ru(S_2COEt)_2(dppe)]$ (**2**)

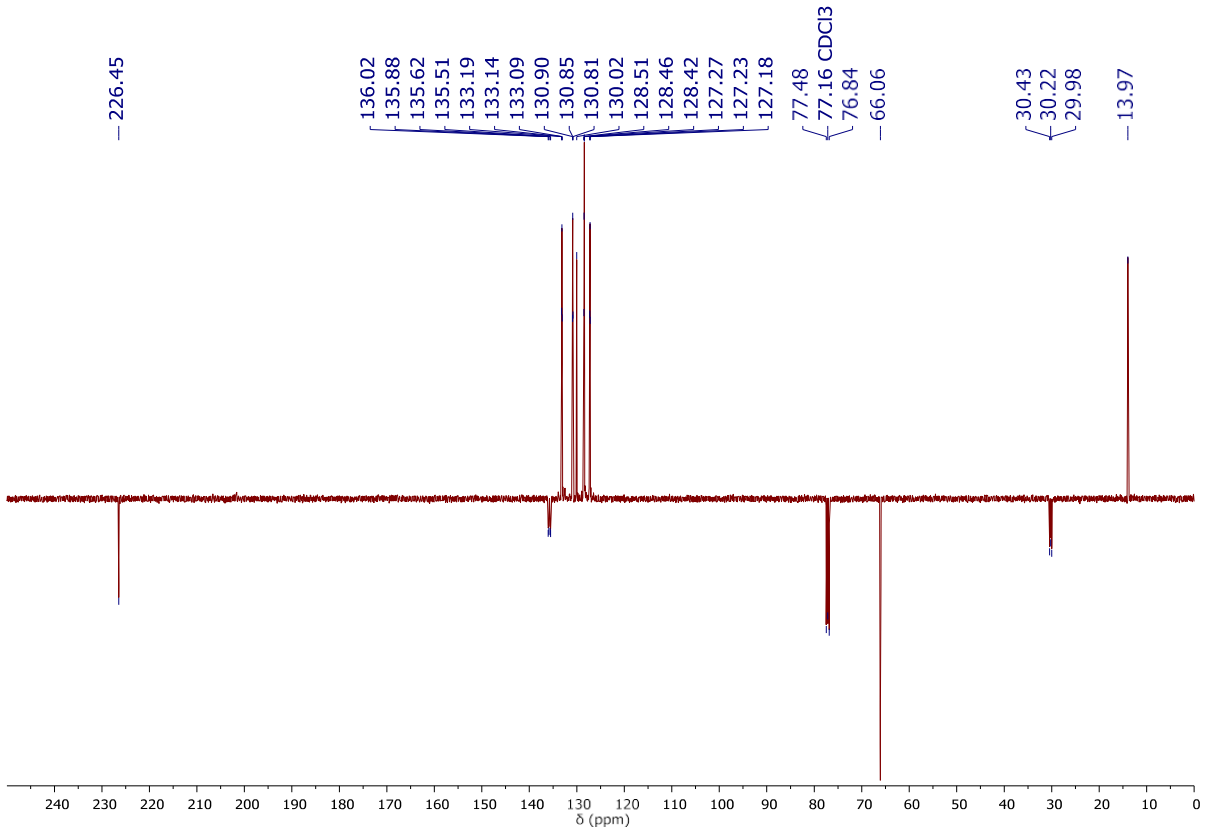

Fig. S10. $^{13}C\{^{1}H\}$ APT NMR spectrum (101 MHz, $CDCl_3$, 298 K) of $[Ru(S_2COEt)_2(dppe)]$ (**2**)

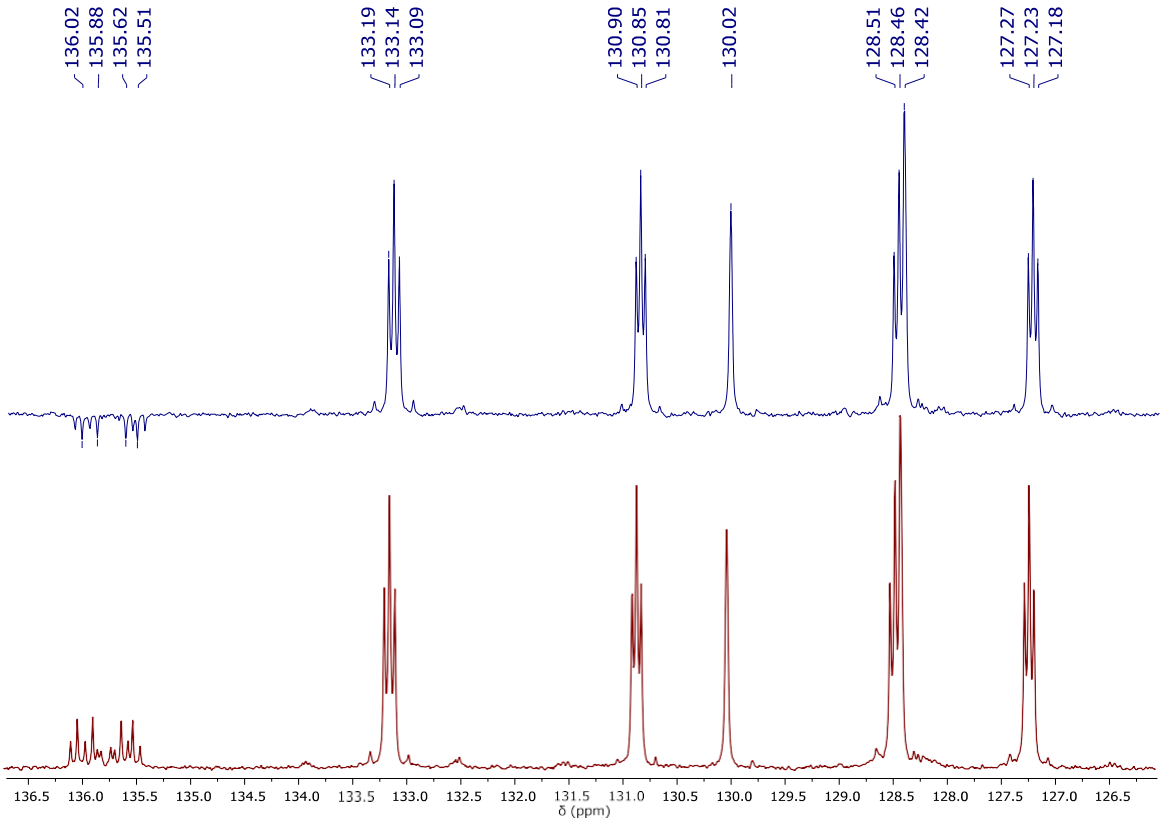

Fig. S11. ^{13}C CPD and APT NMR spectra (101 MHz, $CDCl_3$, 298 K) of $[Ru(S_2COEt)_2(dppe)]$ (**2**)

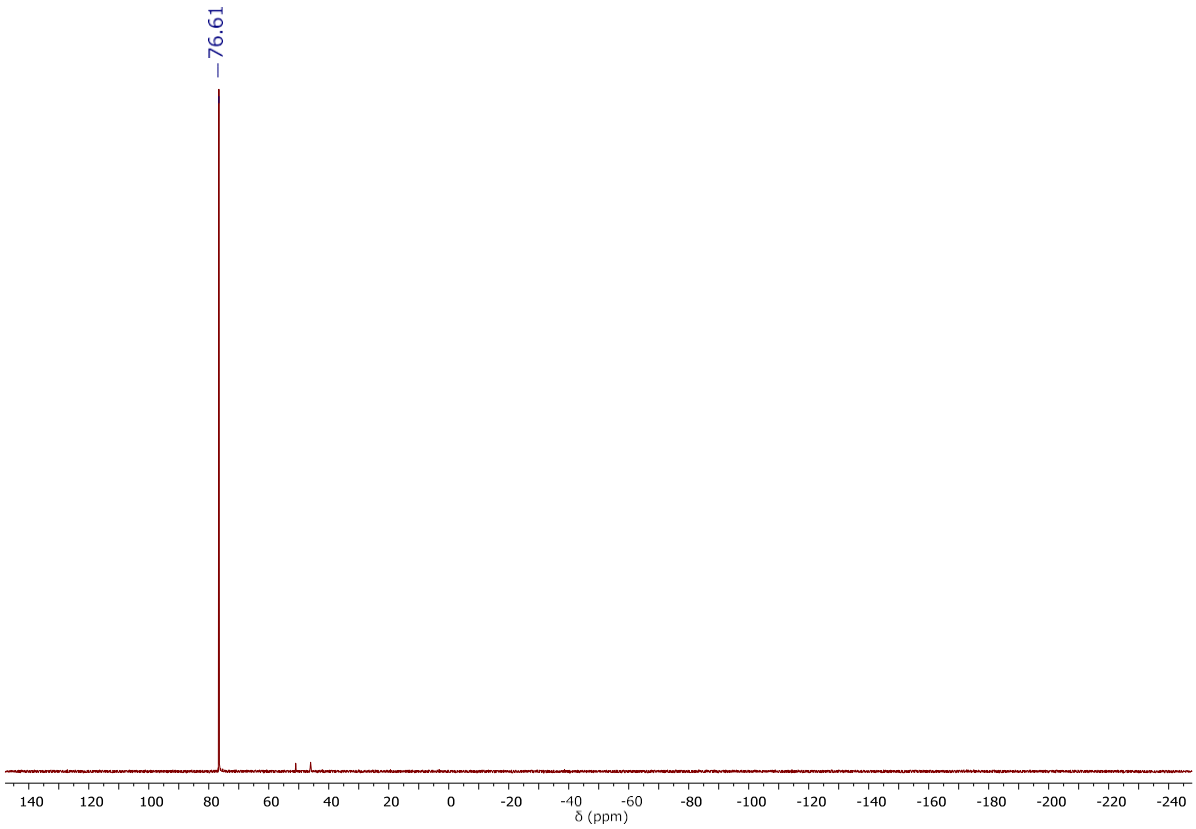

Fig. S12. ^{31}P NMR spectrum (162 MHz, $CDCl_3$, 298 K) of [Ru($S_2COEt)_2$(dppe)] (**2**)

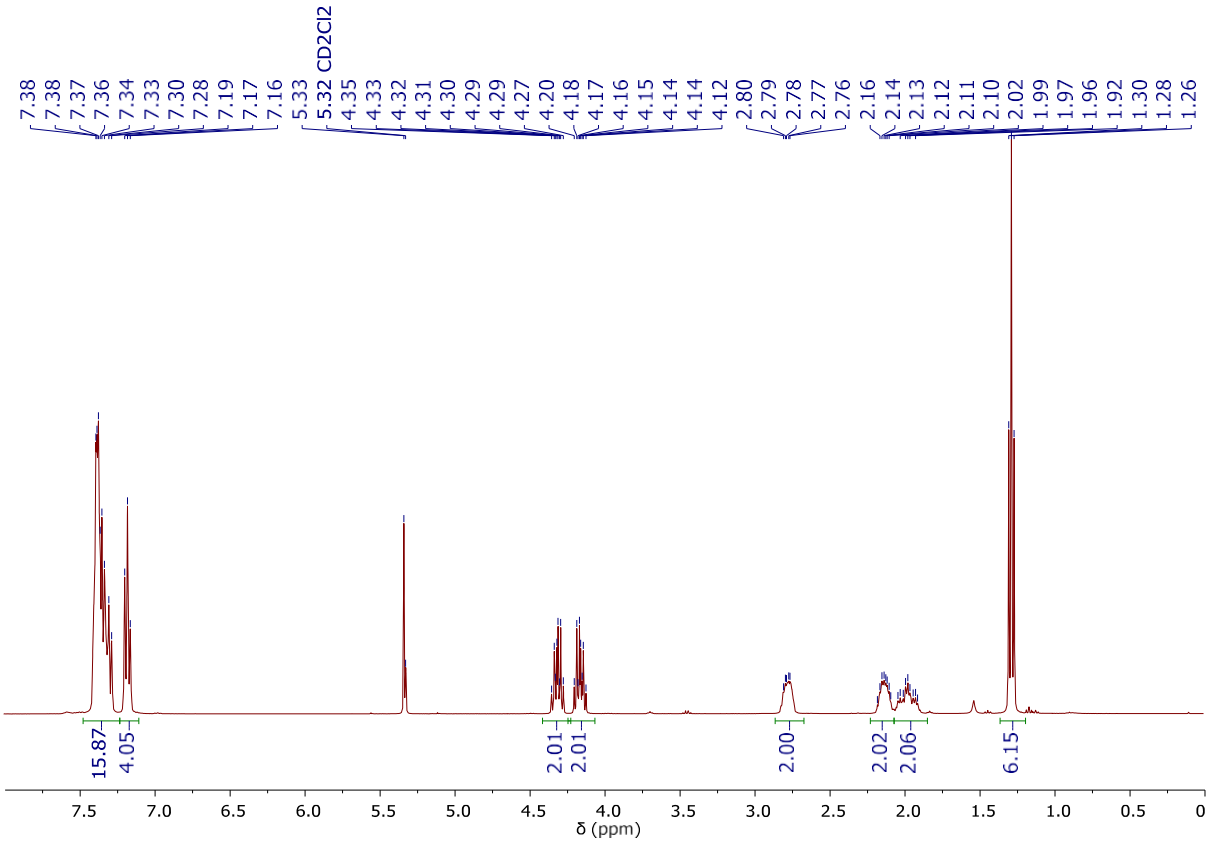

Fig. S13. ^{1}H NMR spectrum (400 MHz, CD_2Cl_2, 298 K) of [Ru($S_2COEt)_2$(dppp)] (**3**)

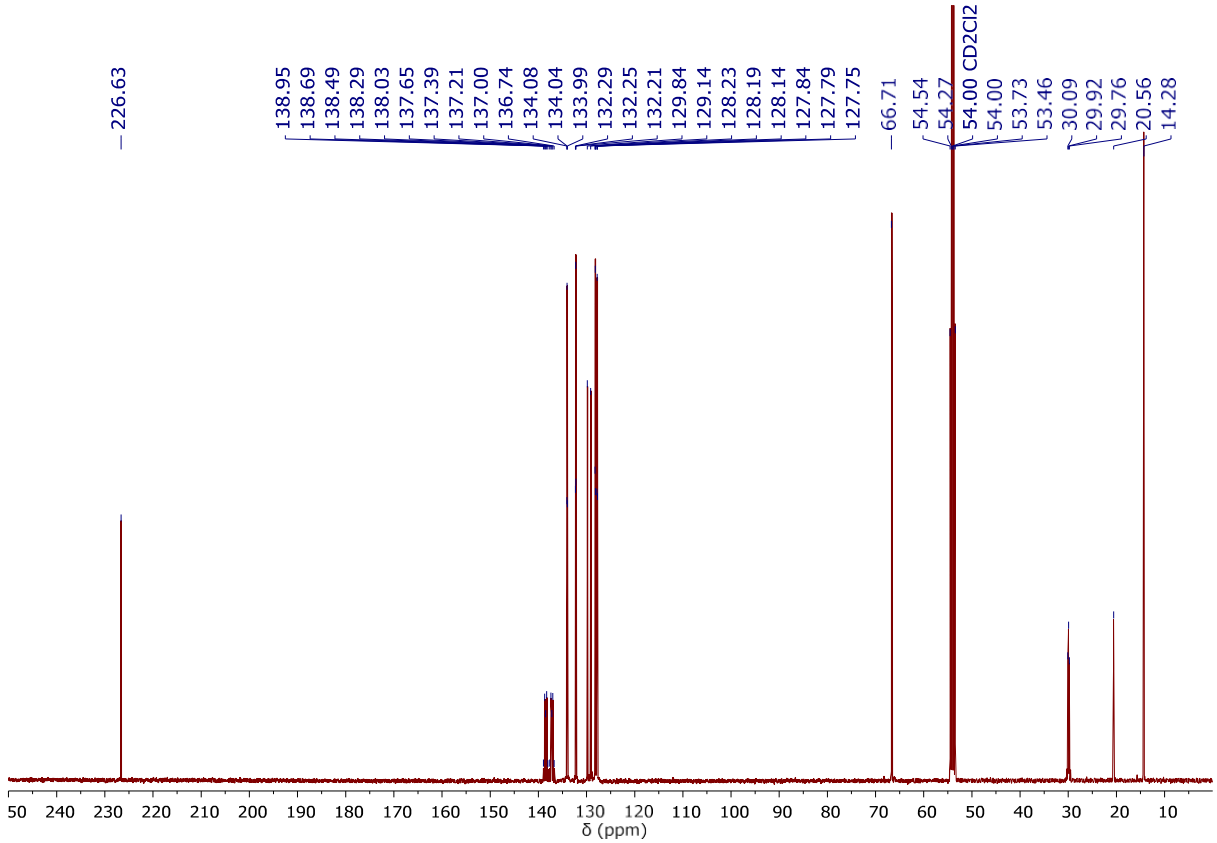

Fig. S14. $^{13}C\{^{1}H\}$ NMR spectrum (101 MHz, CD_2Cl_2, 298 K) of $[Ru(S_2COEt)_2(dppp)]$ (**3**)

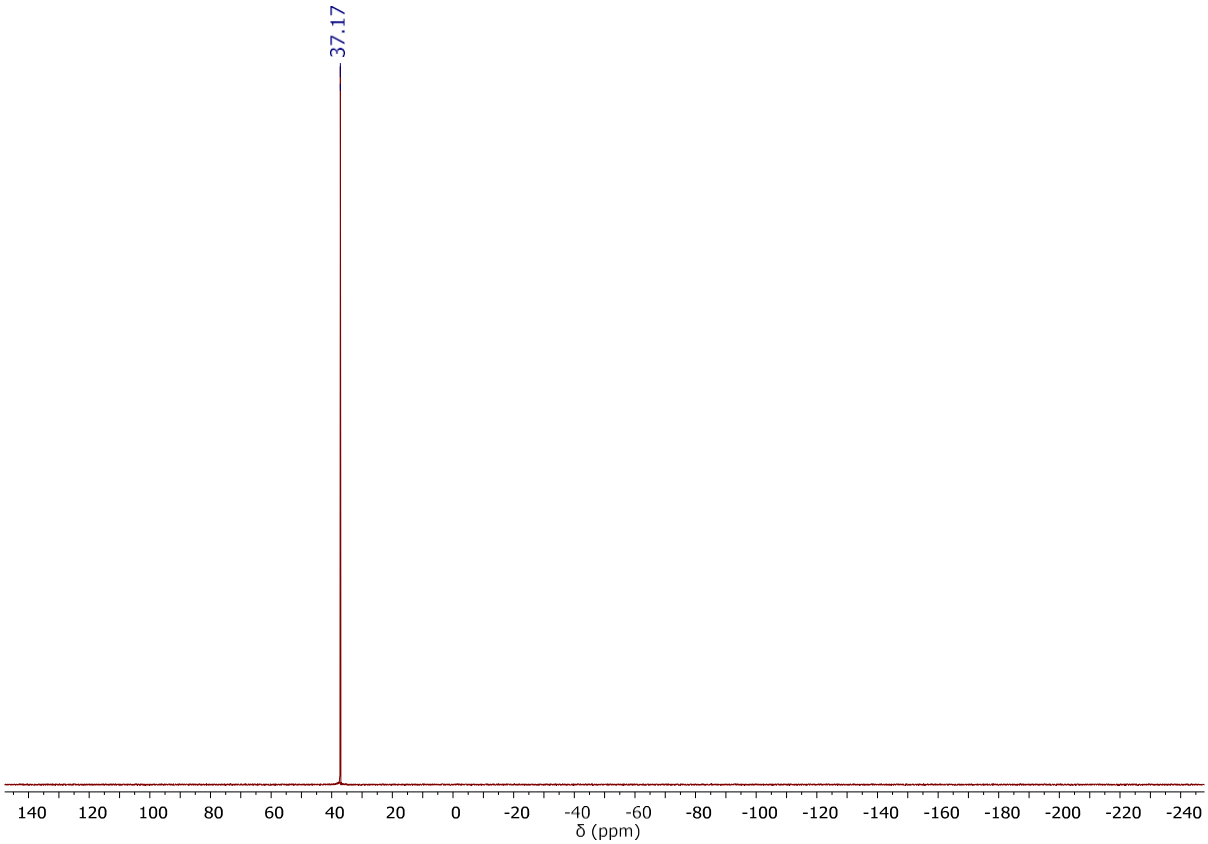

Fig. S15. ^{31}P NMR spectrum (162 MHz, CD_2Cl_2, 298 K) of $[Ru(S_2COEt)_2(dppp)]$ (**3**)

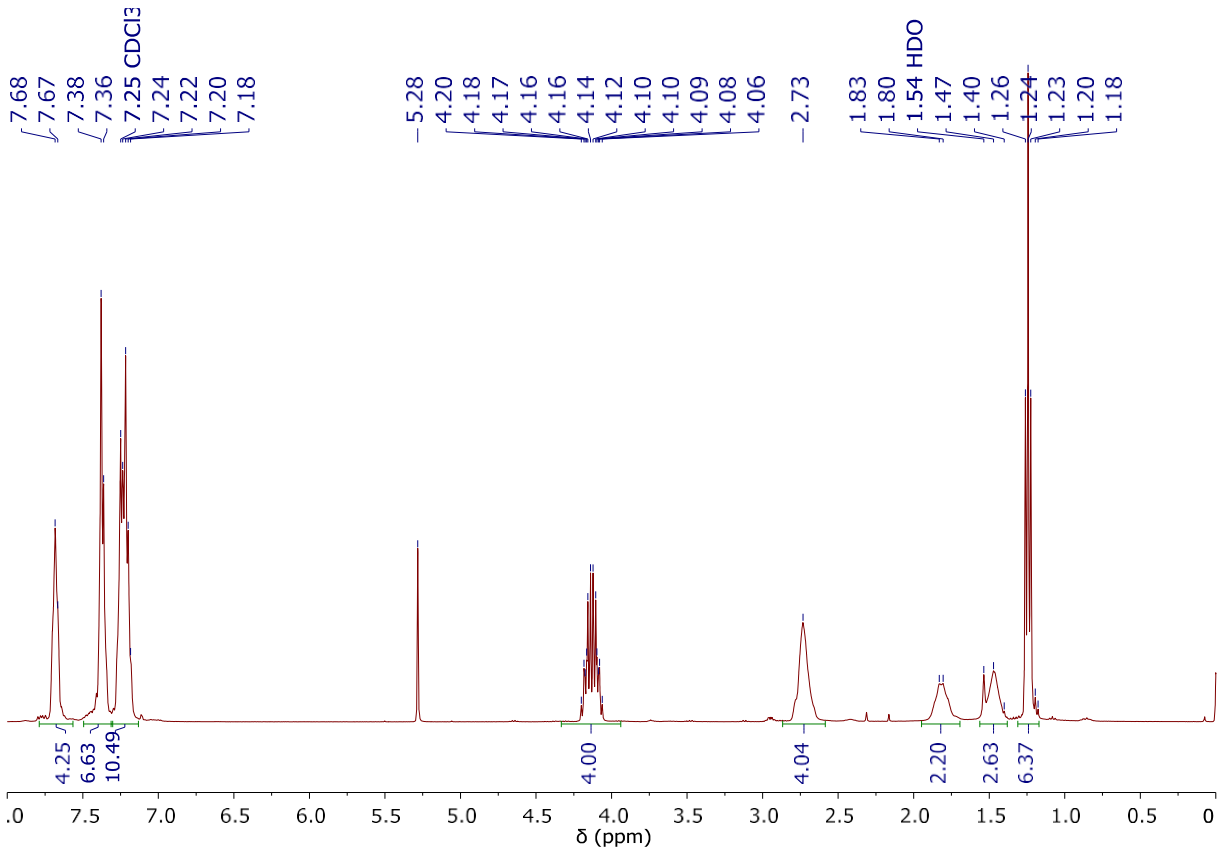

Fig. S16. ^{1}H NMR spectrum (400 MHz, $CDCl_3$, 298 K) of [Ru($S_2COEt)_2$(dppb)] (**4**)

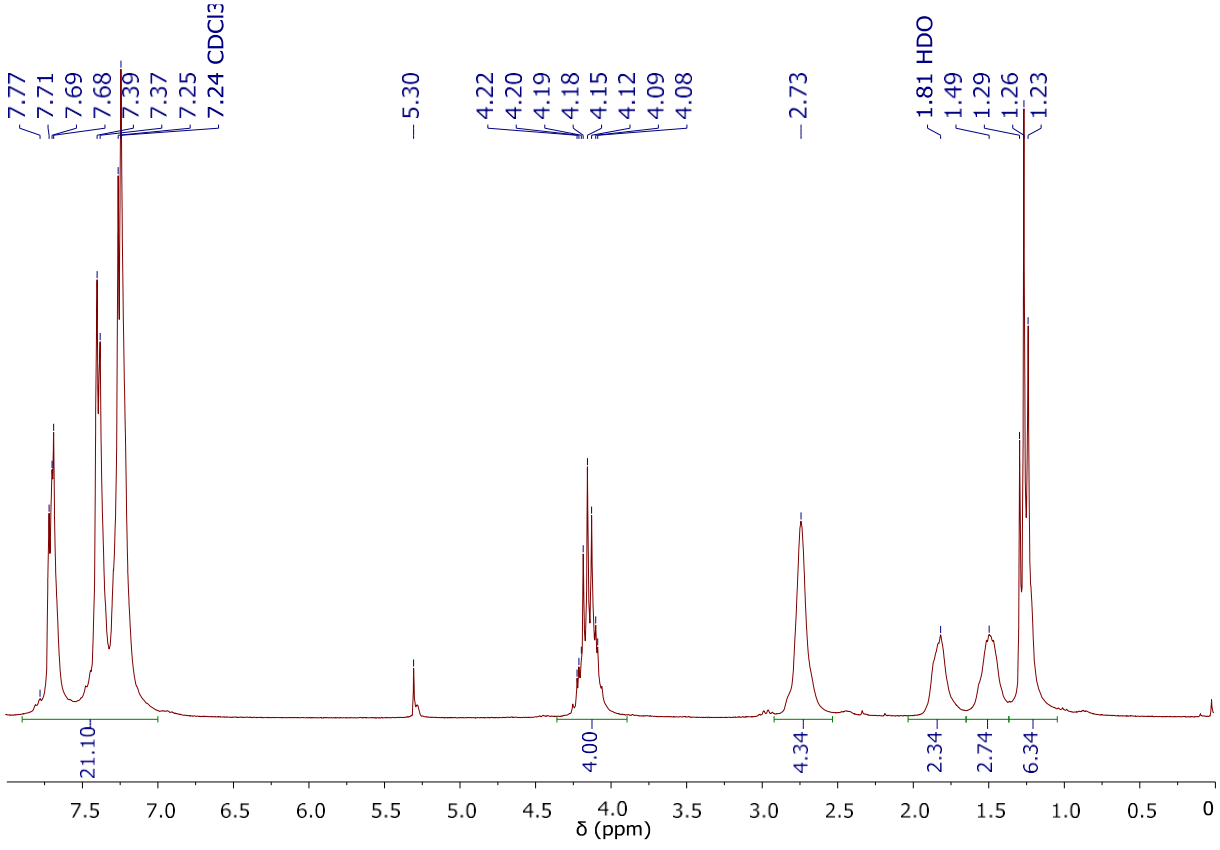

Fig. S17. $^{1}H\{^{31}P\}$ NMR spectrum (250 MHz, $CDCl_3$, 298 K) of [Ru($S_2COEt)_2$(dppb)] (**4**)

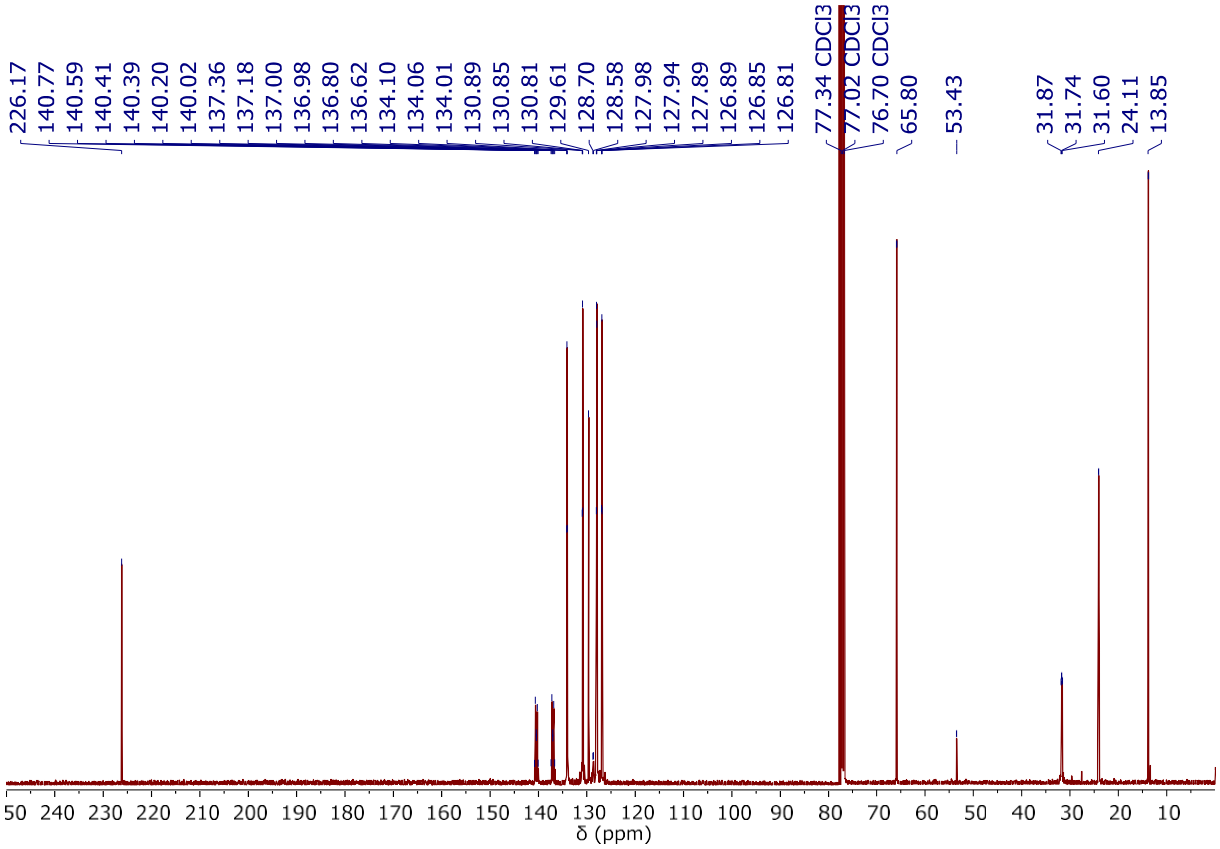

Fig. S18. $^{13}C\{^{1}H\}$ NMR spectrum (101 MHz, $CDCl_3$, 298 K) of $[Ru(S_2COEt)_2(dppb)]$ (**4**)

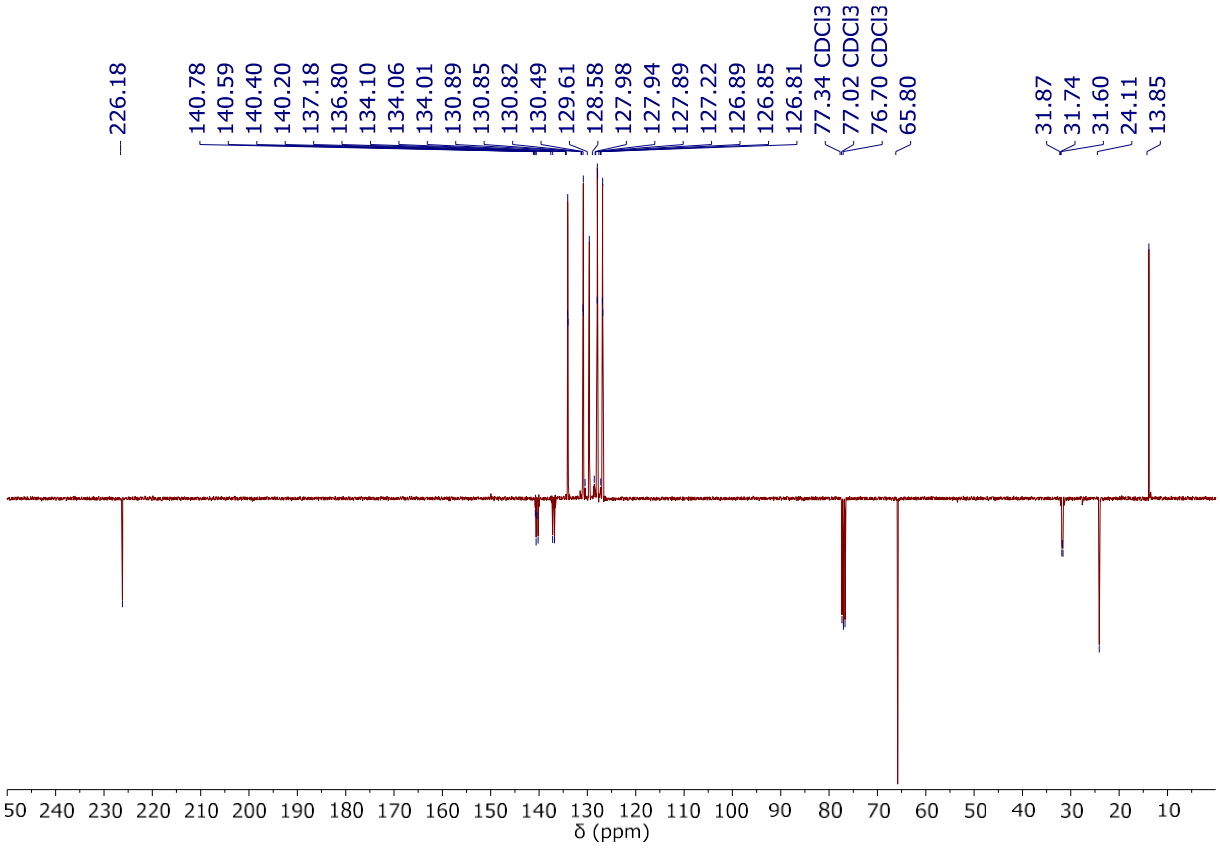

Fig. S19. $^{13}C\{^{1}H\}$ APT NMR spectrum (101 MHz, $CDCl_3$, 298 K) of $[Ru(S_2COEt)_2(dppb)]$ (**4**)

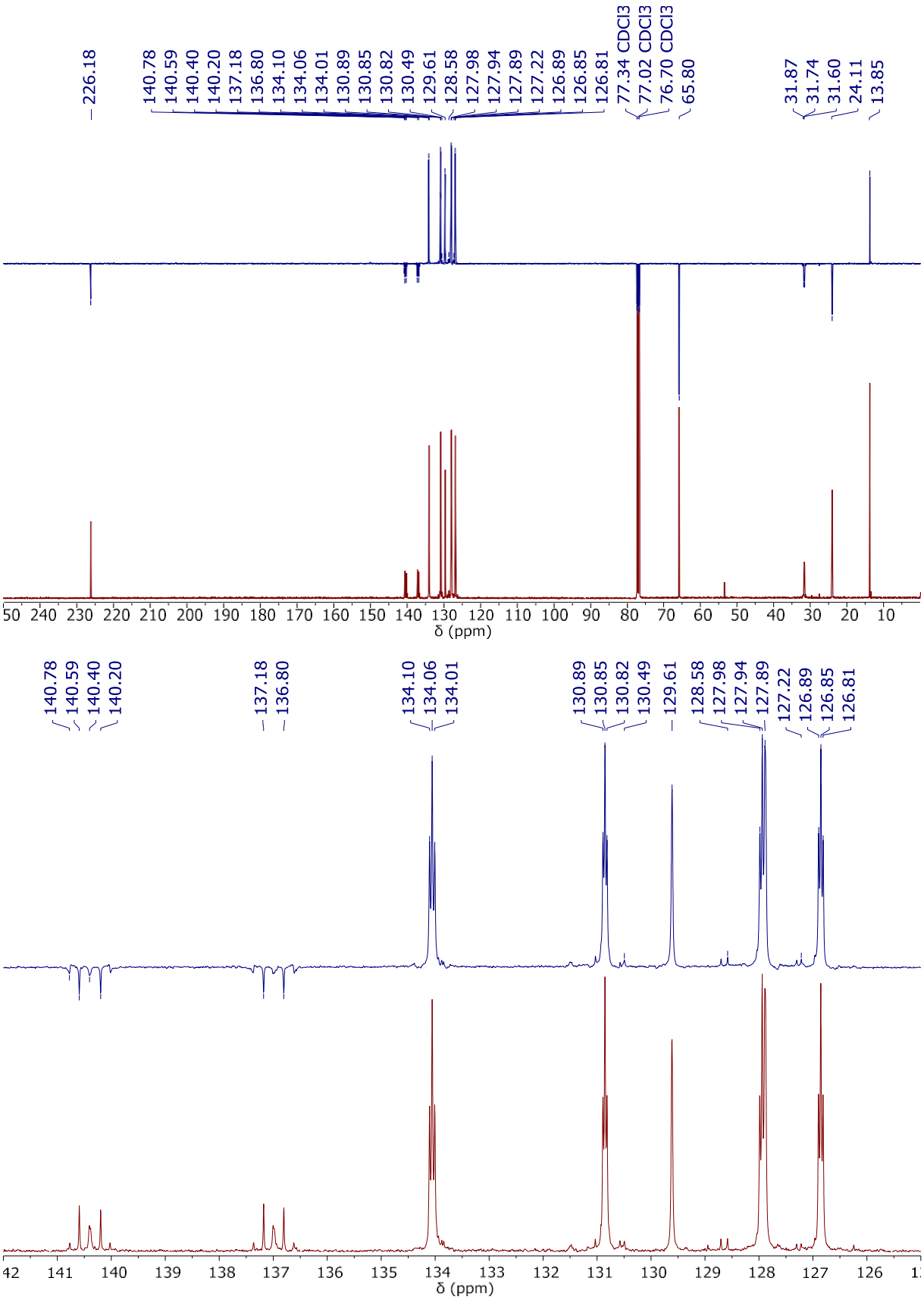

Fig. S20. ^{13}C CPD and APT NMR spectra (101 MHz, $CDCl_3$, 298 K) of [Ru($S_2COEt)_2$(dppb)] (**4**)

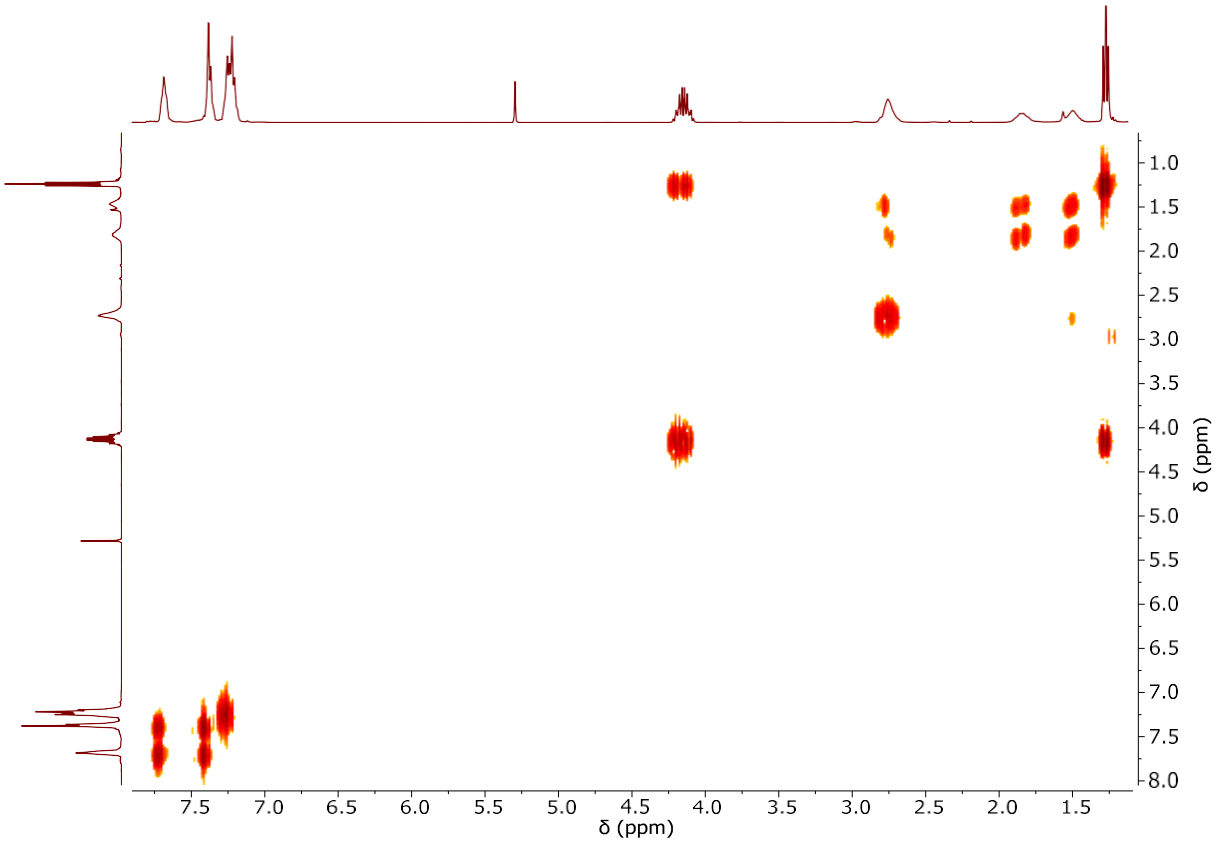

Fig. S21. COSY NMR spectrum (400 MHz, $CDCl_3$, 298 K) of [Ru($S_2COEt)_2$(dppb)] (**4**)

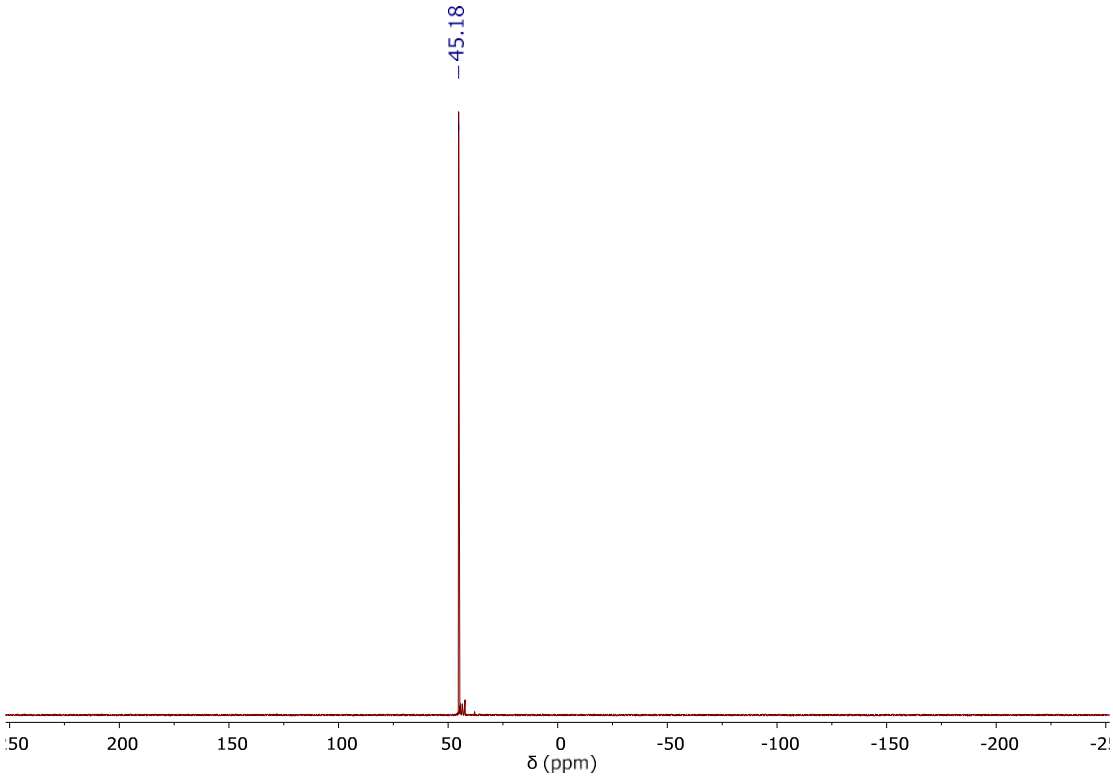

Fig. S22. ^{31}P NMR spectrum (162 MHz, $CDCl_3$, 298 K) of [Ru($S_2COEt)_2$(dppb)] (**4**)

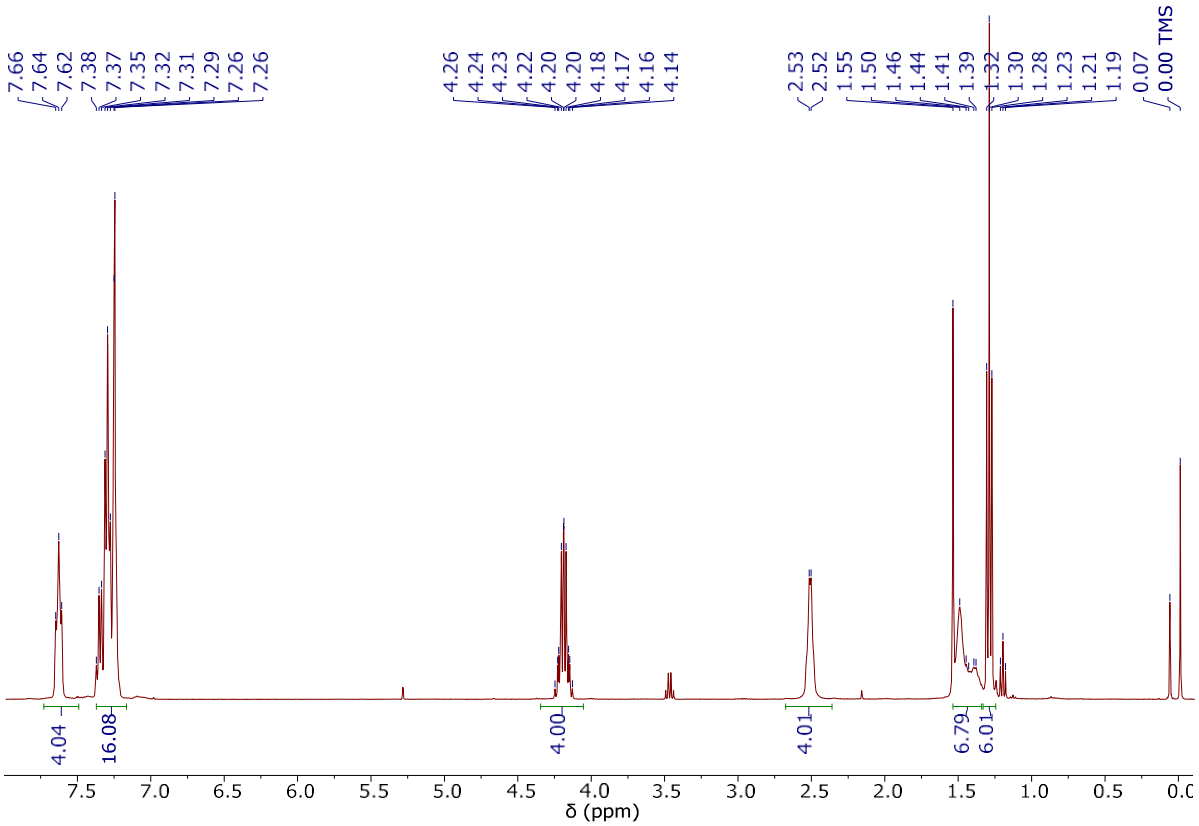

Fig. S23. ^{1}H NMR spectrum (400 MHz, $CDCl_3$, 298 K) of [Ru($S_2COEt)_2$(dpppe)] (**5**)

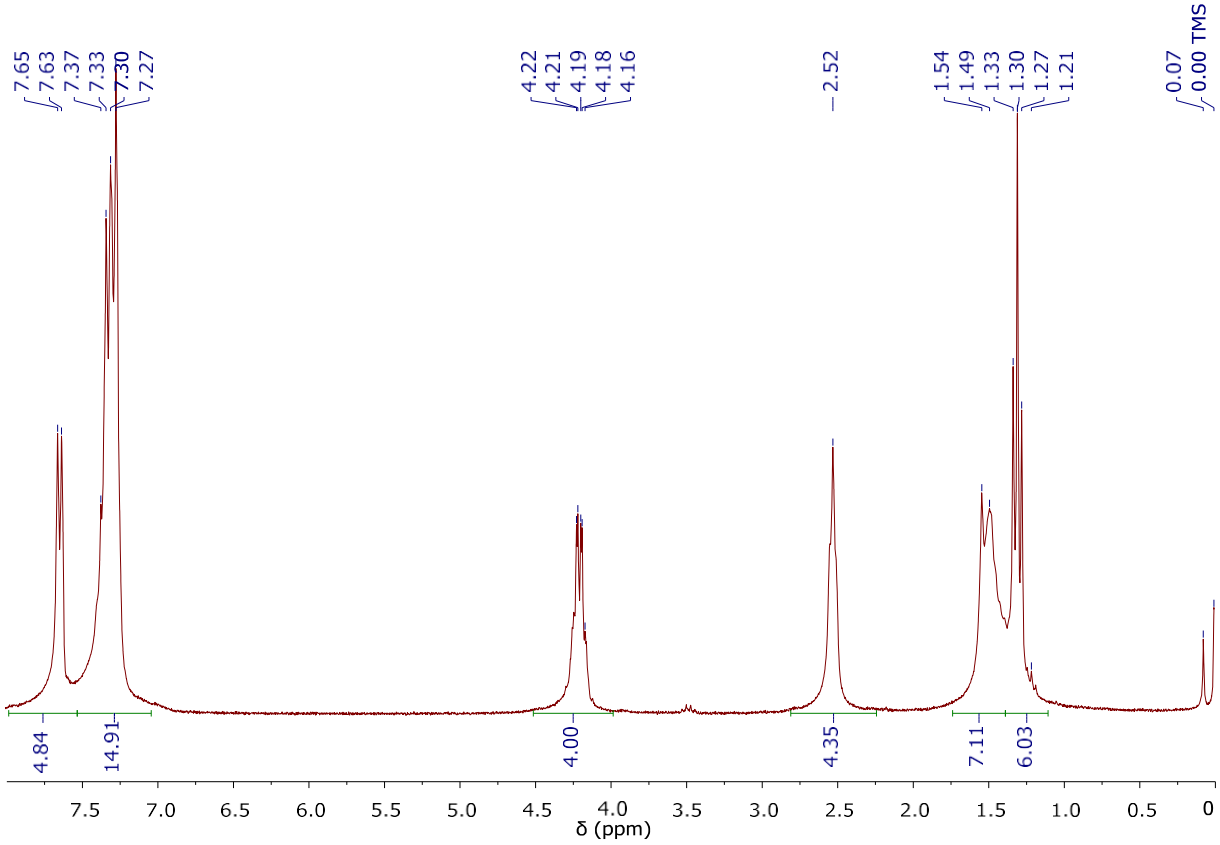

Fig. S24. $^{1}H\{^{31}P\}$ NMR spectrum (250 MHz, $CDCl_3$, 298 K) of [Ru($S_2COEt)_2$(dpppe)] (**5**)

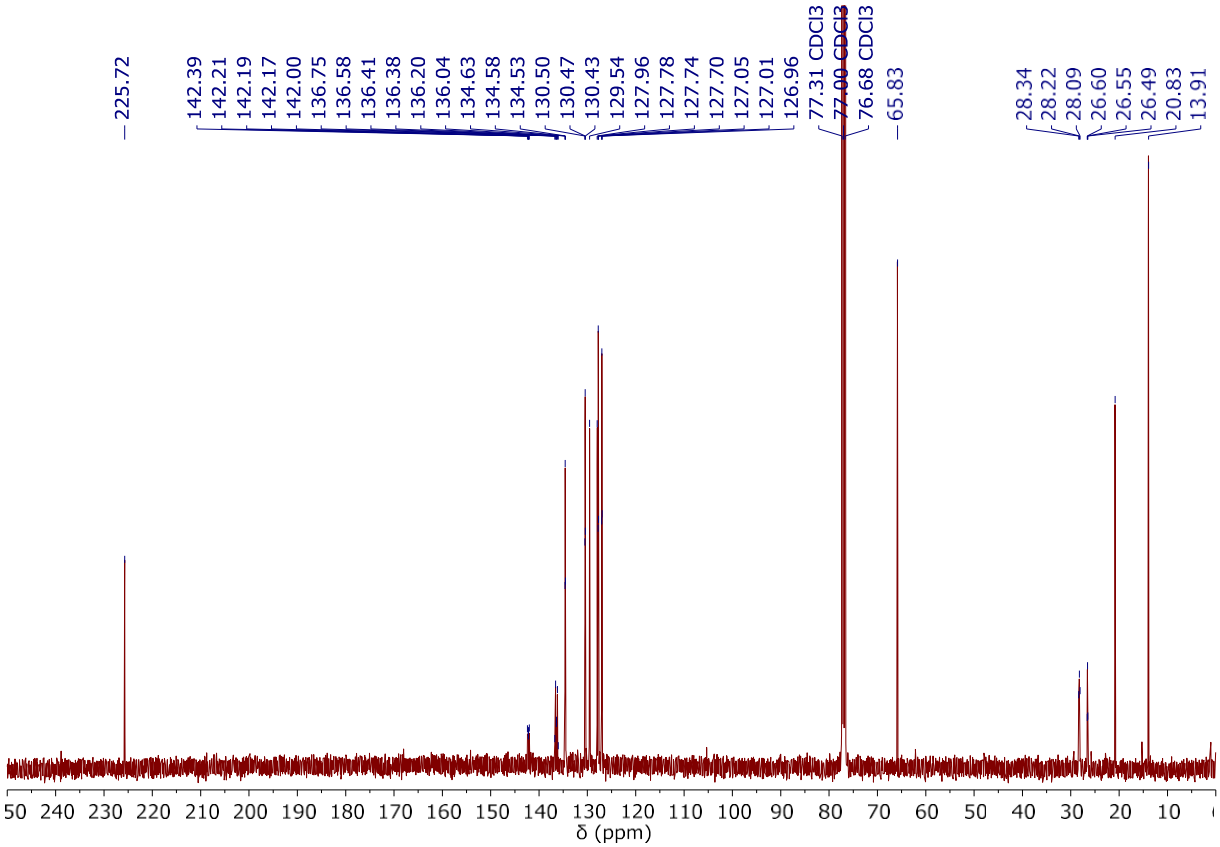

Fig. S25. $^{13}C\{^{1}H\}$ NMR spectrum (101 MHz, $CDCl_3$, 298 K) of $[Ru(S_2COEt)_2(dpppe)]$ (**5**)

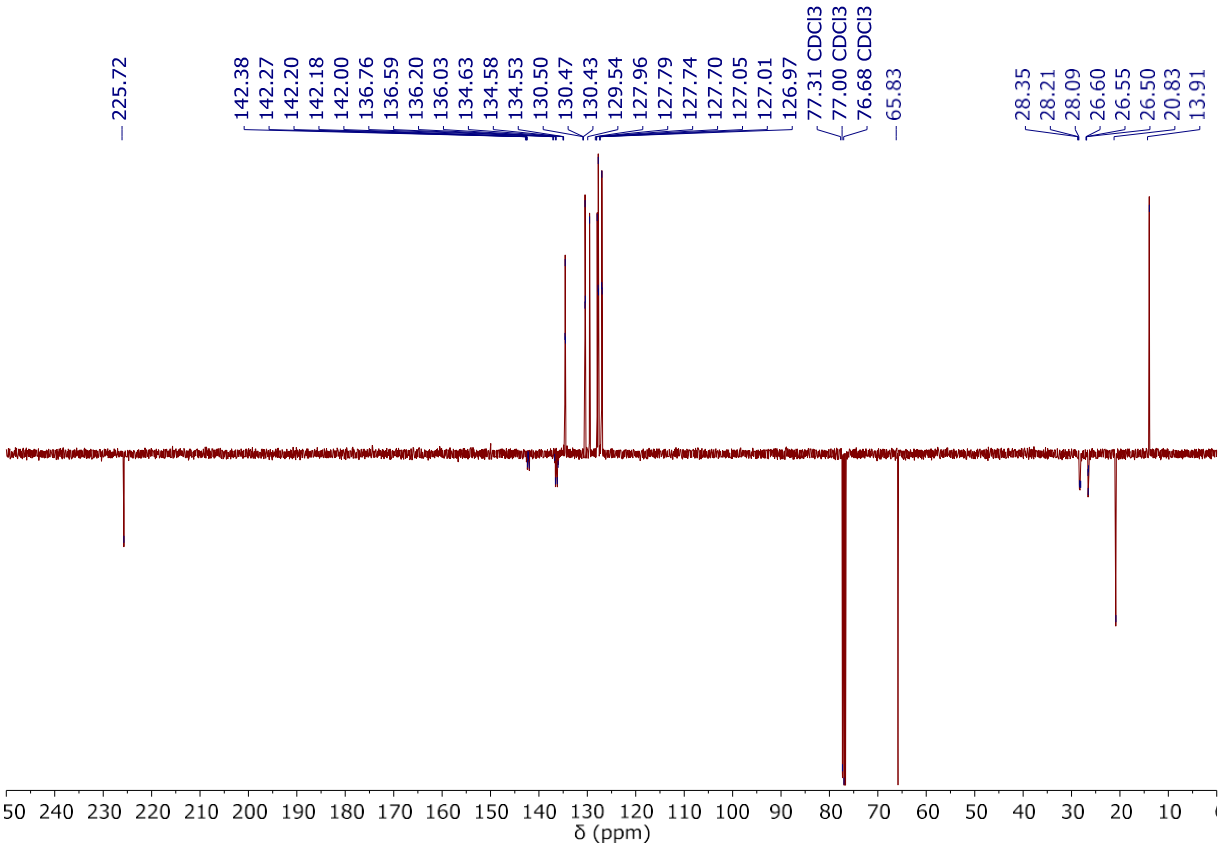

Fig. S26. $^{13}C\{^{1}H\}$ APT NMR spectrum (101 MHz, $CDCl_3$, 298 K) of $[Ru(S_2COEt)_2(dpppe)]$ (**5**)

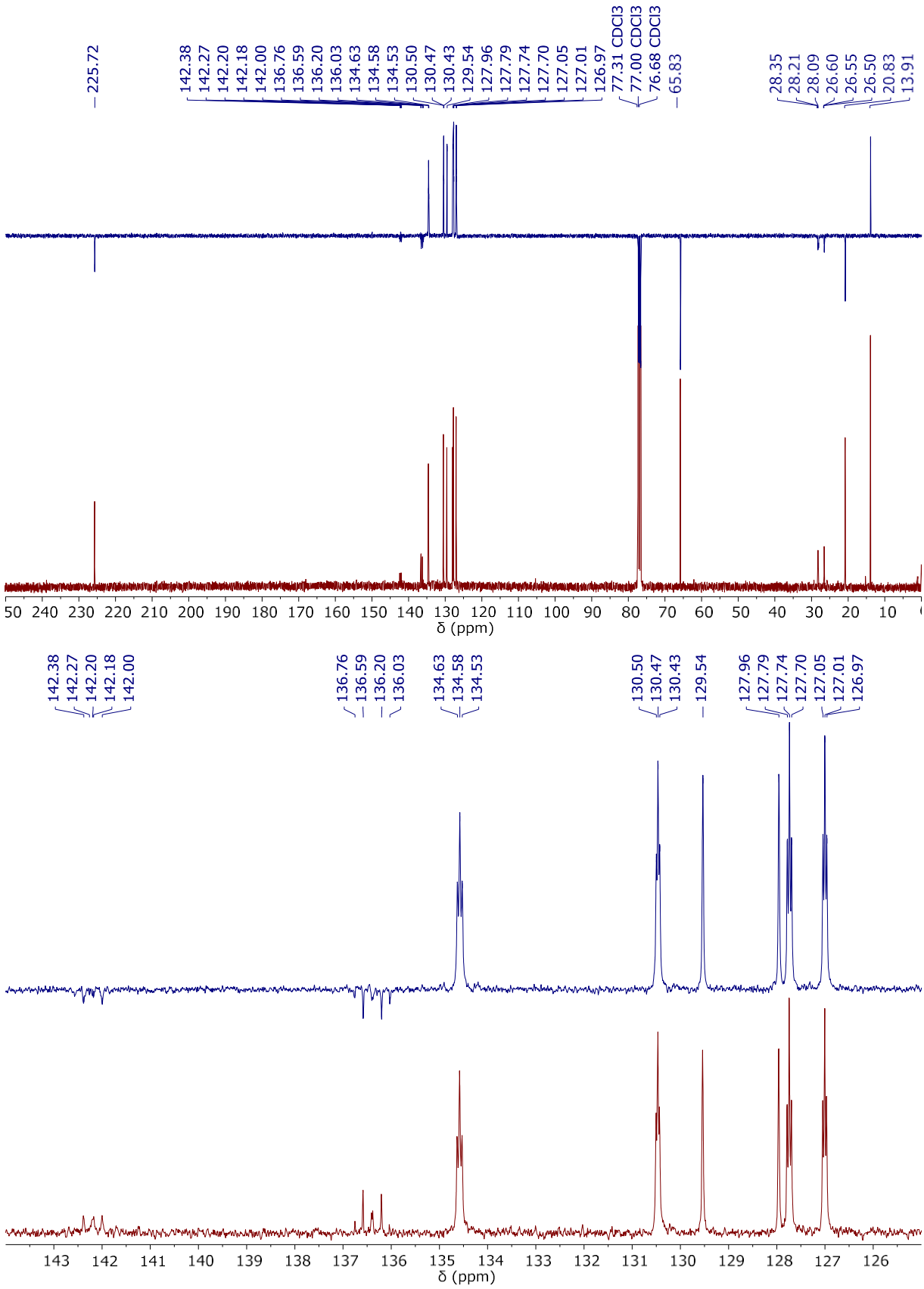

Fig. S27. ^{13}C CPD and APT NMR spectra (101 MHz, $CDCl_3$, 298 K) of [Ru($S_2COEt)_2$(dpppe)] (**5**)

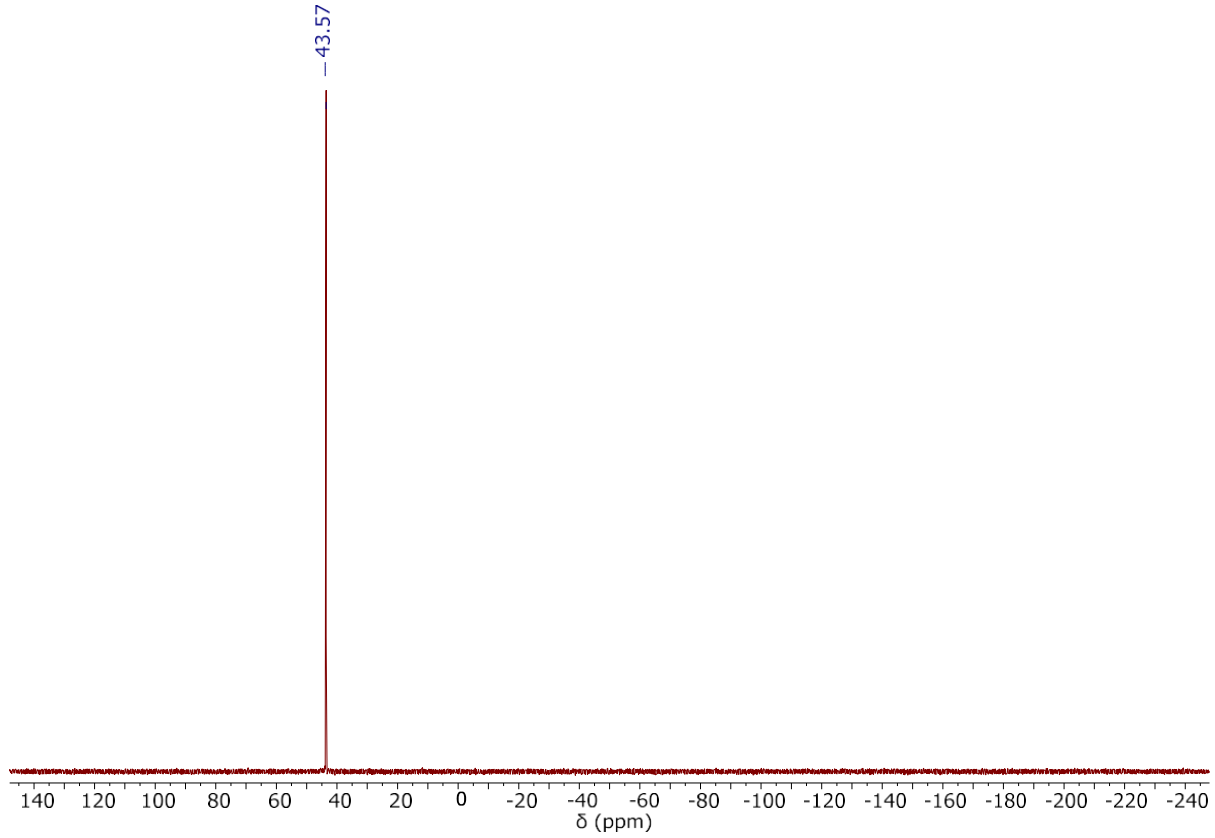

Fig. S28. ^{31}P NMR spectrum (162 MHz, $CDCl_3$, 298 K) of [Ru($S_2COEt)_2$(dpppe)] (**5**)

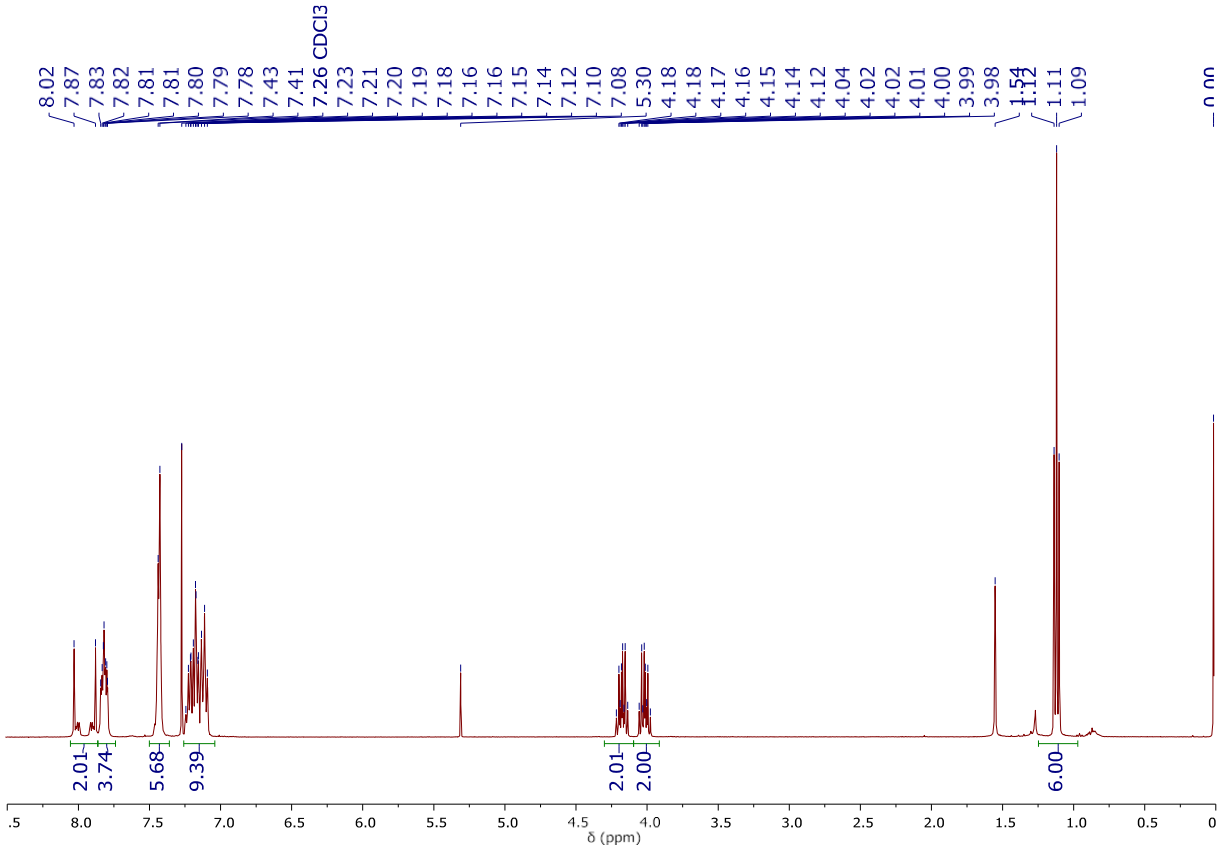

Fig. S29. ^{1}H NMR spectrum (400 MHz, $CDCl_3$, 298 K) of [Ru($S_2COEt)_2$(dppen)] (**6**)

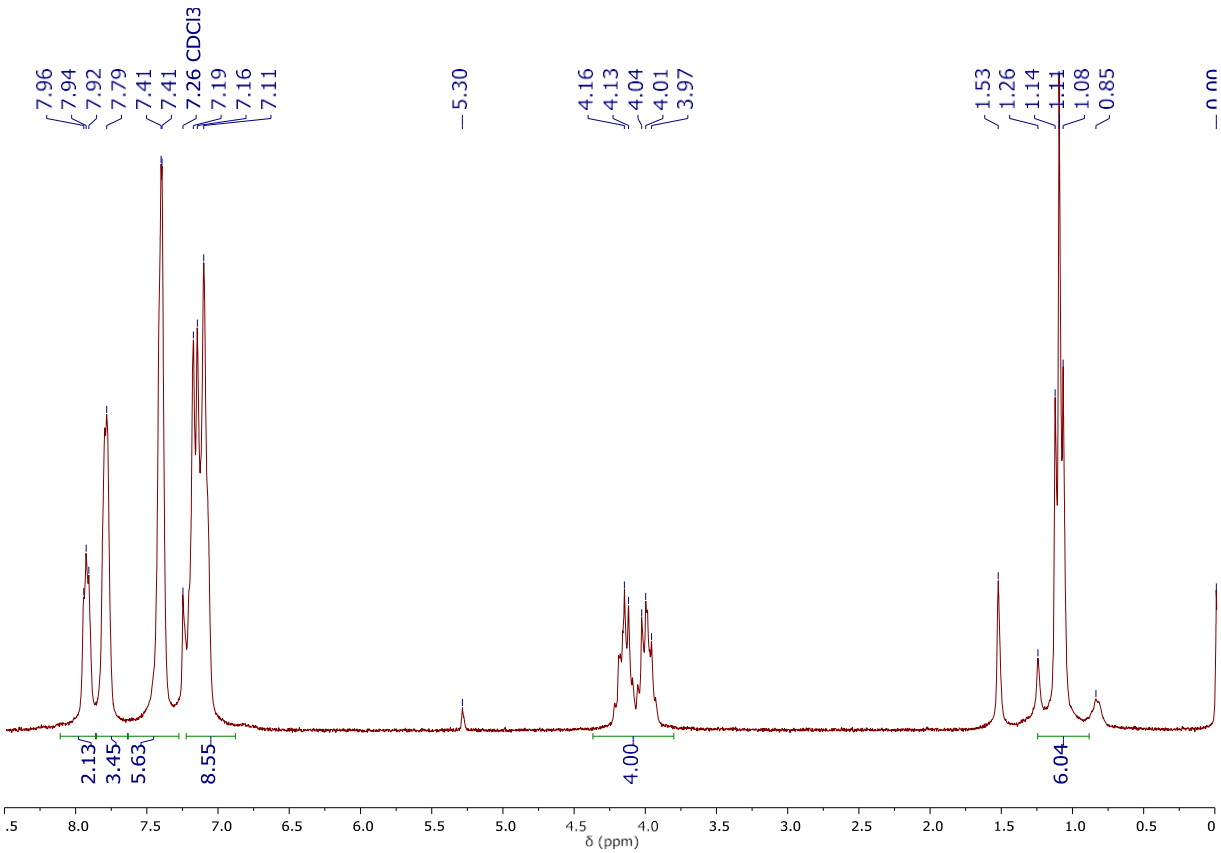

Fig. S30. $^{1}H\{^{31}P\}$ NMR spectrum (250 MHz, $CDCl_3$, 298 K) of $[Ru(S_2COEt)_2(dppen)]$ (**6**)

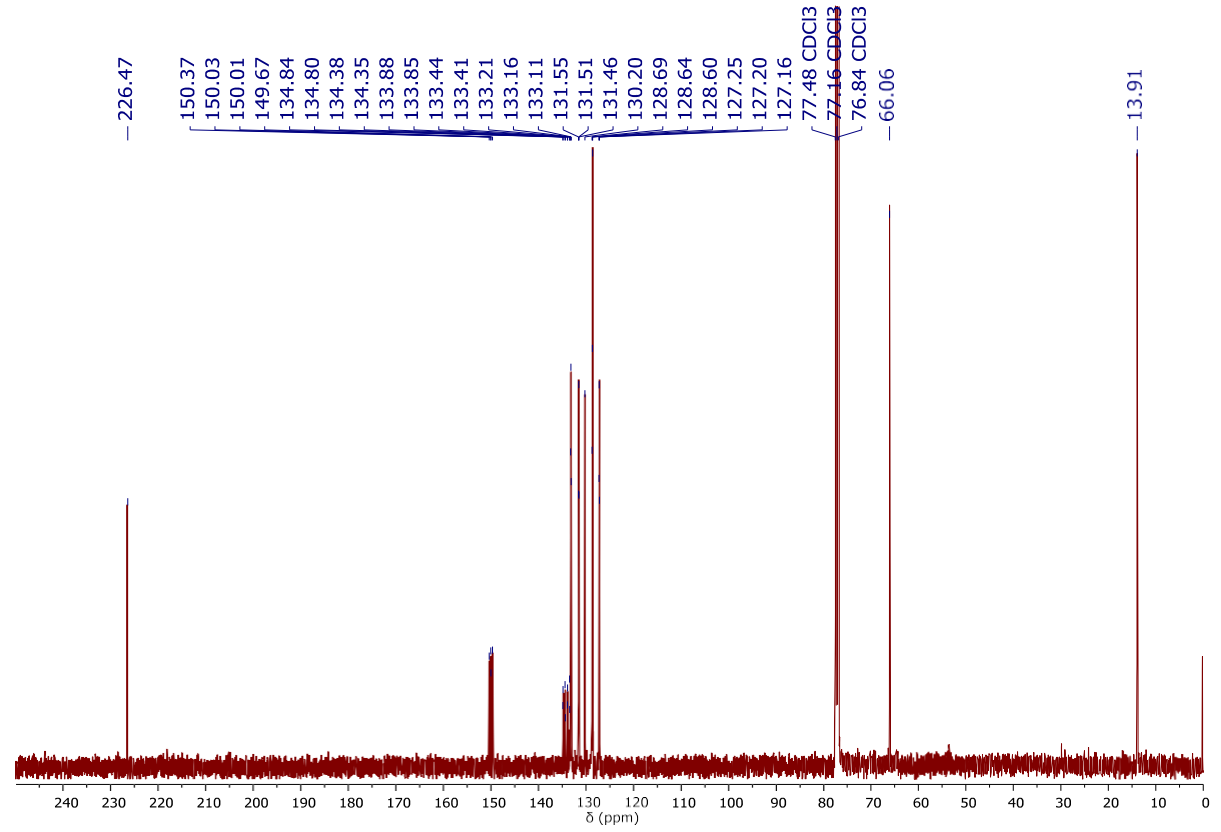

Fig. S31. $^{13}C\{^{1}H\}$ NMR spectrum (101 MHz, $CDCl_3$, 298 K) of $[Ru(S_2COEt)_2(dppen)]$ (**6**)

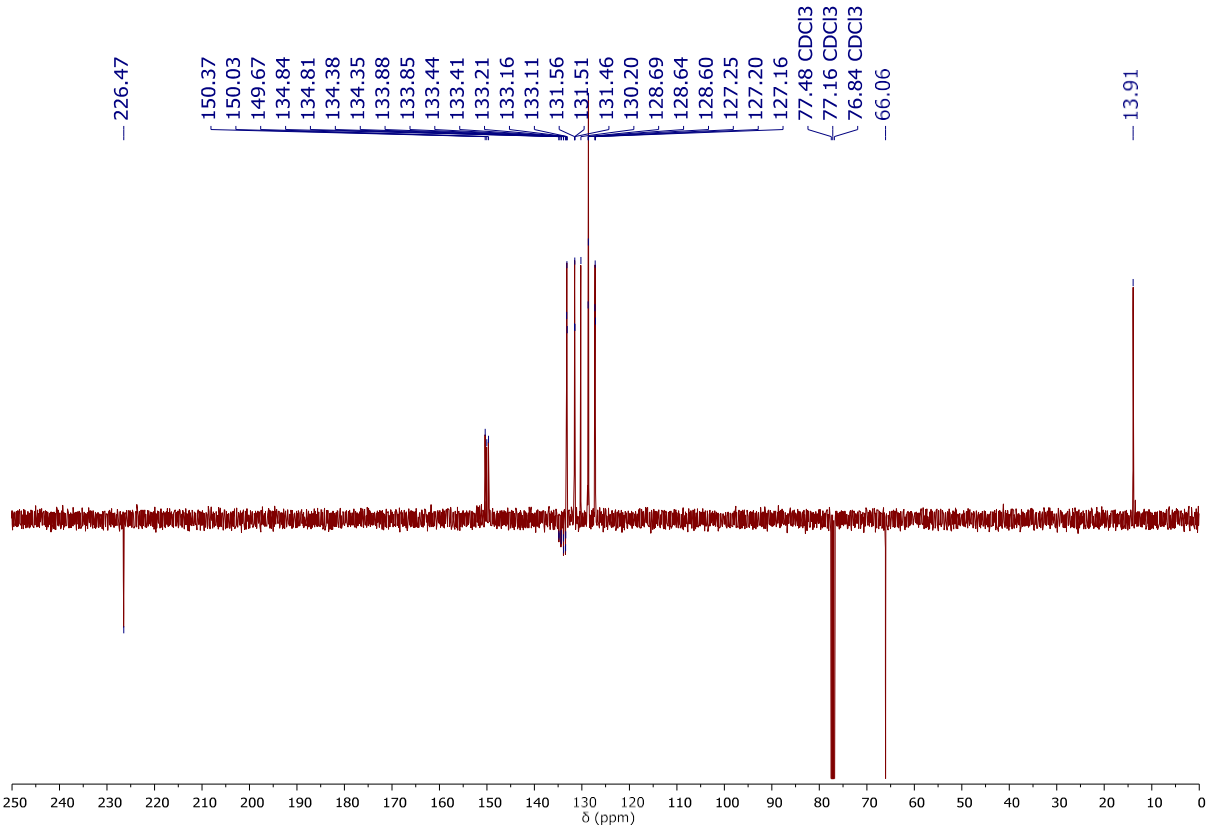

Fig. S32. $^{13}C\{^{1}H\}$ APT NMR spectrum (101 MHz, $CDCl_3$, 298 K) of [Ru($S_2COEt)_2$(dppen)] (**6**)

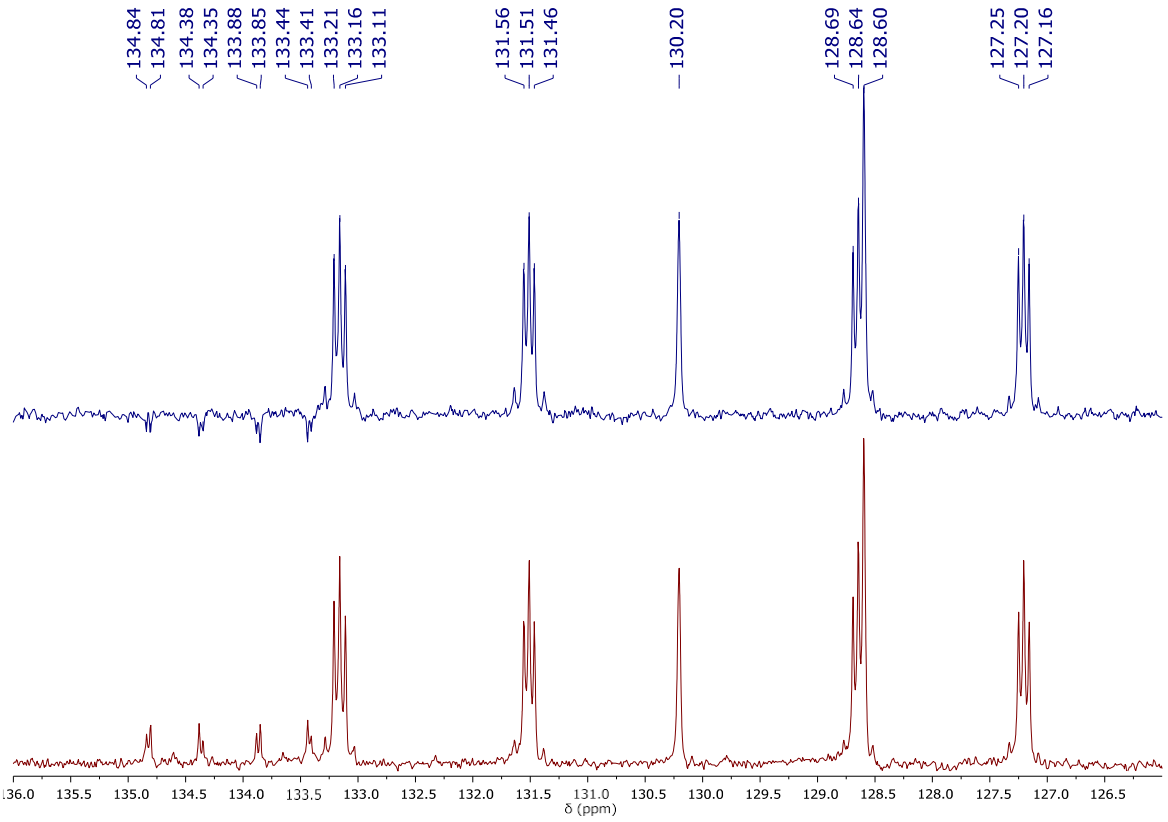

Fig. S33. ^{13}C CPD and APT NMR spectra (101 MHz, $CDCl_3$, 298 K) of [Ru($S_2COEt)_2$(dppen)] (**6**)

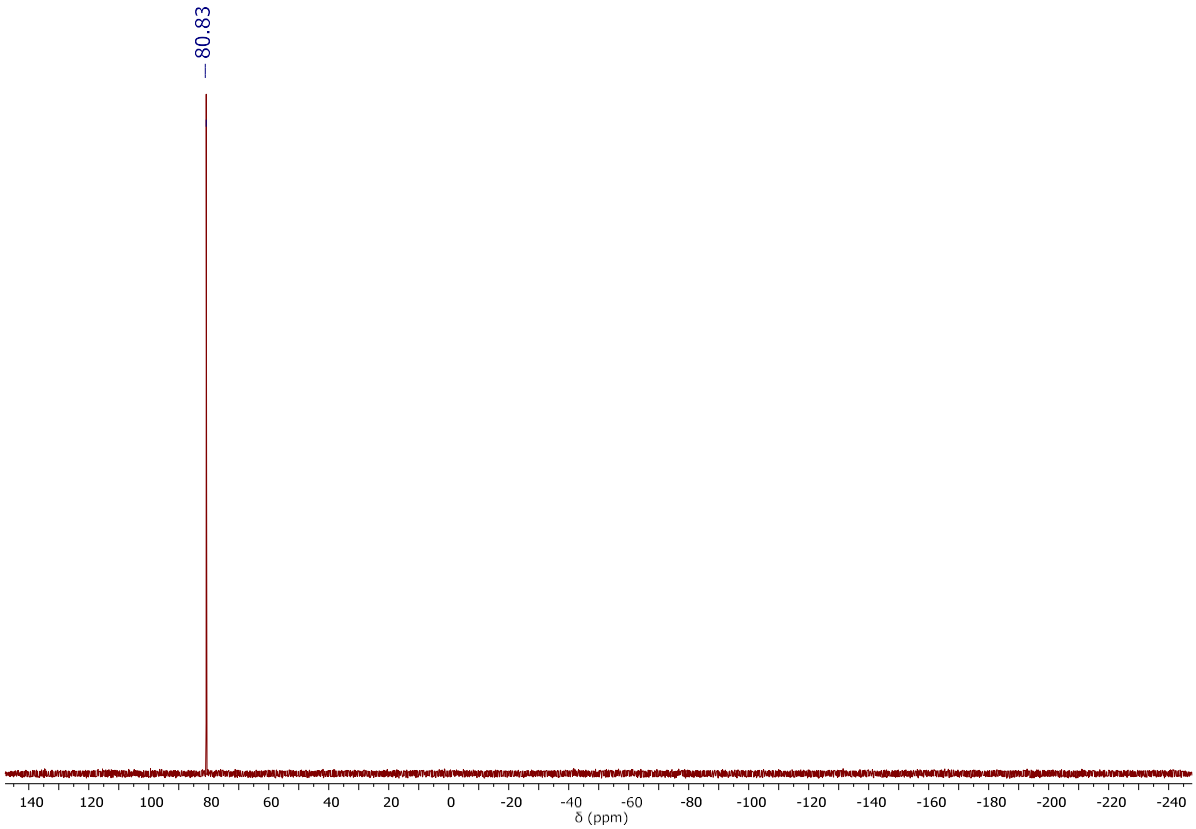

Fig. S34. ^{31}P NMR spectrum (162 MHz, $CDCl_3$, 298 K) of [Ru($S_2COEt)_2$(dppen)] (**6**)

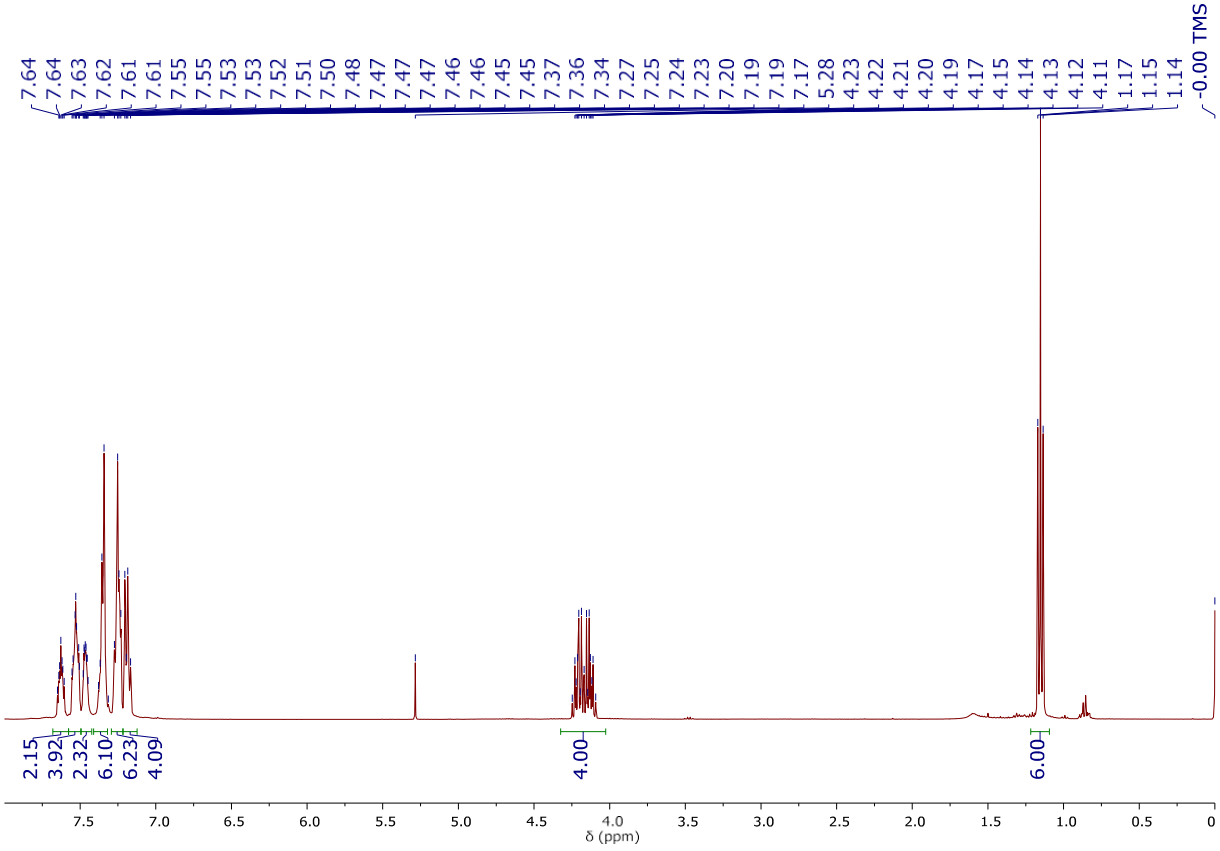

Fig. S35. ^{1}H NMR spectrum (400 MHz, $CDCl_3$, 298 K) of [Ru($S_2COEt)_2$(dppbz)] (**7**)

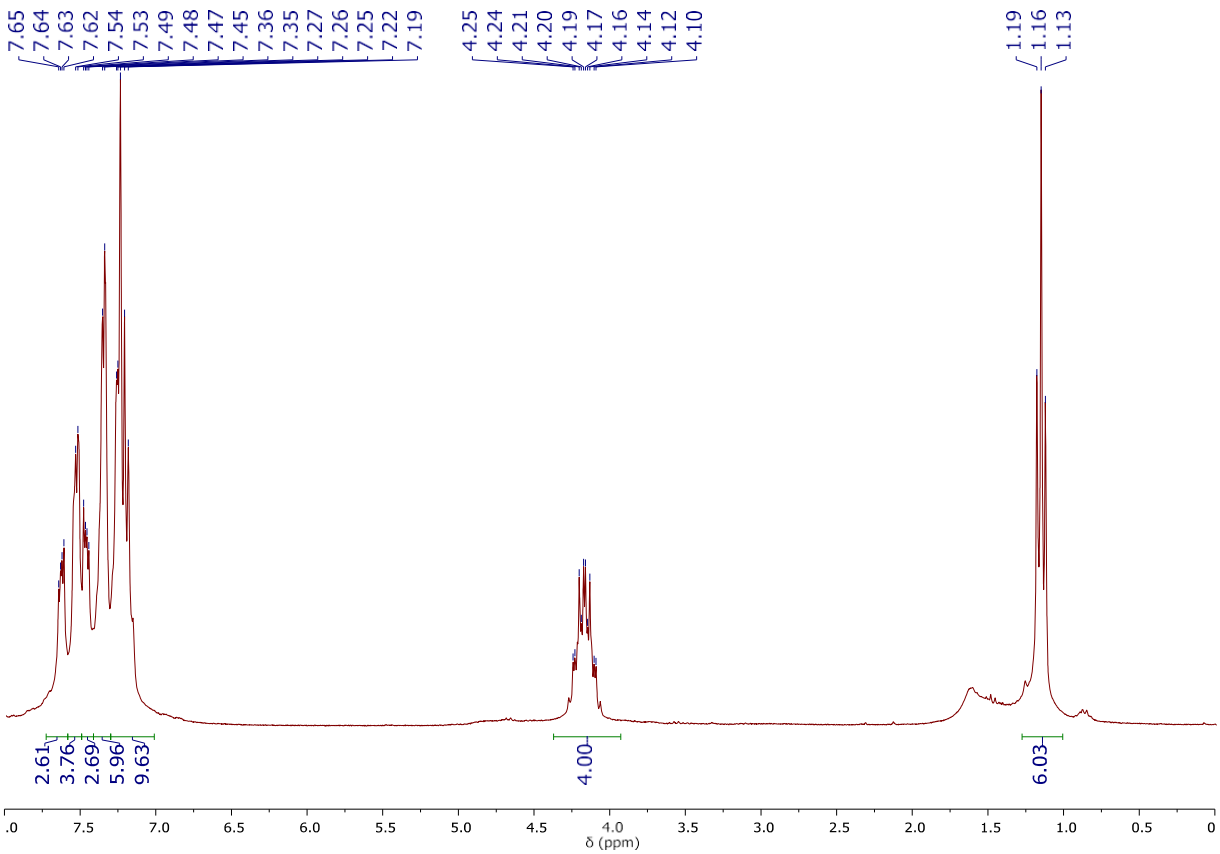

Fig. S36. $^{1}H\{^{31}P\}$ NMR spectrum (250 MHz, $CDCl_3$, 298 K) of $[Ru(S_2COEt)_2(dppbz)]$ (**7**)

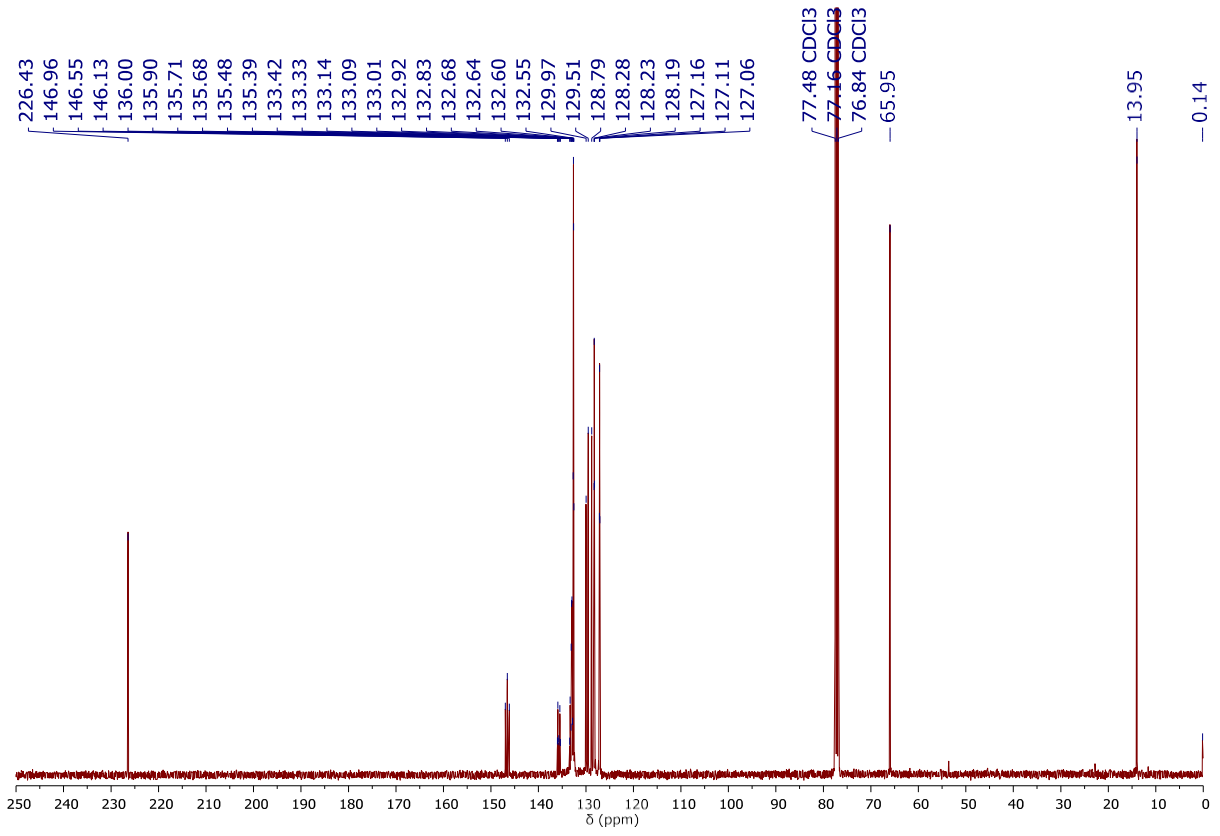

Fig. S37. $^{13}C\{^{1}H\}$ NMR spectrum (101 MHz, $CDCl_3$, 298 K) of $[Ru(S_2COEt)_2(dppbz)]$ (**7**)

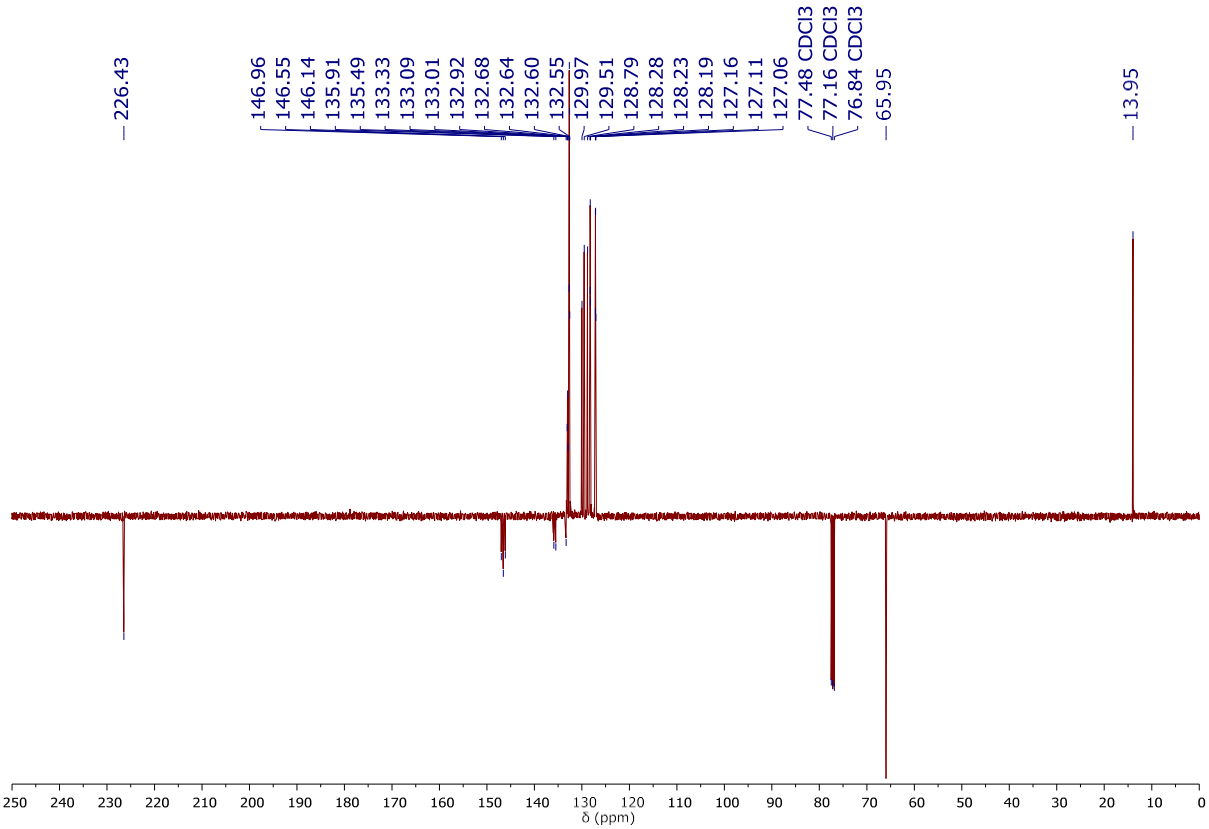

Fig. S38. $^{13}C\{^{1}H\}$ APT NMR spectrum (101 MHz, $CDCl_3$, 298 K) of $[Ru(S_2COEt)_2(dppbz)]$ (**7**)

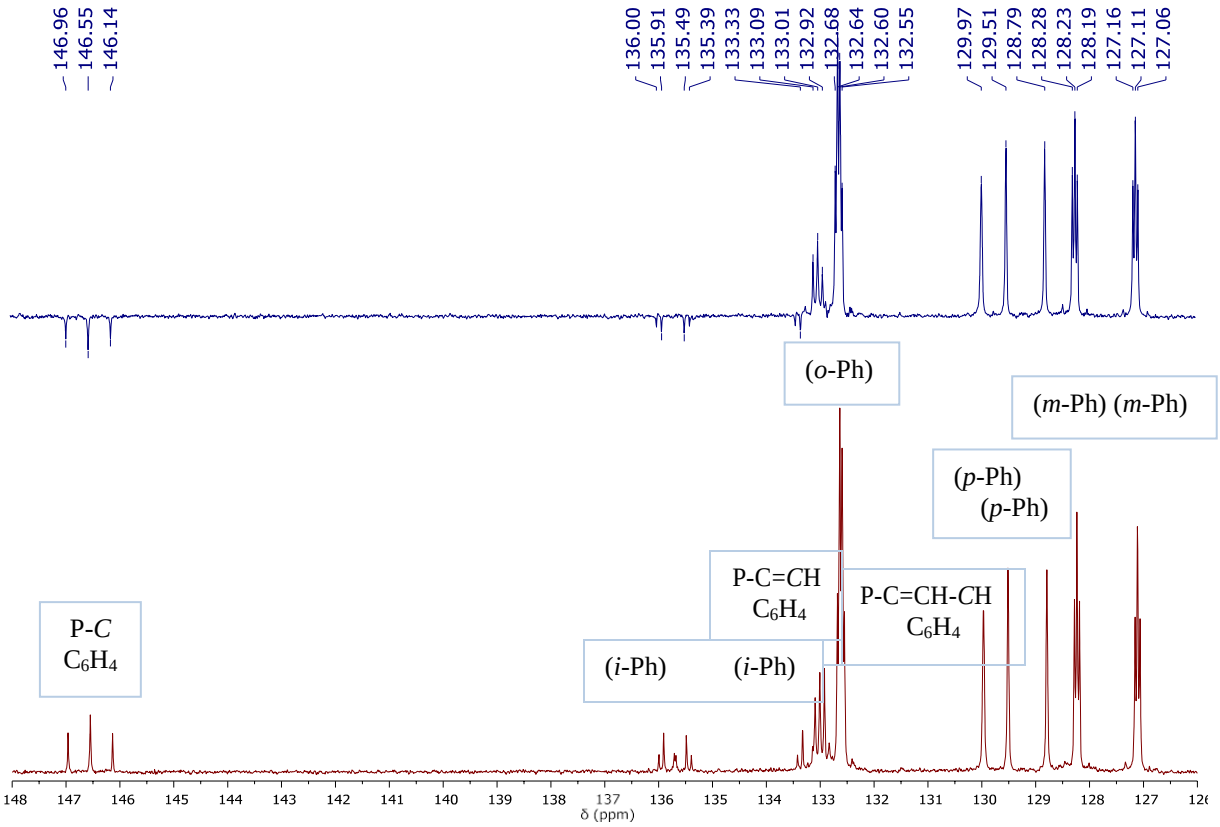

Fig. S39. ^{13}C CPD and APT NMR spectra (101 MHz, $CDCl_3$, 298 K) of $[Ru(S_2COEt)_2(dppbz)]$ (**7**)

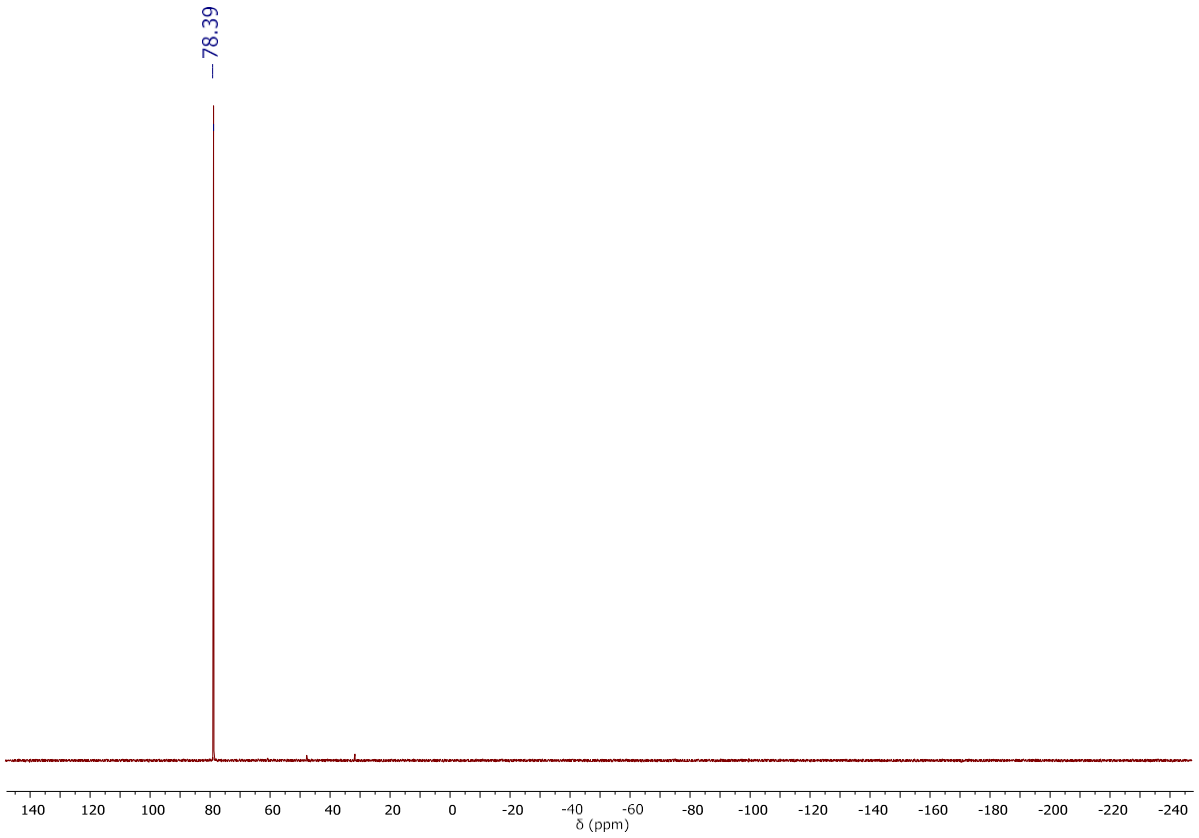

Fig. S40. ^{31}P NMR spectrum (162 MHz, $CDCl_3$, 298 K) of [Ru($S_2COEt)_2$(dppbz)] (**7**)

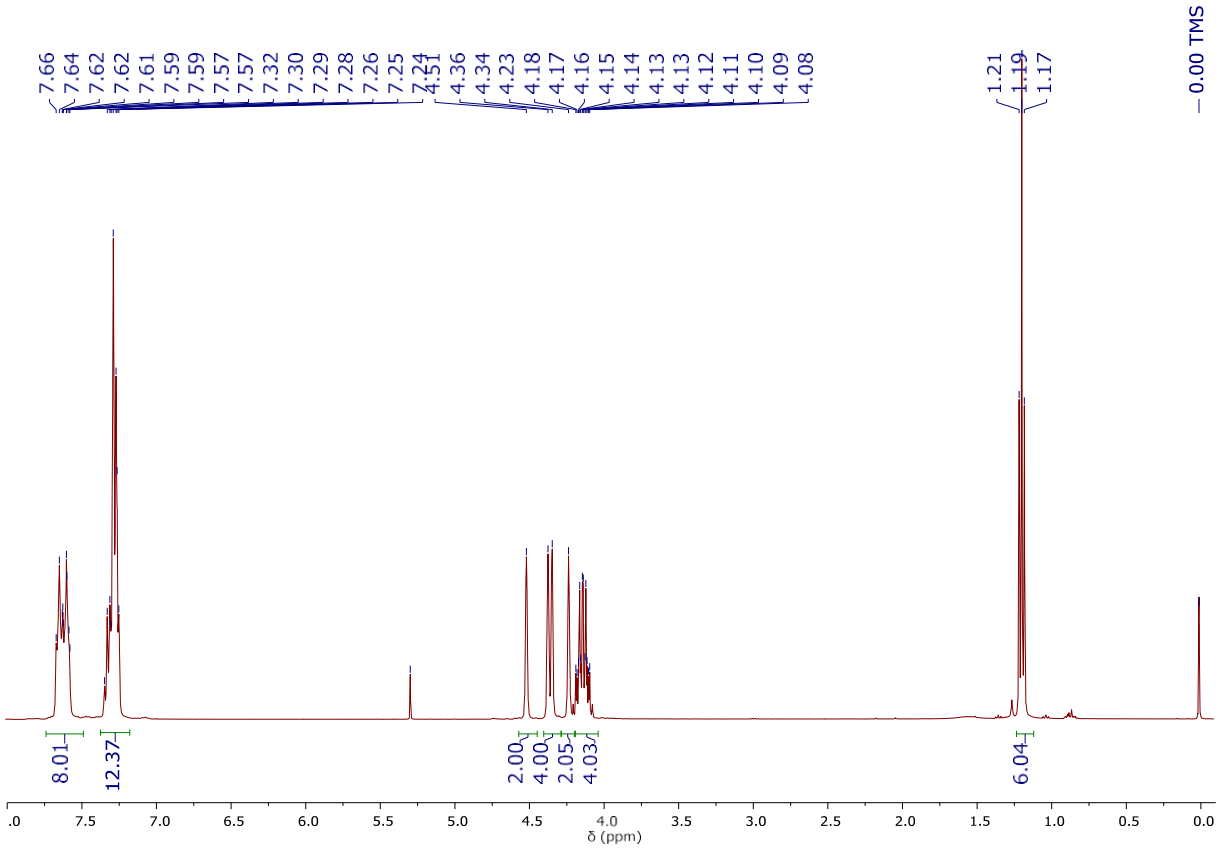

Fig. S41. ^{1}H NMR spectrum (400 MHz, $CDCl_3$, 298 K) of [Ru($S_2COEt)_2$(dppf)] (**8**)

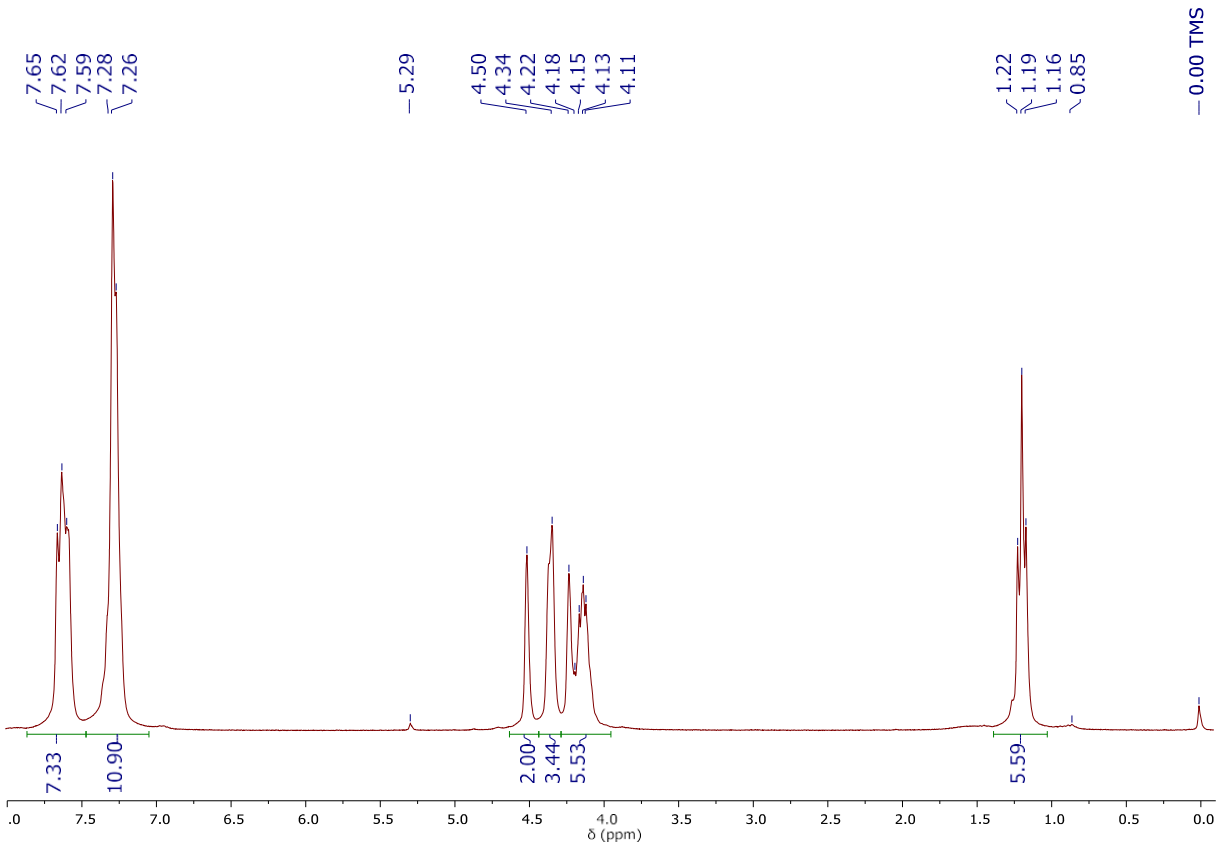

Fig. S42. $^{1}H\{^{31}P\}$ NMR spectrum (250 MHz, $CDCl_3$, 298 K) of $[Ru(S_2COEt)_2(dppf)]$ (**8**)

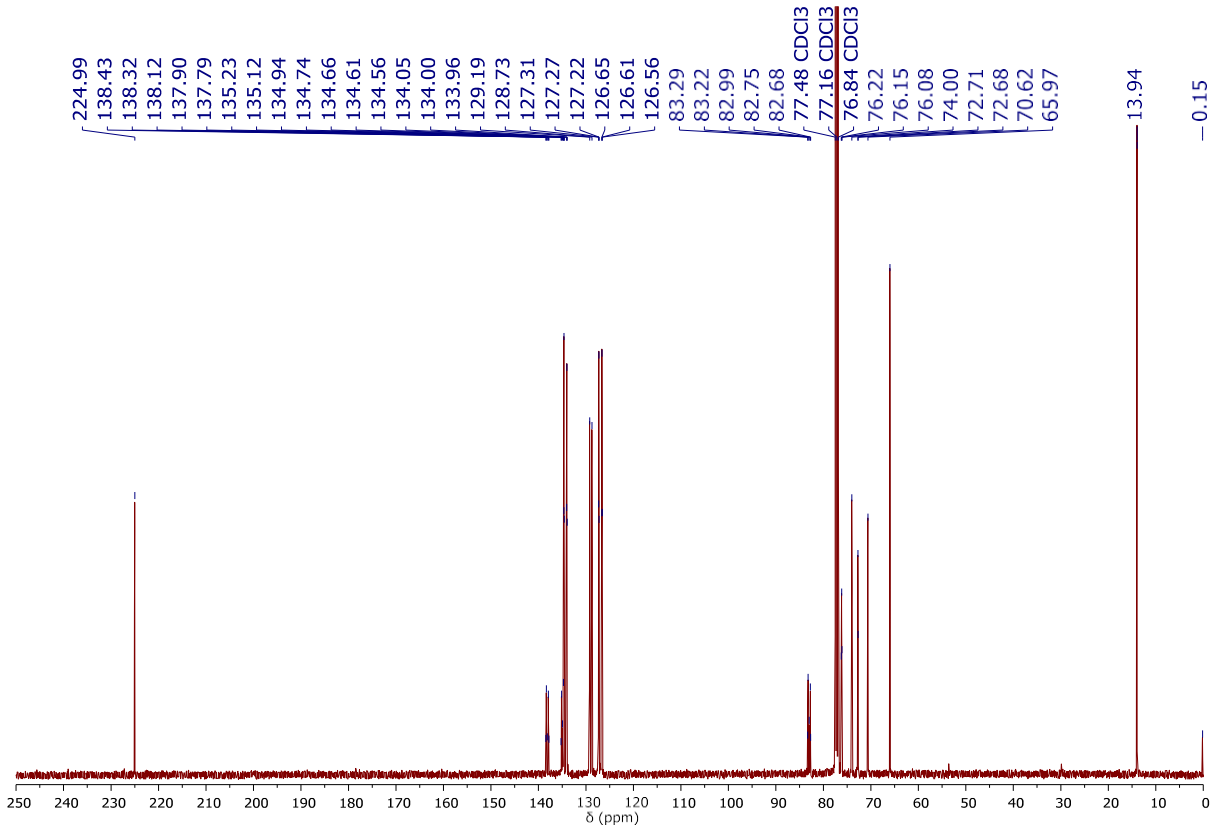

Fig. S43. $^{13}C\{^{1}H\}$ NMR spectrum (101 MHz, $CDCl_3$, 298 K) of $[Ru(S_2COEt)_2(dppf)]$ (**8**)

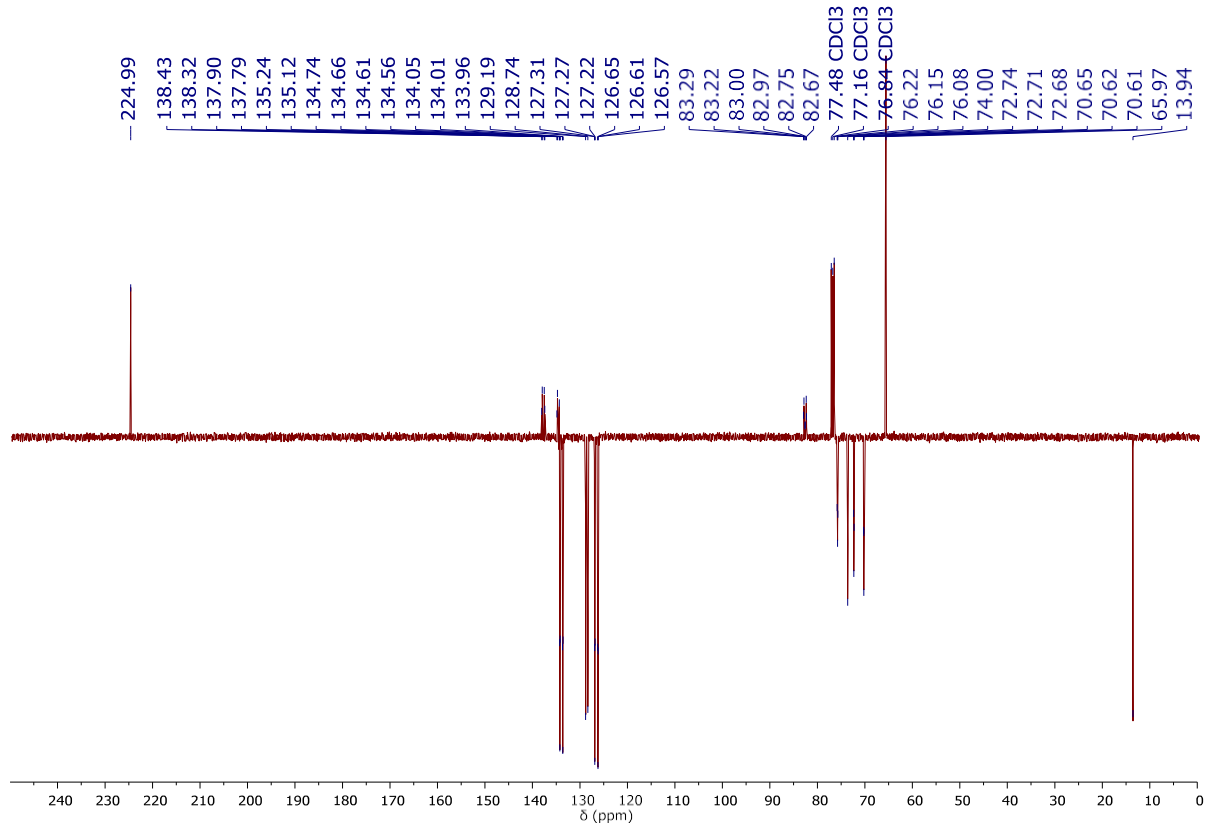

Fig. S44. $^{13}C\{^{1}H\}$ APT NMR spectrum (101 MHz, $CDCl_3$, 298 K) of $[Ru(S_2COEt)_2(dppf)]$ (**8**)

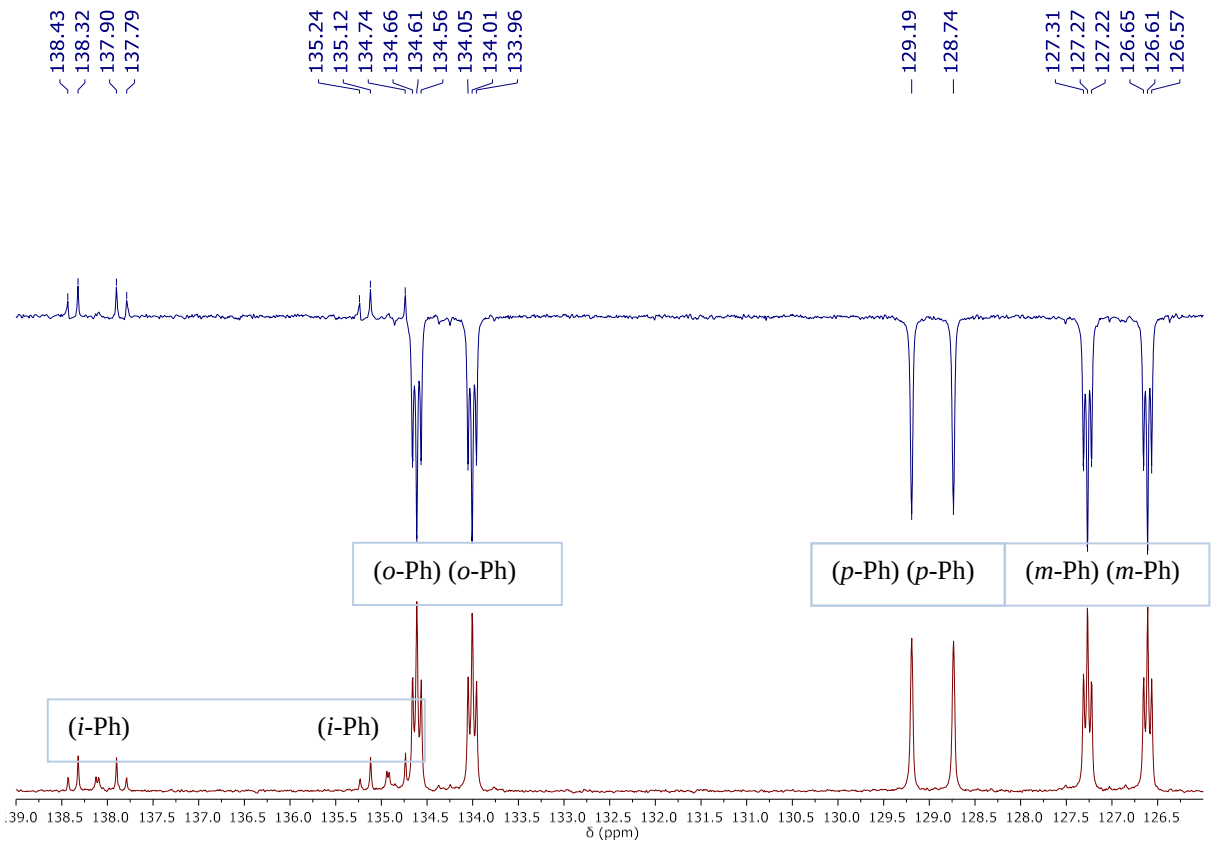

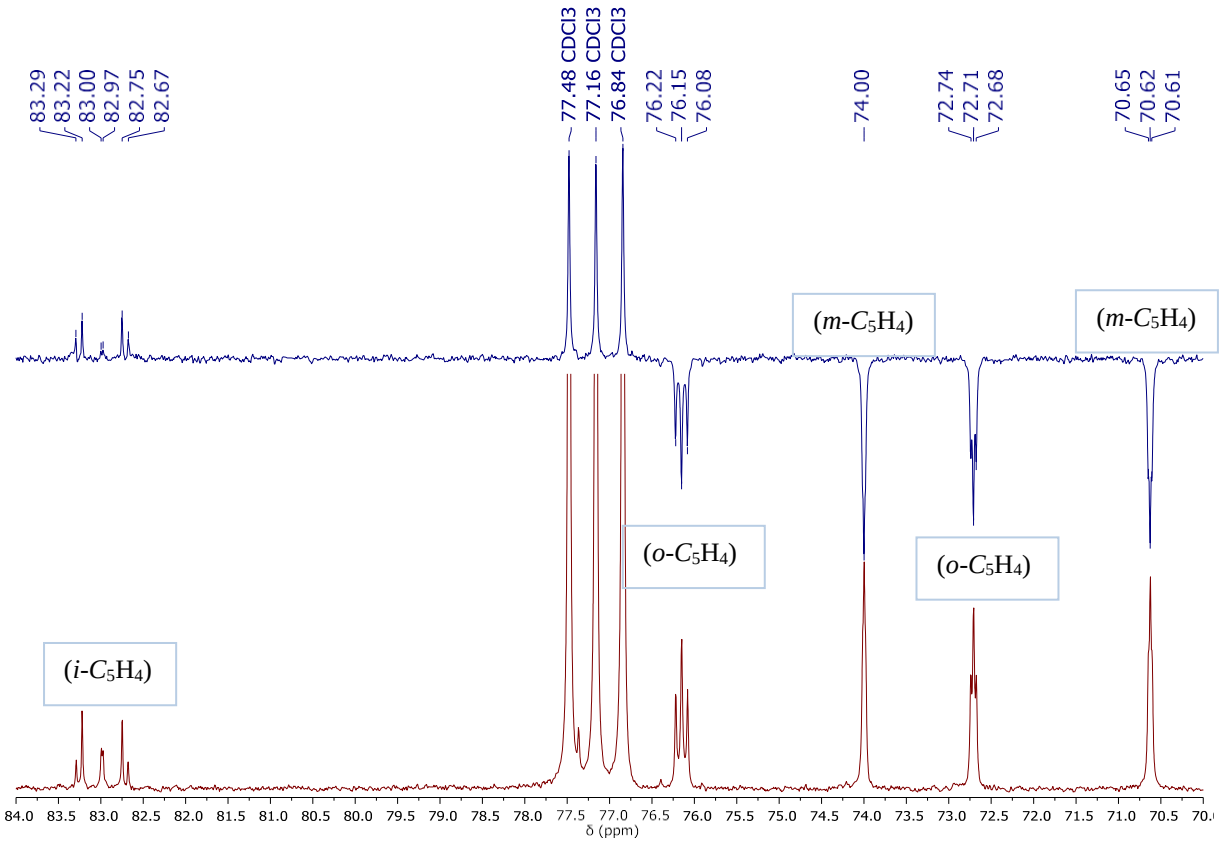

Fig. S45. ^{13}C CPD and APT NMR spectra (101 MHz, $CDCl_3$, 298 K) of [Ru($S_2COEt)_2$(dppf)] (**8**)

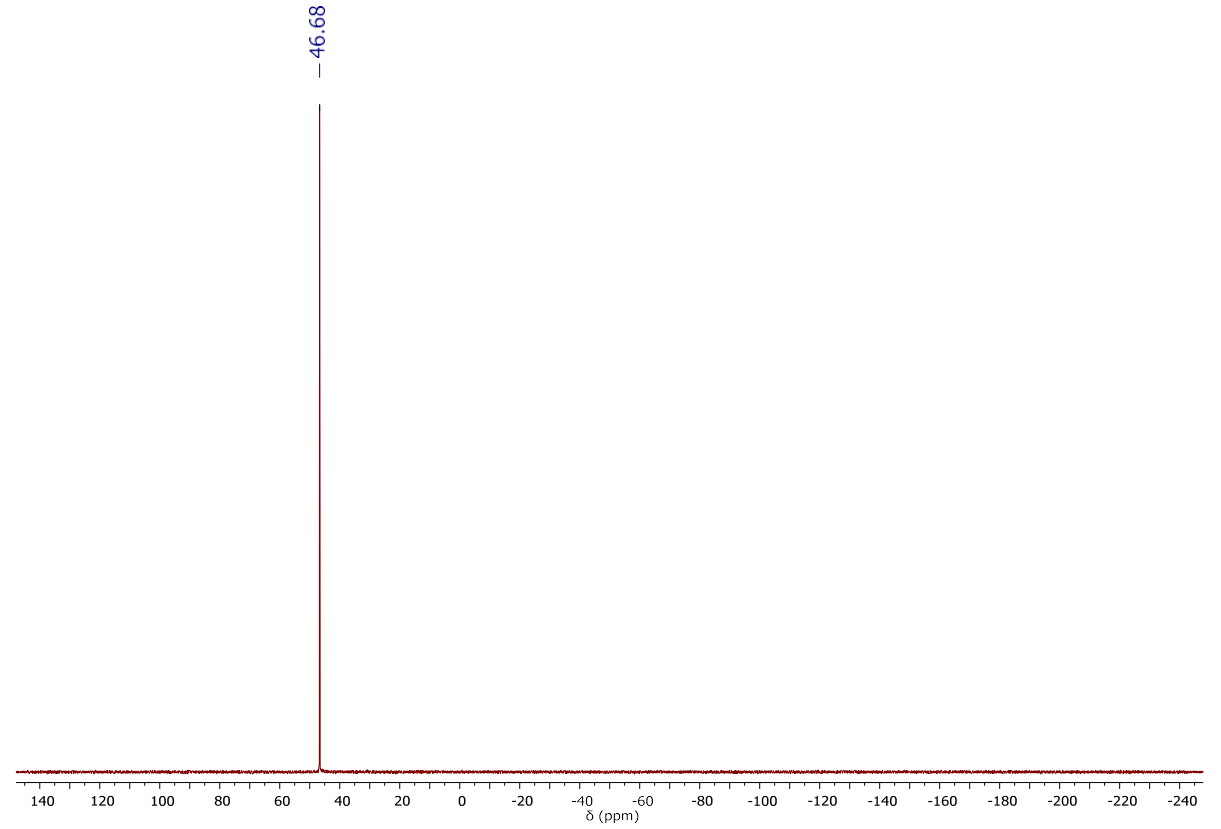

Fig. S46. ^{31}P NMR spectrum (162 MHz, $CDCl_3$, 298 K) of [Ru($S_2COEt)_2$(dppf)] (**8**)

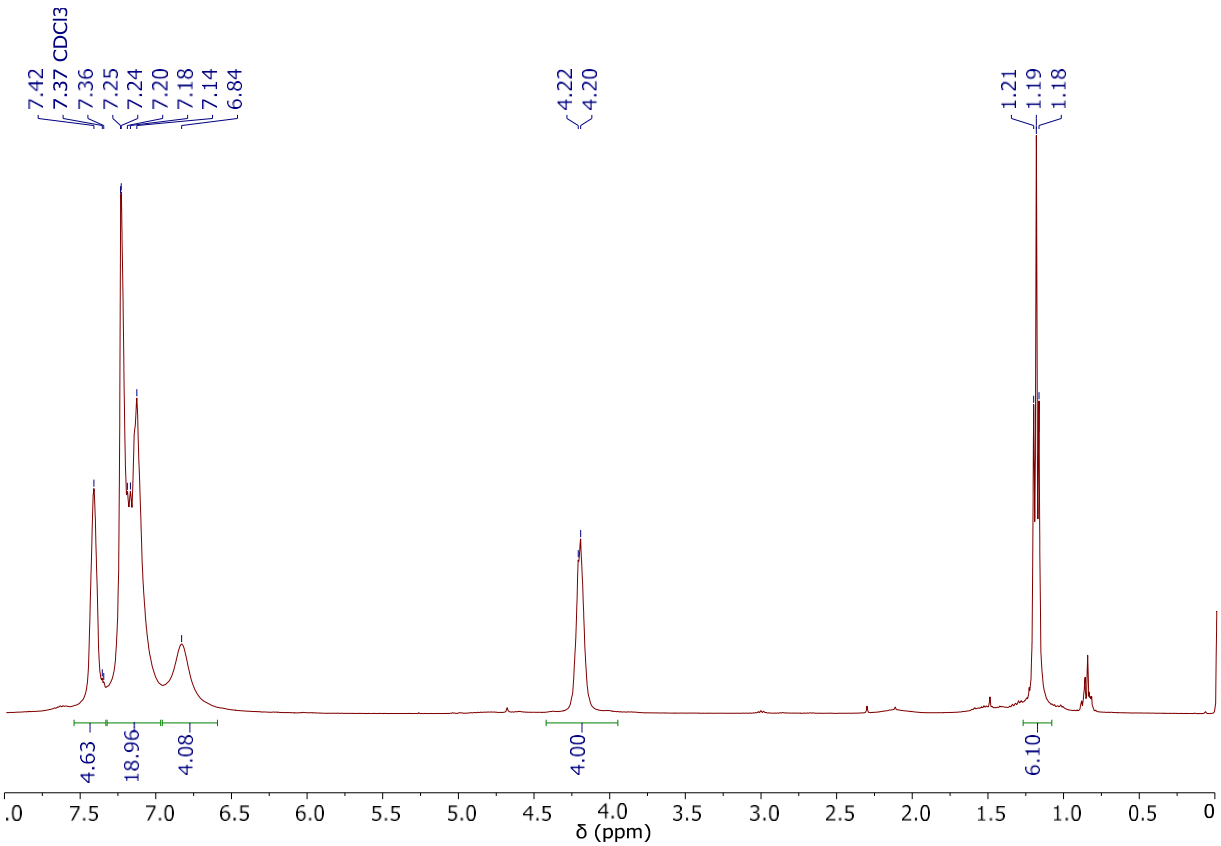

Fig. S47. ^{1}H NMR spectrum (400 MHz, $CDCl_3$, 298 K) of [Ru($S_2COEt)_2$(DPEphos)] (**9**)

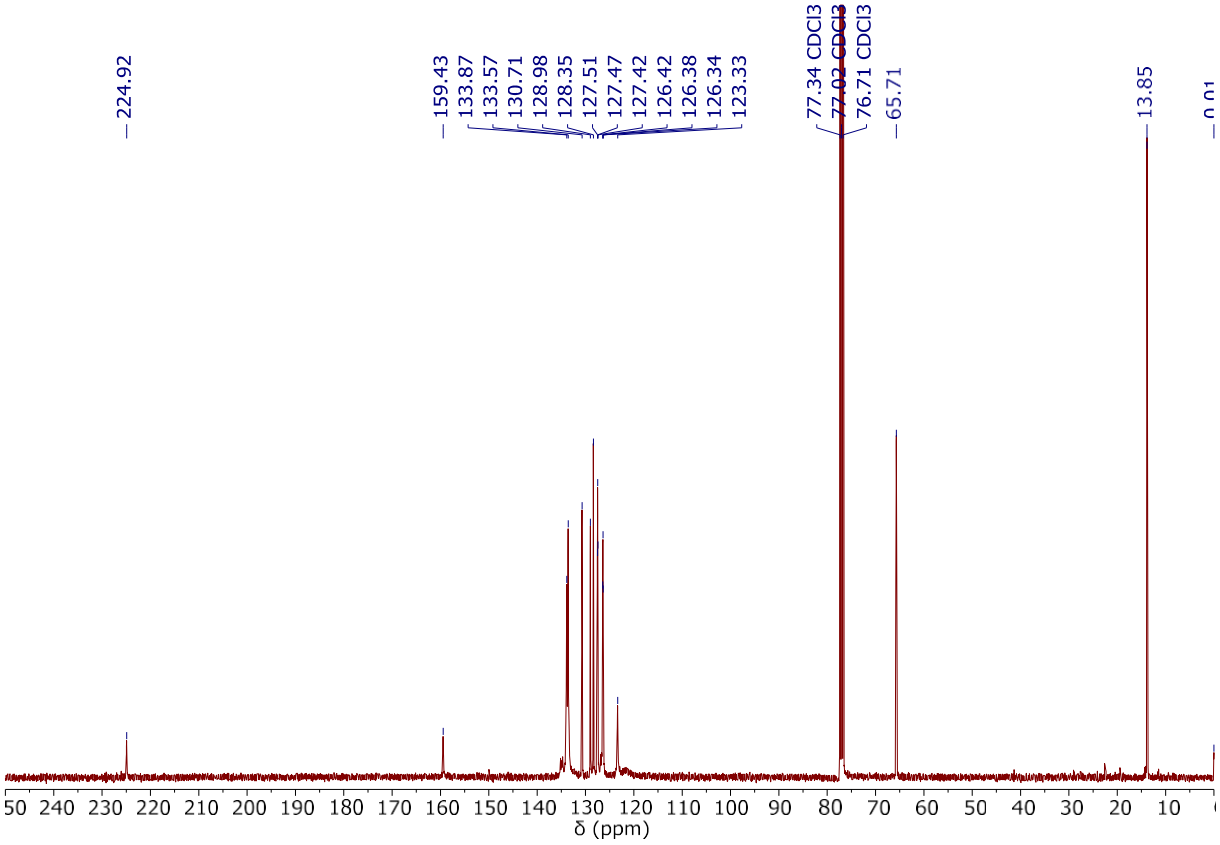

Fig. S48. ^{13}C{^{1}H} NMR spectrum (101 MHz, $CDCl_3$, 298 K) of [Ru($S_2COEt)_2$(DPEphos)] (**9**)

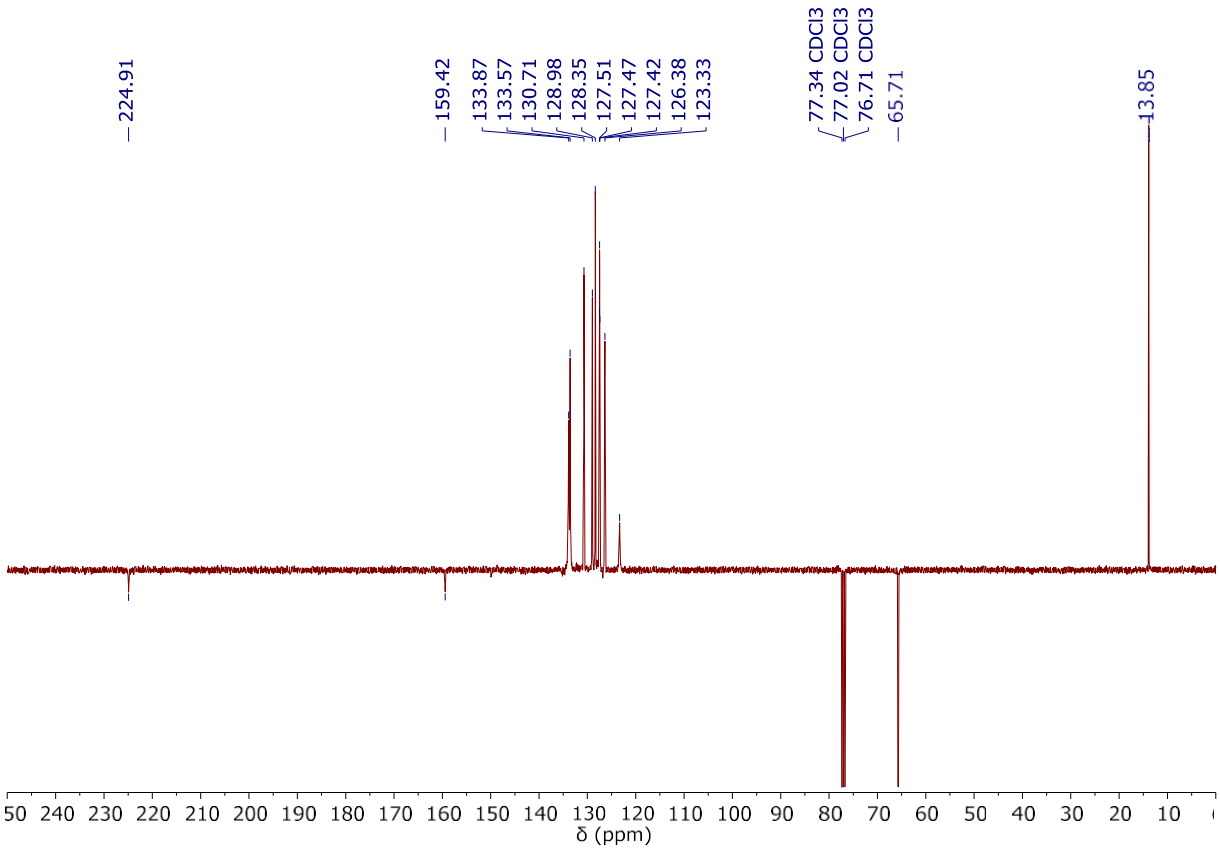

Fig. S49. $^{13}C\{^{1}H\}$ APT NMR spectrum (101 MHz, $CDCl_3$, 298 K) of $[Ru(S_2COEt)_2(DPEphos)]$ (**9**)

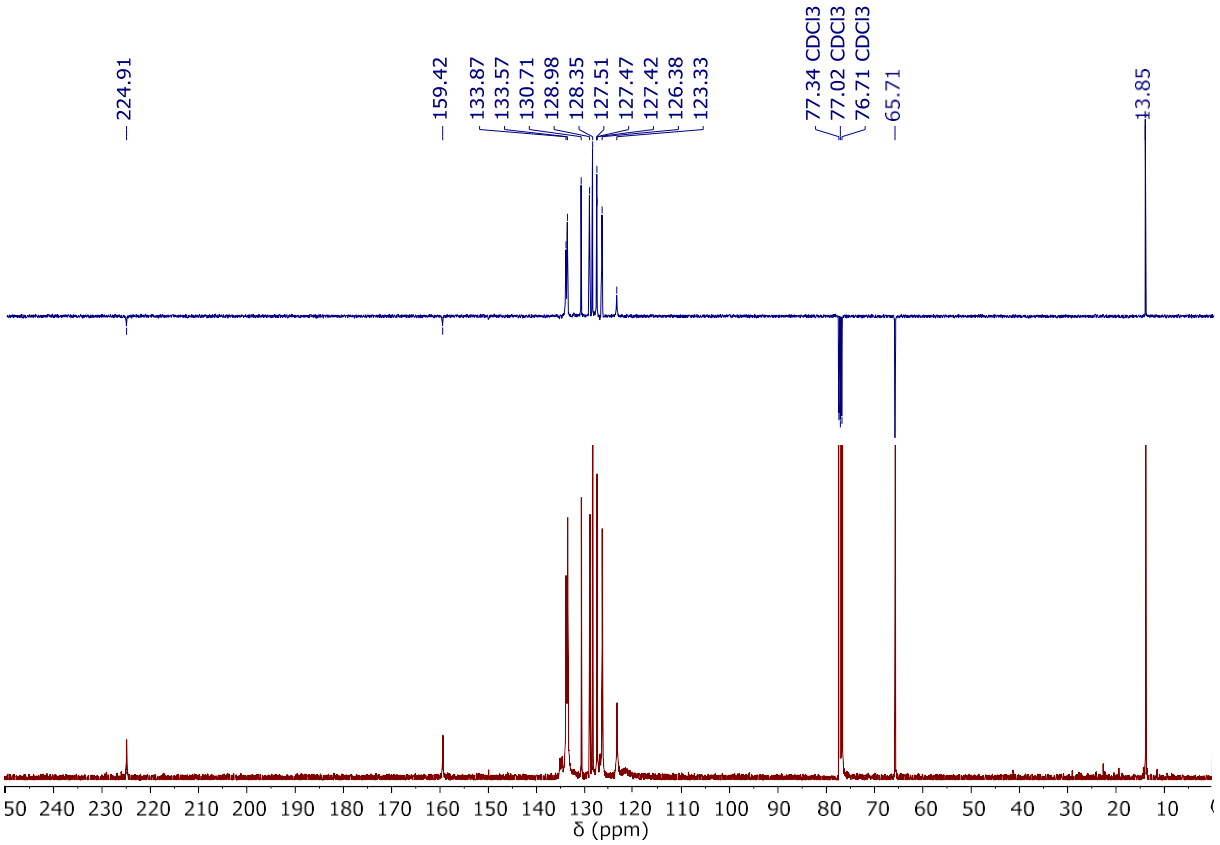

Fig. S50. ^{13}C CPD and APT NMR spectra (101 MHz, $CDCl_3$, 298 K) of $[Ru(S_2COEt)_2(DPEphos)]$ (**9**)

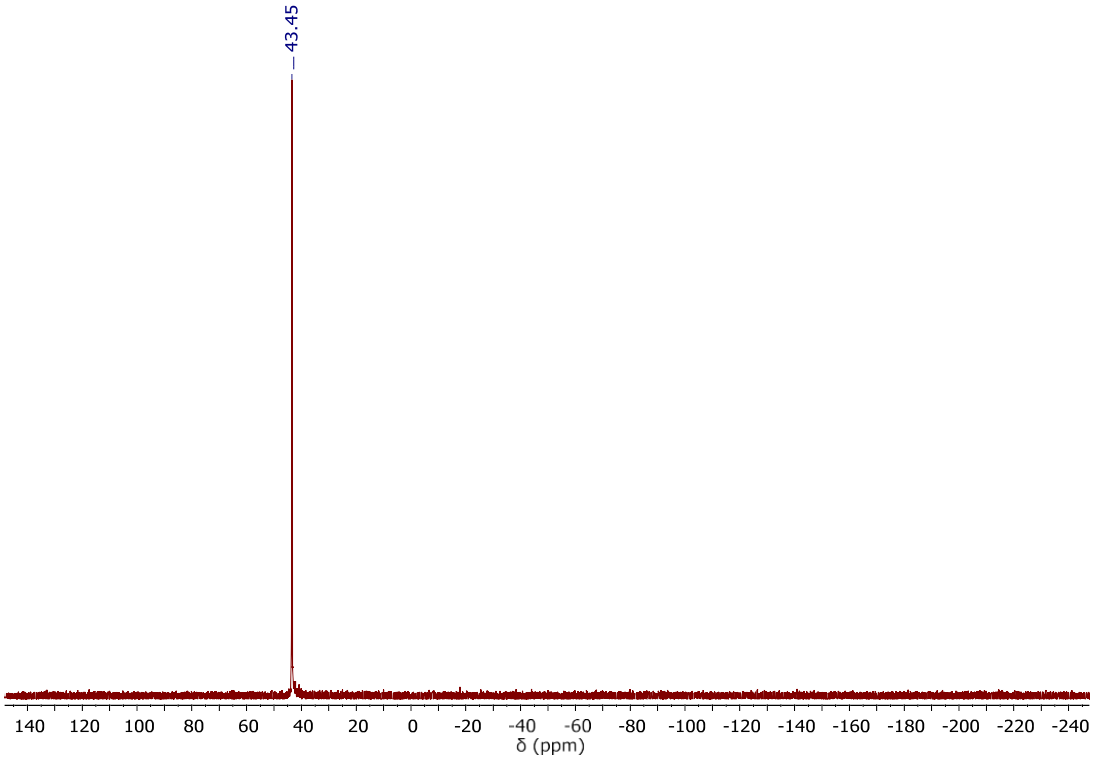

Fig. S51. ^{31}P NMR spectrum (162 MHz, $CDCl_3$, 298 K) of [Ru($S_2COEt)_2$(DPEphos)] (**9**)

Part 2 – IR spectra

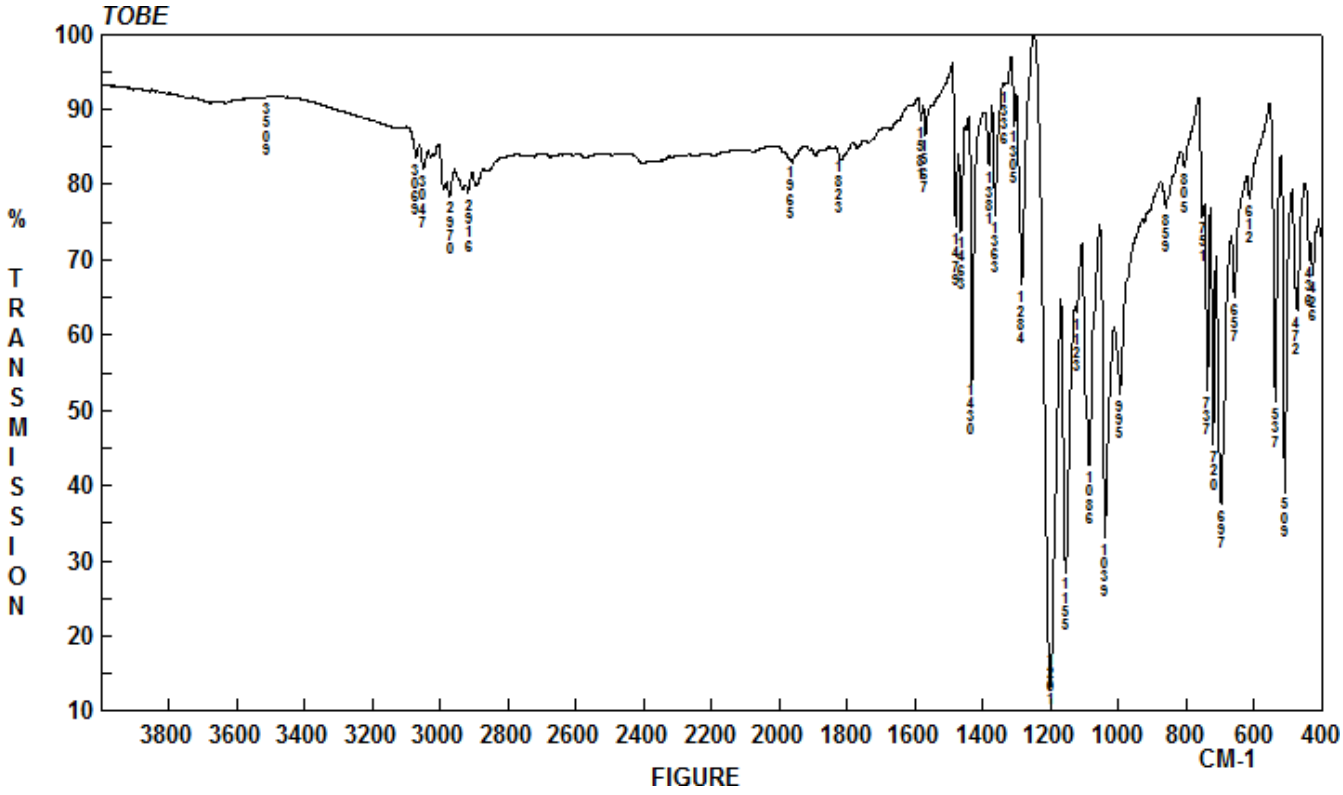

Fig. S52. FT-IR spectrum (KBr) of [Ru(S_2COEt)$_2$(dppm)] (**1**)

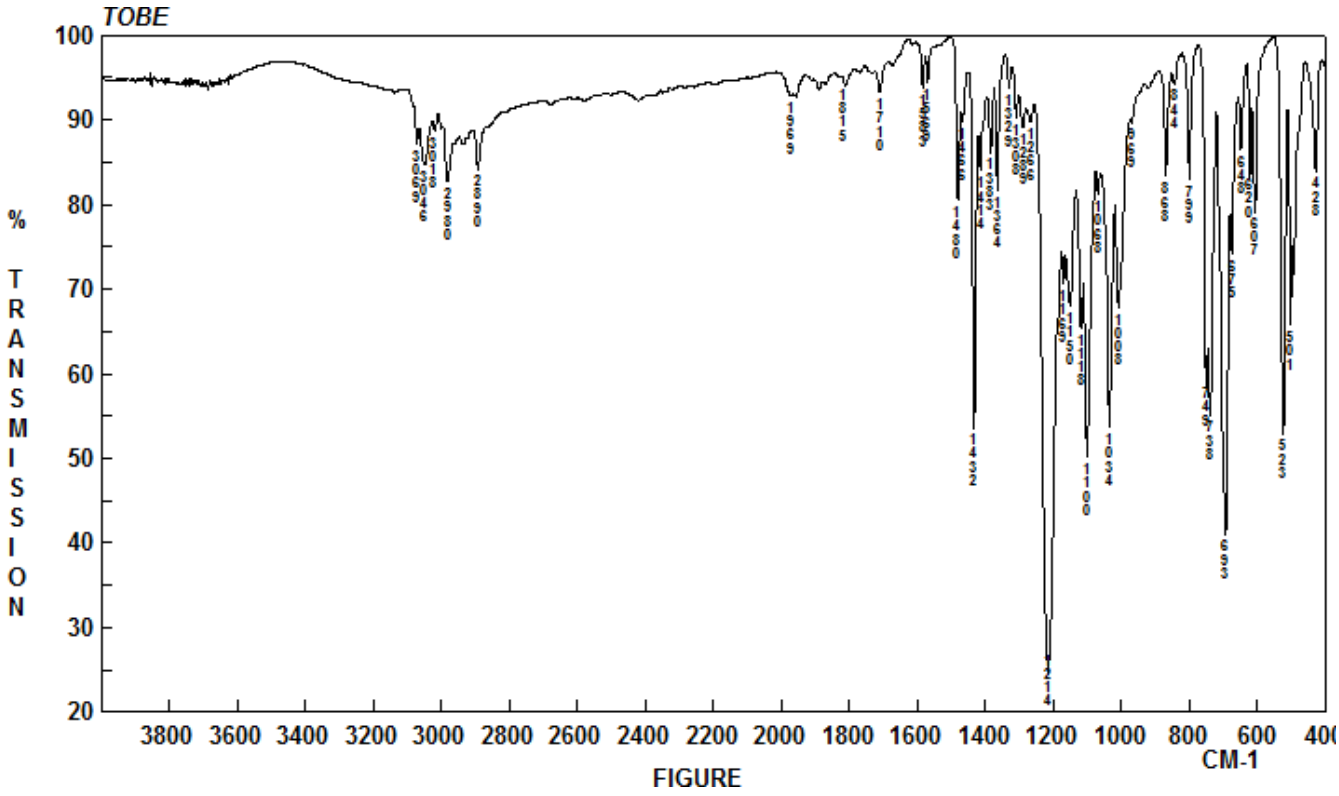

Fig. S53. FT-IR spectrum (KBr) of [Ru(S_2COEt)$_2$(dppe)] (**2**)

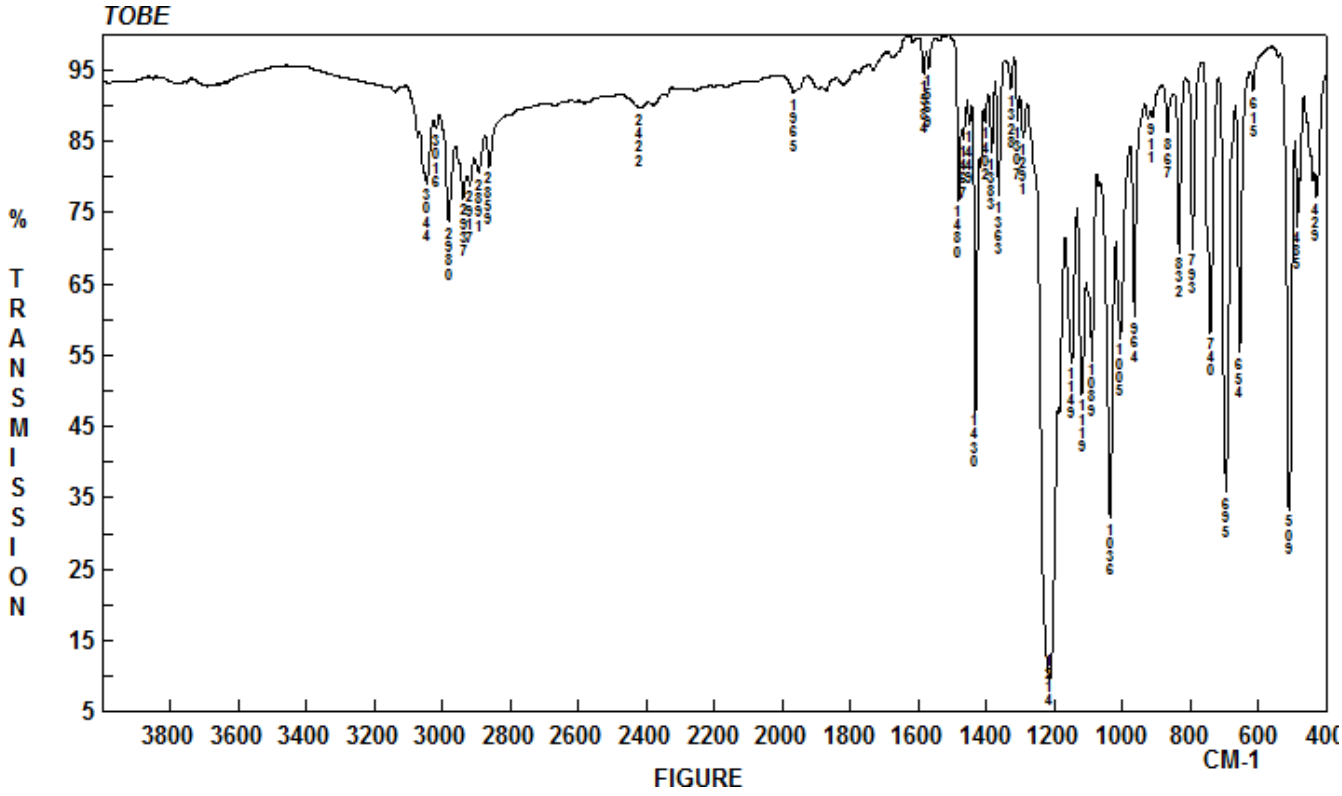

Fig. S54. FT-IR spectrum (KBr) of [Ru(S_2COEt)$_2$(dppp)] (**3**)

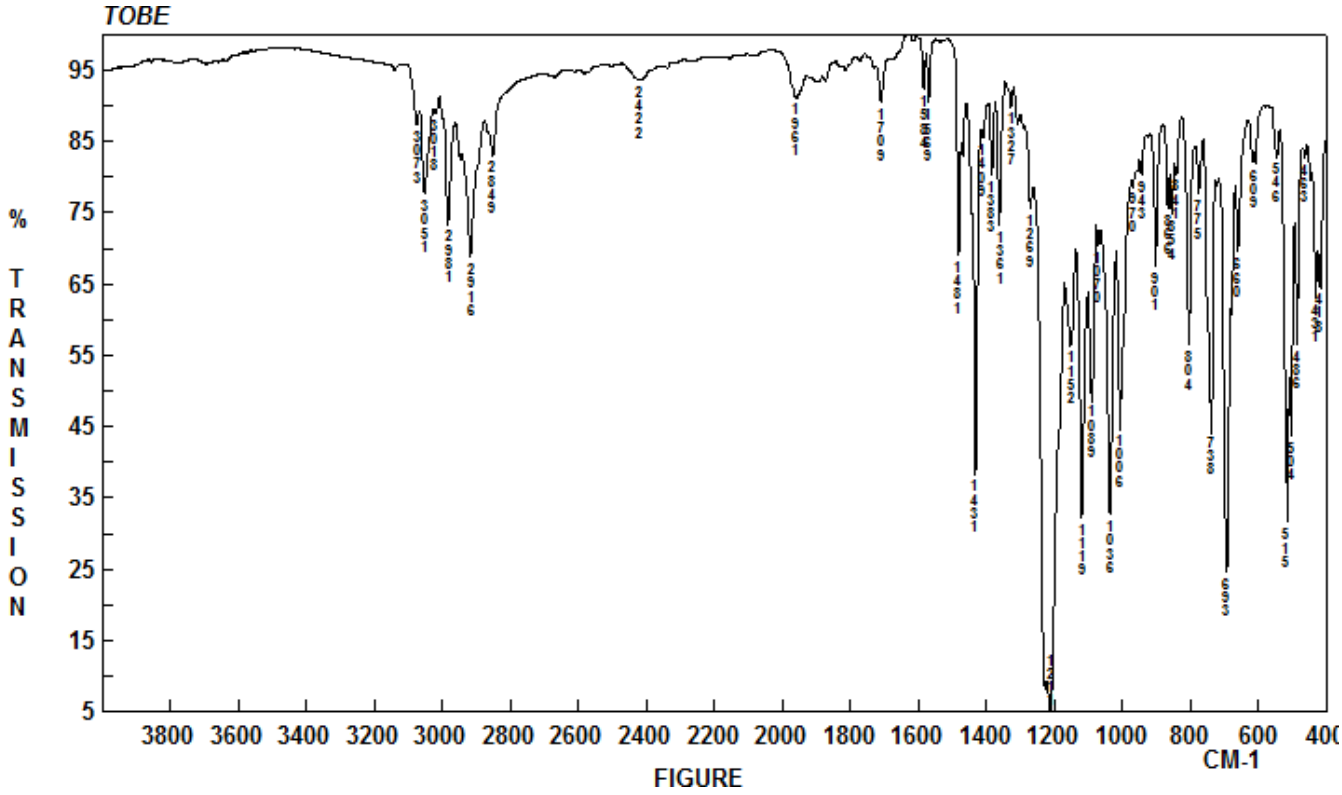

Fig. S55. FT-IR spectrum (KBr) of [Ru(S_2COEt)$_2$(dppb)] (**4**)

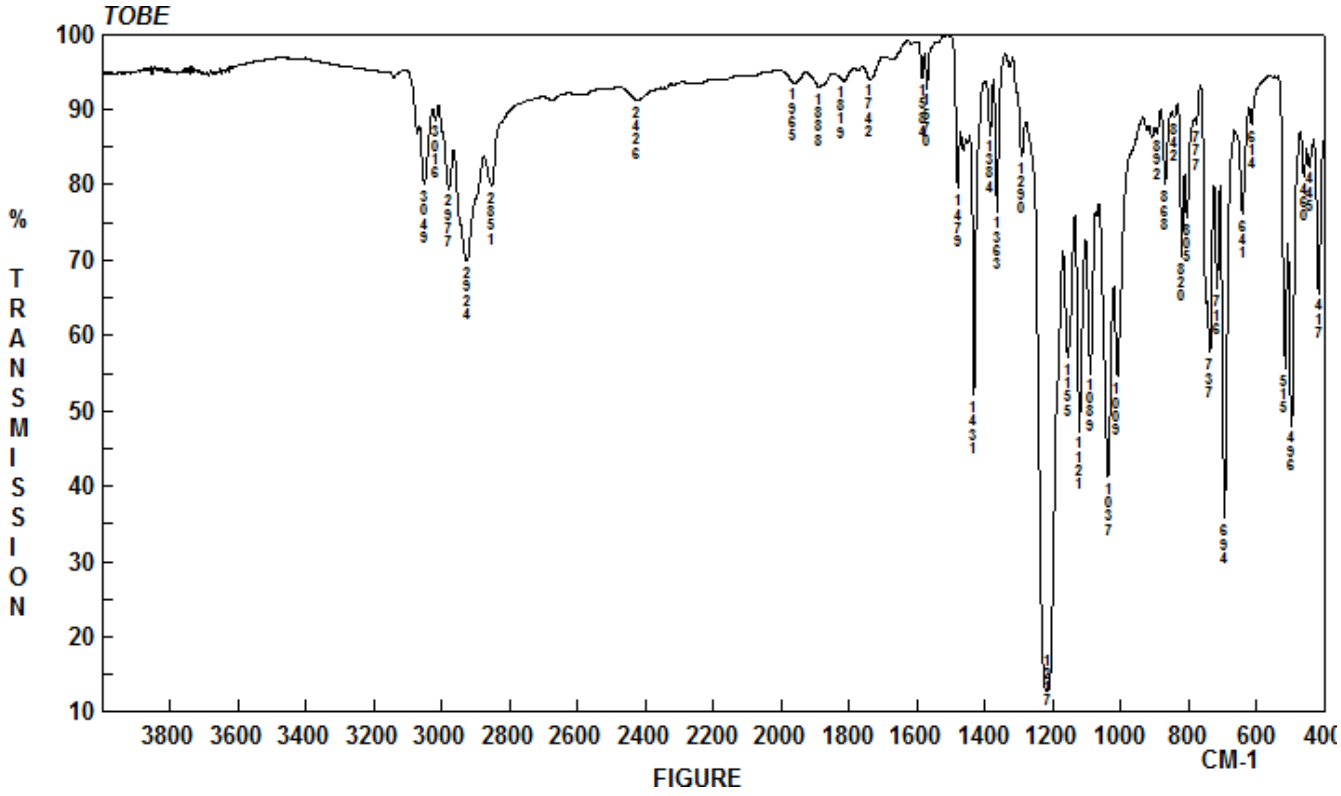

Fig. S56. FT-IR spectrum (KBr) of [Ru($S_2COEt)_2$(dpppe)] (**5**)

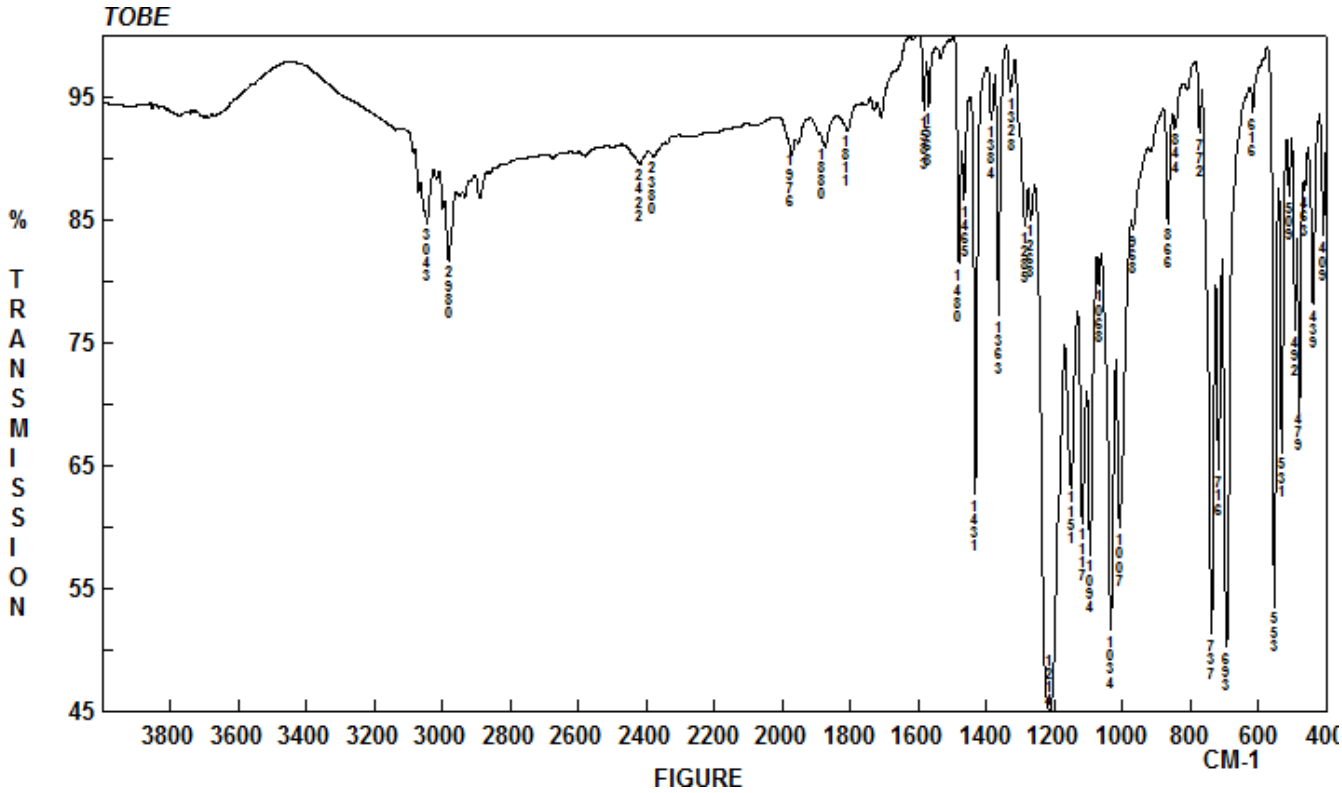

Fig. S57. FT-IR spectrum (KBr) of [Ru($S_2COEt)_2$(dppen)] (**6**)

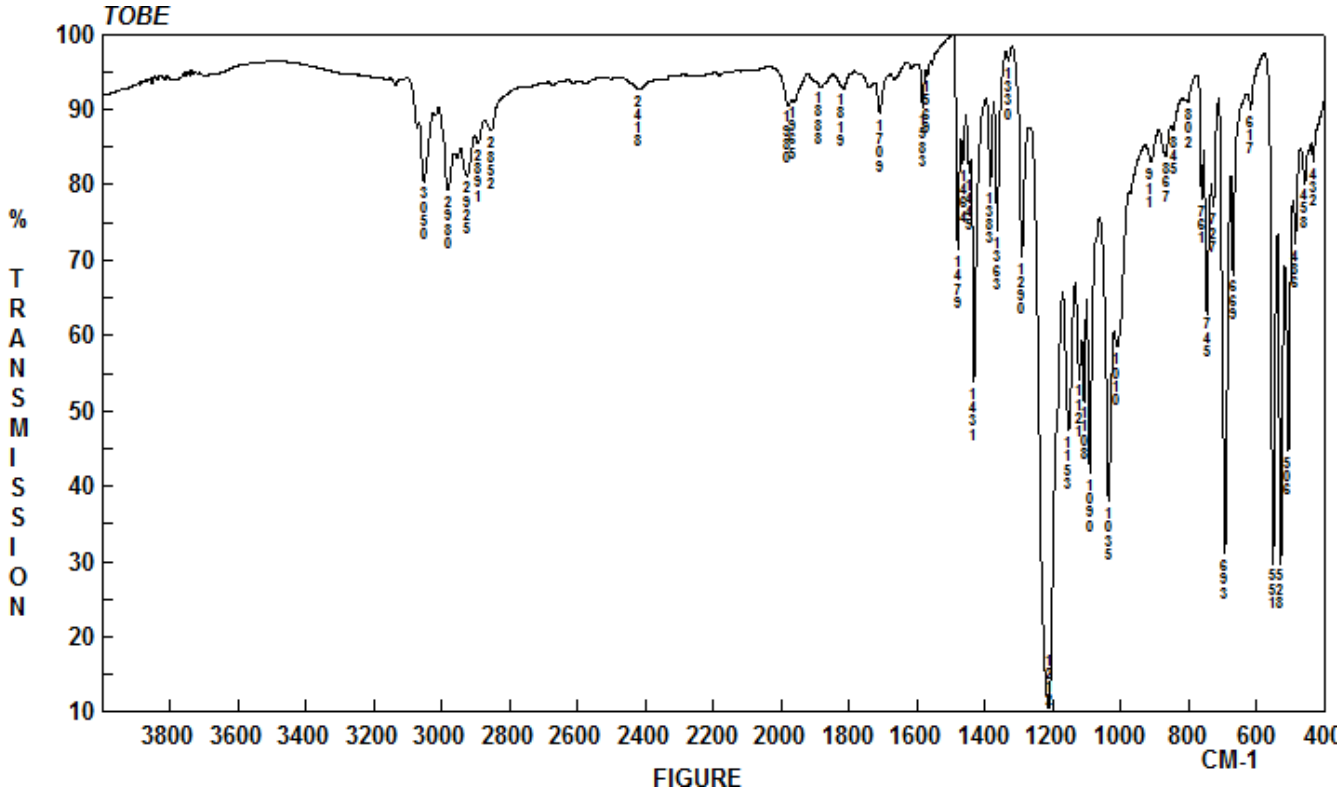

Fig. S58. FT-IR spectrum (KBr) of $[Ru(S_2COEt)_2(dppbz)]$ (**7**)

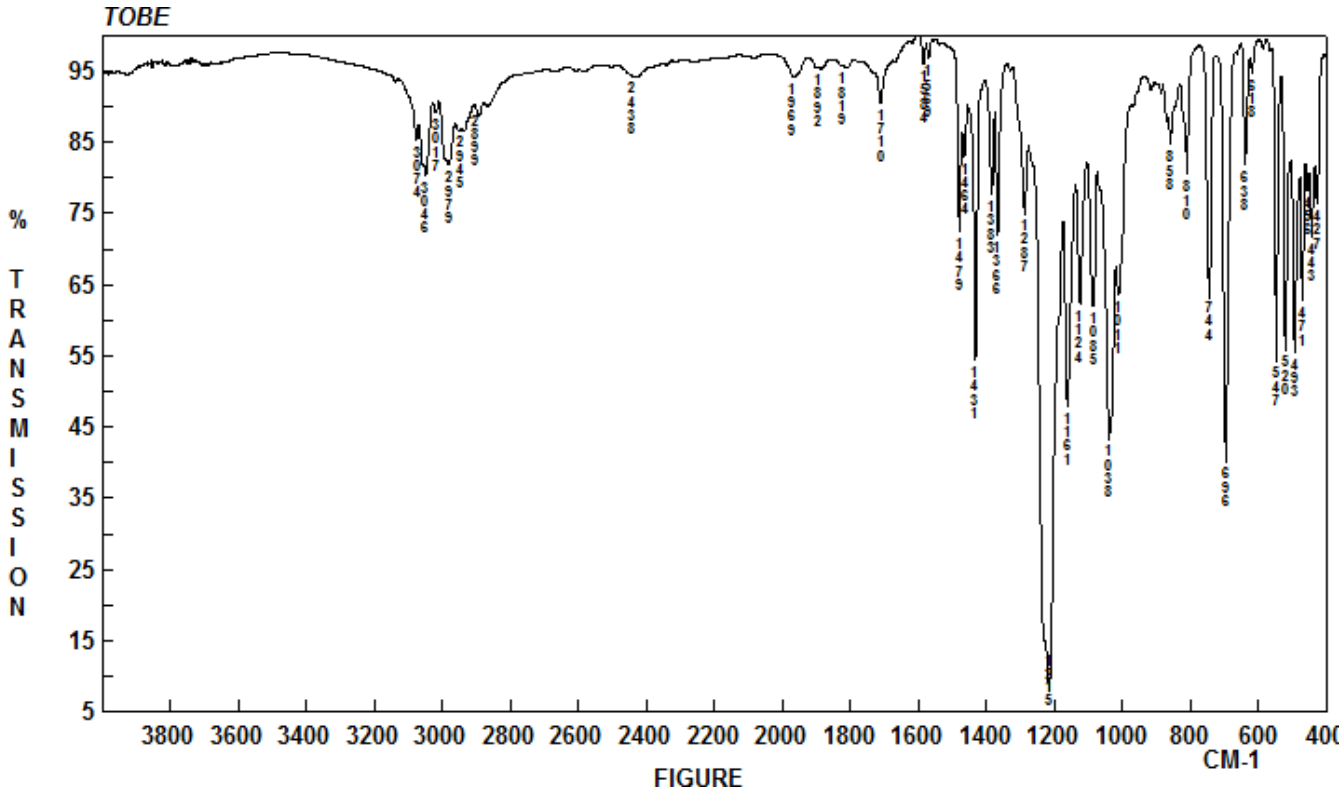

Fig. S59. FT-IR spectrum (KBr) of $[Ru(S_2COEt)_2(dppf)]$ (**8**)

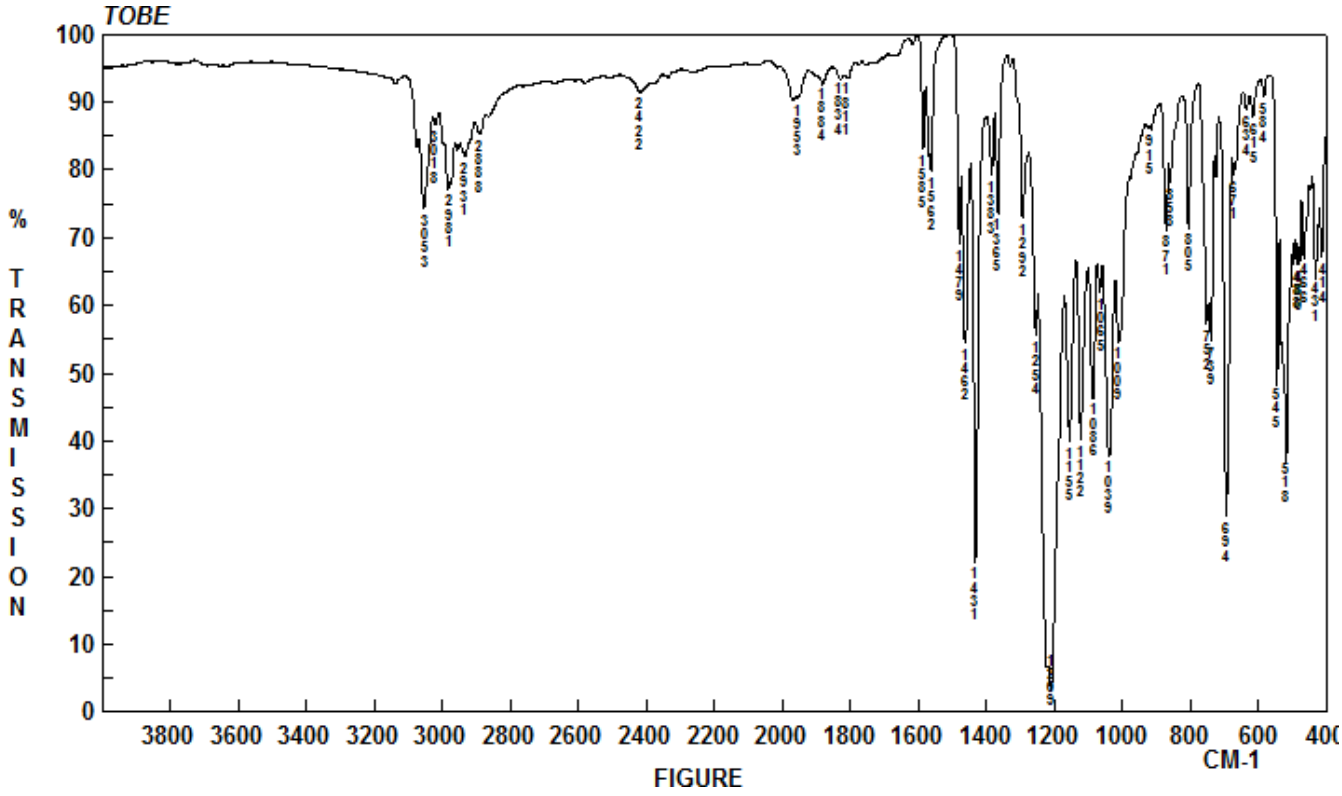

Fig. S60. FT-IR spectrum (KBr) of [Ru(S_2COEt)$_2$(DPEphos)] (**9**)

Part 3 – Mass spectra

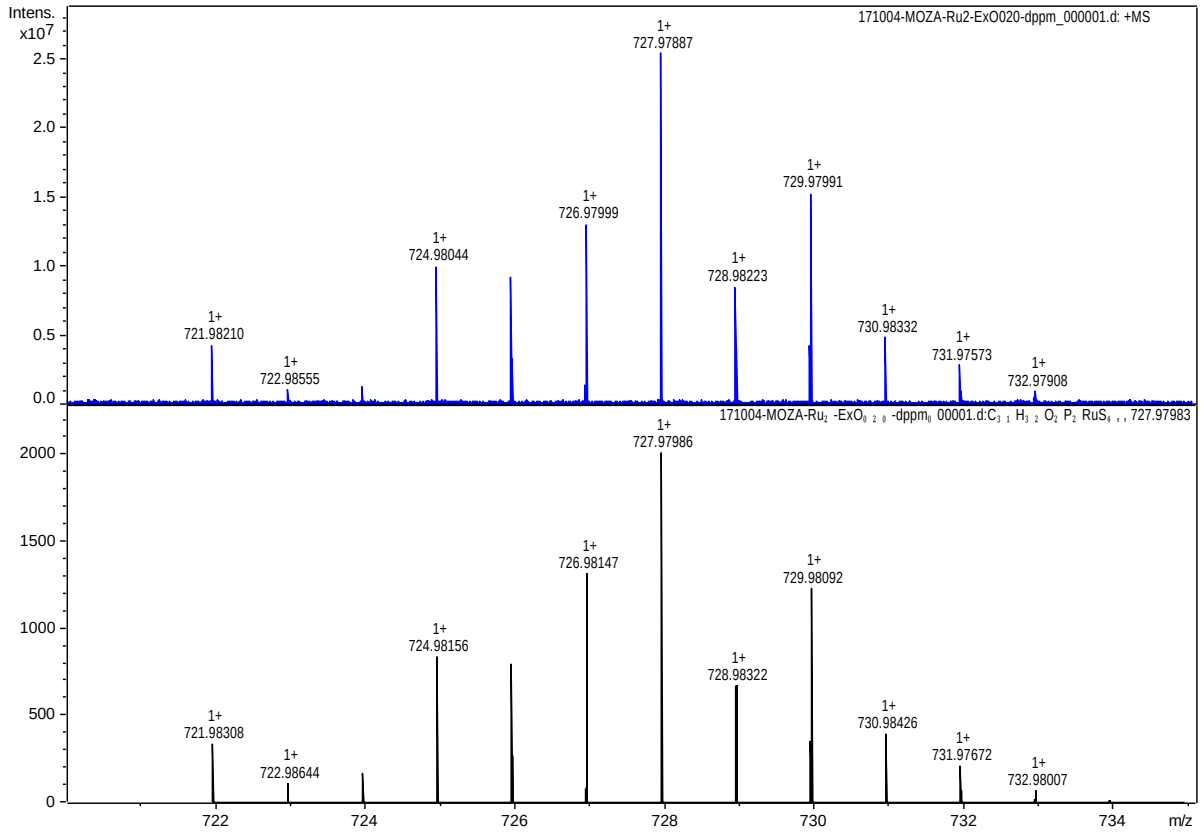

Fig. S61. Isotope profiles of [Ru(S_2COEt)$_2$(dppm)] (**1**) obtained by ESI-MS (in blue) and simulated isotope patterns of the corresponding ion (in black)

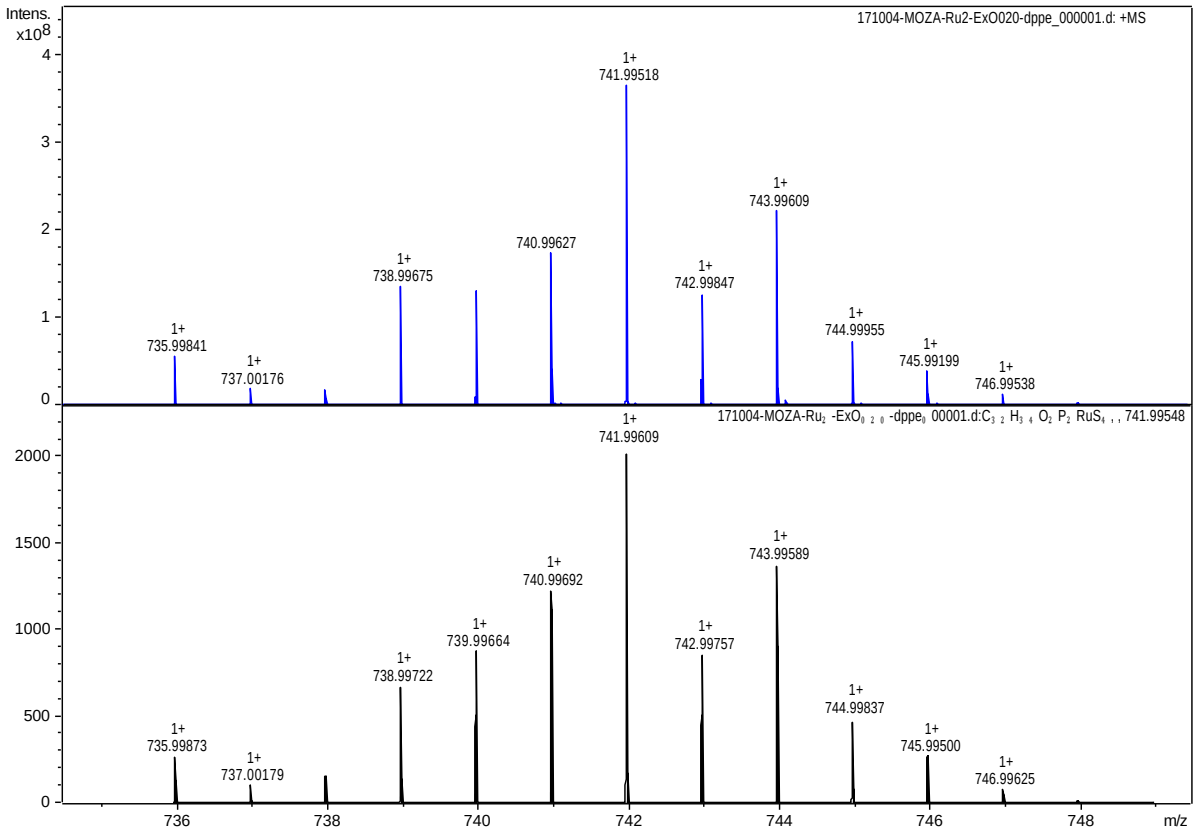

Fig. S62. Isotope profiles of [Ru(S_2COEt)$_2$(dppe)] (**2**) obtained by ESI-MS (in blue) and simulated isotope patterns of the corresponding ion (in black)

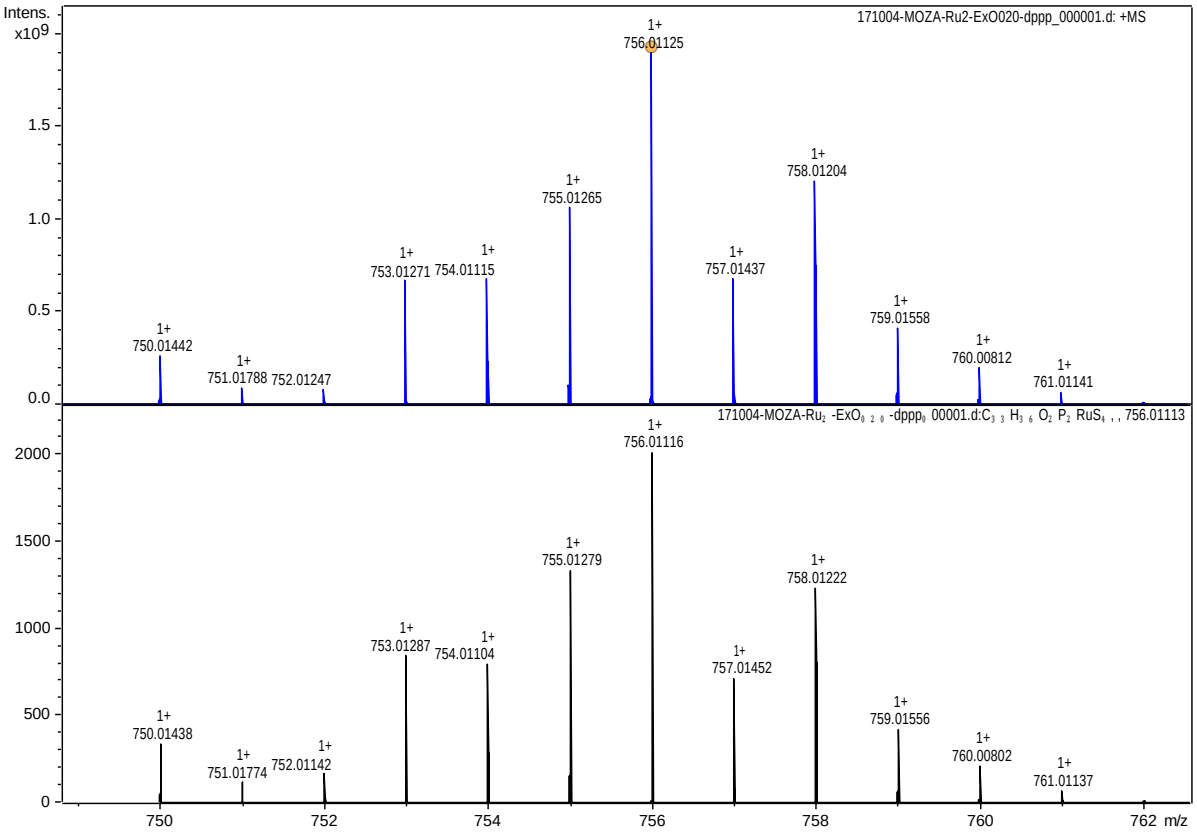

Fig. S63. Isotope profiles of [Ru(S_2COEt)$_2$(dppp)] (**3**) obtained by ESI-MS (in blue) and simulated isotope patterns of the corresponding ion (in black)

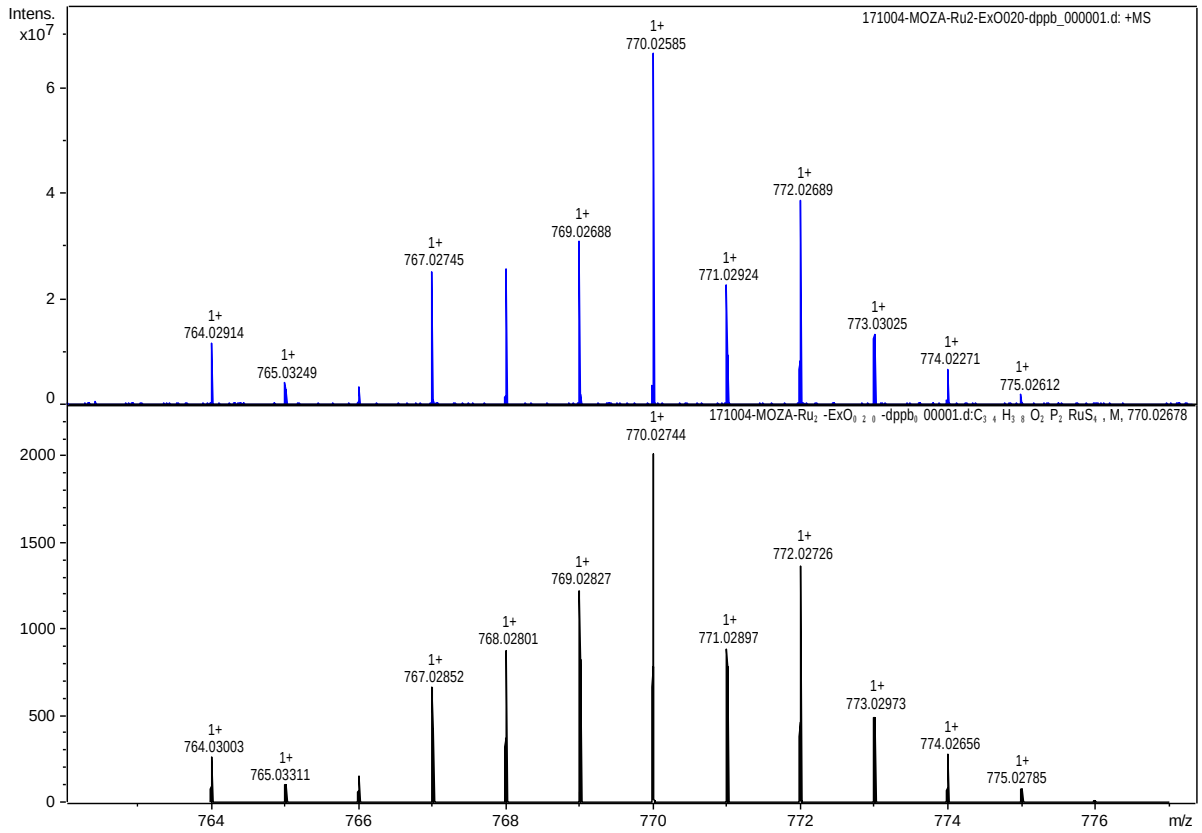

Fig. S64. Isotope profiles of [Ru(S_2COEt)$_2$(dppb)] (**4**) obtained by ESI-MS (in blue) and simulated isotope patterns of the corresponding ion (in black)

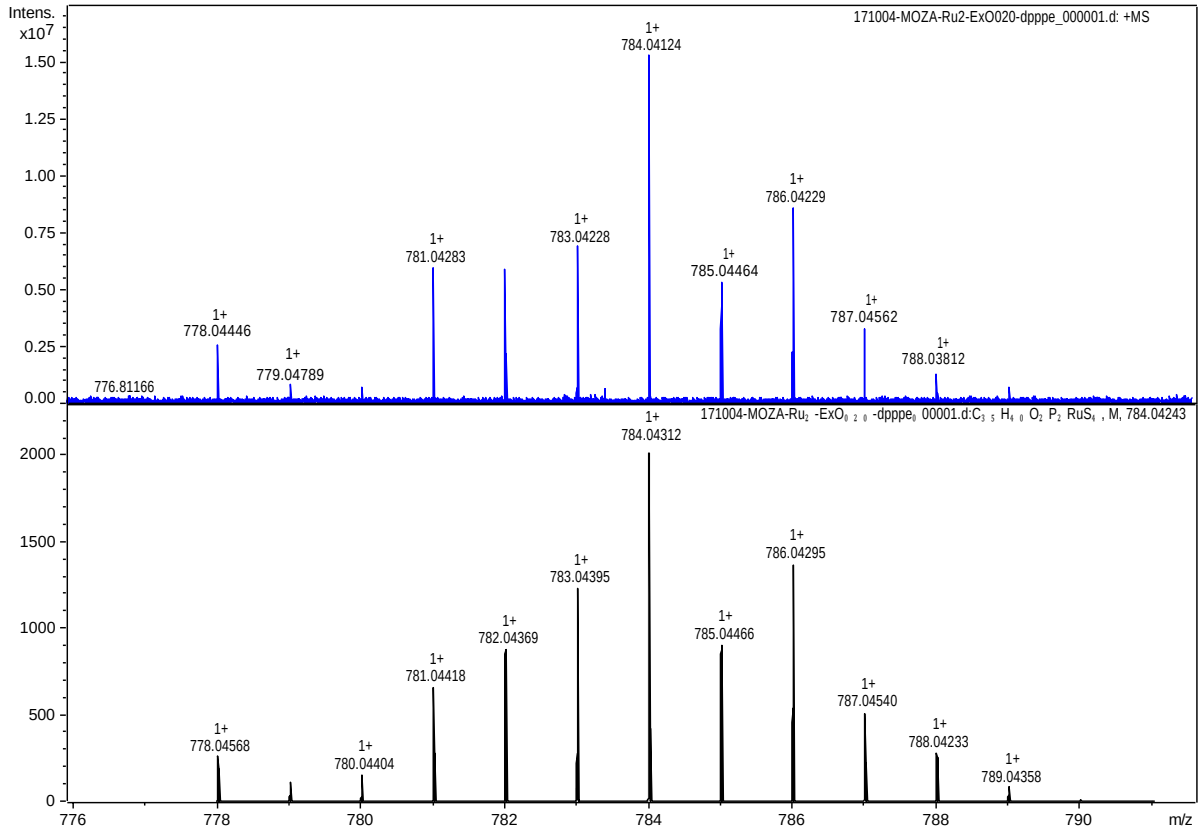

Fig. S65. Isotope profiles of [Ru(S_2COEt)$_2$(dpppe)] (**5**) obtained by ESI-MS (in blue) and simulated isotope patterns of the corresponding ion (in black)

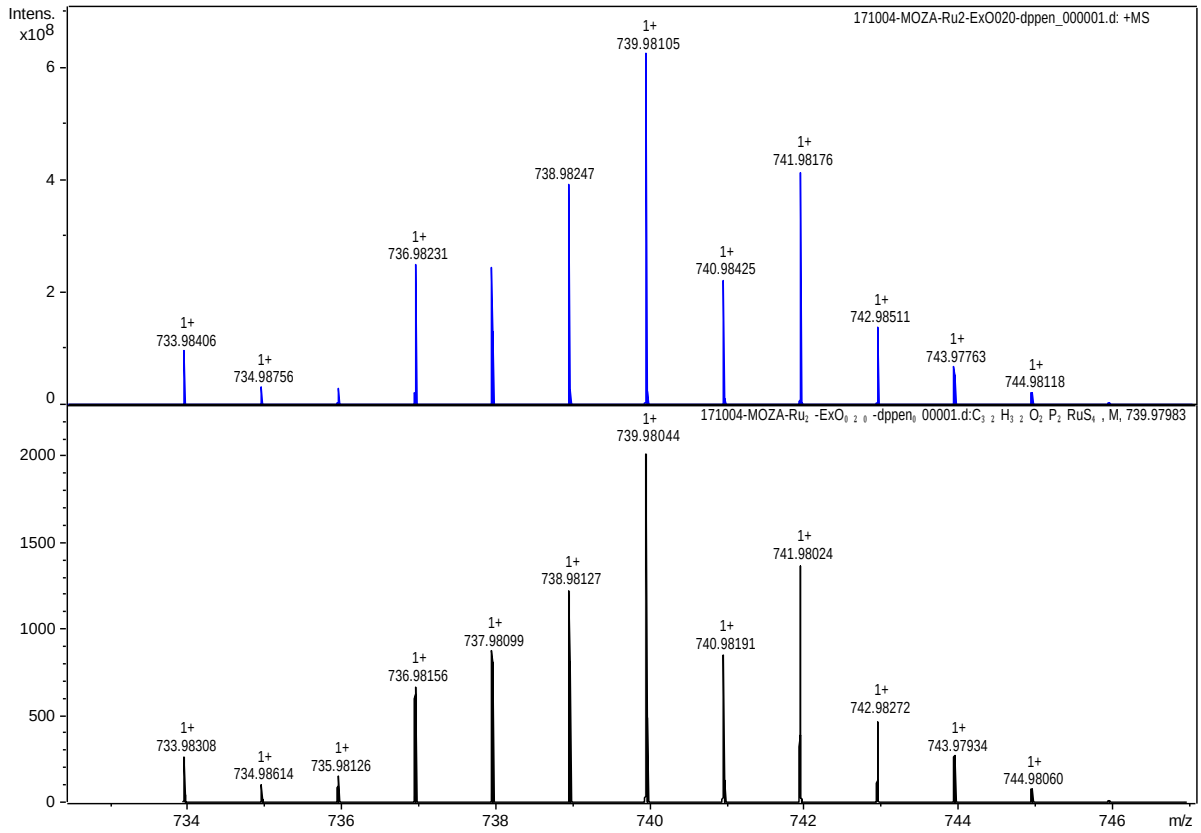

Fig. S66. Isotope profiles of [Ru(S_2COEt)$_2$(dppen)] (**6**) obtained by ESI-MS (in blue) and simulated isotope patterns of the corresponding ion (in black)

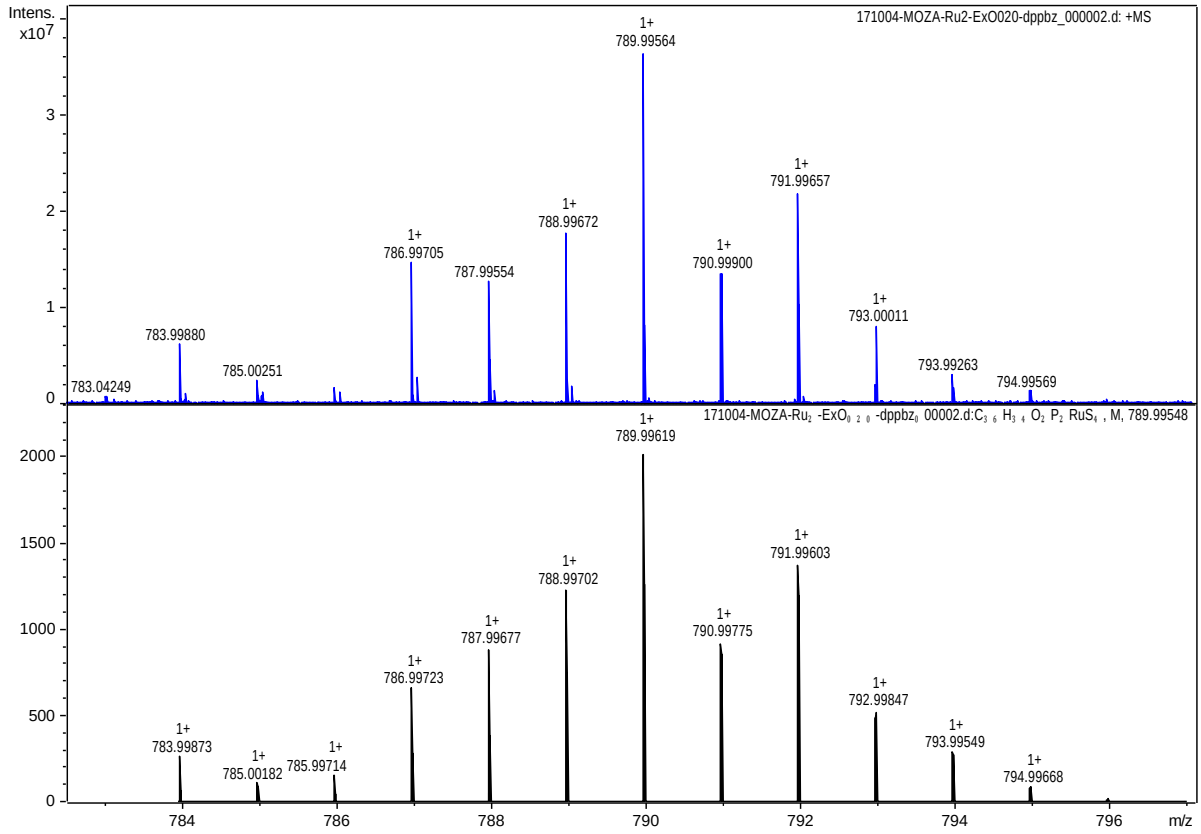

Fig. S67. Isotope profiles of [Ru(S_2COEt)$_2$(dppbz)] (**7**) obtained by ESI-MS (in blue) and simulated isotope patterns of the corresponding ion (in black)

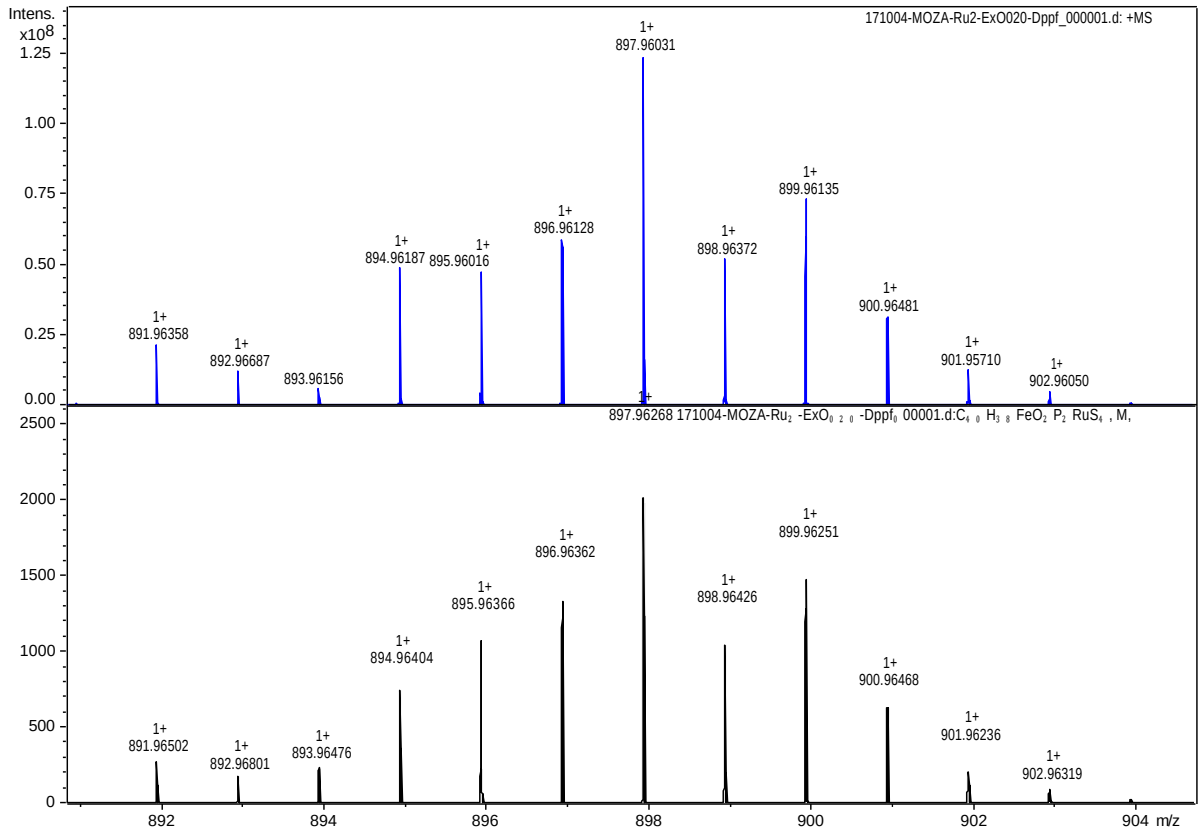

Fig. S68. Isotope profiles of [Ru(S_2COEt)$_2$(dppf)] (**8**) obtained by ESI-MS (in blue) and simulated isotope patterns of the corresponding ion (in black)

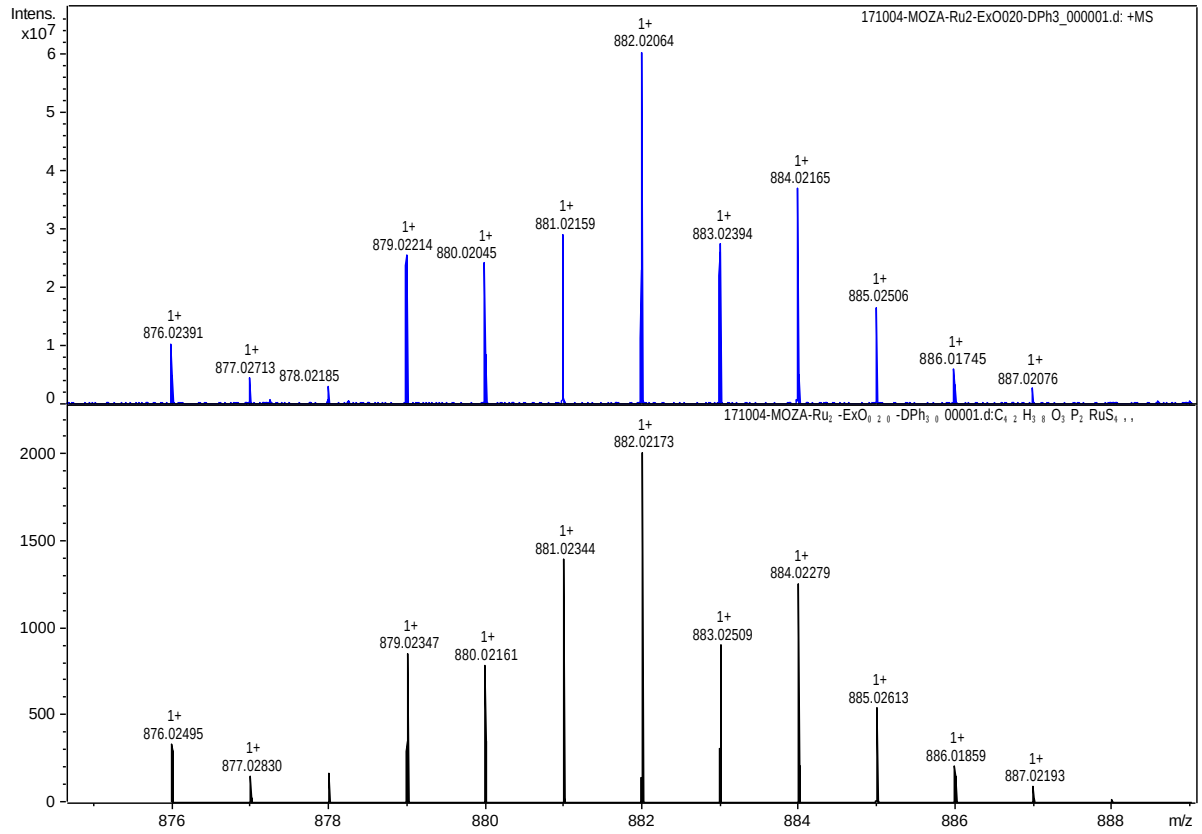

Fig. S69. Isotope profiles of [Ru(S_2COEt)$_2$(DPEphos)] (**9**) obtained by ESI-MS (in blue) and simulated isotope patterns of the corresponding ion (in black)

Part 4 – Crystallography

Table S1. Crystal data and structure refinement parameters for compounds **1**–**9**

Complex	**1**	**2**	**3**	**4**	**5**
Chemical formula	$C_{31}H_{32}O_2P_2RuS_4$	$C_{32}H_{34}O_2P_2RuS_4$	$2(C_{33}H_{36}O_2P_2RuS_4)\cdot CH_2Cl_2$	$C_{34}H_{38}O_2P_2RuS_4$	$C_{35}H_{40}O_2P_2RuS_4$
M (g mol^{-1})	727.81	741.84	1596.66	769.89	783.92
Crystal system	Triclinic	Orthorhombic	Orthorhombic	Monoclinic	Triclinic
Space group	P–1	$P2_12_12_1$	$Aba2$	$P2_1/n$	P–1
a (Å)	9.0261(7)	11.1196(6)	20.1261(7)	12.8809(10)	11.3144(3)
b (Å)	11.1233(9)	14.0834(10)	21.5909(8)	16.5329(11)	11.4472(3)
c (Å)	16.9387(14)	20.6451(12)	16.4408(7)	16.3601(9)	13.6613(4)
α (°)	72.137(4)	90	90	90	94.926(2)
β (°)	80.855(4)	90	90	105.668(3)	93.661(2)
γ (°)	73.704(5)	90	90	90	97.305(2)
V (Å^3)	1548.7(2)	3233.1(3)	7144.2(5)	3354.6(4)	1743.53(8)
Z	2	4	4	4	2
D_x (g cm^{-3})	1.561	1.524	1.484	1.524	1.493
μ(Mo Kα) (mm^{-1})	0.908	0.871	0.867	0.843	0.812
Reflns collected	58899	51408	36877	41282	19804
Indpndt reflns	7671	9865	6994	8244	6359
R_{int}	0.055	0.098	0.095	0.048	0.055
R_1[a] (all data)	0.038	0.057	0.069	0.040	0.075
wR_2[b] (all data)	0.059	0.073	0.103	0.068	0.086
GOF[c] on F^2	1.059	0.996	1.012	1.046	0.994

Complex	**6**	**7**	**8**	**9**
Chemical formula	$C_{32}H_{32}O_2P_2RuS_4$	$C_{36}H_{34}O_2P_2RuS_4$	$C_{40}H_{38}FeO_2P_2RuS_4$	$C_{42}H_{38}O_3P_2RuS_4$
M (g mol^{-1})	739.82	789.88	897.8	881.97
Crystal system	Orthorhombic	Triclinic	Monoclinic	Triclinic
Space group	$P2_12_12_1$	P–1	$P2_1/n$	P–1
a (Å)	11.301(2)	11.3572(7)	19.1300(9)	10.8511(6)
b (Å)	13.968(3)	11.7146(10)	9.7269(3)	11.1779(7)
c (Å)	20.344(3)	13.7193(12)	22.0104(10)	17.2515(10)
α (°)	90	95.488(6)	90	82.595(4)
β (°)	90	105.893(5)	115.313(2)	73.977(3)
γ (°)	90	96.247(5)	90	73.322(3)
V (Å^3)	3211.4(10)	1730.0(2)	3702.4(3)	1923.7(2)
Z	4	2	4	2
D_x (g cm^{-3})	1.53	1.516	1.611	1.523
μ(Mo Kα) (mm^{-1})	0.877	0.819	1.148	0.748
Reflns collected	30577	32670	56273	35910
Indpndt reflns	7935	8558	7566	9179
R_{int}	0.093	0.083	0.108	0.047
R_1[a] (all data)	0.069	0.072	0.065	0.050
wR_2[b] (all data)	0.078	0.093	0.083	0.077
GOF[c] on F^2	0.98	0.989	1.017	1.067

[a] $R_1 = \sum||F_o| - |F_c||/\sum|F_o|$. [b] $wR_2 = [(\sum w(F_o^2 - F_c^2)^2/\sum|F_o|^2)]^{1/2}$. [c] GOF = $[\sum[w(F_o^2 - F_c^2)^2]/(N_o - N_v)]^{1/2}$ (N_o = number of observations; N_v = number of variables).

Part 5 – Cyclic voltammetry

Table S2. Electrochemical data obtained from cyclic voltammetry experiments for compounds **1**–**9**[a]

Complex	$I_{p,ox}$ (mA/cm²)	$I_{p,red}$ (mA/cm²)	$E_{p,ox}$ (V)	$E_{p,red}$ (V)	$E_{1/2}$ (V)[b]
1 (dppm)	0.192	–0.097	0.785	0.551	0.668
2 (dppe)	0.140	–0.107	0.861	0.676	0.769
3 (dppp)	0.183	–0.124	0.857	0.661	0.759
4 (dppb)	0.232	–0.190	0.841	0.645	0.743
5 (dpppe)	0.275	–0.215	0.824	0.655	0.740
6 (dppen)	0.305	–0.227	0.890	0.710	0.800
7 (dppbz)	0.224	–0.174	0.861	0.684	0.773
8 (dppf)	0.121	–0.113	0.764	0.525	0.645
9 (DPEphos)	0.276	–0.238	0.754	0.590	0.672

[a] Peak current densities (I_p) and peak potentials (E_p) correspond to the Ru^{3+}/Ru^{2+} redox couple.

[b] $E_{1/2} = (E_{p,ox} + E_{p,red})/2$.

Part 6 – Catalytic tests

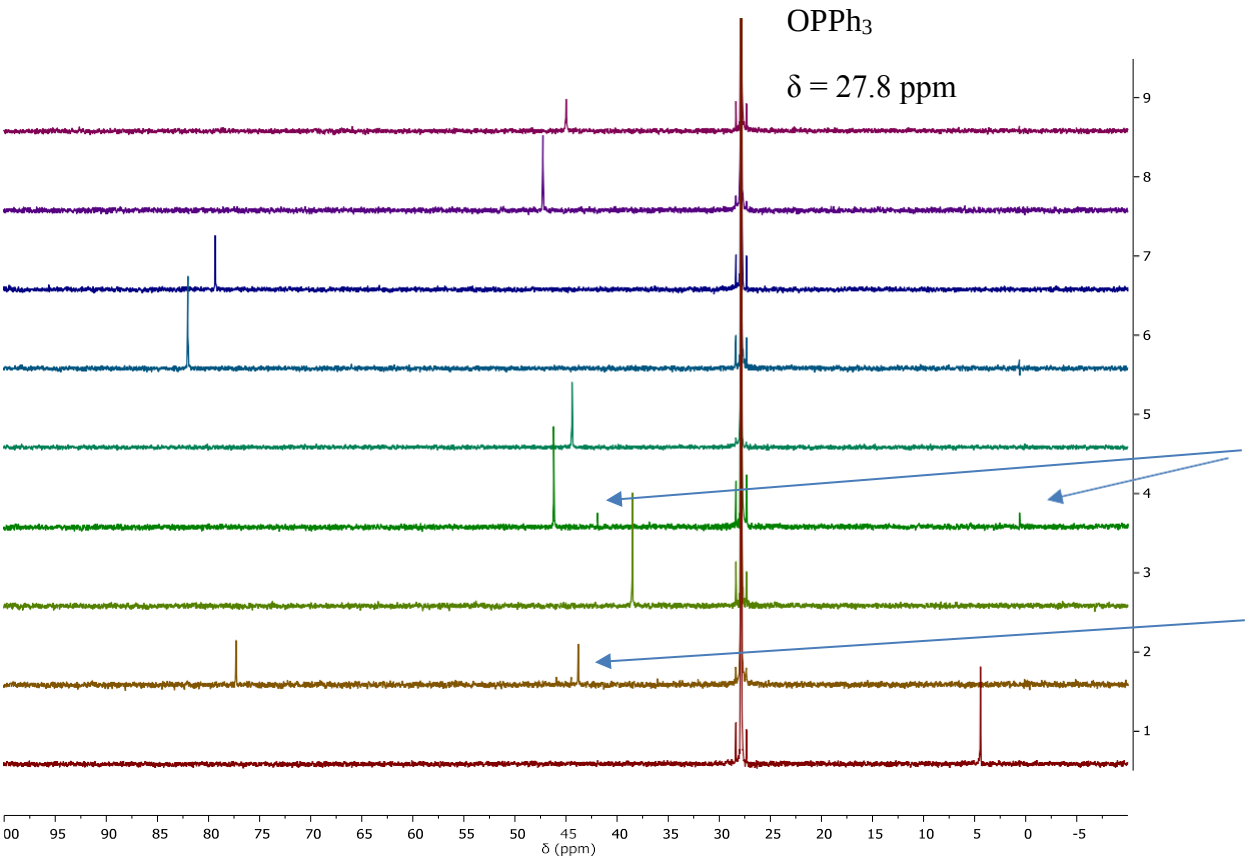

Fig. S70. ^{31}P NMR spectra of the reaction mixtures obtained after heating benzoic acid and 1-hexyne in toluene at 160 °C for 30 min in the presence of [Ru(S_2COEt)$_2$(diphos)] complexes **1**–**9** (a sealed capillary tube containing Ph_3PO in CD_2Cl_2 was used as an external reference)

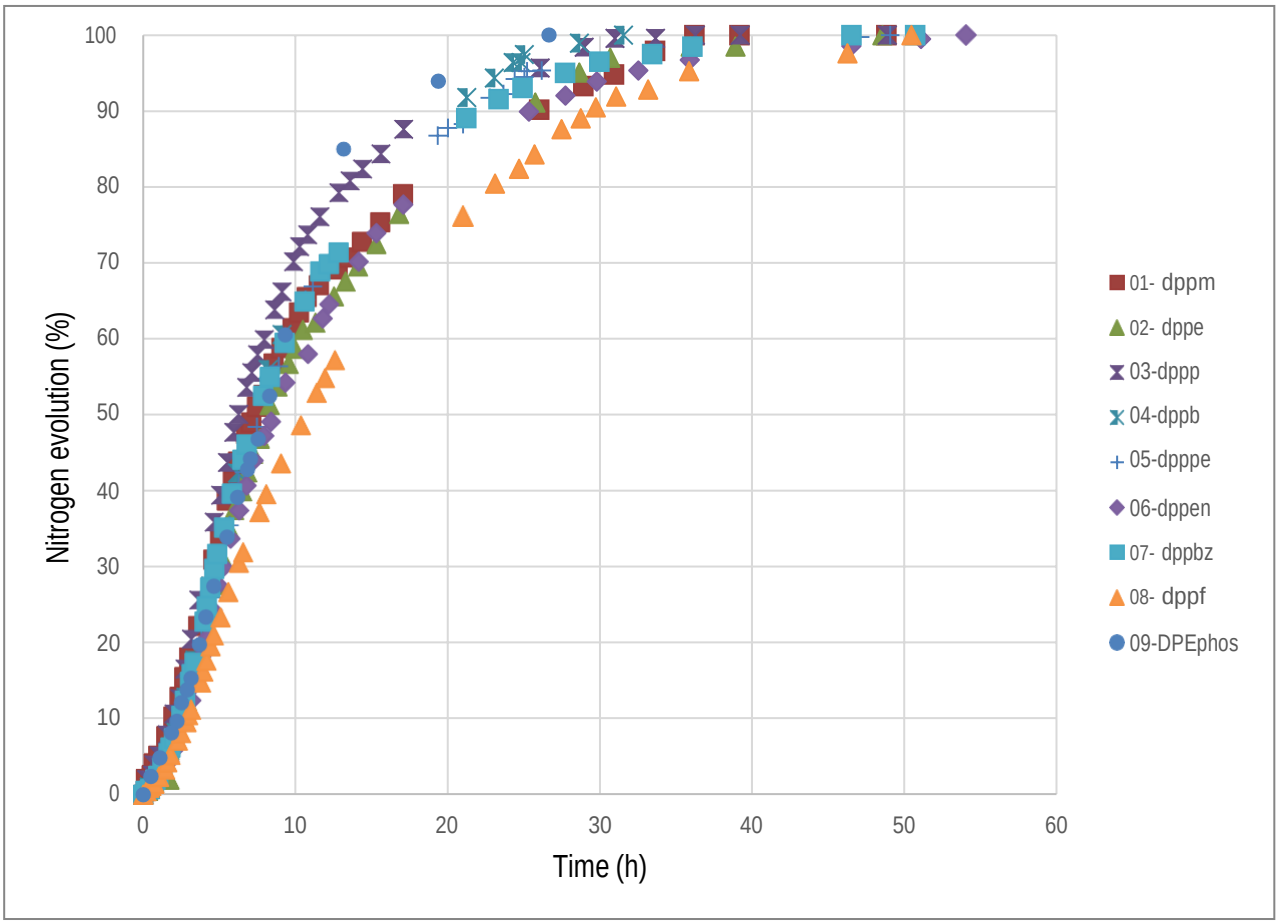

Fig. S71. Rate of nitrogen evolution monitored with a gas burette during the cyclopropanation of styrene catalyzed by [Ru(S_2COEt)$_2$(diphos)] complexes **1**–**9** at 60 °C

I.2. Supporting Information (SI) for Chapter VI: Synthesis of ruthenium–dithiocarbamate chelates bearing diphosphine ligands and their use as latent initiators for atom transfer radical additions

Supporting Information for:

Synthesis of Ruthenium–dithiocarbamate chelates bearing diphosphine ligands and their use as latent initiators for atom transfer radical additions

Mohammed Zain Aldin,[a] Guillermo Zaragoza,[b] and Lionel Delaude*[a]

[a]*Laboratory of Organometallic Chemistry, and Homogeneous Catalysis, Institut de chimie (B6a), Allée du six Août 13, Quartier Agora, Université de Liège, 4000 Liège, Belgium*

[b]*Unidade de Difracción de Raios X, Edificio CACTUS, Universidade de Santiago de Compostela, Campus Vida, 15782 Santiago de Compostela, Spain*

Table of content

Part 1 – Crystallography

Table S1. Crystal data and structure refinement parameters for compounds **1–3, 5–7,** and **9**

Complex	**1**	**2**	**3**	**5**
Chemical formula	$C_{35}H_{42}N_2P_2RuS_4$	$C_{36}H_{44}N_2P_2RuS_4{\cdot}CH_2Cl_2$	$C_{37}H_{46}N_2P_2RuS_4$	$C_{39}H_{50}N_2P_2RuS_4$
M (g mol^{-1})	781.96	880.91	810.01	838.06
Crystal system	Monoclinic	Triclinic	Triclinic	Monoclinic
Space group	$P2_1/c$	$P\bar{1}$	$P\bar{1}$	$P2_1/c$
a (Å)	20.4582(11)	10.4014(4)	12.6008(6)	12.7822(8)
b (Å)	19.0090(9)	11.6818(5)	12.7124(6)	13.4512(7)
c (Å)	27.2173(13)	17.8804(8)	16.4277(8)	22.4769(13)
α (°)	90	71.2956(17)	94.384(2)	90
β (°)	92.745(2)	79.1086(16)	106.523(2)	91.651(2)
γ (°)	90	82.4133(16)	117.583(2)	90
V (Å^3)	10572.4(9)	2014.82(15)	2167.97(18)	3863.0(4)
Z	12	2	2	4
D_x (g cm^{-3})	1.474	1.452	1.241	1.441
μ(Mo Kα) (mm^{-1})	0.80	0.84	0.65	0.74
Reflns collected	563606	60320	92110	210605
Indpndt reflns	26240	9627	10363	7615
R_{int}	0.058	0.052	0.049	0.096
R_1 (all data)	0.033	0.043	0.035	0.071
wR_2 (all data)	0.056	0.079	0.059	0.132
GOF on F^2	1.08	1.07	1.06	1.17

Complex	**6**	**7**	**9**
Chemical formula	$C_{36}H_{42}N_2P_2RuS_4$	$C_{40}H_{44}N_2P_2RuS_4{\cdot}0.746(CH_2Cl_2)$	$C_{46}H_{48}N_2OP_2RuS_4{\cdot}CH_2Cl_2$
M (g mol^{-1})	793.96	907.42	1021.04
Crystal system	Triclinic	Monoclinic	Triclinic
Space group	$P\bar{1}$	$I2/a$	$P\bar{1}$
a (Å)	11.0423(4)	21.6473(14)	11.1974(10)
b (Å)	11.2383(4)	18.4166(8)	11.5952(11)
c (Å)	16.0783(6)	23.184(1)	19.5399(16)
α (°)	98.688(1)	90	96.424(3)
β (°)	99.621(1)	115.268(1)	99.380(3)
γ (°)	102.287(2)	90	110.767(4)
V (Å^3)	1885.73(12)	8358.4(7)	2300.5(4)
Z	2	8	2
D_x (g cm^{-3})	1.398	1.442	1.474
μ(Mo Kα) (mm^{-1})	0.75	0.78	0.75
Reflns collected	32209	78625	145493
Indpndt reflns	7711	9972	14035
R_{int}	0.082	0.057	0.059
R_1 (all data)	0.070	0.052	0.044
wR_2 (all data)	0.087	0.081	0.063
GOF on F^2	1.05	1.02	1.05

Table S2. Selected bond distances (Å) and angles (°) derived from the molecular structures of complexes **1–9**[a]

Complex	**1**[b]	**1a**	**1b**	**1c**	**2**	**3**	**4**[c]	**5**	**6**	**7**	**8**[d]	**9**
Ru(1)–P(1)	2.241(1)	2.2644(5)	2.2576(5)	2.2634(5)	2.2472(6)	2.2644(5)	2.2772(9)	2.2884(12)	2.2313(10)	2.2535(7)	2.3174(18)	2.3089(5)
Ru(1)–P(2)		2.2582(4)	2.2412(5)	2.2730(5)	2.2479(6)	2.2664(5)	2.2917(9)	2.3019(12)	2.2458(10)	2.2519(7)	2.3174(18)	2.3103(5)
Ru(1)–S(1)	2.384(1)	2.3960(4)	2.4015(4)	2.4155(5)	2.3957(6)	2.4017(5)	2.4054(9)	2.3917(13)	2.4044(10)	2.4002(7)	2.4109(16)	2.3966(5)
Ru(1)–S(2)	2.469(1)	2.4657(4)	2.4601(4)	2.4505(5)	2.4609(6)	2.4547(5)	2.4503(9)	2.4460(12)	2.4621(10)	2.4387(6)	2.4175(18)	2.4445(5)
Δ (Ru-S)	0.085	0.0697	0.0586	0.035	0.0652	0.053	0.0449	0.0543	0.0577	0.0385	0.066	0.0479
Ru(1)–S(3)		2.4004(4)	2.3860(4)	2.3822(5)	2.3966(6)	2.3942(5)	2.4088(9)	2.401(7)	2.3836(9)	2.3959(6)	2.4109(16)	2.4054(5)
Ru(1)–S(4)		2.4511(4)	2.4613(5)	2.4631(5)	2.4650(6)	2.4915(5)	2.4665(9)	2.449(4)	2.4577(10)	2.4510(7)	2.4175(18)	2.4409(5)
Δ (Ru-S)		0.0507	0.0753	0.0809	0.0684	0.0973	0.0577	0.048	0.0741	0.0551	0.066	0.0355
C(1)–S(1)	1.726(3)	1.7213(17)	1.7200(17)	1.7164(18)	1.713(2)	1.7205(19)	1.712(4)	1.715(5)	1.712(4)	1.717(3)	1.715(7)	1.7172(17)
C(1)–S(2)	1.719(4)	1.7180(17)	1.7181(17)	1.7155(118)	1.720(2)	1.707(2)	1.725(4)	1.712(5)	1.724(4)	1.716(2)	1.718(7)	1.7093(17)
C(1)–N(1)	1.321(5)	1.338(2)	1.333(2)	1.340(2)	1.333(3)	1.336(2)	1.336(4)	1.328(6)	1.333(5)	1.336(3)	1.329(9)	1.335(2)
P(1)–Ru(1)–P(2)	73.07(3)	72.726(16)	72.770(16)	**72.695(18)**	86.12(2)	91.467(17)	93.31(3)	95.75(4)	84.95(4)	85.03(2)	**100.64(9)**	99.026(17)
S(1)–Ru(1)–S(2)	72.02(3)	71.814(15)	72.054(15)	71.662(15)	71.58(2)	71.663(16)	71.97(3)	71.81(4)	71.75(3)	72.21(2)	71.94(6)	71.992(15)
S(1)–C(1)–S(2)	111.9(2)	112.03(9)	112.57(9)	112.21(10)	111.70(13)	112.09(10)	112.22(19)	111.8(3)	121.1(3)	112.31(14)	111.4(4)	112.29(10)
S(1)–C(1)–N(1)–C(2)	0.5(5)	-9.3(2)	7.9(2)	-7.7(2)	0.9(3)	-3.9(3)	-0.1(5)	-4.0(7)	3.5(5)	3.4(3)	-3.33(5)	0.1(2)

[a] See Fig. 1 for ORTEP plots and Chart 3 for atom labeling. [b] CCDC 626124. [c] CCDC 1002168. [d] CCDC 202635.

Table S3. Measurement of the distortion from the octahedral geometry in the molecular structures of complexes **1–9**

Complex	**1**[b]	**1a**	**1b**	**1c**	**2**	**3**	**4**[c]	**5**	**6**	**7**	**8**[d]	**9**
Vp (volume polyhedral)		16.87	16.79	16.87	17.07	17.20	17.30	17.206	16.96	16.94	17.14	17.32
Qe (quadratic elongation)		1.04	1.04	1.04	1.03	1.03	1.03	1.03	1.03	1.03	1.03	1.03
Av (angular variance)		130.31	127.69	136.78	87.87	95.22	96.68	99.51	88.26	95.95	113.74	95.04

[a] See Fig. 1 for ORTEP plots and Chart 3 for atom labeling. [b] CCDC 626124. [c] CCDC 1002168. [d] CCDC 202635.

Part 2 – Mass spectrometry

2.1 Experimental procedures

Complexes **1**–**9** were dissolved in a mixture of CH_3CN and CH_2Cl_2 (50/50 v/v). Exact masses were determined by infusing the samples on a Bruker Daltonics SolariX XR 9.4 T spectrometer equipped with an electrospray ionization (ESI) source operating in the positive ion mode. An average MS spectrum was generated from the accumulation of 20 scans within a mass range from m/z = 100 to 2000 and a file size of 2 M (expected mass resolving power: 130000 at m/z 400). The ESI capillary voltage and the end plate offset were set to 4.5 kV and –500 V, respectively. The other optimized settings were as followed: a nebulizer gas pressure of 0.2 bar, a dry gas flow rate of 4.0 L/min, a dry gas temperature of 225 °C, and a quadrupole ion accumulation time of 0.3 s. The mass analyzer was systematically calibrated in the positive ion mode from m/z = 196 ($[(H_3PO_4)_2+H]^+$) to 1372 ($[(H_3PO_4)_{14}+H]^+$) using a 0.8% H_3PO_4 solution in CH_3CN:H_2O 50/50 v/v infused at 4 μL.min^{-1}.

Collision-induced dissociation (CID) experiments were also performed to generate MS/MS spectra. For MS/MS spectral collection, the precursor ions were selected with a mass range window of m/z ± 10 to allow the mass selection of all the isotopes of ruthenium-containing compounds. They were fragmented by CID in the collision cell with a collision energy set at 40 V for all compounds except for the most stable [Ru(S_2CNEt_2)$_2$(DPEphos)] complex (**9**), which required a CID energy of 55 V.

2.2 MS spectra

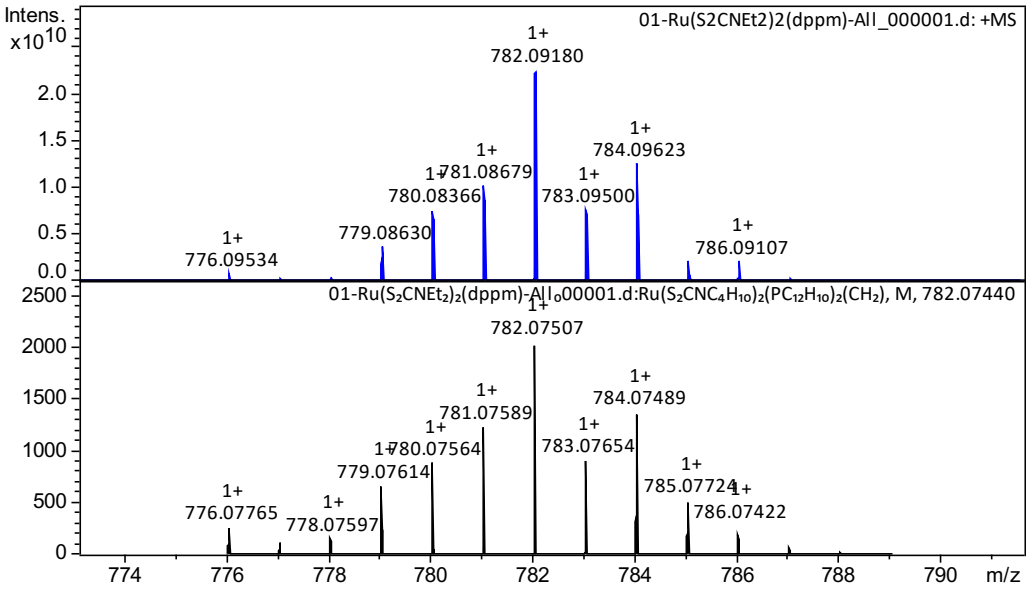

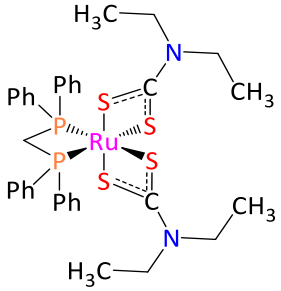

CF: $C_{35}H_{42}N_2P_2RuS_4$
Exact Mass: 782.07495

Fig. S1. Isotope profile of [Ru(S_2CNEt_2)$_2$(dppm)] (**1**) obtained by ESI-MS (top) and simulated isotope pattern of the corresponding ion (bottom)

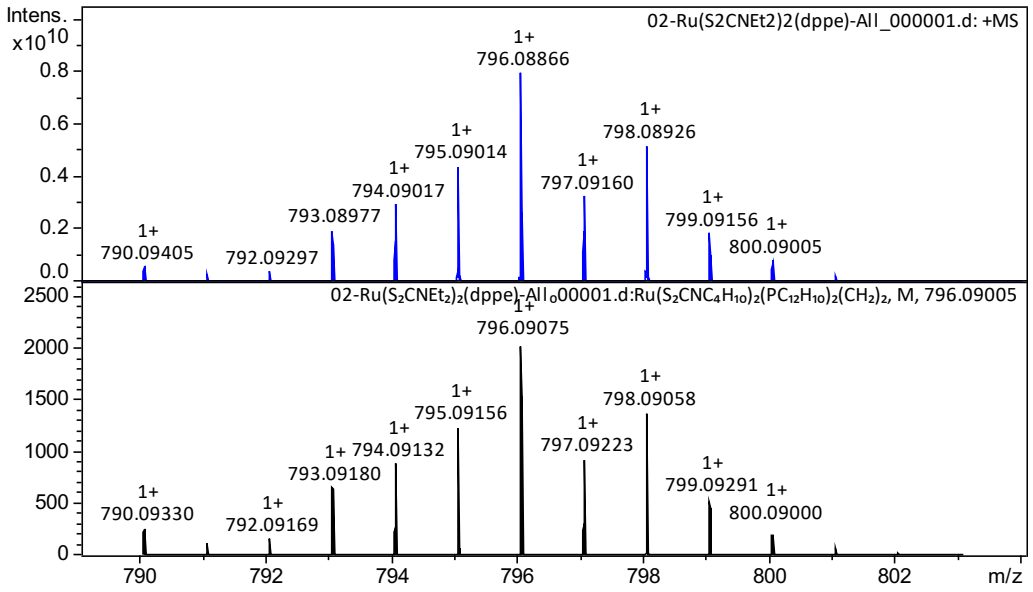

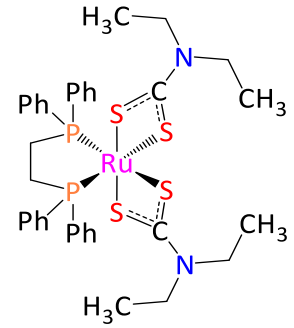

CF: $C_{36}H_{44}N_2P_2RuS_4$
Exact Mass: 796.09060

Fig. S2. Isotope profile of [Ru(S_2CNEt_2)$_2$(dppe)] (**2**) obtained by ESI-MS (top) and simulated isotope pattern of the corresponding ion (bottom)

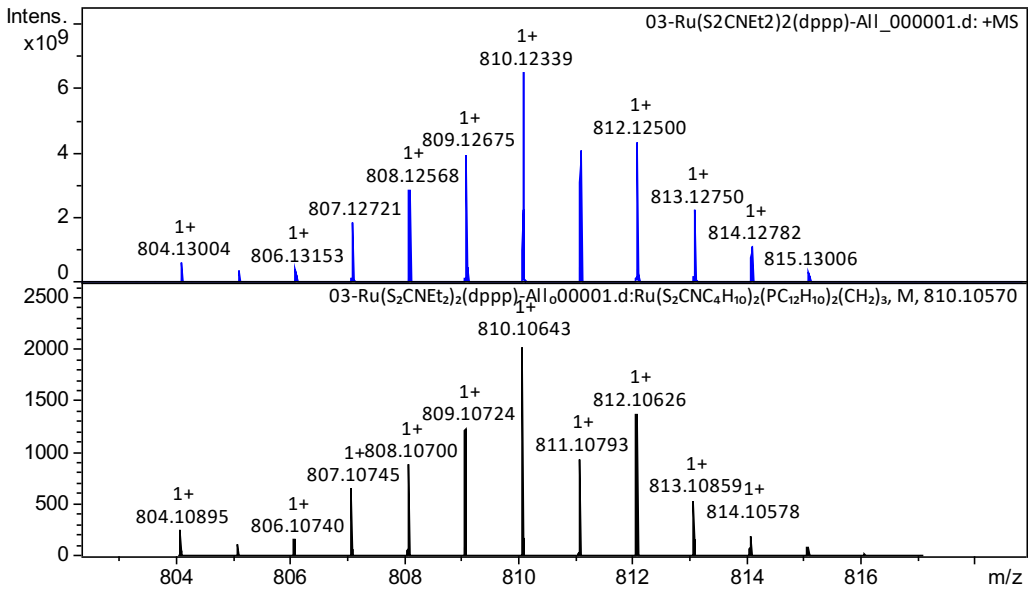

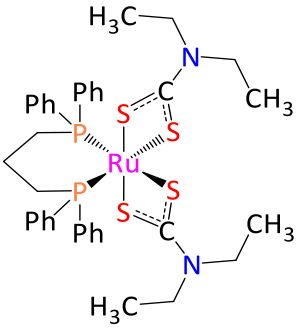

CF: $C_{37}H_{46}N_2P_2RuS_4$
Exact Mass: 810.10625

Fig. S3. Isotope profile of [Ru(S_2CNEt_2)$_2$(dppp)] (**3**) obtained by ESI-MS (top) and simulated isotope pattern of the corresponding ion (bottom)

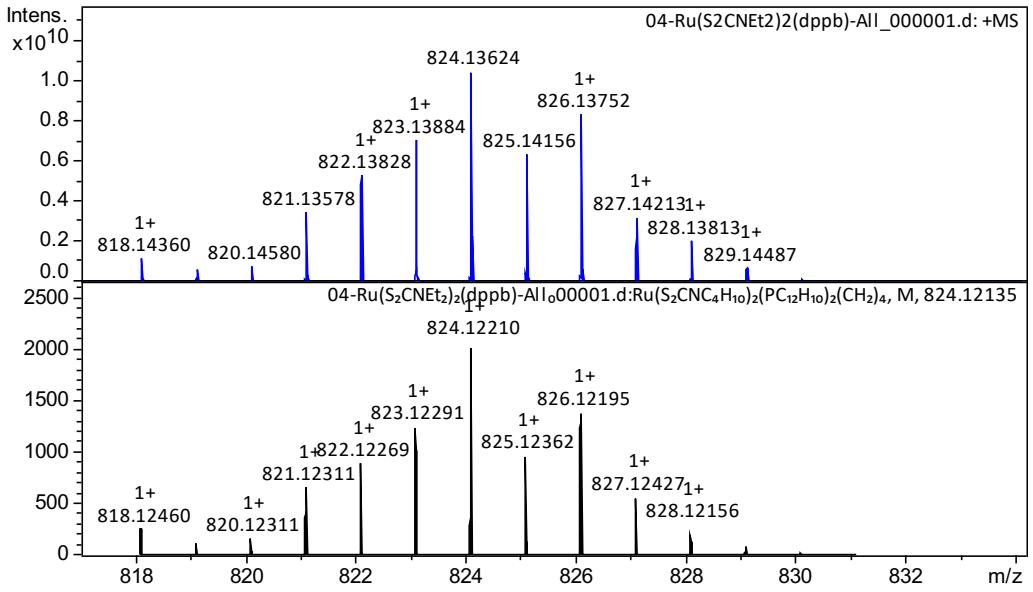

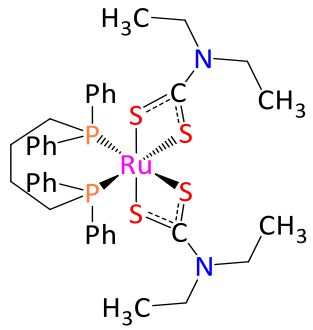

CF: $C_{38}H_{48}N_2P_2RuS_4$

Exact Mass: 824.12190

Fig. S4. Isotope profile of [Ru(S_2CNEt_2)$_2$(dppb)] (**4**) obtained by ESI-MS (top) and simulated isotope pattern of the corresponding ion (bottom)

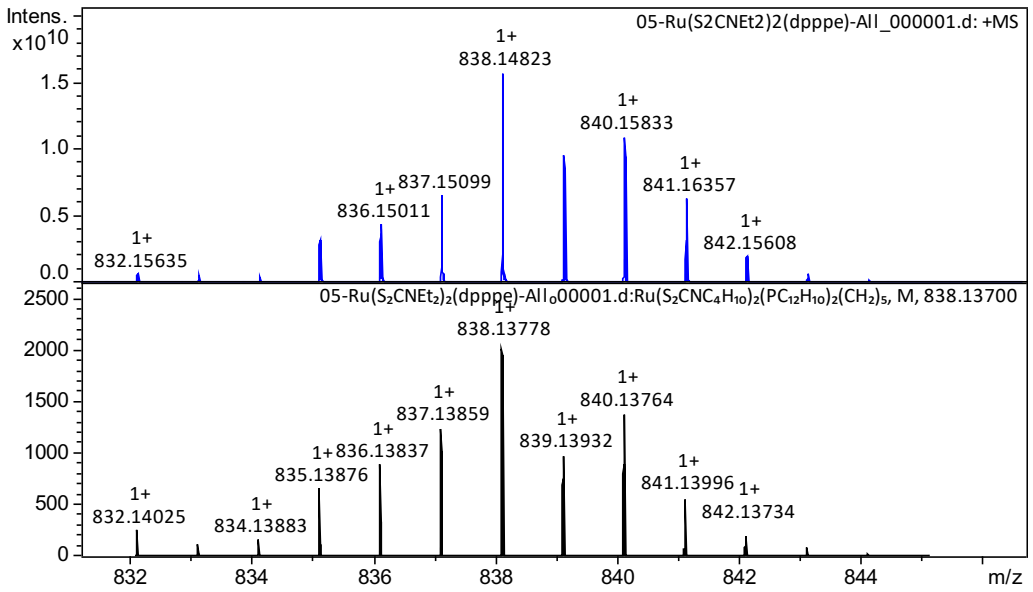

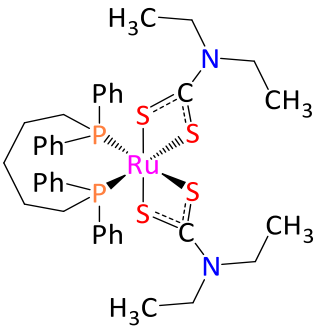

CF: $C_{39}H_{50}N_2P_2RuS_4$

Exact Mass: 838.13755

Fig. S5. Isotope profile of [Ru(S_2CNEt_2)$_2$(dpppe)] (**5**) obtained by ESI-MS (top) and simulated isotope pattern of the corresponding ion (bottom)

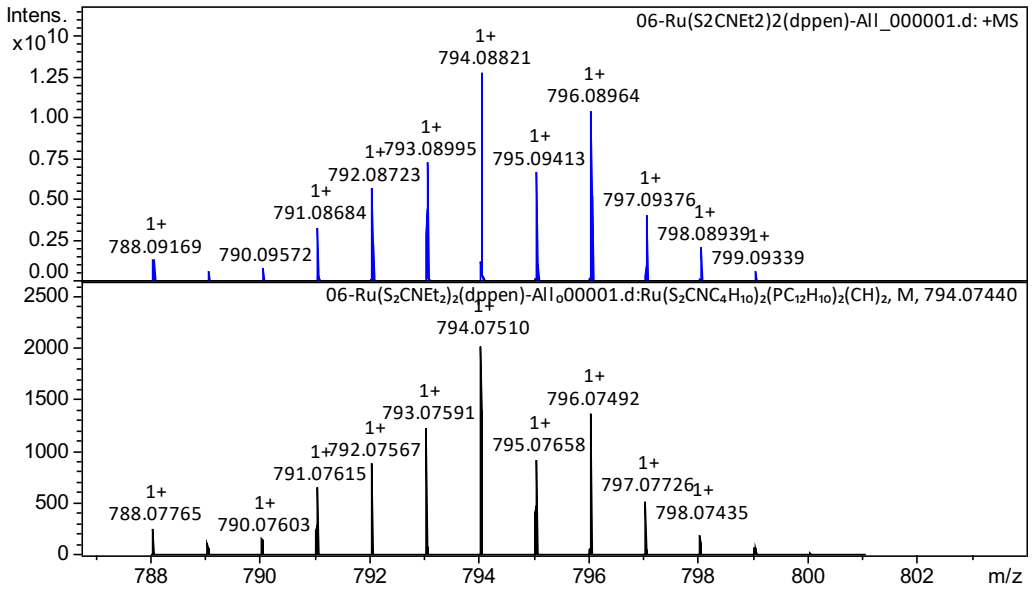

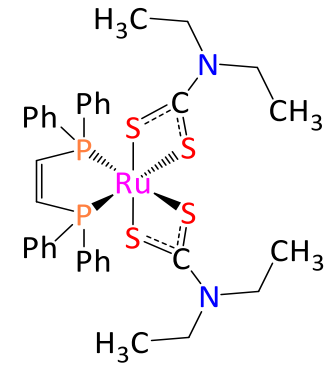

CF: $C_{36}H_{42}N_2P_2RuS_4$

Exact Mass: 794.07495

Fig. S6. Isotope profile of [Ru(S_2CNEt_2)$_2$(dppen)] (**6**) obtained by ESI-MS (top) and simulated isotope pattern of the corresponding ion (bottom)

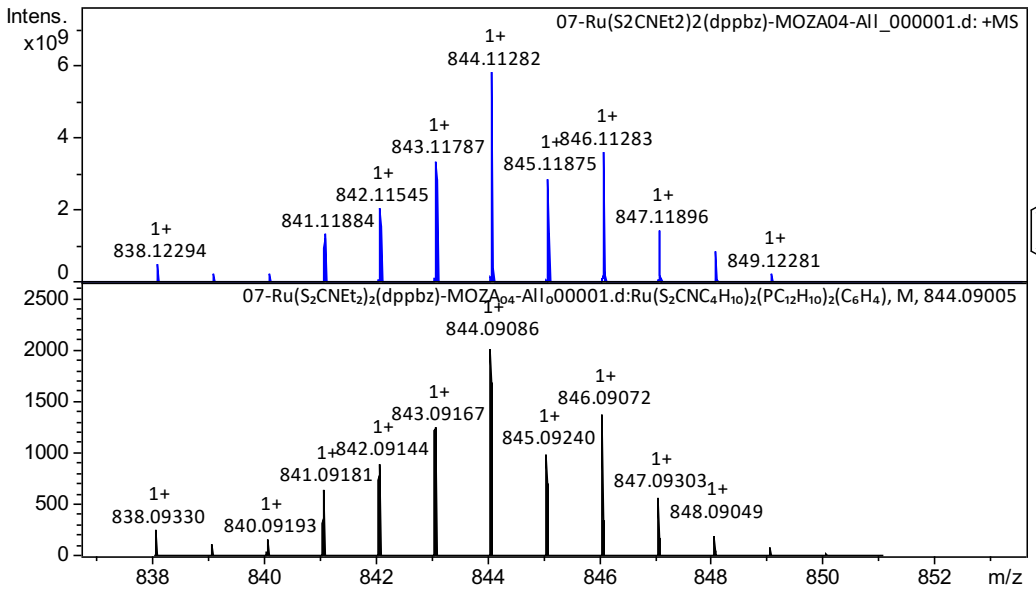

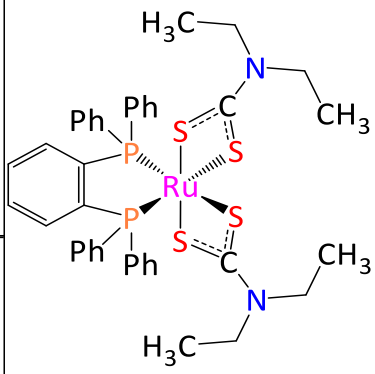

CF: $C_{40}H_{44}N_2P_2RuS_4$

Exact Mass: 844.09060

Fig. S7. Isotope profile of [Ru(S_2CNEt_2)$_2$(dppbz)] (**7**) obtained by ESI-MS (top) and simulated isotope pattern of the corresponding ion (bottom)

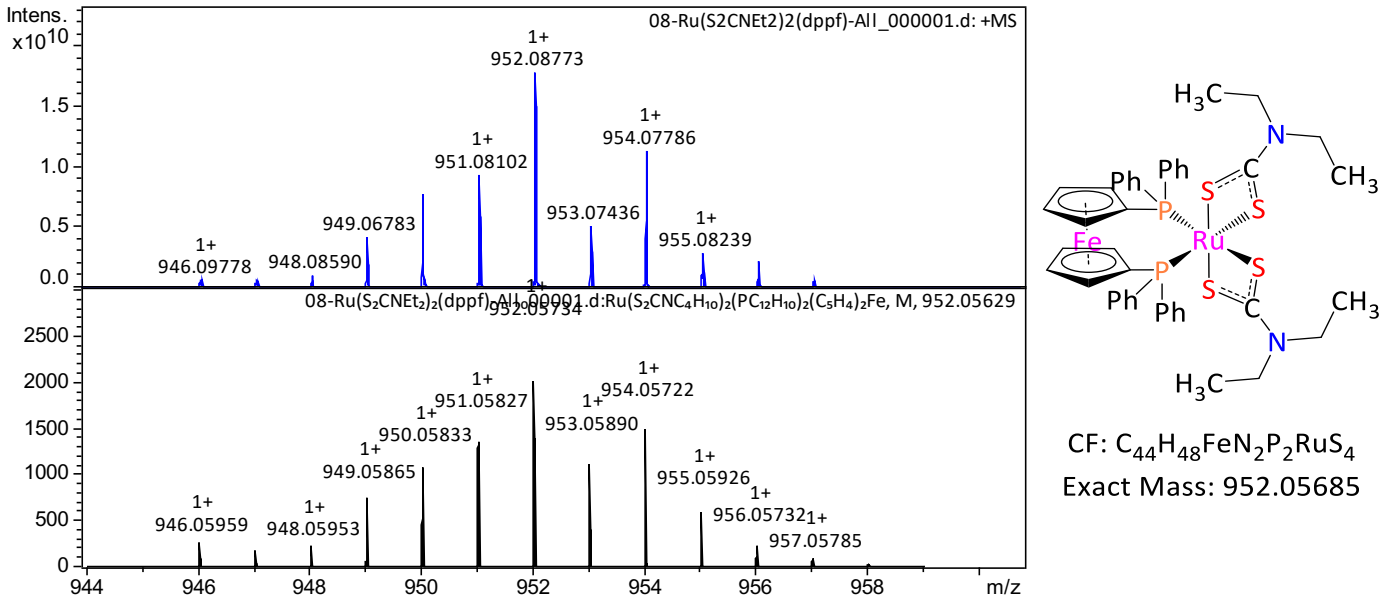

Fig. S8. Isotope profile of [Ru(S_2CNEt_2)$_2$(dppf)] (**8**) obtained by ESI-MS (top) and simulated isotope pattern of the corresponding ion (bottom)

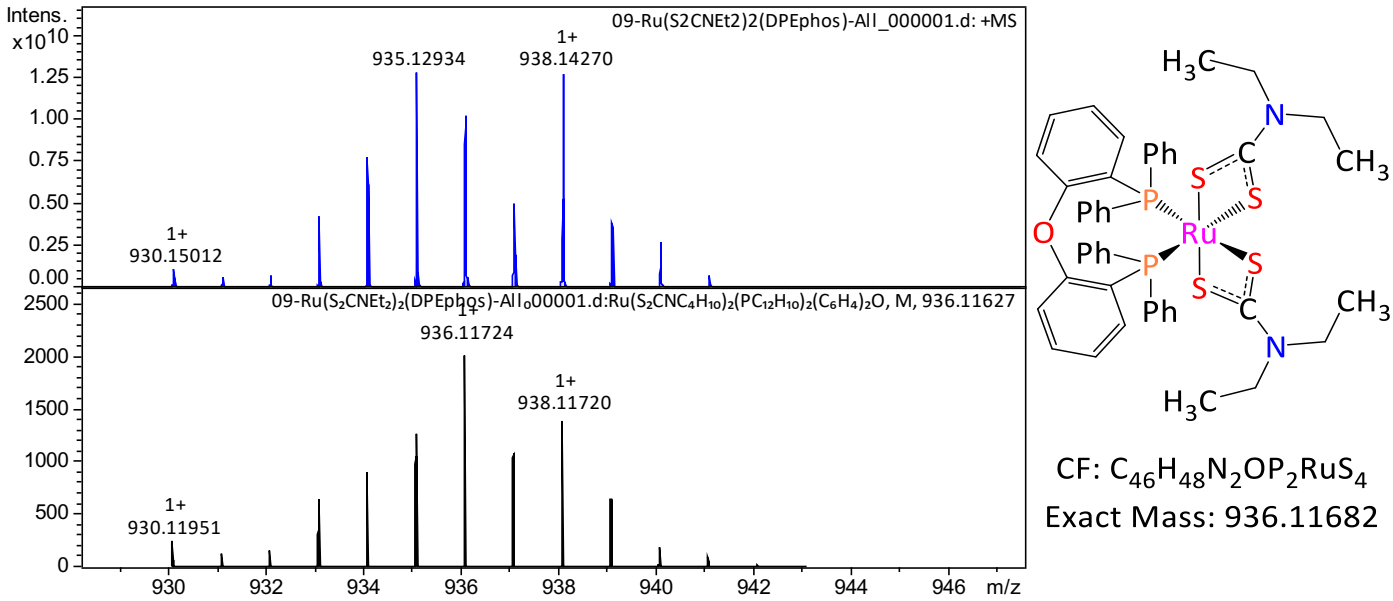

Fig. S9. Isotope profile of [Ru(S_2CNEt_2)$_2$(DPEphos)] (**9**) obtained by ESI-MS (top) and simulated isotope pattern of the corresponding ion (bottom)

2.3 MS/MS spectra

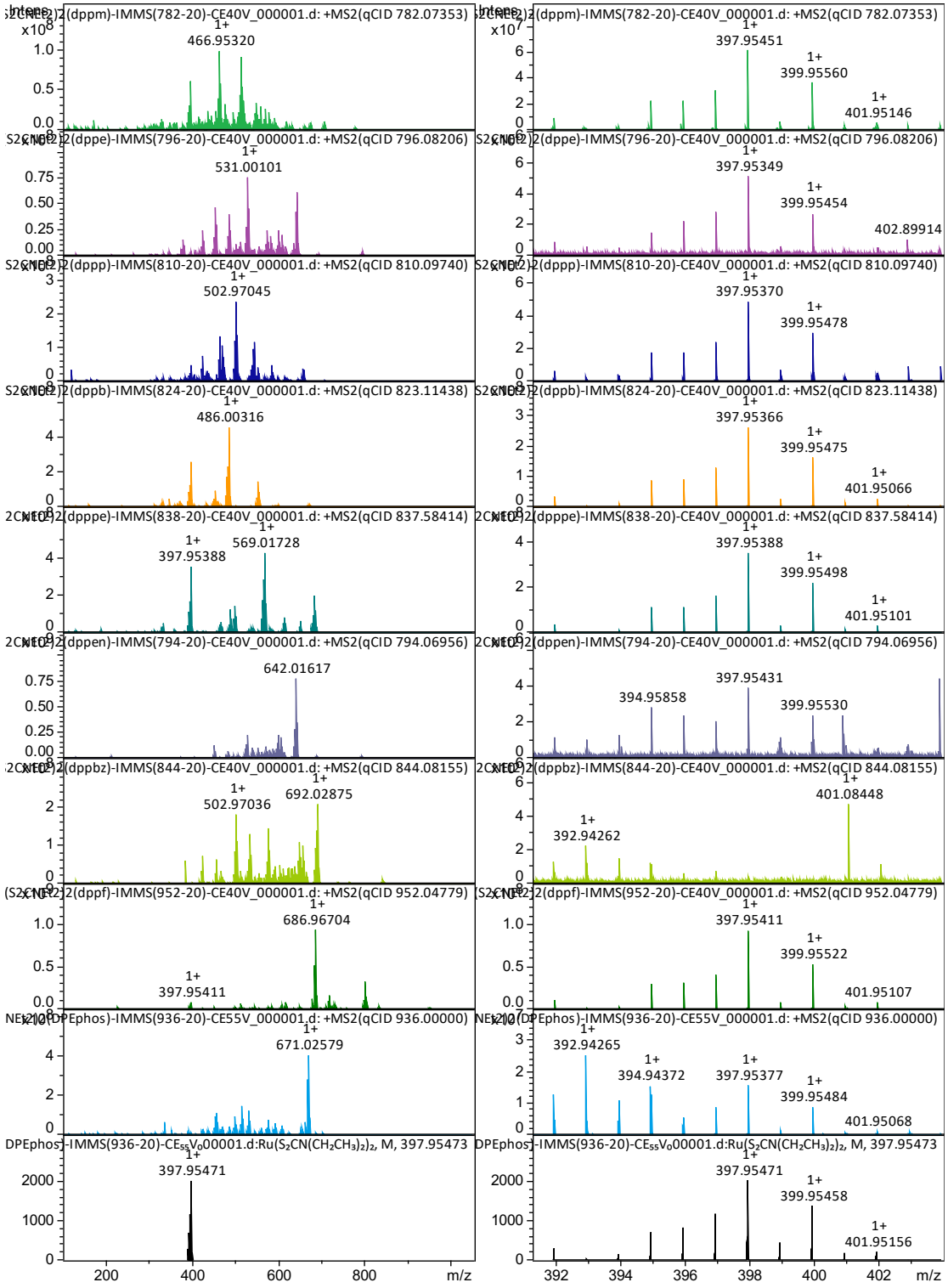

Fig. S10. MS/MS spectra of the [Ru $S_2CNEt_2)_2$(diphos)] complexes **1**–**9** and simulated isotope pattern for the $[Ru(S_2CNEt_2)_2]^+$ cation

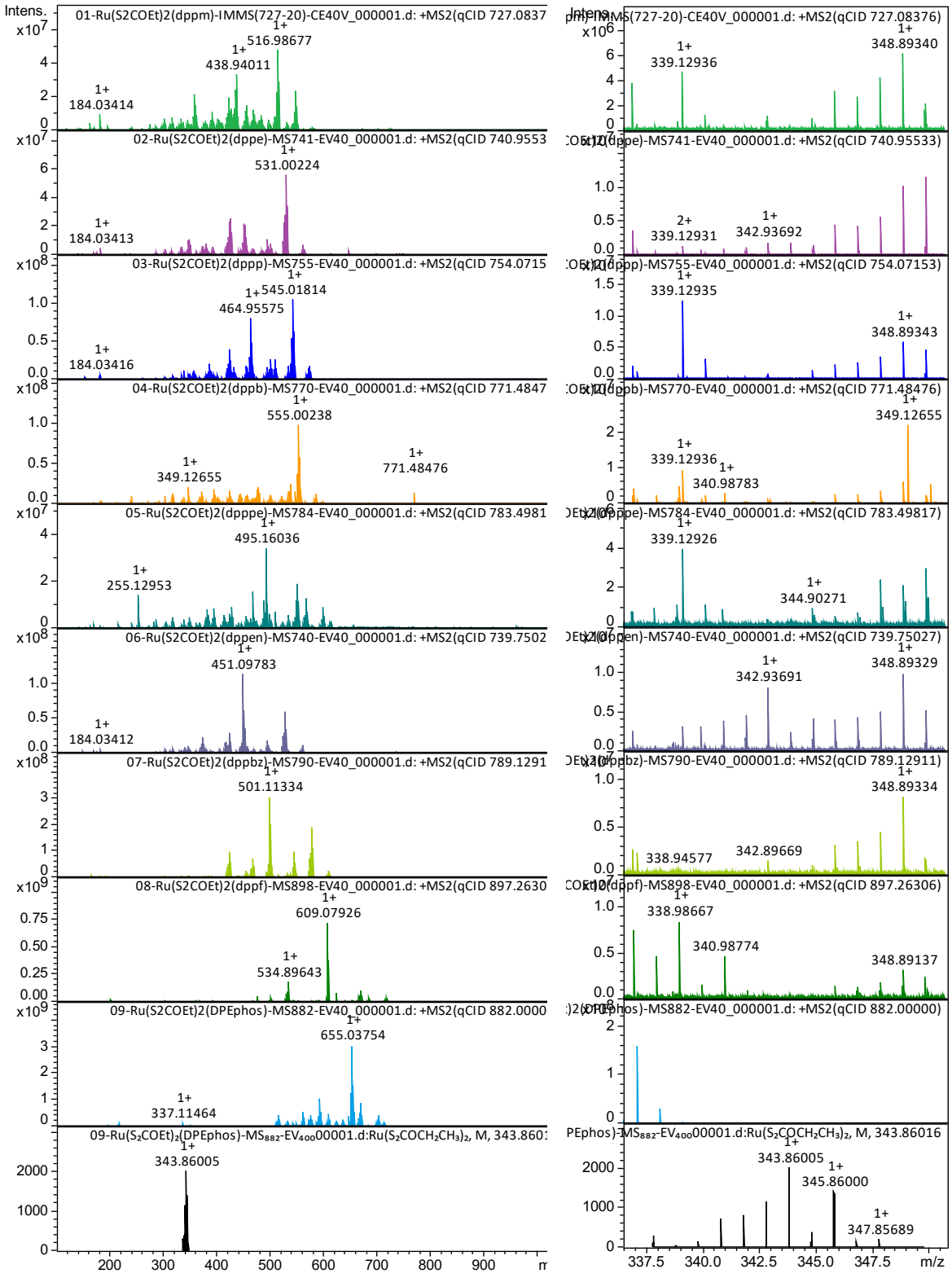

Fig. S11. MS/MS spectra of the $[Ru(S_2COEt)_2(diphos)]$ complexes and simulated isotope pattern for the $[Ru(S_2COEt)_2]^+$ cation

Part 3 – Catalytic tests

3.1 Cyclopropanation of styrene with ethyl diazoacetate

A 10 mL vial equipped with a magnetic stirring bar and a septum was charged with a [Ru(S_2CNEt_2)$_2$(diphos)] complex (5 μmol), styrene (1 mL), and chlorobenzene (1 mL). The mixture was stirred in an oil bath thermostated at 60 °C. Ethyl diazoacetate (120 ± 5 mg, 1 mmol) was diluted up to 1 mL with chlorobenzene in a 1 mL syringe. This solution was added dropwise to the reaction mixture in 4.5 h using a syringe pump. Stirring was maintained for an additional 43.5 h at 60 °C. The rate of nitrogen evolution was monitored with a water column connected to the reaction flask via the septum and a metallic cannula. After a total reaction time of 48 h, the reaction mixture was analyzed by gas chromatography and its composition was established by comparison with authentic samples.

Table S4. Cyclopropanation of styrene catalyzed by ruthenium complexes **1–9**

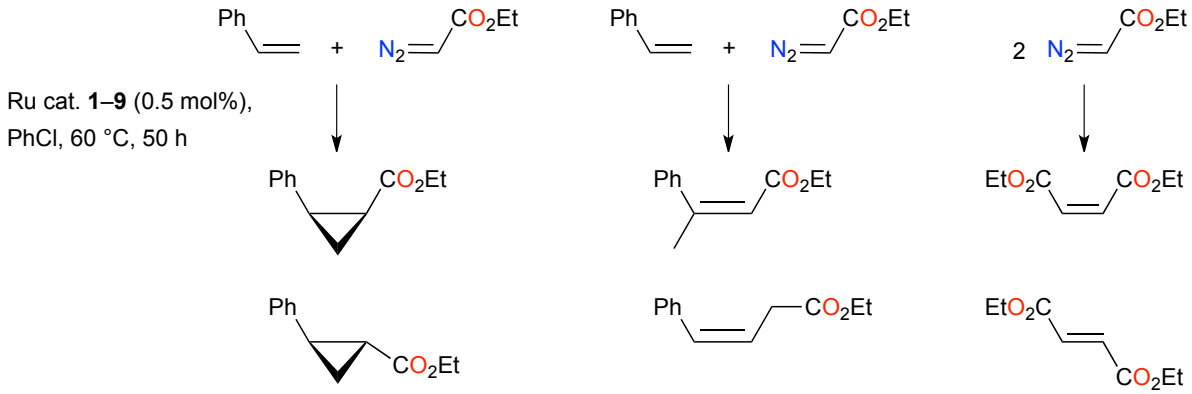

	Cyclopropanation		Homologation	Dimerization	
	Yield (%)	*cis*/*trans* ratio	Yield (%)	Yield (%)	*cis*/*trans* ratio
[Ru(S_2CNEt_2)$_2$(dppm)] (**1**)	92	0.32	2	7	1.59
[Ru(S_2CNEt_2)$_2$(dppe)] (**2**)	93	0.31	1	6	1.67
[Ru(S_2CNEt_2)$_2$(dppp)] (**3**)	90	0.29	3	7	1.74
[Ru(S_2CNEt_2)$_2$(dppb)] (**4**)	91	0.29	2	7	2.57
[Ru(S_2CNEt_2)$_2$(dpppe)] (**5**)	91	0.32	1	7	4.94
[Ru(S_2CNEt_2)$_2$(dppen)] (**6**)	94	0.32	1	4	2.09
[Ru(S_2CNEt_2)$_2$(dppbz)] (**7**)	94	0.29	1	5	1.21
[Ru(S_2CNEt_2)$_2$(dppf)] (**8**)	93	0.30	2	5	5.11
[Ru(S_2CNEt_2)$_2$(DPEphos)] (**9**)	91	0.28	1	8	4.95

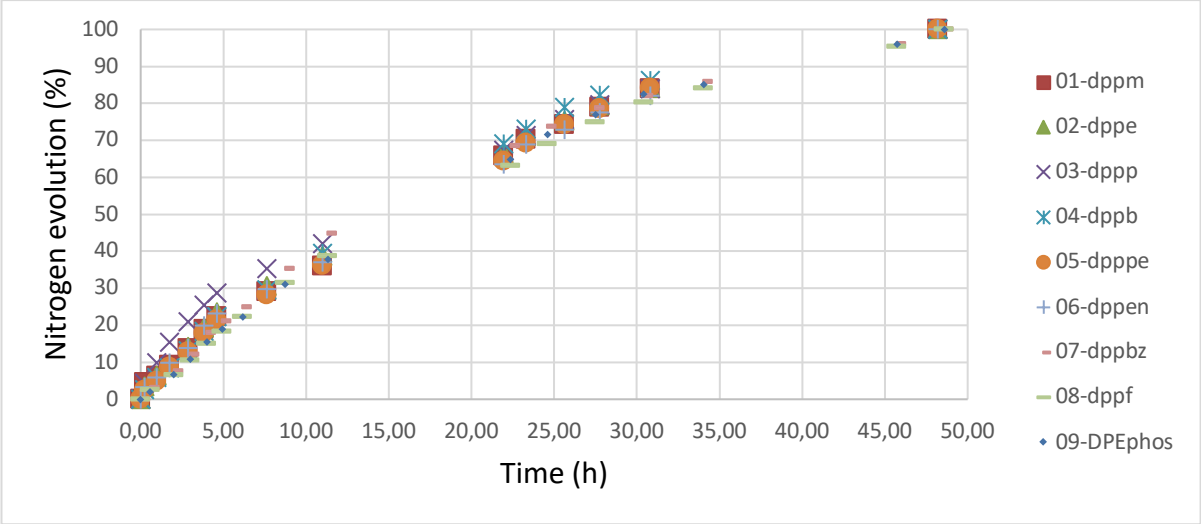

Fig. S12. Rate of nitrogen evolution monitored with a gas burette during the cyclopropanation of styrene catalyzed by [Ru(S_2CNEt_2)$_2$(diphos)] chelates **1–9** at 60 °C

3.2 Synthesis of vinyl esters (enol esters)

A 10 mL pressure vial containing a magnetic stirring bar was charged with a [Ru(S_2CNEt_2)$_2$-(diphos)] complex (4 μmol) and benzoic acid (61.1 mg, 0.5 mmol). The reactor was purged of air by applying five vacuum/nitrogen cycles before a stock solution of 1-hexyne (0.75 mmol) and isooctane (0.13 mmol) in dry toluene was added (2.6 mL). The vial was capped and heated to 160 °C in a CEM Discover microwave reactor with a 170 W maximum power. It was held at that temperature for 30 min. After rapid air-cooling by the unit, the reaction mixture was analyzed by gas chromatography using isooctane as an internal standard.

Table S5. Synthesis of vinyl esters catalyzed by ruthenium complexes **1–9**

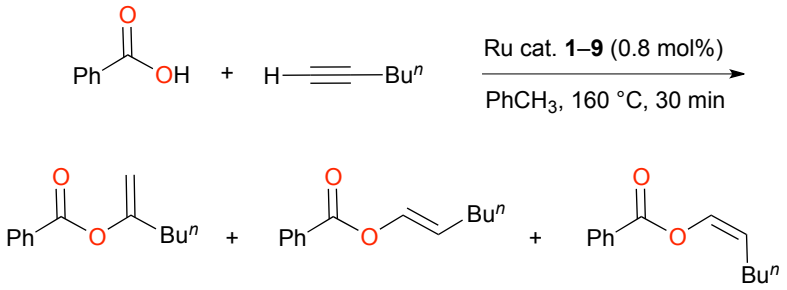

Catalyst	Conversion (%)	Product selectivity		
		Branched	(*Z*)-Linear	(*E*)-Linear
[Ru(S_2CNEt_2)$_2$(dppm)] (**1**)	4	26	45	29
[Ru(S_2CNEt_2)$_2$(dppe)] (**2**)	4	32	43	25
[Ru(S_2CNEt_2)$_2$(dppp)] (**3**)	4	38	40	22
[Ru(S_2CNEt_2)$_2$(dppb)] (**4**)	3	34	47	19
[Ru(S_2CNEt_2)$_2$(dpppe)] (**5**)	5	34	31	35
[Ru(S_2CNEt_2)$_2$(dppen)] (**6**)	5	22	41	37
[Ru(S_2CNEt_2)$_2$(dppbz)] (**7**)	10	30	44	26
[Ru(S_2CNEt_2)$_2$(dppf)] (**8**)	5	30	42	28
[Ru(S_2CNEt_2)$_2$(DPEphos)] (**9**)	2	21	43	35

3.3 ATRA of carbon tetrachloride to methyl methacrylate

General procedure for the reactions with a 0.05 mol% catalyst loading: The $[Ru(S_2CNEt_2)_2$-(dppm)] complex (**1**) (4.7 mg, 6 μmol) was dissolved in dichloromethane (1 mL). Using a syringe, 0.2 mL of this solution was transferred into a 10 mL pressure vial containing a magnetic stirring bar. The solvent was removed under vacuum and the reactor was purged of air by applying five vacuum/nitrogen cycles before a stock solution (1.2 mL) containing methyl methacrylate (2 M), carbon tetrachloride (8 M), and dodecane (0.3 M) was added. The vial was capped with a septum under nitrogen, heated to 160 °C (monitored by an IR sensor) under microwave irradiation, and held at that temperature for various periods of time. After rapid air-cooling by the unit, the reaction mixture was analyzed by gas chromatography using dodecane as an internal standard. The results are listed below.

Table S6. ATRA of MMA and CCl_4 catalyzed by $[Ru(S_2CNEt_2)_2(dppm)]$ (**1**)

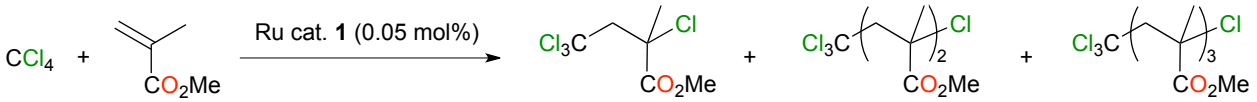

Time (h)	Conv. (%)	TOF (h^{-1})	Mono (%)	Di (%)	Tri (%)	Mono/Bi
0.25	26	2080	61	35	3	1.72
0.50	38	1500	65	32	3	2.03
0.75	56	1493	69	27	3	2.52
1.00	68	1360	74	23	3	3.18
1.25	89	1424	80	18	2	4.50
1.50	100	**1333**	82	16	2	5.03
2.00	100	1000	83	16	2	5.21

Part 4 – NMR spectra

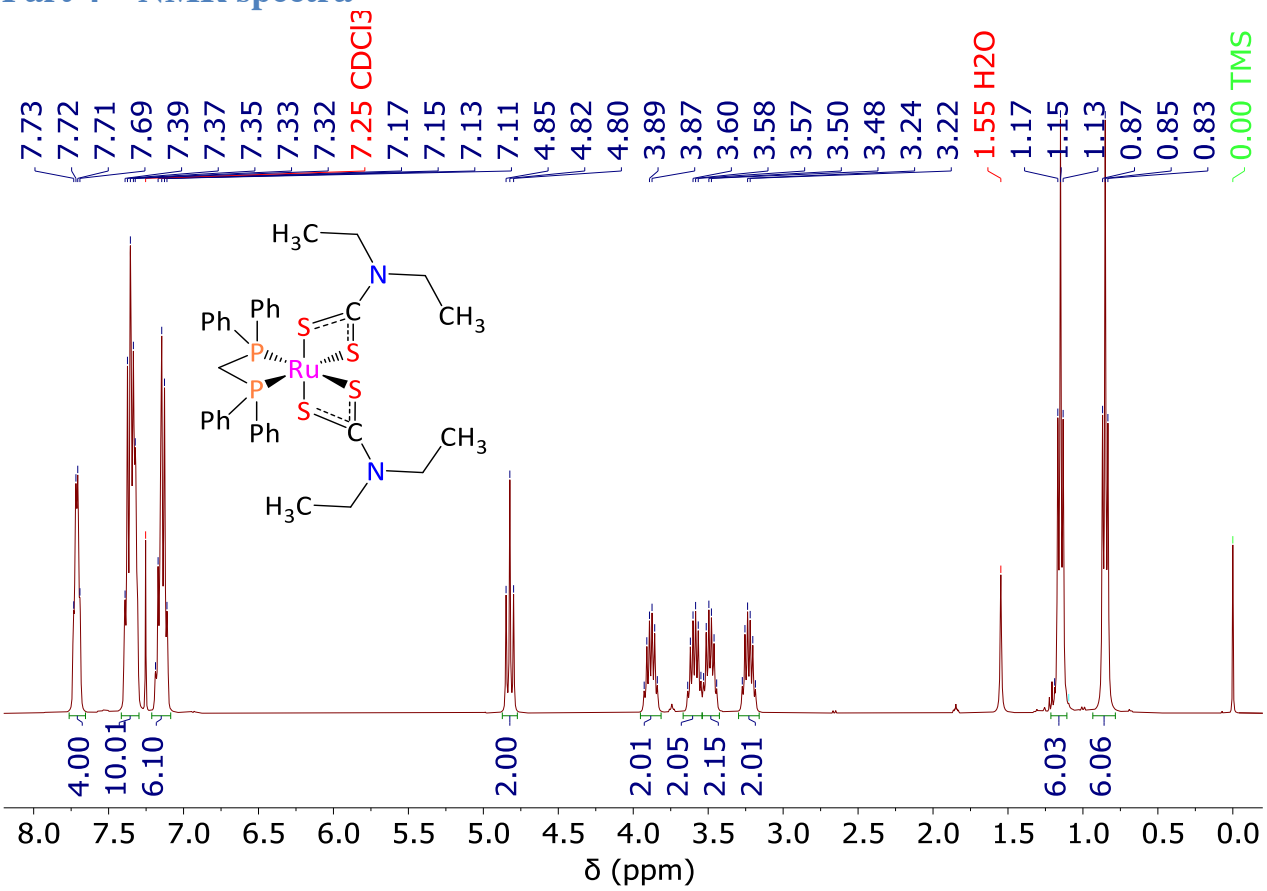

Fig. S13. ^{1}H NMR spectrum (400 MHz, $CDCl_3$, 298 K) of [Ru(S_2CNEt_2)$_2$(dppm)] (**1**)

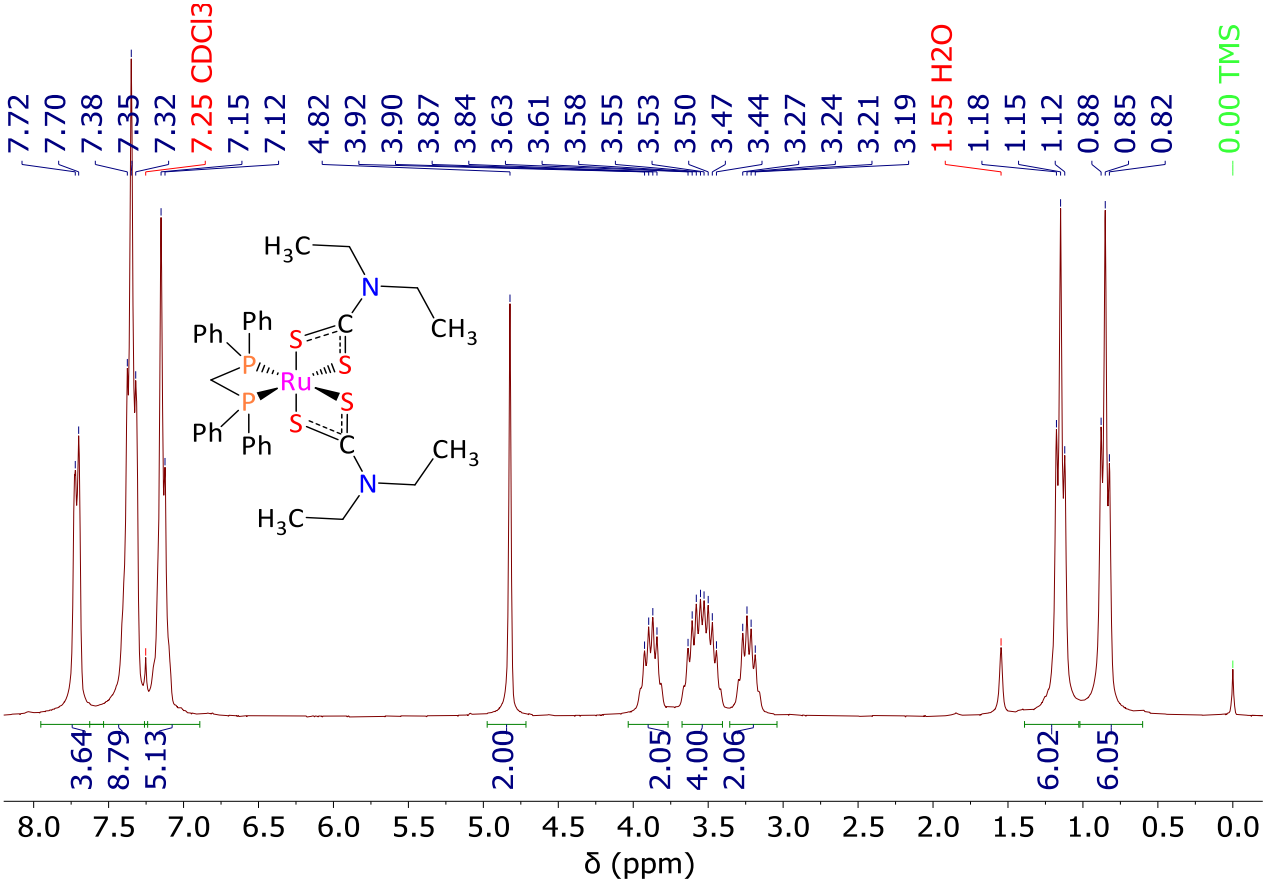

Fig. S14. ^{1}H{^{31}P} NMR spectrum (250 MHz, $CDCl_3$, 298 K) of [Ru(S_2CNEt_2)$_2$(dppm)] (**1**)

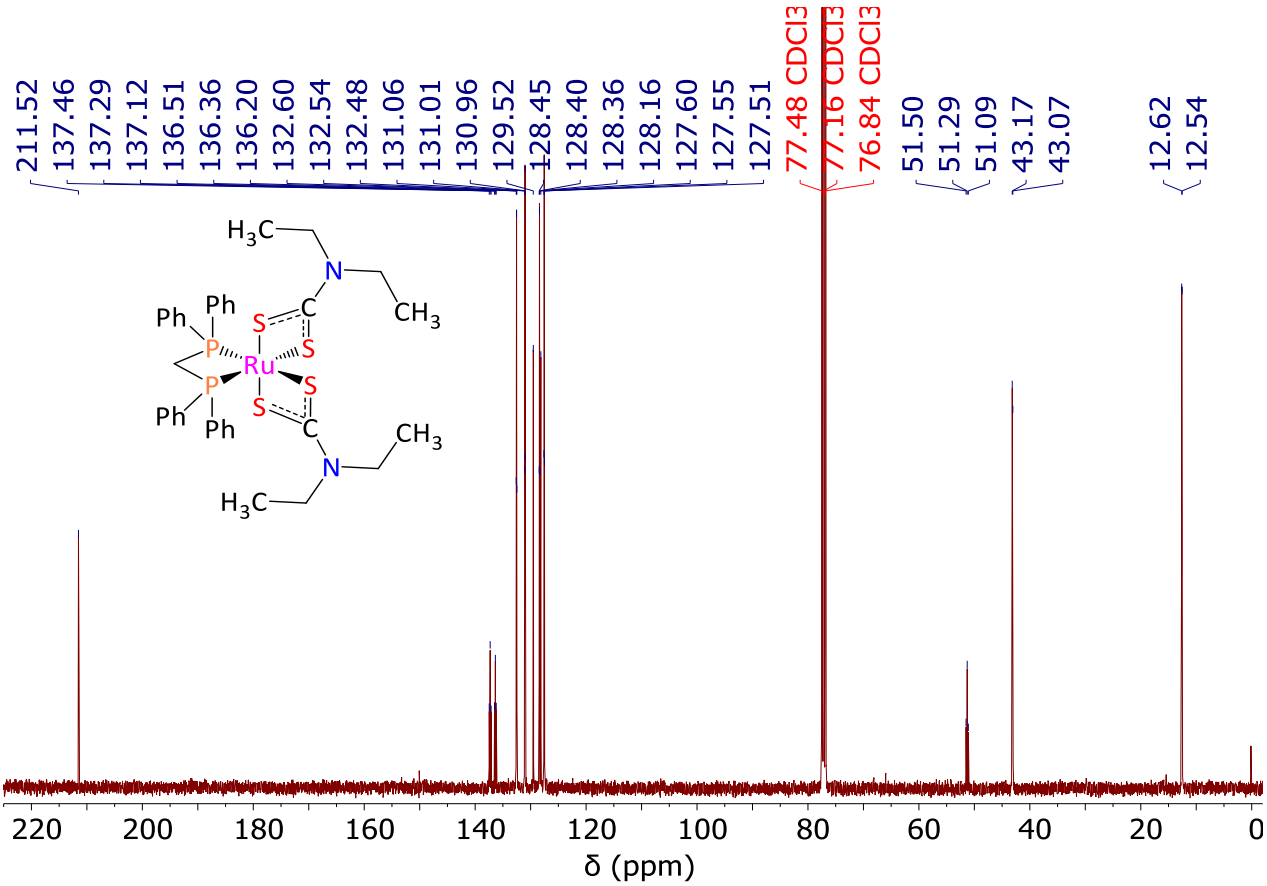

Fig. S15. $^{13}C\{^{1}H\}$ NMR spectrum (101 MHz, $CDCl_3$, 298 K) of $[Ru(S_2CNEt_2)_2(dppm)]$ (**1**)

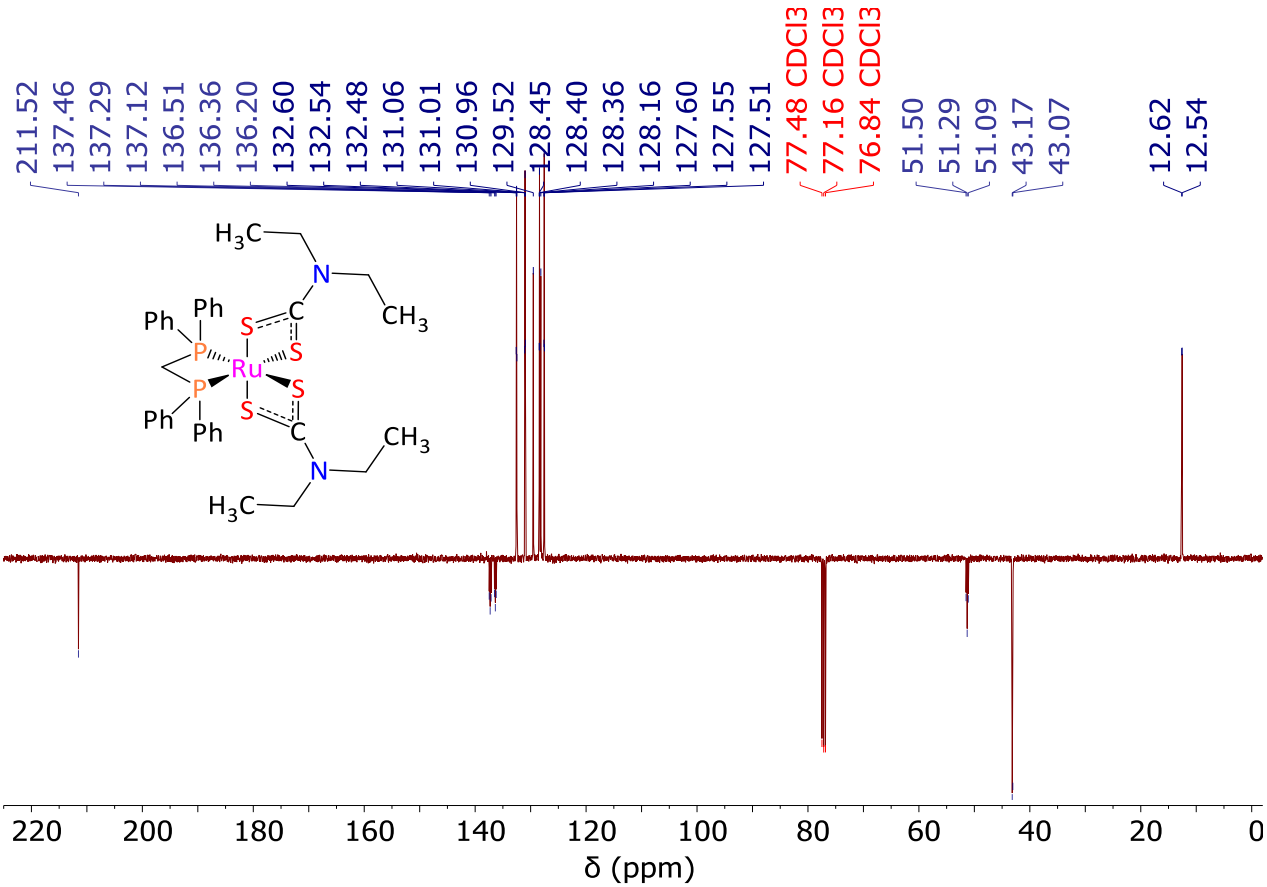

Fig. S16. $^{13}C\{^{1}H\}$ APT NMR spectrum (101 MHz, $CDCl_3$, 298 K) of $[Ru(S_2CNEt_2)_2(dppm)]$ (**1**)

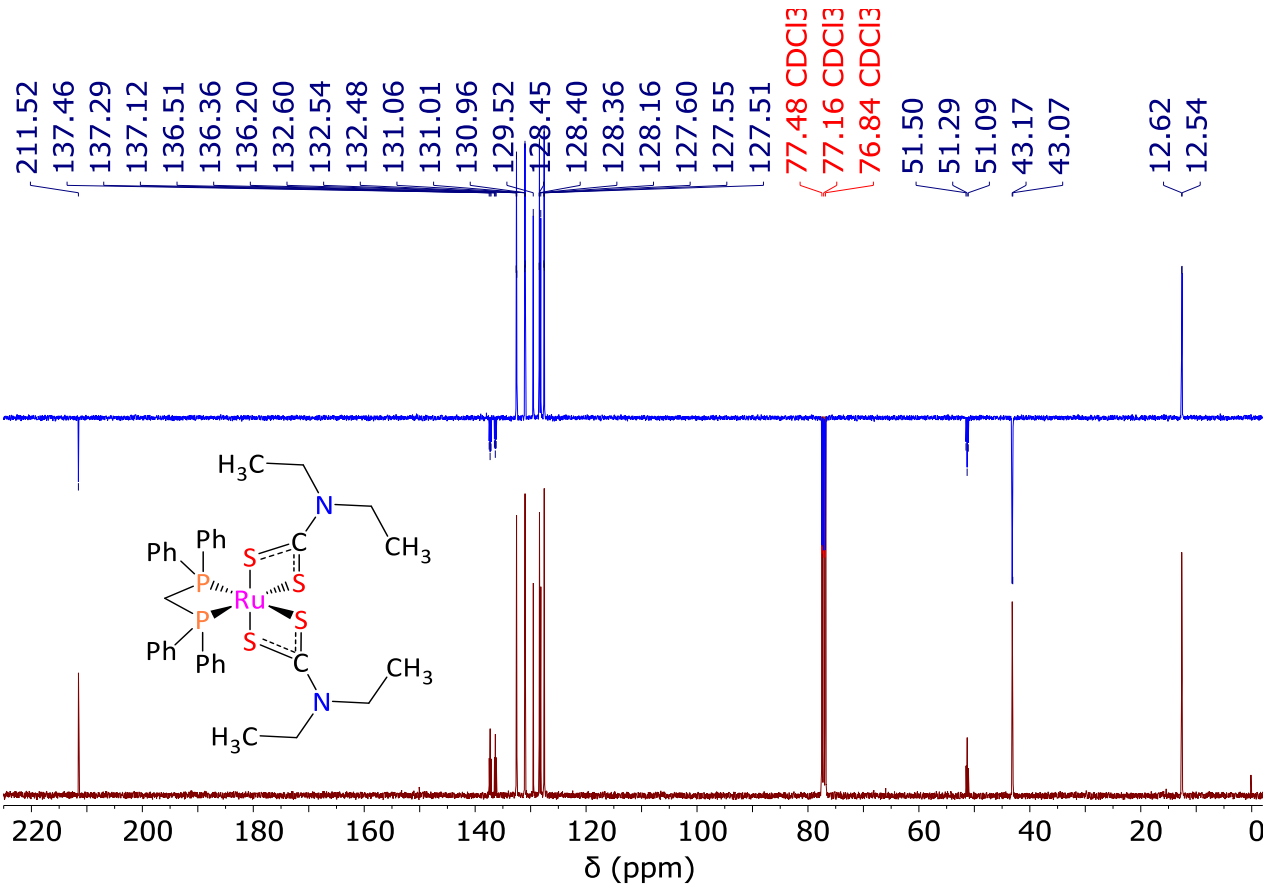

Fig. S17. ^{13}C CPD and APT NMR spectra (101 MHz, $CDCl_3$, 298 K) of [Ru(S_2CNEt_2)$_2$(dppm)] (**1**)

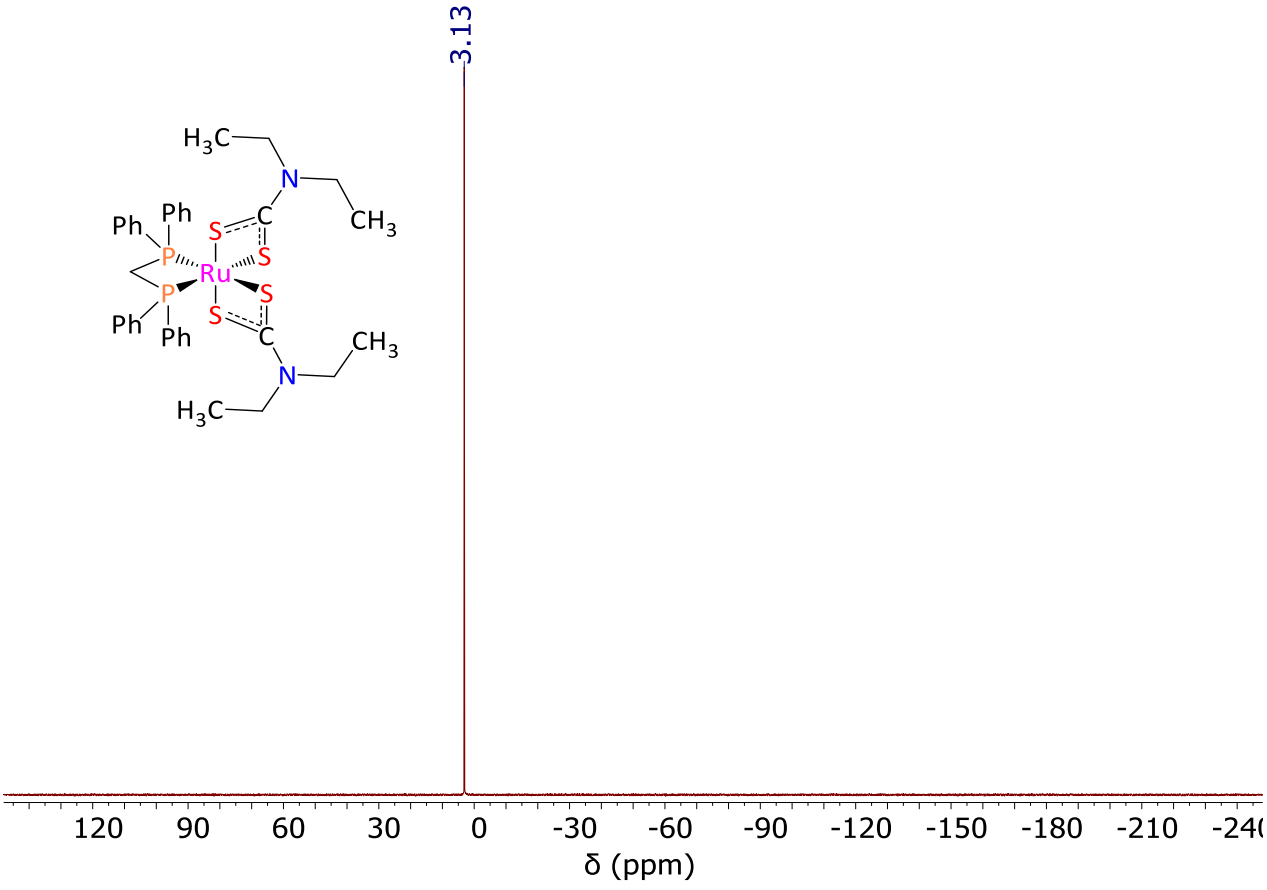

Fig. S18. ^{31}P NMR spectrum (162 MHz, $CDCl_3$, 298 K) of [Ru(S_2CNEt_2)$_2$(dppm)] (**1**)

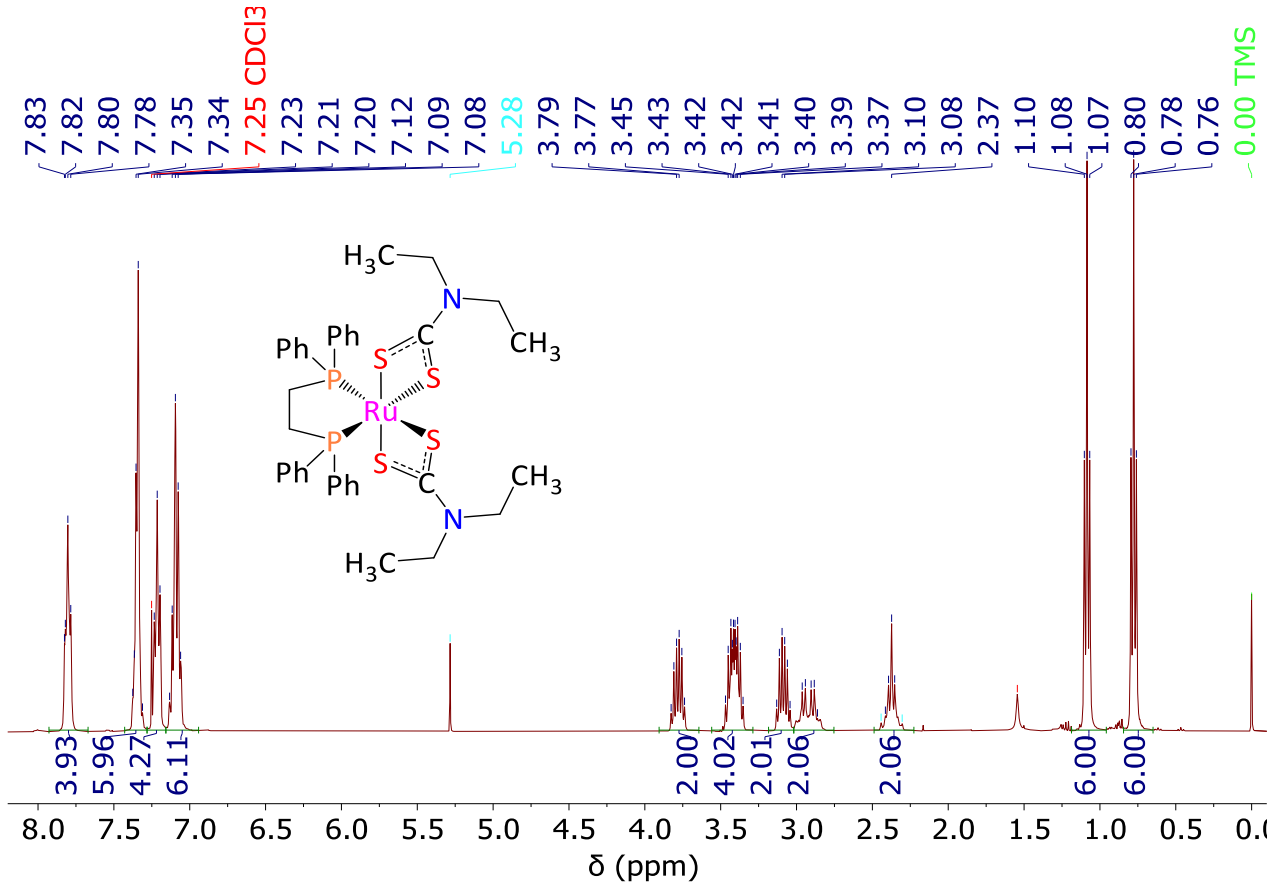

Fig. S19. ^{1}H NMR spectrum (400 MHz, $CDCl_3$, 298 K) of $[Ru(S_2CNEt_2)_2(dppe)]$ (**2**)

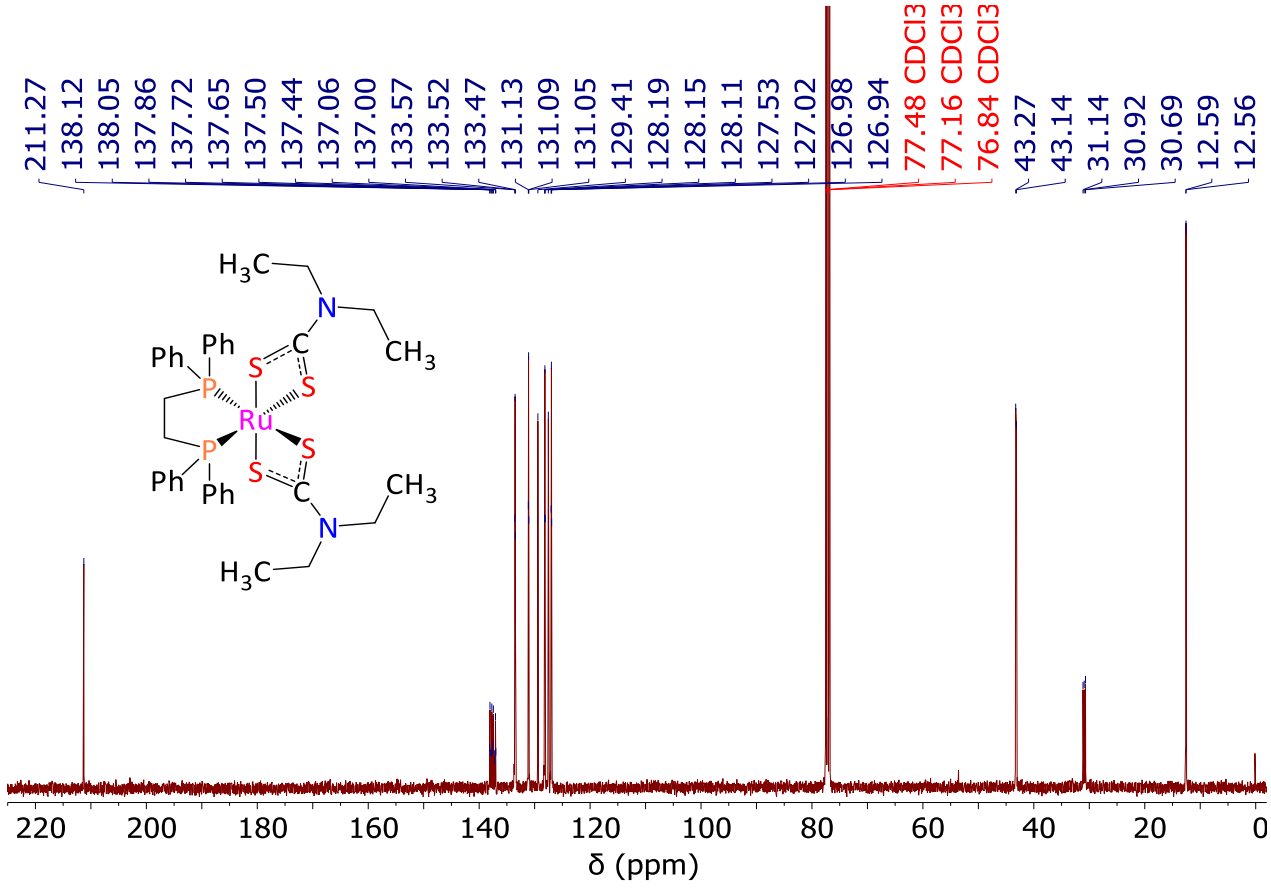

Fig. S20. $^{13}C\{^{1}H\}$ NMR spectrum (101 MHz, $CDCl_3$, 298 K) of $[Ru(S_2CNEt_2)_2(dppe)]$ (**2**)

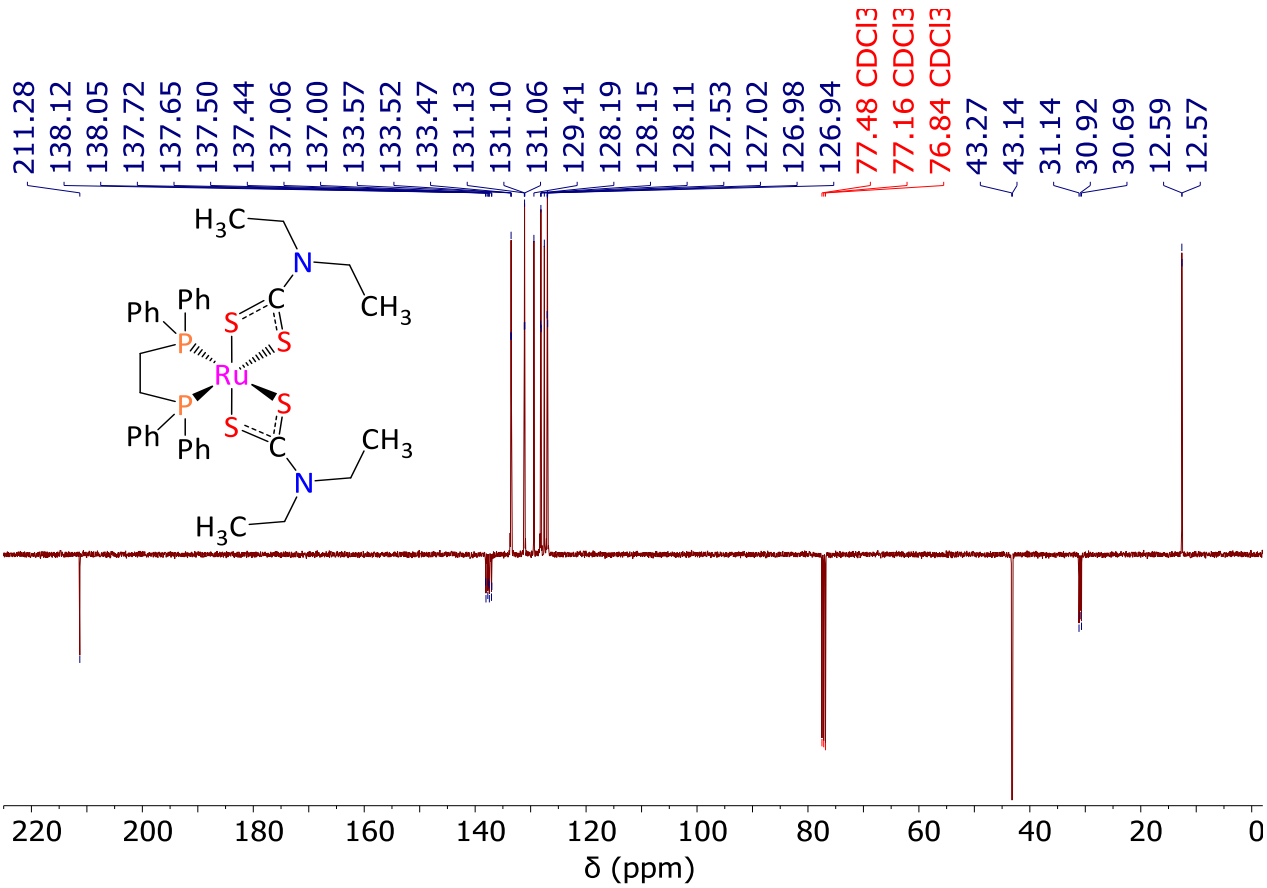

Fig. S21. $^{13}C\{^{1}H\}$ APT NMR spectrum (101 MHz, $CDCl_3$, 298 K) of $[Ru(S_2CNEt_2)_2(dppe)]$ (**2**)

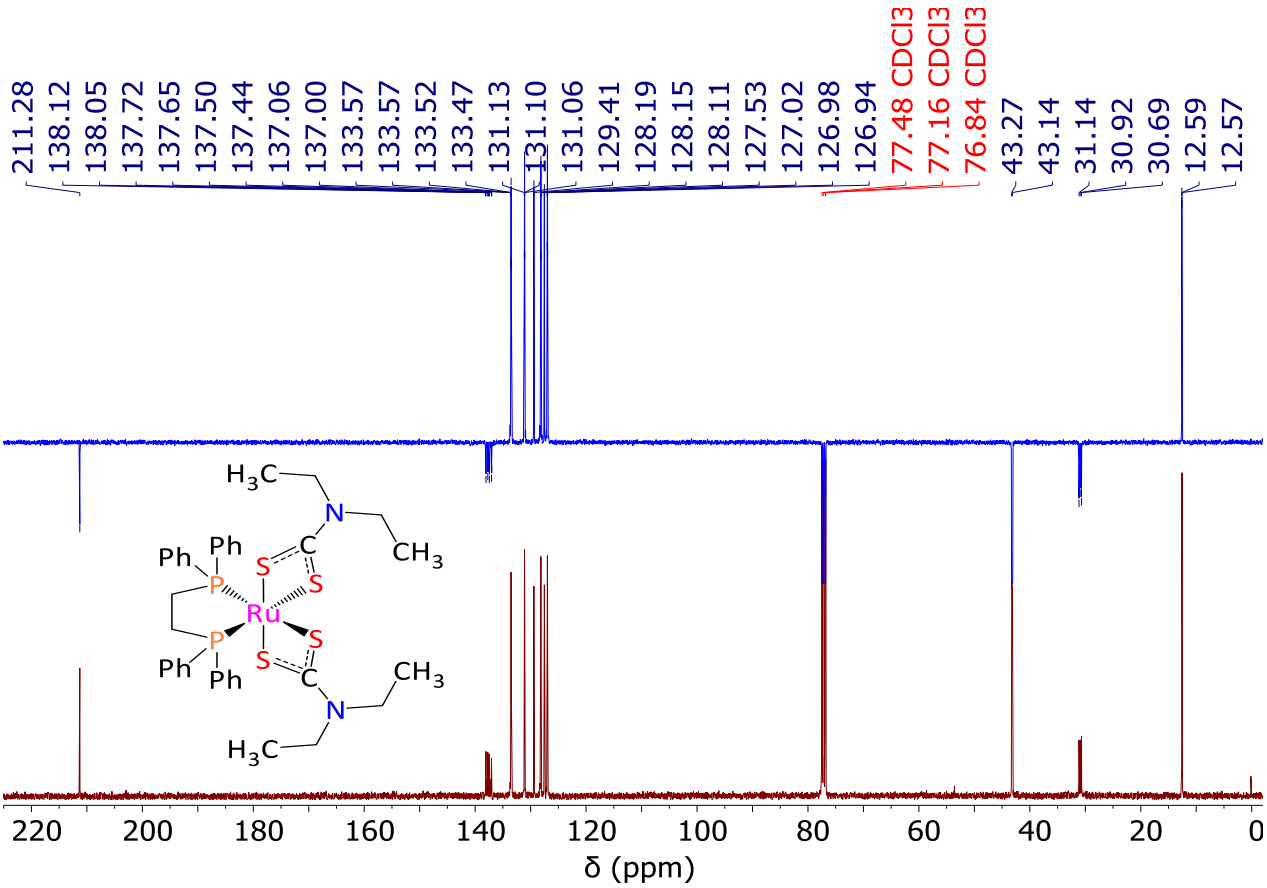

Fig. S22. ^{13}C CPD and APT NMR spectra (101 MHz, $CDCl_3$, 298 K) of $[Ru(S_2CNEt_2)_2(dppe)]$ (**2**)

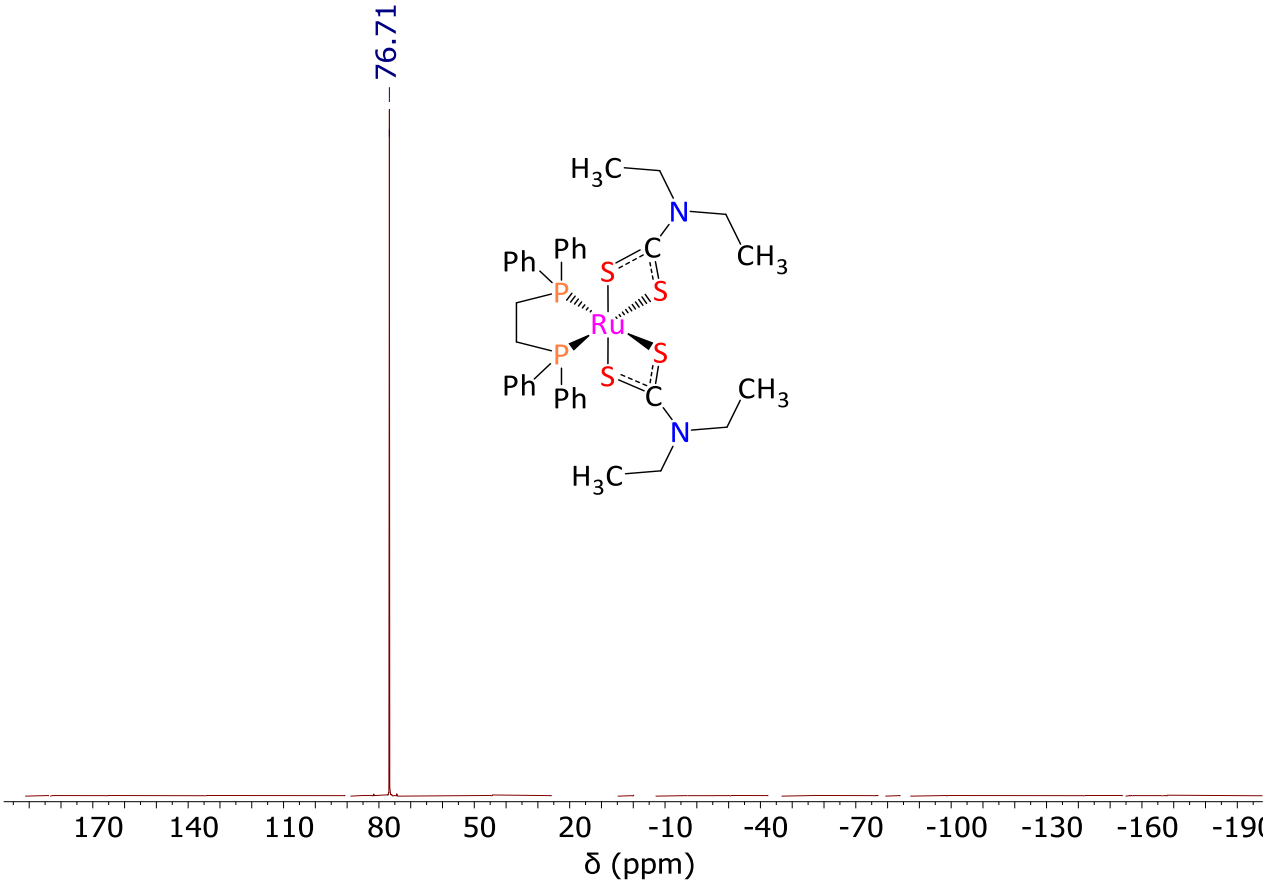

Fig. S23. ^{31}P NMR spectrum (162 MHz, $CDCl_3$, 298 K) of [Ru(S_2CNEt_2)$_2$(dppe)] (**2**)

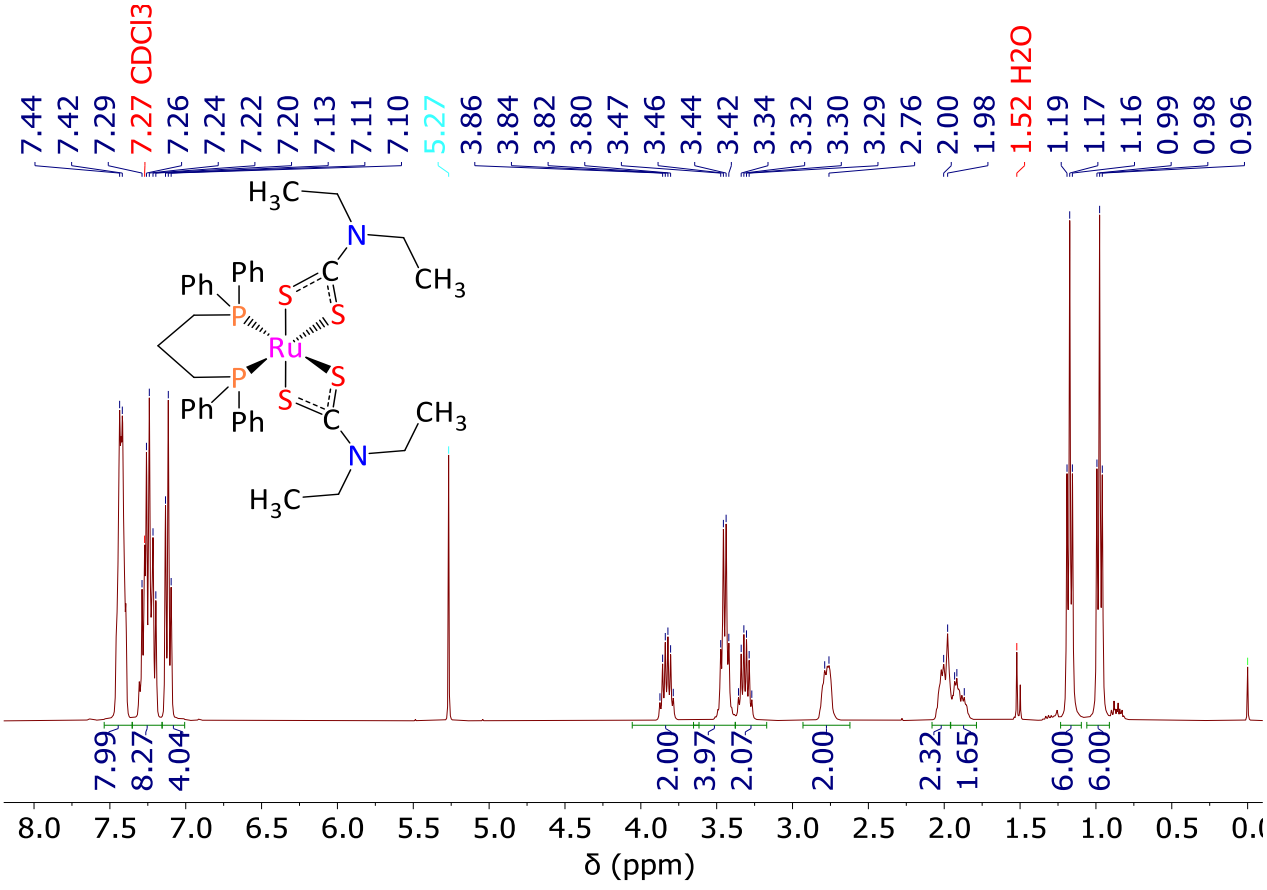

Fig. S24. ^{1}H NMR spectrum (400 MHz, CD_2Cl_2, 298 K) of [Ru(S_2CNEt_2)$_2$(dppp)] (**3**)

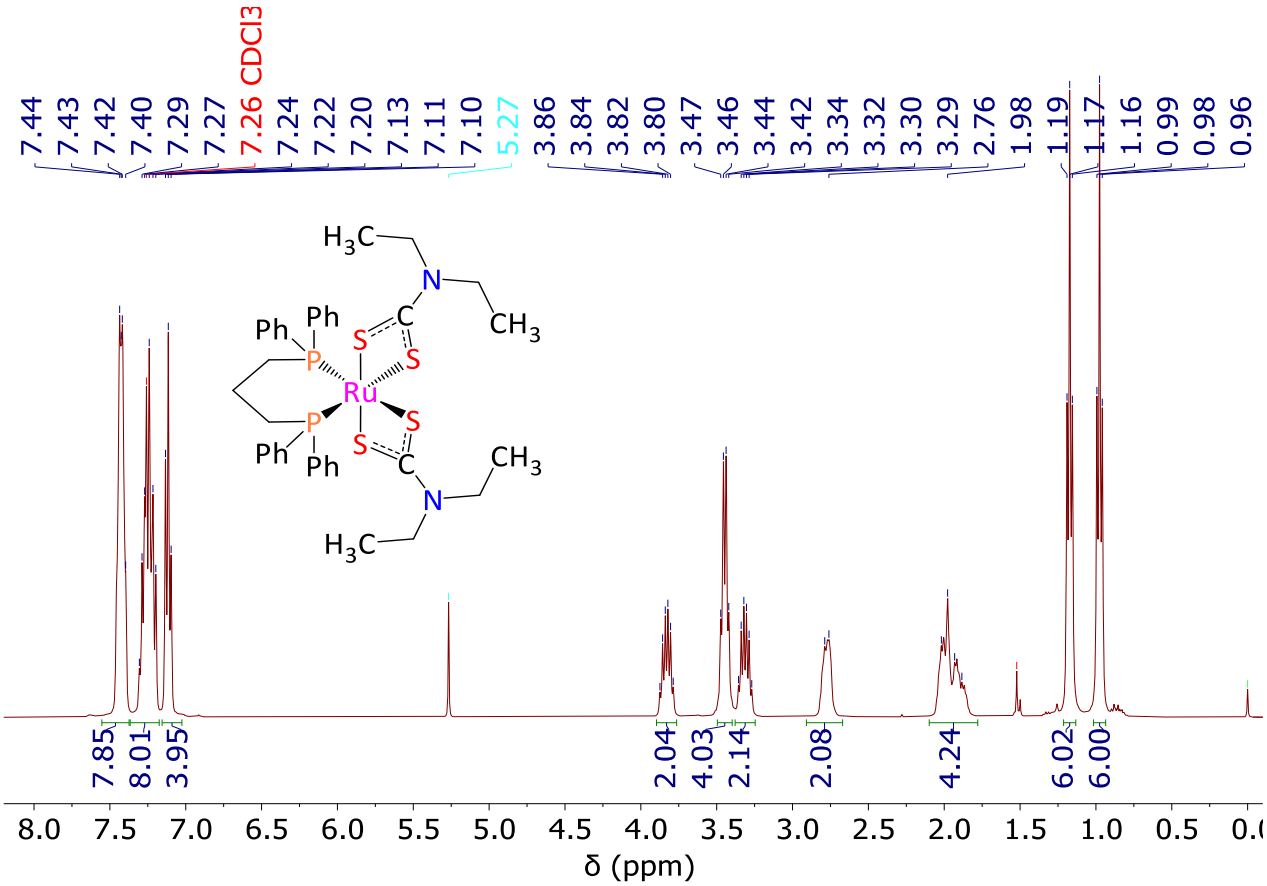

Fig. S25. $^{1}H\{^{31}P\}$ NMR spectrum (250 MHz, $CDCl_3$, 298 K) of $[Ru(S_2CNEt_2)_2(dppp)]$ (**3**)

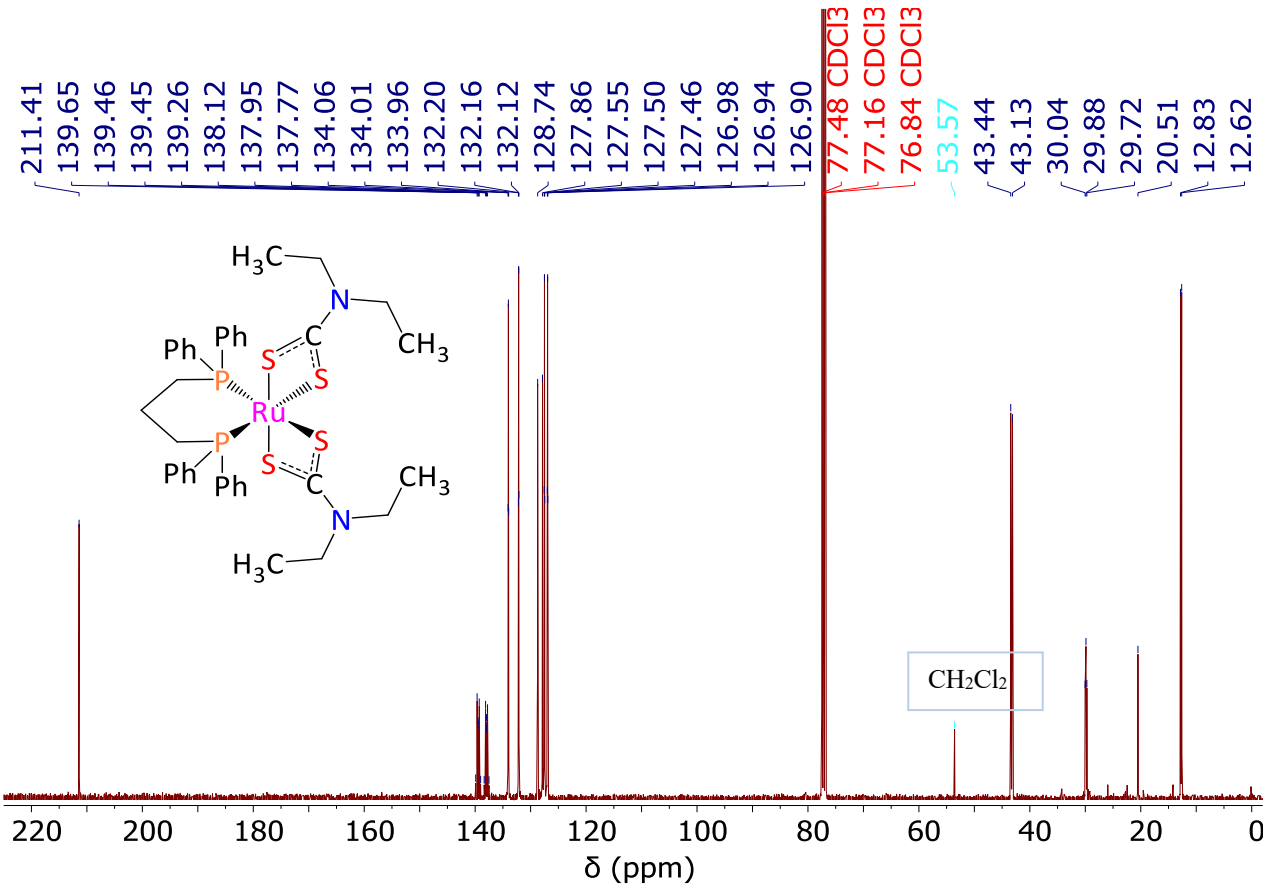

Fig. S26. $^{13}C\{^{1}H\}$ NMR spectrum (101 MHz, CD_2Cl_2, 298 K) of $[Ru(S_2CNEt_2)_2(dppp)]$ (**3**)

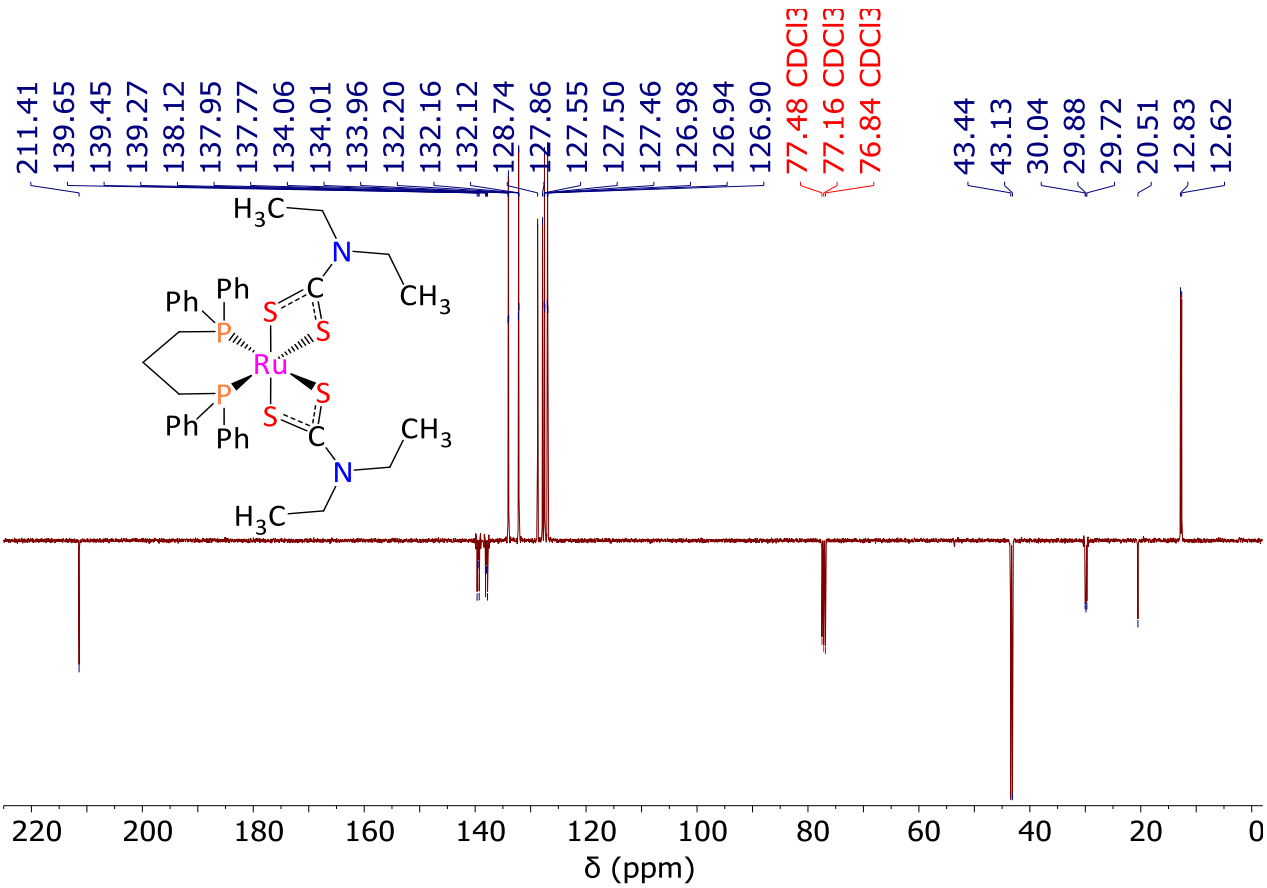

Fig. S27. $^{13}C\{^{1}H\}$ APT NMR spectrum (101 MHz, $CDCl_3$, 298 K) of $[Ru(S_2CNEt_2)_2(dppp)]$ (**3**)

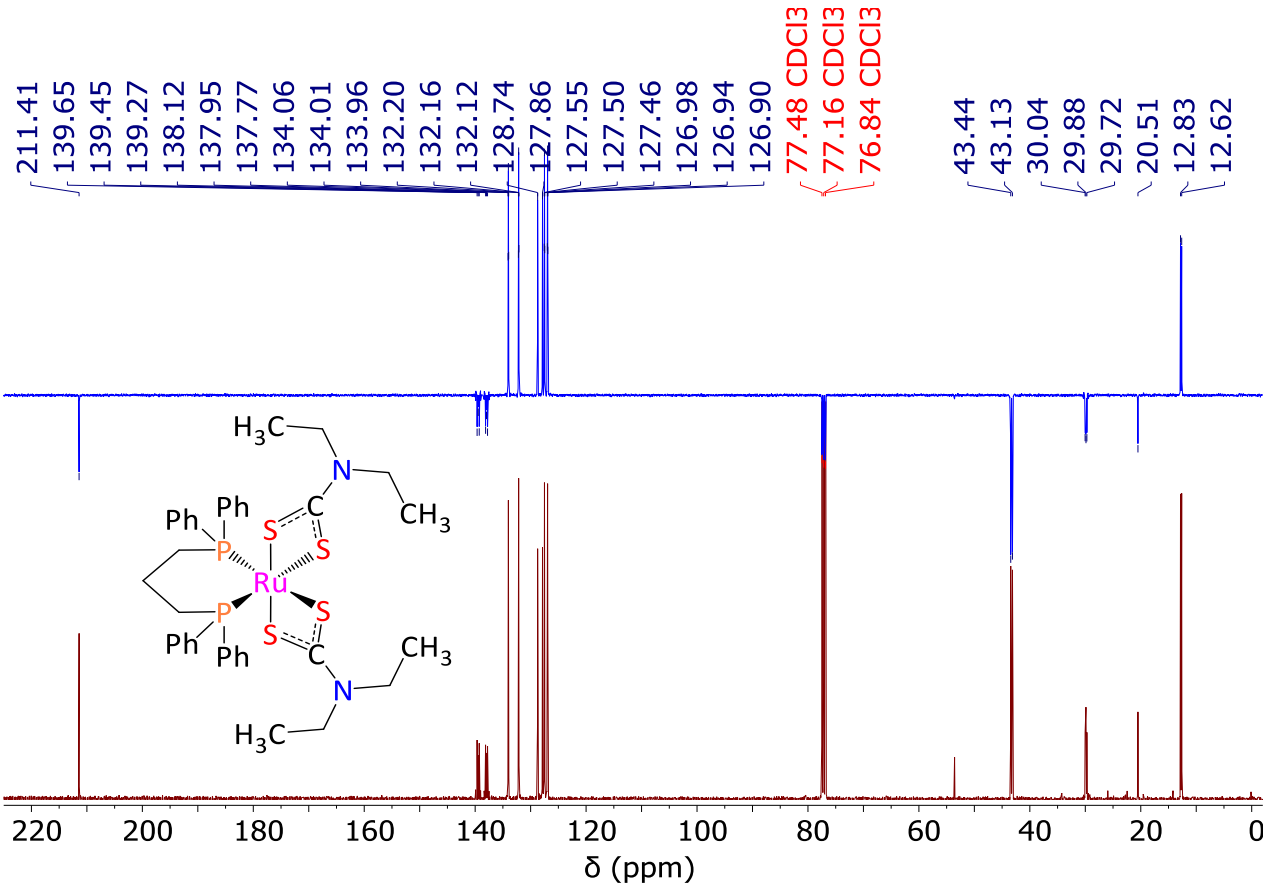

Fig. S28. ^{13}C CPD and APT NMR spectra (101 MHz, $CDCl_3$, 298 K) of $[Ru(S_2CNEt_2)_2(dppp)]$ (**3**)

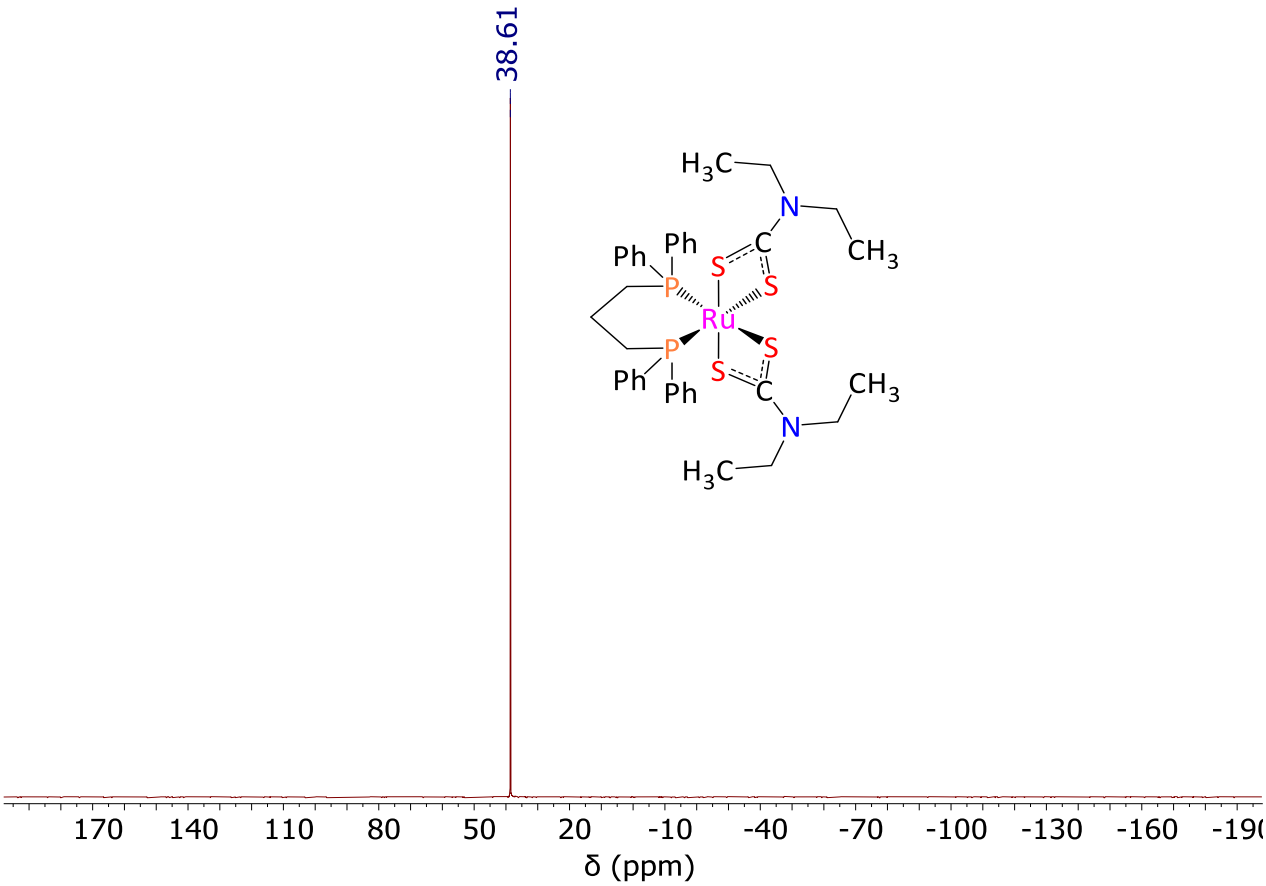

Fig. S29. ^{31}P NMR spectrum (162 MHz, CD_2Cl_2, 298 K) of [Ru(S_2CNEt_2)$_2$(dppp)] (**3**)

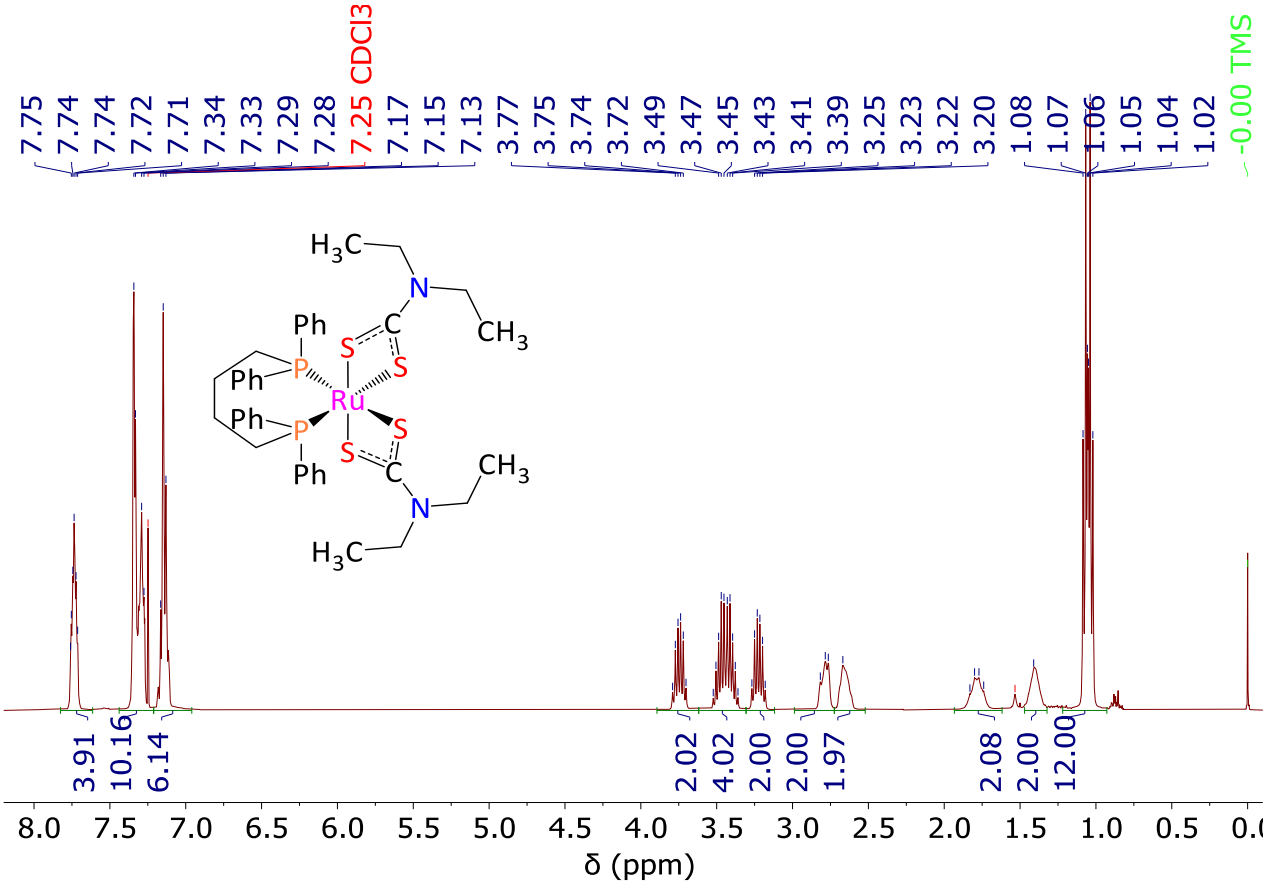

Fig. S30. ^{1}H NMR spectrum (400 MHz, $CDCl_3$, 298 K) of [Ru(S_2CNEt_2)$_2$(dppb)] (**4**)

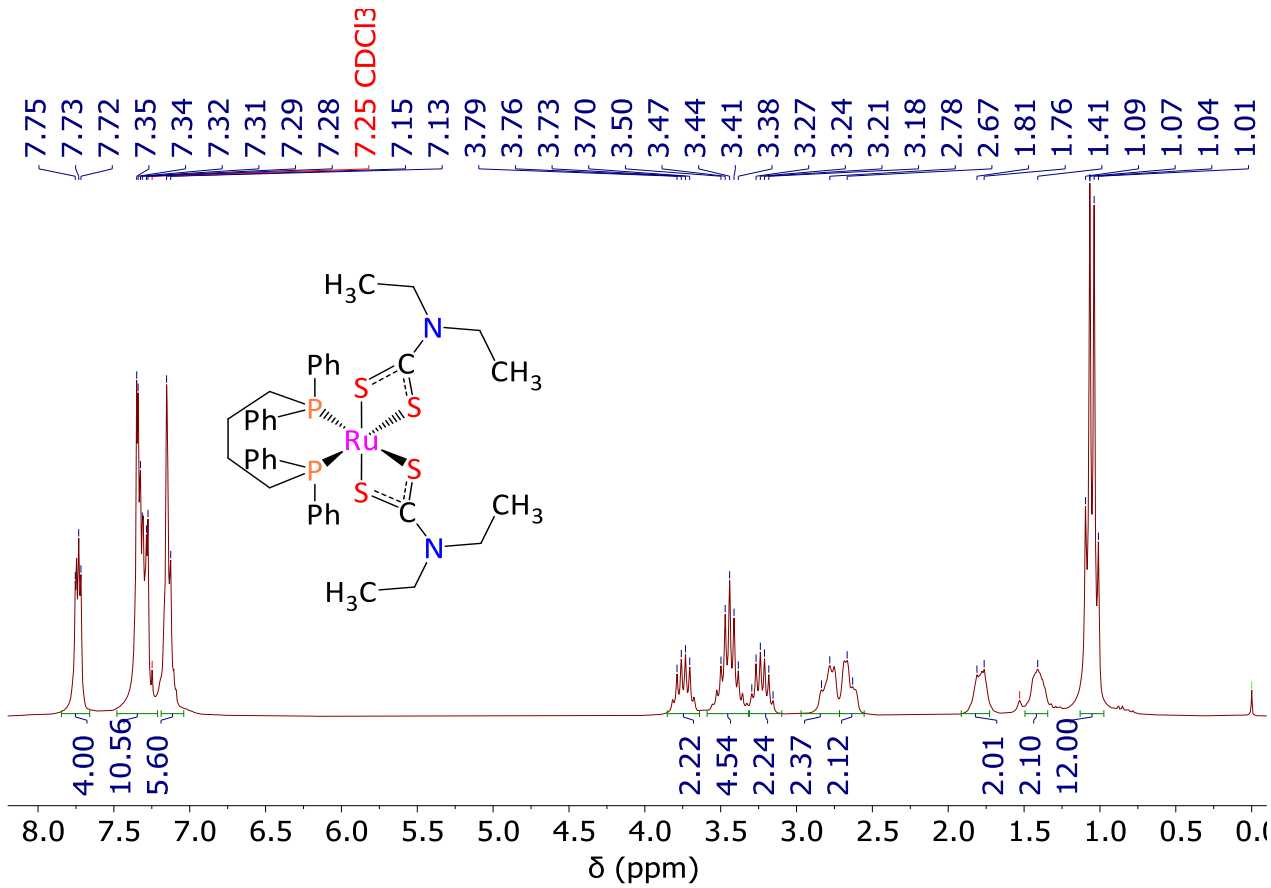

Fig. S31. $^{1}H\{^{31}P\}$ NMR spectrum (250 MHz, $CDCl_3$, 298 K) of $[Ru(S_2CNEt_2)_2(dppb)]$ (**4**)

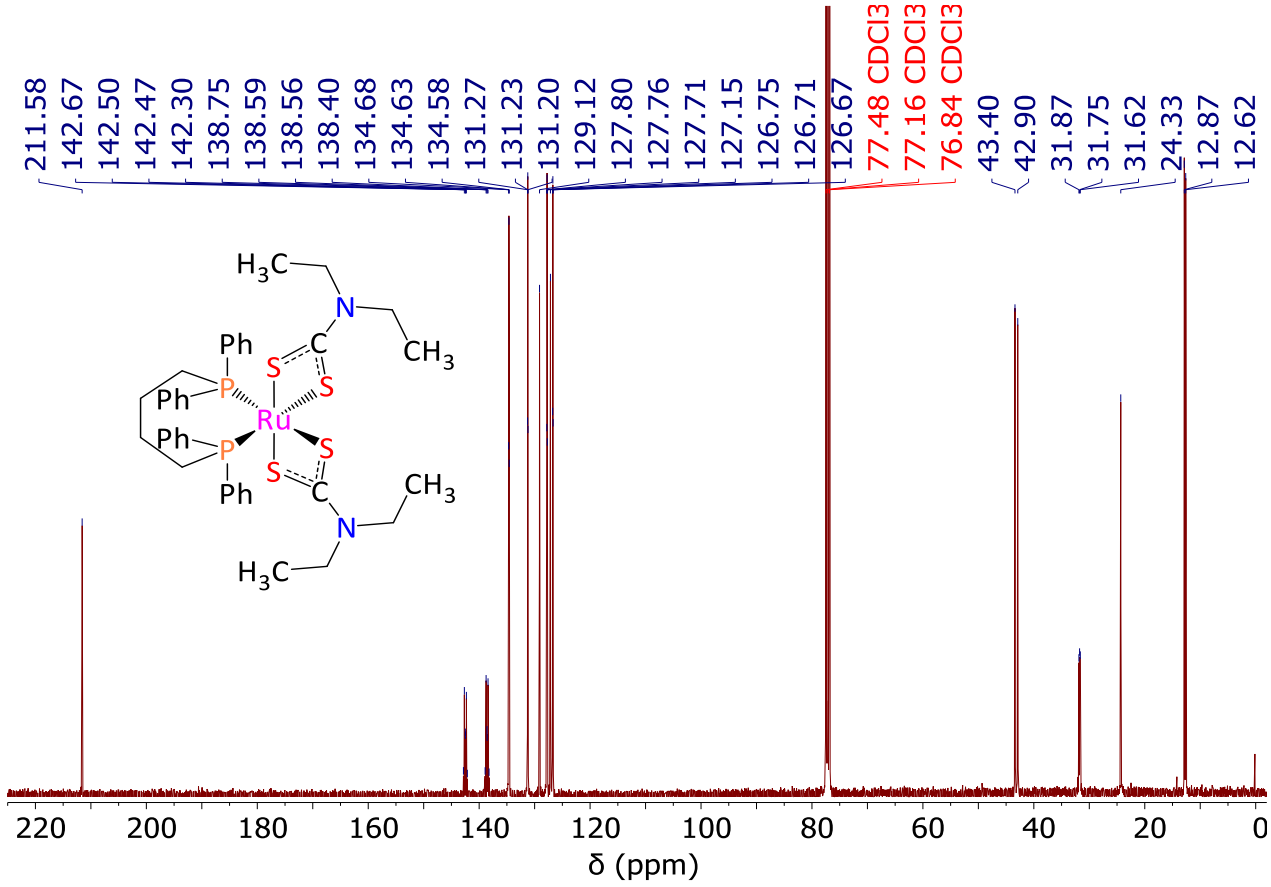

Fig. S32. $^{13}C\{^{1}H\}$ NMR spectrum (101 MHz, $CDCl_3$, 298 K) of $[Ru(S_2CNEt_2)_2(dppb)]$ (**4**)

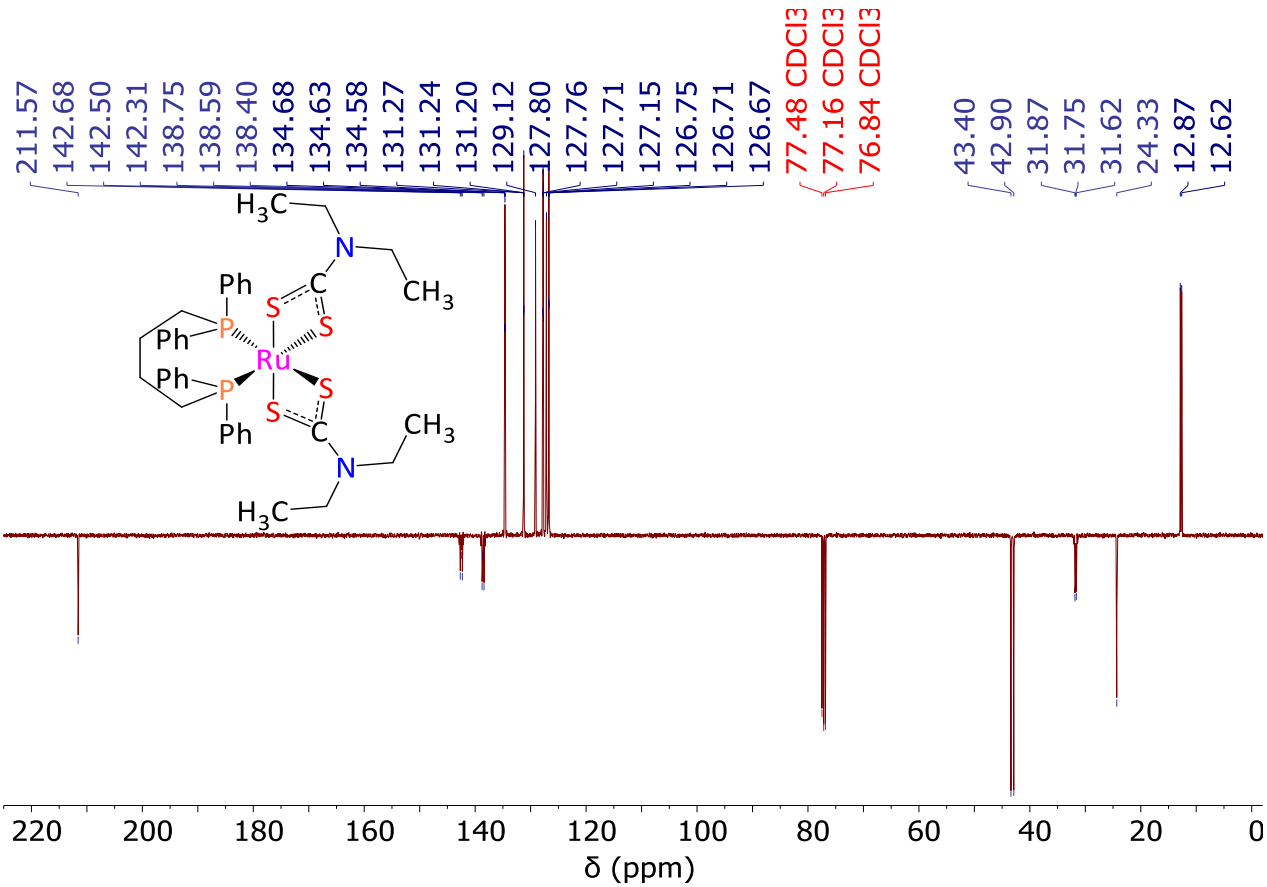

Fig. S33. $^{13}C\{^{1}H\}$ APT NMR spectrum (101 MHz, $CDCl_3$, 298 K) of $[Ru(S_2CNEt_2)_2(dppb)]$ (**4**)

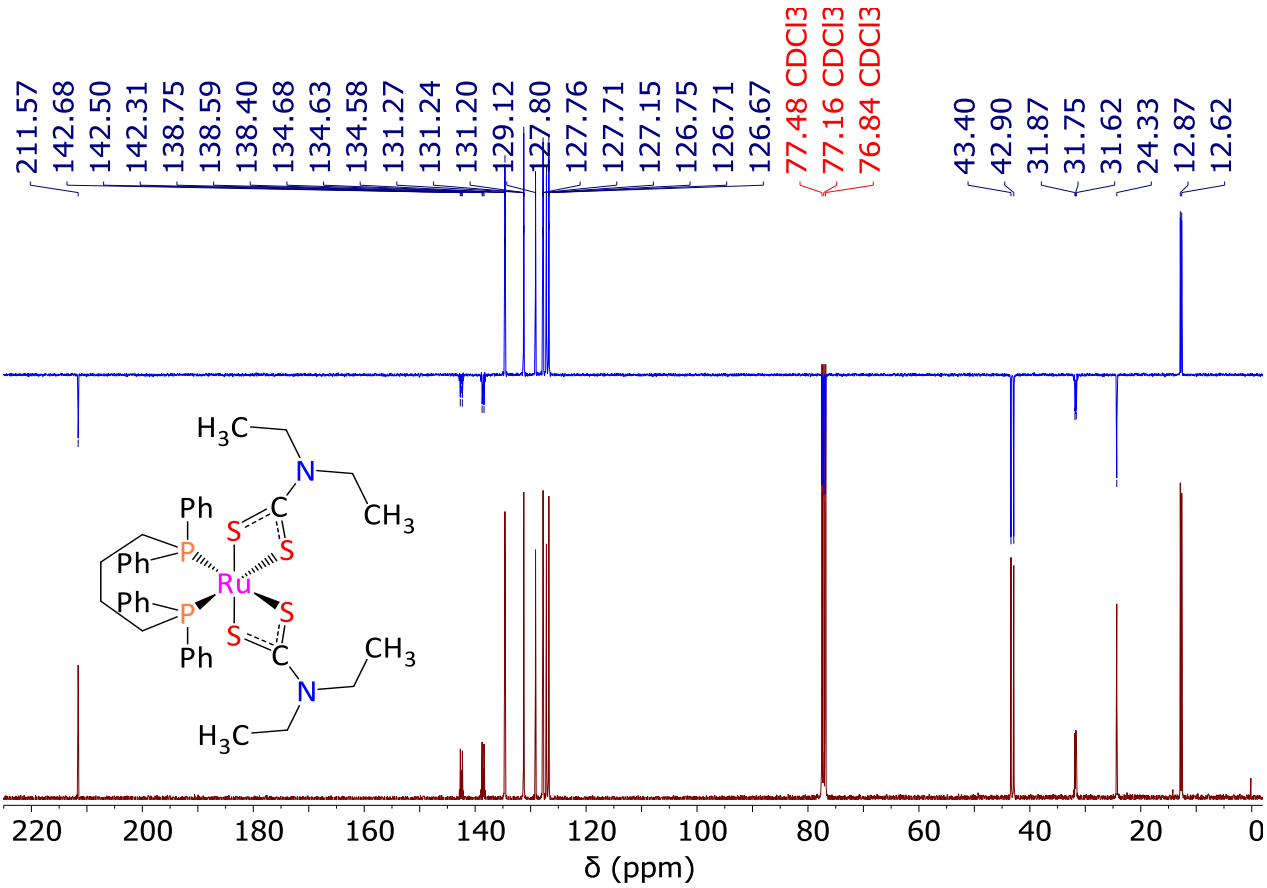

Fig. S34. ^{13}C CPD and APT NMR spectra (101 MHz, $CDCl_3$, 298 K) of $[Ru(S_2CNEt_2)_2(dppb)]$ (**4**)

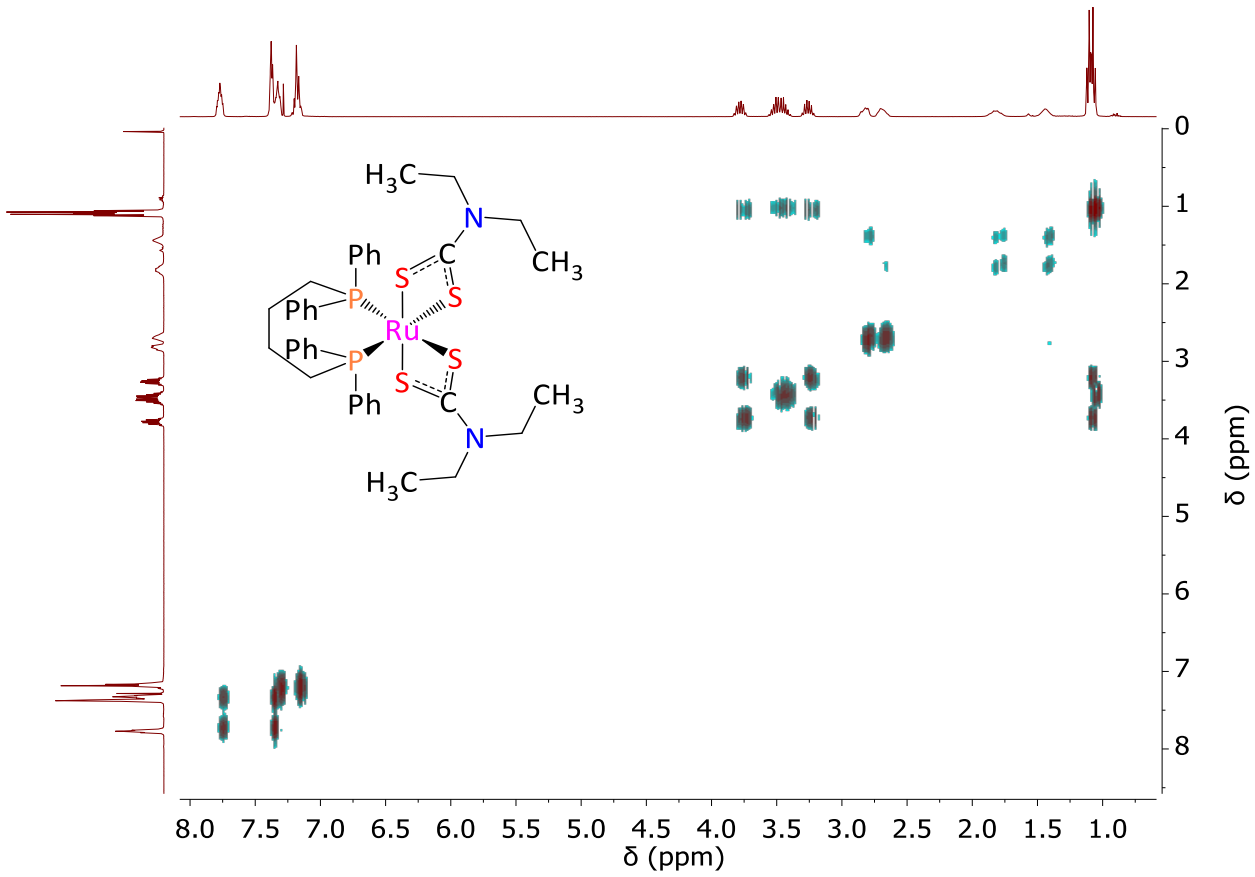

Fig. S35. COSY NMR spectrum (400 MHz, $CDCl_3$, 298 K) of [Ru(S_2CNEt_2)$_2$(dppb)] (**4**)

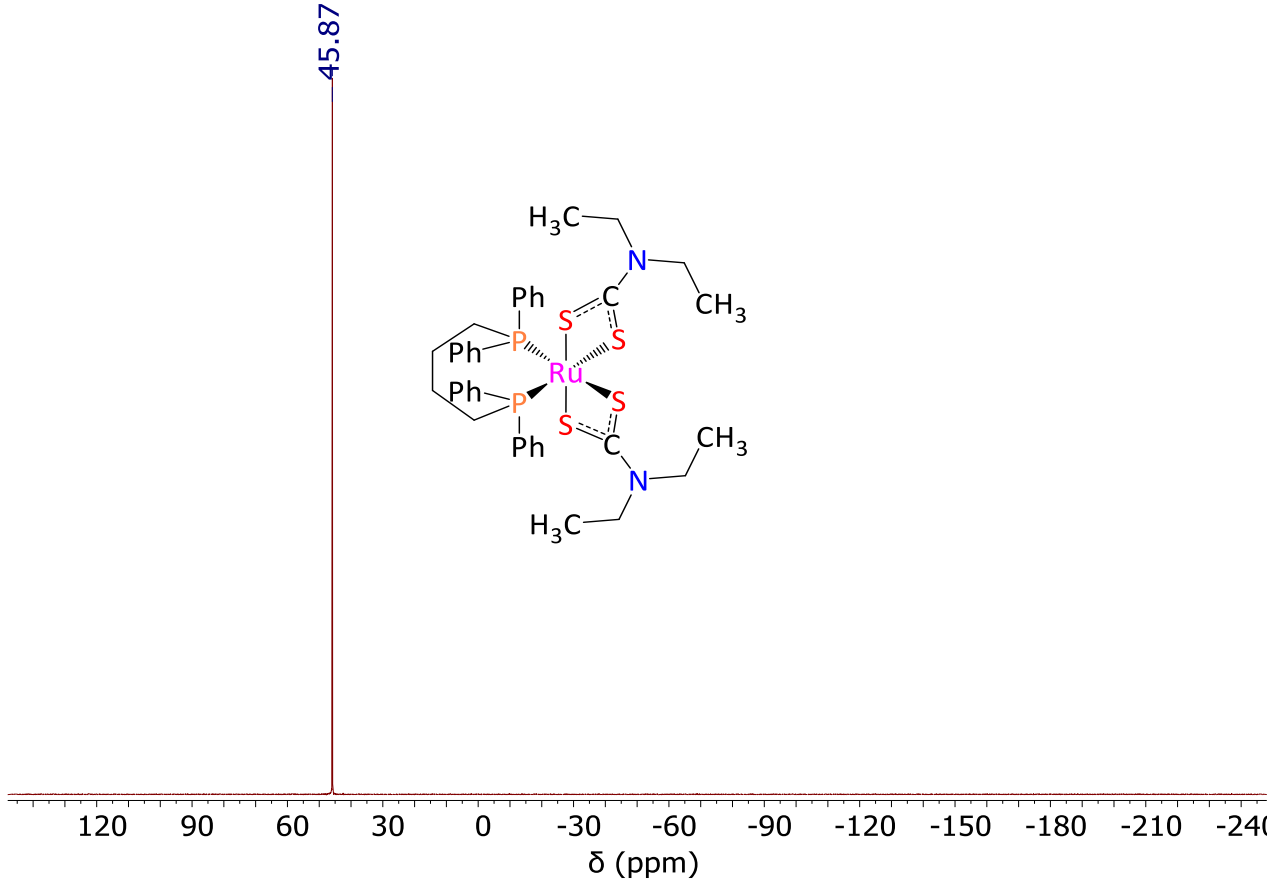

Fig. S36. ^{31}P NMR spectrum (162 MHz, $CDCl_3$, 298 K) of [Ru(S_2CNEt_2)$_2$(dppb)] (**4**)

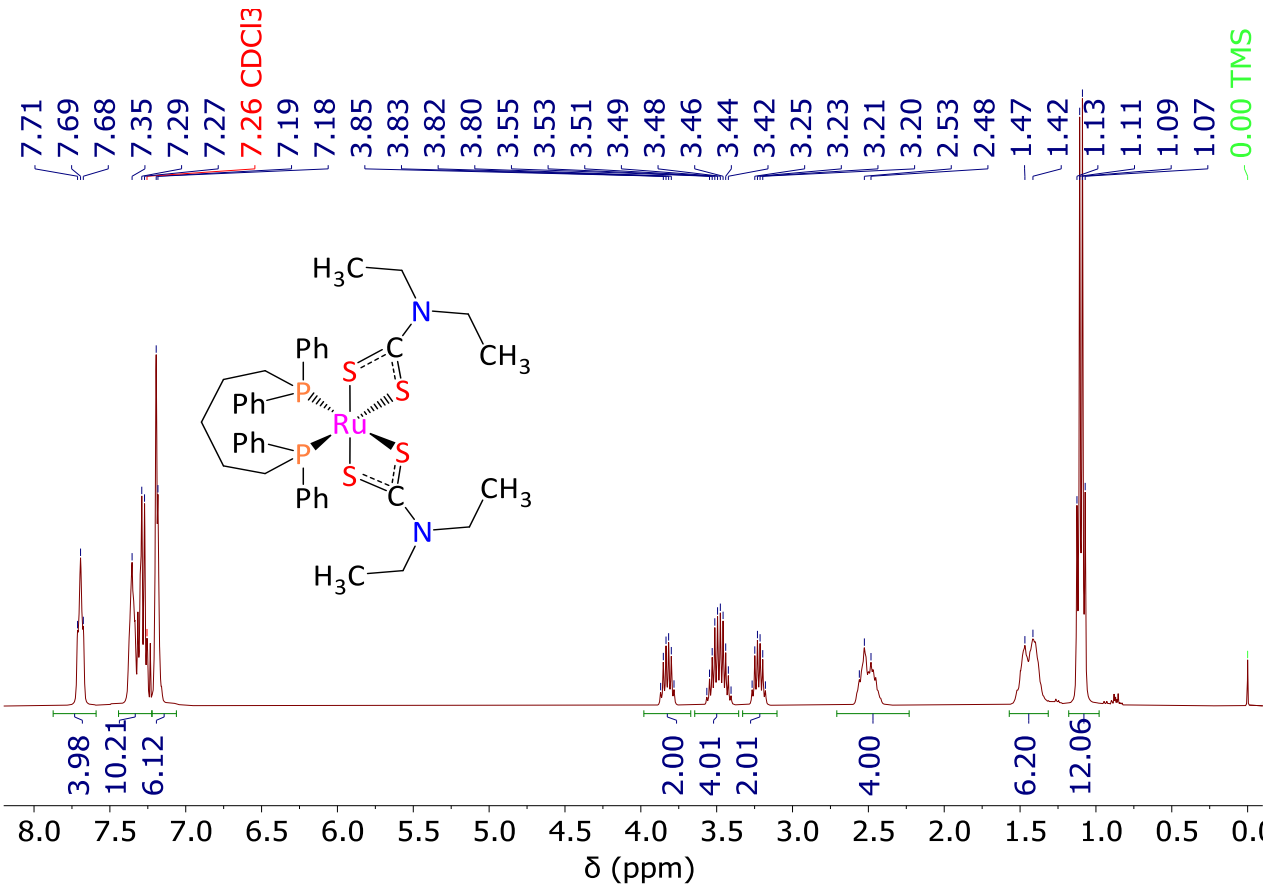

Fig. S37. ^{1}H NMR spectrum (400 MHz, $CDCl_3$, 298 K) of $[Ru(S_2CNEt_2)_2(dpppe)]$ (**5**)

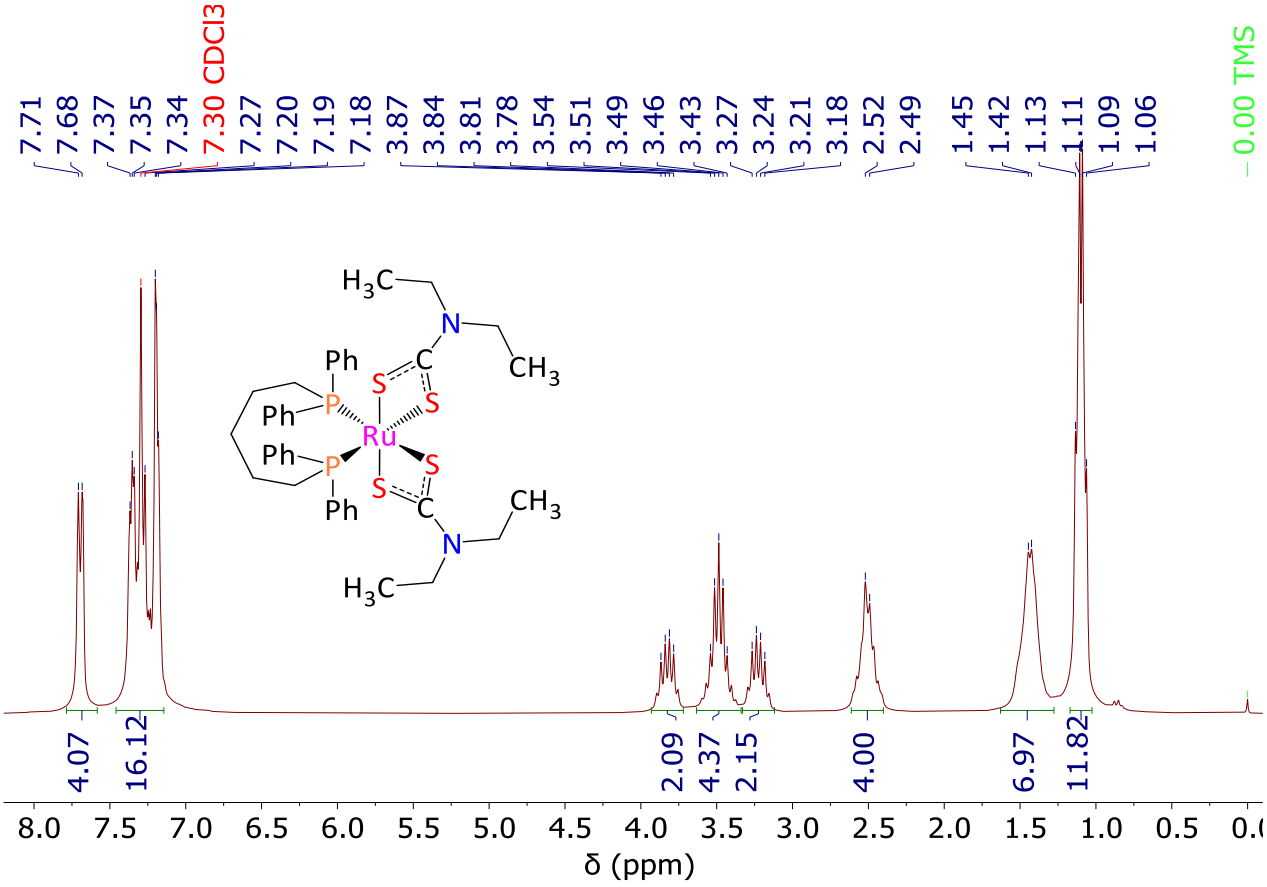

Fig. S38. $^{1}H\{^{31}P\}$ NMR spectrum (250 MHz, $CDCl_3$, 298 K) of $[Ru(S_2CNEt_2)_2(dpppe)]$ (**5**)

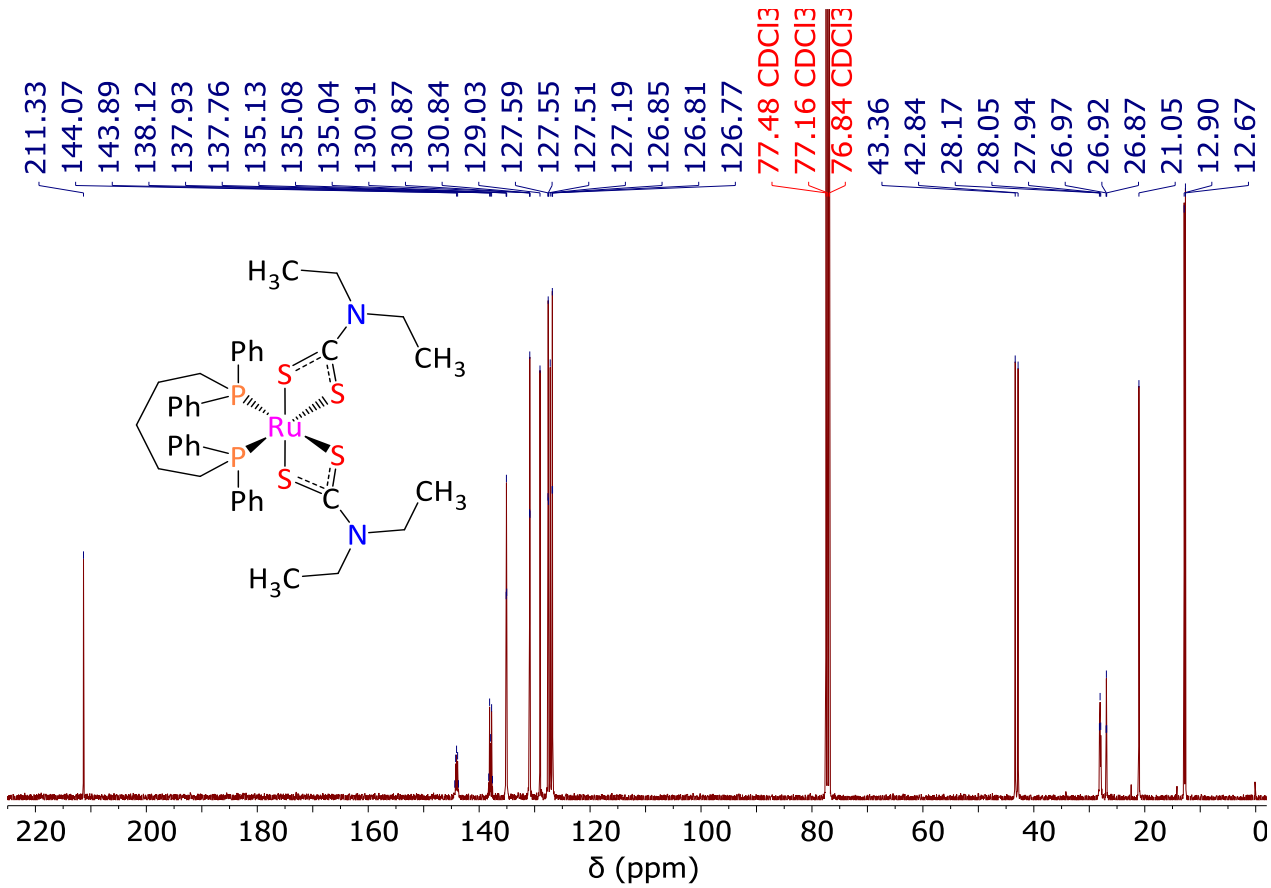

Fig. S39. $^{13}C\{^{1}H\}$ NMR spectrum (101 MHz, $CDCl_3$, 298 K) of $[Ru(S_2CNEt_2)_2(dpppe)]$ (**5**)

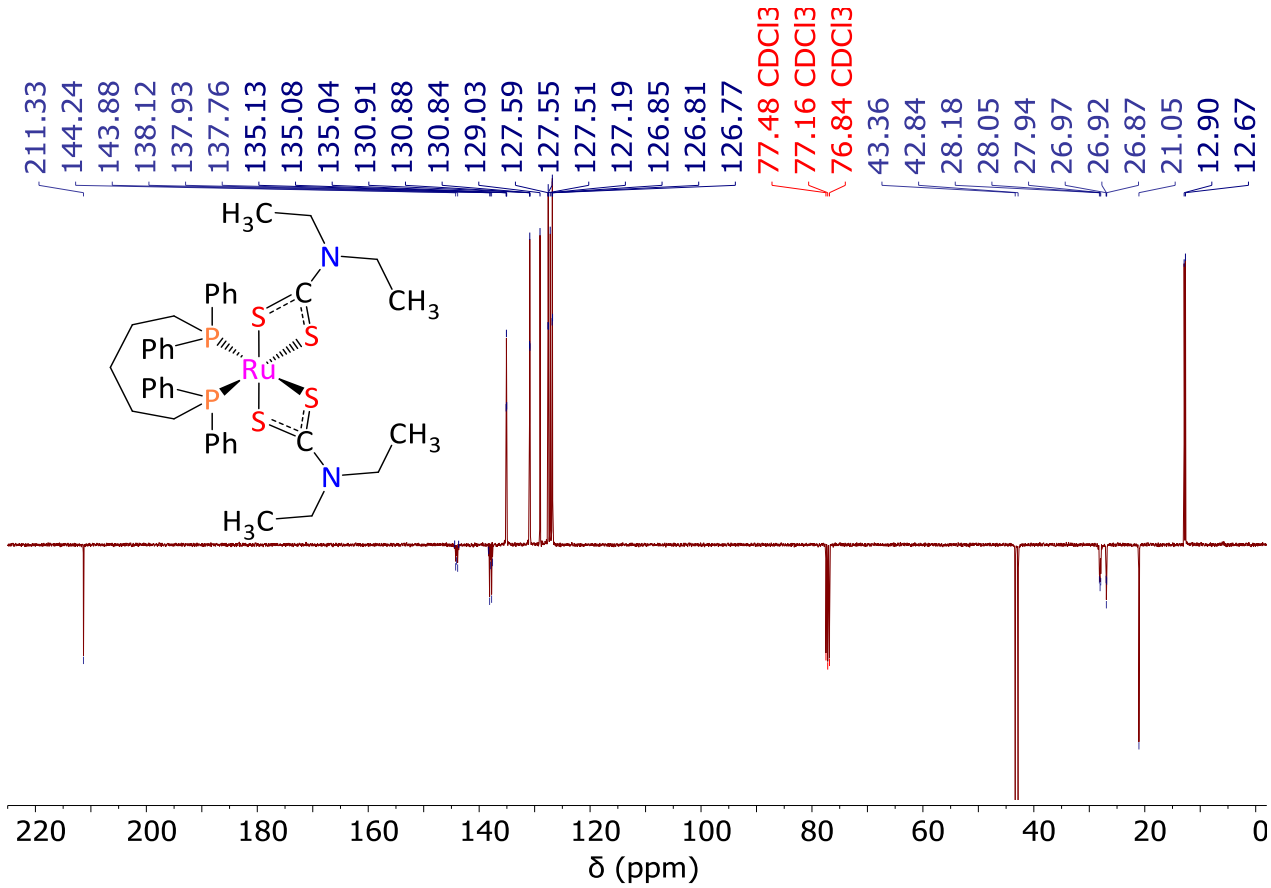

Fig. S40. $^{13}C\{^{1}H\}$ APT NMR spectrum (101 MHz, $CDCl_3$, 298 K) of $[Ru(S_2CNEt_2)_2(dpppe)]$ (**5**)

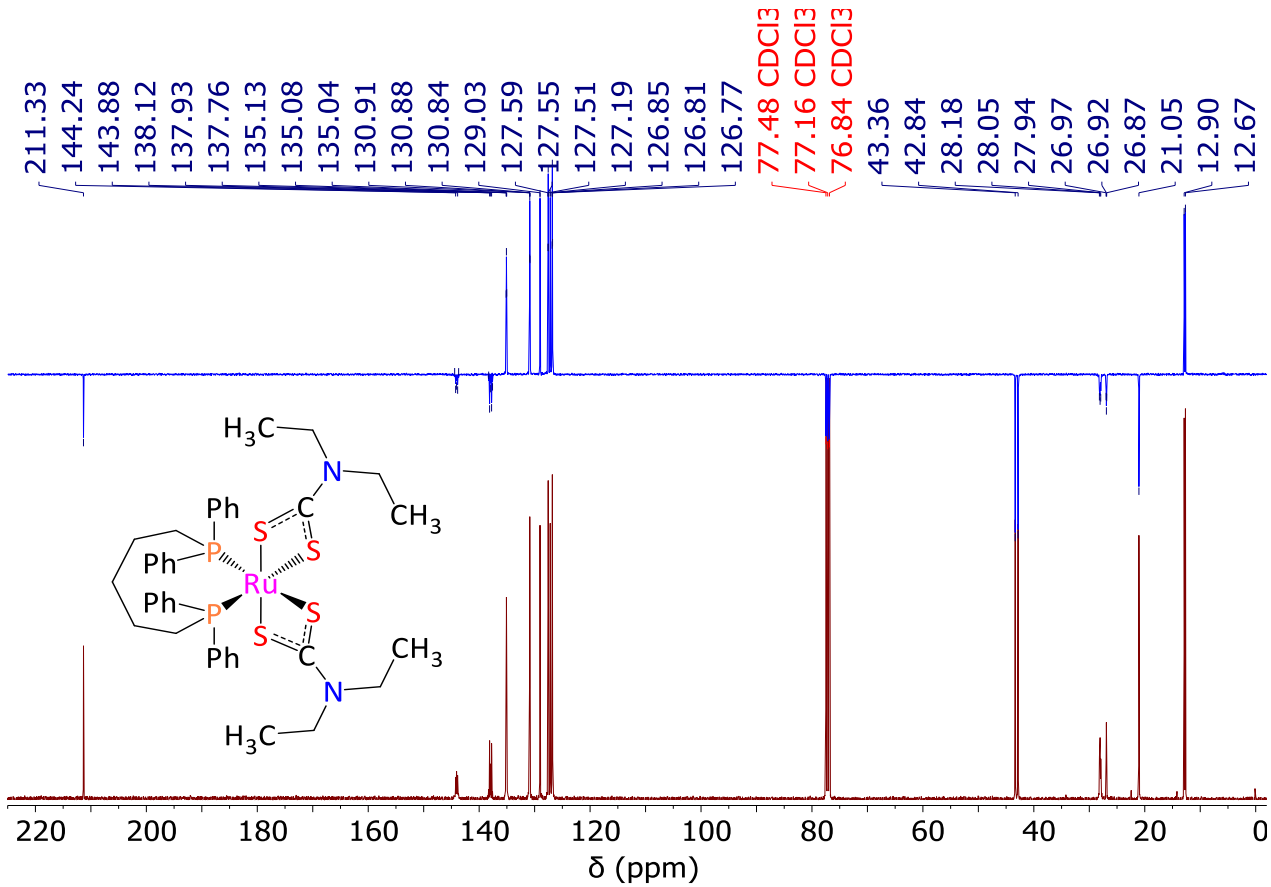

Fig. S41. ^{13}C CPD and APT NMR spectra (101 MHz, $CDCl_3$, 298 K) of [Ru(S_2CNEt_2)$_2$(dpppe)] (**5**)

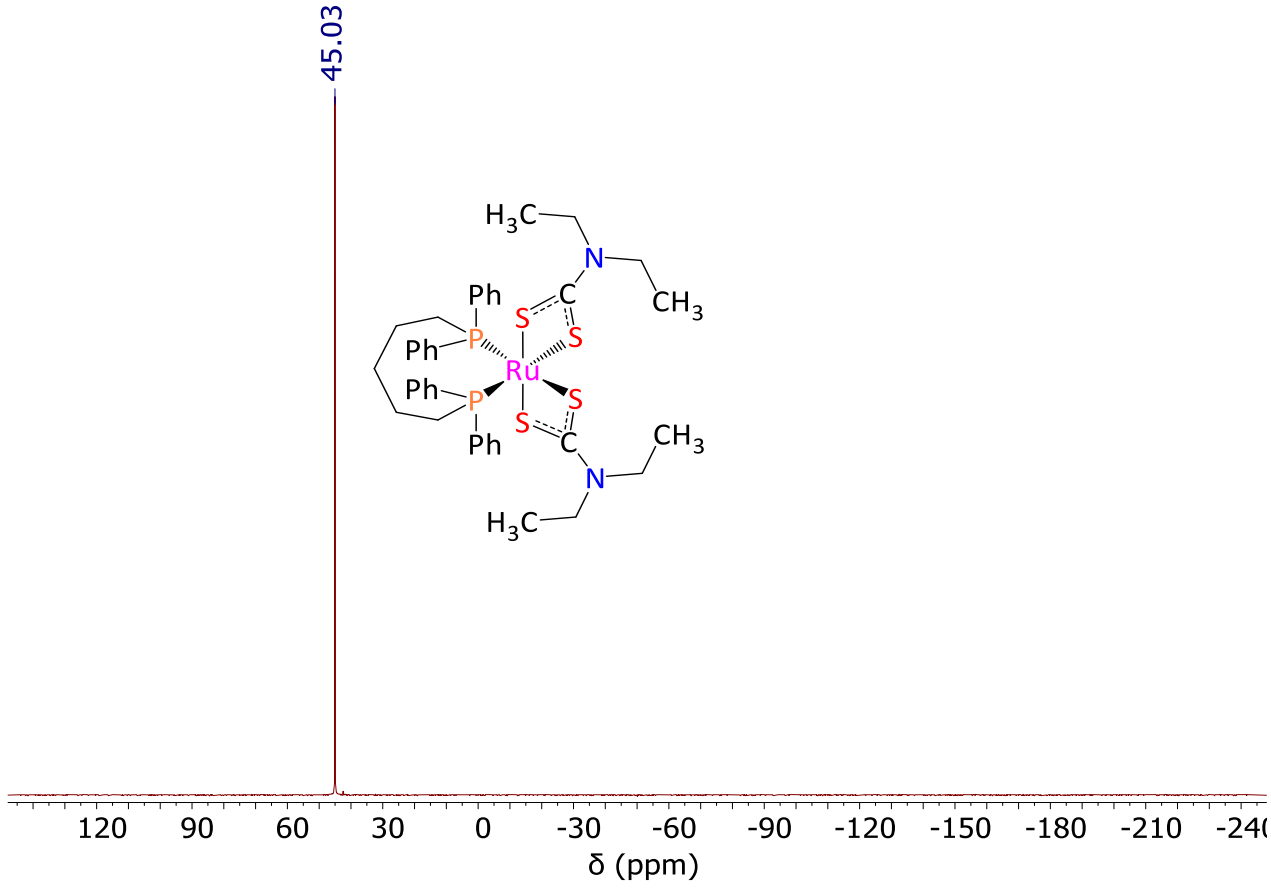

Fig. S42. ^{31}P NMR spectrum (162 MHz, $CDCl_3$, 298 K) of [Ru(S_2CNEt_2)$_2$(dpppe)] (**5**)

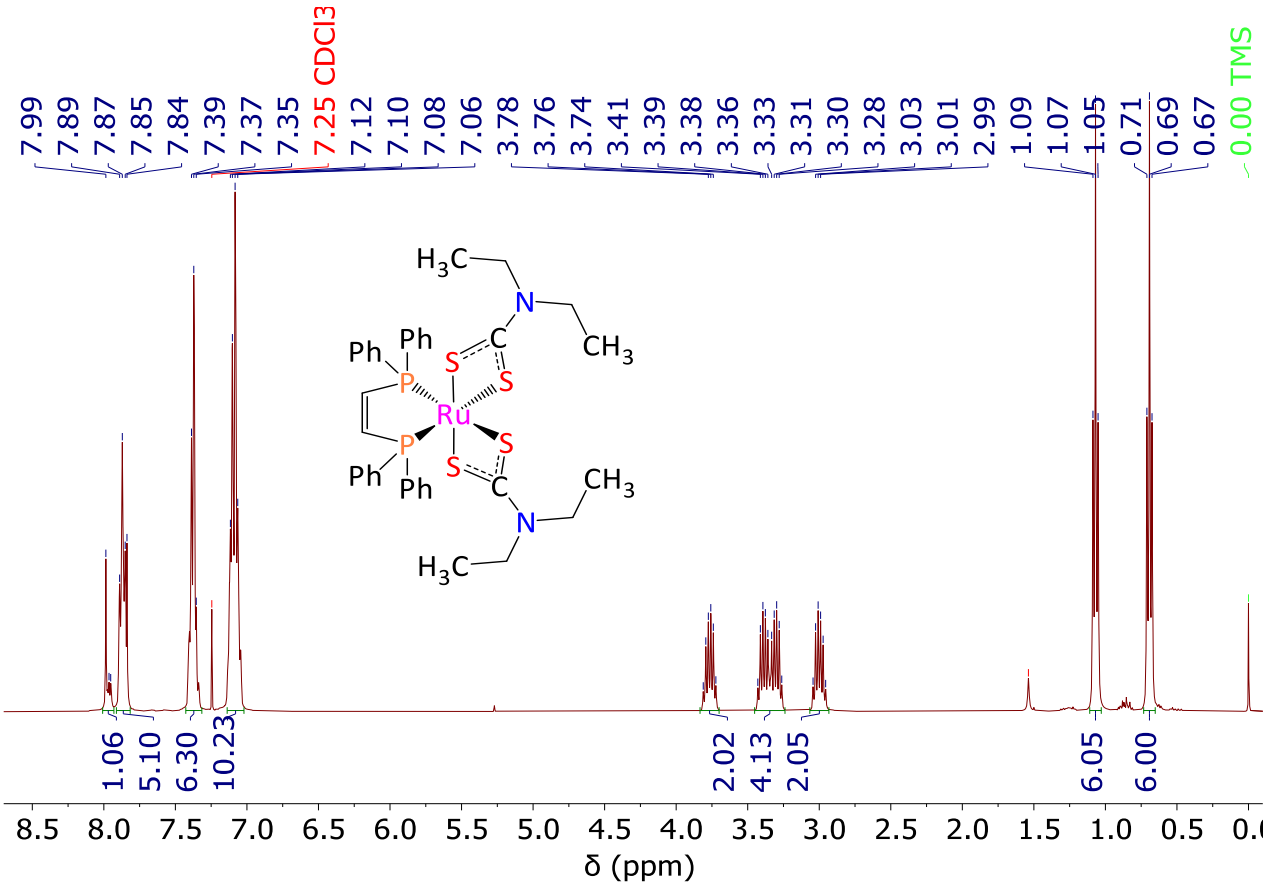

Fig. S43. ^{1}H NMR spectrum (400 MHz, $CDCl_3$, 298 K) of [Ru(S_2CNEt_2)$_2$(dppen)] (**6**)

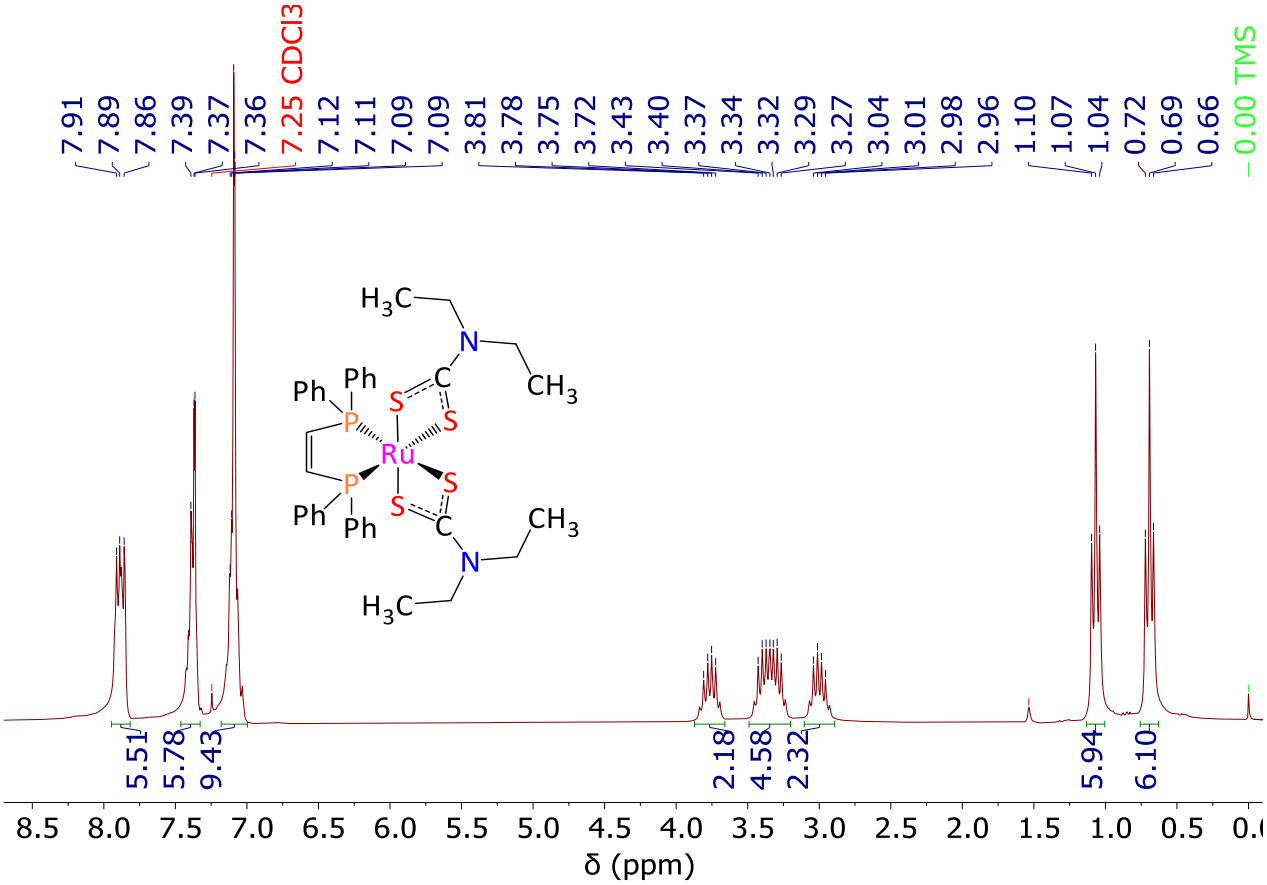

Fig. S44. $^{1}H\{^{31}P\}$ NMR spectrum (250 MHz, $CDCl_3$, 298 K) of [Ru(S_2CNEt_2)$_2$(dppen)] (**6**)

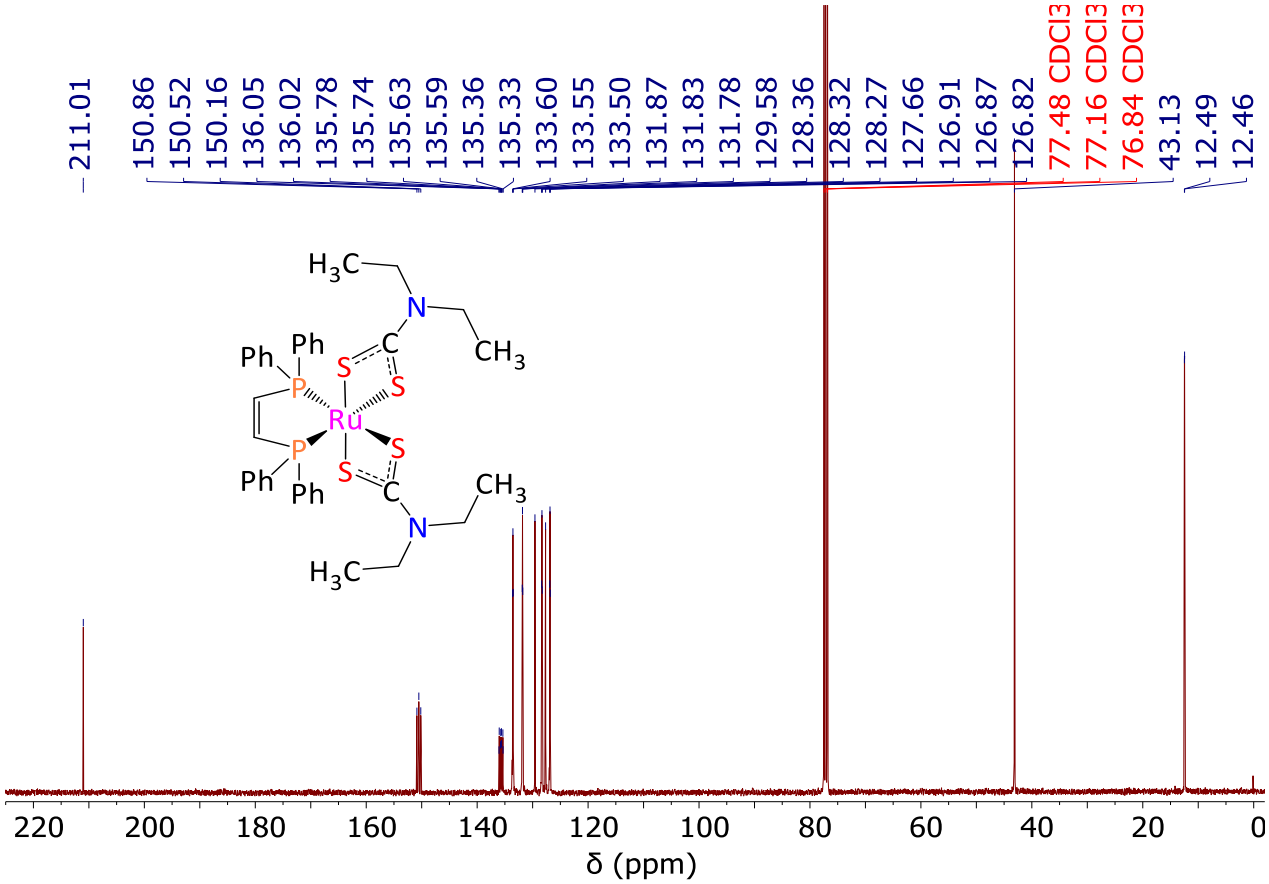

Fig. S45. $^{13}C\{^{1}H\}$ NMR spectrum (101 MHz, $CDCl_3$, 298 K) of $[Ru(S_2CNEt_2)_2(dppen)]$ (**6**)

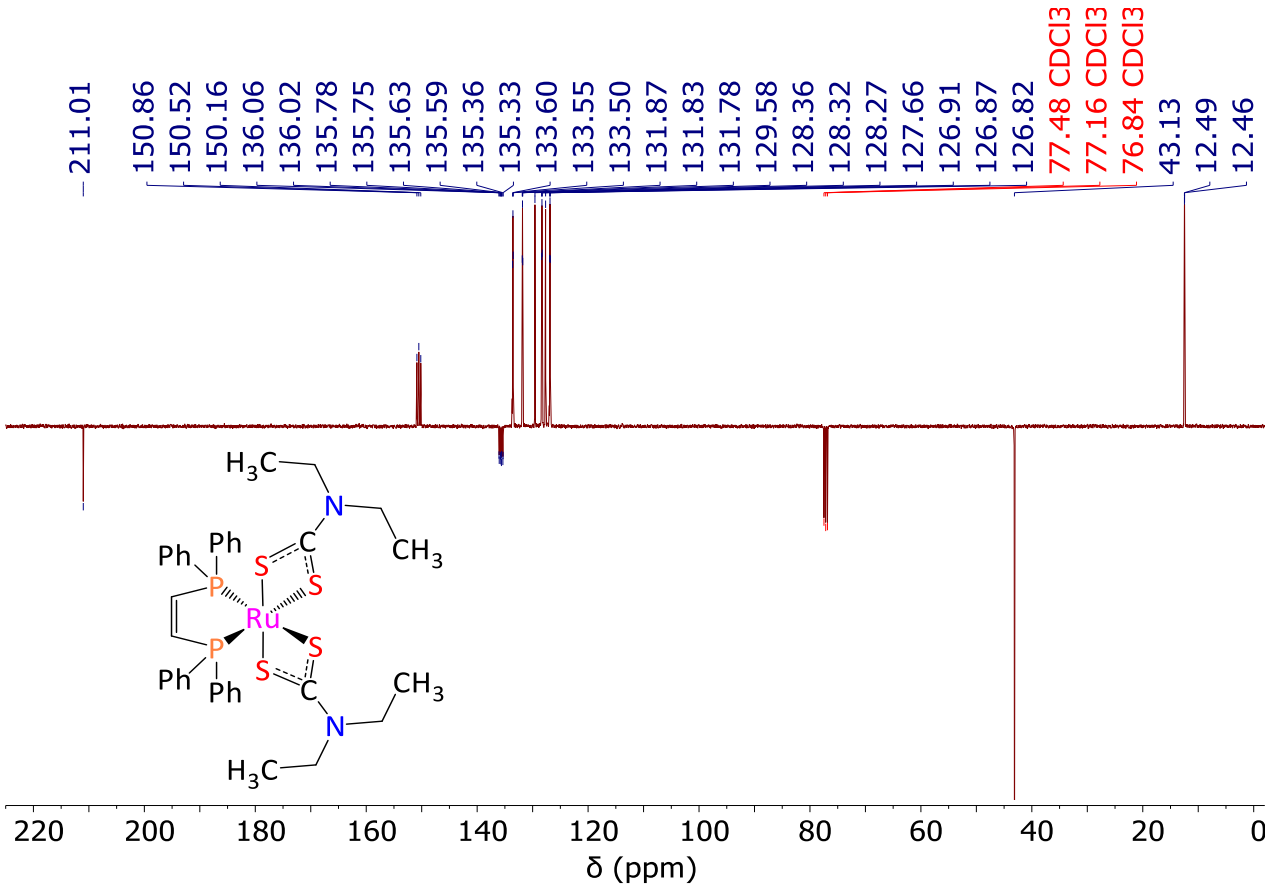

Fig. S46. $^{13}C\{^{1}H\}$ APT NMR spectrum (101 MHz, $CDCl_3$, 298 K) of $[Ru(S_2CNEt_2)_2(dppen)]$ (**6**)

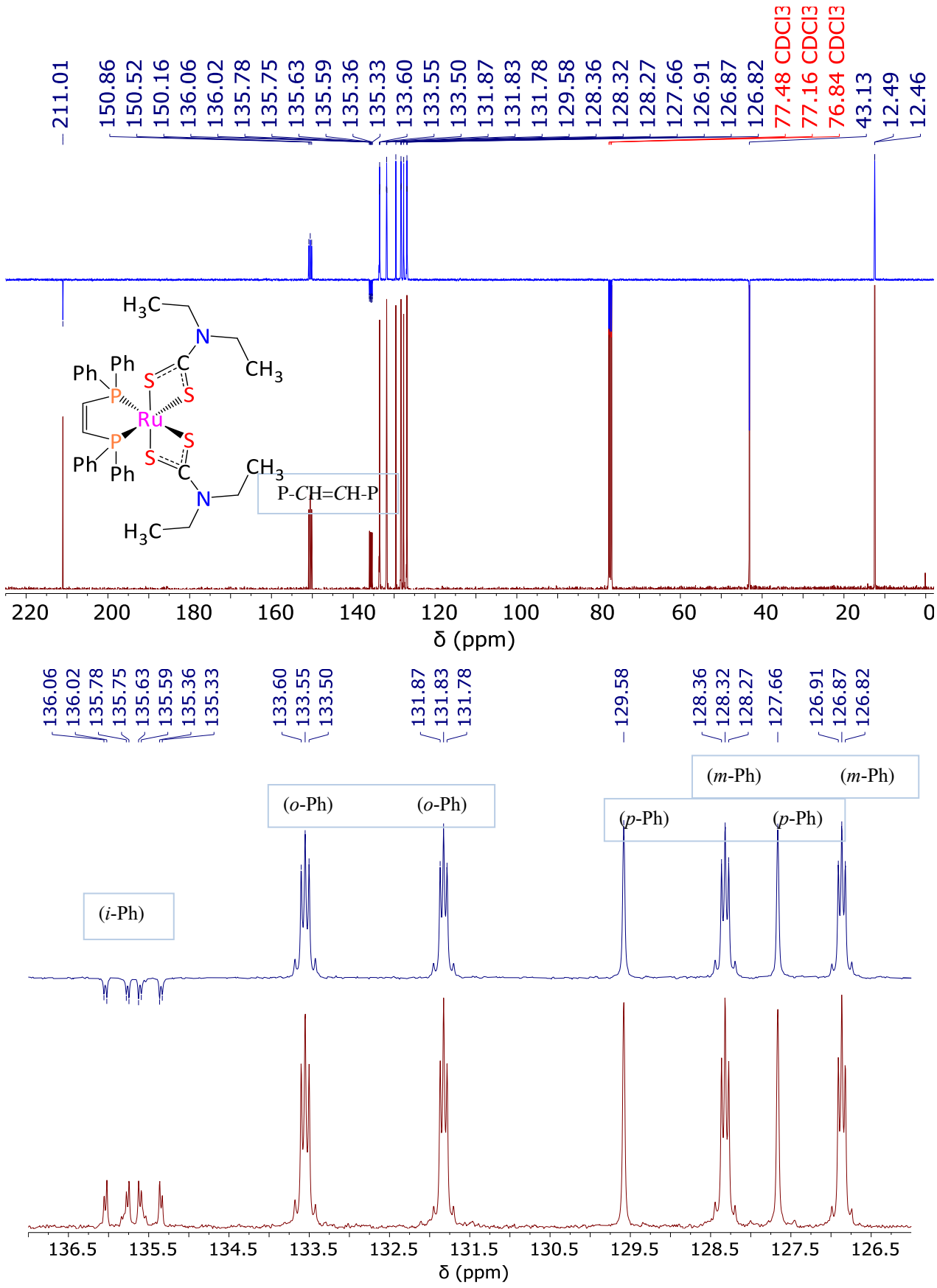

Fig. S47. ^{13}C CPD and APT NMR spectra (101 MHz, $CDCl_3$, 298 K) of [$Ru(S_2CNEt_2)_2$(dppen)] (**6**)

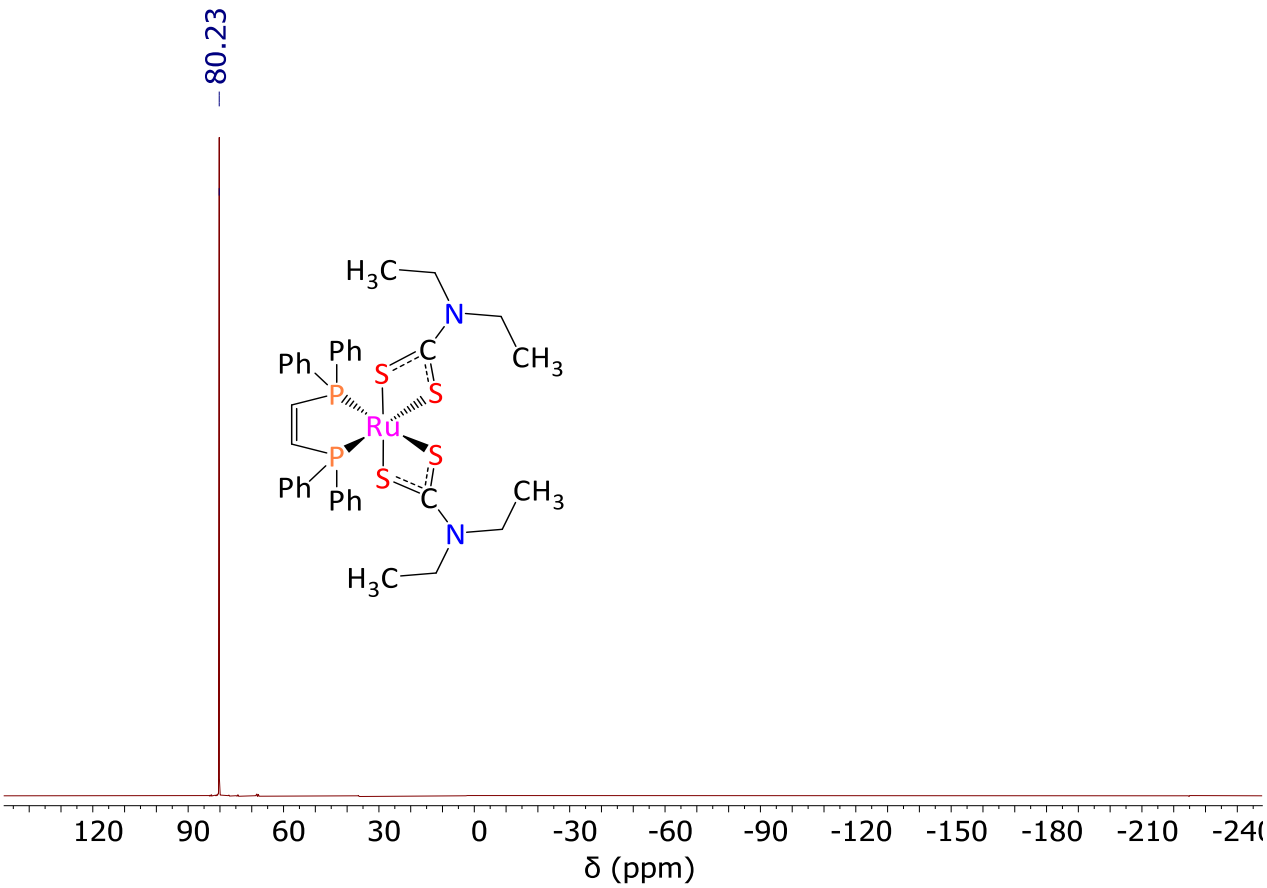

Fig. S48. ^{31}P NMR spectrum (162 MHz, $CDCl_3$, 298 K) of [Ru(S_2CNEt_2)$_2$(dppen)] (**6**)

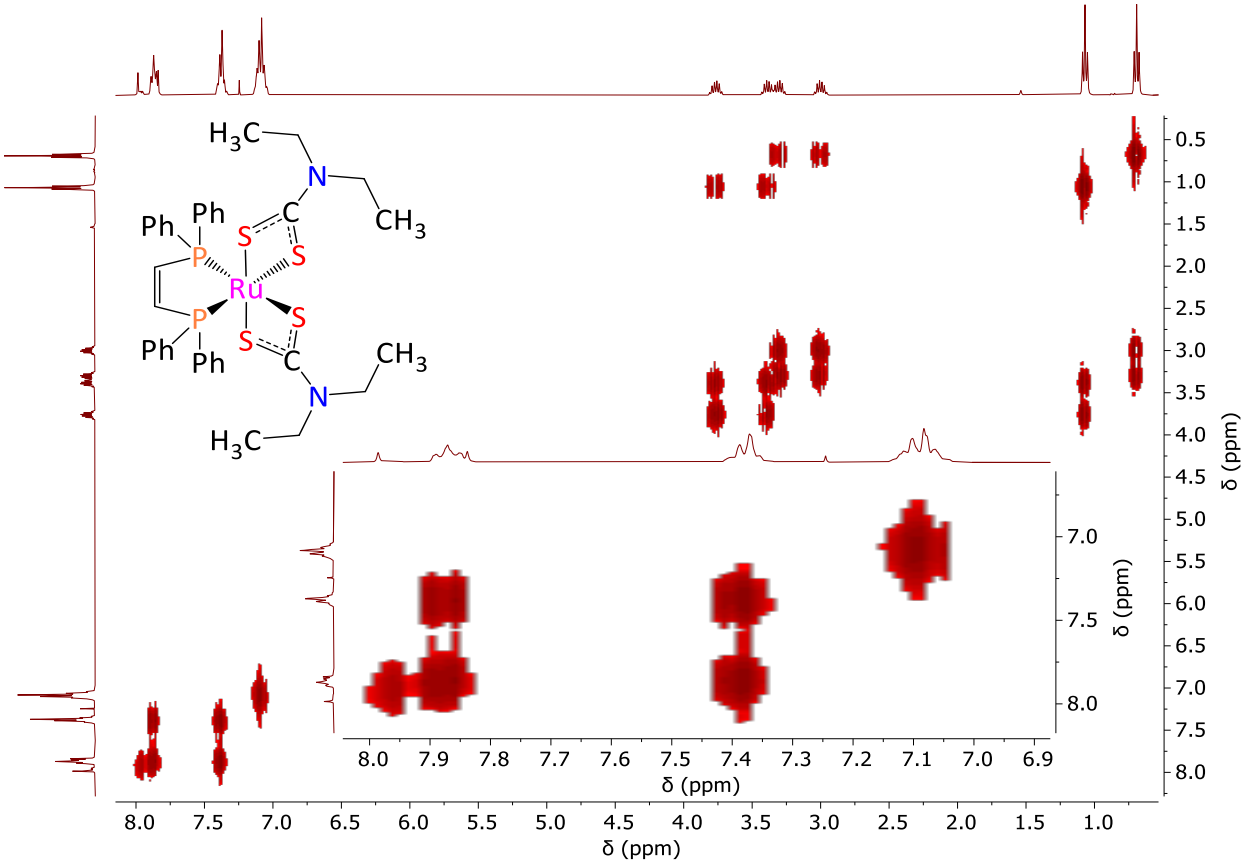

Fig. S49. COSY NMR spectrum (400 MHz, $CDCl_3$, 298 K) of [Ru(S_2CNEt_2)$_2$(dppen)] (**6**)

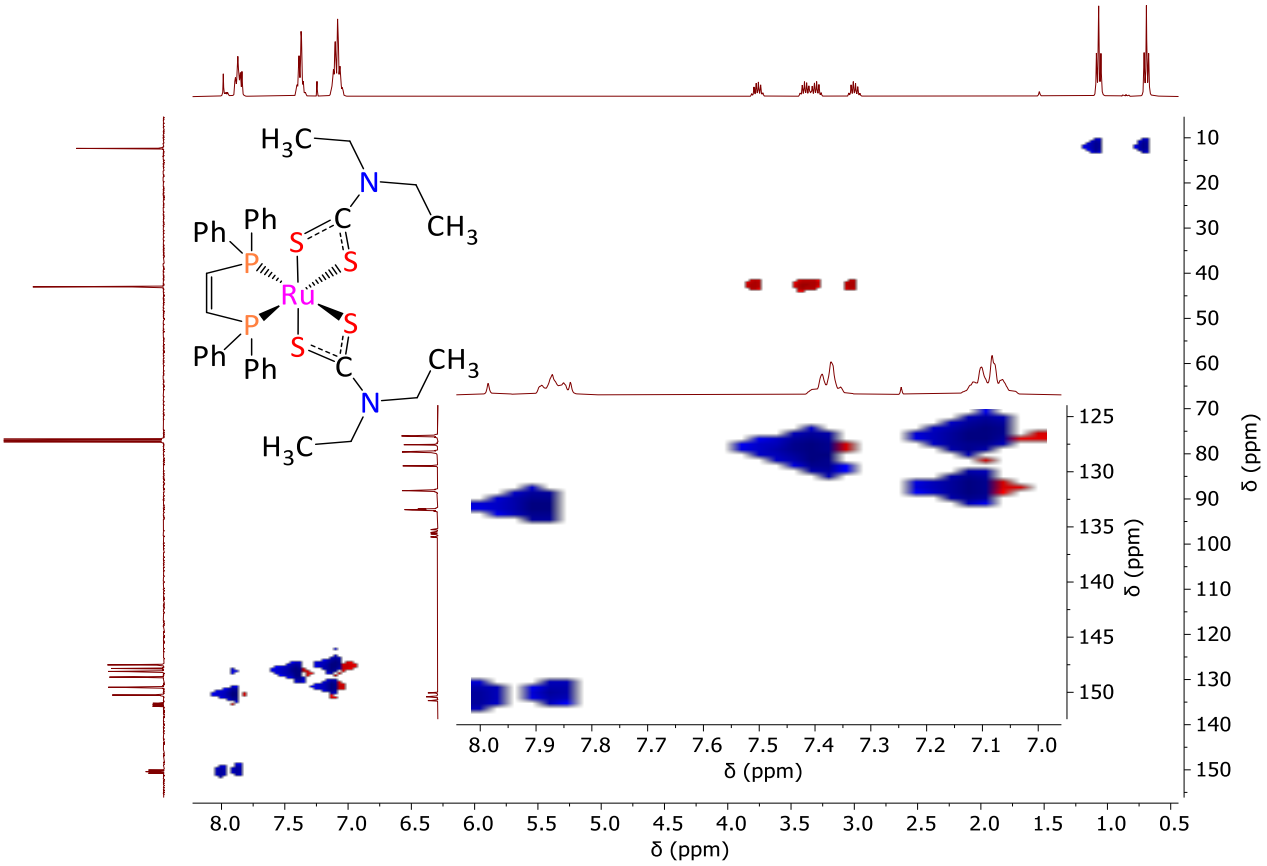

Fig. S50. HSQC NMR spectrum (400 MHz, $CDCl_3$, 298 K) of [Ru(S_2CNEt_2)$_2$(dppen)] (**6**)

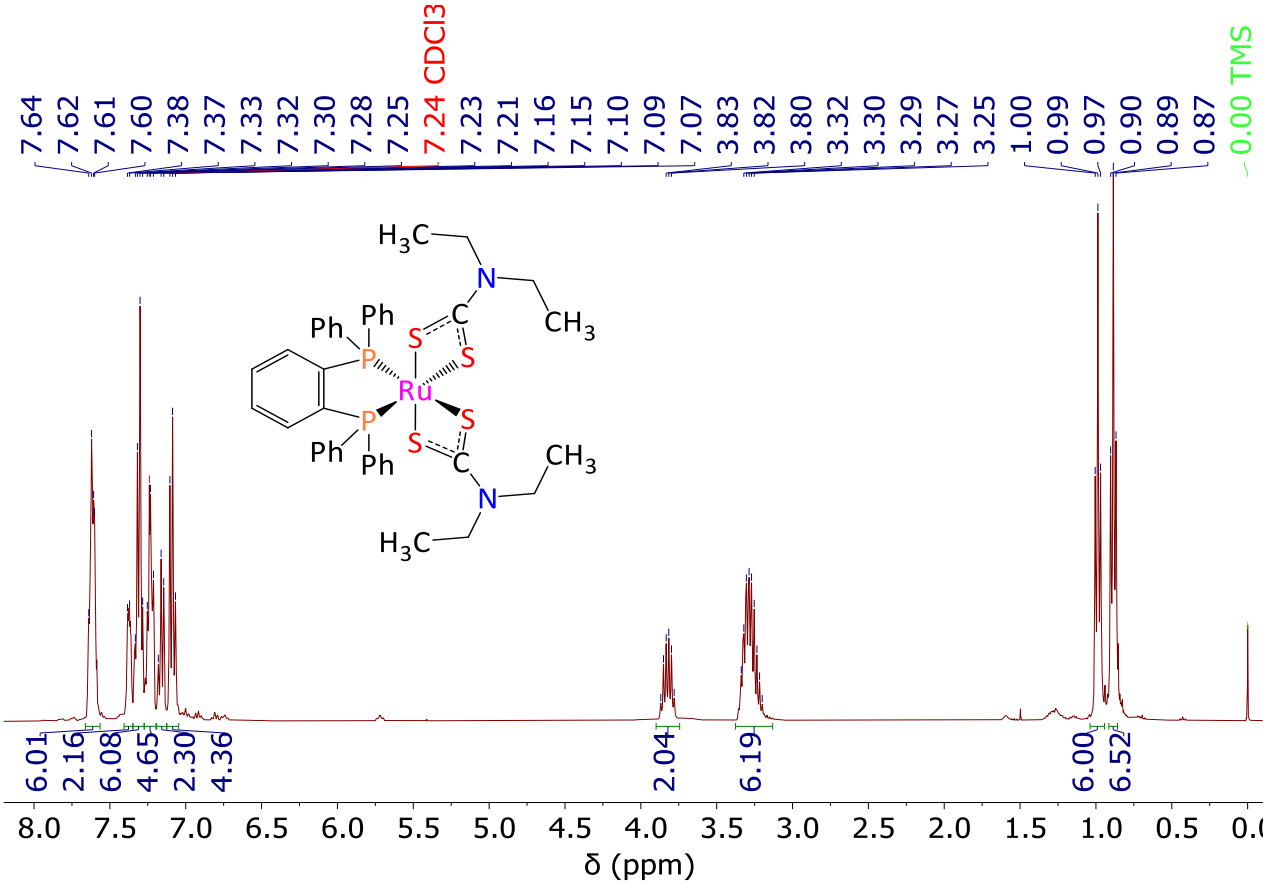

Fig. S51. ^{1}H NMR spectrum (400 MHz, $CDCl_3$, 298 K) of [Ru(S_2CNEt_2)$_2$(dppbz)] (**7**)

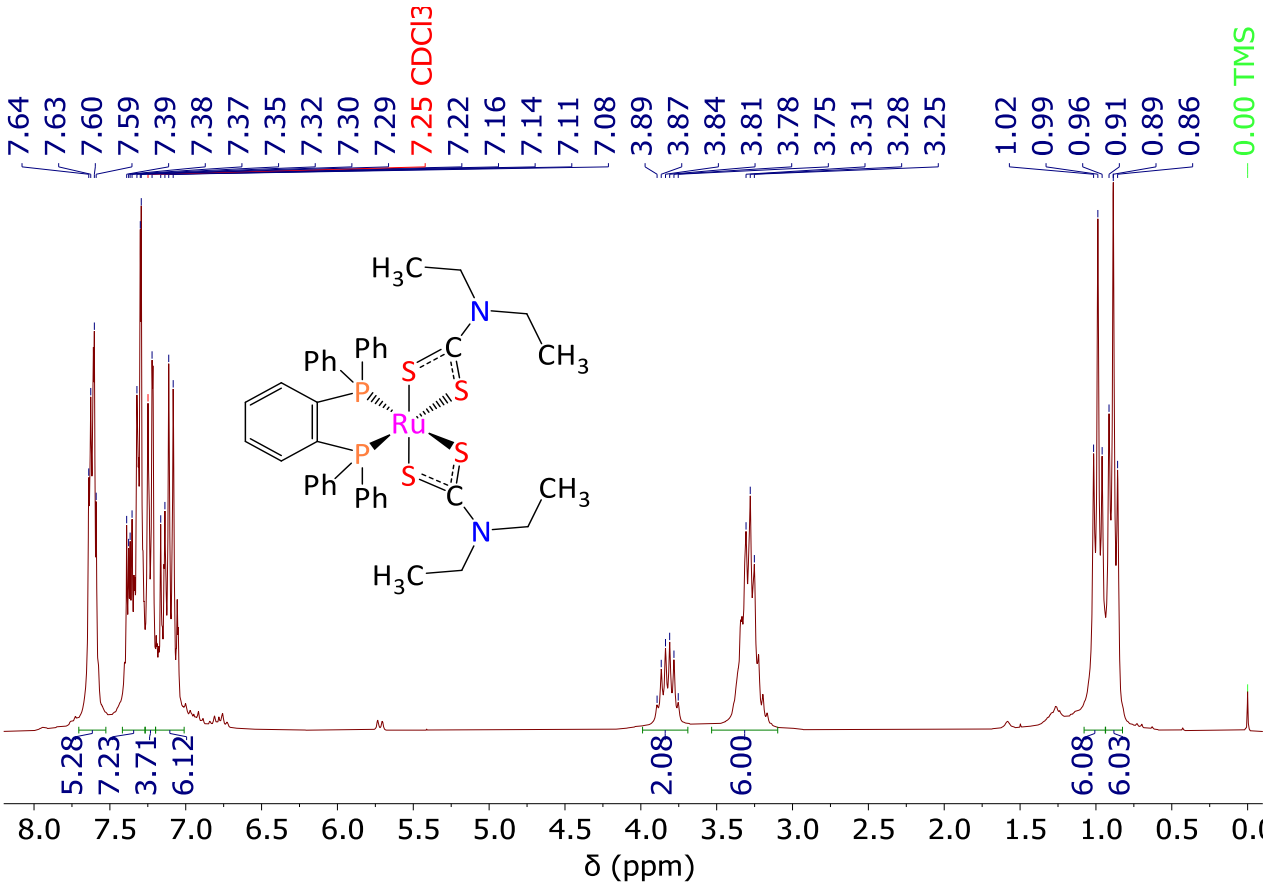

Fig. S52. $^{1}H\{^{31}P\}$ NMR spectrum (250 MHz, $CDCl_3$, 298 K) of $[Ru(S_2CNEt_2)_2(dppbz)]$ (**7**)

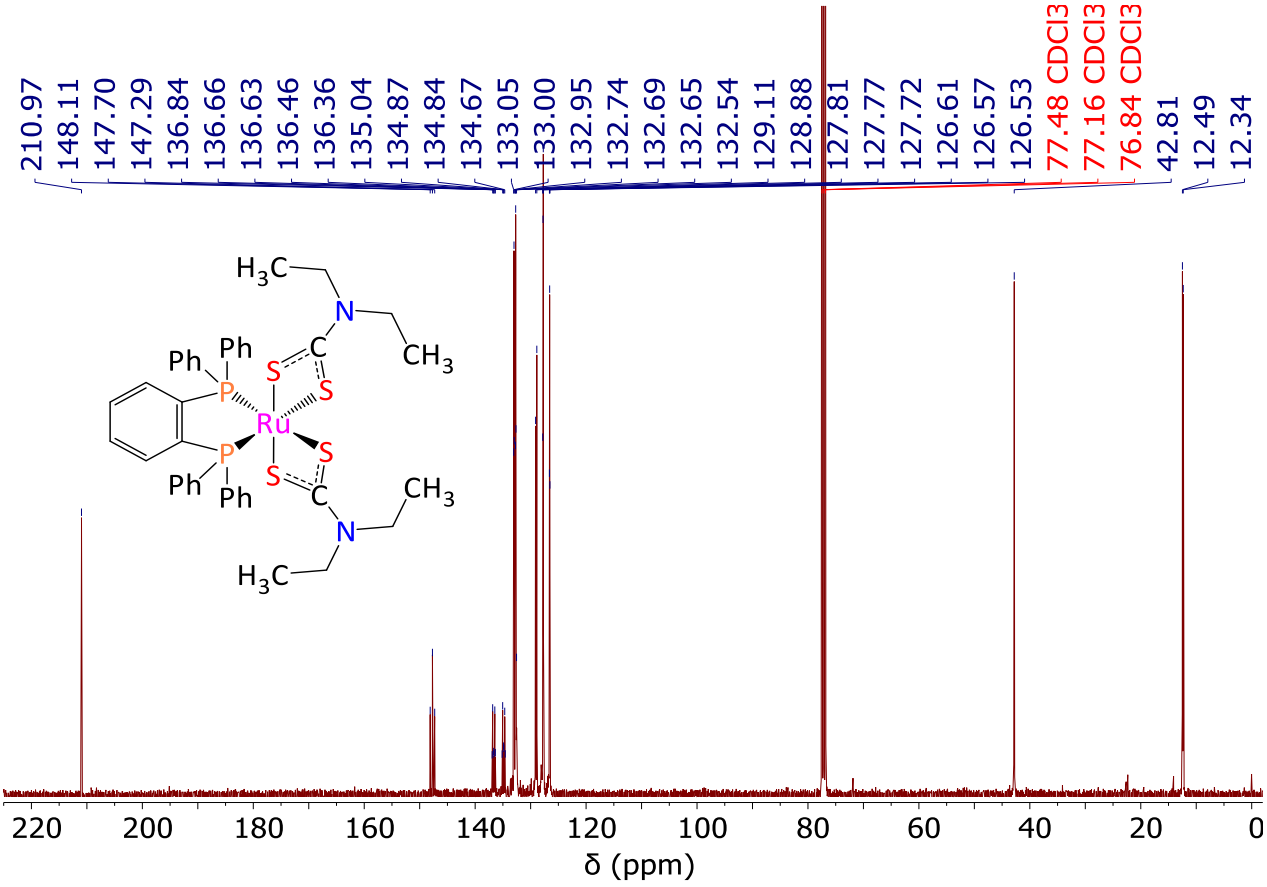

Fig. S53. $^{13}C\{^{1}H\}$ NMR spectrum (101 MHz, $CDCl_3$, 298 K) of $[Ru(S_2CNEt_2)_2(dppbz)]$ (**7**)

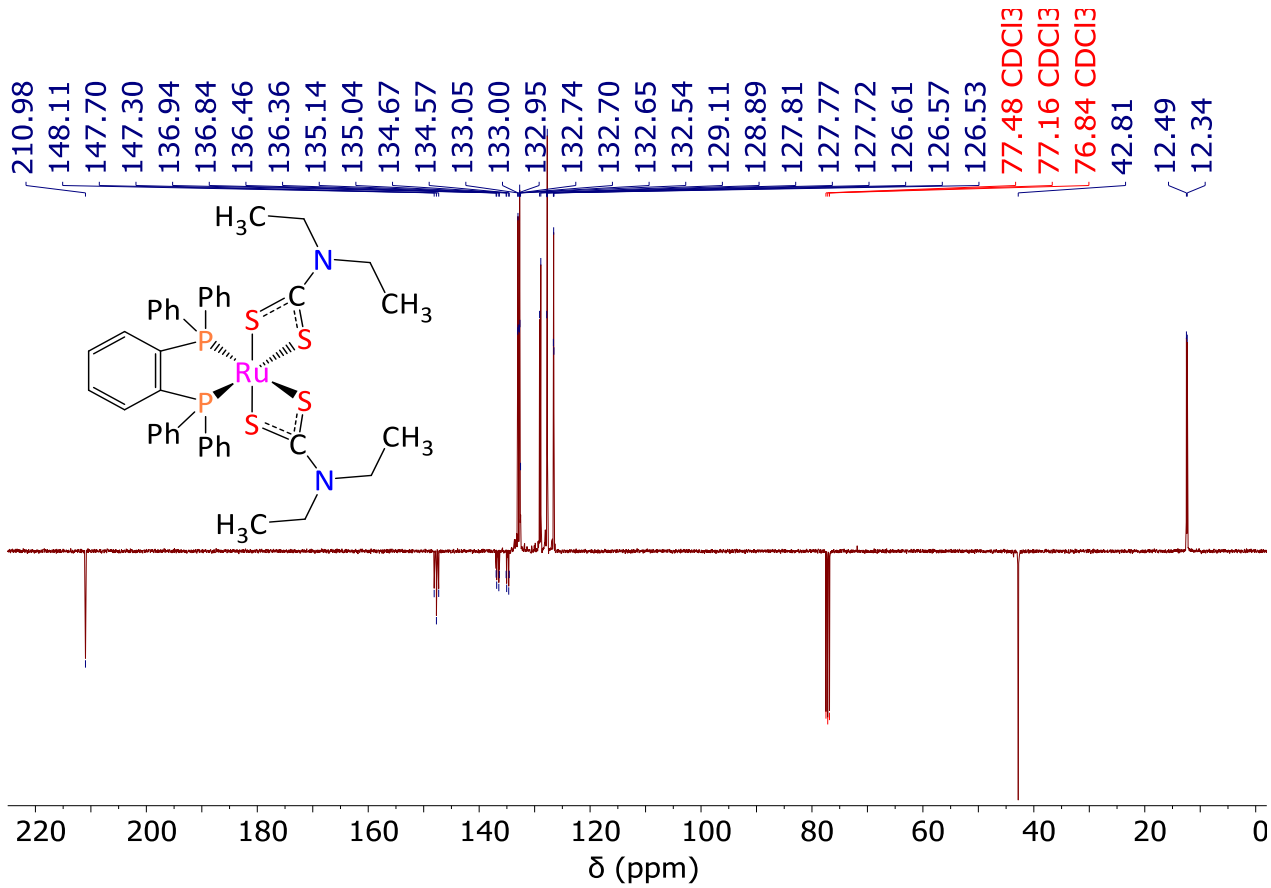

Fig. S54. $^{13}C\{^{1}H\}$ APT NMR spectrum (101 MHz, $CDCl_3$, 298 K) of $[Ru(S_2CNEt_2)_2(dppbz)]$ (**7**)

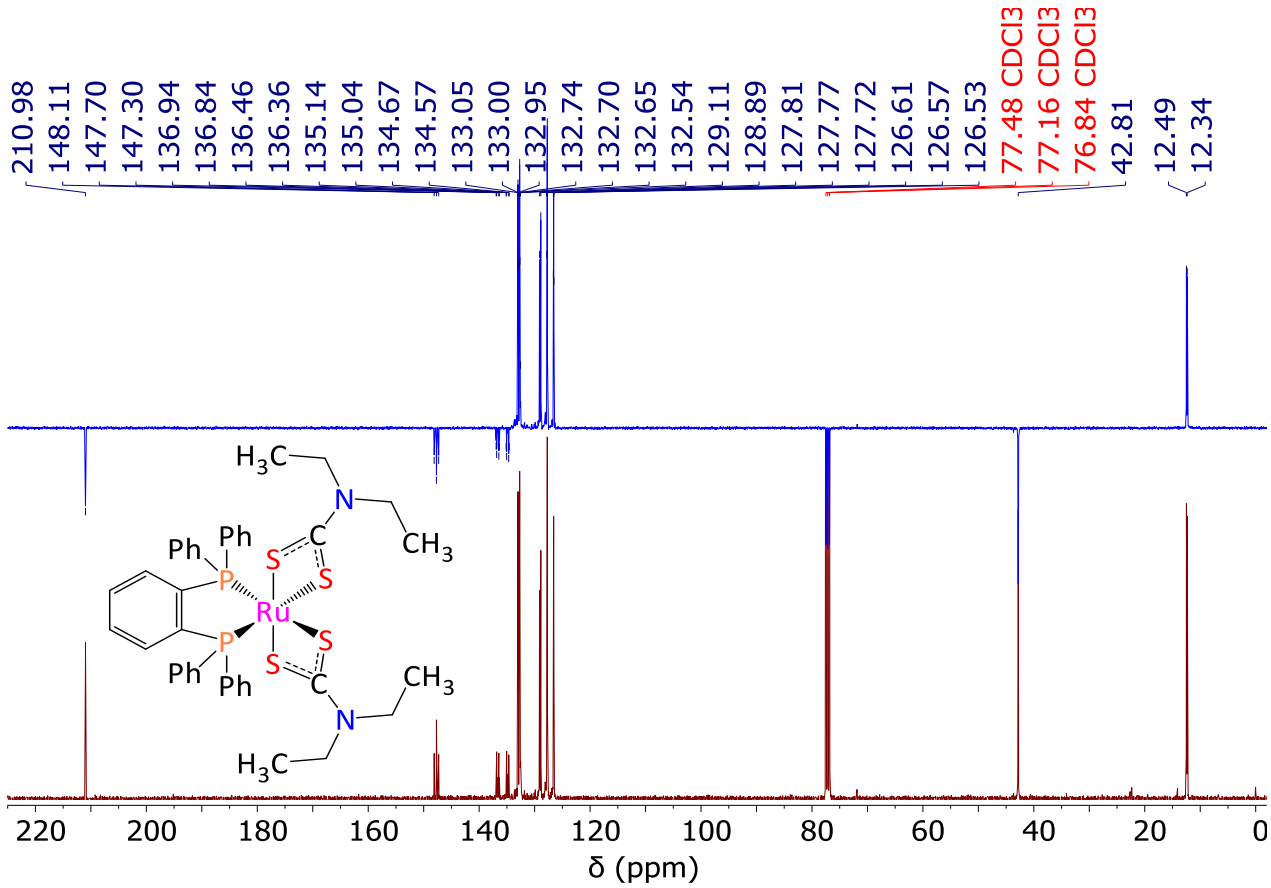

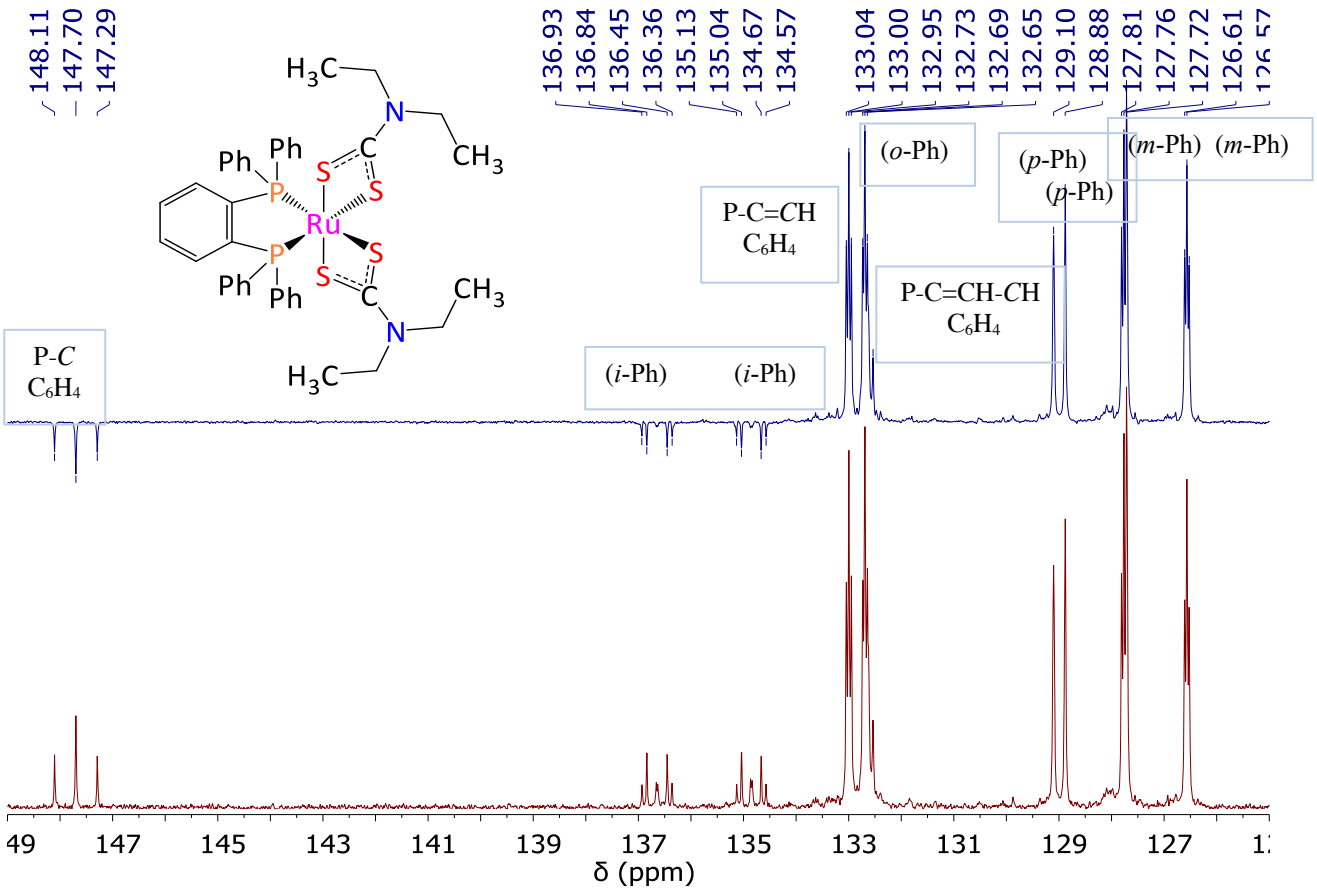

Fig. S55. ^{13}C CPD and APT NMR spectra (101 MHz, $CDCl_3$, 298 K) of $[Ru(S_2CNEt_2)_2(dppbz)]$ (**7**)

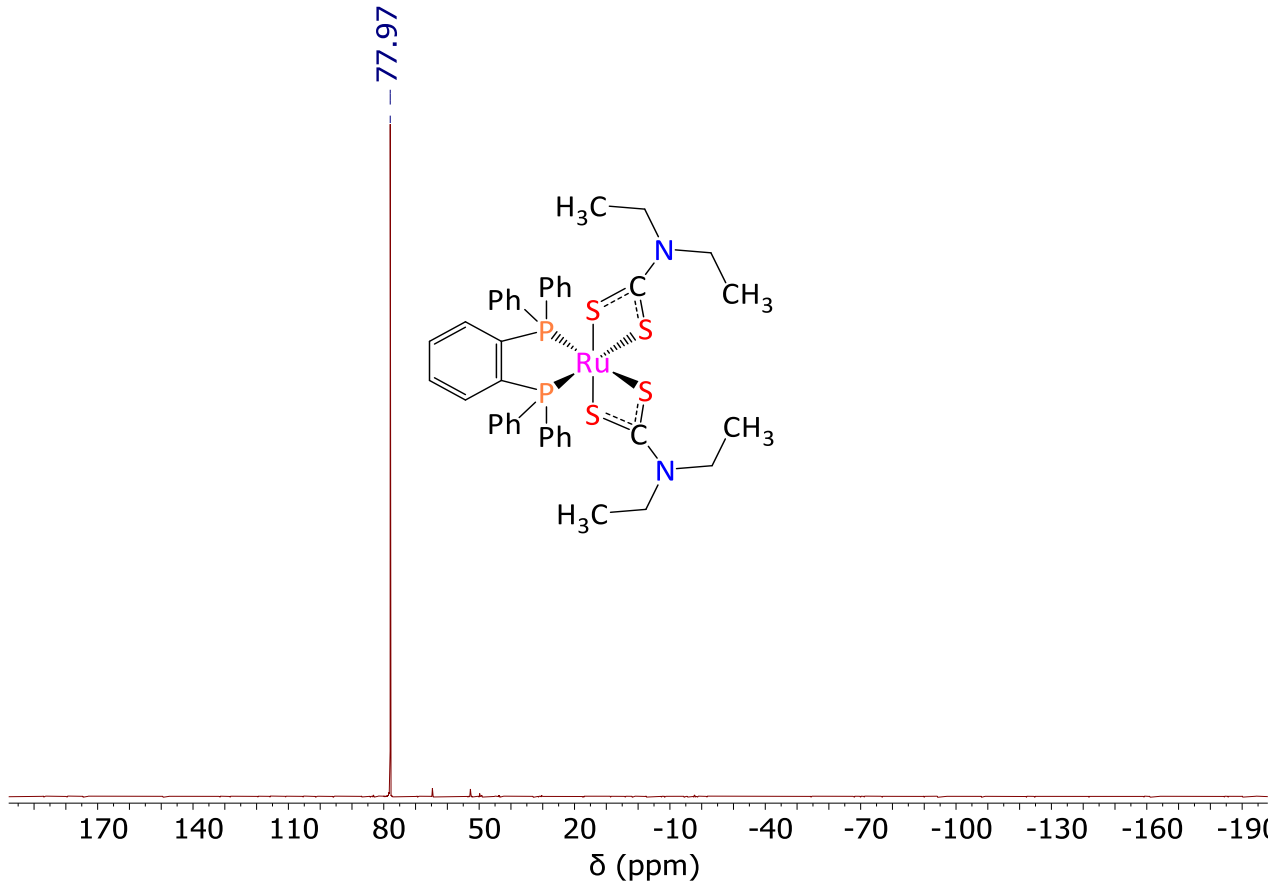

Fig. S56. ^{31}P NMR spectrum (162 MHz, $CDCl_3$, 298 K) of $[Ru(S_2CNEt_2)_2(dppbz)]$ (**7**)

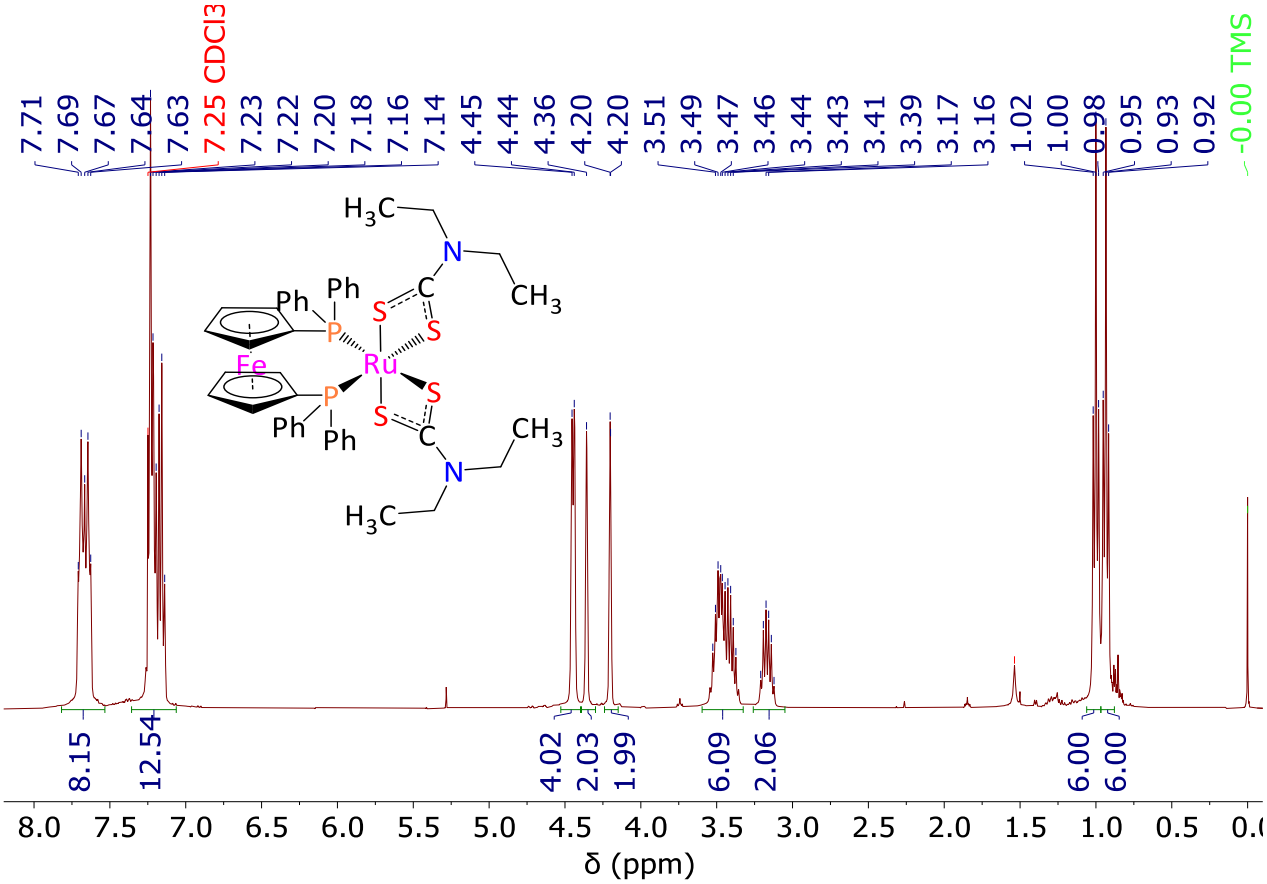

Fig. S57. ^{1}H NMR spectrum (400 MHz, $CDCl_3$, 298 K) of [Ru(S_2CNEt_2)$_2$(dppf)] (**8**)

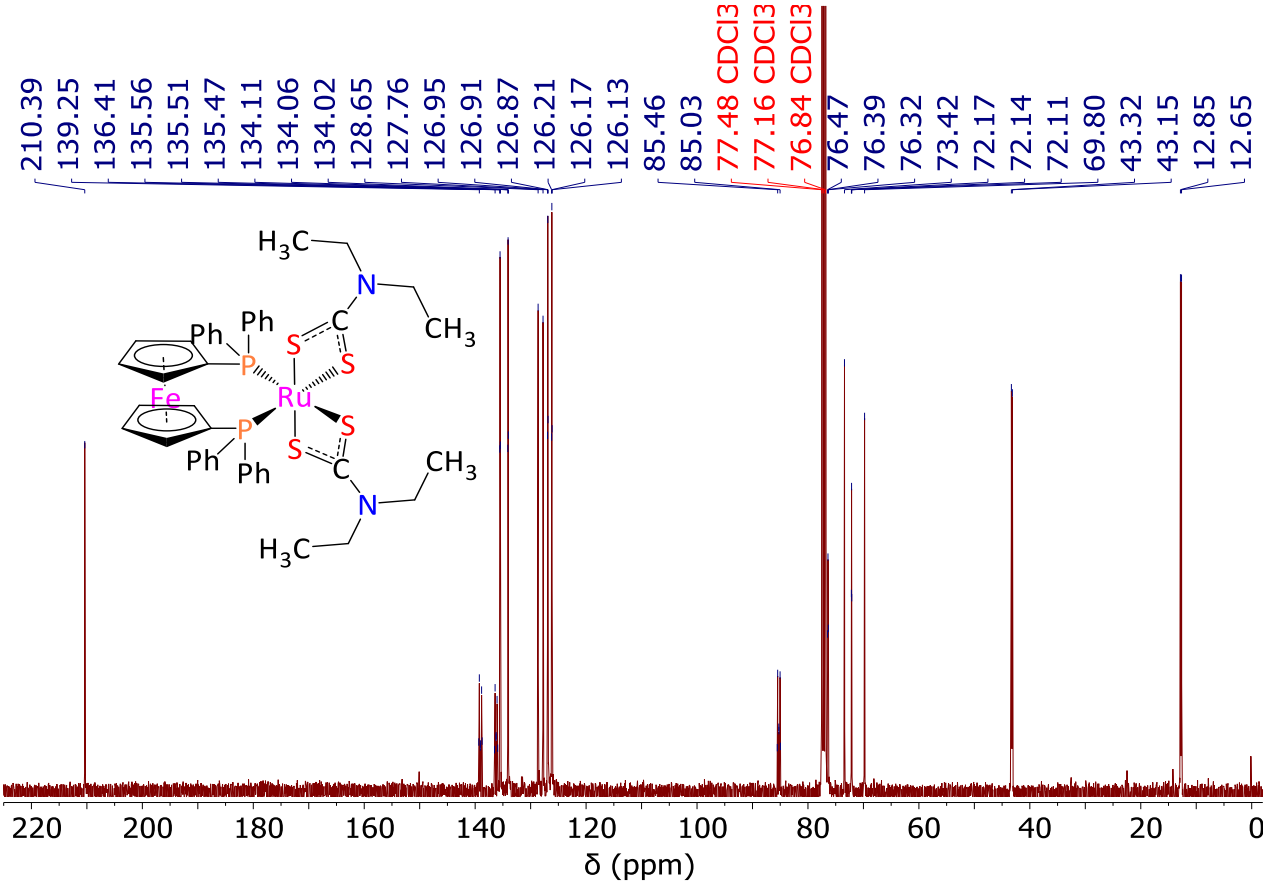

Fig. S58. ^{13}C{^{1}H} NMR spectrum (101 MHz, $CDCl_3$, 298 K) of [Ru(S_2CNEt_2)$_2$(dppf)] (**8**)

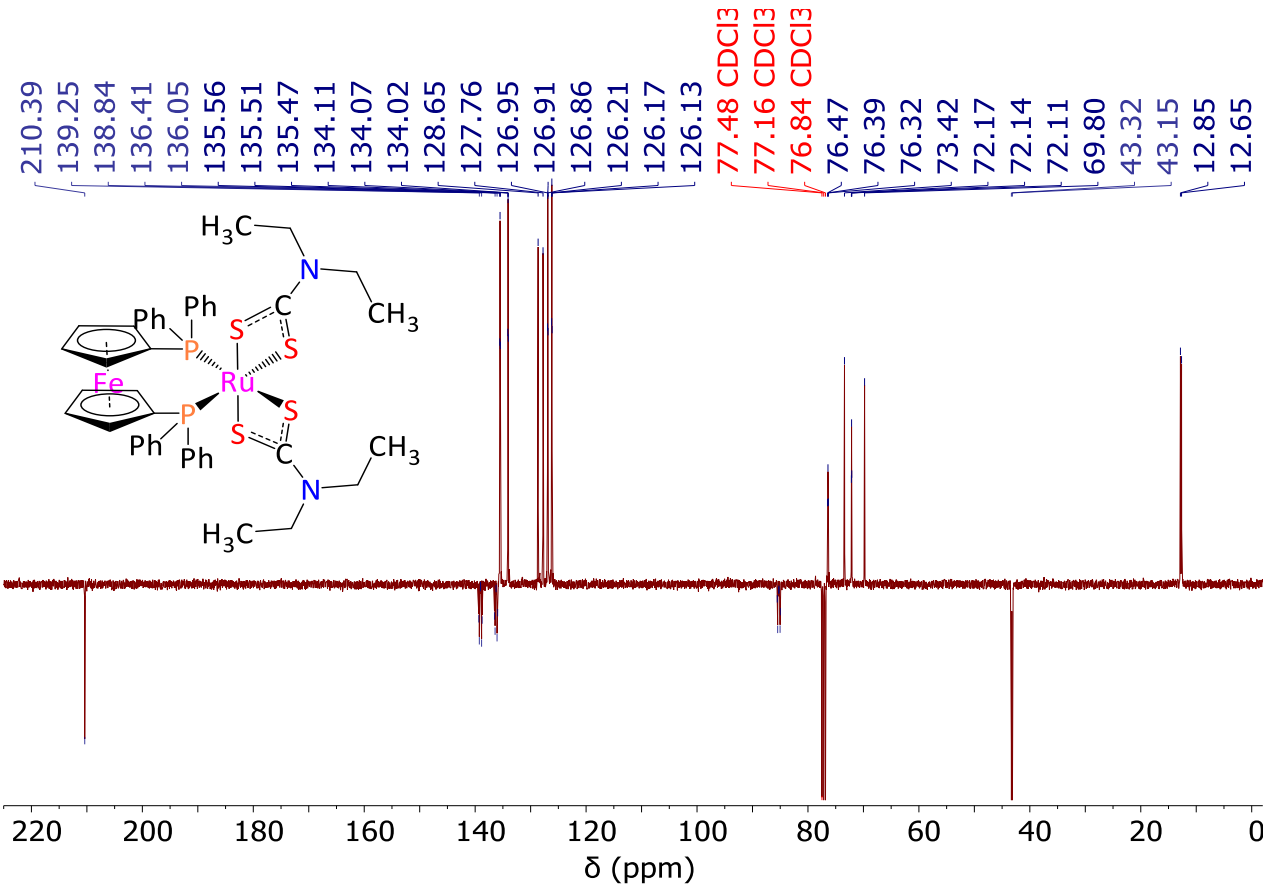

Fig. S59. $^{13}C\{^{1}H\}$ APT NMR spectrum (101 MHz, $CDCl_3$, 298 K) of $[Ru(S_2CNEt_2)_2(dppf)]$ (**8**)

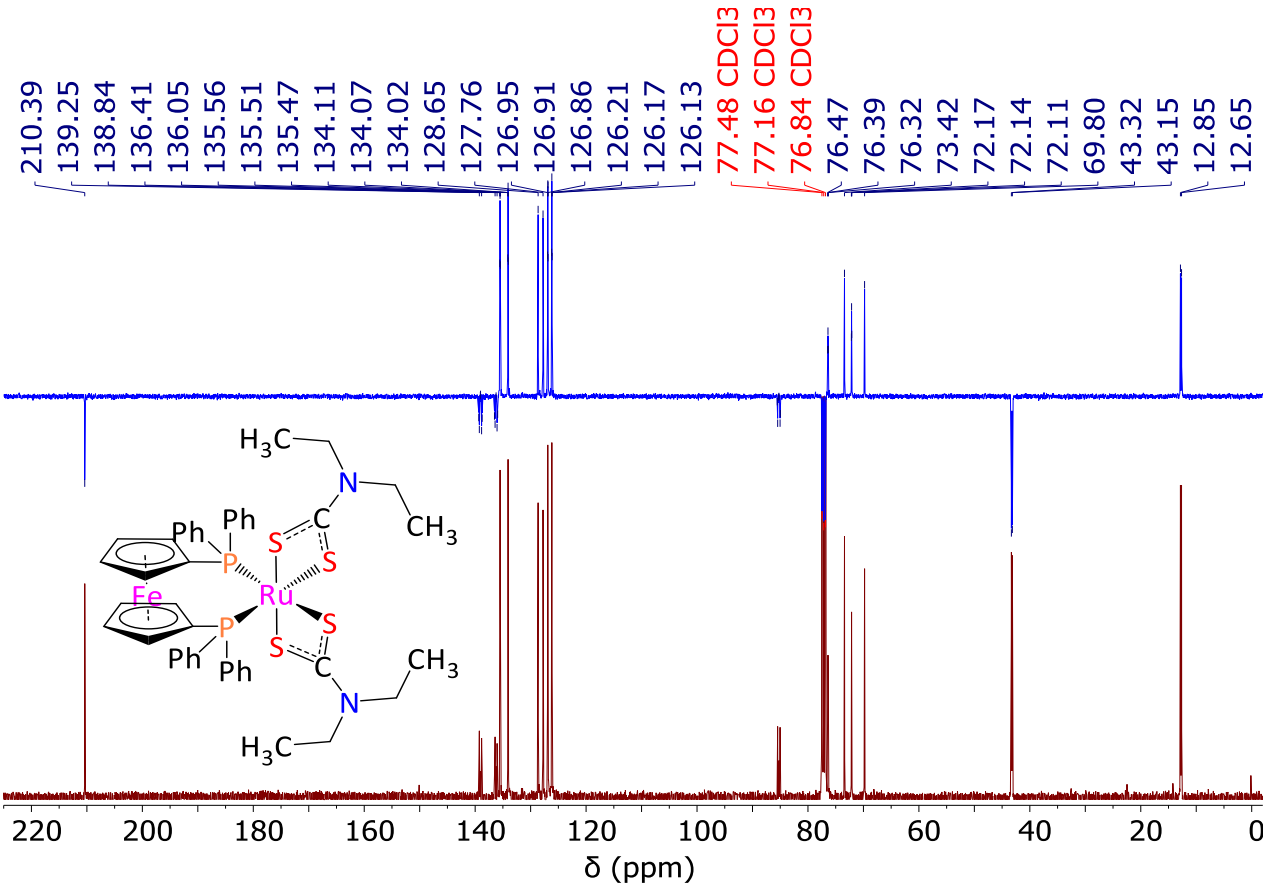

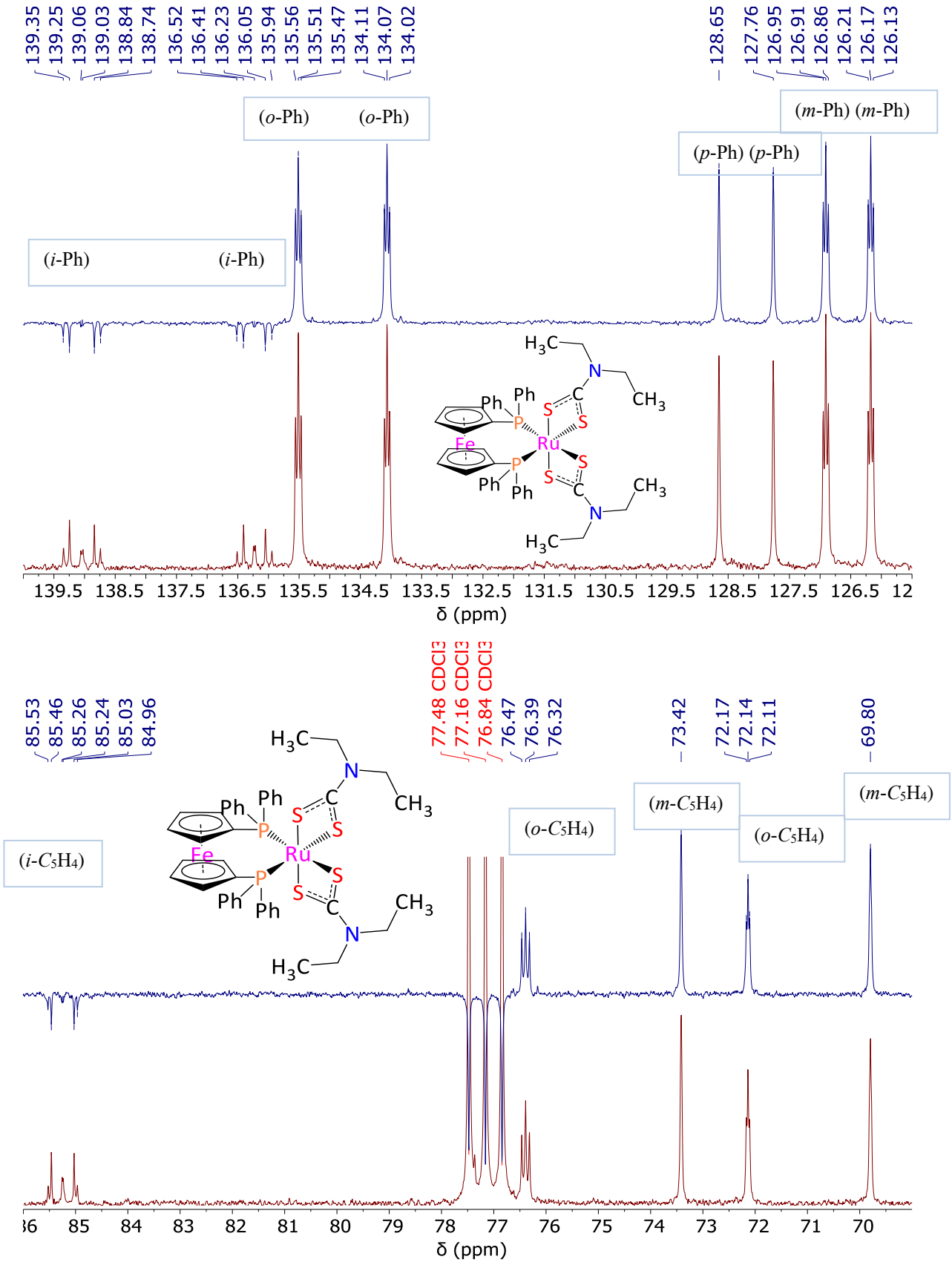

Fig. S60. ^{13}C CPD and APT NMR spectra (101 MHz, $CDCl_3$, 298 K) of $[Ru(S_2CNEt_2)_2(dppf)]$ (**8**)

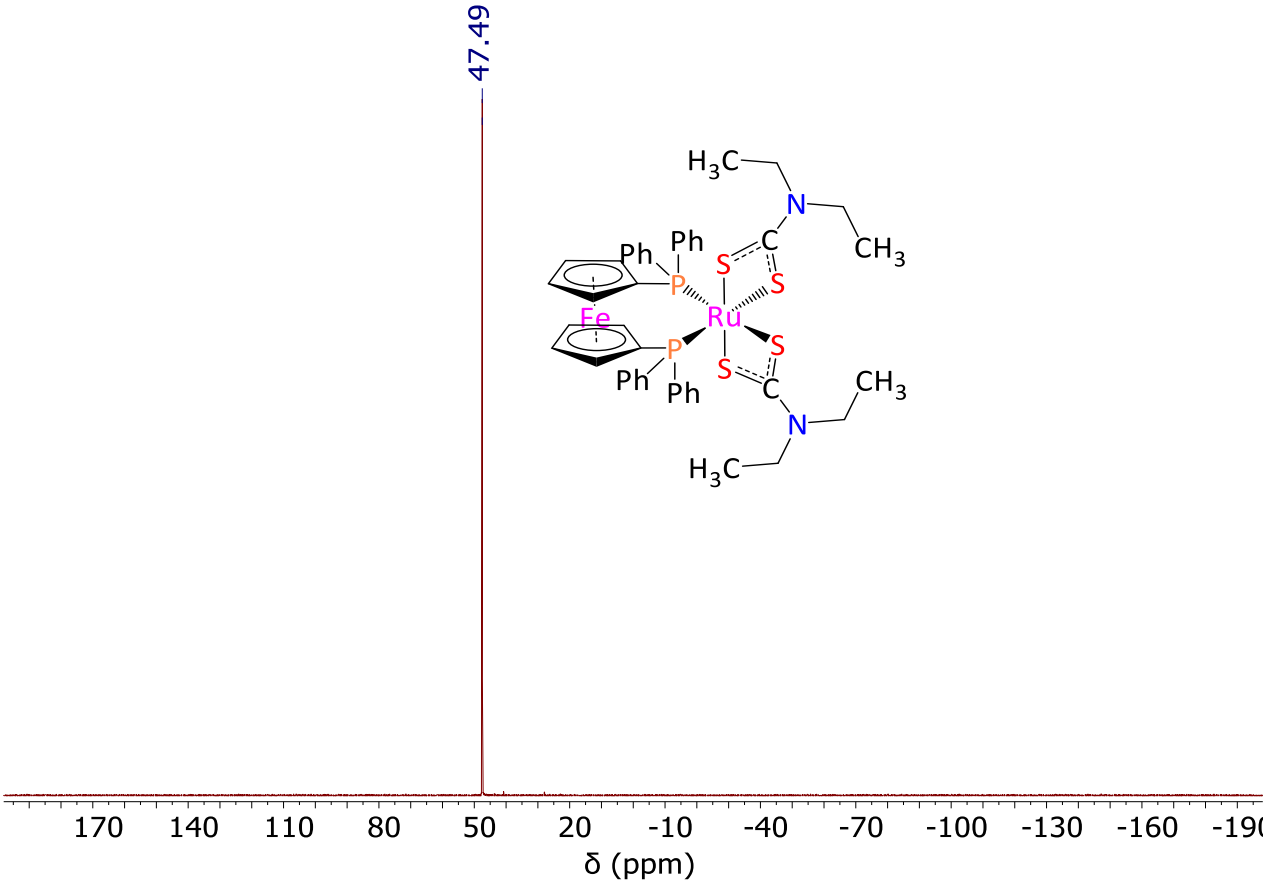

Fig. S61. ^{31}P NMR spectrum (162 MHz, $CDCl_3$, 298 K) of [Ru(S_2CNEt_2)$_2$(dppf)] (**8**)

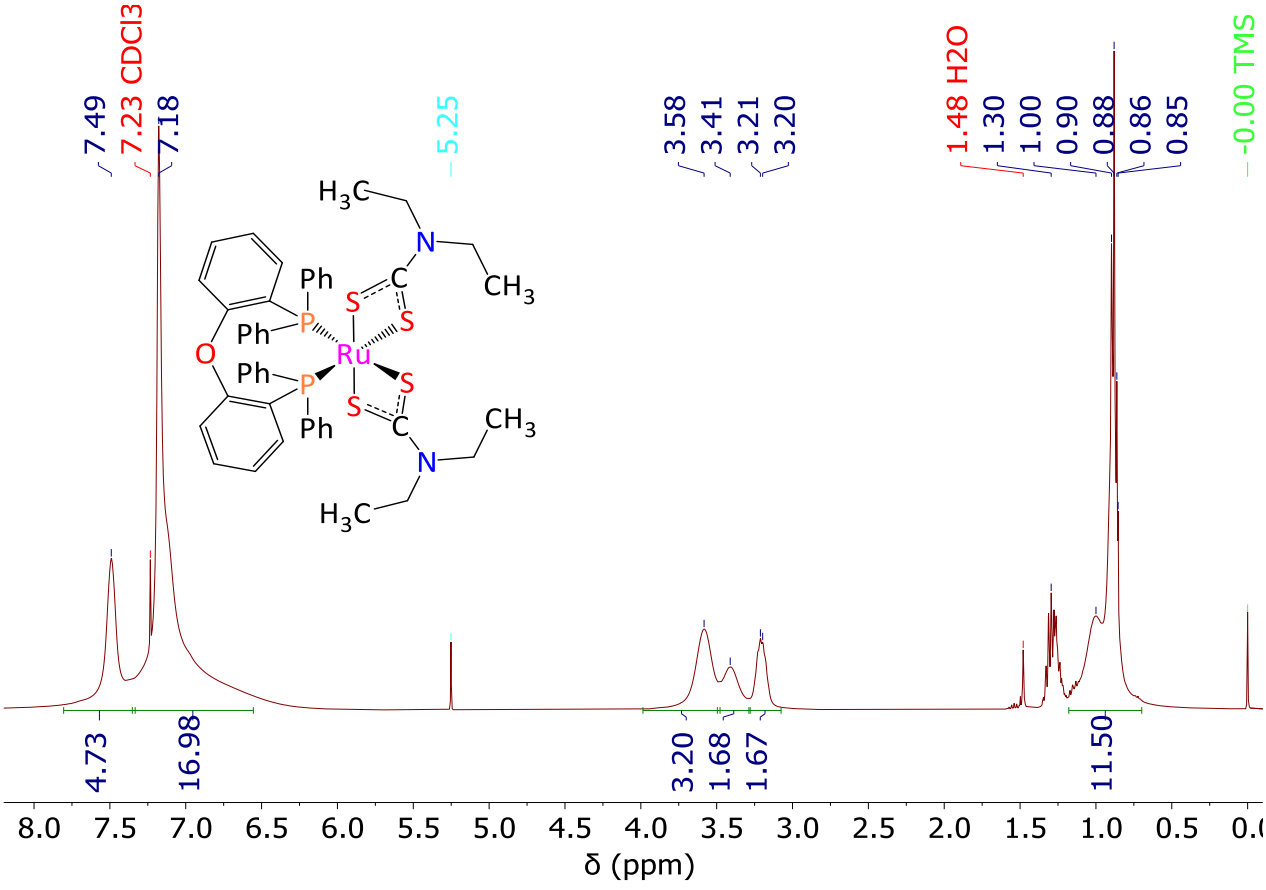

Fig. S62. ^{1}H NMR spectrum (400 MHz, $CDCl_3$, 298 K) of [Ru(S_2CNEt_2)$_2$(DPEphos)] (**9**)

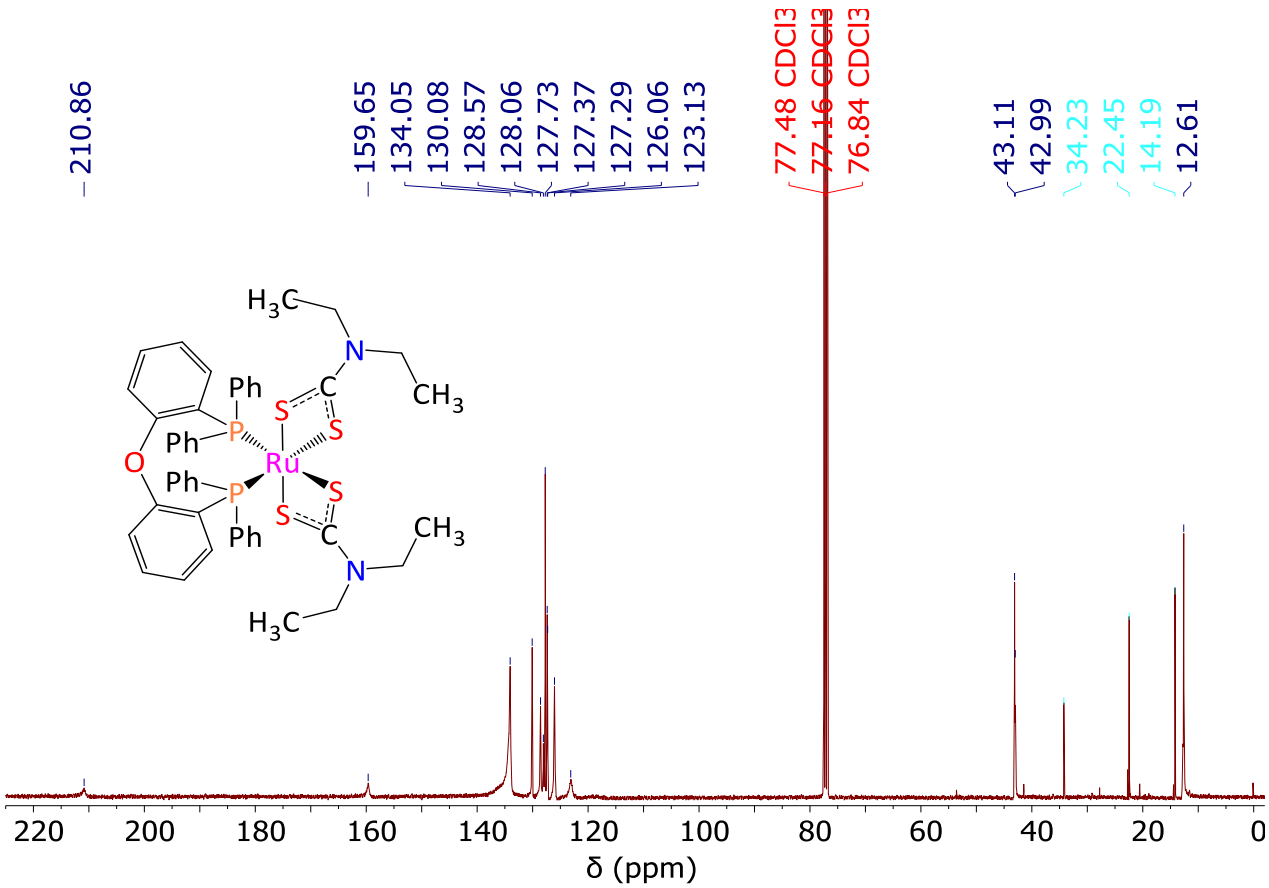

Fig. S63. $^{13}C\{^{1}H\}$ NMR spectrum (101 MHz, $CDCl_3$, 298 K) of $[Ru(S_2CNEt_2)_2(DPEphos)]$ (**9**)

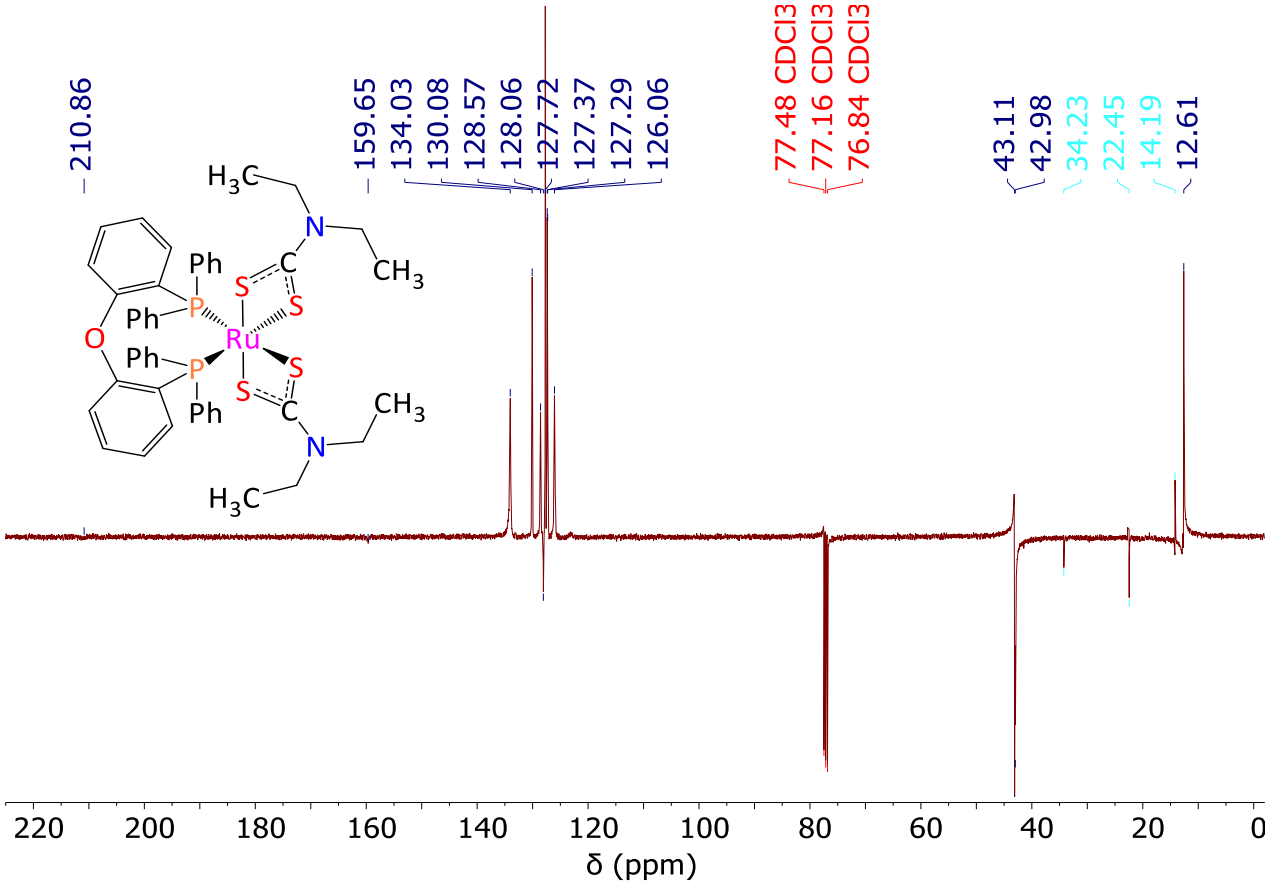

Fig. S64. $^{13}C\{^{1}H\}$ APT NMR spectrum (101 MHz, $CDCl_3$, 298 K) of $[Ru(S_2CNEt_2)_2(DPEphos)]$ (**9**)

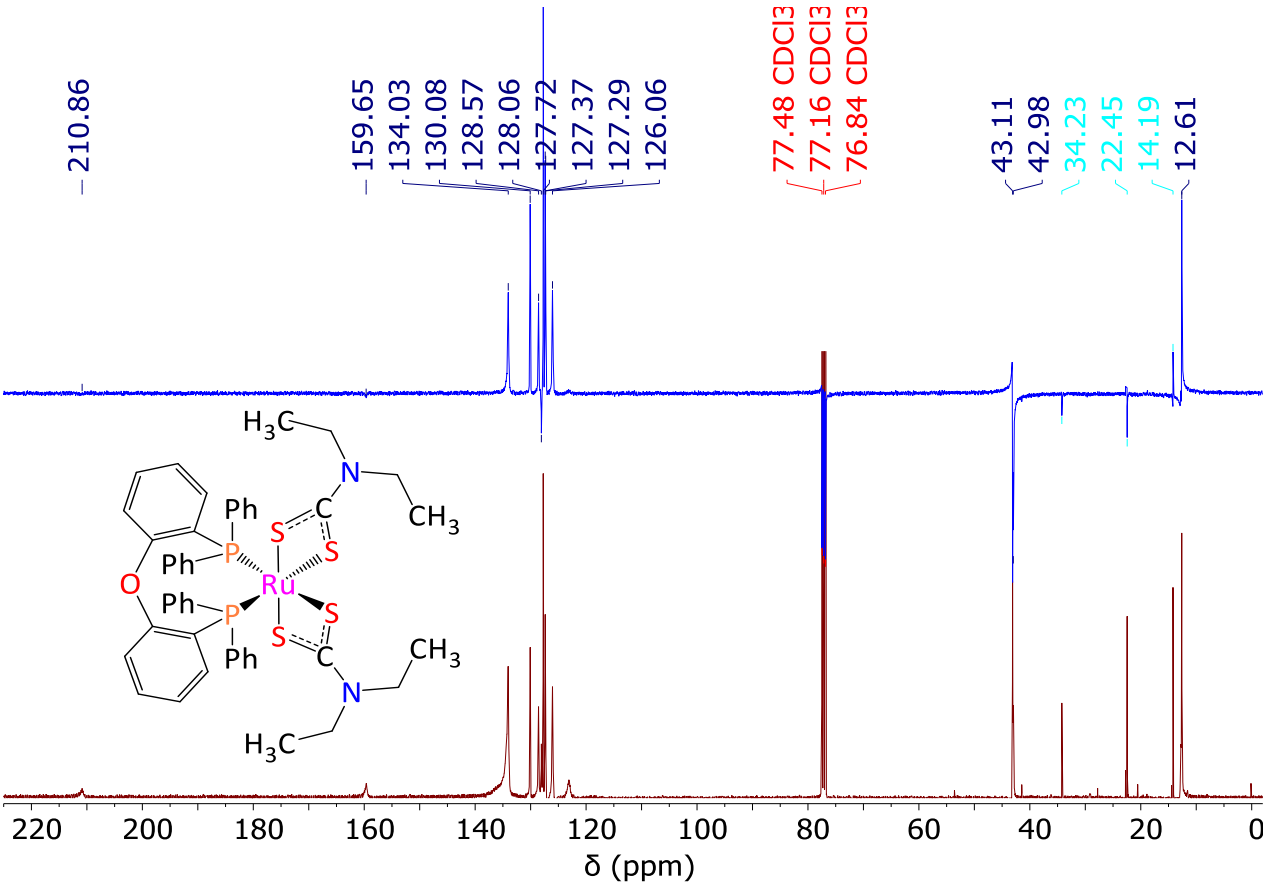

Fig. S65. ^{13}C CPD and APT NMR spectra (101 MHz, $CDCl_3$, 298 K) of [$Ru(S_2CNEt_2)_2$(DPEphos)] (**9**)

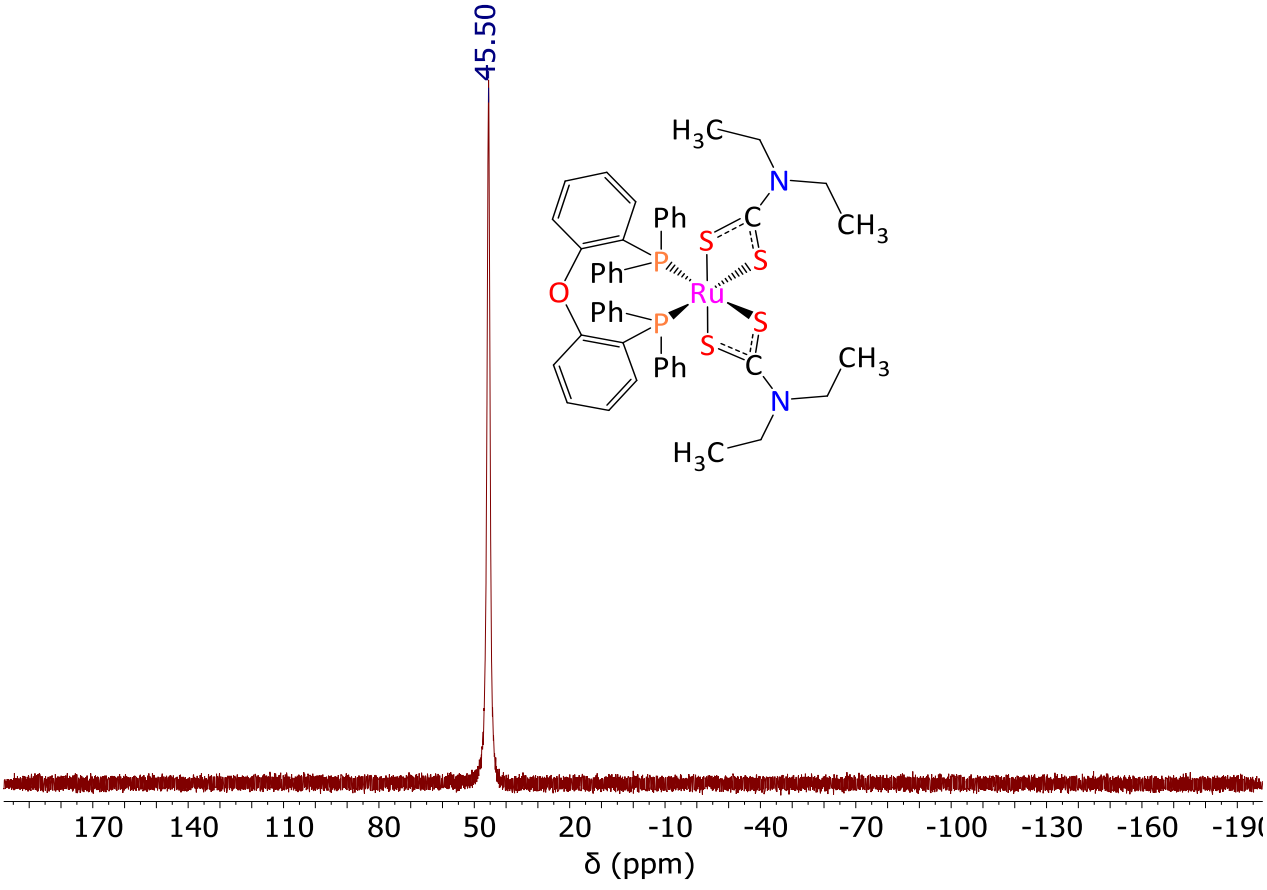

Fig. S66. ^{31}P NMR spectrum (162 MHz, $CDCl_3$, 298 K) of [$Ru(S_2CNEt_2)_2$(DPEphos)] (**9**)

Part 5 – IR spectra

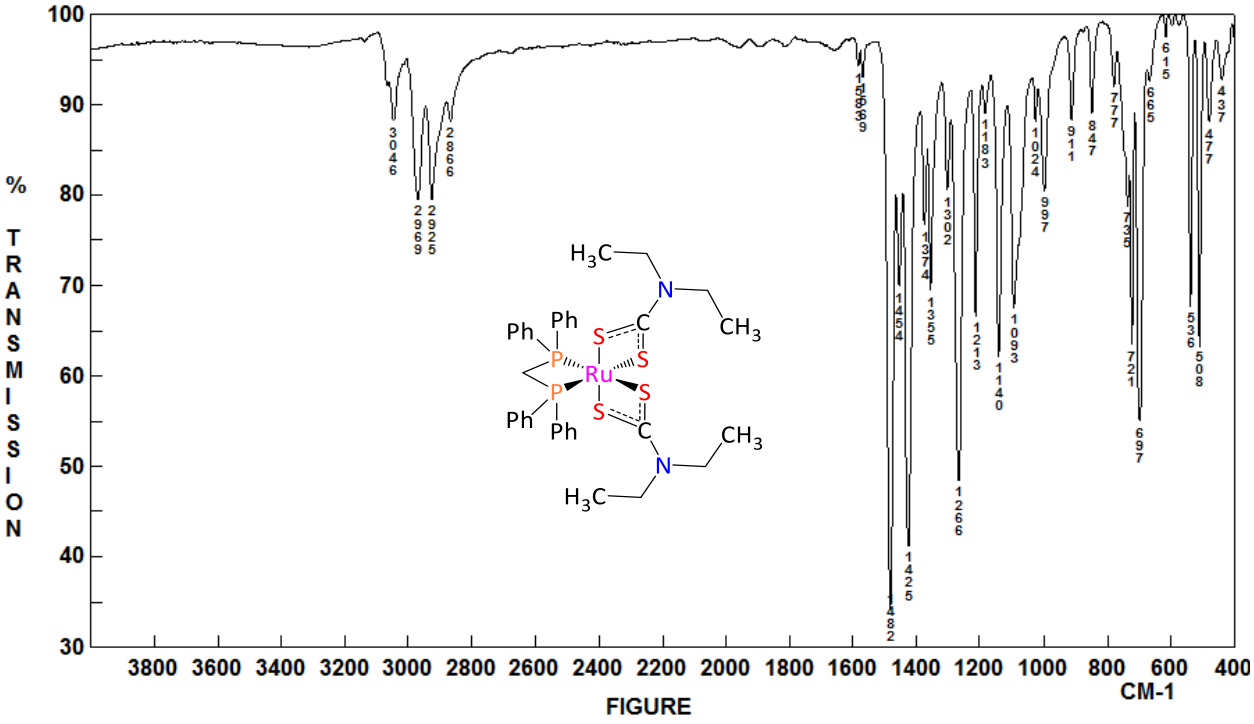

Fig. S67. FT-IR spectrum (KBr) of [Ru(S_2CNEt_2)$_2$(dppm)] (**1**)

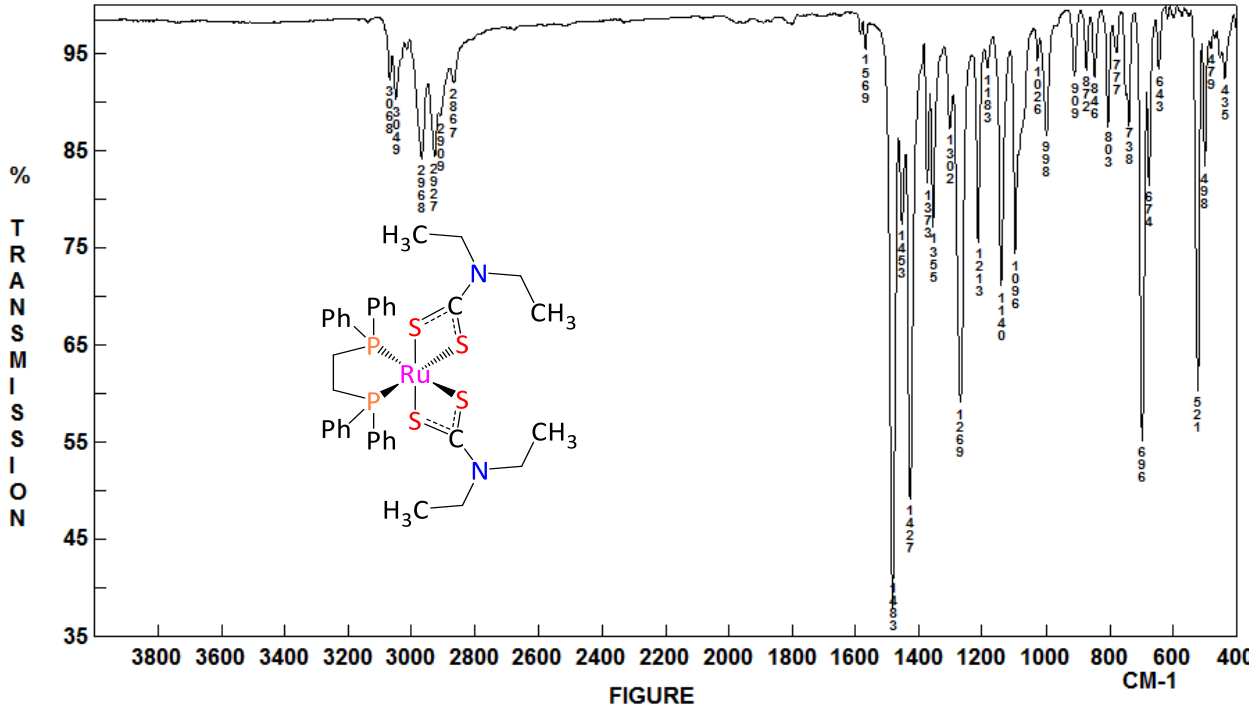

Fig. S68. FT-IR spectrum (KBr) of [Ru(S_2CNEt_2)$_2$(dppe)] (**2**)

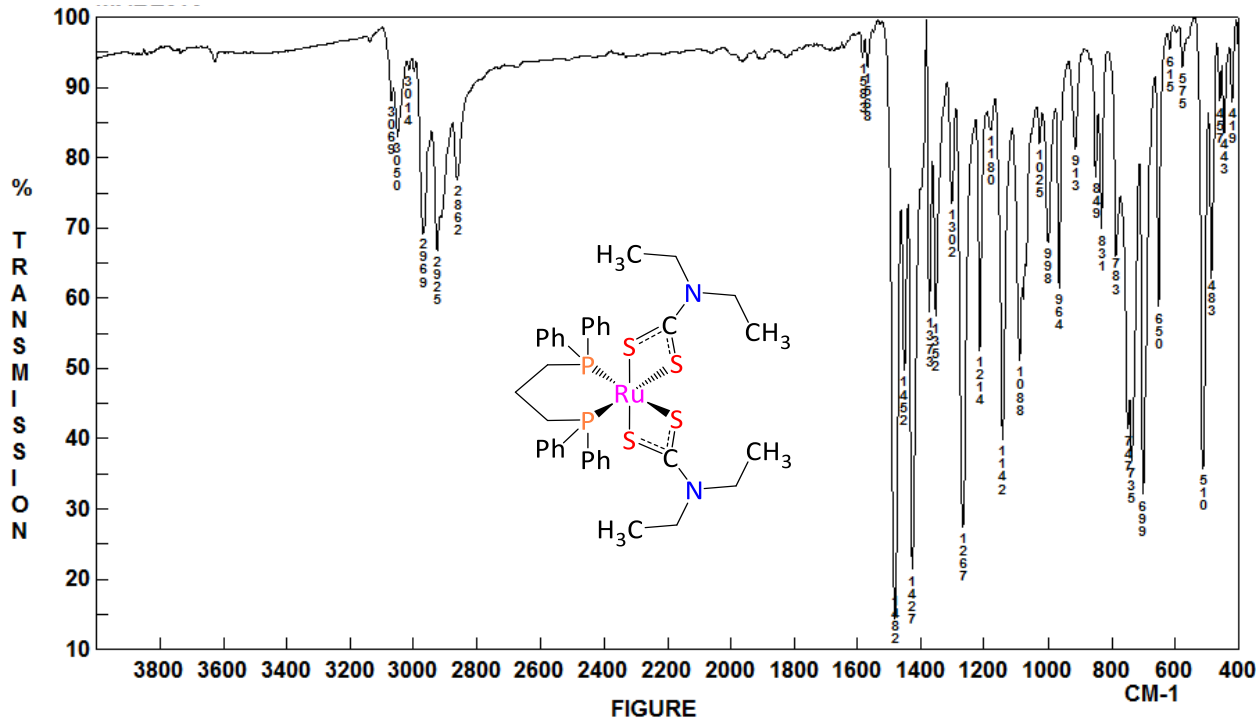

Fig. S69. FT-IR spectrum (KBr) of [Ru(S_2CNEt_2)$_2$(dppp)] (**3**)

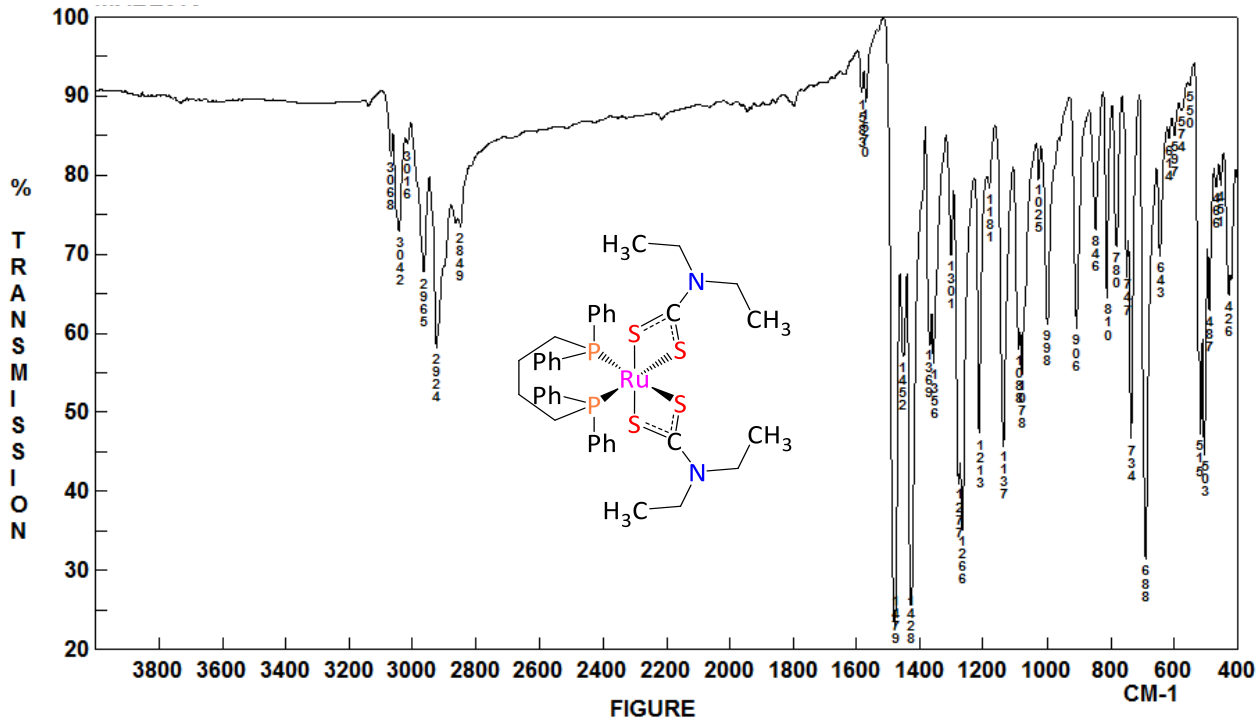

Fig. S70. FT-IR spectrum (KBr) of [Ru(S_2CNEt_2)$_2$(dppb)] (**4**)

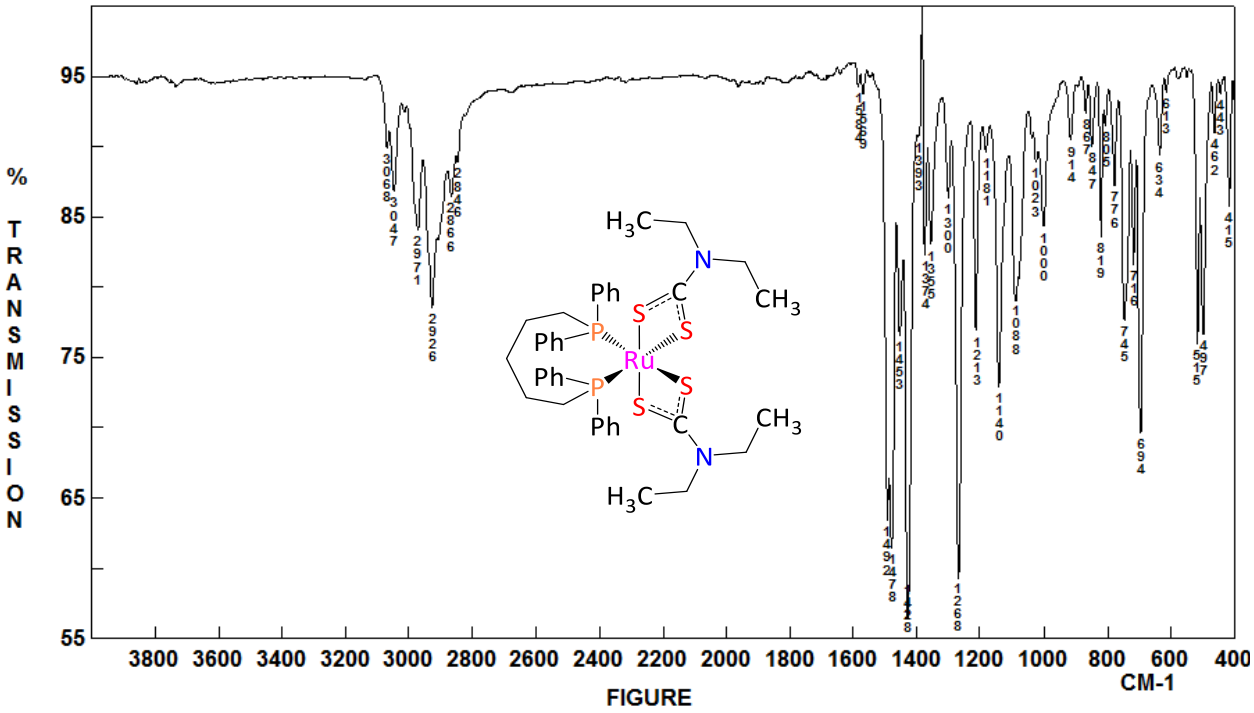

Fig. S71. FT-IR spectrum (KBr) of [Ru(S_2CNEt_2)$_2$(dpppe)] (**5**)

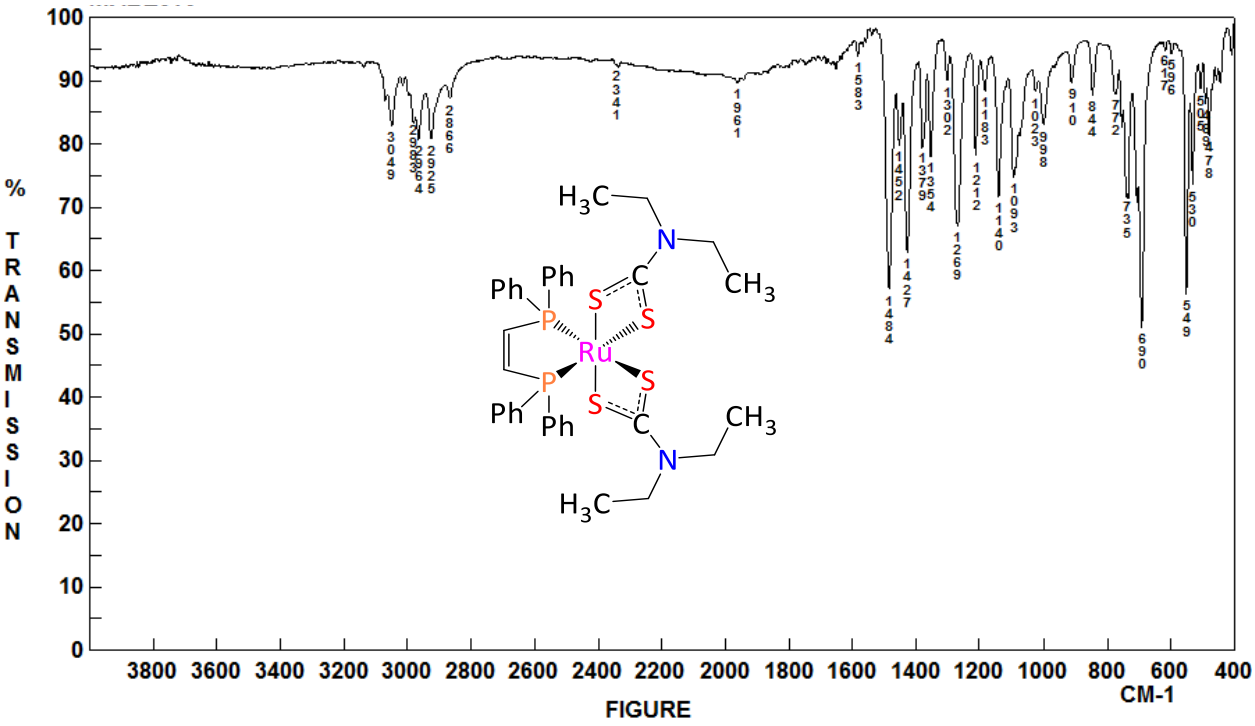

Fig. S72. FT-IR spectrum (KBr) of [Ru(S_2CNEt_2)$_2$(dppen)] (**6**)

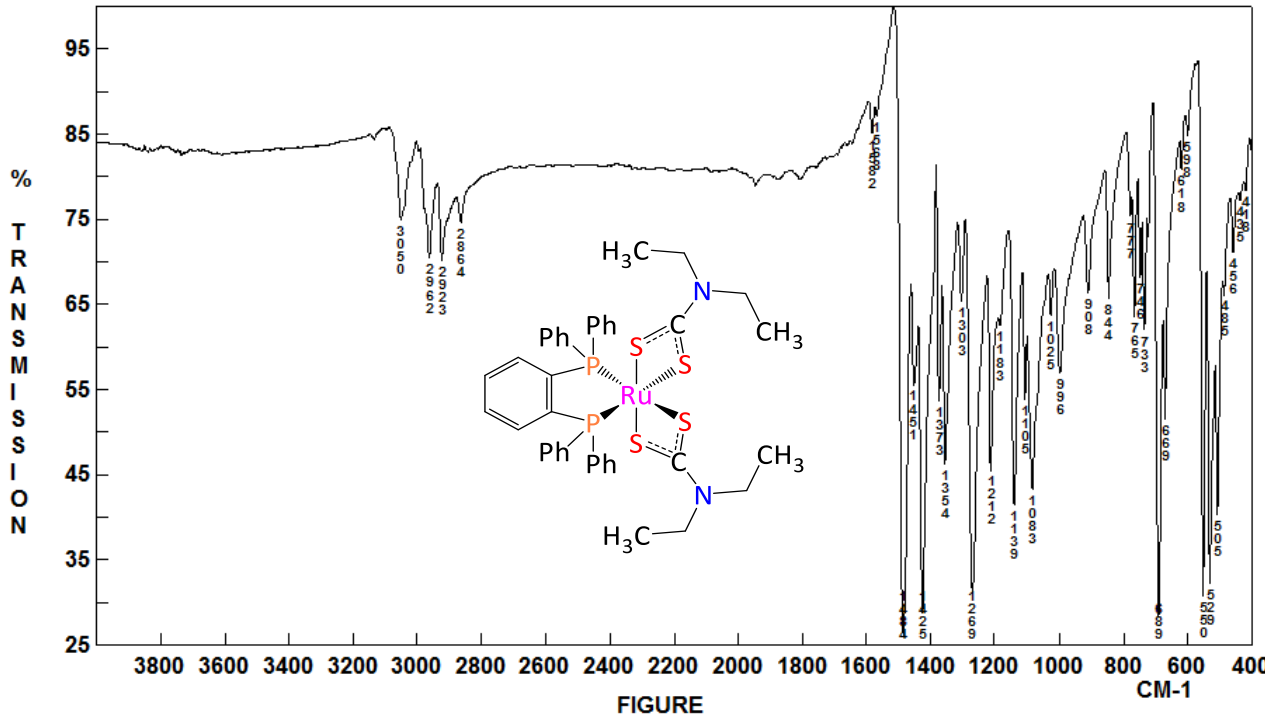

Fig. S73. FT-IR spectrum (KBr) of $[Ru(S_2CNEt_2)_2(dppbz)]$ (**7**)

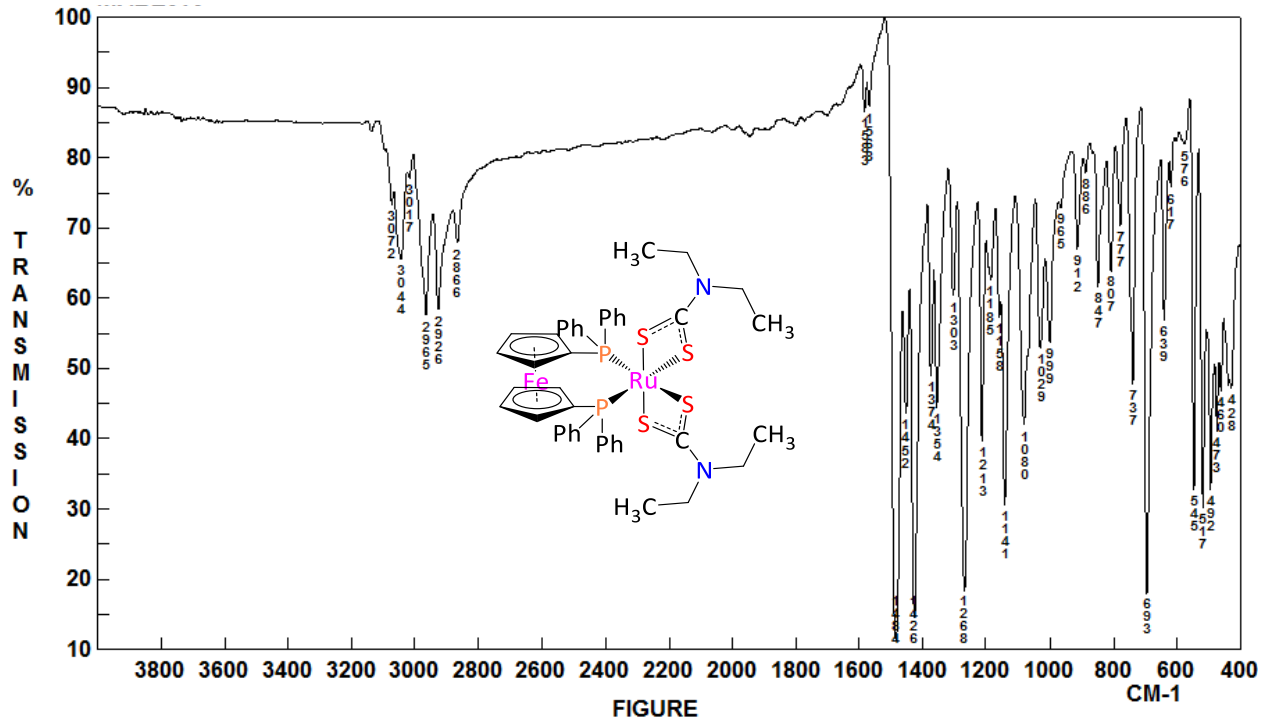

Fig. S74. FT-IR spectrum (KBr) of $[Ru(S_2CNEt_2)_2(dppf)]$ (**8**)

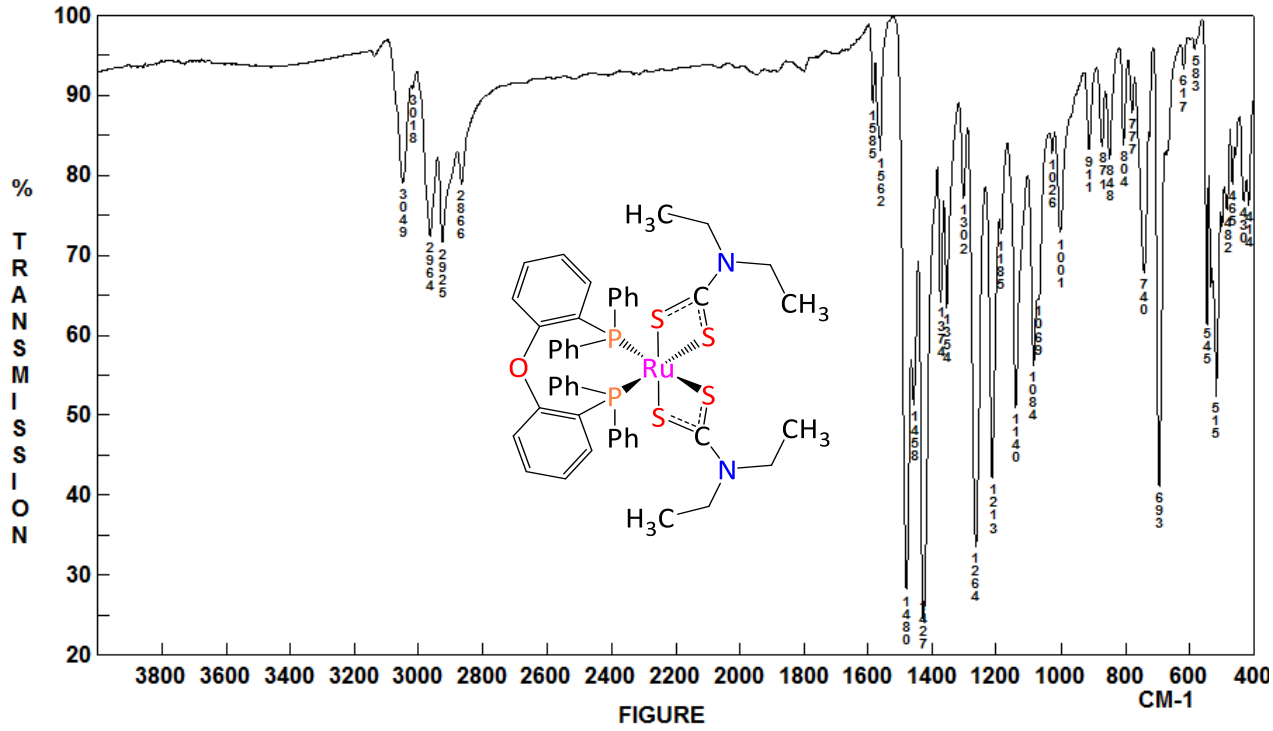

Fig. S75. FT-IR spectrum (KBr) of [Ru(S_2CNEt_2)$_2$(DPEphos)] (**9**)

I.3. Supporting Information (SI) for Chapter VII: Synthesis, Characterization, and Biological Activity of Water-Soluble, Dual Anionic and Cationic Ruthenium–Arene Complexes Bearing Imidazol(in)ium-2-dithiocarboxylate Ligands

Supporting Information for:

Synthesis, Characterization, and Biological Activity of Water-Soluble, Dual Anionic and Cationic Ruthenium–Arene Complexes Bearing Imidazol(in)ium-2-dithiocarboxylate Ligands

Mohammed Zain Aldin,[†] Guillermo Zaragoza,[‡] William Deschamps,[§] Jean-Claude Didelot Tomani,[§] Jacob Souopgui,[§] and Lionel Delaude[*,†]

[†]*Laboratory of Catalysis, MolSys Research Unit, Institut de Chimie Organique (B6a), Allée du six Août 13, Université de Liège, 4000 Liège, Belgium*

[‡]*Unidade de Difracción de Raios X, RIAIDT, Universidade de Santiago de Compostela, Campus Vida, 15782 Santiago de Compostela, Spain*

[§]*Department of Molecular Biology, Institute for Molecular Biology and Medicine, Université Libre de Bruxelles, 6041 Gosselies, Belgium*

[*] *E-mail: l.delaude@uliege.be*

Table of Contents

Part 1 – Experimental section

General Information

Unless otherwise specified, all the syntheses were carried out under a dry nitrogen atmosphere using standard Schlenk techniques. Solvents were distilled from appropriate drying agents and deoxygenated prior to use. Imidazol(in)ium-2-dithiocarboxylates were synthesized according to published procedures.[1] The $[RuCl_2(p\text{-cymene})]_2$ dimer was purchased from Strem. Petroleum ether refers to the fraction of boiling point 40–60 °C and was purchased from VWR. All the other chemicals were obtained from Aldrich or TCI. ^1H and ^{13}C NMR spectra were recorded at 298 K with a Bruker DRX 400 spectrometer operating at 400.13 and 100.62 MHz, respectively. Chemical shifts are listed in parts per million downfield from TMS and are referenced from the solvent peaks or TMS. COSY, HSQC, and HMBC sequences were used for peak assignments. Infrared spectra were recorded with a Bruker Equinox 55 FT-IR spectrometer. Electrospray mass spectra were obtained using a Micromass LCT Premier instrument.

Synthesis of Monometallic Complexes 2a–e

A 10-mL glass vial equipped with a magnetic stirring bar and a rubber stopcock was charged with $[RuCl_2(p\text{-cymene})]_2$ (0.0613 g, 0.1 mmol) and an imidazol(in)ium-2-dithiocarboxylate zwitterion (0.2 mmol). Reagent grade dichloromethane (2–3 mL) taken straight from the bottle was added and the reaction mixture was stirred for 10 min at room temperature under a normal atmosphere. The solvent was evaporated under vacuum. The remaining solid was finely powdered, washed with petroleum ether (5 mL), and dried under high vacuum.

[RuCl(η⁶-p-cymene)(κ²-S,S'-S₂C·IMes)]Cl (***2a***). Dark red-purple microcrystalline powder (0.137 g, 99.7% yield). ^1H NMR (400 MHz, $CDCl_3$): δ 1.07 (d, $^3J_{HH}$ = 6.9 Hz, 6 H, *p*-cym $CH(CH_3)_2$), 2.04 (s, 12 H, Mes *o*-CH_3), 2.15 (s, 3 H, *p*-cym CH_3), 2.38 (s, 6 H, Mes *p*-CH_3), 2.53 (sept, $^3J_{HH}$ = 6.8 Hz, 1 H, *p*-cym $CH(CH_3)_2$), 5.52 (d, $^3J_{HH}$ = 6.1 Hz, 2 H, *p*-cym CH_{ar}), 5.68 (d, $^3J_{HH}$ = 6.1 Hz, 2 H, *p*-cym CH_{ar}), 7.02 (s, 4 H, Mes *m*-CH_{ar}), 8.25 ppm (s, 2 H, Im =CHN). ^{13}C NMR (101 MHz, $CDCl_3$): δ 17.3, 19.0, 21.1, 22.3, 31.9, 85.9, 86.3, 106.0, 106.5, 127.0, 129.7, 129.9, 134.1, 136.2, 141.6, 212.2 ppm (CS_2). ESI-MS (CH_3CN, positive mode) *m/z* calcd for $C_{32}H_{38}ClN_2RuS_2$ ($[M]^+$), 651.12071; found, 651.12106.

[RuCl(η⁶-p-cymene)(κ²-S,S'-S₂C·IDip)]Cl (***2b***). Dark red-purple microcrystalline powder (0.151 g, 98% yield). ^1H NMR (400 MHz, $CDCl_3$): δ 1.06 (d, $^3J_{HH}$ = 6.9 Hz, 6 H, *p*-cym $CH(CH_3)_2$), 1.21 (d, $^3J_{HH}$ = 6.5 Hz, 24 H, Dip $CH(CH_3)_2$), 2.09 (s, 2 H, *p*-cym CH_3), 2.33 (sept, $^3J_{HH}$ = 6.5 Hz 4 H, Dip $CH(CH_3)_2$), 2.47 (sept, $^3J_{HH}$ = 7.0 Hz, 1 H, *p*-cym $CH(CH_3)_2$), 5.44 (d, $^3J_{HH}$ = 6.1 Hz, 2 H, *p*-cym CH_{ar}), 5.59 (d, $^3J_{HH}$ = 6.1 Hz, 2 H, *p*-cym CH_{ar}), 7.34 (d, $^3J_{HH}$ = 7.8 Hz, 4 H, Dip *m*-CH_{ar}), 7.61 (t, $^3J_{HH}$ = 7.8 Hz, 2 H, Dip *p*-CH_{ar}), 8.39 ppm (s, 2 H, Im =CHN). ^{13}C NMR (101 MHz, $CDCl_3$): δ 19.3, 22.5, 22.9, 24.9, 29.3, 32.0, 86.8, 87.0, 106.2, 106.9, 125.2, 128.6, 129.9, 132.4, 136.3, 144.8, 211.8 ppm (CS_2). ESI-MS (CH_3CN, positive mode) *m/z* calcd for $C_{38}H_{50}ClN_2RuS_2$ ($[M]^+$), 735.21478; found, 735.22701.

[RuCl(η⁶-p-cymene)(κ²-S,S'-S₂C·ICy)]Cl (***2c***). Dark yellow-green microcrystalline powder (0.119 g, 97% yield). ^1H NMR (400 MHz, $CDCl_3$): δ 1.19 – 1.45(m, 6 H, Cy), 1.33 (d, $^3J_{HH}$ = 6.9 Hz, 6 H, *p*-cym $CH(CH_3)_2$), 1.60 – 1.75 (m, 2 H, Cy), 1.75 – 1.92 (m, 8 H, Cy), 1.92 – 2.06 (m, 4 H, Cy), 2.38 (s, 3 H, *p*-cym CH_3), 2.89 (sept, $^3J_{HH}$ = 6.7 Hz, 1 H, *p*-cym $CH(CH_3)_2$), 4.47 (tt, $^3J_{HH}$ = 11.8, 3.5 Hz, 2 H, Cy CHN), 5.80 (d, $^3J_{HH}$ = 6.1 Hz, 2 H, *p*-cym CH_{ar}), 6.03 (d, $^3J_{HH}$ = 6.1 Hz, 2 H, *p*-cym CH_{ar}), 8.13 ppm (s, 2 H, Im =CHN). ^{13}C NMR (101

MHz, $CDCl_3$): δ 19.3, 22.2, 22.8, 24.2, 24.8, 32.3, 33.3, 58.8, 85.5, 85.5, 105.6, 106.2, 121.4, 140.4, 218.8 ppm (CS_2). ESI-MS (CH_3CN, positive mode) *m/z* calcd for $C_{26}H_{38}ClN_2RuS_2$ ($[M]^+$), 579.12055; found, 579.12080.

*[RuCl(η⁶-p-cymene)(κ²-S,S'-S_2C·SIMes)]Cl (**2d**)*. Dark red-purple microcrystalline powder (0.136 g, 99% yield). ^{1}H NMR (400 MHz, $CDCl_3$): δ 0.96 (d, $^3J_{HH}$ = 6.9 Hz, 6 H, *p*-cym $CH(CH_3)_2$), 2.11 (s, 3 H, *p*-cym CH_3), 2.29 (s, 6 H, Mes *p*-CH_3), 2.33 (s, 12 H, Mes *o*-CH_3), 2.42 (sept, $^3J_{HH}$ = 6.9, 1 H, *p*-cym $CH(CH_3)_2$), 4.64 (s, 4 H, Im CH_2N), 5.50 (d, $^3J_{HH}$ = 6.1 Hz, 2 H, *p*-cym CH_{ar}), 5.66 (d, $^3J_{HH}$ = 6.1 Hz, 2 H, *p*-cym CH_{ar}), 6.90 ppm (s, 4 H, Mes *m*-CH_{ar}). ^{13}C NMR (101 MHz, $CDCl_3$): δ 18.0, 19.0, 21.0, 22.1, 22.3, 31.9, 51.8, 85.7, 86.3, 106.5, 107.2, 129.9, 129.9, 135.2, 140.4, 155.4, 213.9 ppm (CS_2). ESI-MS (CH_3CN, positive mode) *m/z* calcd for $C_{32}H_{40}ClN_2RuS_2$ ($[M]^+$), 653.13636; found, 653.14533.

*[RuCl(η⁶-p-cymene)(κ²-S,S'-S_2C·SIDip)]Cl (**2e**)*. Dark red-purple microcrystalline powder (0.153 g, 99% yield). ^{1}H NMR (400 MHz, $CDCl_3$): δ 1.02 (d, $^3J_{HH}$ = 6.9 Hz, 6 H, *p*-cym $CH(CH_3)_2$), 1.28 (d, $^3J_{HH}$ = 6.8 Hz, 12 H, Dip $CH(CH_3)_2$), 1.34 (d, $^3J_{HH}$ = 6.8 Hz, 12 H, Dip $CH(CH_3)_2$), 2.05 (s, 3 H , *p*-cym CH_3), 2.42 (sept, $^3J_{HH}$ = 6.9 Hz, 1 H, *p*-cym $CH(CH_3)_2$), 2.95 (sept, $^3J_{HH}$ = 6.3 Hz, 4 H, Dip $CH(CH_3)_2$), 4.68 (br s, 4 H, Im CH_2N), 5.44 (d, $^3J_{HH}$ = 6.1 Hz, 2 H, *p*-cym CH_{ar}), 5.59 (d, $^3J_{HH}$ = 6.1 Hz, 2 H, *p*-cym CH_{ar}), 7.24 (d, $^3J_{HH}$ = 7.8 Hz, 4 H, Dip *m*-CH_{ar}), 7.48 ppm (t, $^3J_{HH}$ = 7.8 Hz, 2 H, Dip *p*-CH_{ar}). ^{13}C NMR (101 MHz, $CDCl_3$): δ 19.4, 22.5, 23.7, 25.6, 29.3, 31.9, 54.6, 87.6, 87.7, 105.8, 108.7, 125.3, 129.9, 131.4, 146.0, 152.5, 211.7 ppm (CS_2). ESI-MS (CH_3CN, positive mode) *m/z* calcd for $C_{38}H_{52}ClN_2RuS_2$ ($[M]^+$), 737.23043; found, 737.24248.

Synthesis of Bimetallic Complexes 3a–e

A 10-mL glass vial equipped with a magnetic stirring bar and a rubber stopcock was charged with $[RuCl_2(p\text{-cymene})]_2$ (0.0613 g, 0.1 mmol) and an imidazol(in)ium-2-dithiocarboxylate zwitterion (0.1 mmol). Reagent grade dichloromethane (3 mL) taken straight from the bottle was added and the reaction mixture was stirred for 10 min at room temperature under a normal atmosphere. The solvent was evaporated under vacuum. The remaining solid was washed with petroleum ether (3 × 10 mL) and dried under high vacuum.

*[RuCl(η⁶-p-cymene)(κ²-S,S'-S_2C·IMes)][$RuCl_3$(η⁶-p-cymene)] (**3a**)*. Dark red-purple microcrystalline powder (0.099 g, 99.8% yield). ^{1}H NMR (400 MHz, $CDCl_3$): δ 1.02 (d, $^3J_{HH}$ = 6.9 Hz, 6 H, *p*-cym $CH(CH_3)_2$), 1.25 (t, $^3J_{HH}$ = 6.6 Hz, 6 H, *p*-cym $CH(CH_3)_2$), 1.99 (s, 12 H, Mes *o*-CH_3), 2.11 (s, 3 H, *p*-cym CH_3), 2.12 (s, 1 H, *p*-cym CH_3), 2.18 (s, 2 H, *p*-cym CH_3), 2.31 (s, 6 H, Mes *p*-CH_3), 2.47 (sept, $^3J_{HH}$ = 6.9 Hz, 1 H, *p*-cym $CH(CH_3)_2$), 3.07 (sept, $^3J_{HH}$ = 7.0 Hz, 1 H, *p*-cym $CH(CH_3)_2$), 5.12 (d, $^3J_{HH}$ = 5.8 Hz, 1 H, *p*-cym CH_{ar}), 5.30 (d, $^3J_{HH}$ = 5.9 Hz, 1 H, *p*-cym CH_{ar}), 5.36 (d, $^3J_{HH}$ = 5.8 Hz, 1 H, *p*-cym CH_{ar}), 5.39 (d, $^3J_{HH}$ = 6.1 Hz, 2 H, *p*-cym CH_{ar}), 5.43 (d, $^3J_{HH}$ = 5.9 Hz, 1 H, *p*-cym CH_{ar}), 5.56 (d, $^3J_{HH}$ = 6.1 Hz, 2 H, *p*-cym CH_{ar}), 6.93 (s, 4 H, Mes *m*-CH_{ar}), 8.30 ppm (s, 2 H, Im =CHN). ^{13}C NMR (101 MHz, $CDCl_3$): δ 17.8, 18.8, 19.0, 19.3, 21.4, 22.2, 22.4, 22.6, 30.6, 30.7, 32.3, 79.7, 80.6, 81.3, 81.7, 85.8, 86.3, 96.2, 96.8, 100.7, 101.3, 105.8, 106.7, 129.0, 130.0, 130.3, 134.7, 135.7, 141.6, 214.2 ppm (CS_2). IR (KBr): ν 3063 (s), 2956 (s), 2916 (s), 2867 (m), 1606 (m), 1544 (s), 1484 (s), 1465 (s), 1424 (s), 1376 (m), 1230 (m), 1009 (m), 854 (m), 722 (m) cm^{-1}. ESI-MS (CH_3CN, positive mode) *m/z* calcd for $[C_{32}H_{38}ClN_2RuS_2]^+$ ($[M_{cation}]^+$), 651.12071; found, 651.11968. ESI-MS (CH_3CN, negative mode) *m/z* calcd for $[C_{10}H_{14}Cl_3Ru]^-$ ($[M_{anion}]^-$), 340.92101; found, 340.92111.

[RuCl(η⁶-p-cymene)(κ²-S,S'-S₂C·IDip)][RuCl₃(η⁶-p-cymene)] (***3b***). Dark red-purple microcrystalline powder (0.1018 g, 95% yield). ^{1}H NMR (400 MHz, $CDCl_3$): δ 1.06 (d, $^3J_{HH}$ = 6.9 Hz, 6 H, *p*-cym CH(CH_3)$_2$), 1.11 – 1.38 (m, 30 H, Dip CH(CH_3)$_2$ and *p*-cym CH(CH_3)$_2$), 2.09 (s, 2 H, *p*-cym CH_3), 2.16 (s, 3 H, *p*-cym CH_3), 2.21 (s, 2 H, *p*-cym CH_3), 2.26 – 2.41 (m, 4 H, Dip C*H*(CH$_3$)$_2$), 2.41 – 2.59 (m, 1 H, *p*-cym C*H*(CH$_3$)$_2$), 2.92 (sept, $^3J_{HH}$ = 6.8 Hz, 1 H, *p*-cym C*H*(CH$_3$)$_2$), 3.01 – 3.28 (m, 1 H, *p*-cym C*H*(CH$_3$)$_2$), 5.15 (d, $^3J_{HH}$ = 5.2 Hz, 1 H, *p*-cym CH_{ar}), 5.34 (d, $^3J_{HH}$ = 5.8 Hz, 2 H, *p*-cym CH_{ar}), 5.38 (d, $^3J_{HH}$ = 5.9 Hz, 2 H, *p*-cym CH_{ar}), 5.48 (d, $^3J_{HH}$ = 5.8 Hz, 2 H, *p*-cym CH_{ar}), 5.54 (d, $^3J_{HH}$ = 6.0 Hz, 2 H, *p*-cym CH_{ar}), 7.31 (d, $^3J_{HH}$ = 7.8 Hz, 4 H, Dip *m*-CH_{ar}), 7.57 (t, $^3J_{HH}$ = 7.8 Hz, 2 H, Dip *p*-CH_{ar}), 8.49 ppm (s, 2H, Im =CHN). ^{13}C NMR (101 MHz, $CDCl_3$): δ 18.8, 19.0, 19.4, 22.2, 22.4, 22.8, 23.1, 23.9, 24.9, 25.1, 29.0, 29.4, 30.7, 32.2, 79.6, 80.6, 81.3, 81.7, 86.7, 86.9, 96.8, 100.7, 101.2, 106.1, 106.8, 125.3, 130.3, 130.6, 132.3, 136.0, 145.2, 213.2 ppm (CS_2). IR (KBr): ν 3054 (m), 2962 (s), 2926 (m), 2868 (m), 1624 (w), 1543 (s), 1468 (s), 1388 (m), 1001 (m), 802 (m) cm^{-1}. ESI-MS (CH_3CN, positive mode): *m/z* calcd for $[C_{32}H_{38}ClN_2RuS_2]^+$ ($[M_{cation}]^+$), 735.21478; found, 735.21374. ESI-MS (CH_3CN, negative mode): *m/z* calcd for $[C_{10}H_{14}Cl_3Ru]^-$ ($[M_{anion}]^-$), 340.92101; found, 340.92113.

[RuCl(η⁶-p-cymene)(κ²-S,S'-S₂C·ICy)][RuCl₃(η⁶-p-cymene)] (***3c***). Dark yellow-green microcrystalline powder (0.0910 g, 99% yield). ^{1}H NMR (400 MHz, $CDCl_3$): δ 1.10 – 1.41 (m, 21 H, *p*-cym CH(CH_3)$_2$ and Cy), 1.53 – 2.02 (m, 14 H, Cy), 2.11 (s, 3 H, *p*-cym CH_3), 2.32 (s, 3 H, *p*-cym CH_3), 2.67 – 3.01 (m, 2 H, *p*-cym C*H*(CH$_3$)$_2$), 5.30 (d, *J* = 5.9 Hz, 2 H, *p*-cym CH_{ar}), 5.43 (d, *J* = 5.8 Hz, 3 H, *p*-cym CH_{ar}), 5.69 (d, *J* = 5.7 Hz, 1 H, *p*-cym CH_{ar}), 5.91 (d, *J* = 5.8 Hz, 1 H, *p*-cym CH_{ar}), 8.06 ppm (s, 2 H, Im =CHN). ^{13}C NMR (101 MHz, $CDCl_3$): δ 18.9, 19.0, 19.5, 22.2, 22.4, 23.0, 23.1, 24.4, 25.1, 30.7, 32.6, 33.4, 59.0, 80.6, 81.3, 85.55, 85.60, 96.8, 101.2, 105.8, 106.2, 122.6, 140.0, 220.2 ppm (CS_2). IR (KBr): ν 3054 (m), 2931 (s), 2858 (s), 1631 (w), 1562 (w), 1464 (s), 1449 (s), 1388 (m), 1375 (m), 1248 (m), 1201 (s), 1026 (s) cm^{-1}. ESI-MS (CH_3CN, positive mode): *m/z* calcd for $[C_{32}H_{38}ClN_2RuS_2]^+$ ($[M_{cation}]^+$), 579.12029; found, 579.12005. ESI-MS (CH_3CN, negative mode): *m/z* calcd for $[C_{10}H_{14}Cl_3Ru]^-$ ($[M_{anion}]^-$), 340.92101; found, 340.92119.

[RuCl(η⁶-p-cymene)(κ²-S,S'-S₂C·SIMes)][RuCl₃(η⁶-p-cymene)] (***3d***). Dark red-purple microcrystalline powder (0.0965 g, 97% yield). ^{1}H NMR (400 MHz, $CDCl_3$): δ 0.96 (d, $^3J_{HH}$ = 6.9 Hz, 6 H, *p*-cym CH(CH_3)$_2$), 1.28 (t, $^3J_{HH}$ = 6.7 Hz, 6 H, *p*-cym CH(CH_3)$_2$), 2.11 (s, 3 H, *p*-cym CH_3), 2.15 (s, 2 H, *p*-cym CH_3), 2.23 (s, 1 H, *p*-cym CH_3), 2.27 (s, 6 H, Mes *p*-CH_3), 2.34 (s, 12 H, Mes *o*-CH_3), 2.37 – 2.49 (m, 1 H, *p*-cym C*H*(CH$_3$)$_2$), 2.91 (m, 1 H, *p*-cym C*H*(CH$_3$)$_2$), 3.11 (m, 1 H, *p*-cym C*H*(CH$_3$)$_2$), 4.64 (br s, 4 H, Im CH_2N), 5.17 (d, $^3J_{HH}$ = 5.6 Hz, 1 H, *p*-cym CH_{ar}), 5.33 (d, $^3J_{HH}$ = 5.8 Hz, 1 H, *p*-cym CH_{ar}), 5.39 (d, $^3J_{HH}$ = 5.6 Hz, 3 H, *p*-cym CH_{ar}), 5.47 (d, $^3J_{HH}$ = 5.8 Hz, 1 H, *p*-cym CH_{ar}), 5.56 (d, $^3J_{HH}$ = 5.8 Hz, 2 H, *p*-cym CH_{ar}), 6.87 ppm (s, 4 H, Mes *m*-CH_{ar}). ^{13}C NMR (101 MHz, $CDCl_3$): δ 18.3, 18.8, 19.2, 21.2, 22.2, 22.4, 22.6, 30.6, 32.1, 53.1, 79.7, 80.6, 81.3, 81.5, 85.6, 86.2, 106.4, 107.2, 129.9, 130.4, 135.7, 140.3, 155.8, 215.8 ppm (CS_2). IR (KBr): ν 3045 (w), 2967 (m), 2915 (m), 2865 (w), 1628 (w), 1607 (m), 1553 (s), 1510 (m), 1465 (s), 1378 (m), 1352 (w), 1284 (s), 1190 (w), 1031 (m), 851 (m) cm^{-1}. ESI-MS (CH_3CN, positive mode): *m/z* calcd for $[C_{32}H_{38}ClN_2RuS_2]^+$ ($[M_{cation}]^+$), 653.13636; found, 653.13590. ESI-MS (CH_3CN, negative mode): *m/z* calcd for $[C_{10}H_{14}Cl_3Ru]^-$ ($[M_{anion}]^-$), 340.92101; found, 340.92110.

[RuCl(η⁶-p-cymene)(κ²-S,S'-S₂C·SIDip)][RuCl₃(η⁶-p-cymene)] (***3e***). Dark red-purple microcrystalline powder (0.1060 g, 98% yield). ^{1}H NMR (400 MHz, $CDCl_3$): δ 0.99 (d, $^3J_{HH}$ = 6.9 Hz, 6 H, *p*-cym CH(CH_3)$_2$), 1.12 – 1.29 (m, 20 H, Dip CH(CH_3)$_2$), 1.28 – 1.43 (m, 12 H, *p*-cym CH(CH_3)$_2$ and Dip CH(CH_3)$_2$), 2.01 (s, 3 H, *p*-cym CH_3), 2.12 (s, 2 H, *p*-cym CH_3), 2.18

(d, $^3J_{HH}$ = 7.7 Hz, 2 H, *p*-cym CH_3), 2.39 (sept, $^3J_{HH}$ = 6.9 Hz, 1 H, *p*-cym C*H*(CH_3)$_2$), 2.76 – 3.15 (m, 5 H, *p*-cym C*H*(CH_3)$_2$ and Dip C*H*(CH_3)$_2$), 4.65 (br s, 4 H, Im CH_2N), 5.11 (s, 1 H, *p*-cym CH_{ar}), 5.30 (d, $^3J_{HH}$ = 5.9 Hz, 1 H, *p*-cym CH_{ar}), 5.34 (d, $^3J_{HH}$ = 5.8 Hz, 3 H, *p*-cym CH_{ar}), 5.44 (d, $^3J_{HH}$ = 5.9 Hz, 1 H, *p*-cym CH_{ar}), 5.50 (d, $^3J_{HH}$ = 5.8 Hz, 2 H, *p*-cym CH_{ar}), 7.18 (d, $^3J_{HH}$ = 7.7 Hz, 4 H, Dip *m*-CH_{ar}), 7.41 ppm (t, $^3J_{HH}$ = 7.7 Hz, 2H, Dip *p*-CH_{ar}). ^{13}C NMR (101 MHz, $CDCl_3$): δ 18.8, 19.0, 19.5, 22.2, 22.4, 22.8, 23.9, 25.9, 29.4, 30.7, 32.0, 79.7, 80.6, 81.3, 81.5, 87.5, 87.6, 96.8, 101.2, 105.6, 108.7, 125.3, 130.3, 131.3, 146.4, 152.9, 213.3 ppm (CS_2). IR (KBr): ν 3060 (w), 2961 (s), 2925 (m), 2867 (m), 1589 (m), 1541 (s), 1494 (m), 1461 (s), 1442 (s), 1360 (m), 1279 (m), 1055 (m), 803 (m) cm^{-1}. ESI-MS (CH_3CN, positive mode): *m/z* calcd for $[C_{32}H_{38}ClN_2RuS_2]^+$ ($[M_{cation}]^+$), 737.23043; found, 737.22976. ESI-MS (CH_3CN, negative mode): *m/z* calcd for $[C_{10}H_{14}Cl_3Ru]^-$ ($[M_{anion}]^-$), 340.92101; found, 340.92115.

X-Ray Crystallography

Data for complexes **3a** and **3c** were collected on a Bruker APEX II diffractometer using the Mo-Kα radiation (λ = 0.71073 Å) from a fine focus sealed tube source at 100 K. Data for complexes **2a** and **2c** were collected on a Bruker D8 VENTURE PHOTON III-14 diffractometer using an Incoatec multilayer mirror monochromated with the Cu-Kα radiation (λ = 1.54178 Å) from a microfocus sealed tube source at 100 K and with a detector resolution of 7.3910 pixels mm^{-1}. Computing data and reduction was made with the APEX II software for all the samples.[2] Absorption corrections based on the multiscan method were applied.[3] All the structures were solved using SIR2004.[4] They were refined by full-matrix, least-squares based on F^2 using SHELXL.[5] An empirical absorption correction was applied using SADABS.[6] All non-hydrogen atoms were anisotropically refined and the hydrogen atom positions were calculated and refined using a riding model. Soft geometrical restraints were necessary in some cases to refine the water geometry. The occupation factor for disordered parts was refined as an independent free variable and was aggregated in function of the obtained values.

*Crystal data for [RuCl(η^6-p-cymene)(κ^2-S,S'-S_2C·IMes)]Cl (**2a**) co-crystallized with water*. Dark green crystal with dimensions 0.09 × 0.06 × 0.02 mm obtained by slow diffusion of petroleum ether in a CH_2Cl_2 solution saturated with water at 6 °C, $C_{32}H_{38}ClN_2RuS_2$·Cl·H_2O, MW = 704.75 g mol^{-1}, triclinic, *P*–1, *a* = 10.2923(5) Å, *b* = 11.7054(5) Å, *c* = 13.1163(6) Å, α = 84.218(4)°, β = 89.441(3), γ = 87.349(3), *V* = 1570.45(12) Å^3, *Z* = 2, D_x = 1.49 g cm^{-3}, μ(Cu Kα) = 7.065 mm^{-1}, 40392 reflns collected, 6391 independent reflns (R_{int} = 0.09), 5728 reflns with $I > 2\sigma(I)$, R_1 (all data) = 0.032, wR_2 (all data) = 0.054, GOF on F_2 = 1.06, ϱ_{max} = 0.38 e Å^{-3}, ϱ_{min} = –0.42 e Å^{-3}.

*Crystal data for [RuCl(η^6-p-cymene)(κ^2-S,S'-S_2C·ICy)]Cl (**2c**) co-crystallized with water*. Orange crystal with dimensions 0.09 × 0.03 × 0.02 mm obtained by slow diffusion of petroleum ether in a CH_2Cl_2 solution saturated with water at 6 °C, 2($C_{26}H_{38}ClN_2RuS_2$)·2Cl·9.75(H_2O), MW = 1404.84 g mol^{-1}, monoclinic, *C*2/*c*, *a* = 24.5061(9))Å, *b* = 9.7644(4)Å, *c* = 27.0470(9) Å, β = *94.544(2),* *V* = 6451.7(4) Å^3, *Z* = 4, D_x = 1.46 g cm^{-3}, μ(Cu Kα) = 6.967 mm^{-1}, 89737 reflns collected, 6600 independent reflns (R_{int} = 0.093), 5275 reflns with $I > 2\sigma(I)$, R_1 (all data) = 0.055, wR_2 (all data) = 0.111, GOF on F_2 = 1.04, ϱ_{max} = 0.96 e Å^{-3}, ϱ_{min} = –1.16 e Å^{-3}.

*Crystal data for [RuCl(η^6-p-cymene)(κ^2-S,S'-S_2C·IMes)][$RuCl_3$(η^6-p-cymene)] (**3a**) co-crystallized with water*. Orange crystal with dimensions 0.4 × 0.06 × 0.04 mm obtained by slow evaporation of an acetone solution containing a few drops of water at 6 °C,

$C_{32}H_{38}ClN_2RuS_2 \cdot C_{10}H_{14}Cl_3Ru \cdot H_2O$, MW = 1010.93 g mol^{-1}, monoclinic, $P2_1/n$, a = 11.822(3) Å, b = 28.056(5) Å, c = 14.239(2) Å, β = 110.133(8)°, V = 4434.3(14) Å^3, Z = 4, D_x = 1.514 g cm^{-3}, μ(Mo Kα) = 1.05 mm^{-1}, 33992 reflns collected, 8417 independent reflns (R_{int} = 0.098), 5528 reflns with $I > 2\ \sigma(I)$, R_1 (all data) = 0.101, wR_2 (all data) = 0.129, GOF on F_2 = 1.01, ϱ_{max} = 0.80 e Å^{-3}, ϱ_{min} = –0.82 e Å^{-3}.

*Crystal data for [RuCl(η^6-p-cymene)(κ^2-S,S'-S$_2$C·SIMes)][RuCl$_3$(η^6-p-cymene)] (**3d**) co-crystallized with water*. Orange crystal with dimensions 0.28 × 0.08 × 0.04 mm obtained by slow evaporation of a CH_2Cl_2 solution containing a few drops of water at 6 °C, $2(C_{32}H_{40}ClN_2RuS_2) \cdot 2(C_{10}H_{14}Cl_3Ru) \cdot 3(H_2O)$, MW = 2043.91 g mol^{-1}, orthorhombic, *Pbca*, a = 20.292(2) Å, b = 15.6905(17) Å, c = 27.772(3) Å, V = 8842.5(16) Å^3, Z = 4, D_x = 1.535 g cm^{-3}, μ(Mo Kα) = 1.06 mm^{-1}, 112907 reflns collected, 8088 independent reflns (R_{int} = 0.054), 4928 reflns with $I > 2\sigma(I)$, R_1 (all data) = 0.054, wR_2 (all data) = 0.129, GOF on F_2 = 1.01, ϱ_{max} = 0.87 e Å^{-3}, ϱ_{min} = –0.87 e Å^{-3}.

CCDC 2037518 (**2a**), 2037519 (**2c**), 2037521 (**3a**), and 2037520 (**3d**) contain the supplementary crystallographic data for this paper. These data can be obtained free of charge via www.ccdc.cam.ac.uk/data_request/cif, or by emailing data_request@ccdc.cam.ac.uk, or by contacting The Cambridge Crystallographic Data Centre, 12 Union Road, Cambridge CB2 1EZ, UK; fax: +44 1223 336033.

Solubility Tests

NMR tubes were loaded with powdered complexes **2a–e** or **3a–e** (5 μmol each). Distilled water was added in small portions (0.05 mL) at room temperature with a glass microsyringe. The tubes were vigorously shaken after every addition. The process was repeated until complete dissolution of the solids.

Cell Culture and Viability Assay

Human leukemia K562 cells and mice splenocytes were cultured in RPMI 1640 and DMEM (Life Technologies, Waltham, MA, USA), respectively. Both culture media were supplemented with 10% heat-inactivated Fetal Bovine Serum (FBS; Life technologies), 1% glutamine, and 1% of penicillin-streptomycin (Life technologies) and maintained at 37 °C under 5% CO_2 in a humidified atmosphere. K562 Cells were passaged at least 5 times before any experiment. For the determination of cell densities, the cell counting was done using a Neubauer counting chamber with trypan blue staining (0.4% in PBS; pH = 7.4; Life technologies). Stock solutions of the complexes were prepared in dimethyl sulfoxide (DMSO) or water at a concentration of 20 mg/mL and kept in a cold room at 4 °C before use. Due to the cytotoxicity of DMSO, its final concentration was limited to 1%. To study the effect of complexes on the cell viability, a dose-dependent assay for all complexes was performed for three days using the CellTiter-Glo Luminescent Cell Viability Assay (Promega) as previously reported.[7,8] Briefly, both K562 and splenocyte cells were incubated in the presence or absence of complexes for 3 days at 37 °C in a humidified 5% CO_2 atmosphere in 96-well plates. After 3 days of incubation, the cells were allowed to equilibrate at room temperature for approximately 30 min before adding 100 μL of the CellTiter-Glo reagent to each well. The culture plate was then covered with an aluminum sheet to protect it from light and shaken for 2 min on an orbital shaker to induce cell lysis. It was further incubated for 10 min at room temperature for the stabilization of the luminescent signal before reading the luminescence on a Berthold Technologies luminometer (XS3LB 960).

The cell viability (%) was calculated by using the following formula:
Viability (%) = [RLU (treated cells) / RLU (vehicle-treated cells)] × 100

The selectivity index (SI) was calculated by using the following formula:
SI = (CC_{50} Splenocytes) / (IC_{50} K562)

Part 2 – NMR spectra

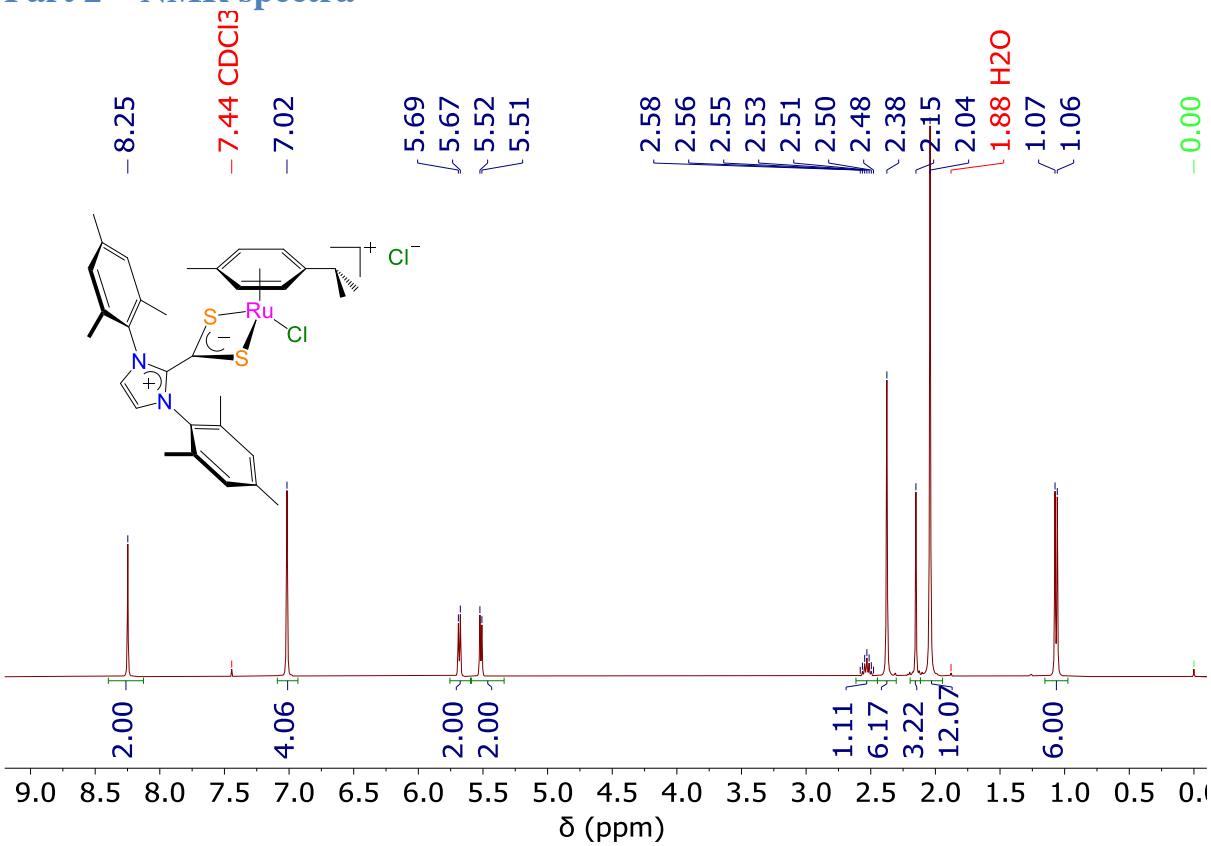

Fig. S1. ^{1}H NMR spectrum (400 MHz, $CDCl_3$, 298 K) of [RuCl(*p*-cymene)(S_2C·IMes)]Cl (**2a**)

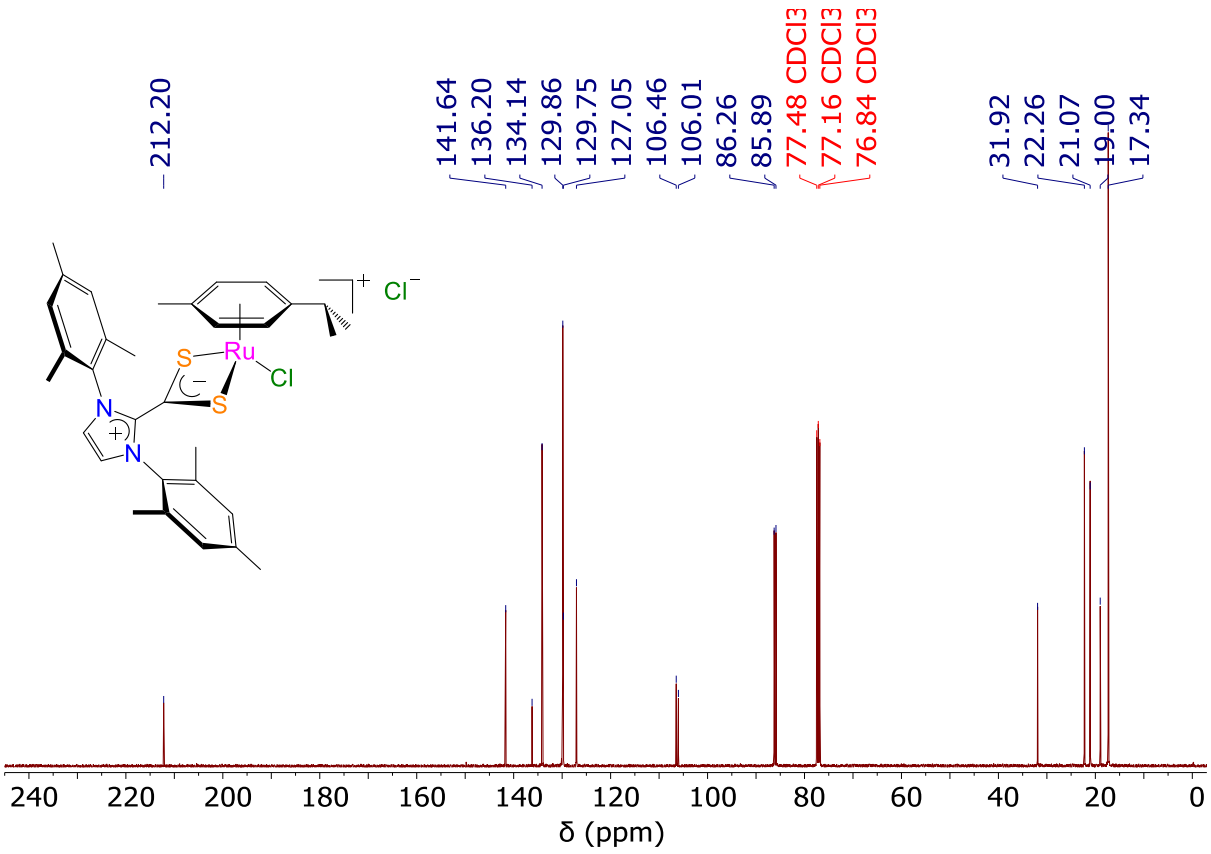

Fig. S2. $^{13}C\{^{1}H\}$ NMR spectrum (101 MHz, $CDCl_3$, 298 K) of [RuCl(*p*-cymene)-(S_2C·IMes)]Cl (**2a**)

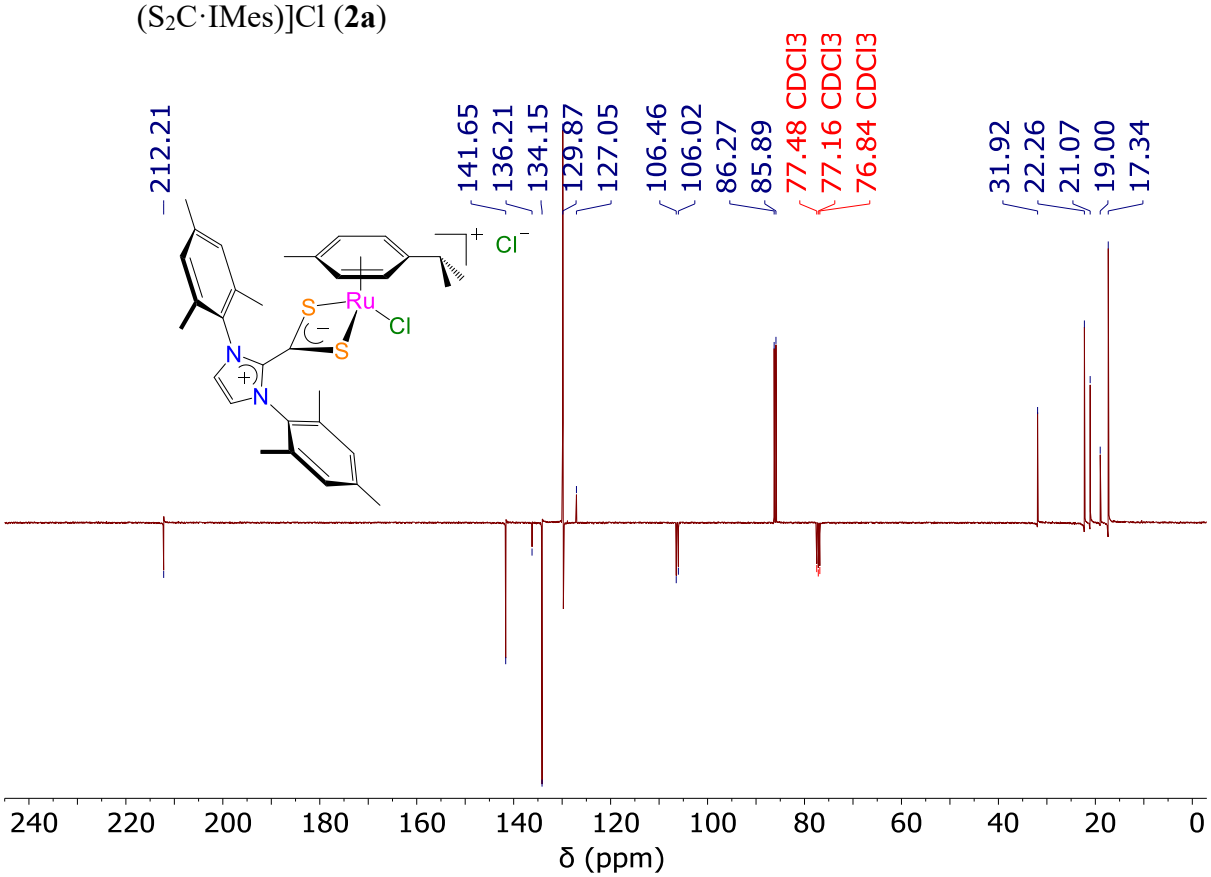

Fig. S3. $^{13}C\{^{1}H\}$ APT NMR spectrum (101 MHz, $CDCl_3$, 298 K) of [RuCl(*p*-cymene)-(S_2C·IMes)]Cl (**2a**)

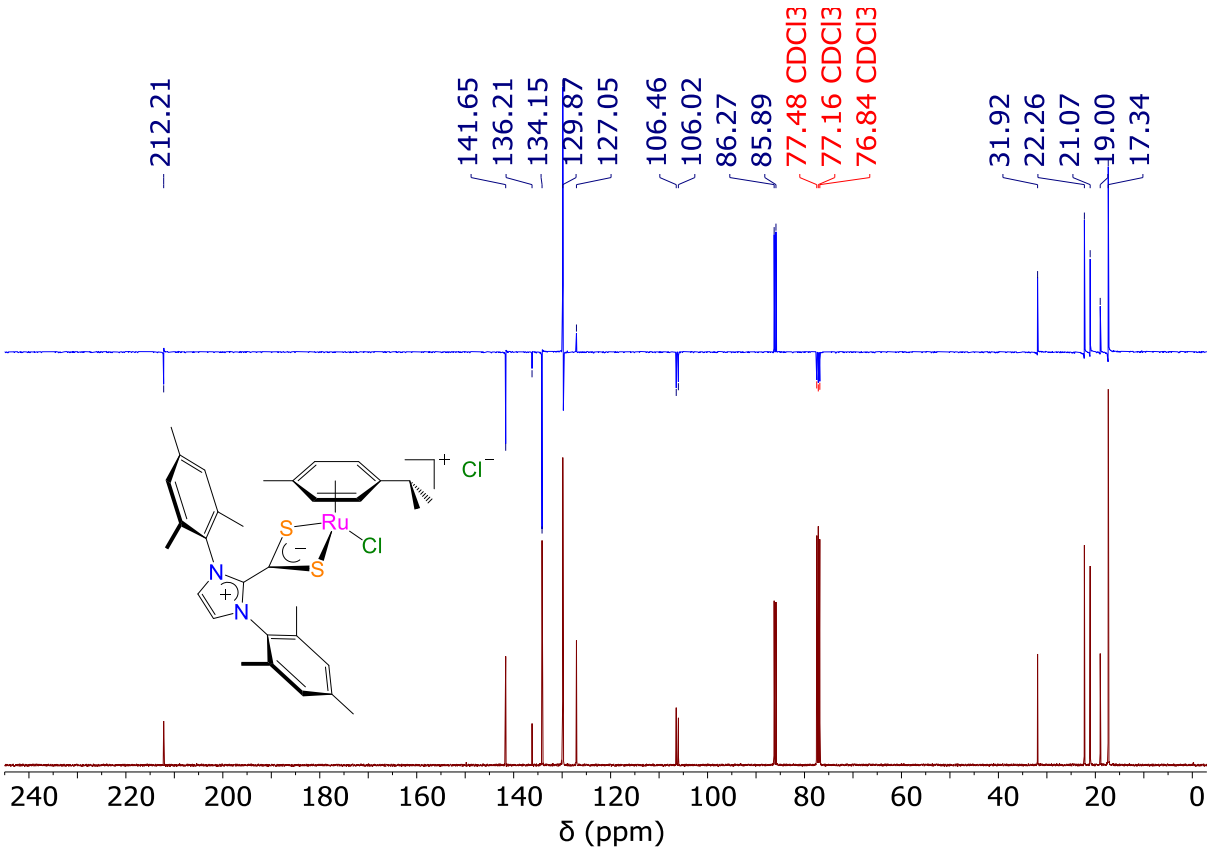

Fig. S4. ^{13}C CPD and APT NMR spectra (101 MHz, $CDCl_3$, 298 K) of [RuCl(*p*-cymene)-(S_2C·IMes)]Cl (**2a**)

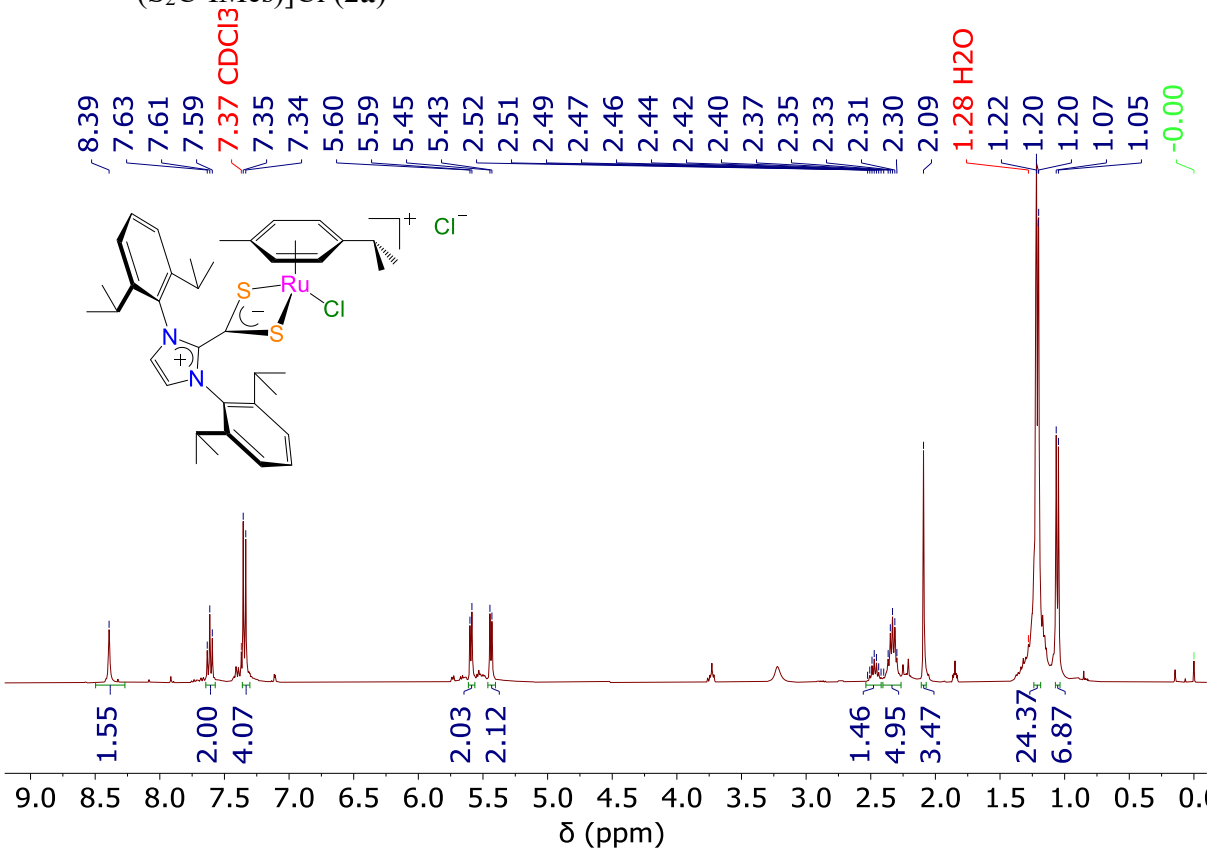

Fig. S5. ^{1}H NMR spectrum (400 MHz, $CDCl_3$, 298 K) of [RuCl(*p*-cymene)(S_2C·IDip)]Cl (**2b**)

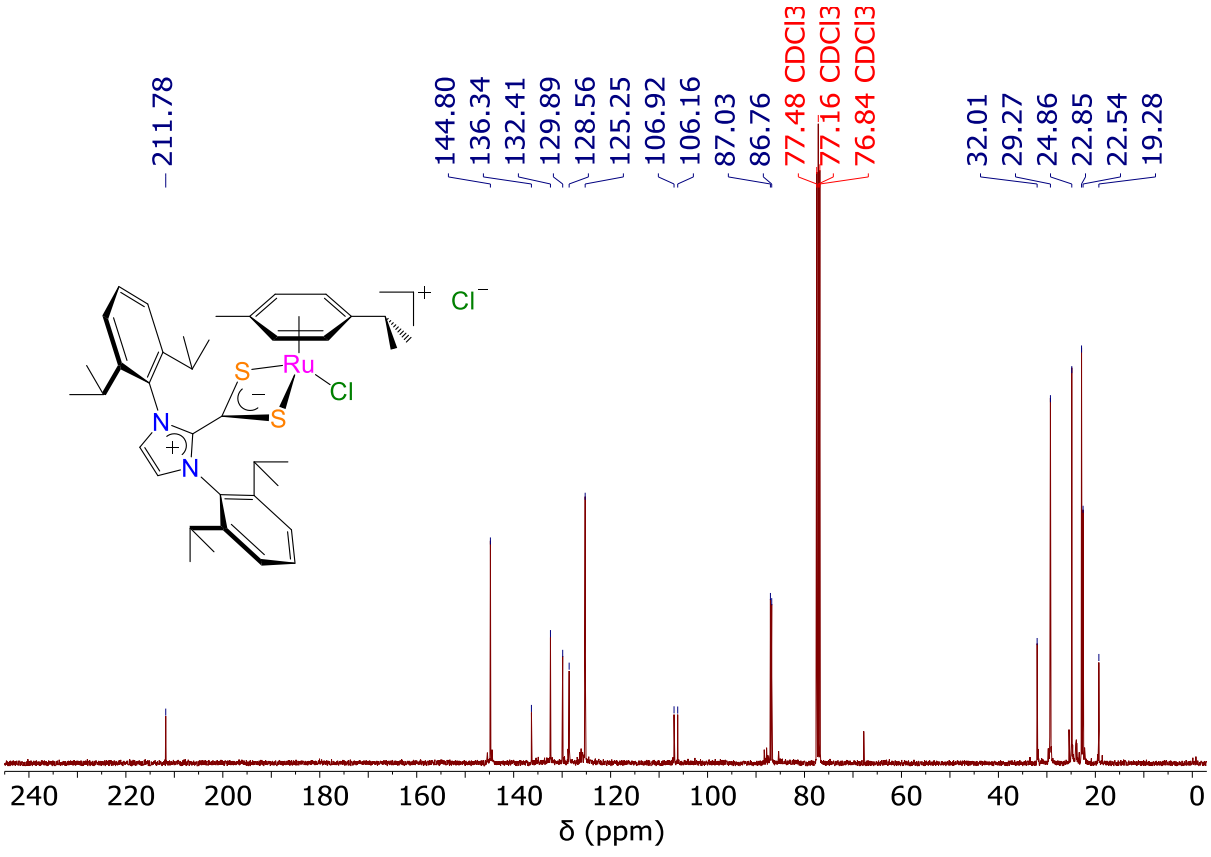

Fig. S6. $^{13}C\{^{1}H\}$ NMR spectrum (101 MHz, $CDCl_3$, 298 K) of [RuCl(*p*-cymene)-(S_2C·IDip)]Cl (**2b**)

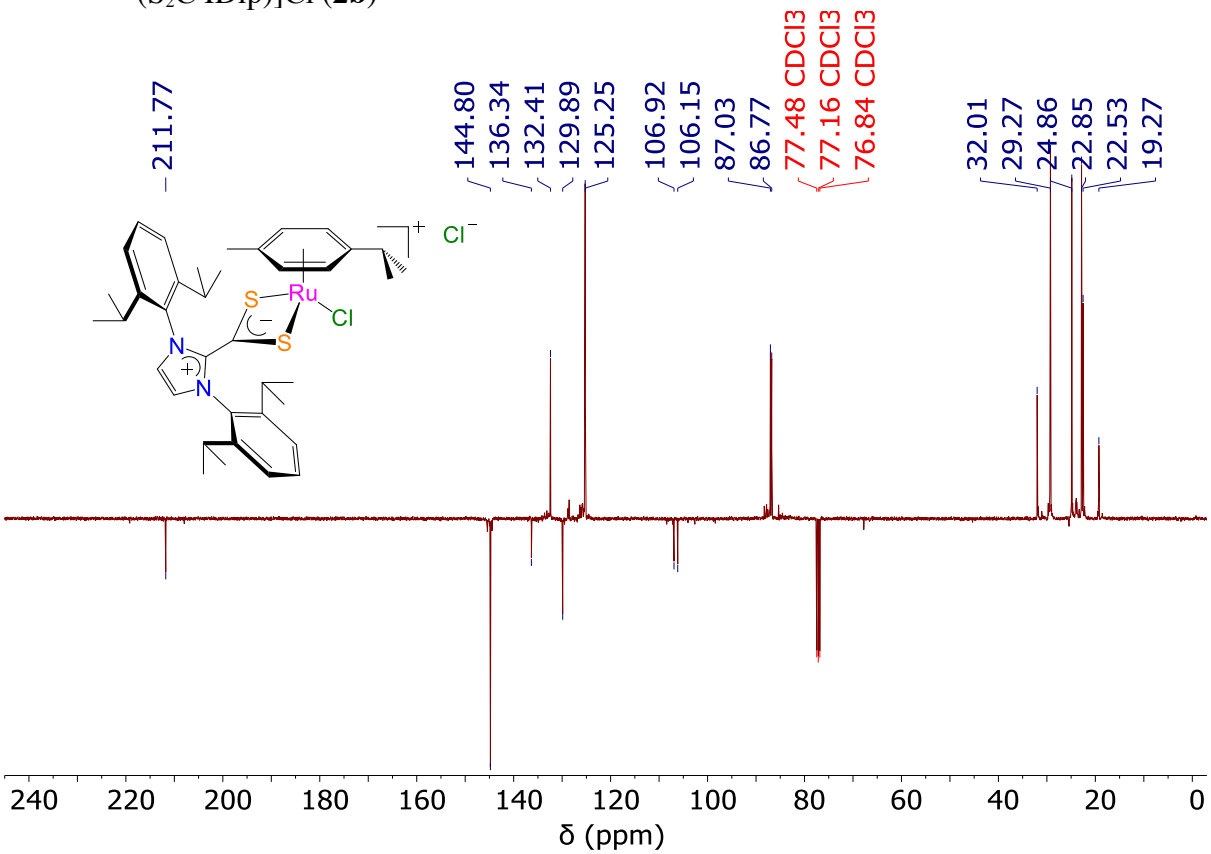

Fig. S7. $^{13}C\{^{1}H\}$ APT NMR spectrum (101 MHz, $CDCl_3$, 298 K) of [RuCl(*p*-cymene)-(S_2C·IDip)]Cl (**2b**)

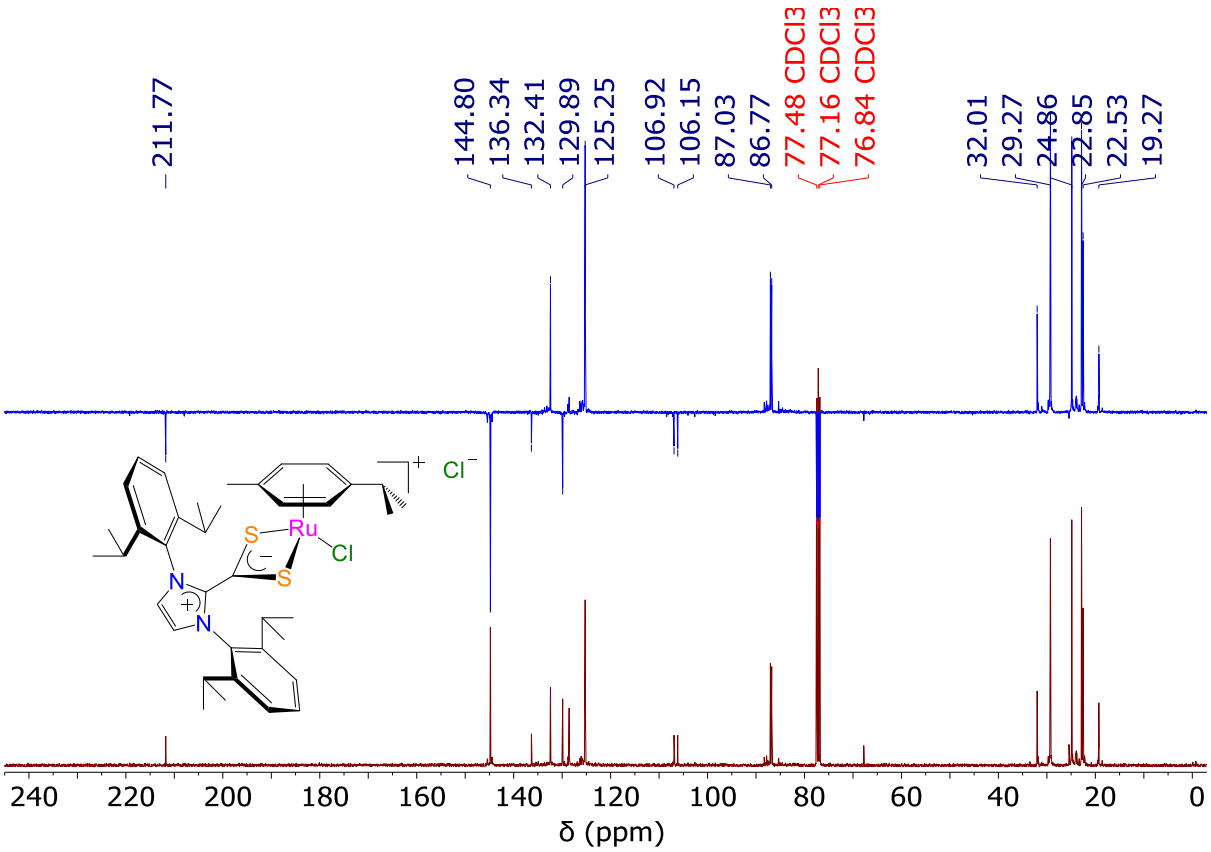

Fig. S8. ^{13}C CPD and APT NMR spectra (101 MHz, $CDCl_3$, 298 K) of [RuCl(*p*-cymene)-(S_2C·IDip)]Cl (**2b**)

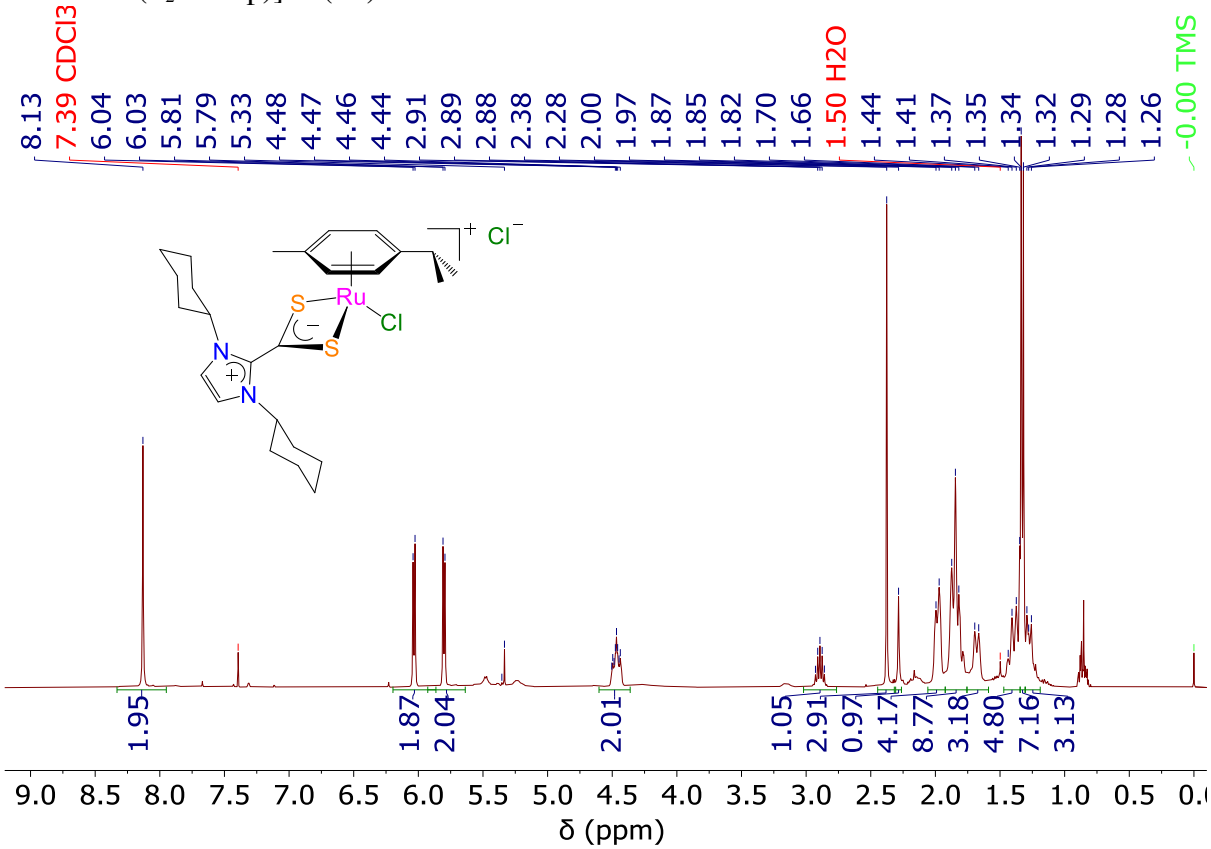

Fig. S9. ^{1}H NMR spectrum (400 MHz, $CDCl_3$, 298 K) of [RuCl(*p*-cymene)(S_2C·ICy)]Cl (**2c**)

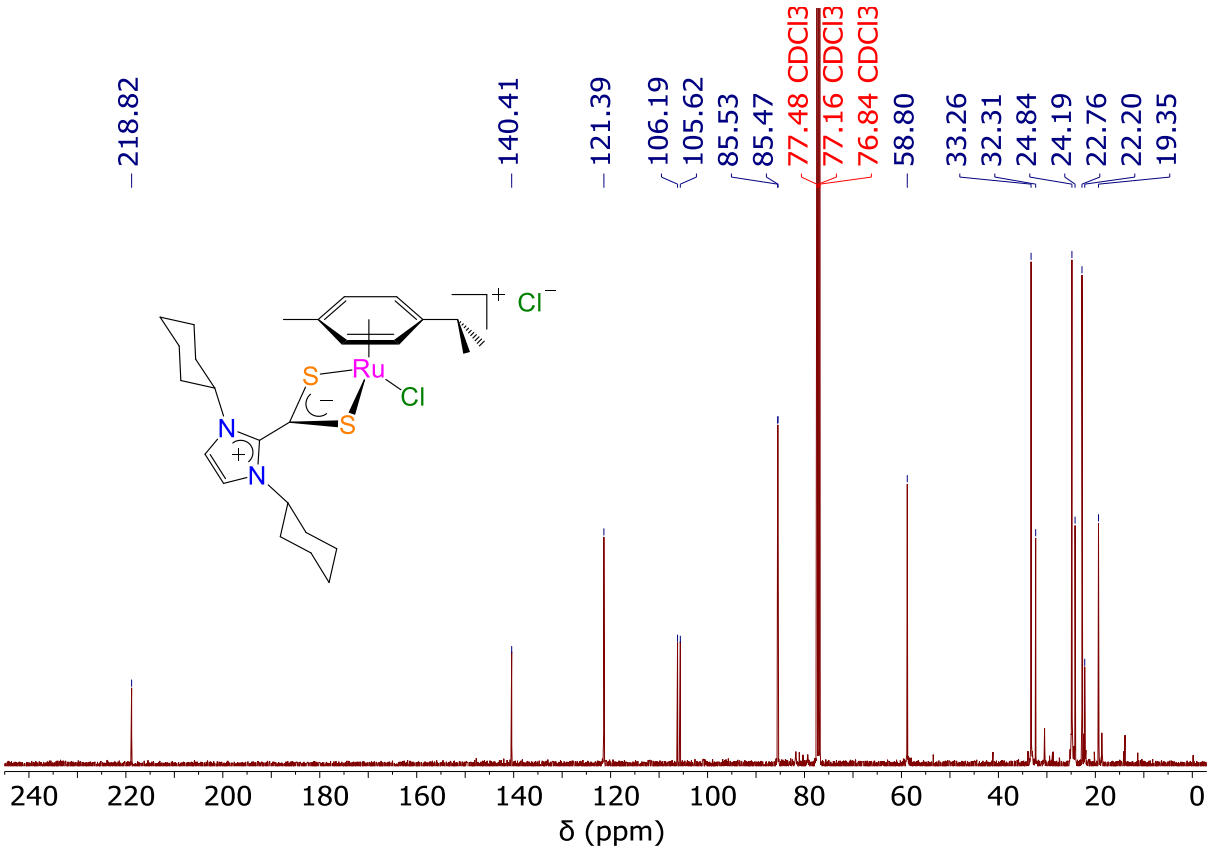

Fig. S10. $^{13}C\{^{1}H\}$ NMR spectrum (101 MHz, $CDCl_3$, 298 K) of [RuCl(*p*-cymene)-(S_2C·ICy)]Cl (**2c**)

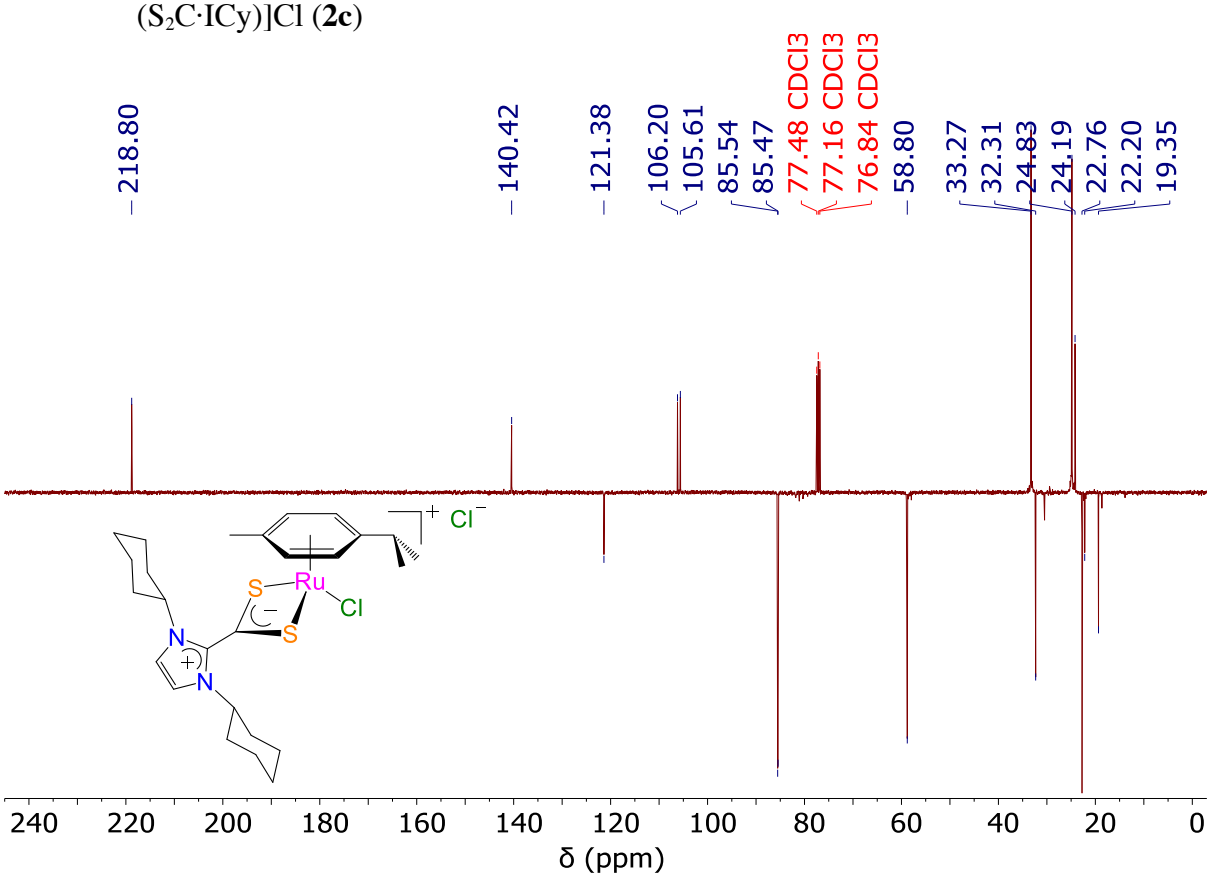

Fig. S11. $^{13}C\{^{1}H\}$ APT NMR spectrum (101 MHz, $CDCl_3$, 298 K) of [RuCl(*p*-cymene)-(S_2C·ICy)]Cl (**2c**)

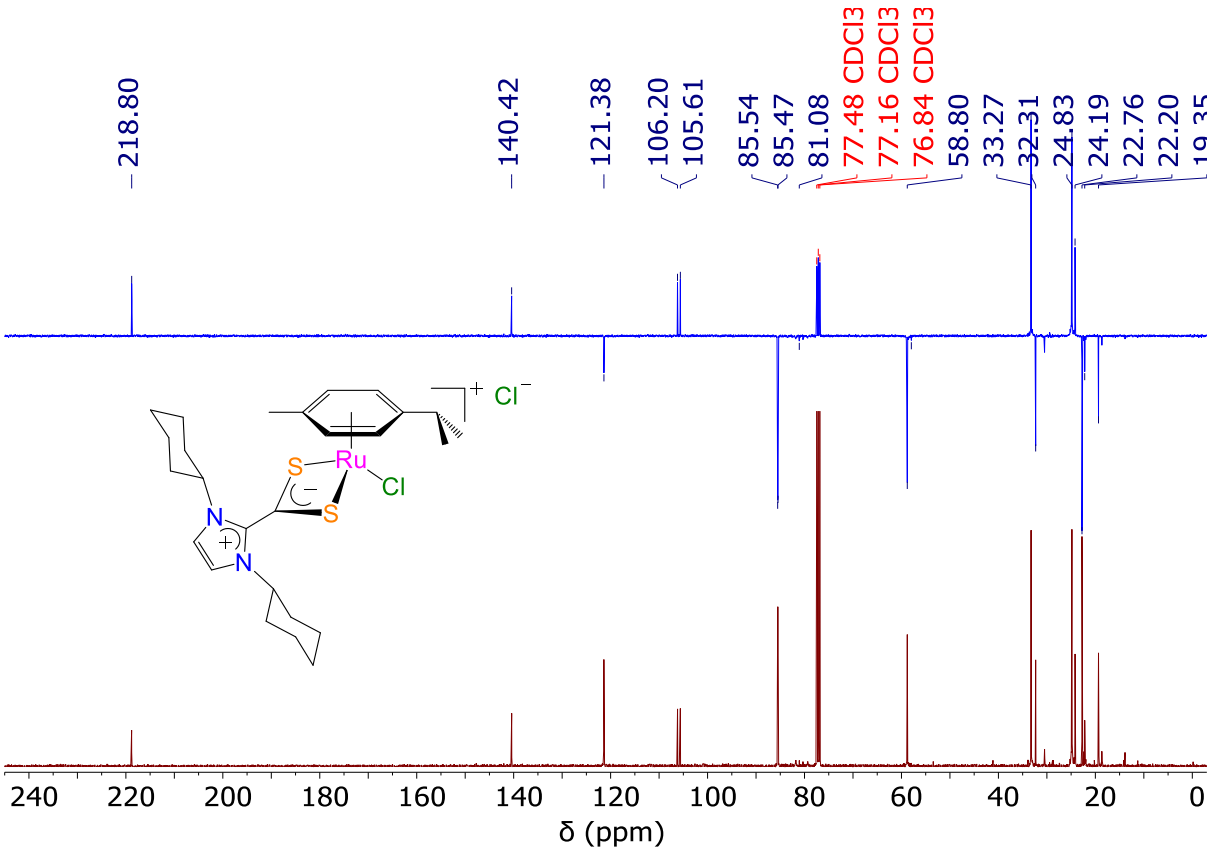

Fig. S12. ^{13}C CPD and APT NMR spectra (101 MHz, $CDCl_3$, 298 K) of [RuCl(*p*-cymene)-(S_2C·ICy)]Cl (**2c**)

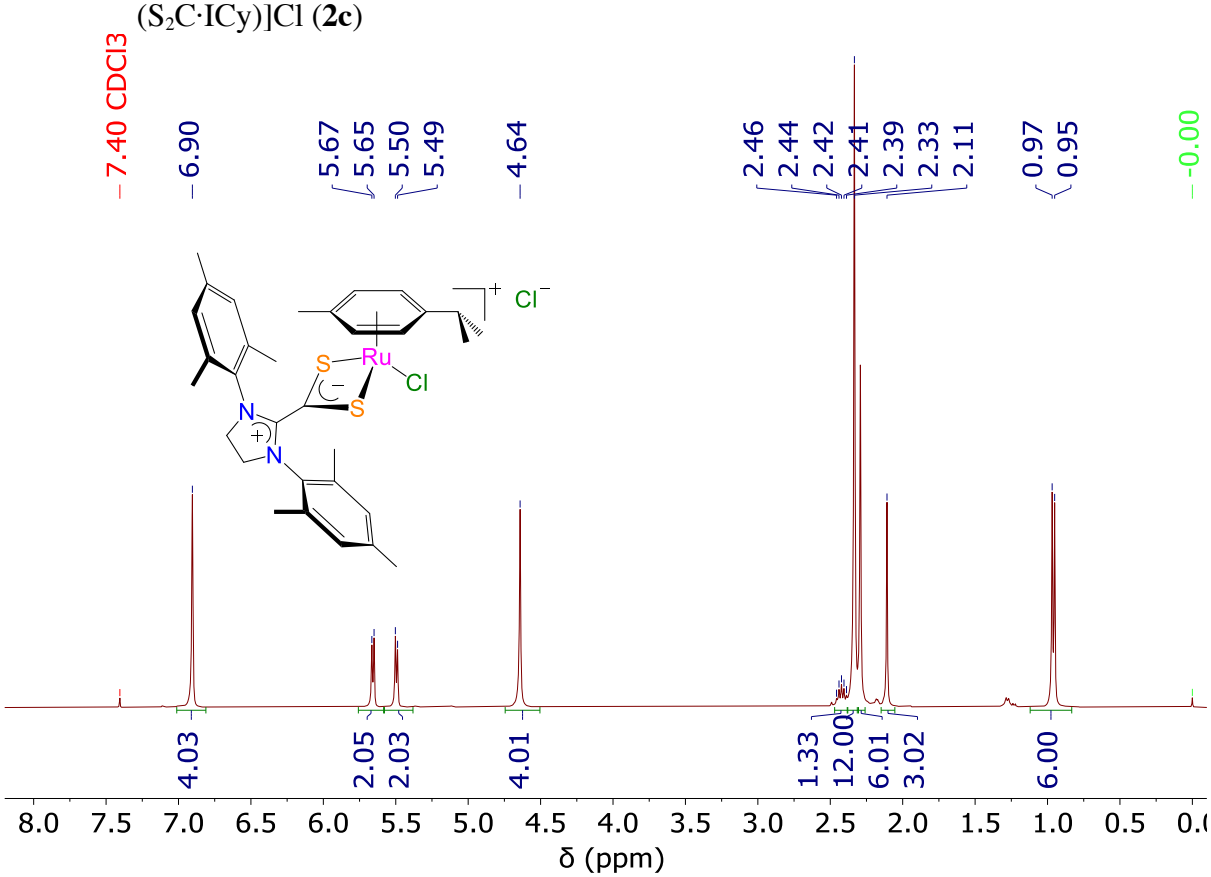

Fig. S13. ^{1}H NMR spectrum (400 MHz, $CDCl_3$, 298 K) of [RuCl(*p*-cymene)(S_2C·SIMes)]Cl (**2d**)

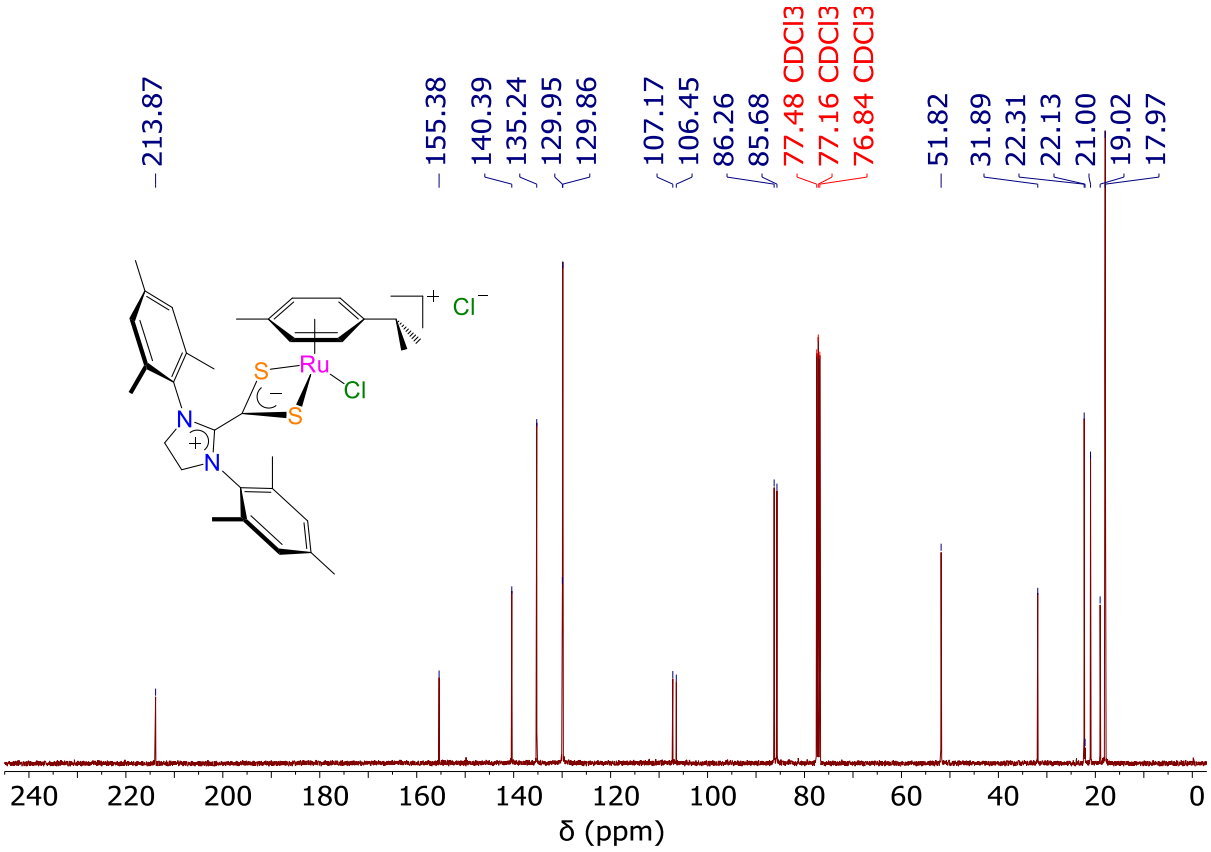

Fig. S14. $^{13}C\{^{1}H\}$ NMR spectrum (101 MHz, $CDCl_3$, 298 K) of [RuCl(*p*-cymene)-(S_2C·SIMes)]Cl (**2d**)

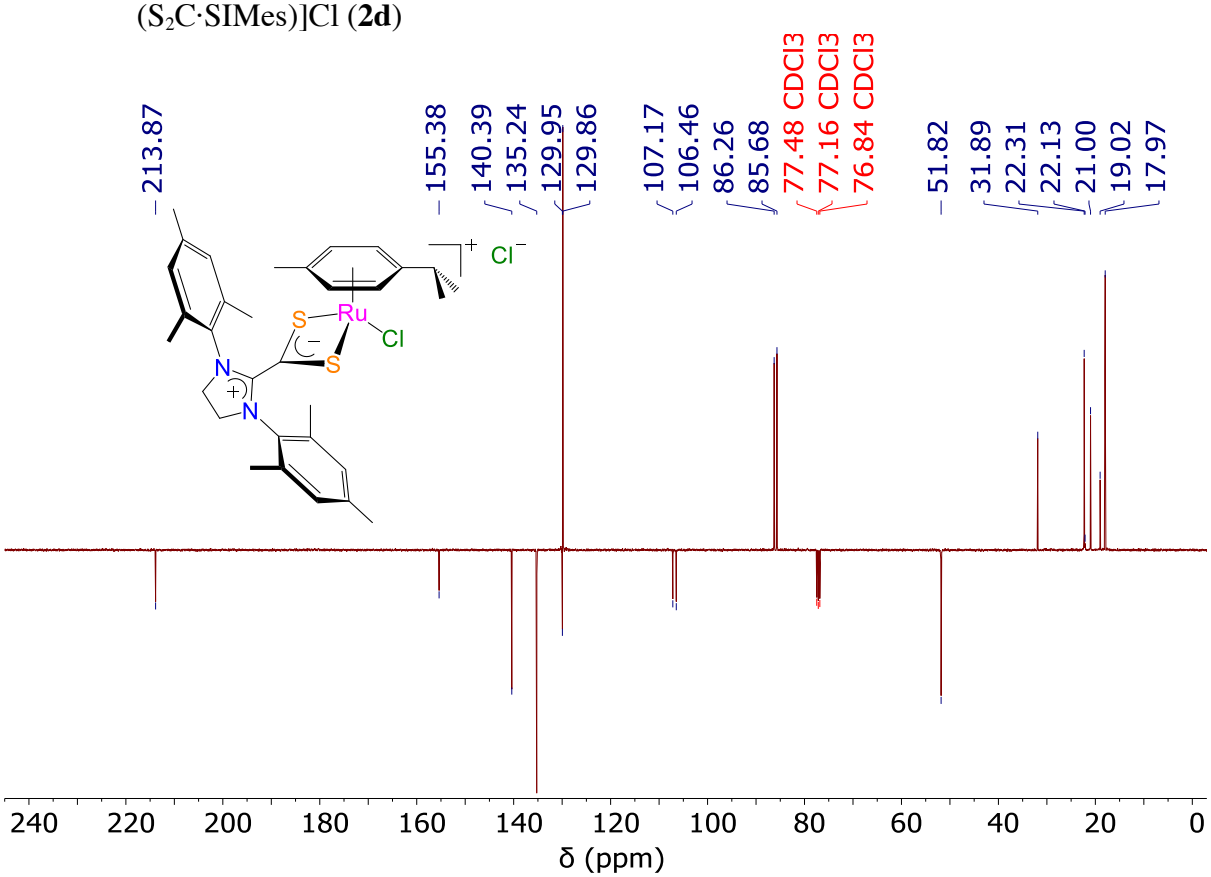

Fig. S15. $^{13}C\{^{1}H\}$ APT NMR spectrum (101 MHz, $CDCl_3$, 298 K) of [RuCl(*p*-cymene)-(S_2C·SIMes)]Cl (**2d**)

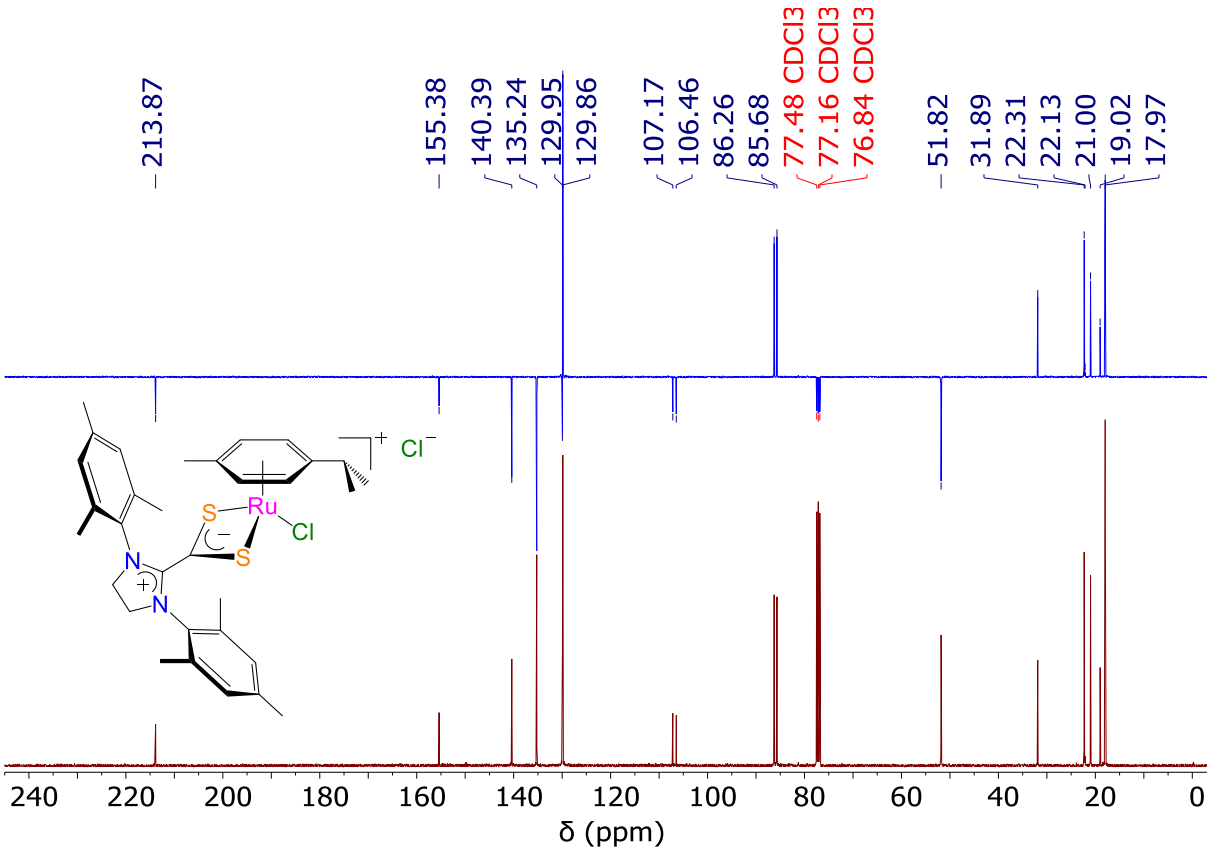

Fig. S16. ^{13}C CPD and APT NMR spectra (101 MHz, $CDCl_3$, 298 K) of [RuCl(*p*-cymene)-(S_2C·SIMes)]Cl (**2d**)

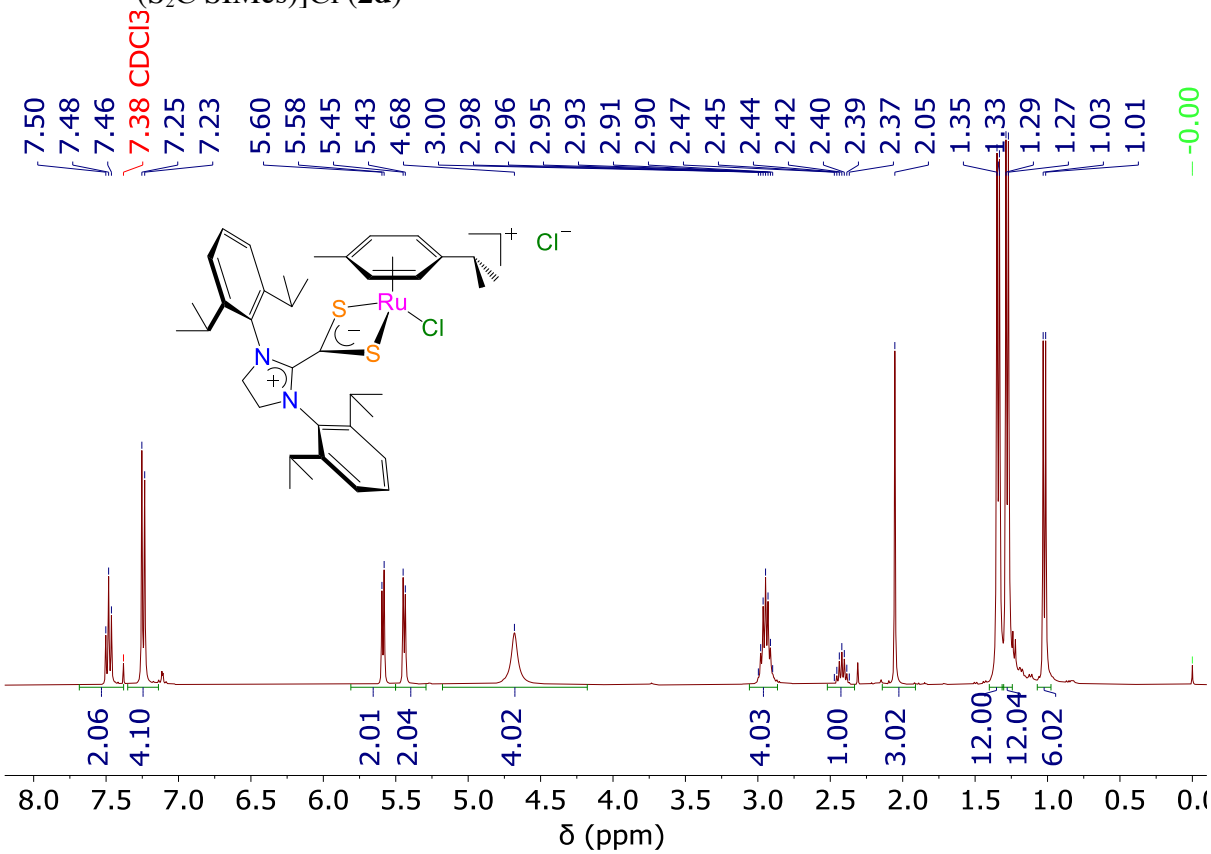

Fig. S17. ^{1}H NMR spectrum (400 MHz, $CDCl_3$, 298 K) of [RuCl(*p*-cymene)(S_2C·SIDip)]Cl (**2e**)

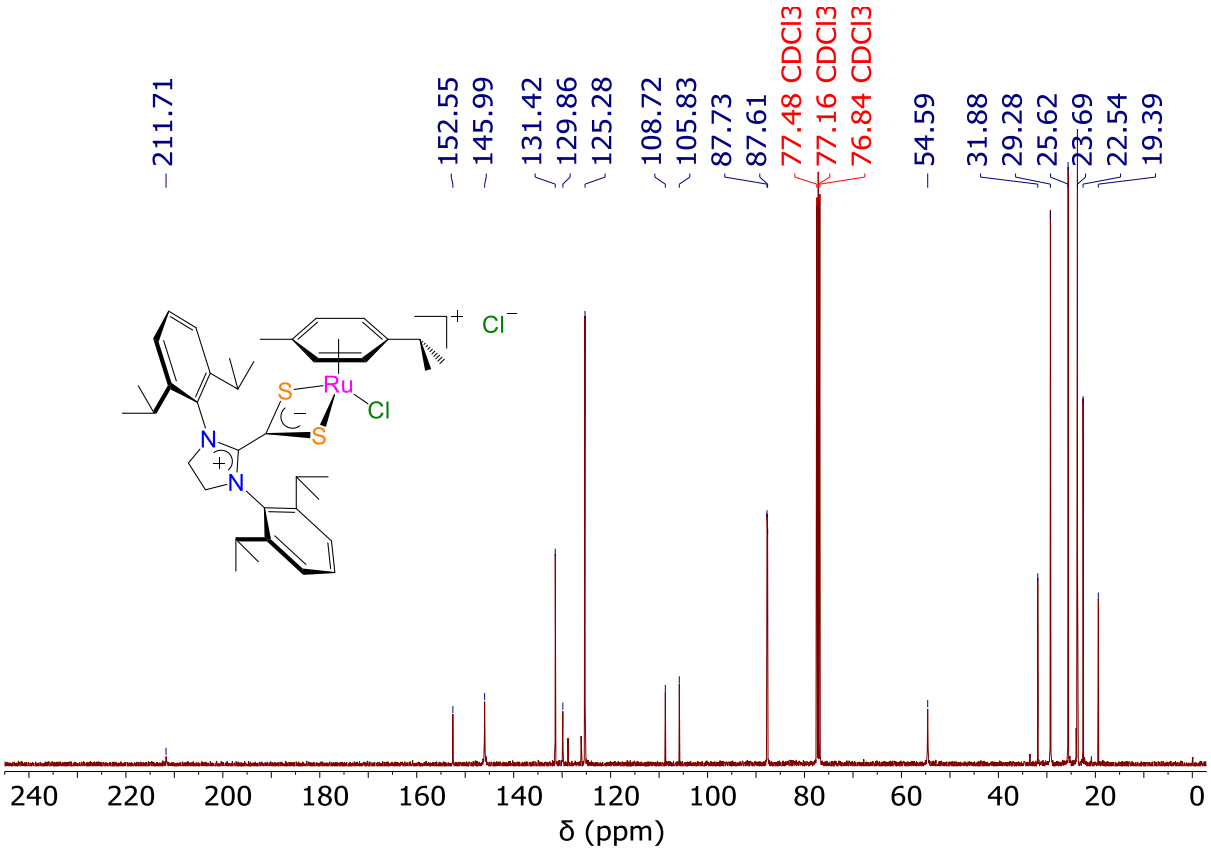

Fig. S18. $^{13}C\{^{1}H\}$ NMR spectrum (101 MHz, $CDCl_3$, 298 K) of [RuCl(*p*-cymene)-(S_2C·SIDip)]Cl (**2e**)

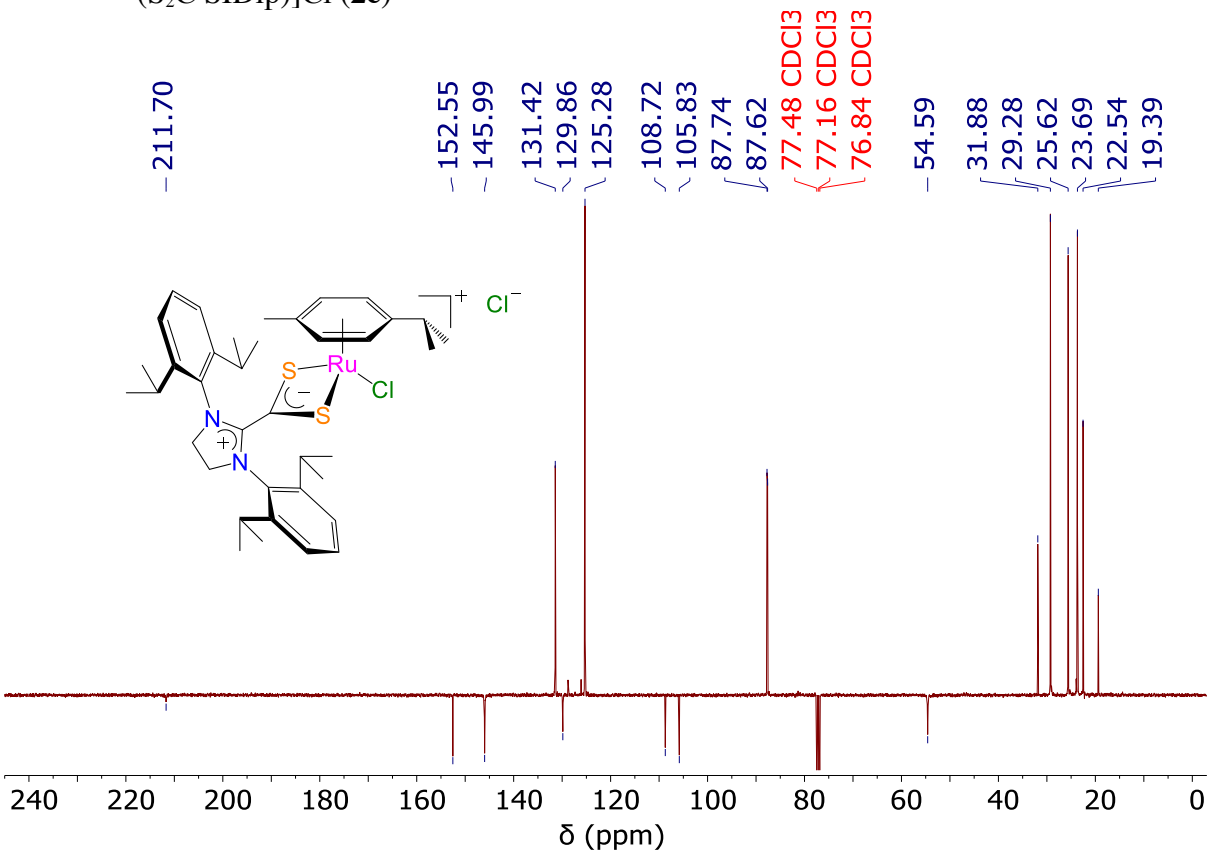

Fig. S19. $^{13}C\{^{1}H\}$ APT NMR spectrum (101 MHz, $CDCl_3$, 298 K) of [RuCl(*p*-cymene)-(S_2C·SIDip)]Cl (**2e**)

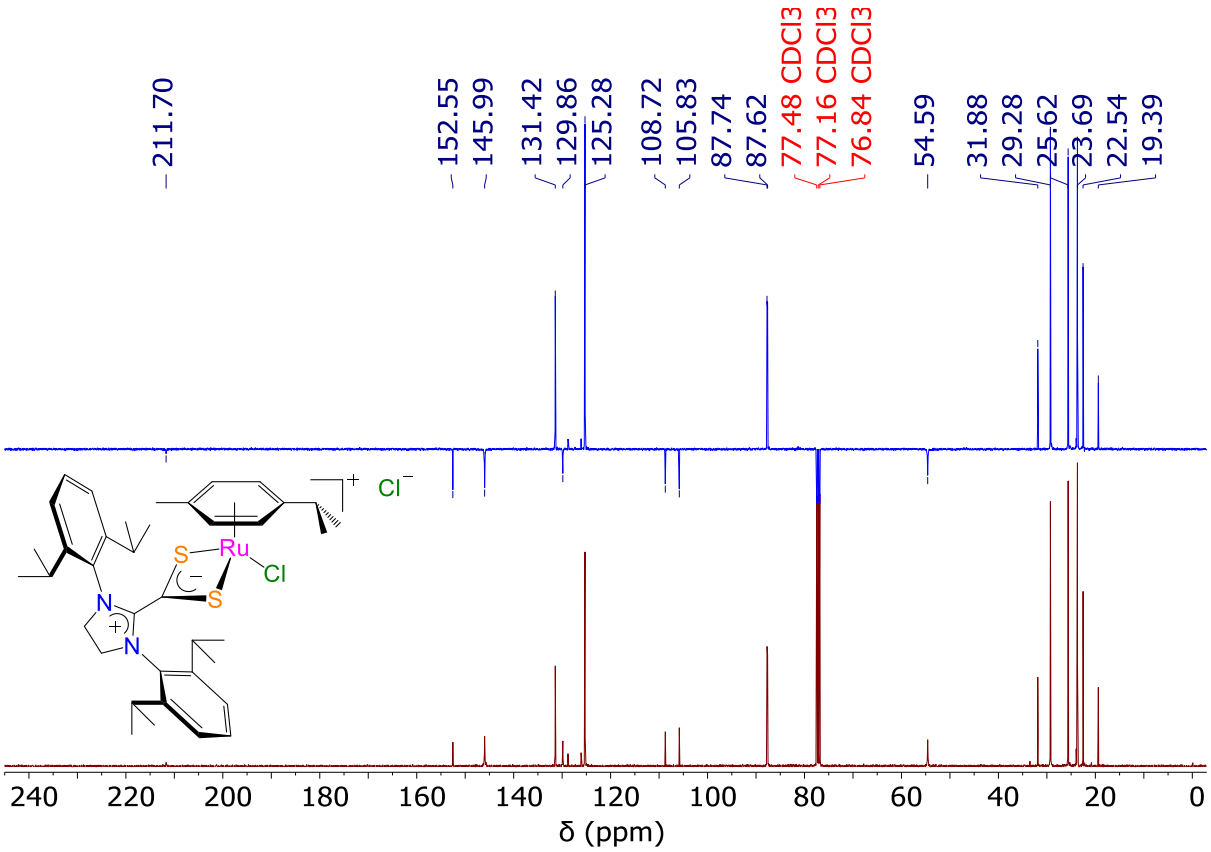

Fig. S20. ^{13}C CPD and APT NMR spectra (101 MHz, $CDCl_3$, 298 K) of [RuCl(*p*-cymene)-(S_2C·SIDip)]Cl (**2e**)

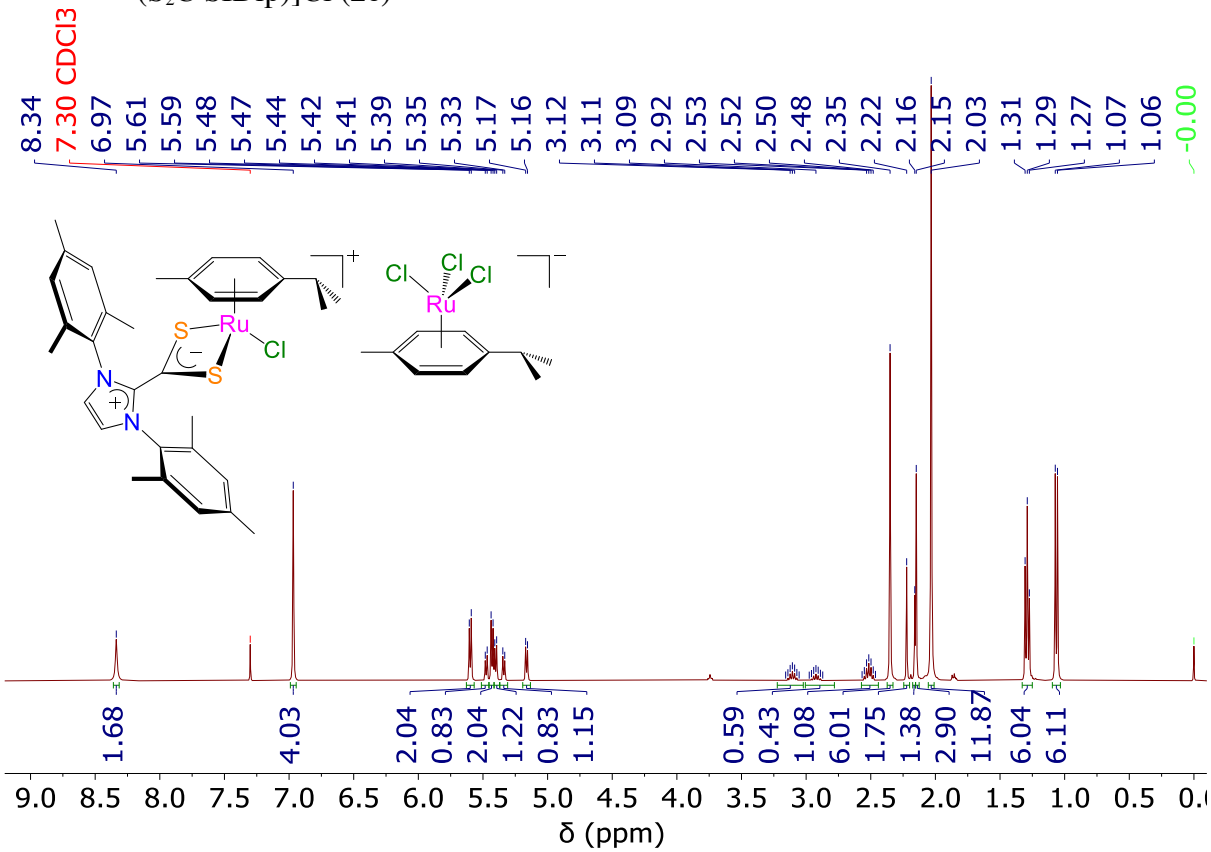

Fig. S21. ^{1}H NMR spectrum (400 MHz, $CDCl_3$, 298 K) of [RuCl(*p*-cymene)(S_2C·IMes)]-[$RuCl_3$(*p*-cymene)] (**3a**)

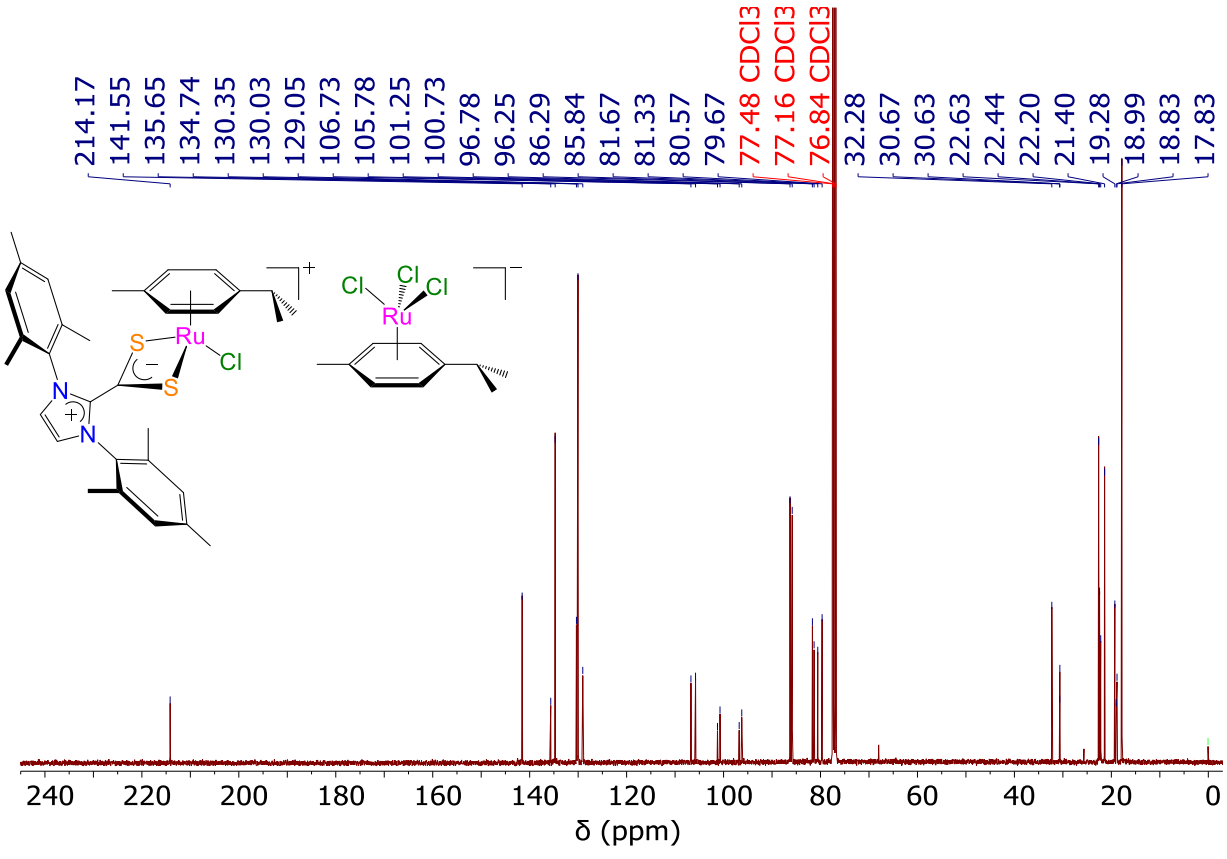

Fig. S22. $^{13}C\{^{1}H\}$ NMR spectrum (101 MHz, $CDCl_3$, 298 K) of [RuCl(*p*-cymene)-(S_2C·IMes)][$RuCl_3$(*p*-cymene)] (**3a**)

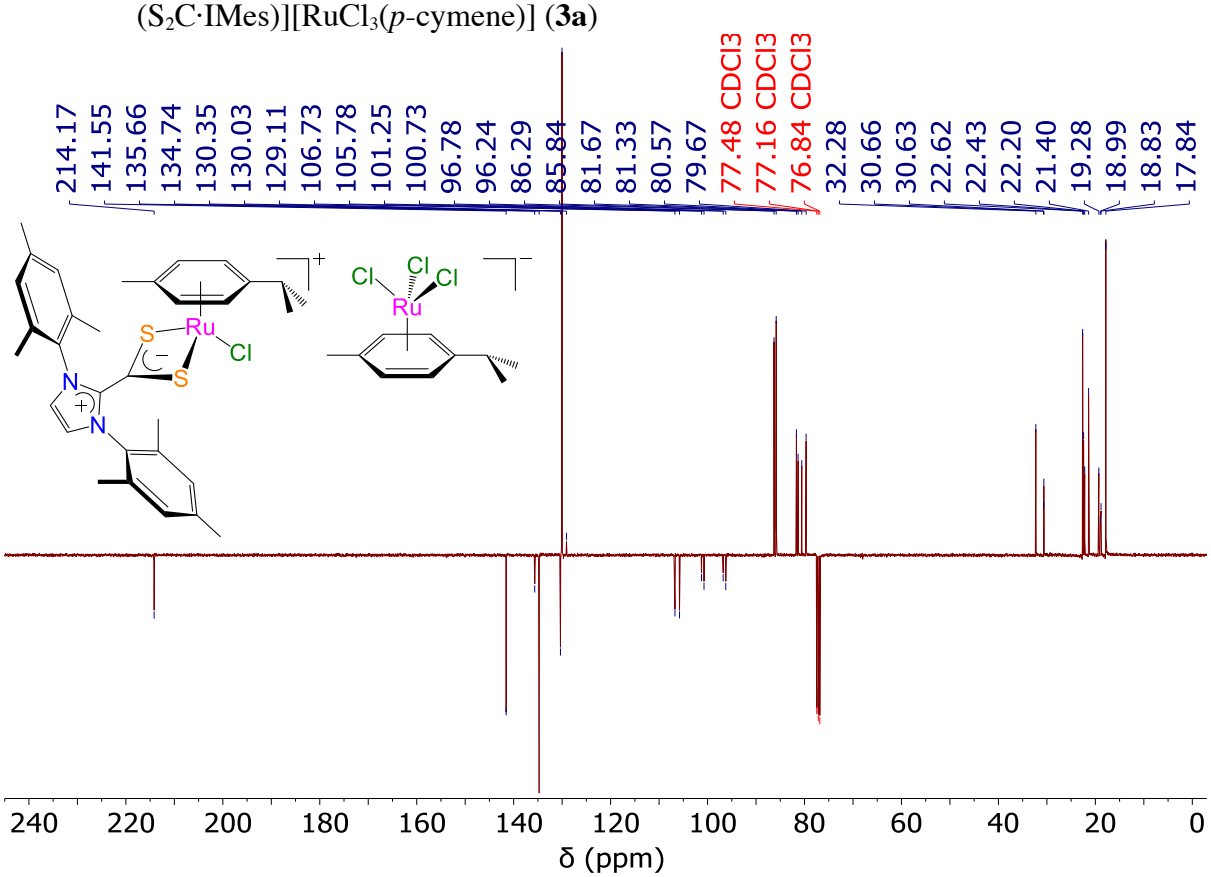

Fig. S23. $^{13}C\{^{1}H\}$ APT NMR spectrum (101 MHz, $CDCl_3$, 298 K) of [RuCl(*p*-cymene)-(S_2C·IMes)][$RuCl_3$(*p*-cymene)] (**3a**)

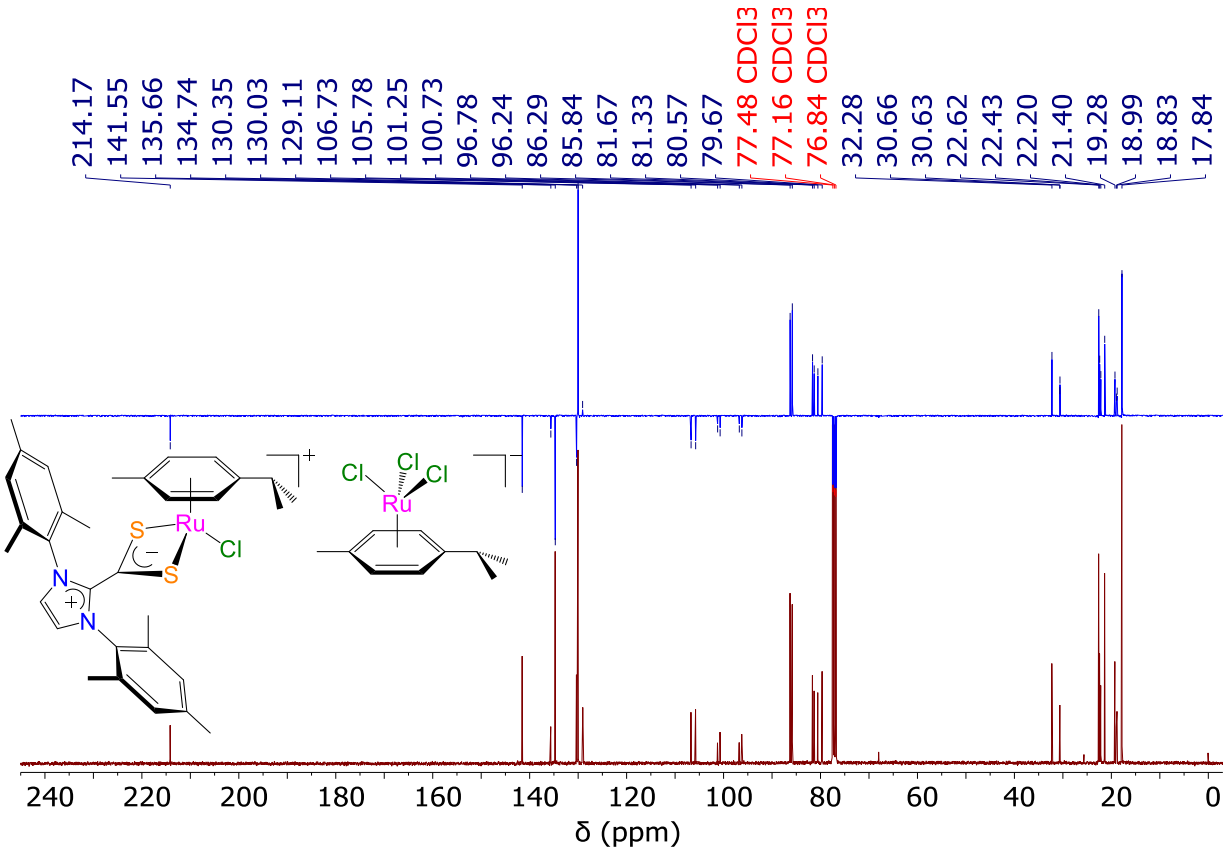

Fig. S24. ^{13}C CPD and APT NMR spectra (101 MHz, $CDCl_3$, 298 K) of [RuCl(*p*-cymene)-(S_2C·IMes)][$RuCl_3$(p-cymene)] (**3a**)

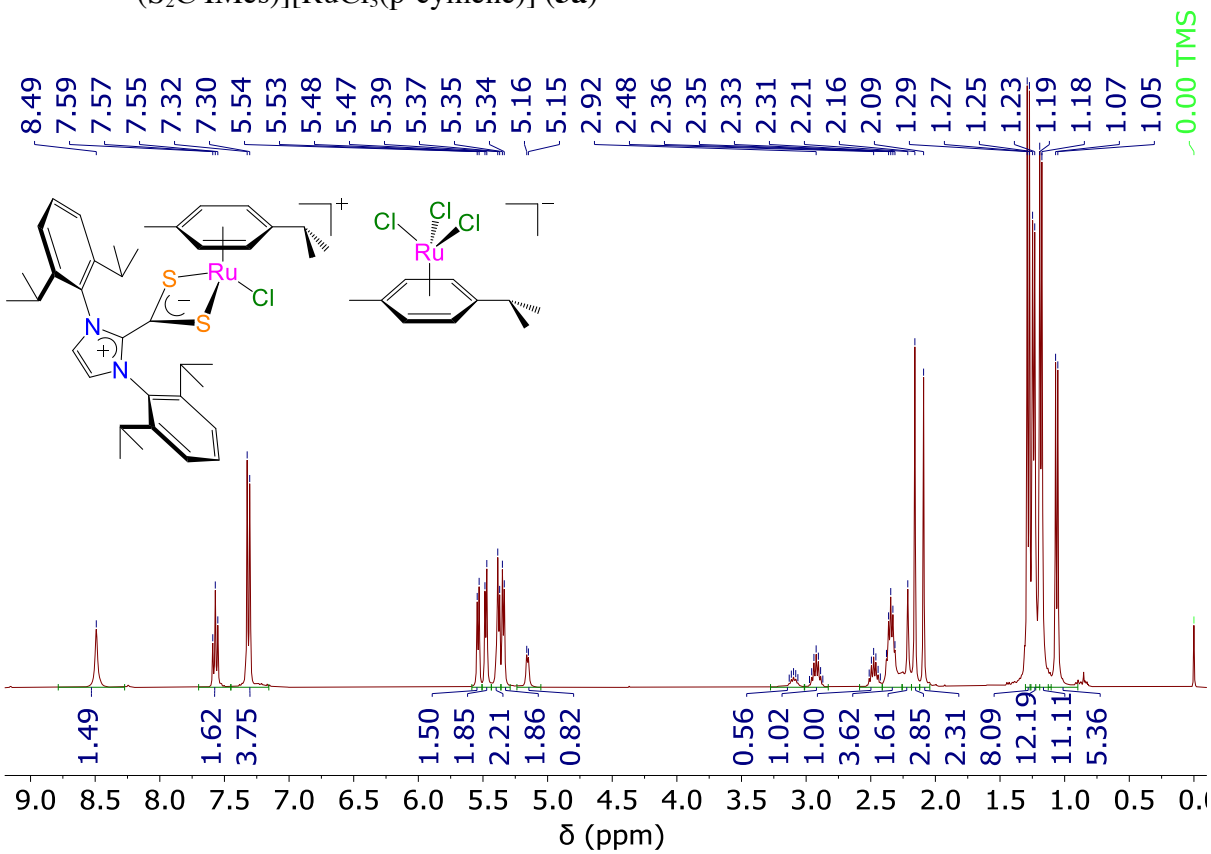

Fig. S25. ^{1}H NMR spectrum (400 MHz, $CDCl_3$, 298 K) of [RuCl(*p*-cymene)(S_2C·IDip)]-[$RuCl_3$(*p*-cymene)] (**3b**)

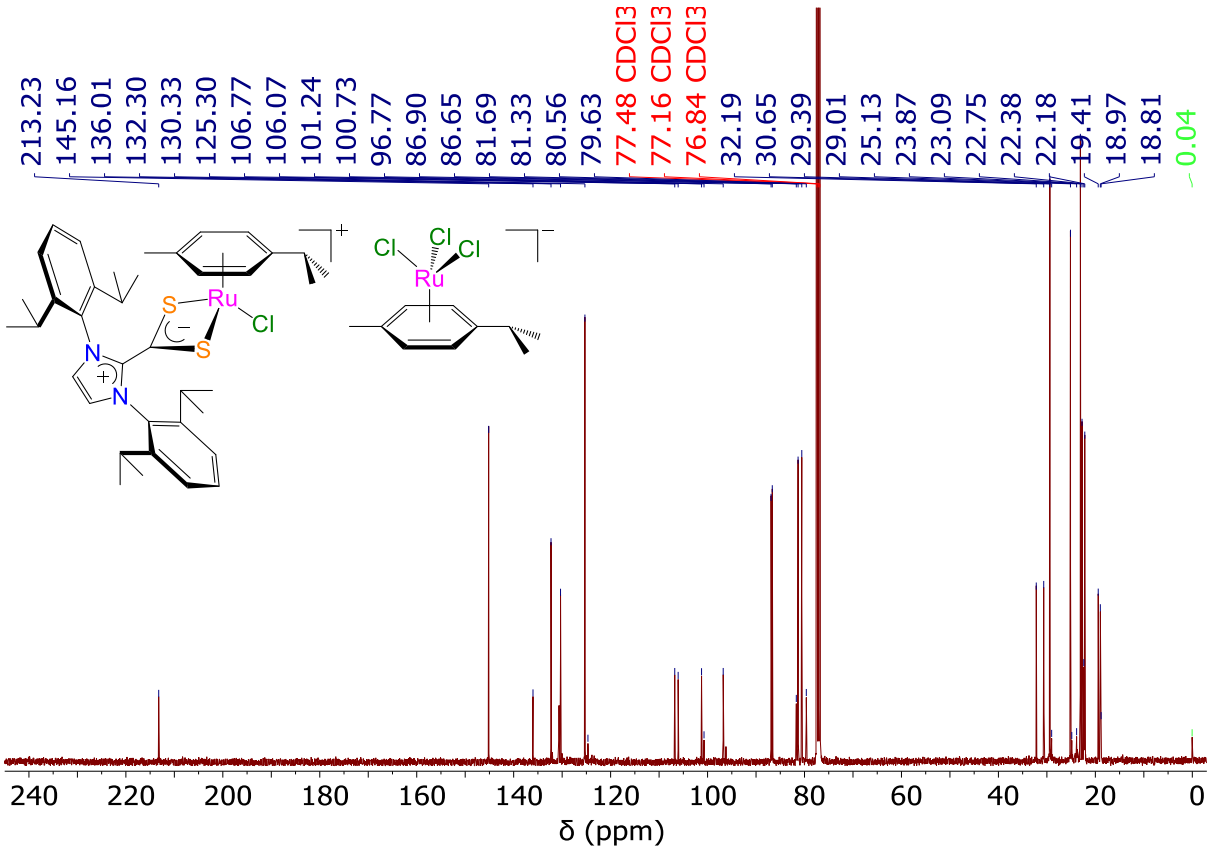

Fig. S26. $^{13}C\{^{1}H\}$ NMR spectrum (101 MHz, $CDCl_3$, 298 K) of [RuCl(*p*-cymene)-(S_2C·IDip)][$RuCl_3$(*p*-cymene)] (**3b**)

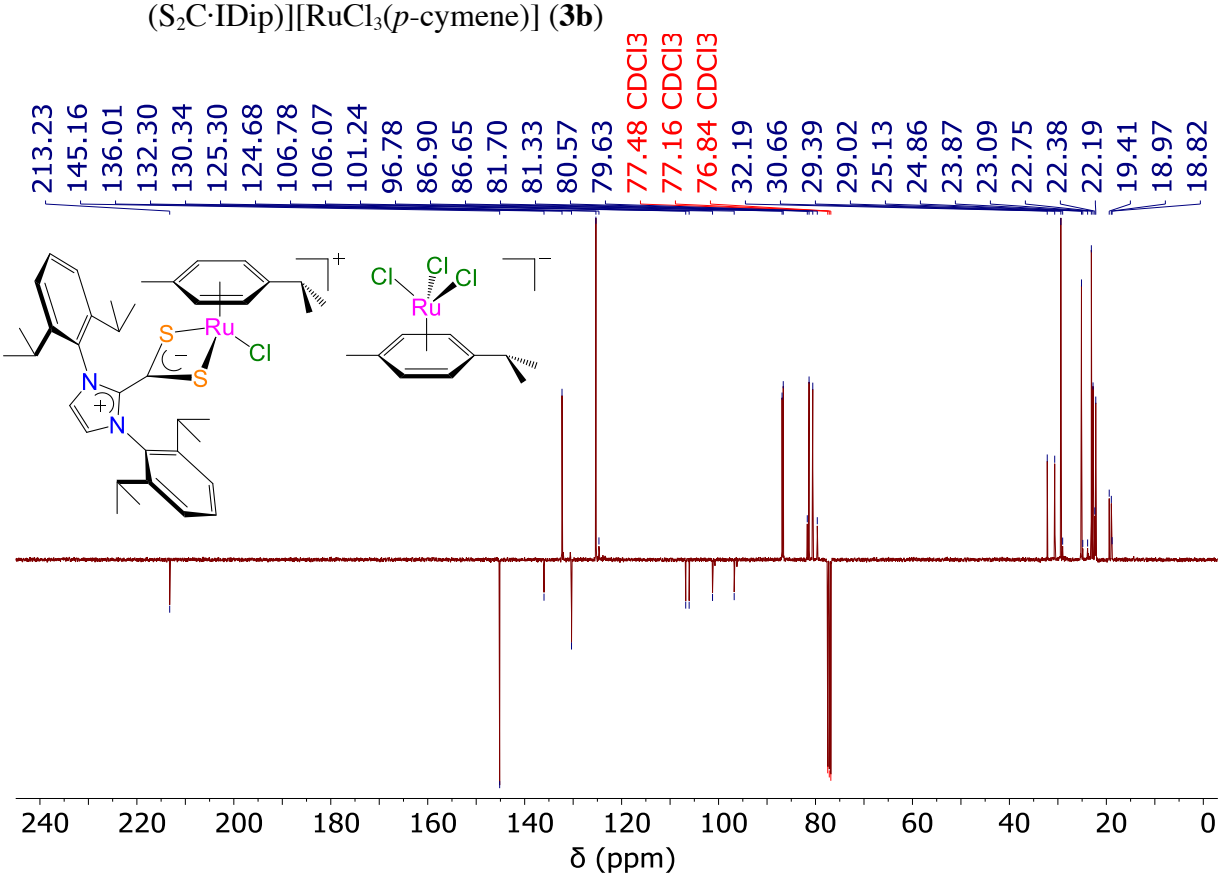

Fig. S27. $^{13}C\{^{1}H\}$ APT NMR spectrum (101 MHz, $CDCl_3$, 298 K) of [RuCl(*p*-cymene)-(S_2C·IDip)][$RuCl_3$(*p*-cymene)] (**3b**)

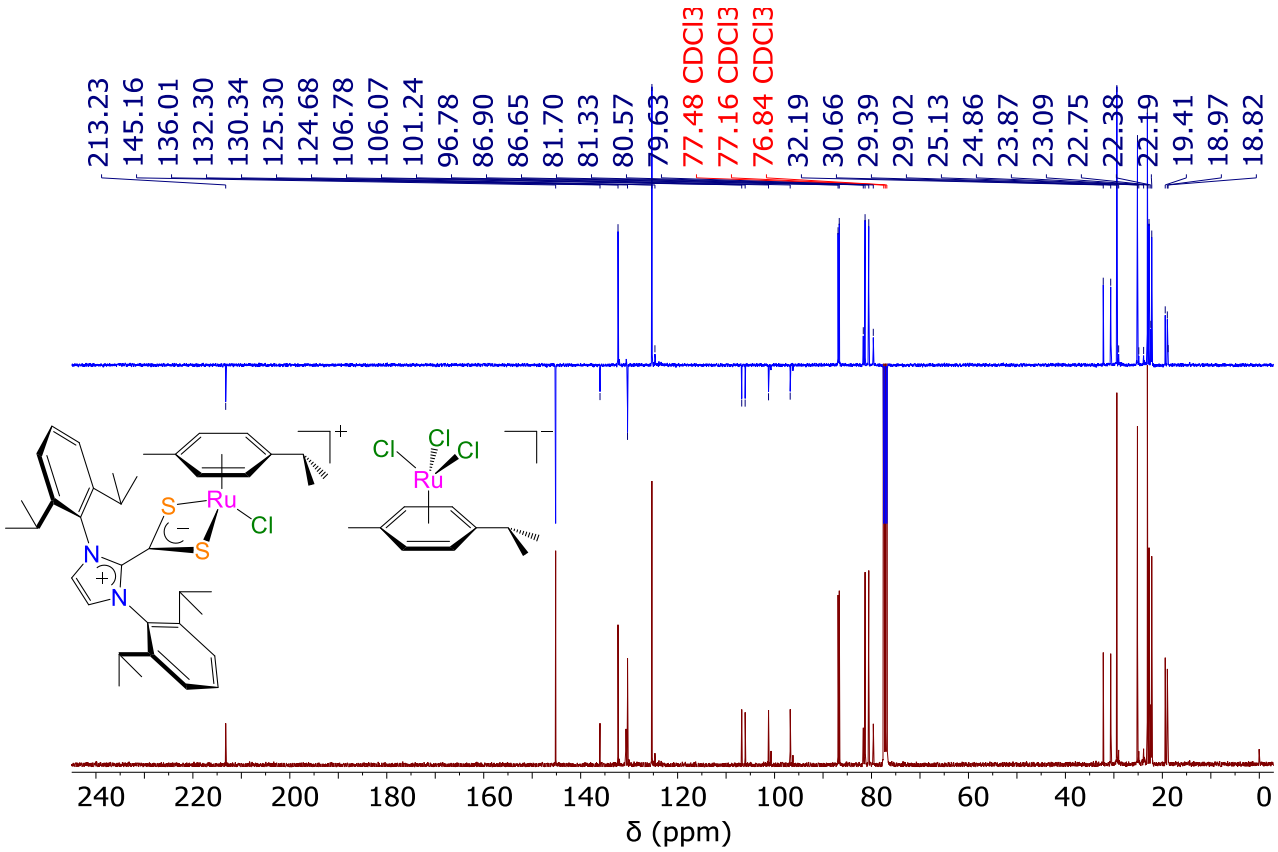

Fig. S28. ^{13}C CPD and APT NMR spectra (101 MHz, $CDCl_3$, 298 K) of [RuCl(*p*-cymene)-(S_2C·IDip)][$RuCl_3$(*p*-cymene)] (**3b**)

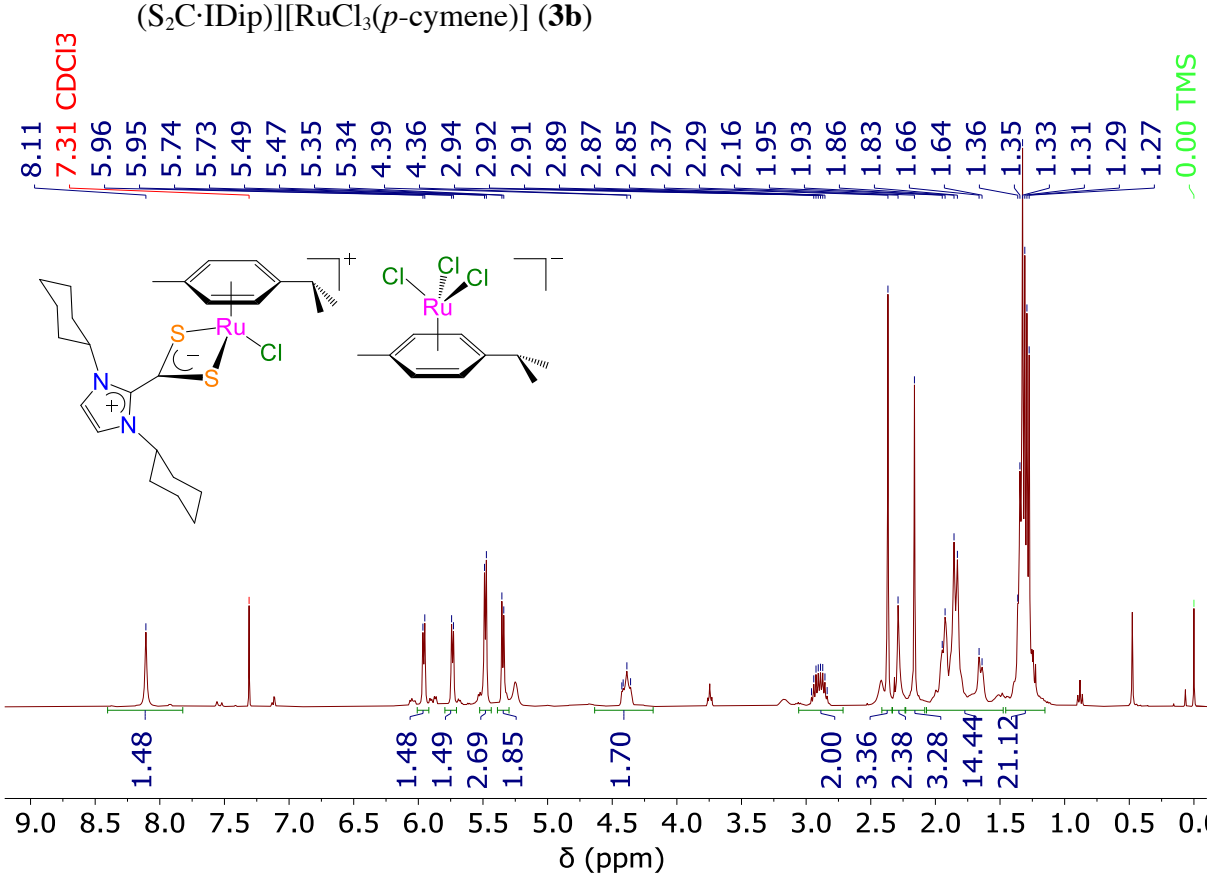

Fig. S29. ^{1}H NMR spectrum (400 MHz, $CDCl_3$, 298 K) of [RuCl(*p*-cymene)(S_2C·ICy)]-[$RuCl_3$(*p*-cymene)] (**3c**)

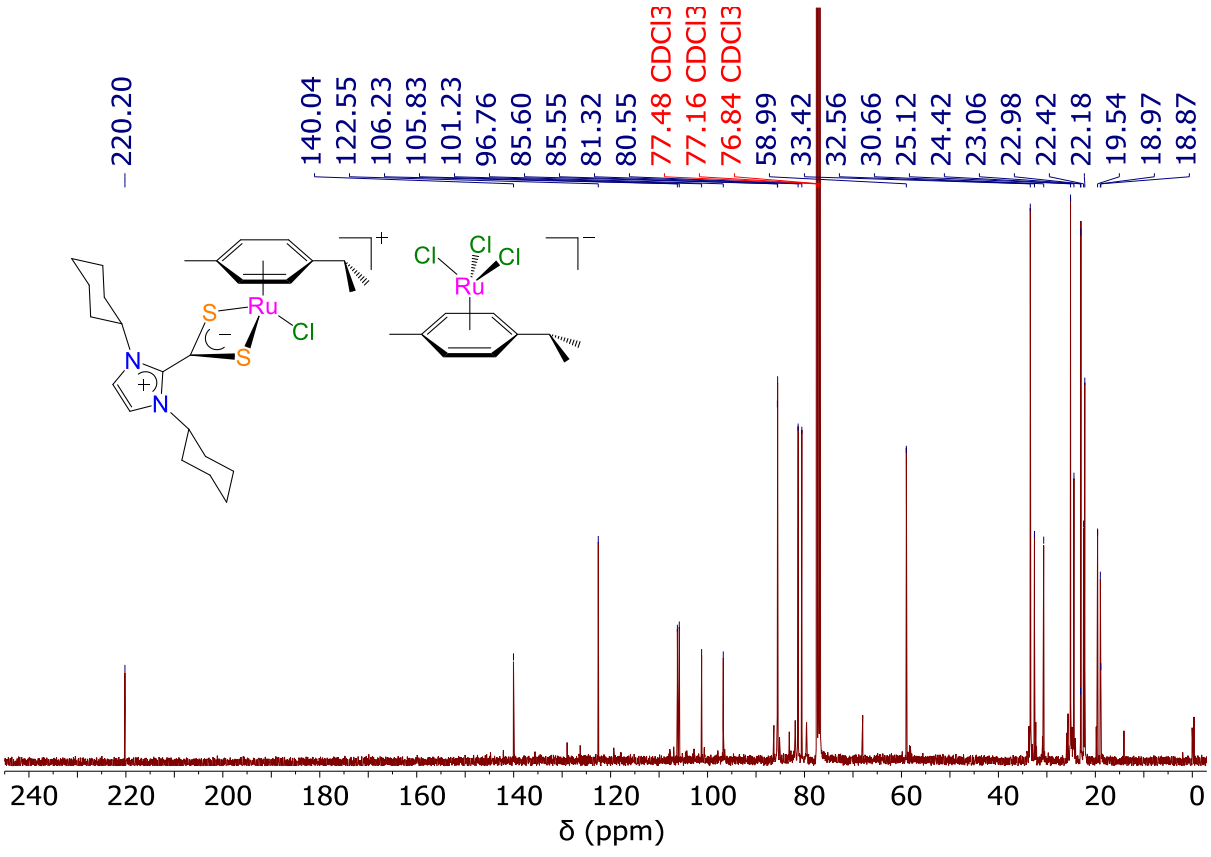

Fig. S30. $^{13}C\{^{1}H\}$ NMR spectrum (101 MHz, $CDCl_3$, 298 K) of [RuCl(*p*-cymene)(S_2C·ICy)]-[$RuCl_3$(*p*-cymene)] (**3c**)

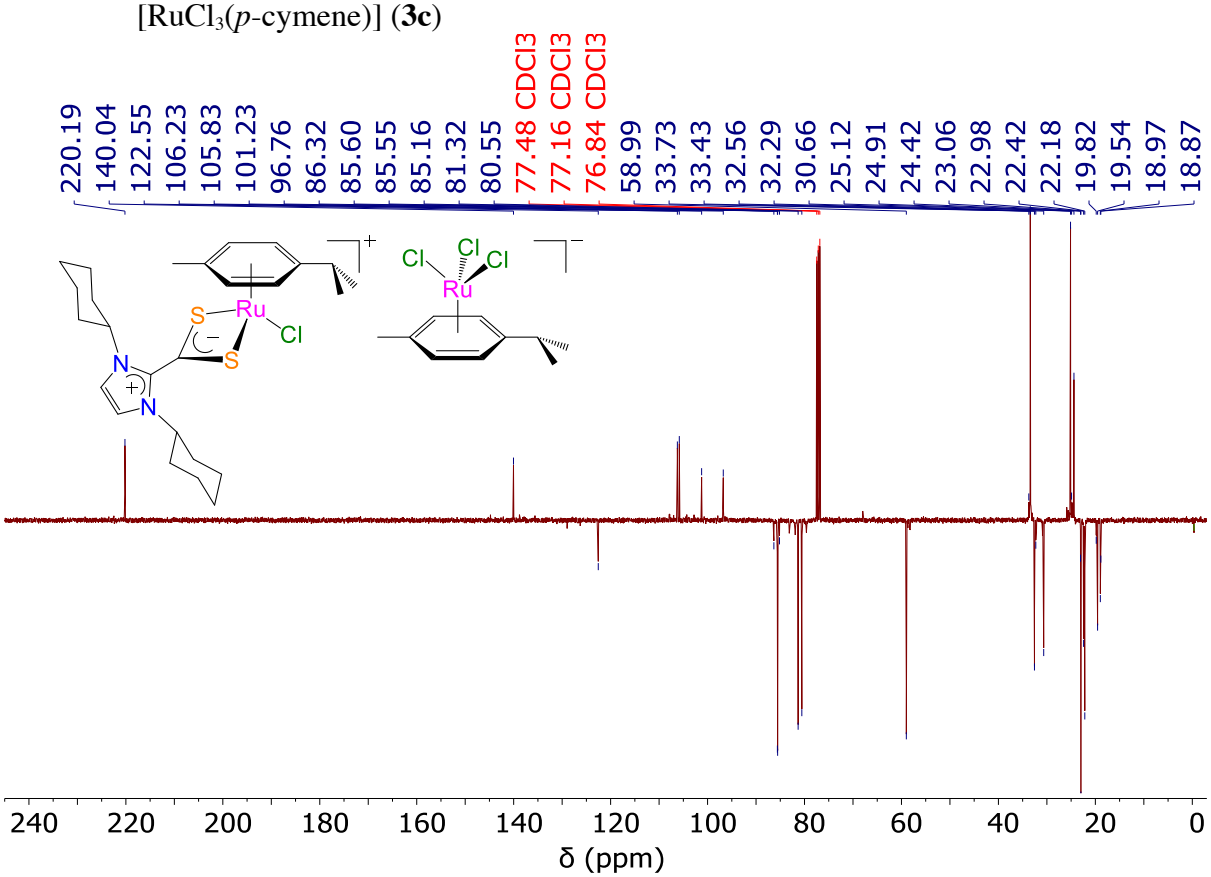

Fig. S31. $^{13}C\{^{1}H\}$ APT NMR spectrum (101 MHz, $CDCl_3$, 298 K) of [RuCl(*p*-cymene)-(S_2C·ICy)][$RuCl_3$(*p*-cymene)] (**3c**)

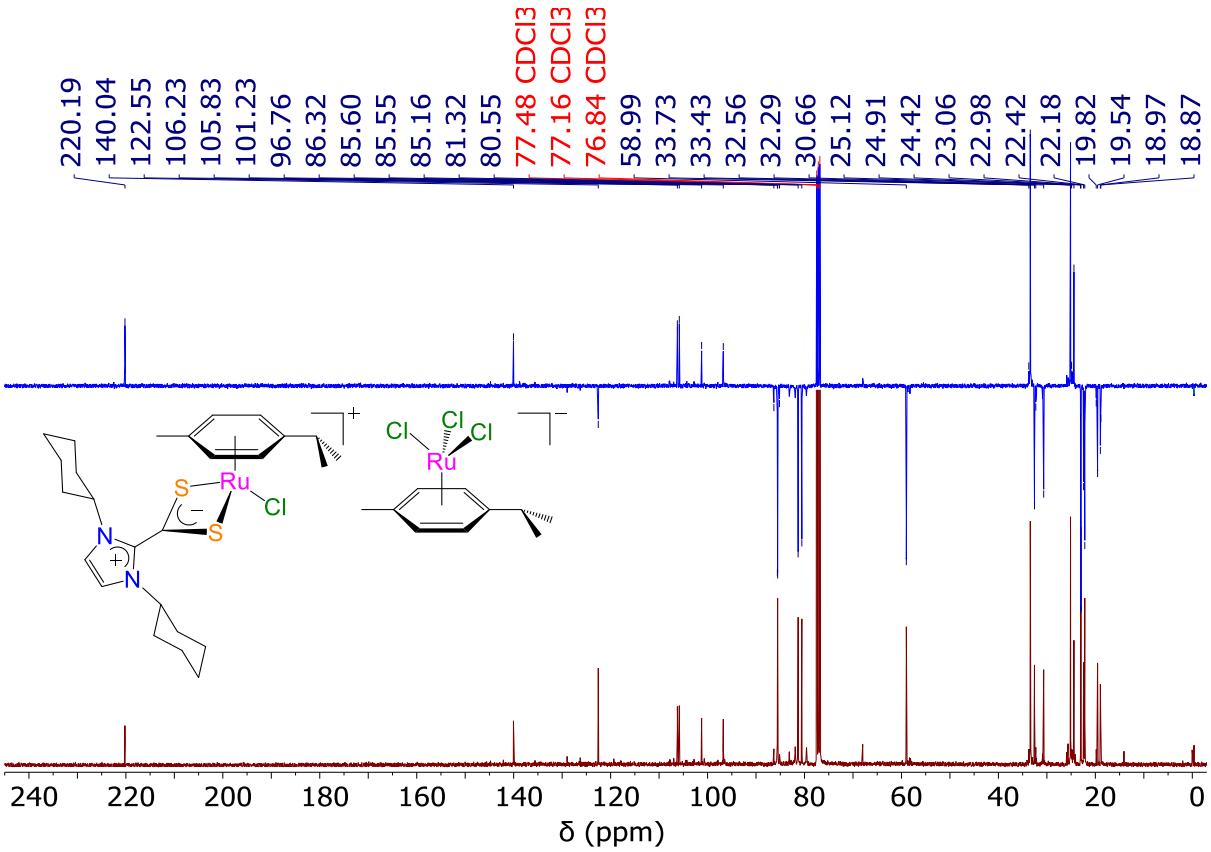

Fig. S32. ^{13}C CPD and APT NMR spectra (101 MHz, $CDCl_3$, 298 K) of [RuCl(*p*-cymene)-(S_2C·ICy)][$RuCl_3$(*p*-cymene)] (**3c**)

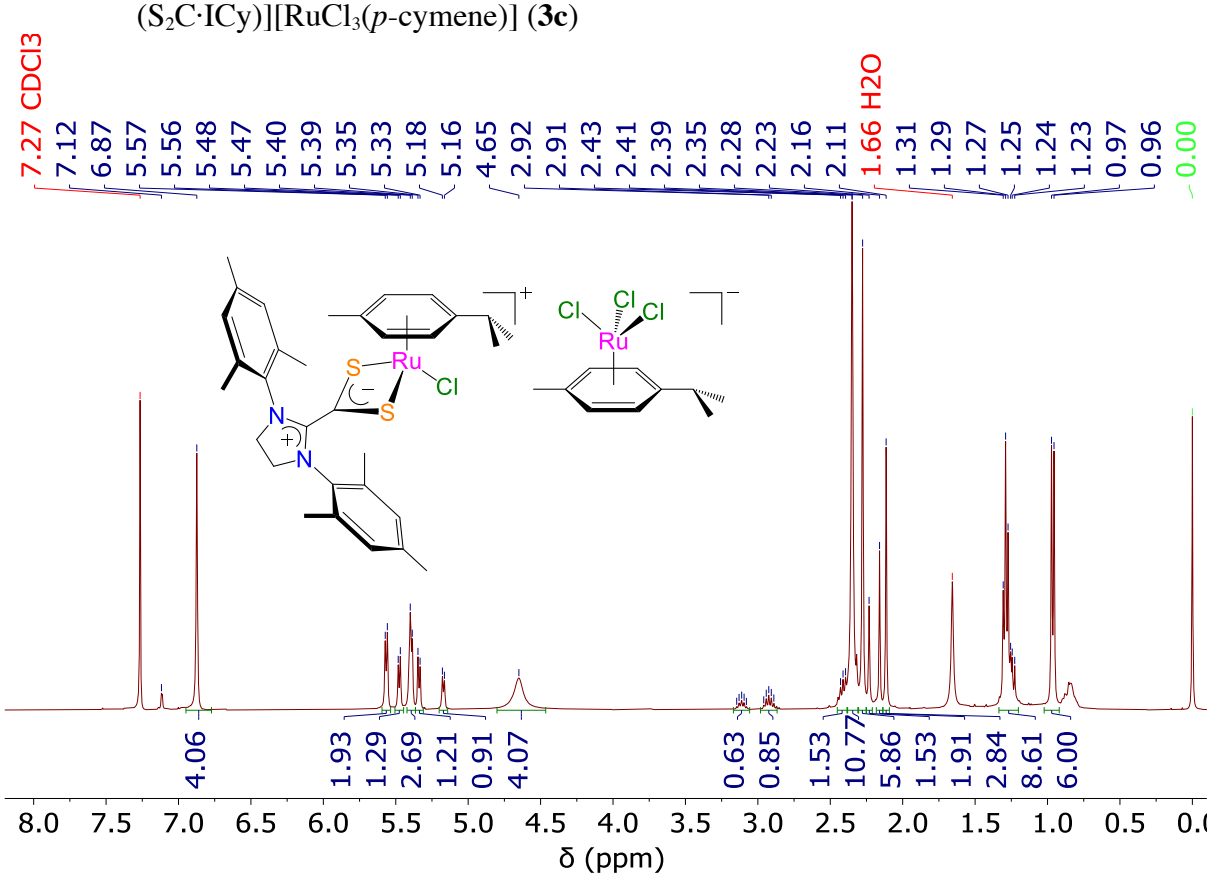

Fig. S33. ^{1}H NMR spectrum (400 MHz, $CDCl_3$, 298 K) of [RuCl(*p*-cymene)(S_2C·SIMes)]-[$RuCl_3$(*p*-cymene)] (**3d**)

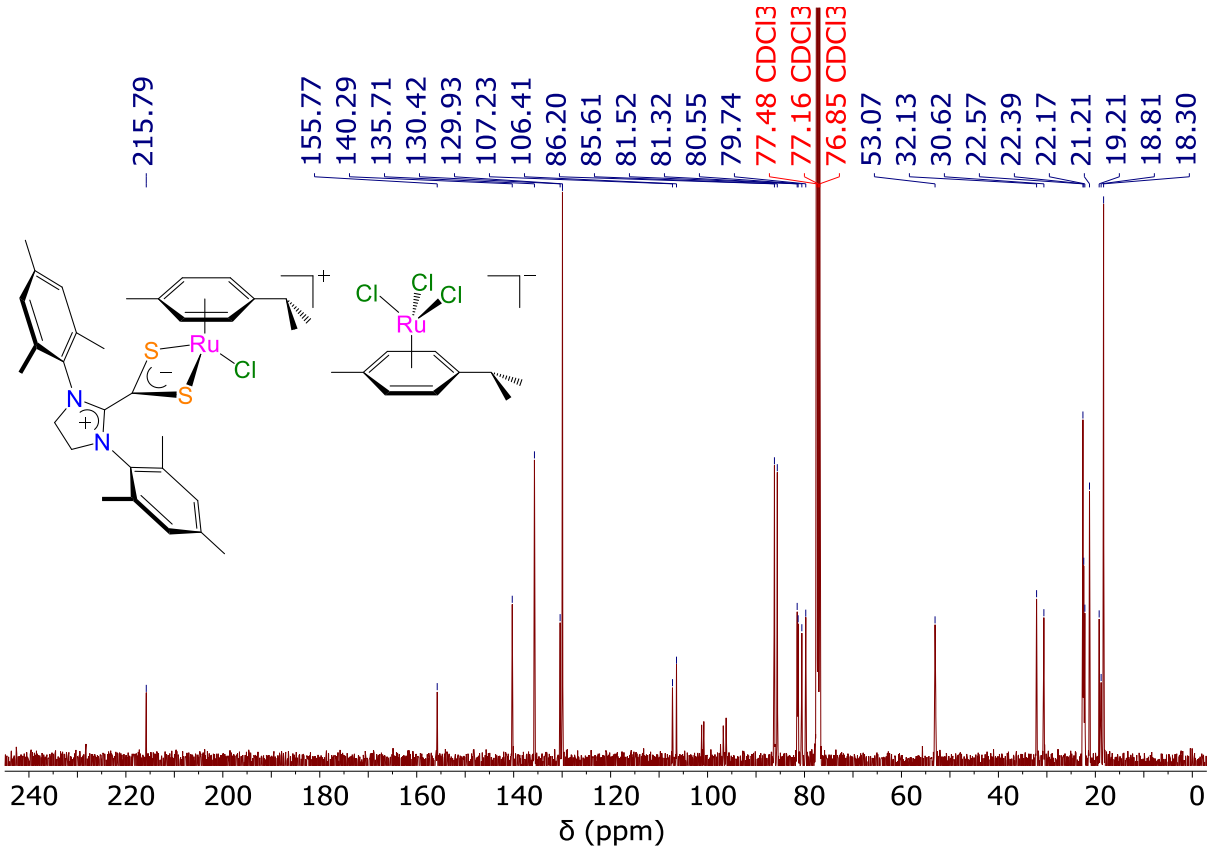

Fig. S34. $^{13}C\{^{1}H\}$ NMR spectrum (101 MHz, $CDCl_3$, 298 K) of [RuCl(*p*-cymene)-(S_2C·SIMes)][$RuCl_3$(*p*-cymene)] (**3d**)

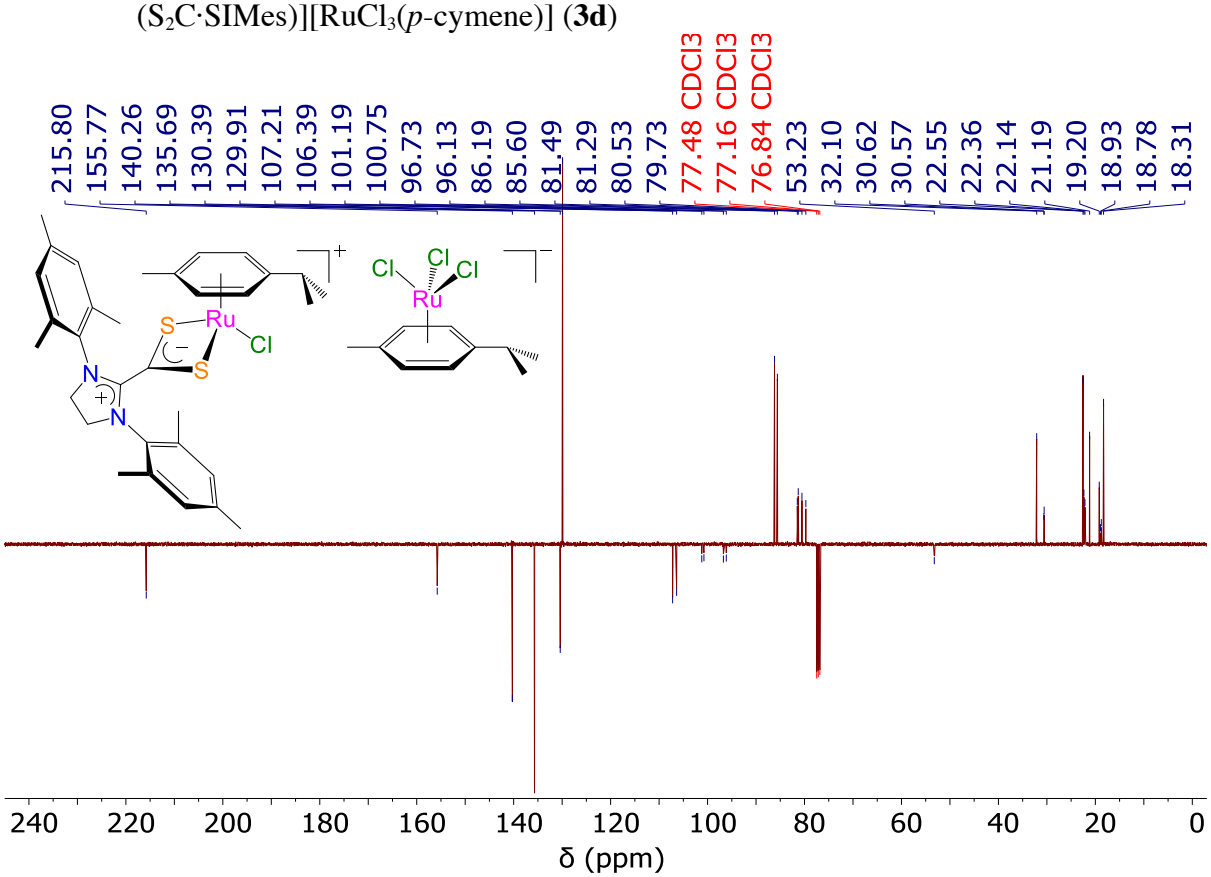

Fig. S35. $^{13}C\{^{1}H\}$ APT NMR spectrum (101 MHz, $CDCl_3$, 298 K) of [RuCl(*p*-cymene)-(S_2C·SIMes)][$RuCl_3$(*p*-cymene)] (**3d**)

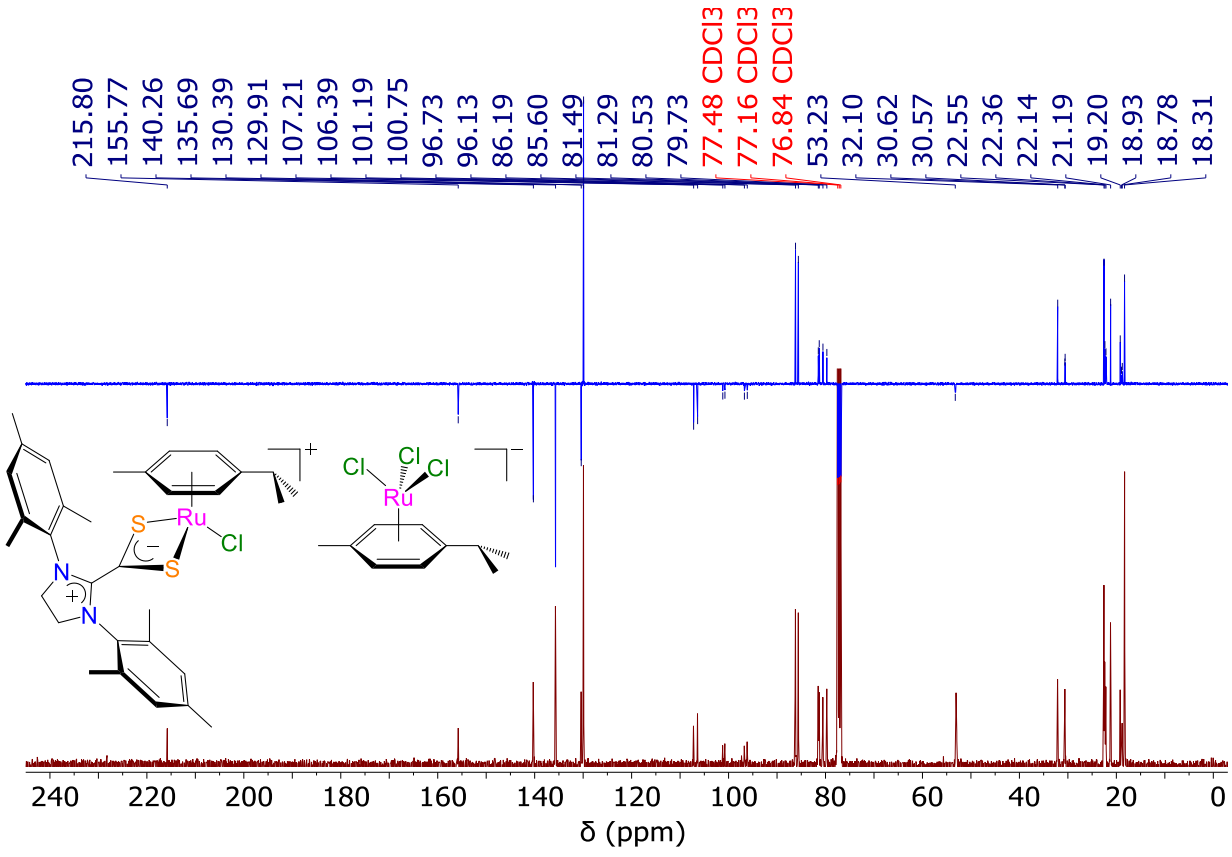

Fig. S36. ^{13}C CPD and APT NMR spectra (101 MHz, $CDCl_3$, 298 K) of [RuCl(*p*-cymene)-(S_2C·SIMes)][$RuCl_3$(*p*-cymene)] (**3d**)

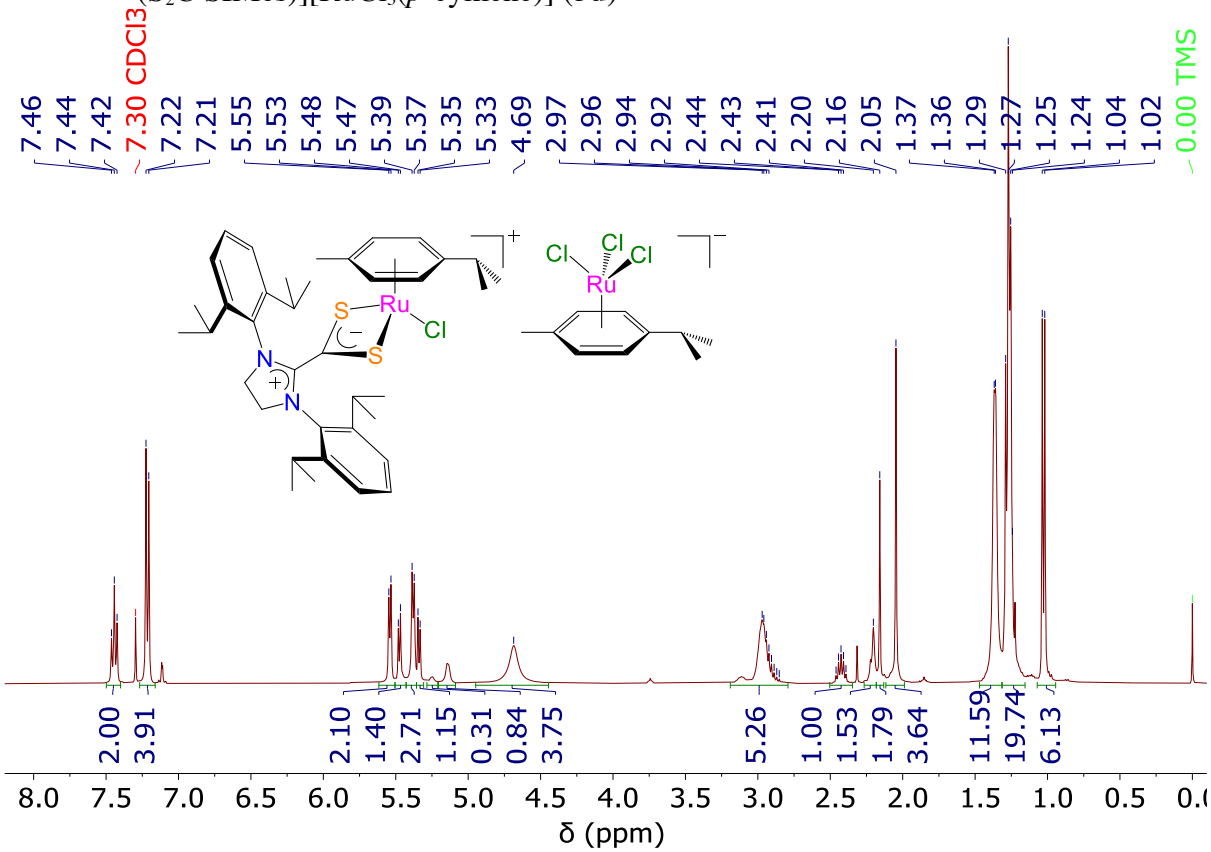

Fig. S37. ^{1}H NMR spectrum (400 MHz, $CDCl_3$, 298 K) of [RuCl(*p*-cymene)-(S_2C·SIDip)][$RuCl_3$(*p*-cymene)] (**3e**)

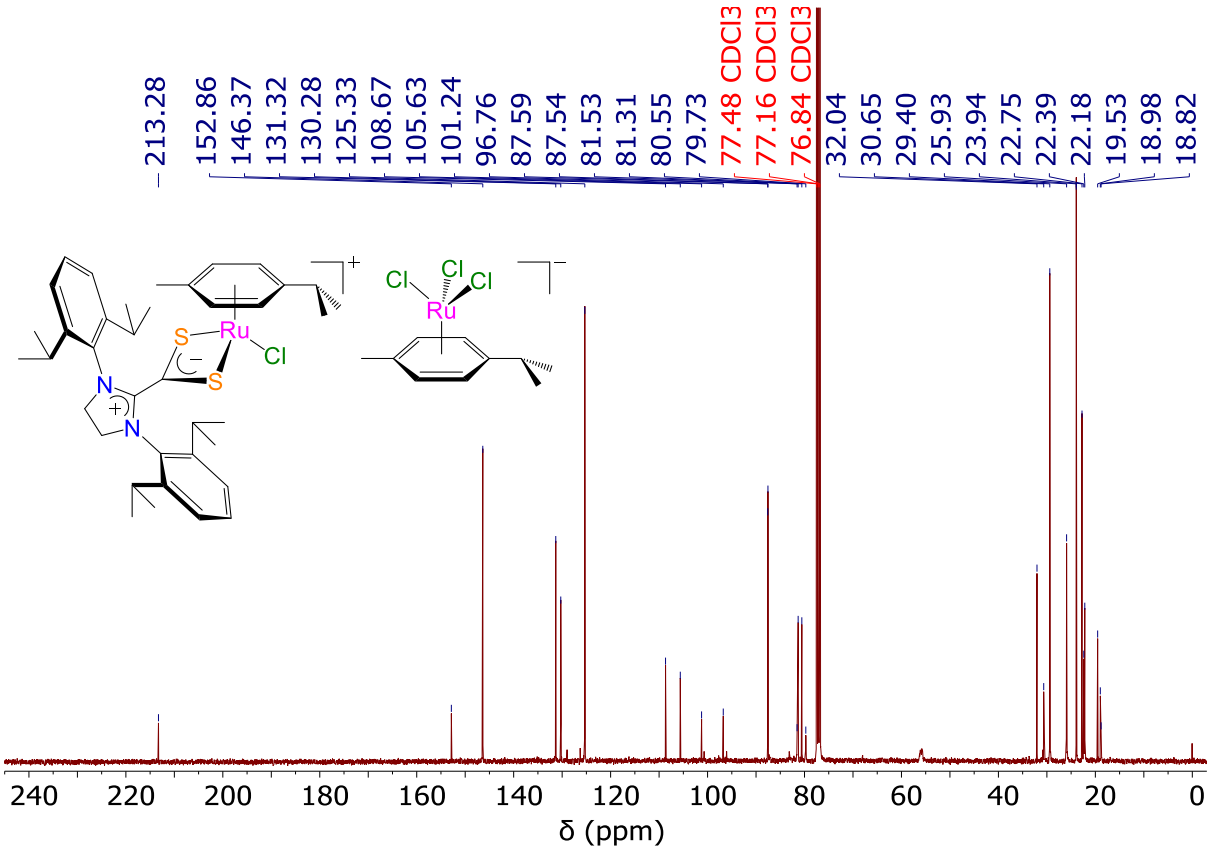

Fig. S38. $^{13}C\{^{1}H\}$ NMR spectrum (101 MHz, $CDCl_3$, 298 K) of [RuCl(*p*-cymene)-(S_2C·SIDip)][$RuCl_3$(*p*-cymene)] (**3e**)

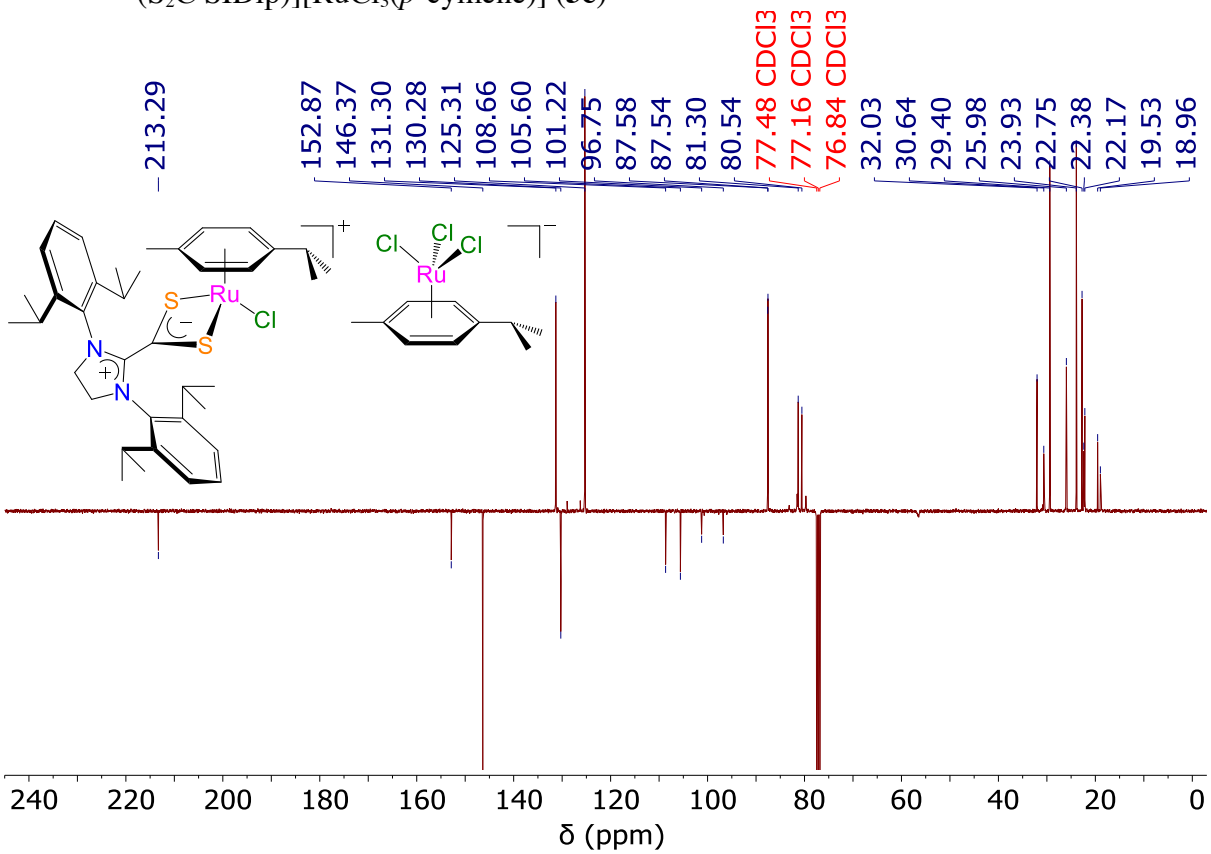

Fig. S39. $^{13}C\{^{1}H\}$ APT NMR spectrum (101 MHz, $CDCl_3$, 298 K) of [RuCl(*p*-cymene)-(S_2C·SIDip)][$RuCl_3$(*p*-cymene)] (**3e**)

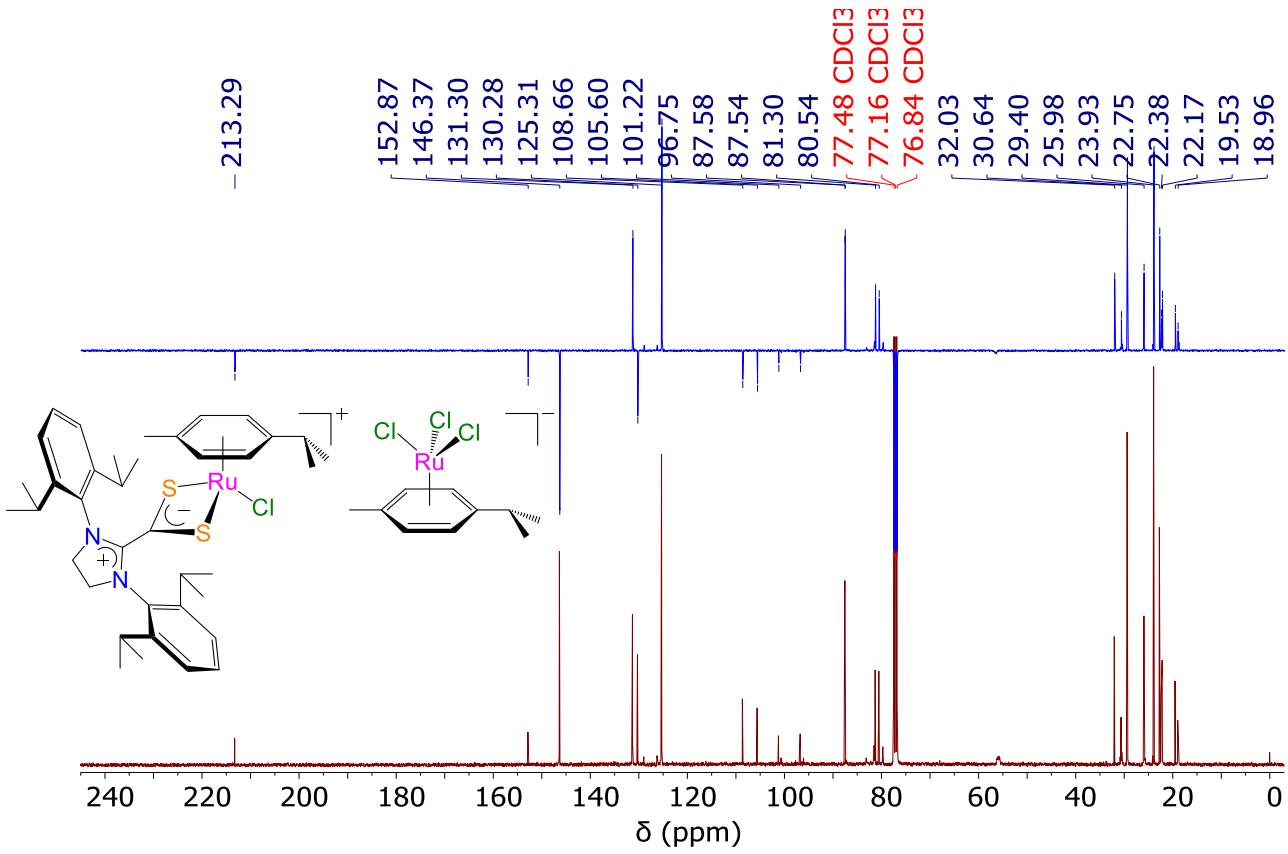

Fig. S40. ^{13}C CPD and APT NMR spectra (101 MHz, $CDCl_3$, 298 K) of [RuCl(*p*-cymene)-(S_2C·SIDip)][$RuCl_3$(*p*-cymene)] (**3e**)

Part 3 – IR spectra

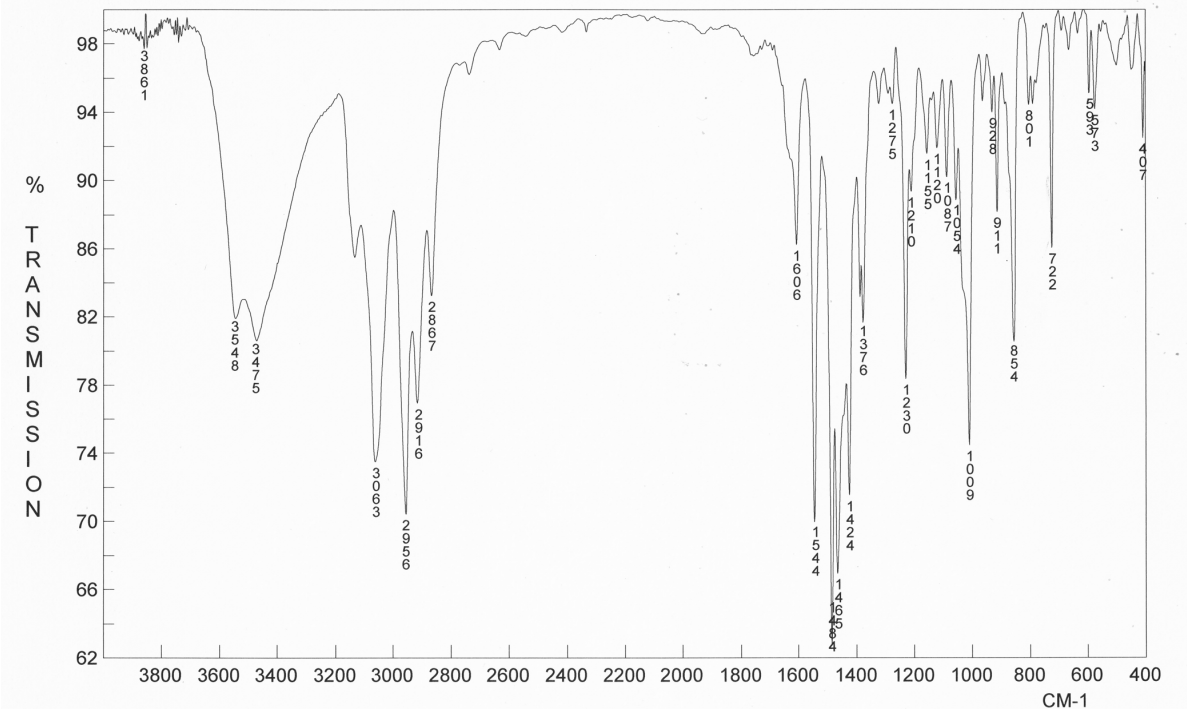

Fig. S41. FT-IR spectrum (KBr) of [RuCl(*p*-cymene)(S_2C·IMes)][$RuCl_3$(*p*-cymene)] (**3a**)

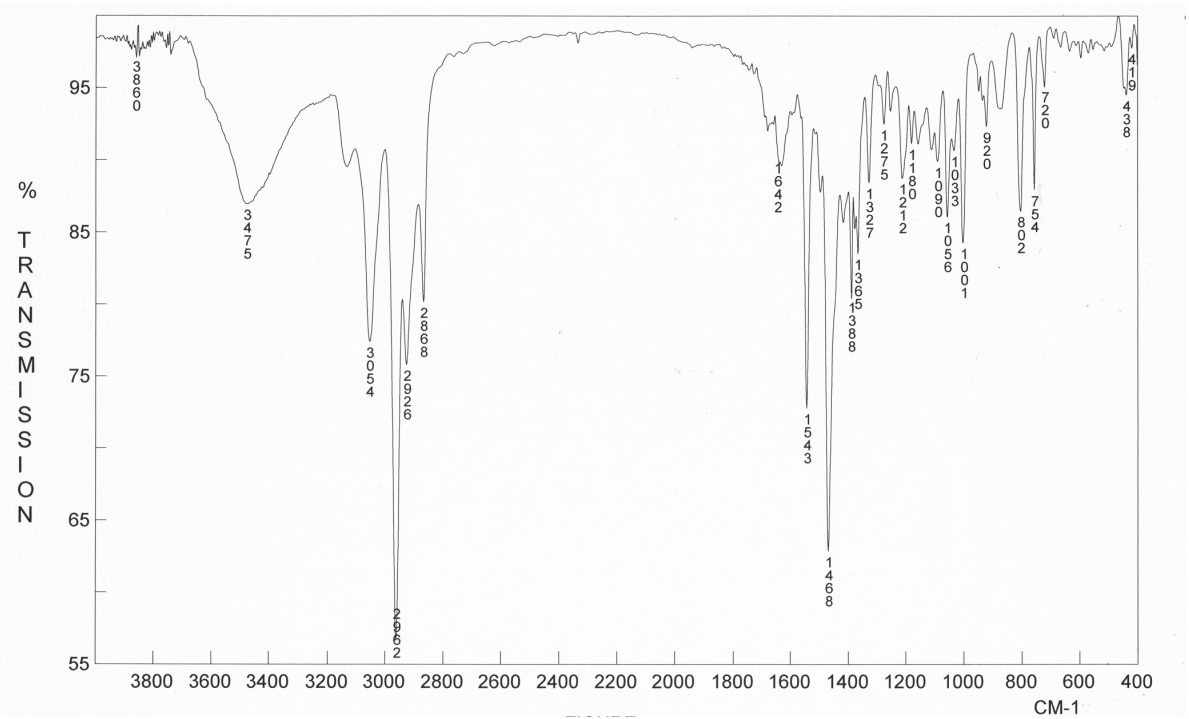

Fig. S42. FT-IR spectrum (KBr) of [RuCl(*p*-cymene)(S_2C·IDip)][$RuCl_3$(*p*-cymene)] (**3b**)

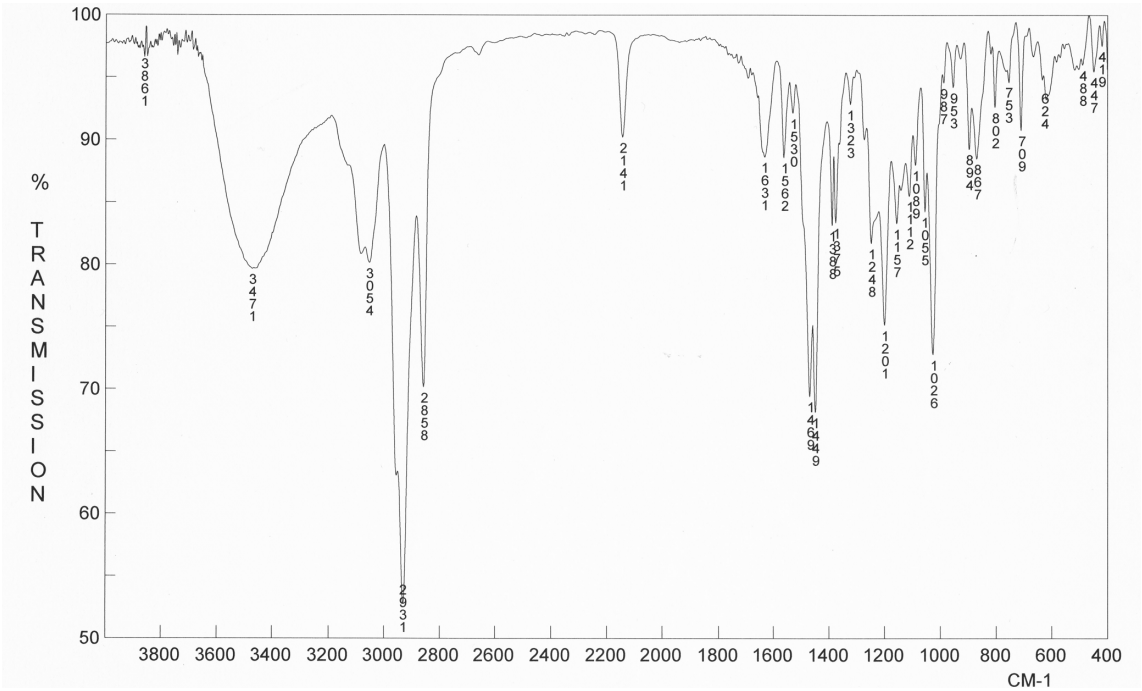

Fig. S43. FT-IR spectrum (KBr) of [RuCl(*p*-cymene)(S_2C·ICy)][$RuCl_3$(*p*-cymene)] (**3c**)

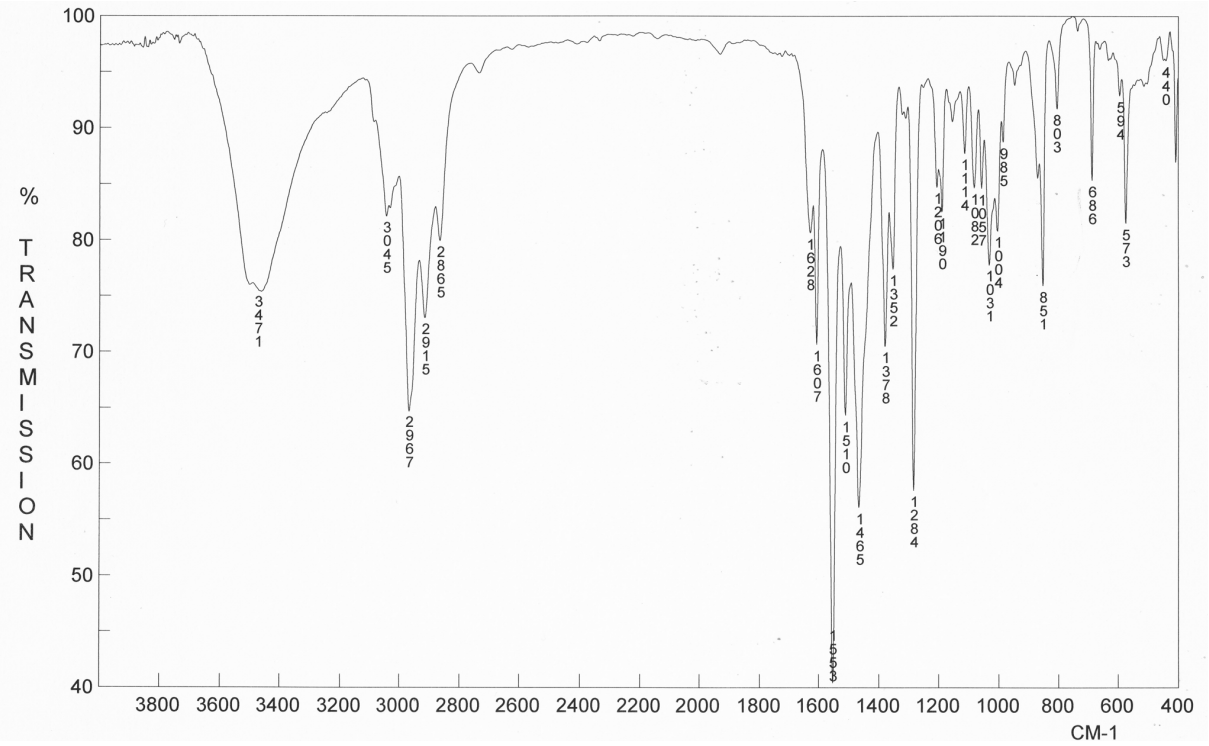

Fig. S44. FT-IR spectrum (KBr) of [RuCl(*p*-cymene)(S_2C·SIMes)][$RuCl_3$(*p*-cymene)] (**3d**)

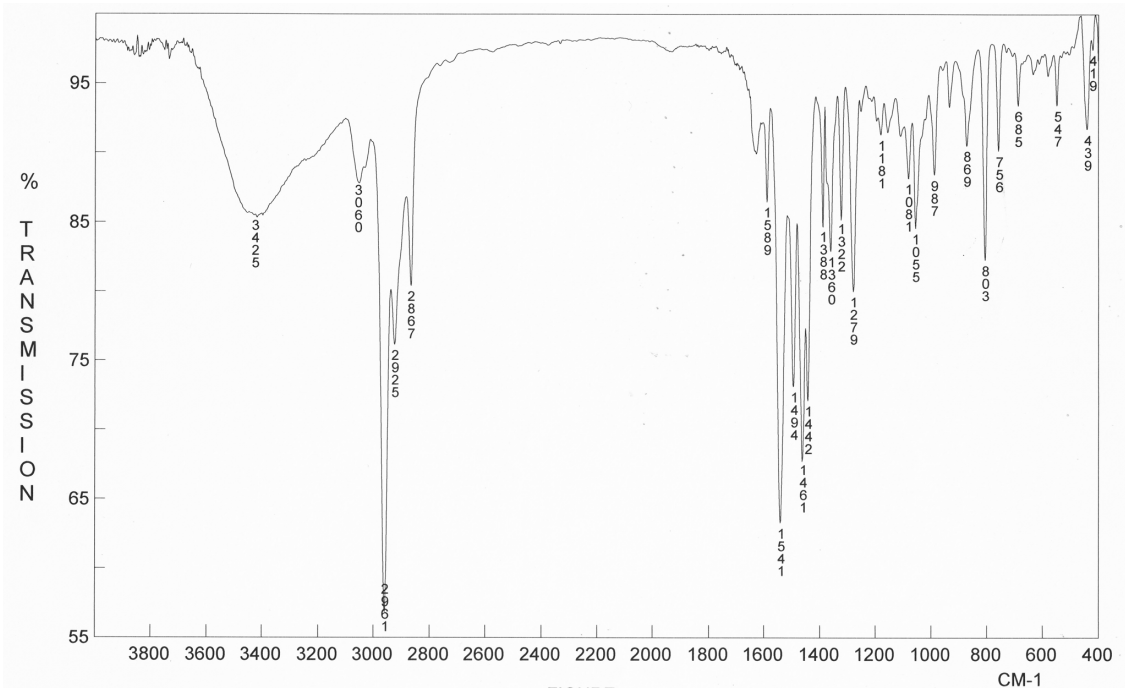

Fig. S45. FT-IR spectrum (KBr) of [RuCl(*p*-cymene)(S_2C·SIDip)][$RuCl_3$(*p*-cymene)] (**3e**)

Part 4 – Mass spectra

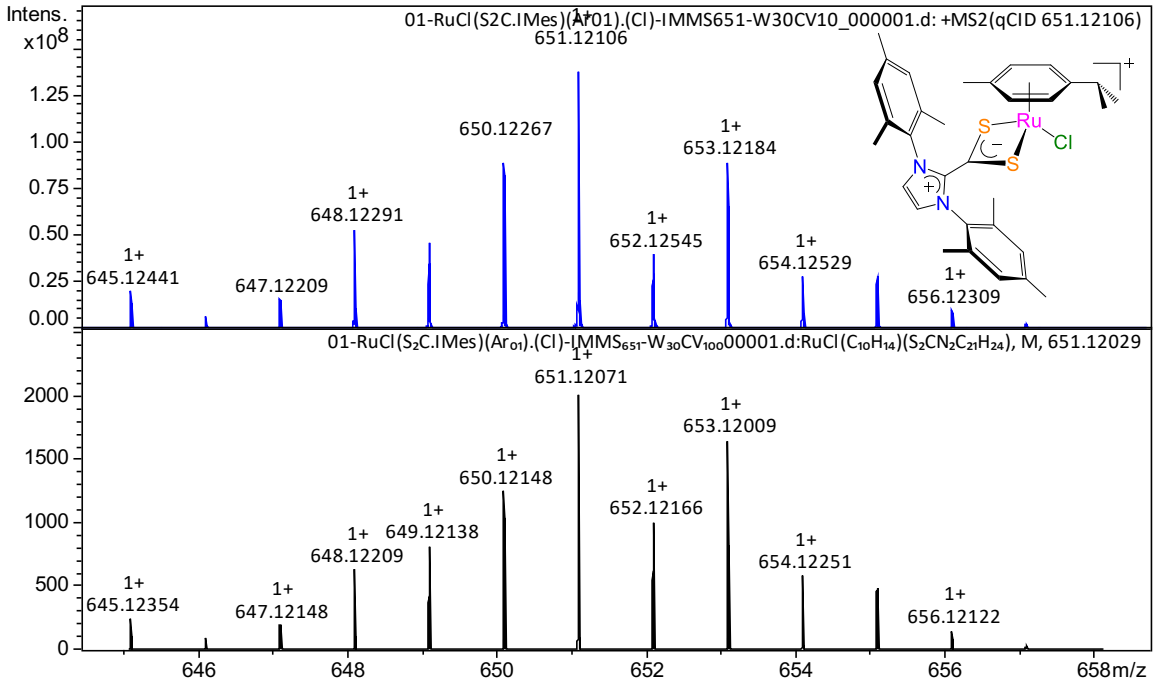

Fig. S46. HR-MS spectrum (CH_3CN, positive mode) of [RuCl(*p*-cymene)(S_2C·IMes)]Cl (**2a**): isotope profile observed by ESI-MS (top) and simulated isotope pattern for the [RuCl(*p*-cymene)(S_2C·IMes)]$^+$ cation (bottom)

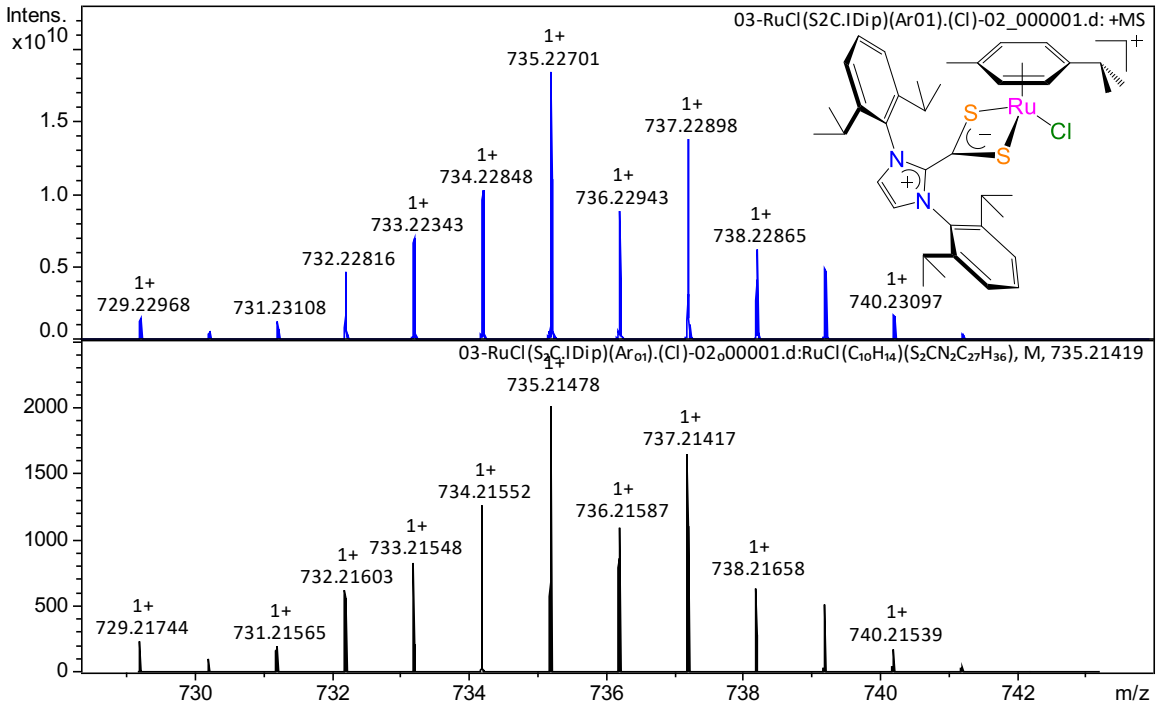

Fig. S47. HR-MS spectrum (CH_3CN, positive mode) of [RuCl(*p*-cymene)(S_2C·IDip)]Cl (**2b**): isotope profile observed by ESI-MS (top) and simulated isotope pattern for the [RuCl(*p*-cymene)(S_2C·IDip)]$^+$ cation (bottom)

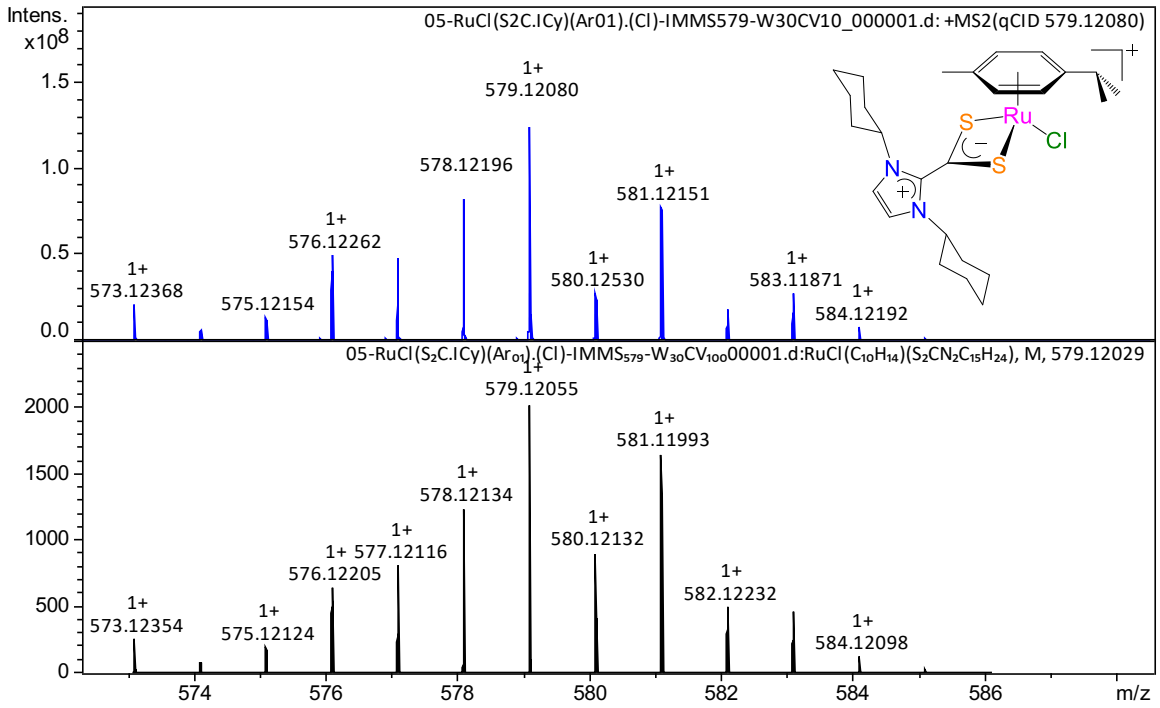

Fig. S48. HR-MS spectrum (CH_3CN, positive mode) of [RuCl(*p*-cymene)(S_2C·ICy)]Cl (**2c**): isotope profile observed by ESI-MS (top) and simulated isotope pattern for the [RuCl(*p*-cymene)(S_2C·ICy)]$^+$ cation (bottom)

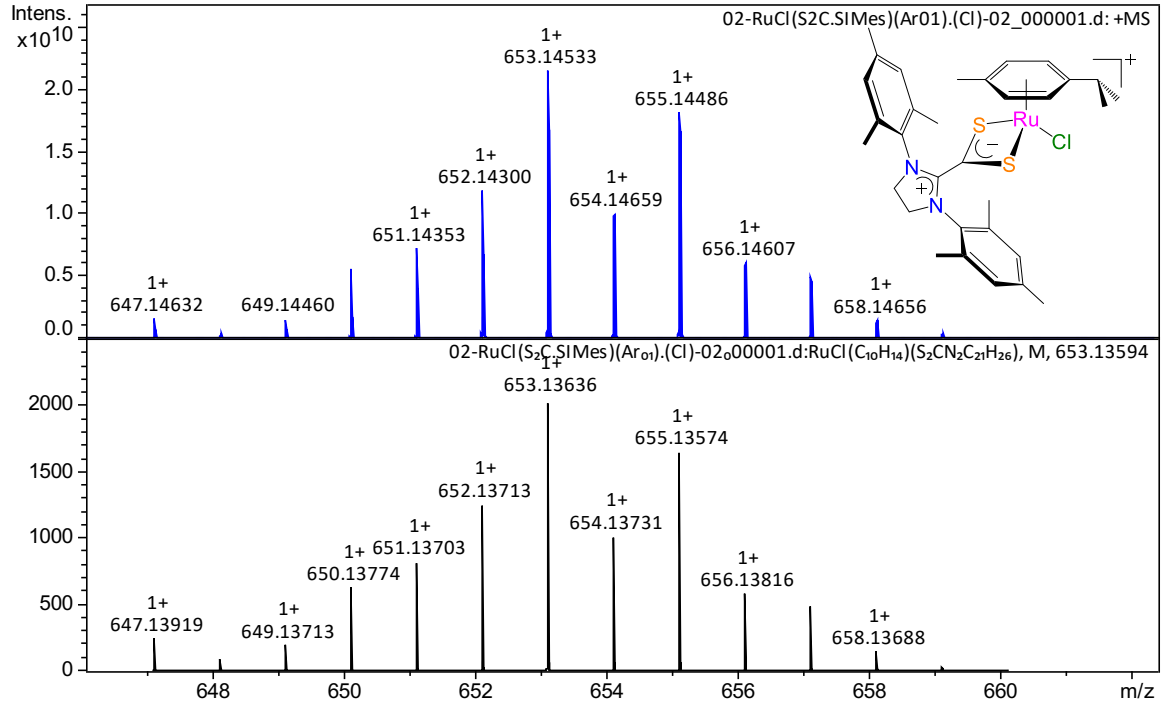

Fig. S49. HR-MS spectrum (CH_3CN, positive mode) of [RuCl(*p*-cymene)(S_2C·SIMes)]Cl (**2d**): isotope profile observed by ESI-MS (top) and simulated isotope pattern for the [RuCl(*p*-cymene)(S_2C·SIMes)]$^+$ cation (bottom)

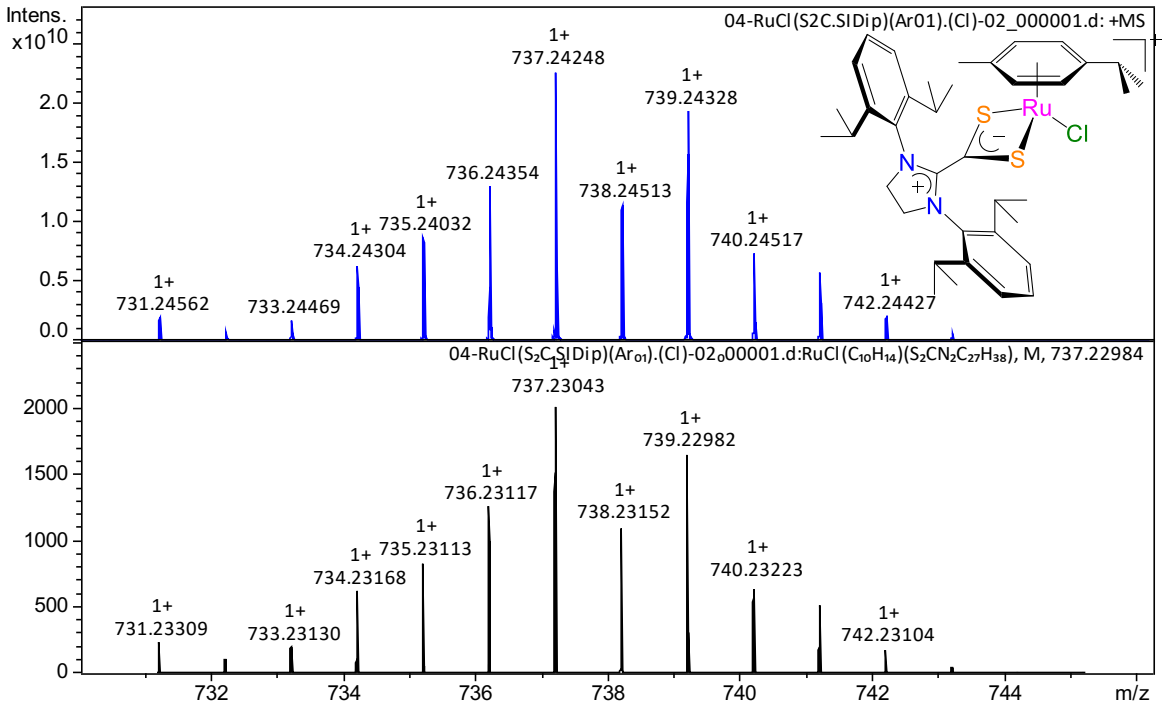

Fig. S50. HR-MS spectrum (CH_3CN, positive mode) of [RuCl(*p*-cymene)(S_2C·SIDip)]Cl (**2e**): isotope profile observed by ESI-MS (top) and simulated isotope pattern for the [RuCl(*p*-cymene)(S_2C·SIDip)]$^+$ cation (bottom)

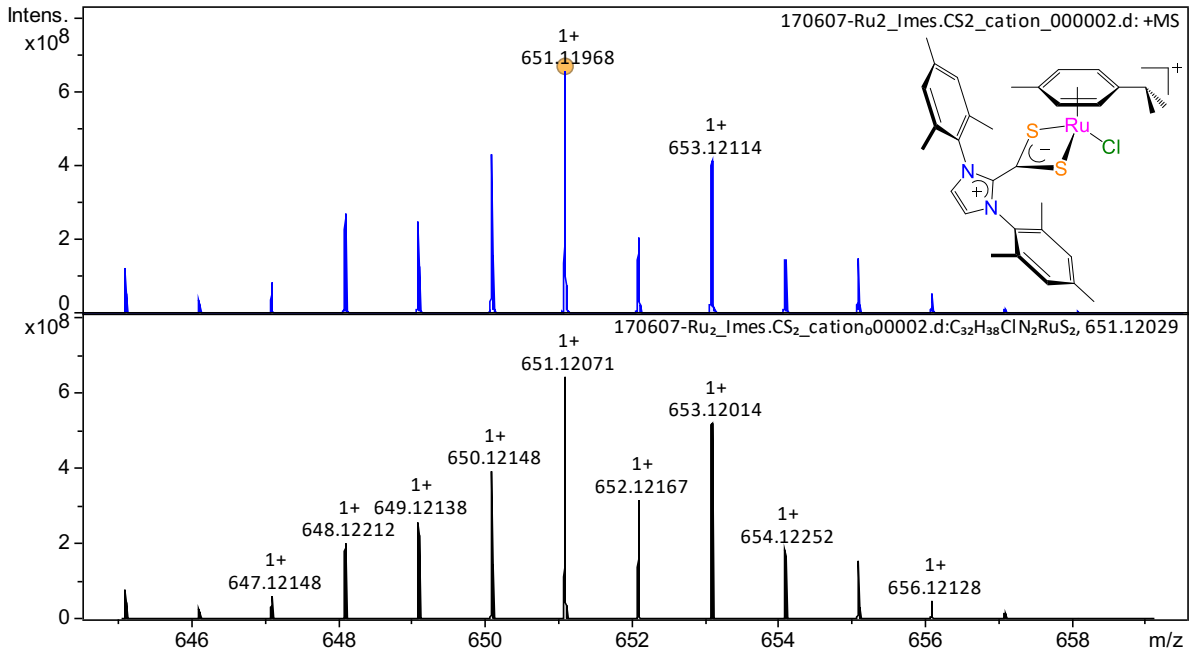

Fig. S51. HR-MS spectrum (CH_3CN, positive mode) of [RuCl(*p*-cymene)(S_2C·IMes)]-[$RuCl_3$(*p*-cymene)] (**3a**): isotope profile observed by ESI-MS (top) and simulated isotope pattern for the [RuCl(*p*-cymene)(S_2C·IMes)]$^+$ cation (bottom)

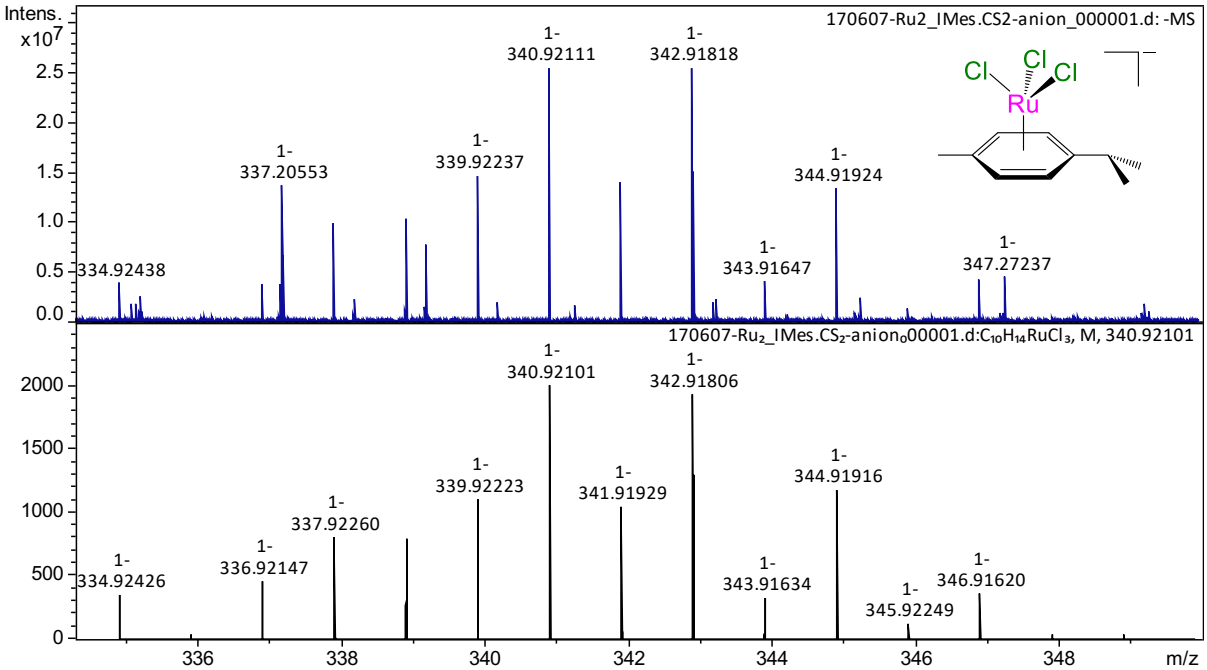

Fig. S52. HR-MS spectrum (CH_3CN, negative mode) of [RuCl(*p*-cymene)(S_2C·IMes)]-[$RuCl_3$(*p*-cymene)] (**3a**): isotope profile observed by ESI-MS (top) and simulated isotope pattern for the [$RuCl_3$(*p*-cymene)]$^-$ anion (bottom)

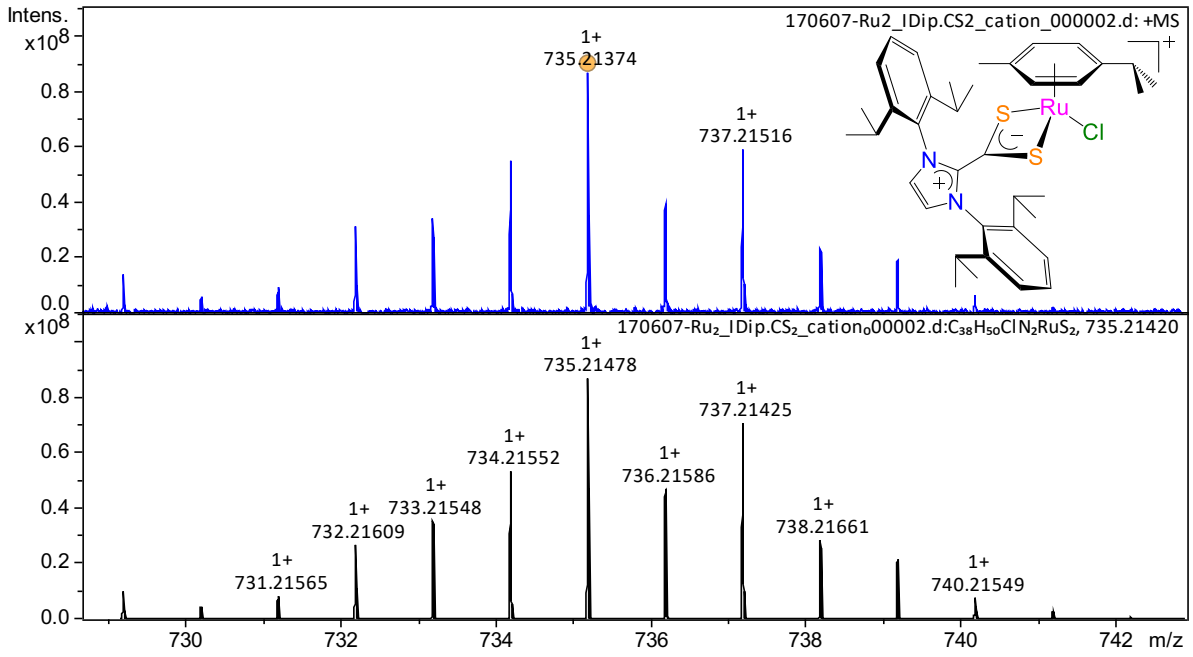

Fig. S53. HR-MS spectrum (CH_3CN, positive mode) of [RuCl(*p*-cymene)(S_2C·IDip)]-[$RuCl_3$(*p*-cymene)] (**3b**): isotope profile observed by ESI-MS (top) and simulated isotope pattern for the [RuCl(*p*-cymene)(S_2C·IDip)]$^+$ cation (bottom)

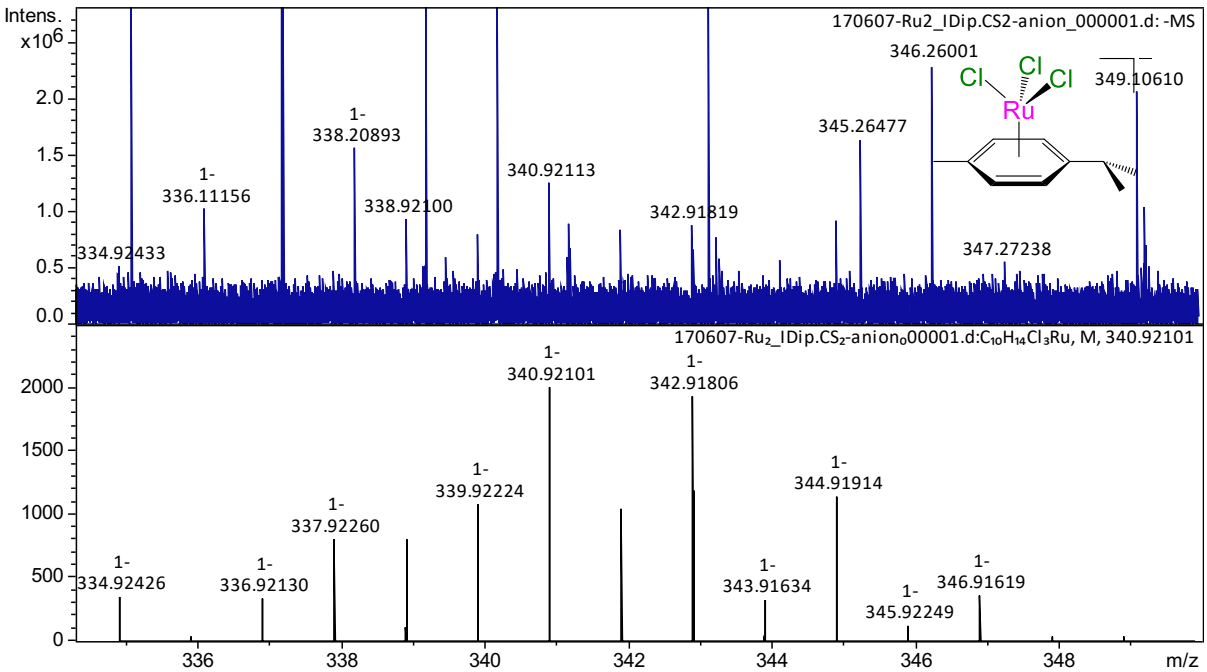

Fig. S54. HR-MS spectrum (CH_3CN, negative mode) of [RuCl(*p*-cymene)(S_2C·IDip)]-[$RuCl_3$(*p*-cymene)] (**3b**): isotope profile observed by ESI-MS (top) and simulated isotope pattern for the [$RuCl_3$(*p*-cymene)]$^-$ anion (bottom)

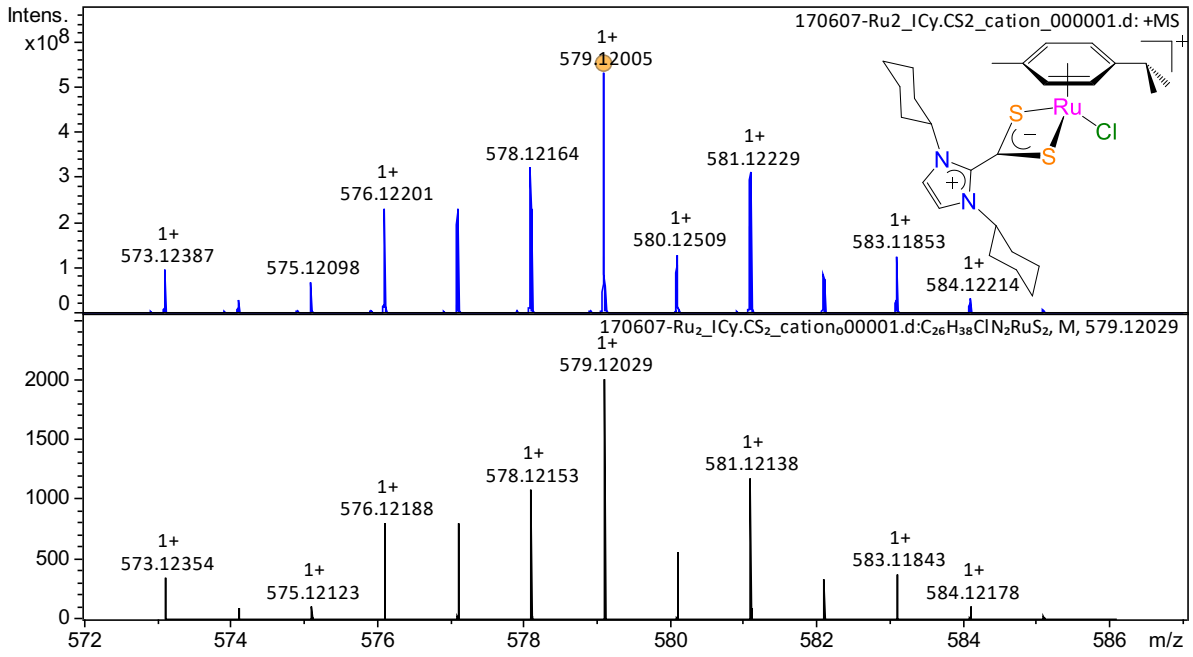

Fig. S55. HR-MS spectrum (CH_3CN, positive mode) of [RuCl(*p*-cymene)(S_2C·ICy)]-[$RuCl_3$(*p*-cymene)] (**3c**): isotope profile observed by ESI-MS (top) and simulated isotope pattern for the [RuCl(*p*-cymene)(S_2C·ICy)]$^+$ cation (bottom)

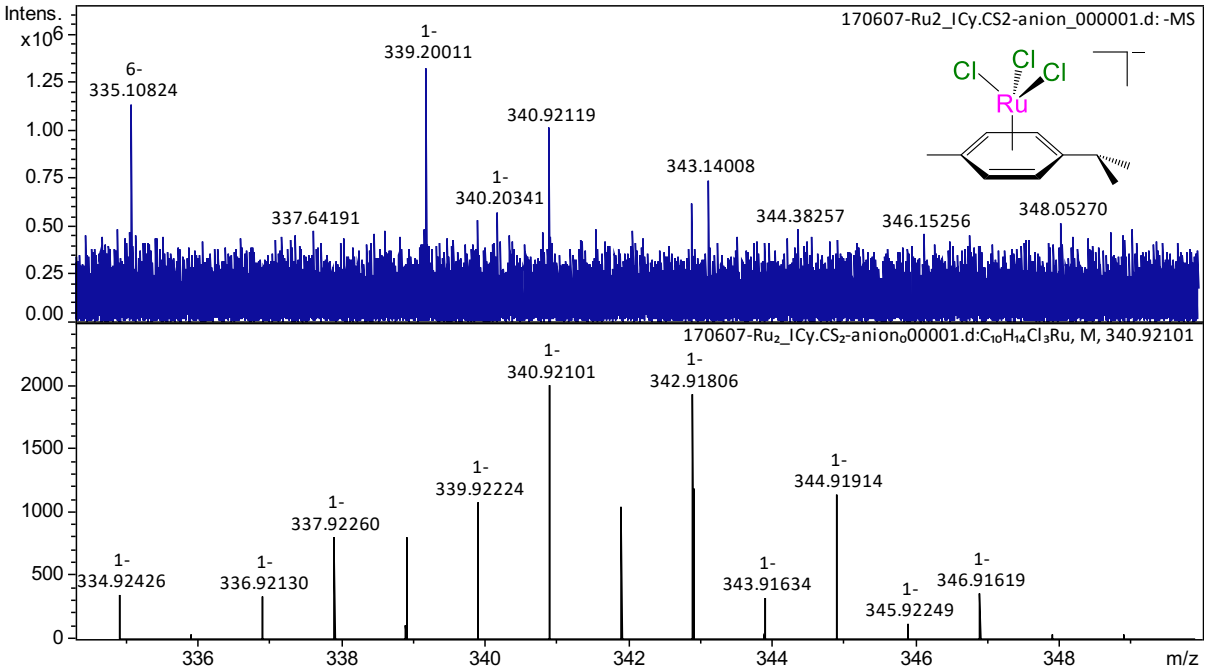

Fig. S56. HR-MS spectrum (CH_3CN, negative mode) of [RuCl(*p*-cymene)(S_2C·ICy)]-[$RuCl_3$(*p*-cymene)] (**3c**): isotope profile observed by ESI-MS (top) and simulated isotope pattern for the [$RuCl_3$(*p*-cymene)]$^-$ anion (bottom)

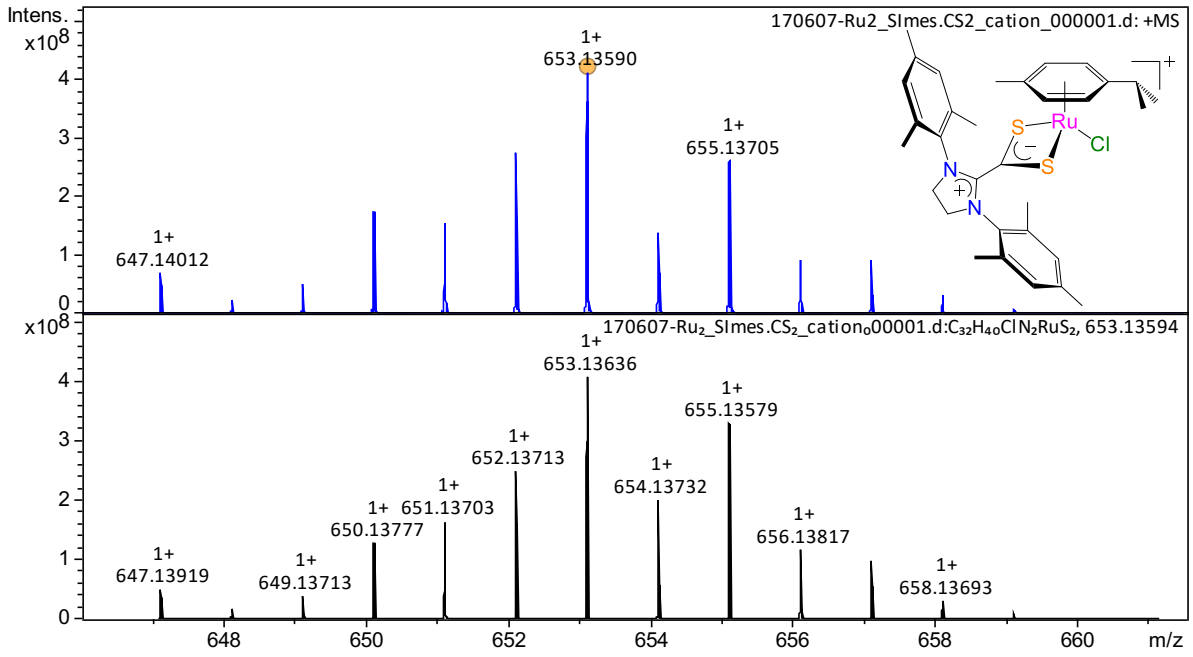

Fig. S57. HR-MS spectrum (CH_3CN, positive mode) of [RuCl(*p*-cymene)(S_2C·SIMes)]-[$RuCl_3$(*p*-cymene)] (**3d**): isotope profile observed by ESI-MS (top) and simulated isotope pattern for the [RuCl(*p*-cymene)(S_2C·SIMes)]$^+$ cation (bottom)

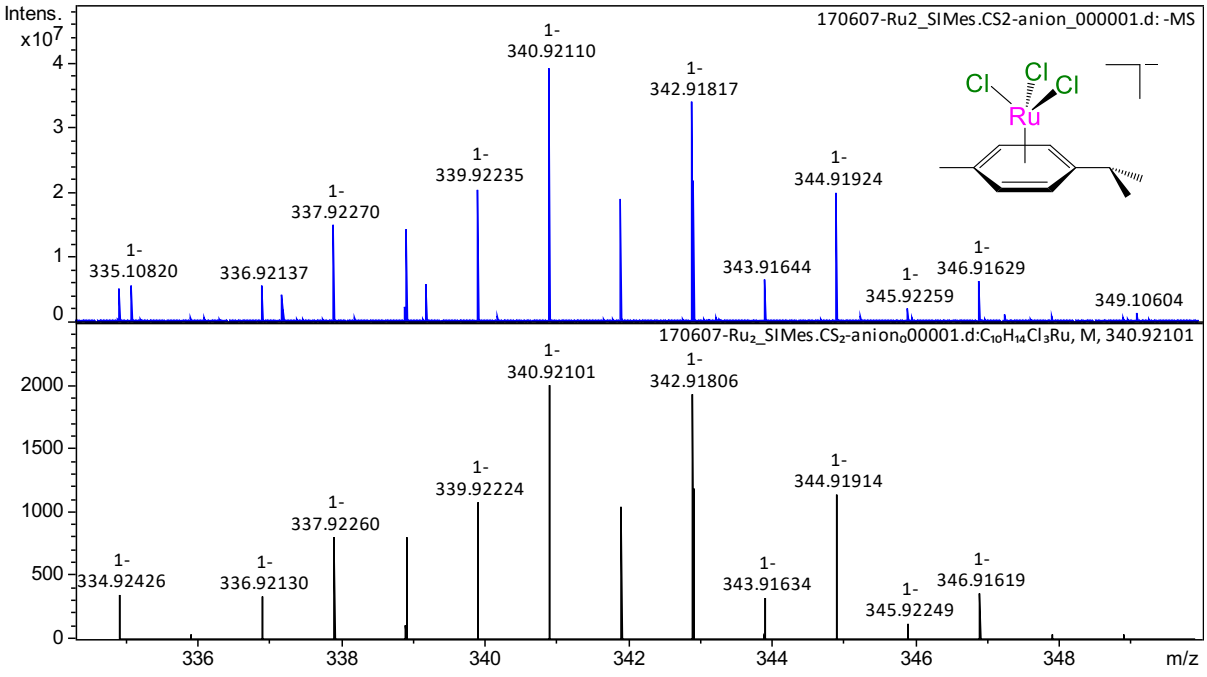

Fig. S58. HR-MS spectrum (CH_3CN, negative mode) of [RuCl(*p*-cymene)(S_2C·SIMes)]-[$RuCl_3$(*p*-cymene)] (**3d**): isotope profile observed by ESI-MS (top) and simulated isotope pattern for the [$RuCl_3$(*p*-cymene)]$^-$ anion (bottom)

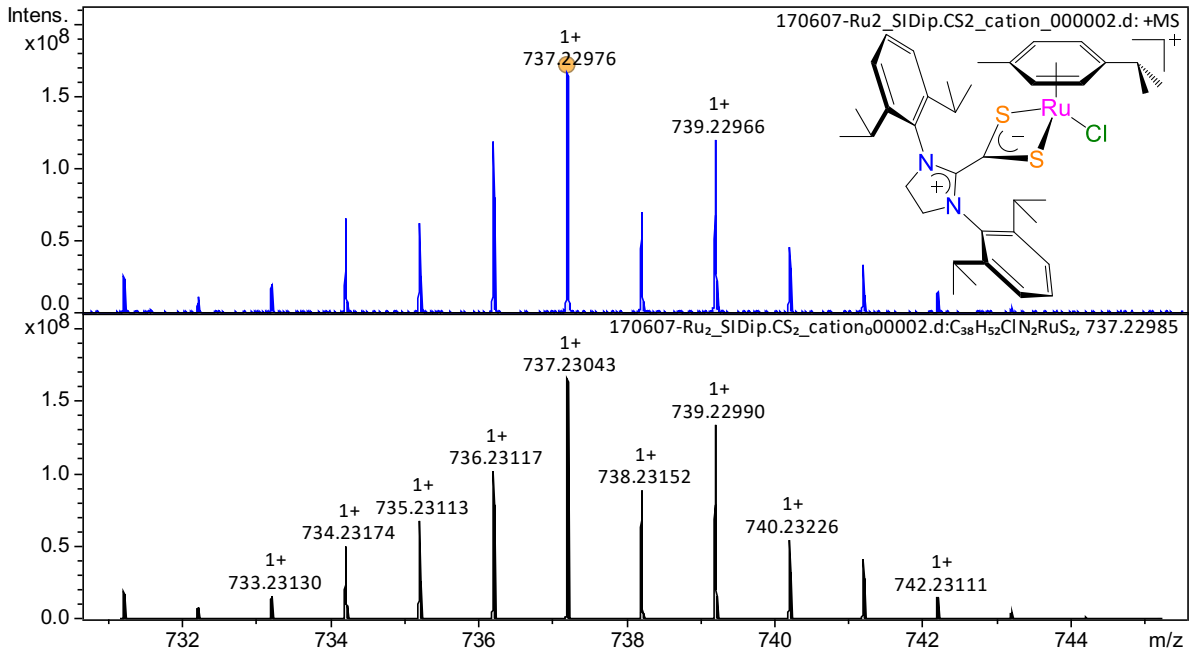

Fig. S59. HR-MS spectrum (CH_3CN, positive mode) of [RuCl(*p*-cymene)(S_2C·SIDip)]-[$RuCl_3$(*p*-cymene)] (**3e**): isotope profile observed by ESI-MS (top) and simulated isotope pattern for the [RuCl(*p*-cymene)(S_2C·SIDip)]$^+$ cation (bottom)

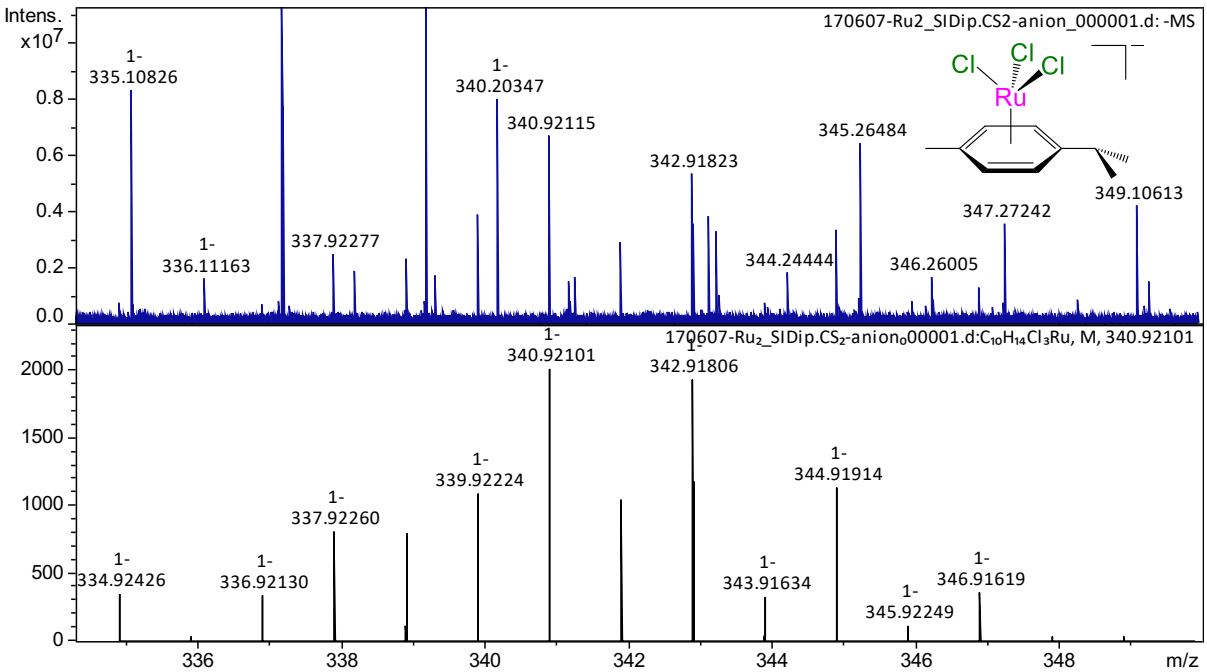

Fig. S60. HR-MS spectrum (CH_3CN, negative mode) of [RuCl(*p*-cymene)(S_2C·SIDip)]-[$RuCl_3$(*p*-cymene)] (**3e**): isotope profile observed by ESI-MS (top) and simulated isotope pattern for the [$RuCl_3$(*p*-cymene)]$^-$ anion (bottom)

Part 5 – Crystallography

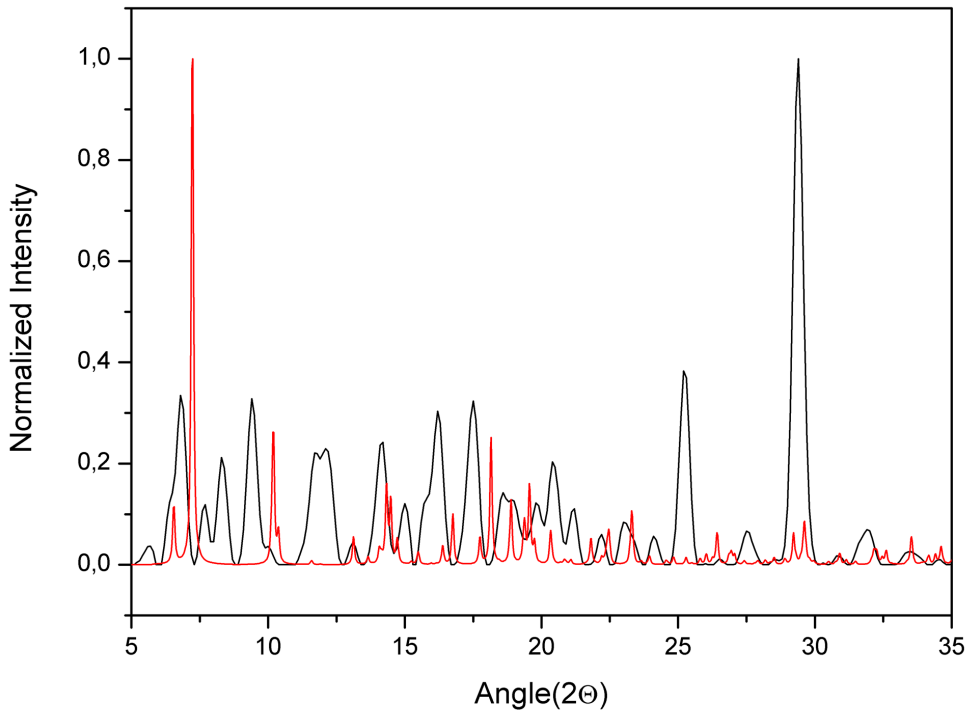

Fig. S61. Powder diffraction pattern recorded for the bulk sample obtained by crystallization of [RuCl(*p*-cymene)(S_2C·ICy)][$RuCl_3$(*p*-cymene)] (**3c**) (black curve) and simulated pattern computed for [RuCl(*p*-cymene)(S_2C·ICy)]Cl (2(**2c**)·9.75(H_2O)) (red curve)

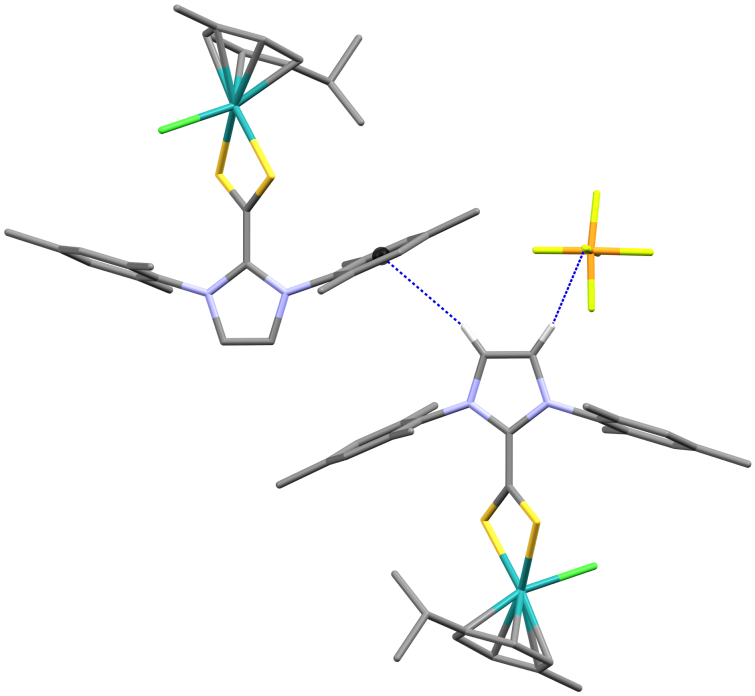

Fig. S62. Molecular structure of [RuCl(*p*-cymene)(S_2C·IMes)]PF_6 (**1a**) showing the H-bonds of the imidazolium protons (hydrogen atoms were omitted except those directly bound to the heterocyclic ring)

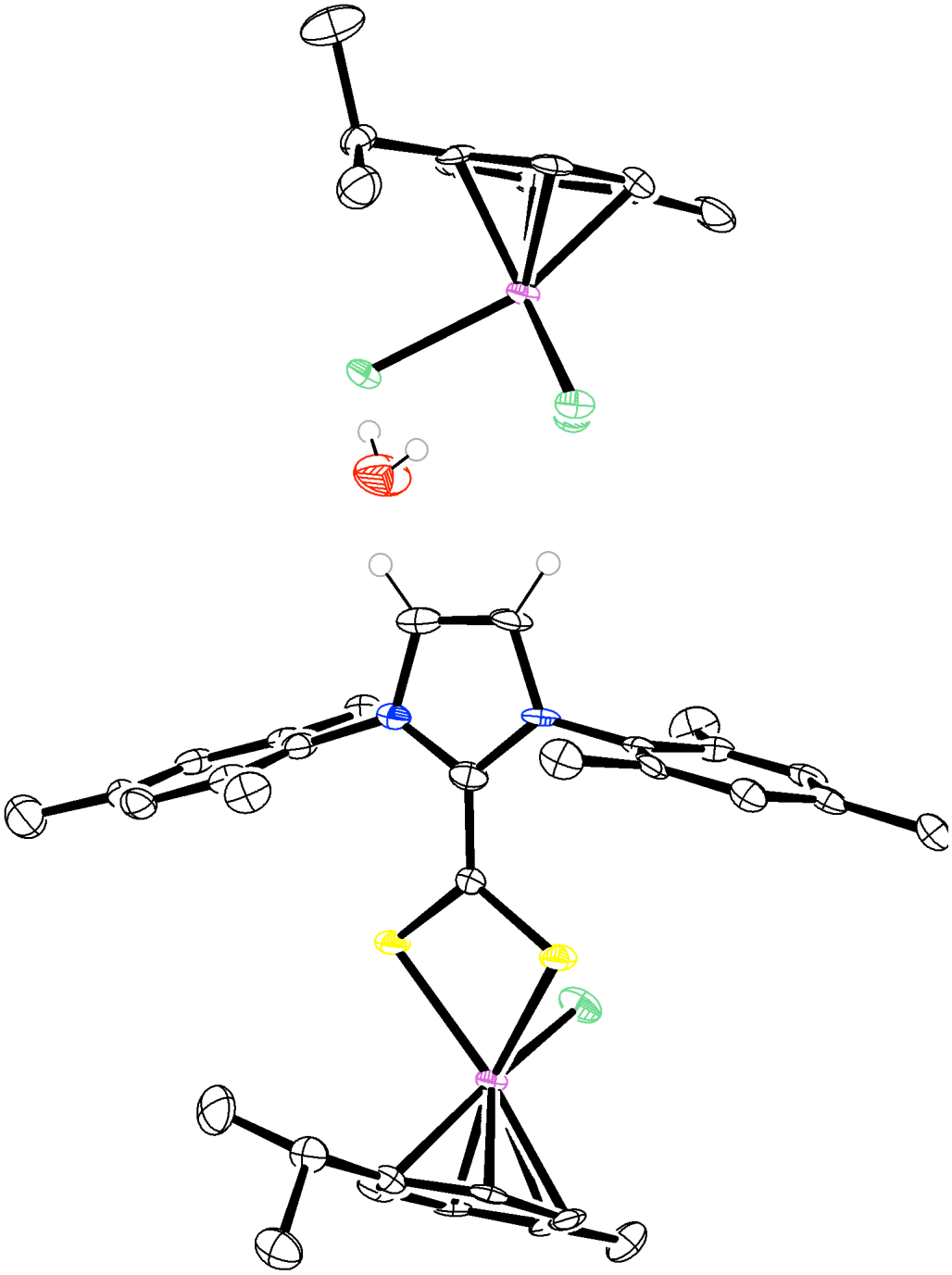

Fig. S63. ORTEP representation of [RuCl(*p*-cymene)(S_2C·IMes)][$RuCl_3$(*p*-cymene)] co-crystallized with water (**3a**·H_2O). Hydrogen atoms were omitted except those directly bound to the heterocyclic ring and oxygen. Thermal ellipsoids were drawn at the 50% probability level

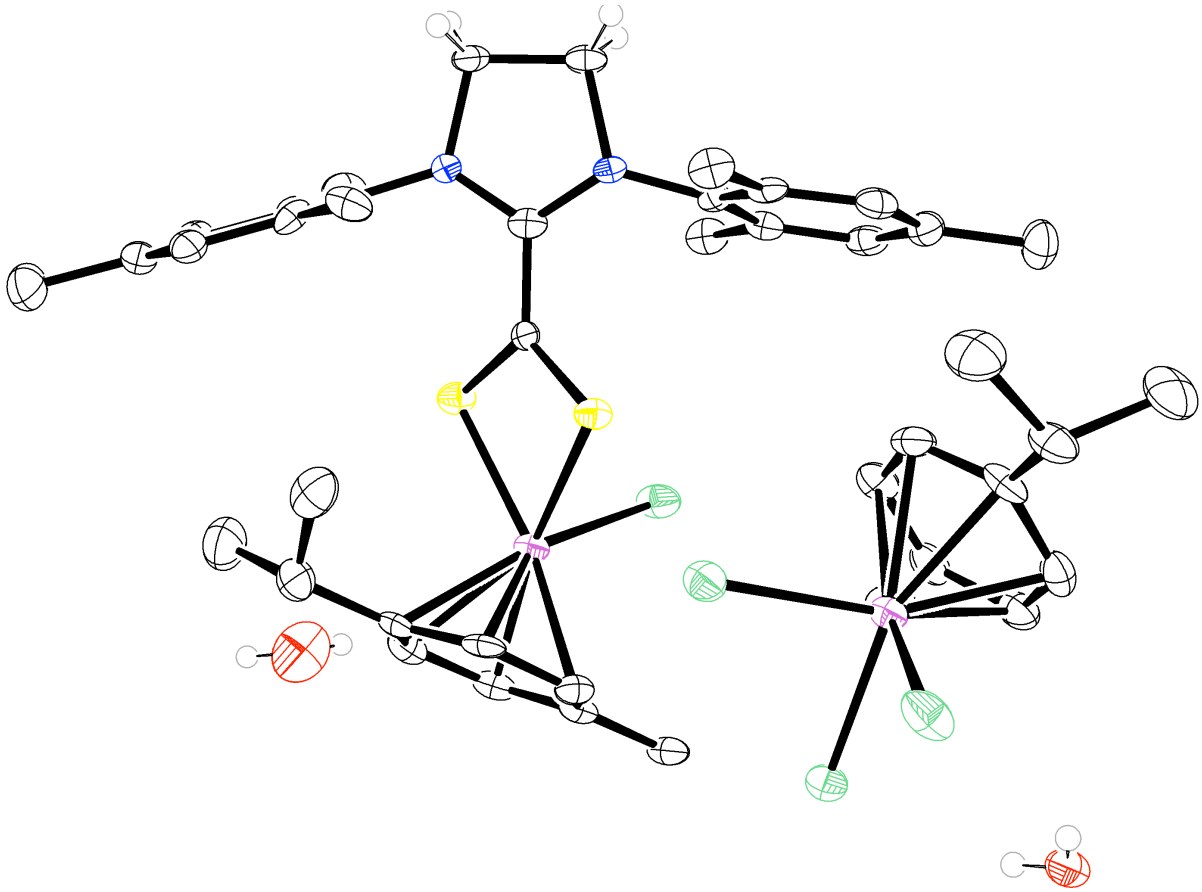

Fig. S64. ORTEP representation of [RuCl(*p*-cymene)(S_2C·SIMes)][$RuCl_3$(*p*-cymene)] co-crystallized with water (2(**3d**)·3(H_2O)). Hydrogen atoms were omitted except those directly bound to the heterocyclic ring and oxygen. Thermal ellipsoids were drawn at the 50% probability level

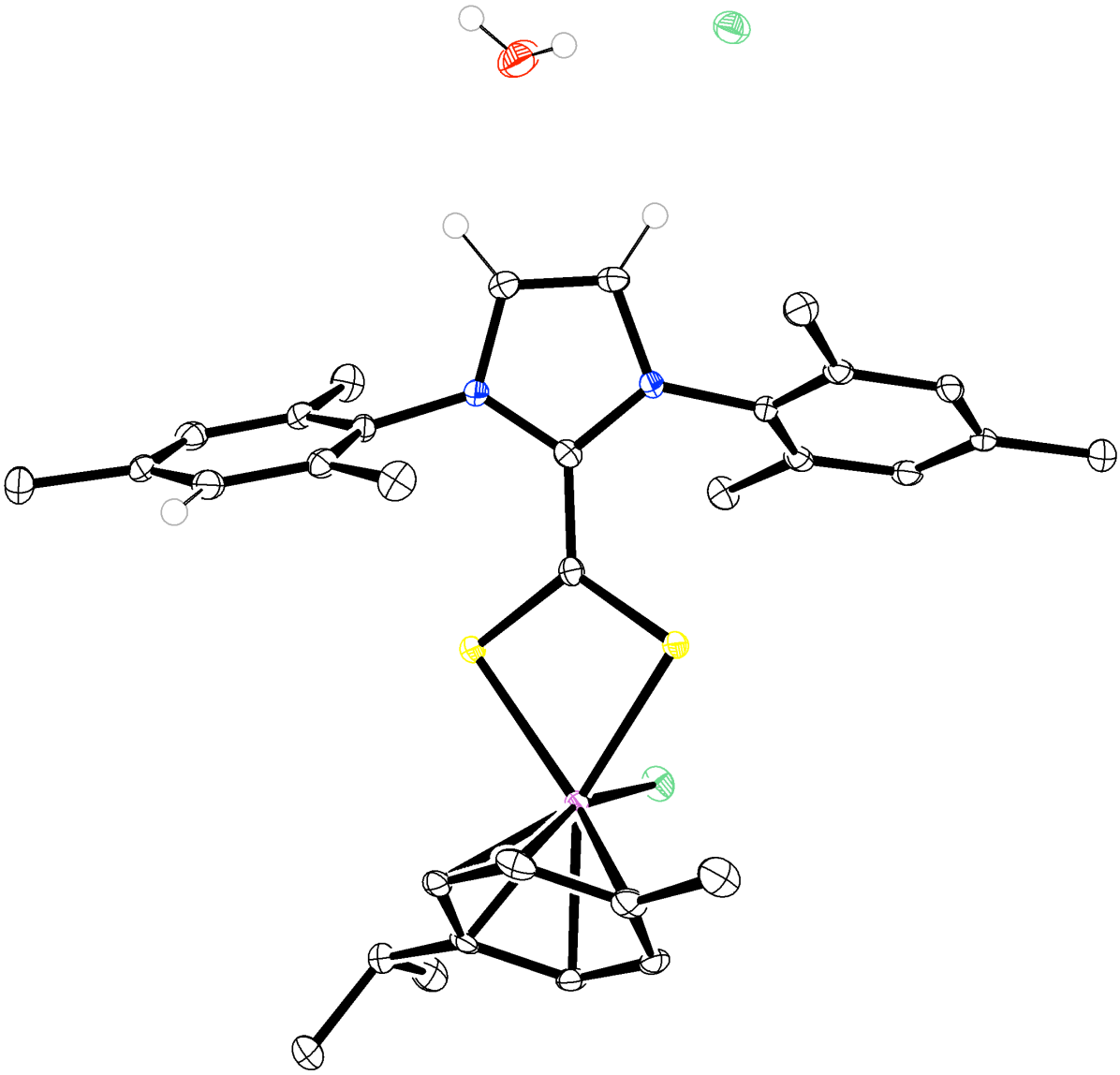

Fig. S65. ORTEP representation of [RuCl(*p*-cymene)(S_2C·IMes)]Cl co-crystallized with water (**2a**·H_2O). Hydrogen atoms were omitted except those directly bound to the heterocyclic ring and oxygen. Thermal ellipsoids were drawn at the 50% probability level

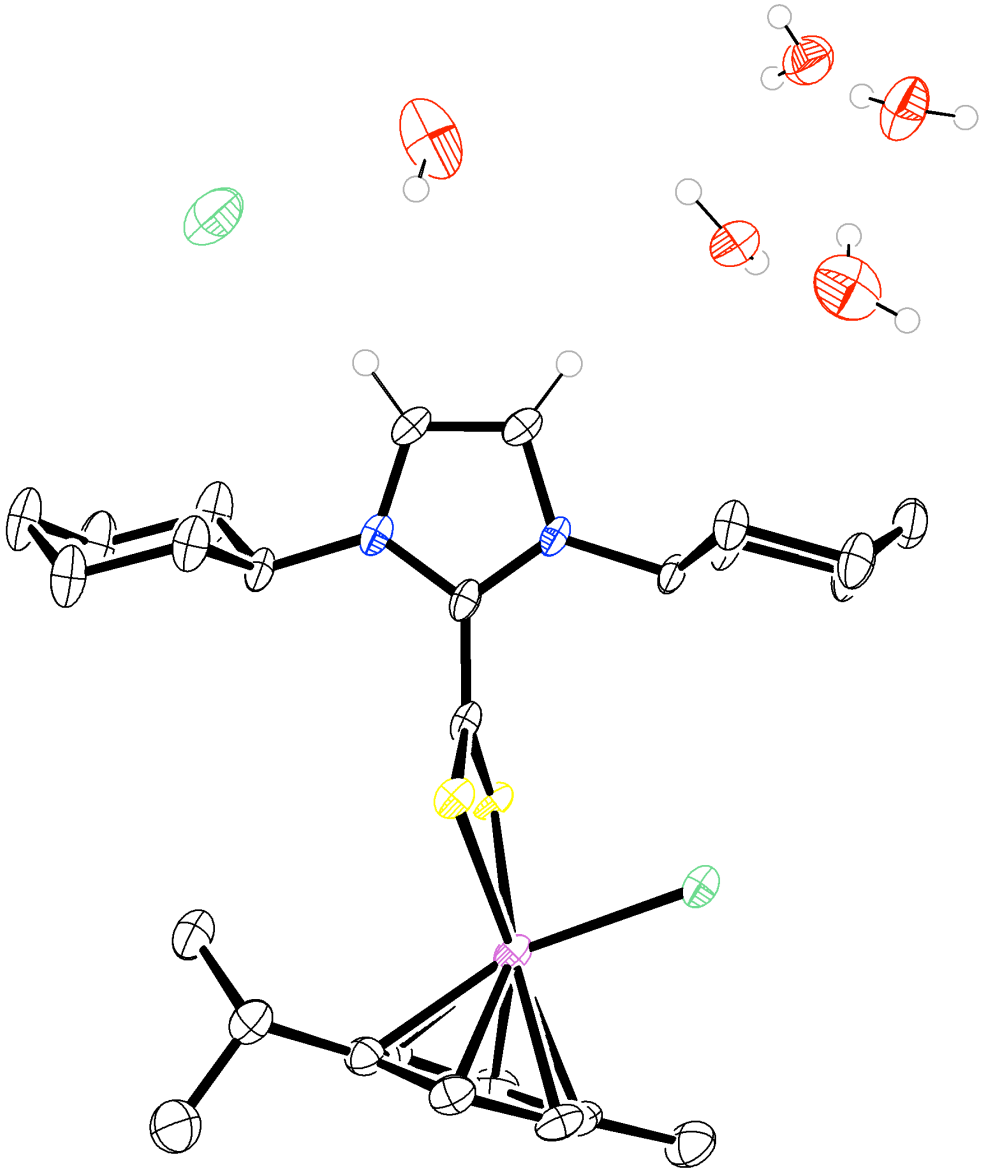

Fig. S66. ORTEP representation of [RuCl(*p*-cymene)(S_2C·ICy)]Cl co-crystallized with water (2(**2c**)·9.75(H_2O)). Hydrogen atoms were omitted except those directly bound to the heterocyclic ring and oxygen. Thermal ellipsoids were drawn at the 50% probability level

Table S1. Analysis of Short Ring-Interactions with Cg–Cg Distances (Å), and Angles (deg) in [RuCl(*p*-cymene)(S_2C·IMes)]Cl (**2a**), [RuCl(*p*-cymene)(S_2C·IMes)][$RuCl_3$(*p*-cymene)] (**3a**), and [RuCl(*p*-cymene)(S_2C·SIMes)][$RuCl_3$(*p*-cymene)] (**3d**). Reciprocal interactions were omitted.

Complex	Cg(I)→Cg(J)	Cg–Cg	Alpha	Beta	Gamma	CgI_Perp	CgJ_Perp
2a·H_2O	Cg(1)→Cg(2)^{i}	5.8119(13)	72.60(11)	20.4	52.4	3.5458(9)	5.4472(9)
	Cg(1)→Cg(4)^{ii}	4.8790(13)	61.22(11)	46.3	34.0	4.0465(9)	3.3729(9)
	Cg(2)→Cg(3)^{iii}	5.2461(13)	44.17(10)	34.7	53.0	3.1572(8)	4.3107(9)
	Cg(3)→Cg(3)^{iv}	5.5539(13)	0.00(10)	54.0	54.0	3.2646(8)	3.2646(8)
	Cg(3)→Cg(4)^{ii}	4.3400(12)	11.71(10)	31.9	34.7	3.5681(8)	3.6840(8)
	Cg(4)→Cg(1)^{v}	4.8790(13)	61.22(11)	34.0	46.3	3.3729(9)	4.0465(9)
3a·H_2O	Cg(1)→Cg(2)^{vi}	5.681(4)	79.9(3)	43.7	53.4	3.383(2)	4.106(3)
	Cg(2)→Cg(2)^{vi}	5.009(3)	0.0(3)	45.0	45.0	3.543(2)	3.543(2)
	Cg(2)→Cg(5)^{ix}	5.626(4)	27.2(3)	59.8	57.7	3.009(3)	2.831(2)
	Cg(3)→Cg(4)^{vii}	4.233(4)	22.0(3)	26.8	5.8	4.212(3)	3.777(2)
	Cg(3)→Cg(5)^{viii}	5.053(4)	11.1(3)	44.3	51.3	3.159(2)	3.618(3)
2(**3d**) ·$3H_2O$	Cg(3)→Cg(4)^{xii}	3.918(4)	11.0(3)	29.2	19.8	3.685(2)	3.419(2)
	Cg(3)→Cg(5)^{x}	4.756(4)	39.2(3)	34.0	61.7	2.252(2)	3.944(2)
	Cg(4)→Cg(1)^{xi}	5.720(4)	68.5(3)	57.3	62.5	2.644(3)	3.091(3)
	Cg(5)→Cg(2)^{xii}	5.783(4)	39.3(3)	42.0	67.8	2.182(3)	4.300(2)

Cg(1): C2 N1 C3 C4 N2; Cg(2): C5 → C10; Cg(3): C14 → C19; Cg(4): C23 → C28; Cg(5): C33 → C38

Symmetry codes: i) 1 – X, 1 – Y, – Z; ii) 1 + X, Y, Z; iii) X, –1 + Y, Z; iv) 1 – X, 2 – Y, –Z; v) –1 + X, Y, Z; vi) 2 – X, –Y, 1 – Z; vii) 1 – X, –Y, 1 – Z; vii) –1/2 + X, 1/2 – Y, 1/2 + Z; viii) 1/2 + X, 1/2 – Y, –1/2 + Z; ix) 1 – X, –Y, 1 – Z; x) –1/2 + X, Y, 3/2 – Z; xi) 1/2 + X, Y, 3/2 – Z; xii) X, 3/2 – Y, –1/2 + Z

Table S2. Selected Bond Lengths (Å), and Angles (deg) for the Hydrogen Bonds Between the Counteranions and Solvent molecules Derived from the Crystal Structures of [RuCl(*p*-cymene)(S_2C·IMes)]Cl (**2a**), [RuCl(*p*-cymene)(S_2C·IMes)][$RuCl_3$(*p*-cymene)] (**3a**), [RuCl(*p*-cymene)(S_2C·ICy)]Cl (**2c**), and [RuCl(*p*-cymene)(S_2C·SIMes)][$RuCl_3$(*p*-cymene)] (**3d**).

Complex	Donor–H···Acceptor	D–H	H···A	D···A	D–H···A
2a·H_2O	O1–H1O···Cl2	0.75(3)	2.50(4)	3.244(2)	171(3)
	O1–H2O···Cl2^{i}	0.81(4)	2.40(4)	3.205(2)	170(3)
3a·H_2O	O1–H1O···Cl3	0.82(2)	2.51(4)	3.275(5)	156(7)
	O1–H2O···Cl4^{ii}	0.83(2)	2.54(3)	3.323(5)	157(6)
2(**2c**)·9.75(H_2O)	O1W–H1O..Cl2	0.843(7)	2.65(7)	3.169(4)	121(6)
	O2W–H21O···Cl2^{iii}	0.847(10)	2.38(3)	3.157(4)	152(6)
	O2W–H22O···O5W	0.848(10)	2.06(3)	2.878(12)	162(7)
	O3W–H31O···O4W	0.848(10)	2.19(3)	2.990(8)	158(6)
	O3W–H32O···O2W^{iv}	0.846(10)	2.07(2)	2.903(8)	166(9)
	O4W–H41O···Cl1^{v}	0.846(10)	2.55(2)	3.342(3)	157(4)
	O4W–H42O···Cl2^{vi}	0.850(10)	2.333(17)	3.165(4)	166(5)
	O5W–H51O···O3W	0.849(10)	2.13(3)	2.943(14)	160(7)
	O5W–H52O···O4W^{vii}	0.855(10)	2.31(5)	3.027(11)	141(7)
2(**3d**)·3H_2O	O1–H11O···Cl4^{viii}	0.83(2)	2.35(3)	3.176(7)	172(9)
	O1–H12O···Cl4^{ix}	0.82(2)	2.49(4)	3.266(6)	157(9)
	O2–H21O···Cl3	0.82(2)	2.54(8)	3.213(10)	139(10)
	O2–H22O···Cl4	0.82(2)	2.80(7)	3.481(10)	142(9)

Symmetry codes: i) 2 – x, 1 – y, –z; ii) 1 – x, –y, 1 – z; iii) 1 – x, y, 3/2 - z; iv) 1 – x, y, 3/2 – z; v) x, 1 – y, 1/2 + z; vi) 1 – x, 1 + y, 3/2 – z; vii) 3/2 – x, –1/2 + y, 3/2 – z; viii) x, 3/2 – y, 1/2 + z; iv) 2 – x, –1/2 + y, 3/2 – z

Part 6 – Cytotoxicity

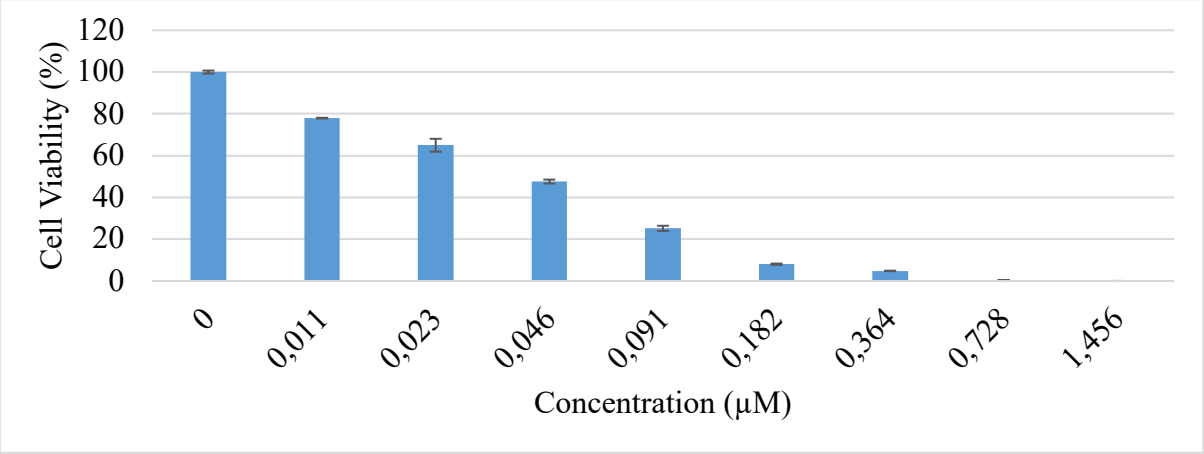

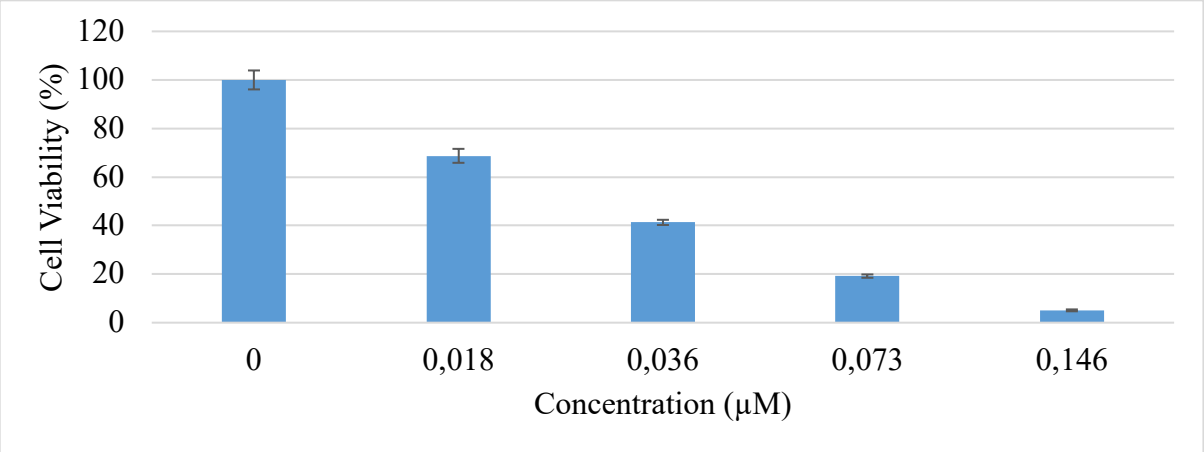

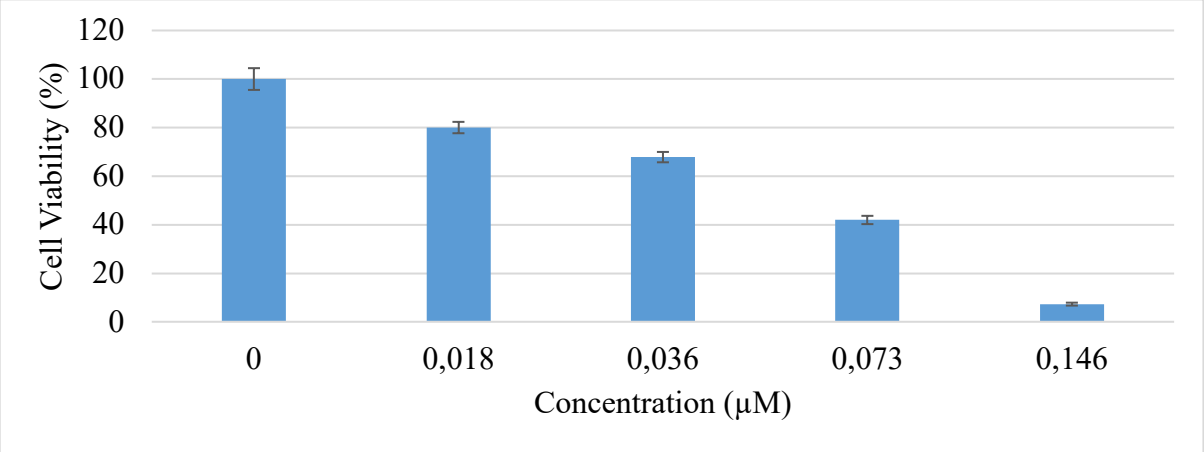

Fig. S67. In vitro cytotoxicity of [RuCl(*p*-cymene)(S_2C·IMes)]Cl (**2a**) against K562 cells measured after 72 h.

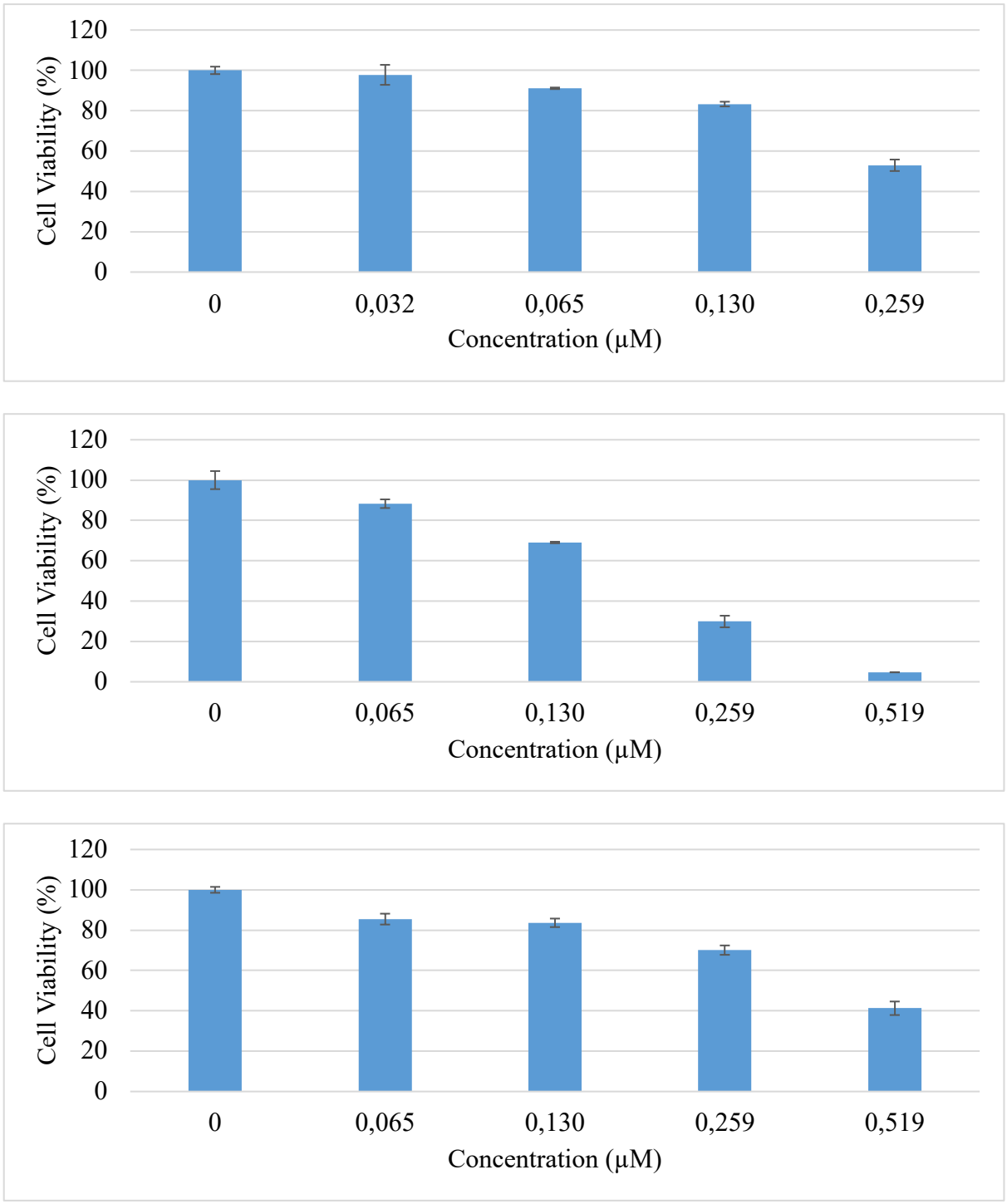

Fig. S68. In vitro cytotoxicity of [RuCl(*p*-cymene)(S_2C·IDip)]Cl (**2b**) against K562 cells measured after 72 h.

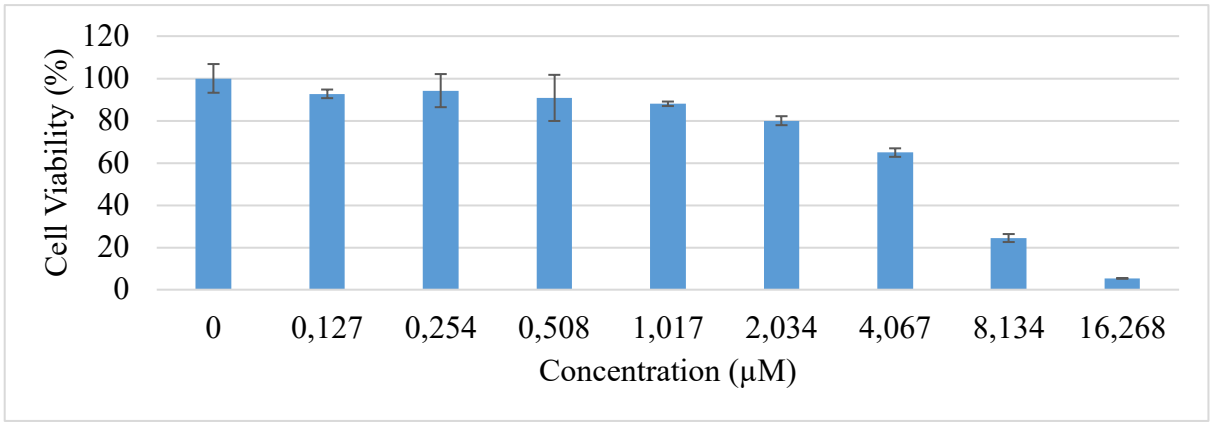

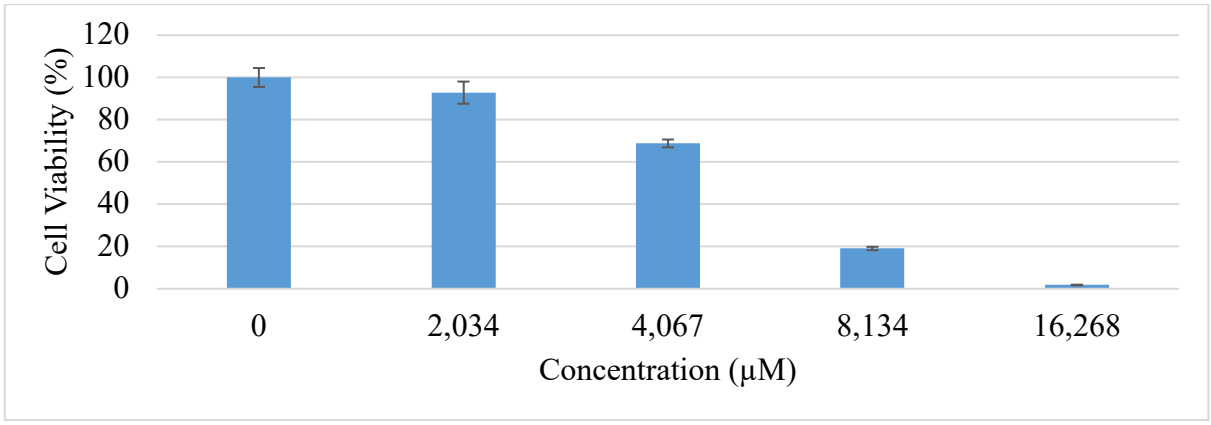

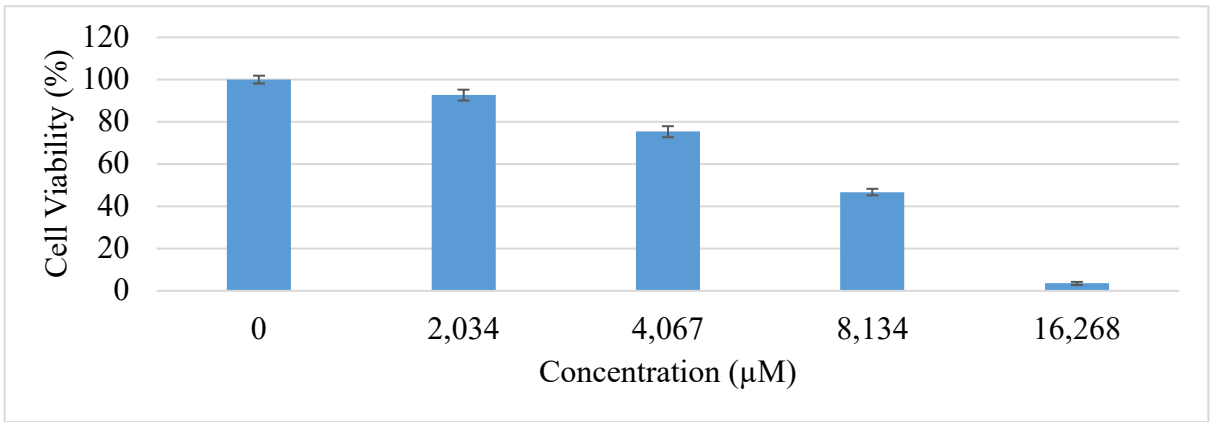

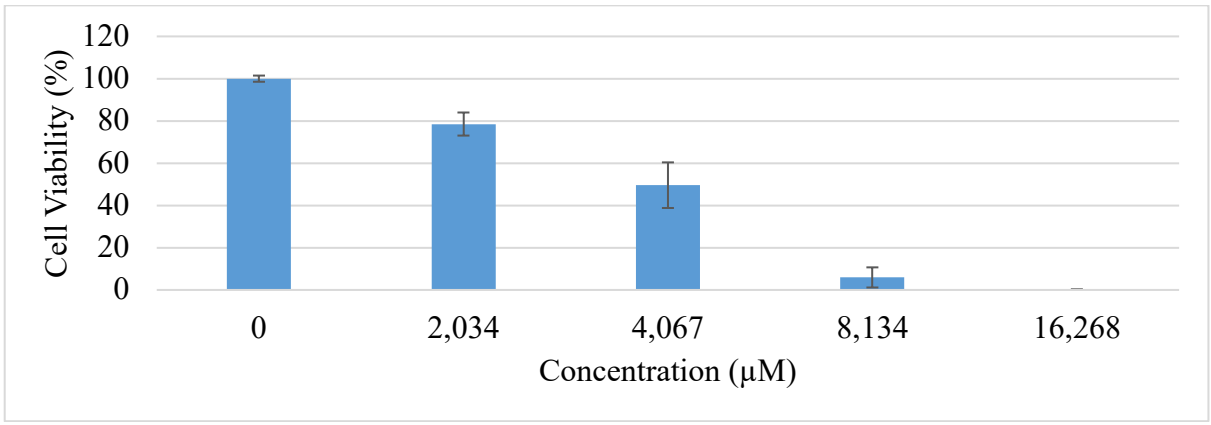

Fig. S69. In vitro cytotoxicity of [RuCl(*p*-cymene)(S_2C·ICy)]Cl (**2c**) against K562 cells measured after 72 h.

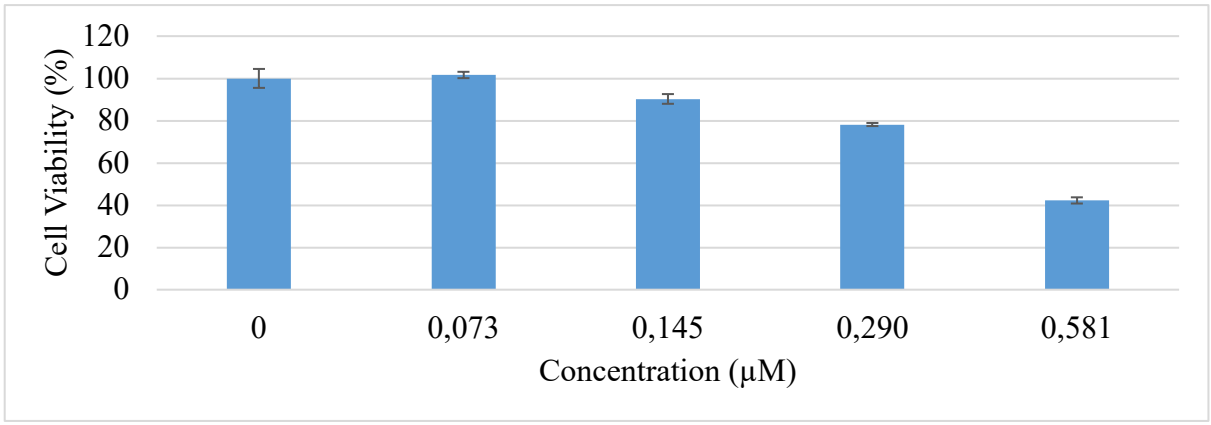

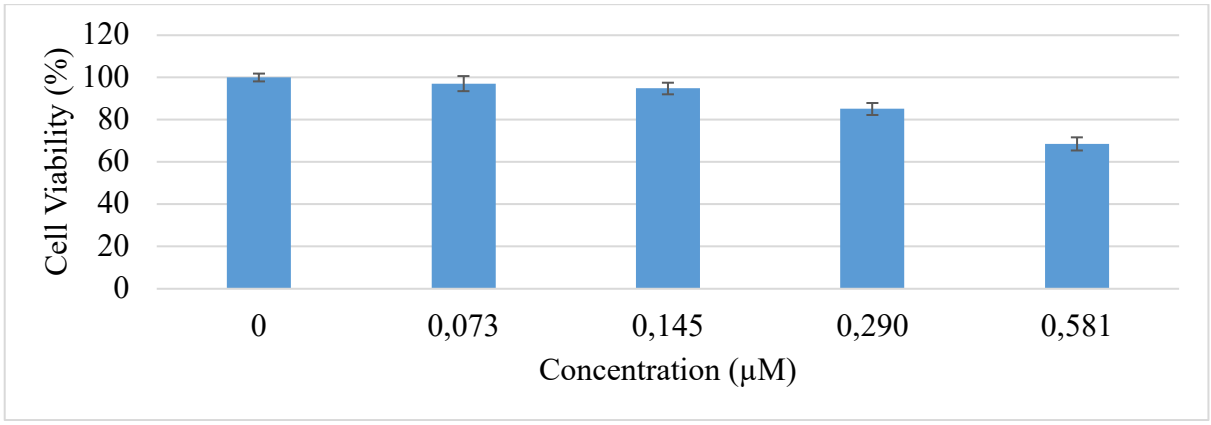

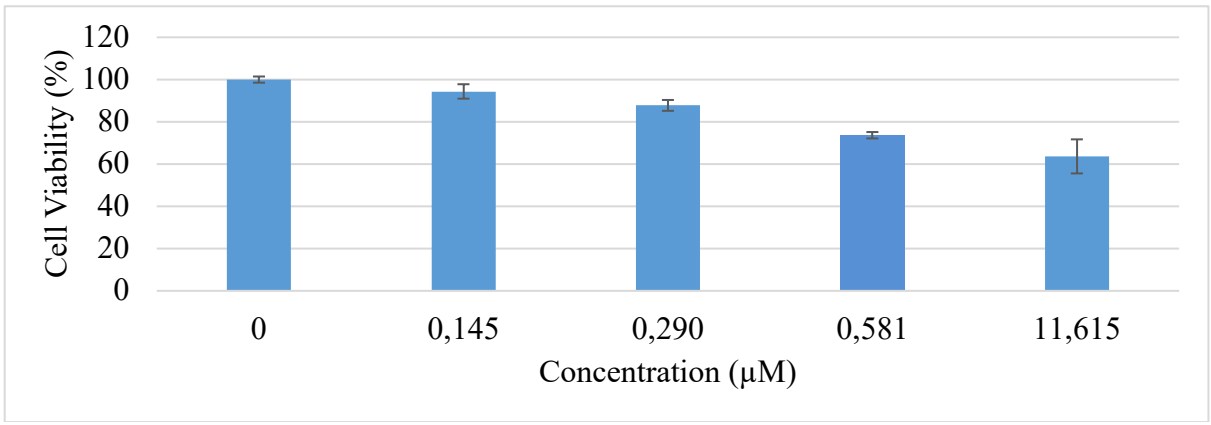

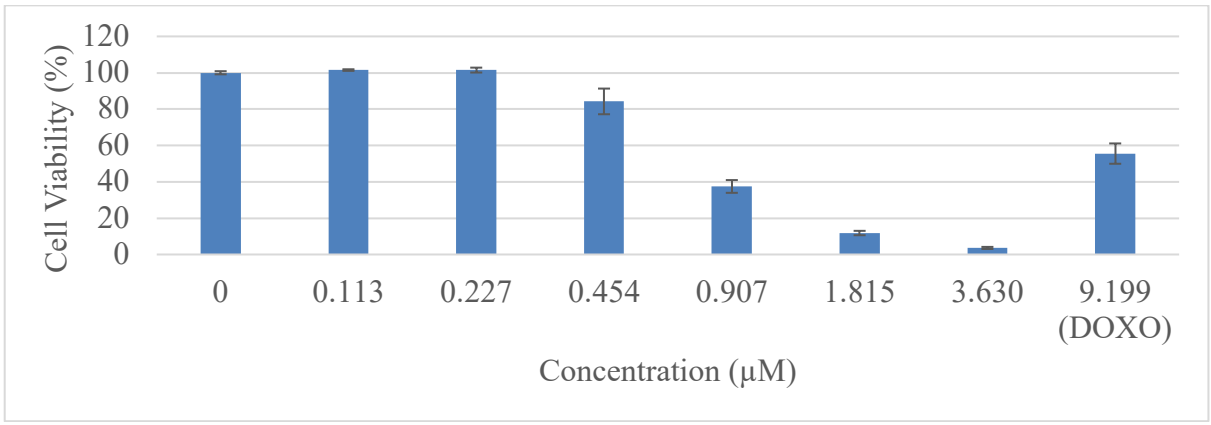

Fig. S70. In vitro cytotoxicity of [RuCl(*p*-cymene)(S_2C·SIMes)]Cl (**2d**) against K562 cells measured after 72 h.

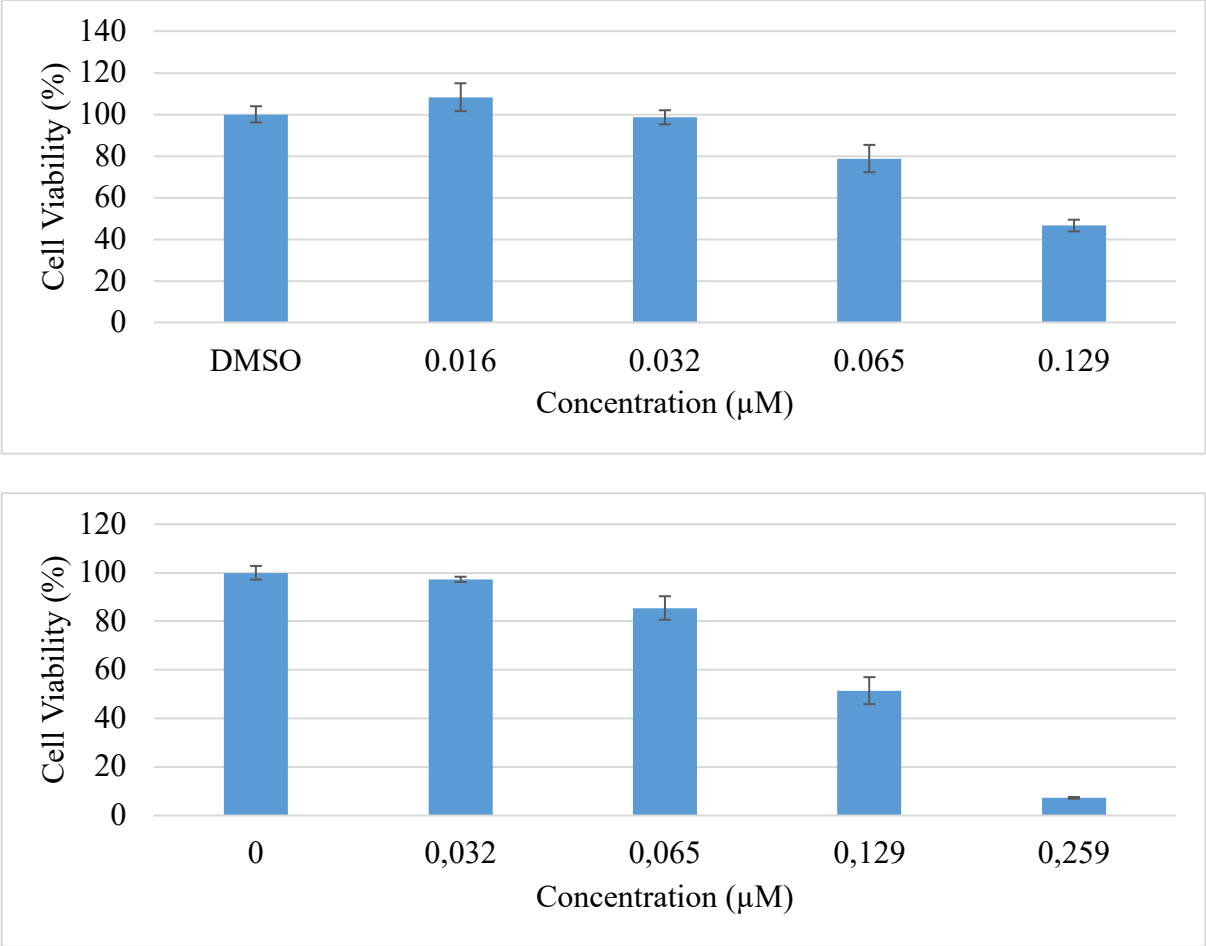

Fig. S71. In vitro cytotoxicity of [RuCl(*p*-cymene)(S_2C·SIDip)]Cl (**2e**) against K562 cells measured after 72 h.

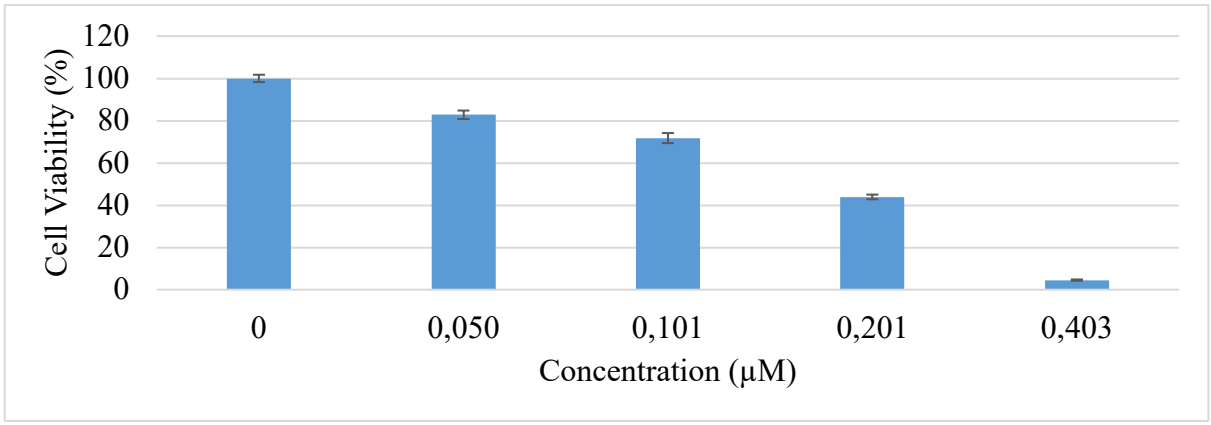

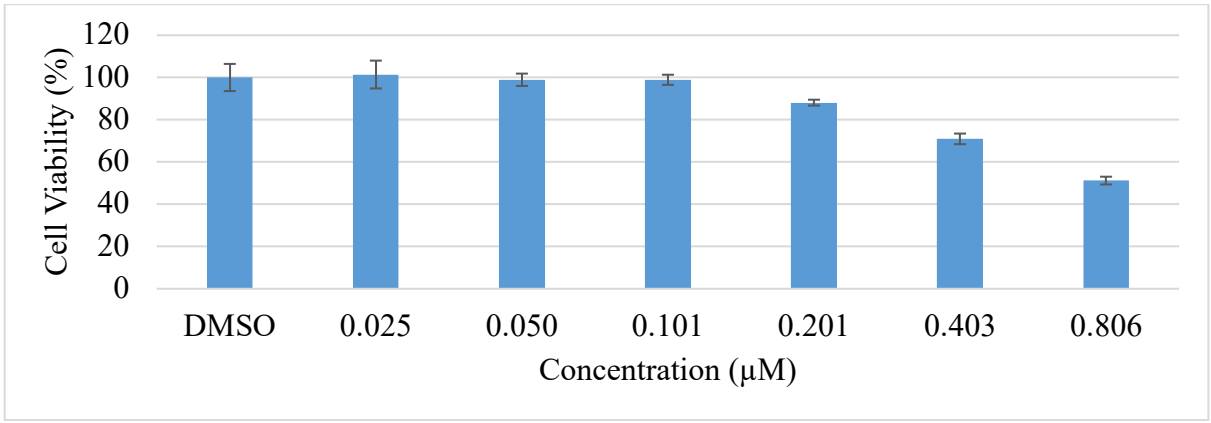

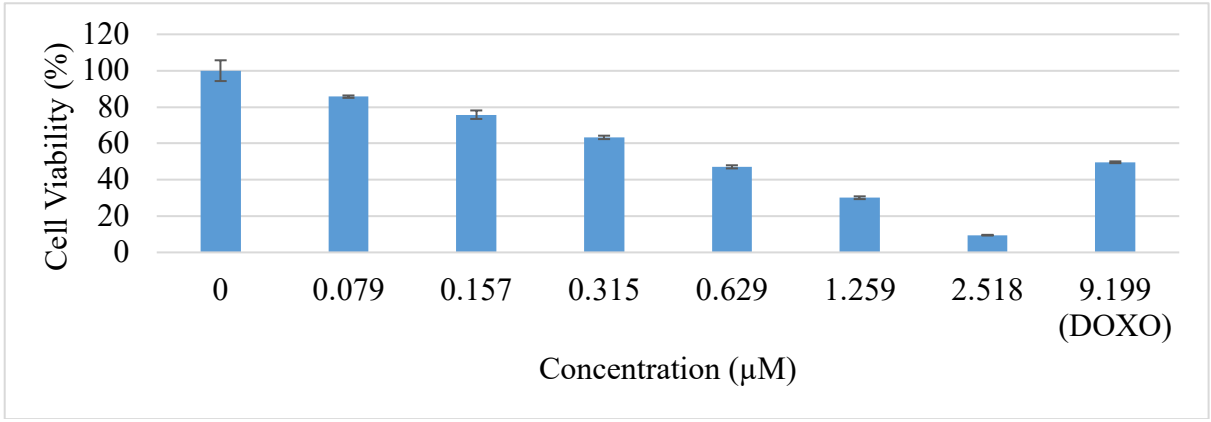

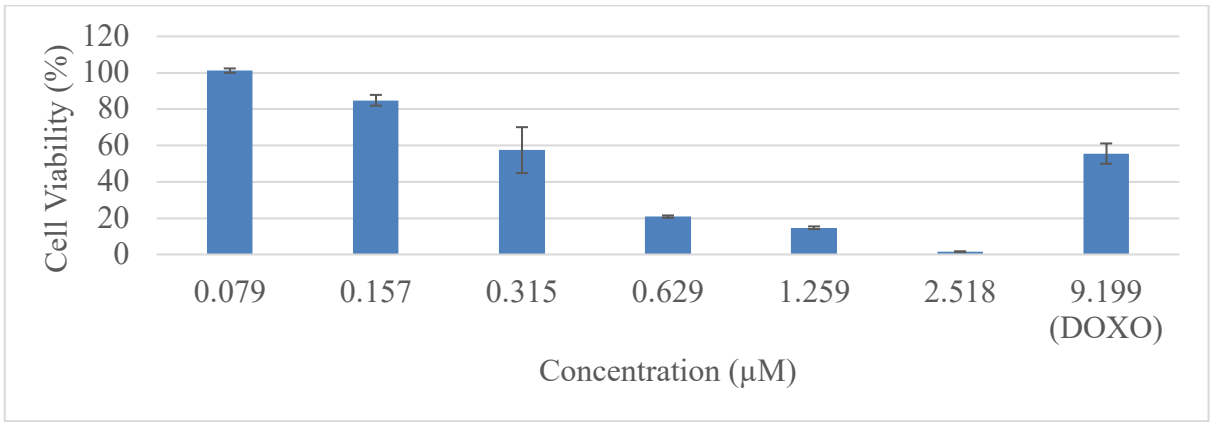

Fig. S72. In vitro cytotoxicity of [RuCl(*p*-cymene)(S_2C·IMes)][$RuCl_3$(p-cymene)] (**3a**) against K562 cells measured after 72 h.

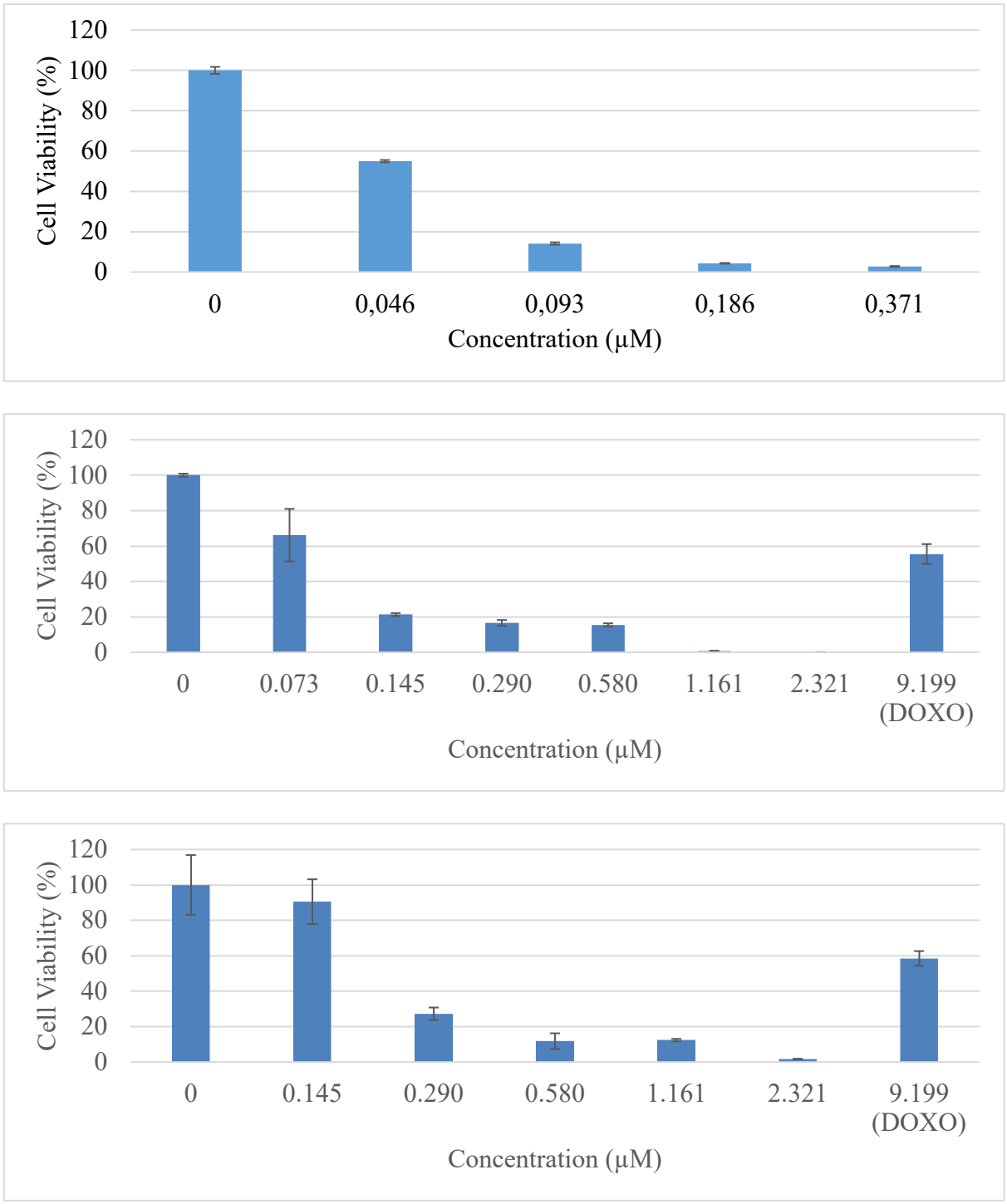

Fig. S73. In vitro cytotoxicity of [RuCl(*p*-cymene)(S_2C·IDip)][$RuCl_3$(p-cymene)] (**3b**) against K562 cells measured after 72 h.

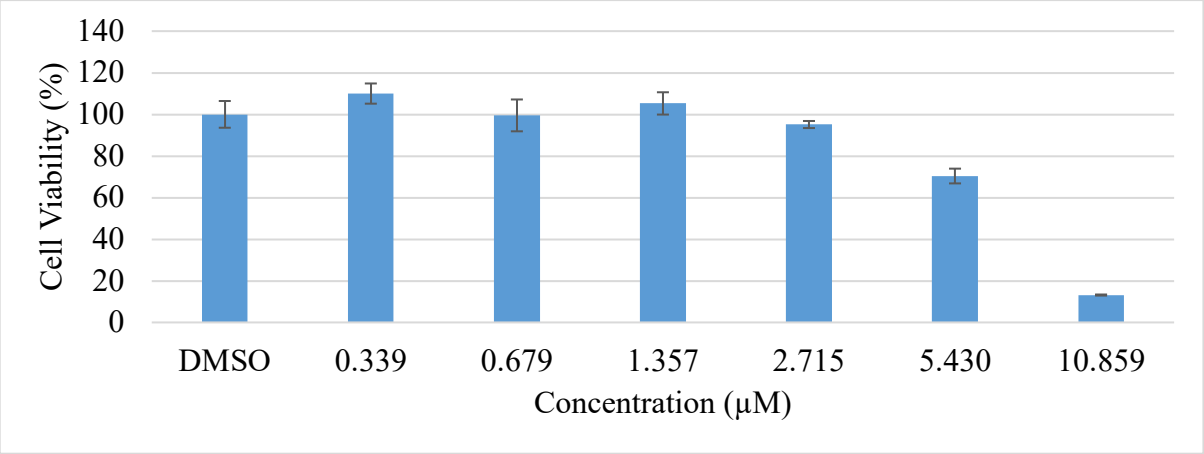

Fig. S74. In vitro cytotoxicity of [RuCl(*p*-cymene)(S_2C·ICy)][$RuCl_3$(p-cymene)] (**3c**) against K562 cells measured after 72 h.

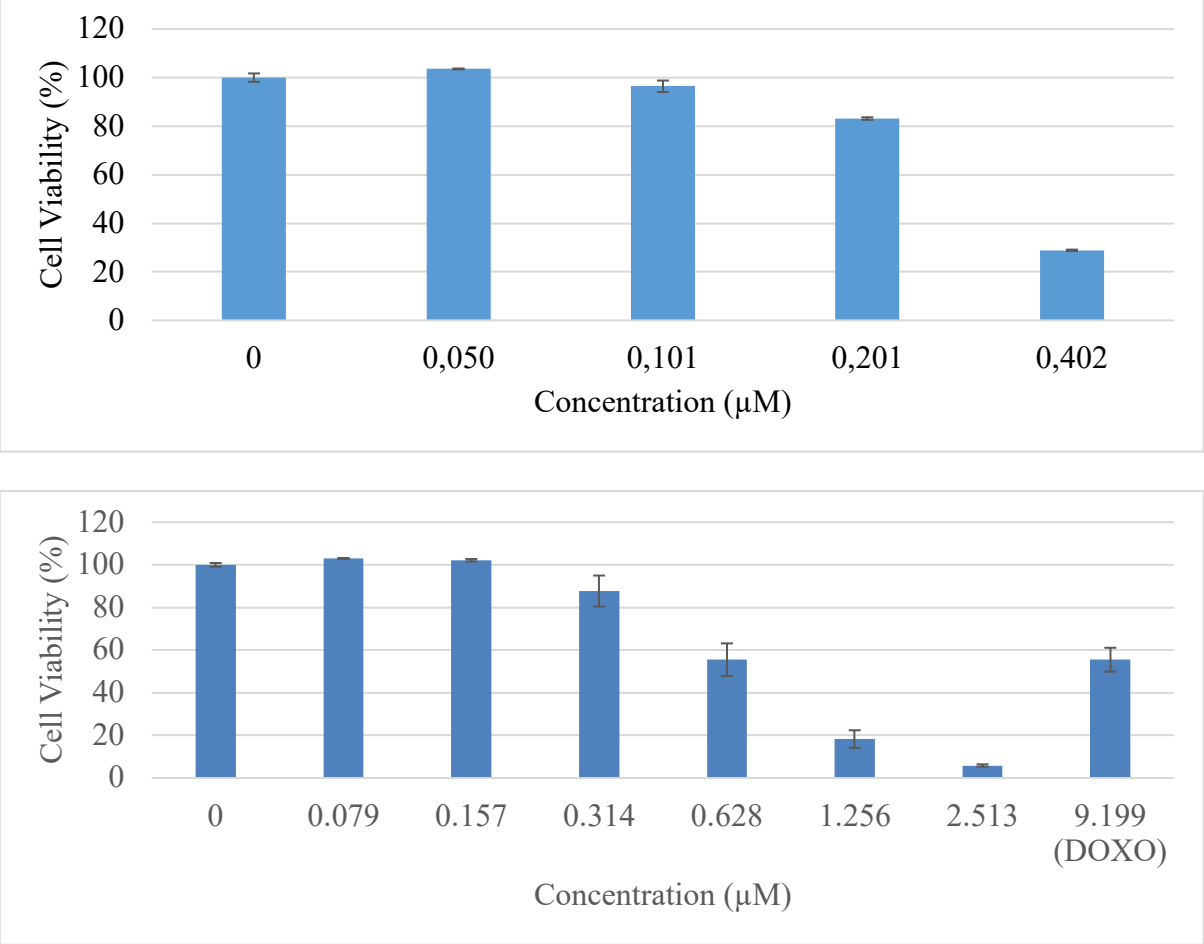

Fig. S75. In vitro cytotoxicity of [RuCl(*p*-cymene)(S_2C·SIMes)][$RuCl_3$(p-cymene)] (**3d**) against K562 cells measured after 72 h.

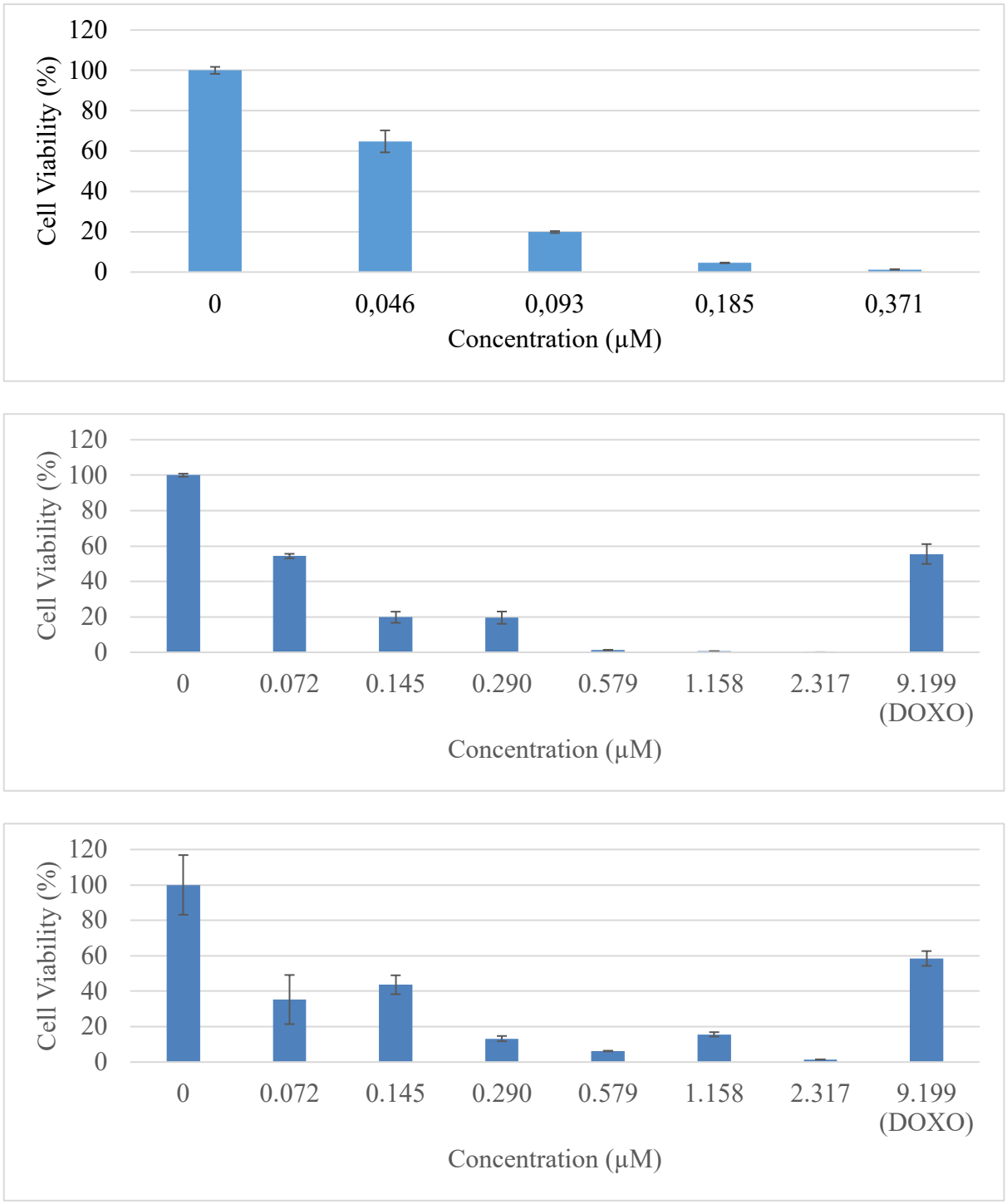

Fig. S76. In vitro cytotoxicity of [RuCl(*p*-cymene)(S_2C·SIDip)][$RuCl_3$(p-cymene)] (**3e**) against K562 cells measured after 72 h.

References

(1) Delaude, L.; Demonceau, A.; Wouters, J. Assessing the Potentials of Zwitterionic NHC·CS_2 Adducts for Probing the Stereoelectronic Parameters of N-Heterocyclic Carbenes. *Eur. J. Inorg. Chem.* **2009**, 1882-1891.
(2) Bruker *APEX II, Bruker AXS Inc.*; Madison, WI, USA, 2004.
(3) Clark, R. C.; Reid, J. S. The Analytical Calculation of Absorption in Multifaceted Crystals. *Acta Crystallogr., Sect. A: Fundam. Crystallogr.* **1995**, *51*, 887-897.
(4) Burla, M. C.; Caliandro, R.; Camalli, M.; Carrozzini, B.; Cascarano, G. L.; De Caro, L.; Giacovazzo, C.; Polidori, G.; Spagna, R. SIR2004: An Improved Tool for Crystal Structure Determination and Refinement. *J. Appl. Crystallogr.* **2005**, *38*, 381-388.
(5) Sheldrick, G. M. *SHELX-97 (SHELXS 97 and SHELXL 97), Programs for Crystal Structure Analyses*; University of Göttingen, Göttingen (Germany), 1998.
(6) Sheldrick, G. M. *SADABS, Programs for Scaling and Correction of Area Detection Data*; University of Göttingen, Göttingen (Germany), 1996.
(7) Tomani, J. C. D.; Gainkam, L. O. T.; Nshutiyayesu, S.; Mukazayire, M. J.; Ribeiro, S. O.; Stevigny, C.; Frederich, M.; Muganga, R.; Souopgui, J. An ethnobotanical survey and inhibitory effects on NLRP3 inflammasomes/Caspase-1 of herbal recipes' extracts traditionally used in Rwanda for asthma treatment. *J. Ethnopharmacol.* **2018**, *227*, 29-40.
(8) Tomani, J. C. D.; Kagisha, V.; Tchinda, A. T.; Jansen, O.; Ledoux, A.; Vanhamme, L.; Frederich, M.; Muganga, R.; Souopgui, J. The inhibition of NLRP3 inflammasome and IL-6 production by hibiscus noldeae baker f. derived constituents provides a link to its anti-inflammatory therapeutic potentials. Molecules **2020**, *25*, art. no. 4693.

I.4. Supporting Information (SI) for Chapter VIII: Synthesis, Characterization, and Biological Activity of Cationic Ruthenium–Arene Complexes with Sulfur Ligands

Supplementary Information for:

Synthesis, characterization, and biological activity of cationic ruthenium–arene complexes with sulfur ligands

Mohammed Zain Aldin,[1] Guillermo Zaragoza,[2] Eva Choquenet,[3] Guillaume Blampain,[3] Gilles Berger,[3] and Lionel Delaude*,[1]

[1]*Laboratory of Catalysis, MolSys Research Unit, Institut de Chimie Organique (B6a), Allée du six Août 13, Université de Liège, 4000 Liège, Belgium*

[2]*Unidade de Difracción de Raios X, RIAIDT, Universidade de Santiago de Compostela, Campus Vida, 15782 Santiago de Compostela, Spain*

[3]*Microbiology, Bioorganic and Macromolecular Chemistry, Faculté de Pharmacie, Université Libre de Bruxelles, 1050 Brussels, Belgium*

*E-mail: l.delaude@uliege.be

Table of content

Part 1 – NMR spectra

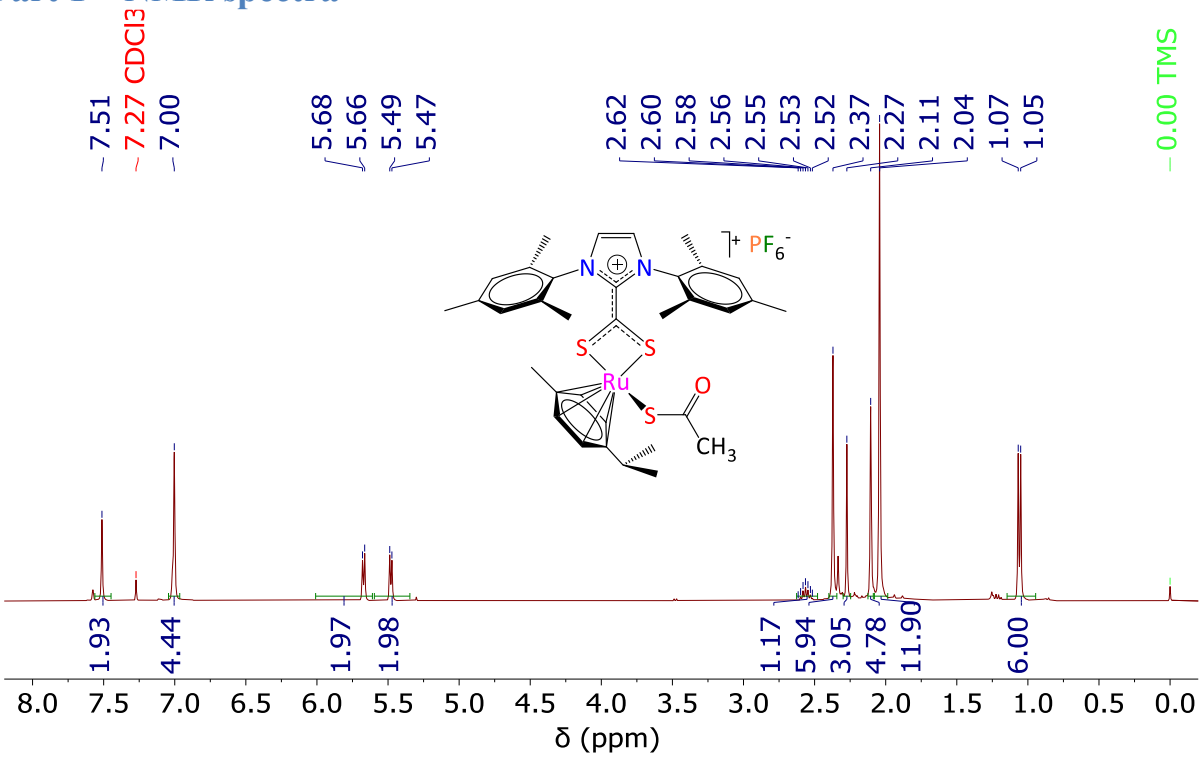

Fig. S1. ^{1}H NMR spectrum (400 MHz, $CDCl_3$, 298 K) of [Ru(κ^1-*S*-SAc)(κ^2-*S,S'*-S_2C·IMes)-(*p*-cymene)](PF_6) (**5a**)

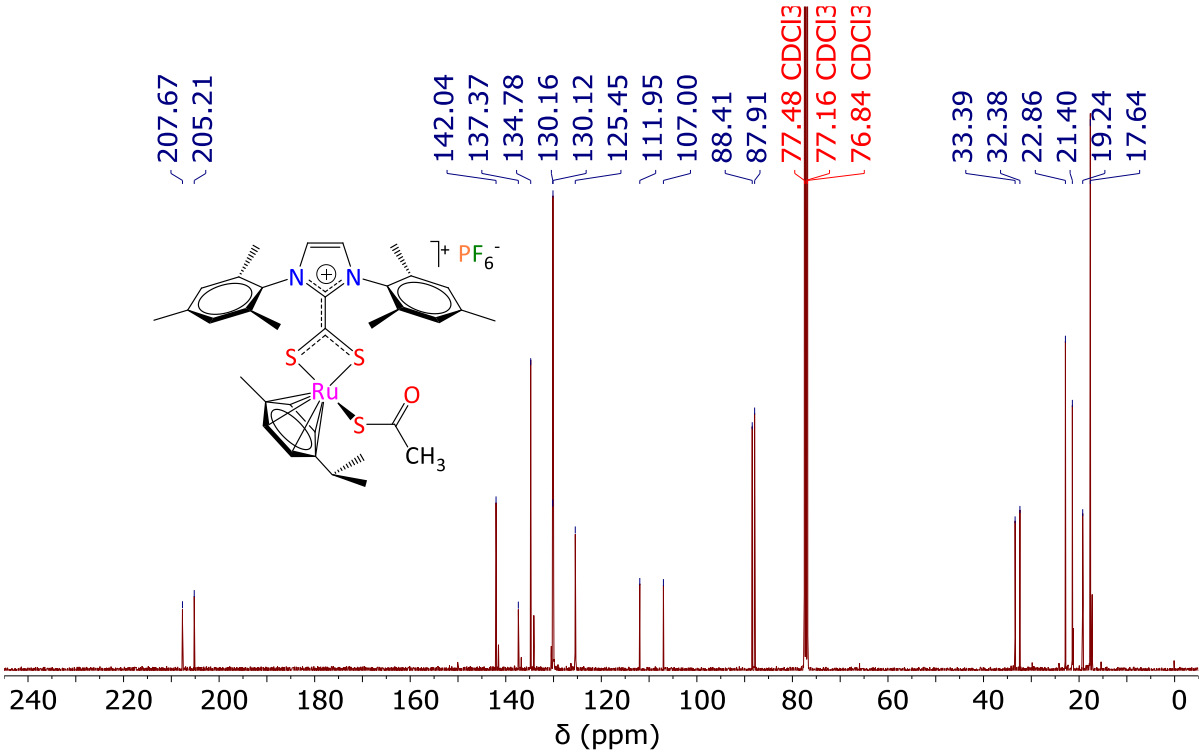

Fig. S2. ^{13}C{^{1}H} NMR spectrum (101 MHz, $CDCl_3$, 298 K) of [Ru(κ^1-*S*-SAc)(κ^2-*S,S'*-S_2C·IMes)(*p*-cymene)](PF_6) (**5a**)

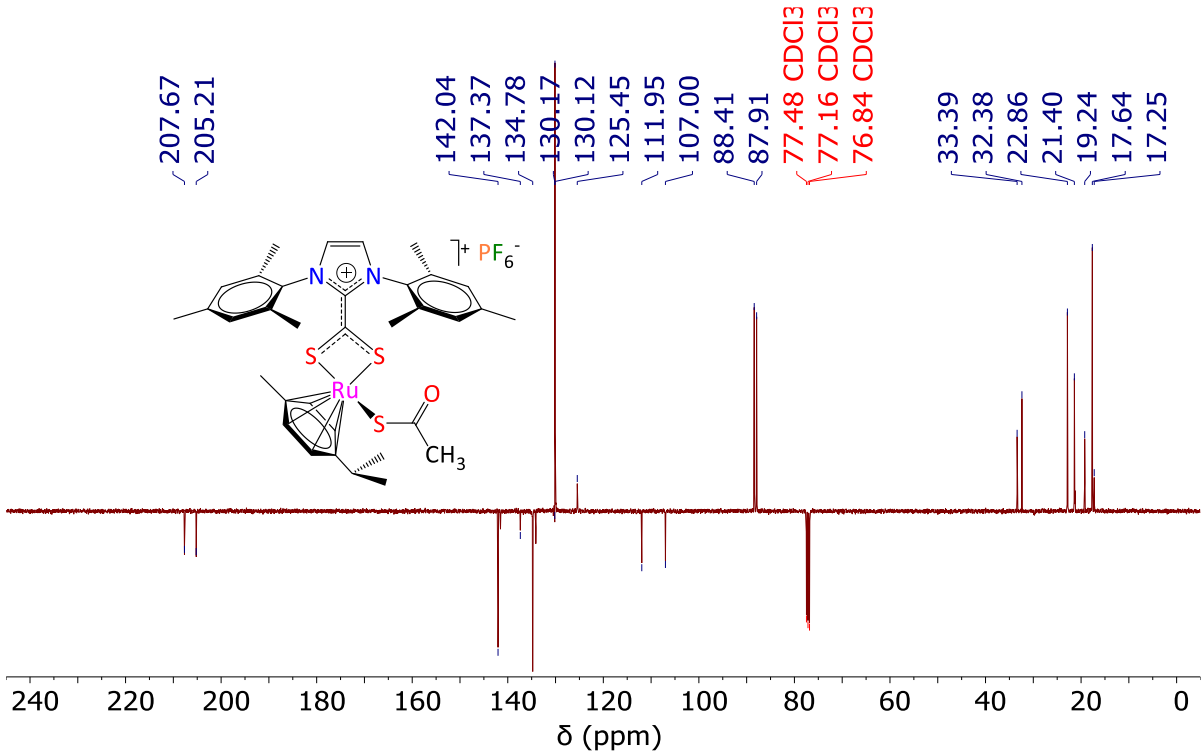

Fig. S3. $^{13}C\{^{1}H\}$ APT NMR spectrum (101 MHz, $CDCl_3$, 298 K) of [Ru(κ^1-*S*-SAc)(κ^2-*S,S'*-S_2C·IMes)(*p*-cymene)](PF_6) (**5a**)

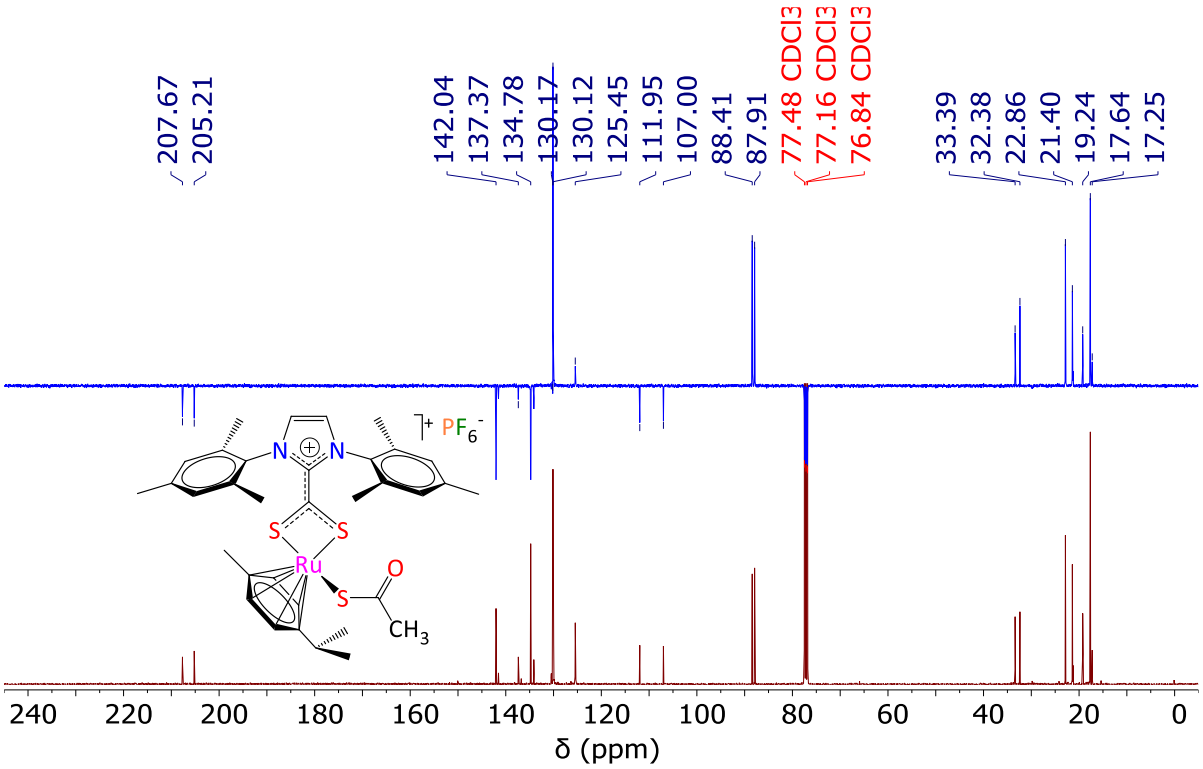

Fig. S4. ^{13}C CPD and APT NMR spectra (101 MHz, $CDCl_3$, 298 K) of [Ru(κ^1-*S*-SAc)(κ^2-*S,S'*-S_2C·IMes)(*p*-cymene)](PF_6) (**5a**)

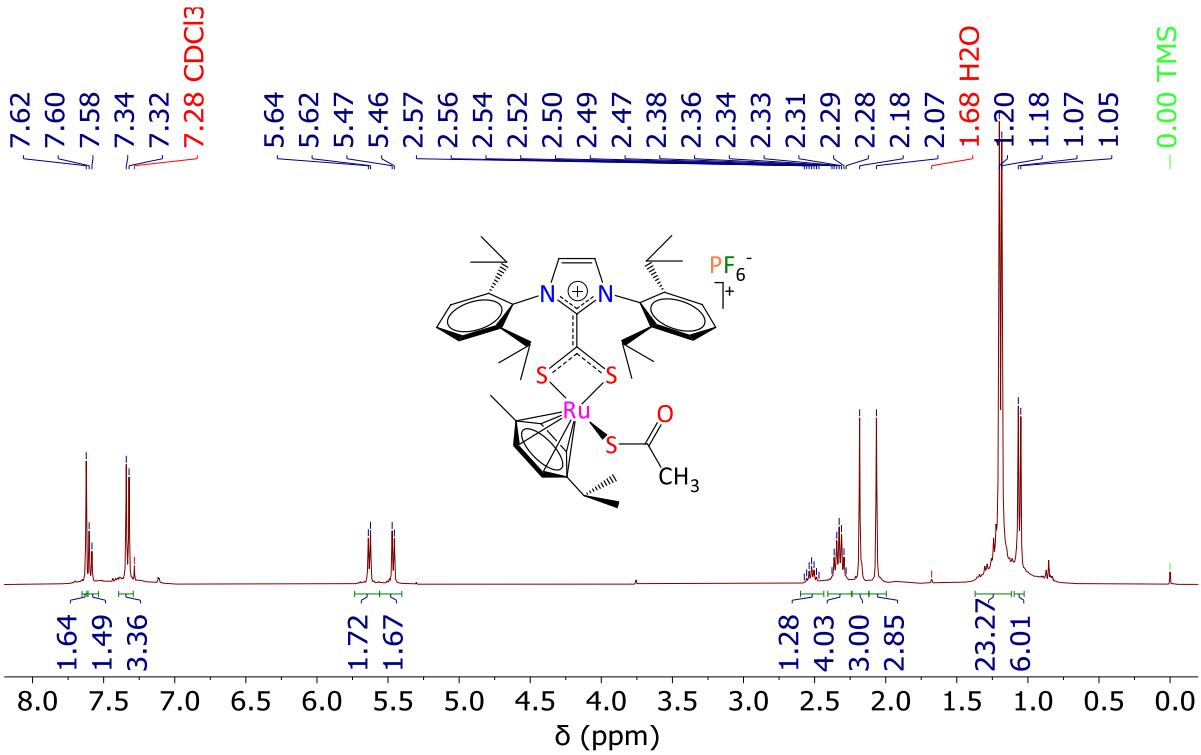

Fig. S5. ^{1}H NMR spectrum (400 MHz, $CDCl_3$, 298 K) of [Ru(κ^1-*S*-SAc)(κ^2-*S,S'*-S_2C·IDip)(*p*-cymene)](PF_6) (**5b**)

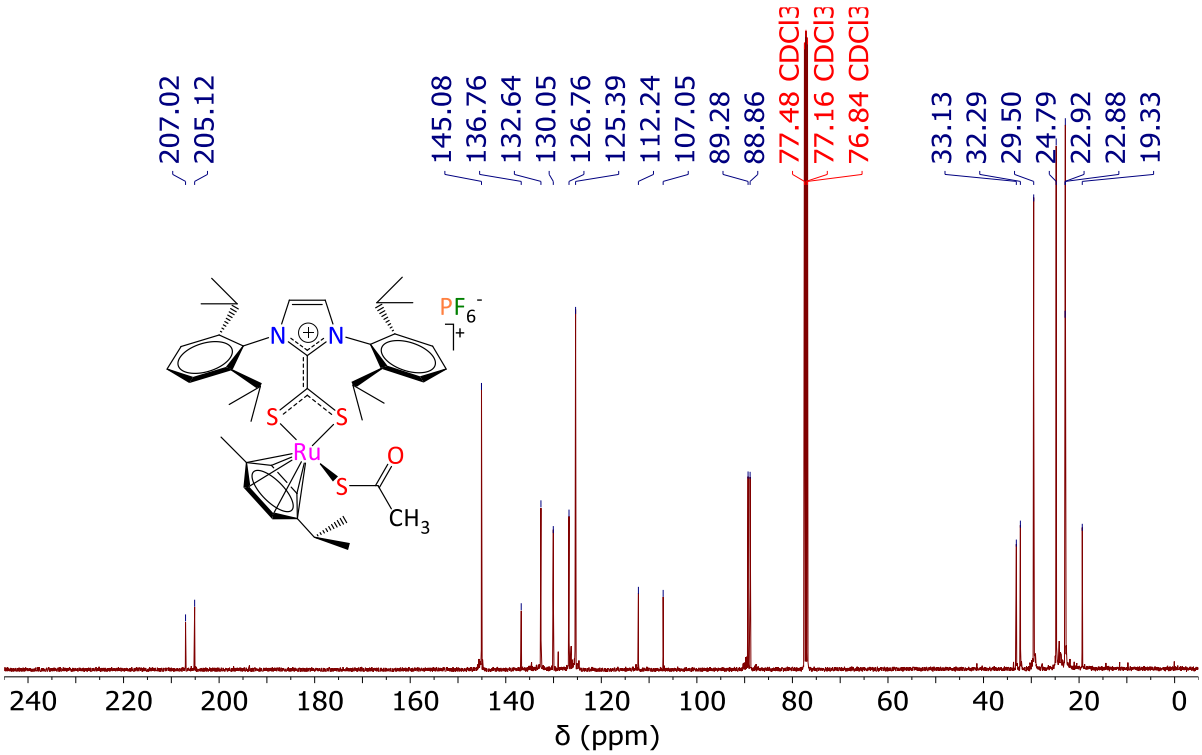

Fig. S6. ^{13}C{^{1}H} NMR spectrum (101 MHz, $CDCl_3$, 298 K) of [Ru(κ^1-*S*-SAc)(κ^2-*S,S'*-S_2C·IDip)(*p*-cymene)](PF_6) (**5b**)

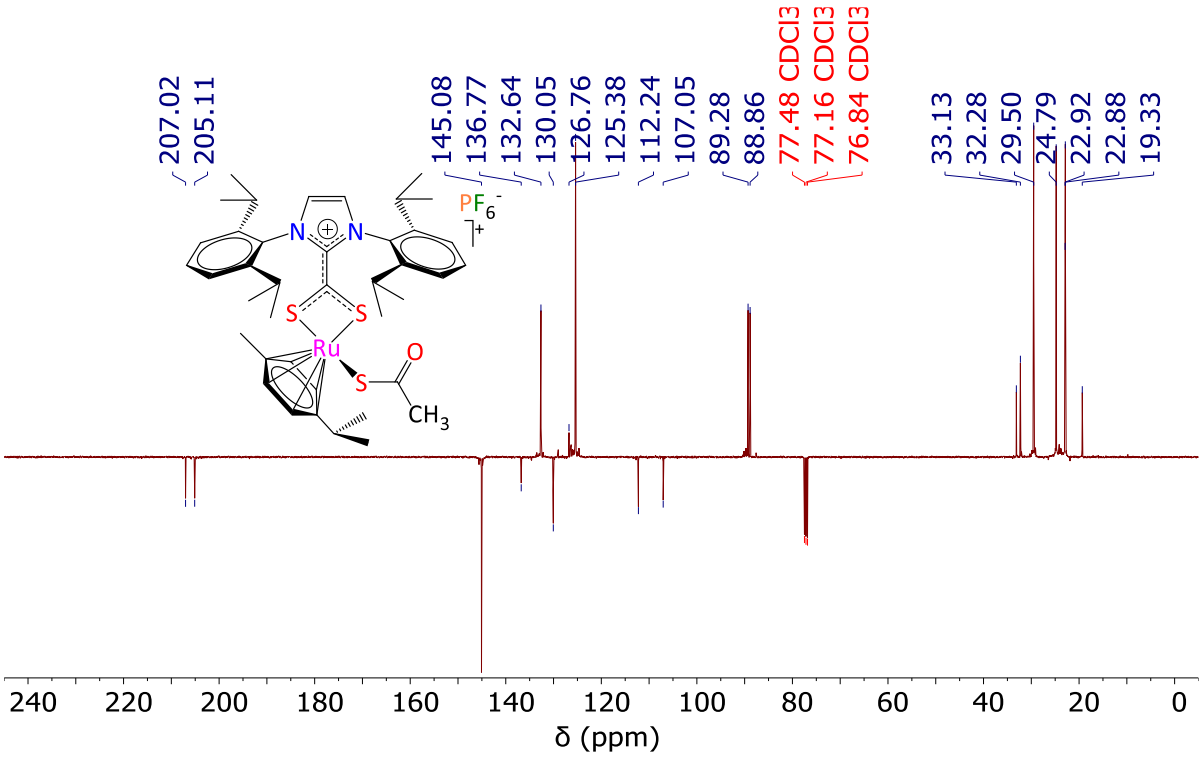

Fig. S7. APT NMR spectrum (101 MHz, $CDCl_3$, 298 K) of [Ru(κ^1-*S*-SAc)(κ^2-*S,S'*-S_2C·IDip)(*p*-cymene)](PF_6) (**5b**)

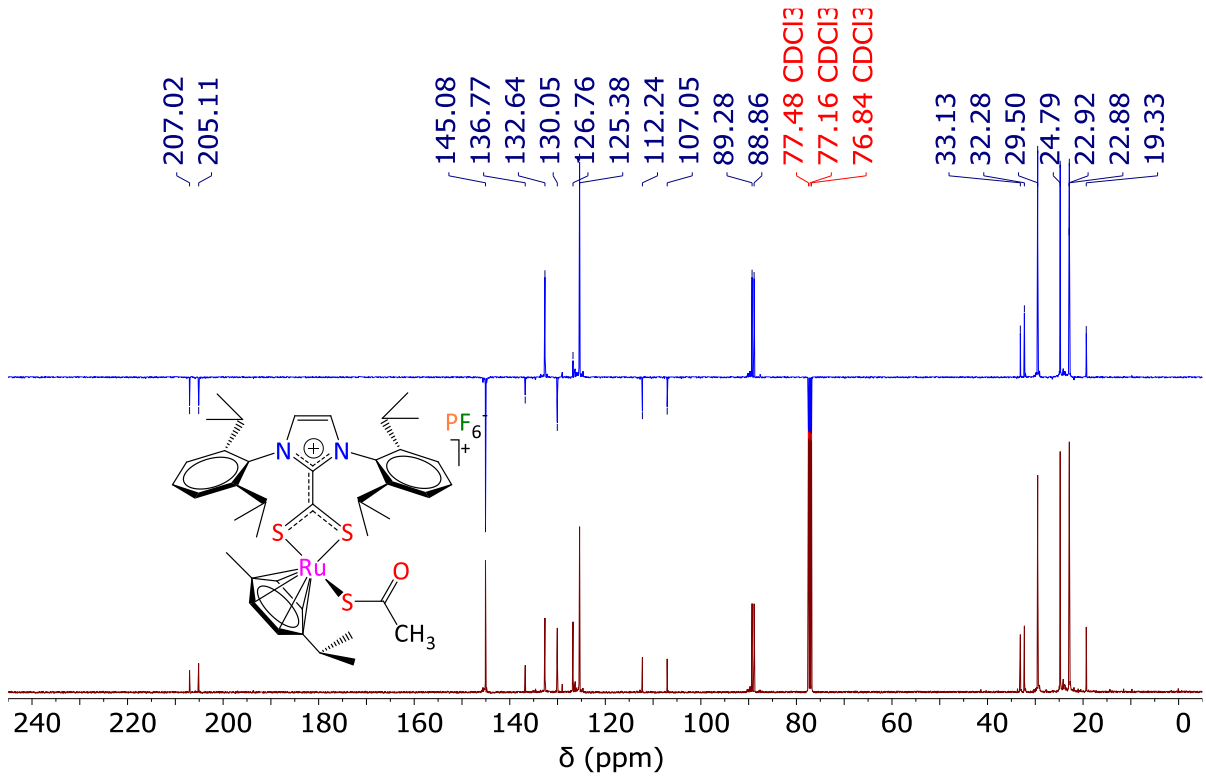

Fig. S8. ^{13}C and APT NMR spectrum (101 MHz, $CDCl_3$, 298 K) of [Ru(κ^1-*S*-SAc)(κ^2-*S,S'*-S_2C·IDip)(*p*-cymene)](PF_6) (**5b**)

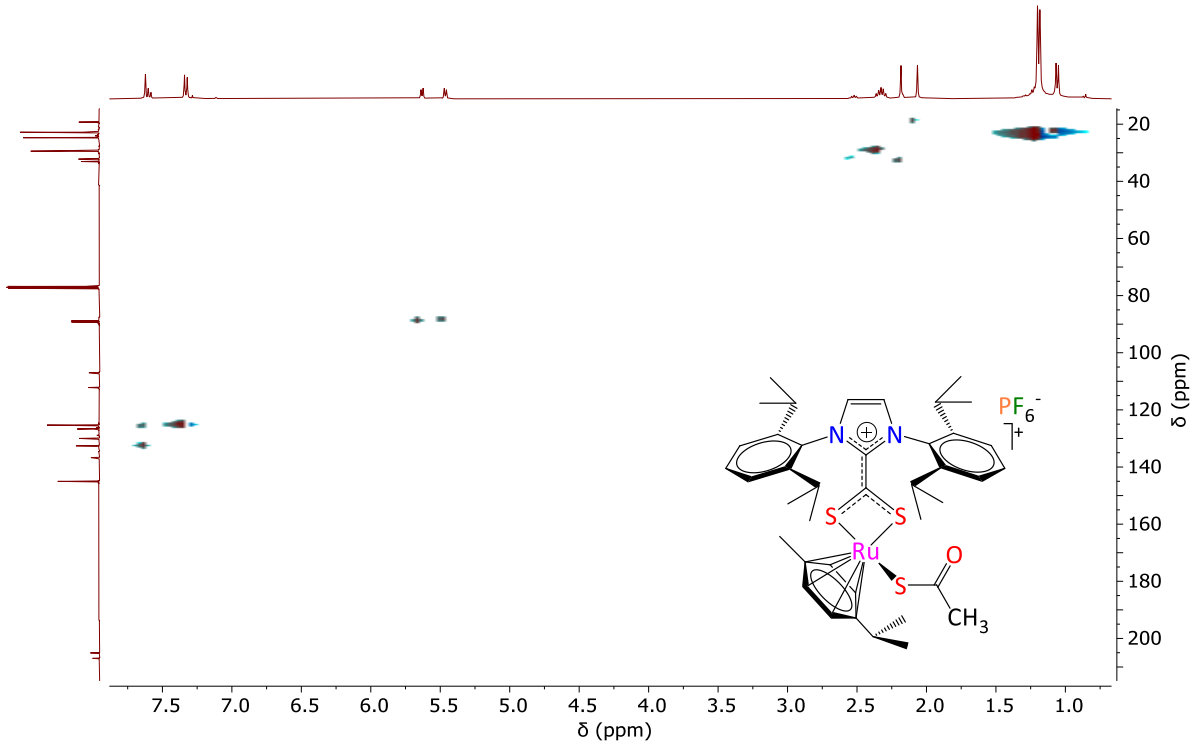

Fig. S9. HSQC spectrum of [Ru(κ^1-*S*-SAc)(κ^2-*S,S'*-S_2C·IDip)(*p*-cymene)](PF_6) (**5b**)

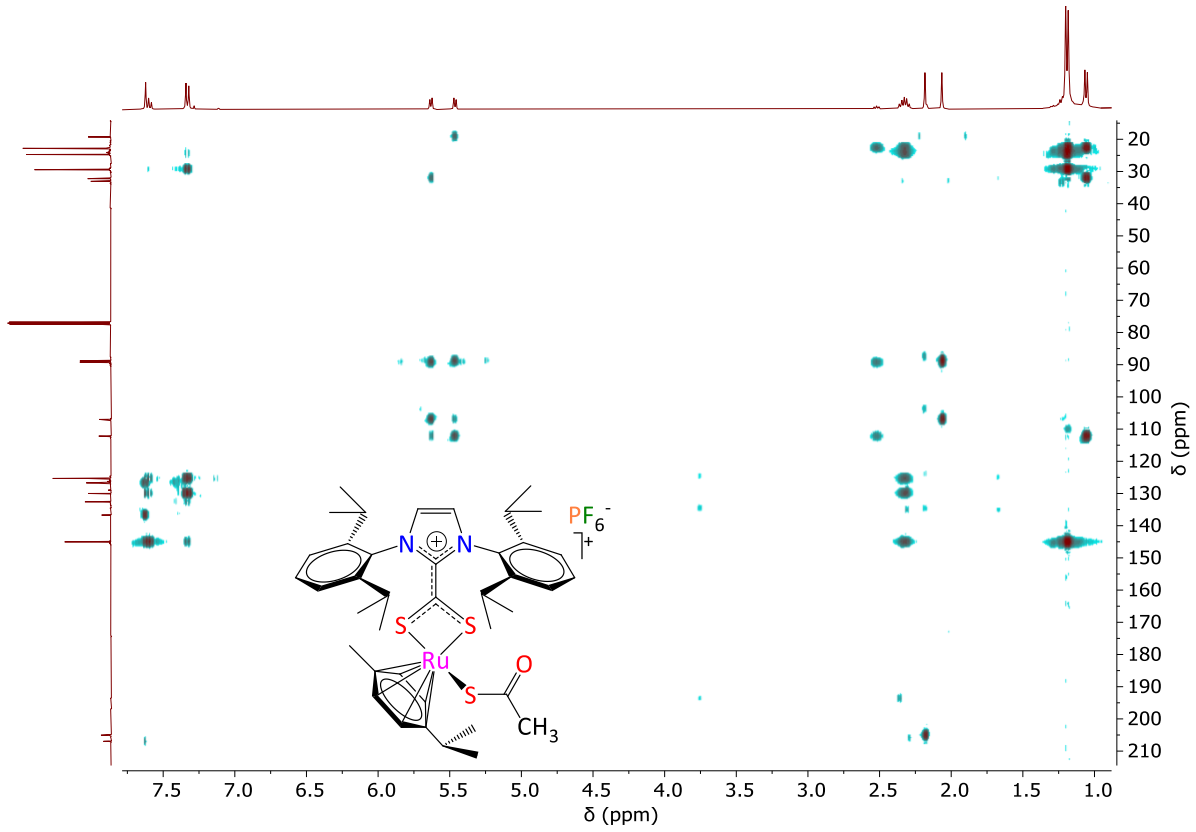

Fig. S10. HMBC spectrum of [Ru(κ^1-*S*-SAc)(κ^2-*S,S'*-S_2C·IDip)(*p*-cymene)](PF_6) (**5b**)

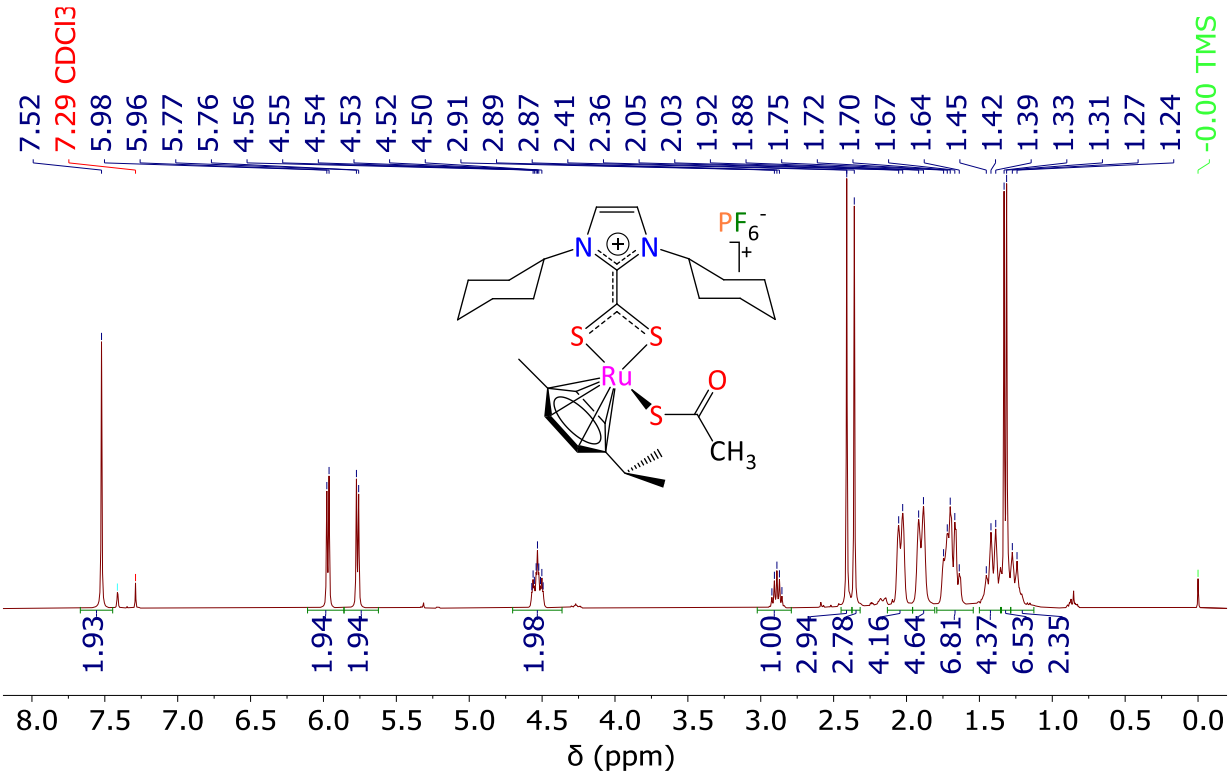

Fig. S11. ^{1}H NMR spectrum (400 MHz, $CDCl_3$, 298 K) of [Ru(κ^1-*S*-SAc)(κ^2-*S,S'*-S_2C·ICy)(*p*-cymene)](PF_6) (**5c**)

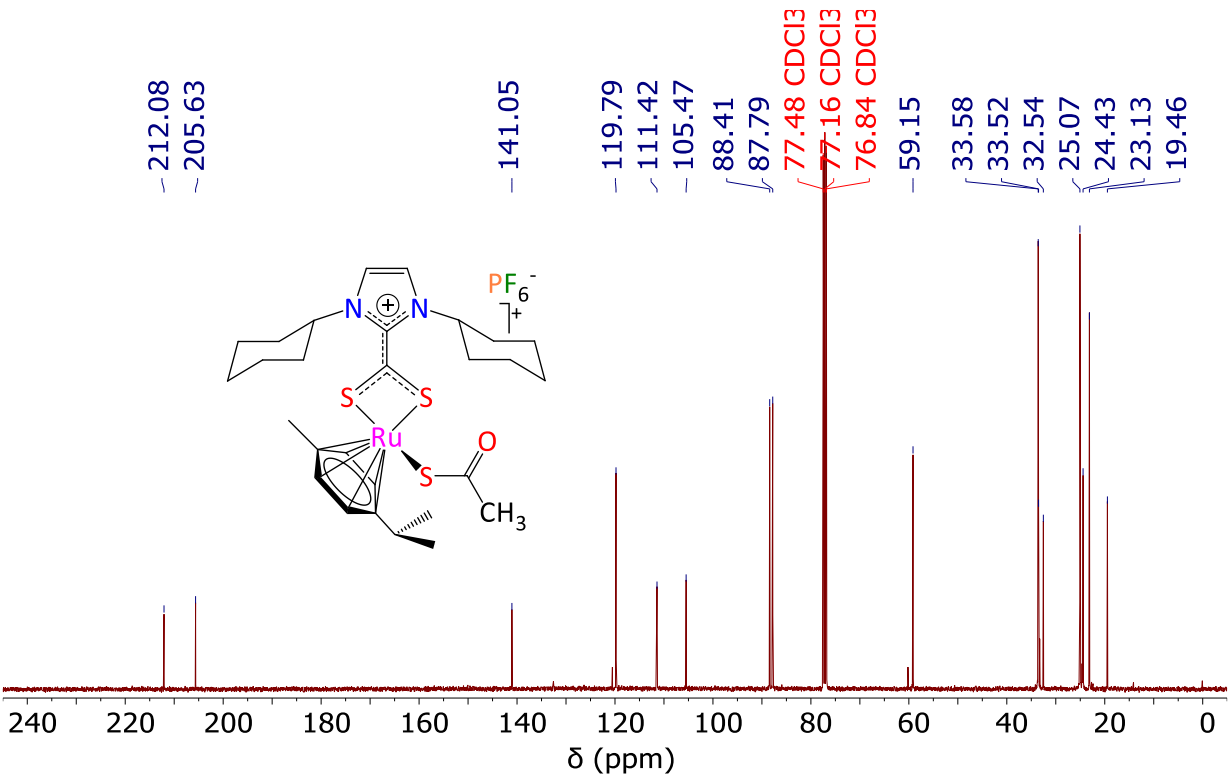

Fig. S12. ^{13}C{^{1}H} NMR spectrum (101 MHz, $CDCl_3$, 298 K) of [Ru(κ^1-*S*-SAc)(κ^2-*S,S'*-S_2C·ICy)(*p*-cymene)](PF_6) (**5c**)

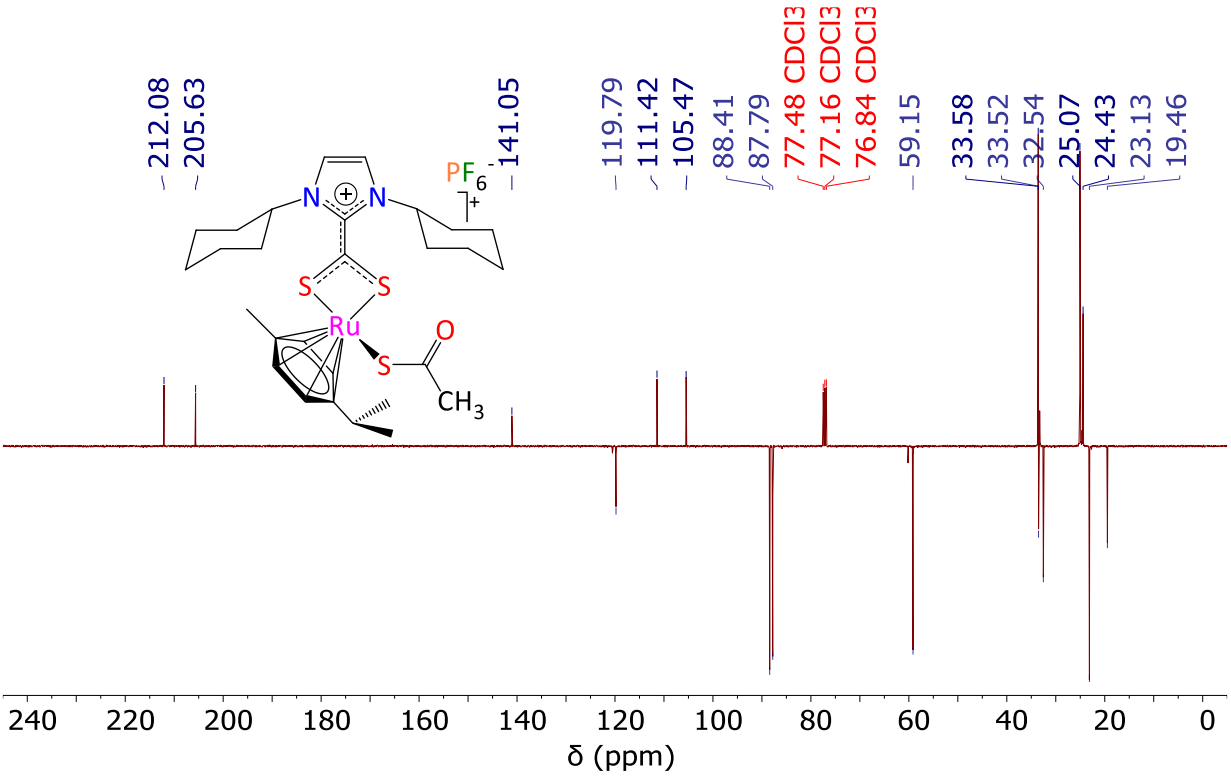

Fig. S13. APT NMR spectrum (101 MHz, $CDCl_3$, 298 K) of [Ru(κ^1-*S*-SAc)(κ^2-*S,S'*-S_2C·ICy)-(*p*-cymene)](PF_6) (**5c**)

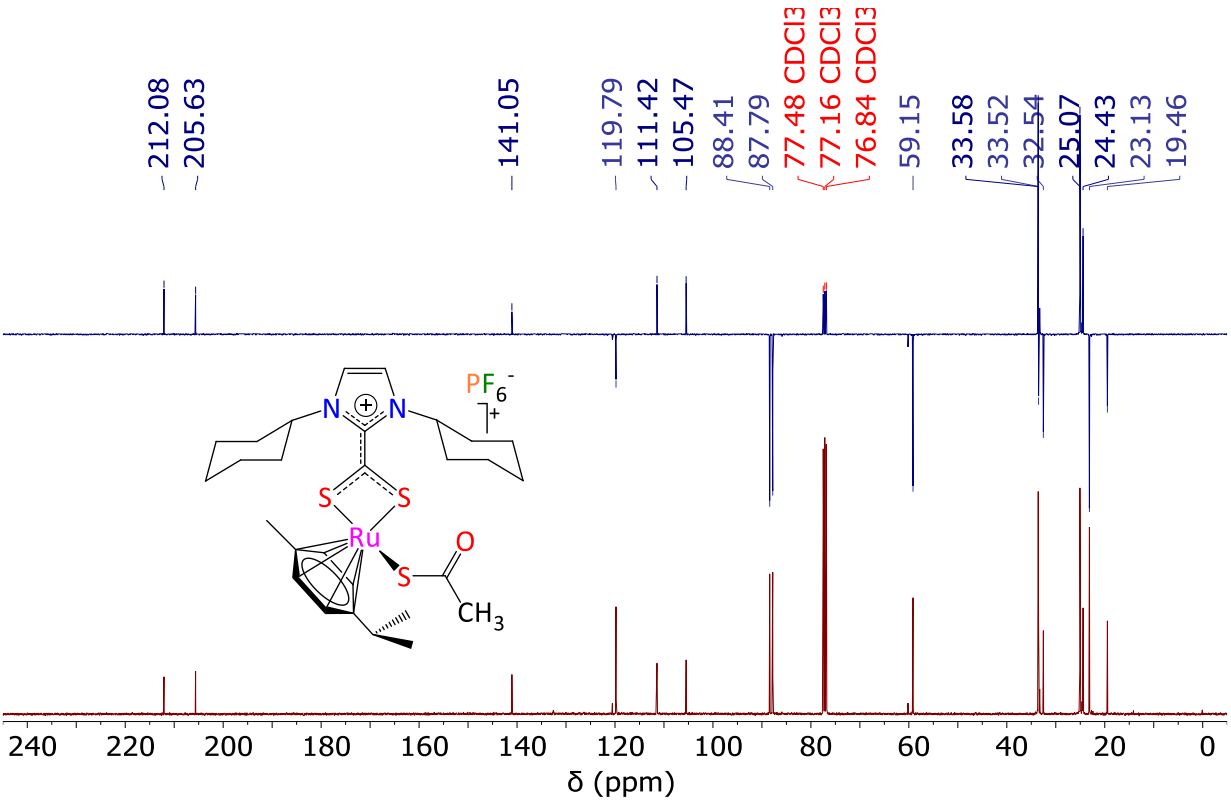

Fig. S14. ^{13}C and APT NMR spectrum (101 MHz, $CDCl_3$, 298 K) of [Ru(κ^1-*S*-SAc)(κ^2-*S,S'*-S_2C·ICy)(*p*-cymene)](PF_6) (**5c**)

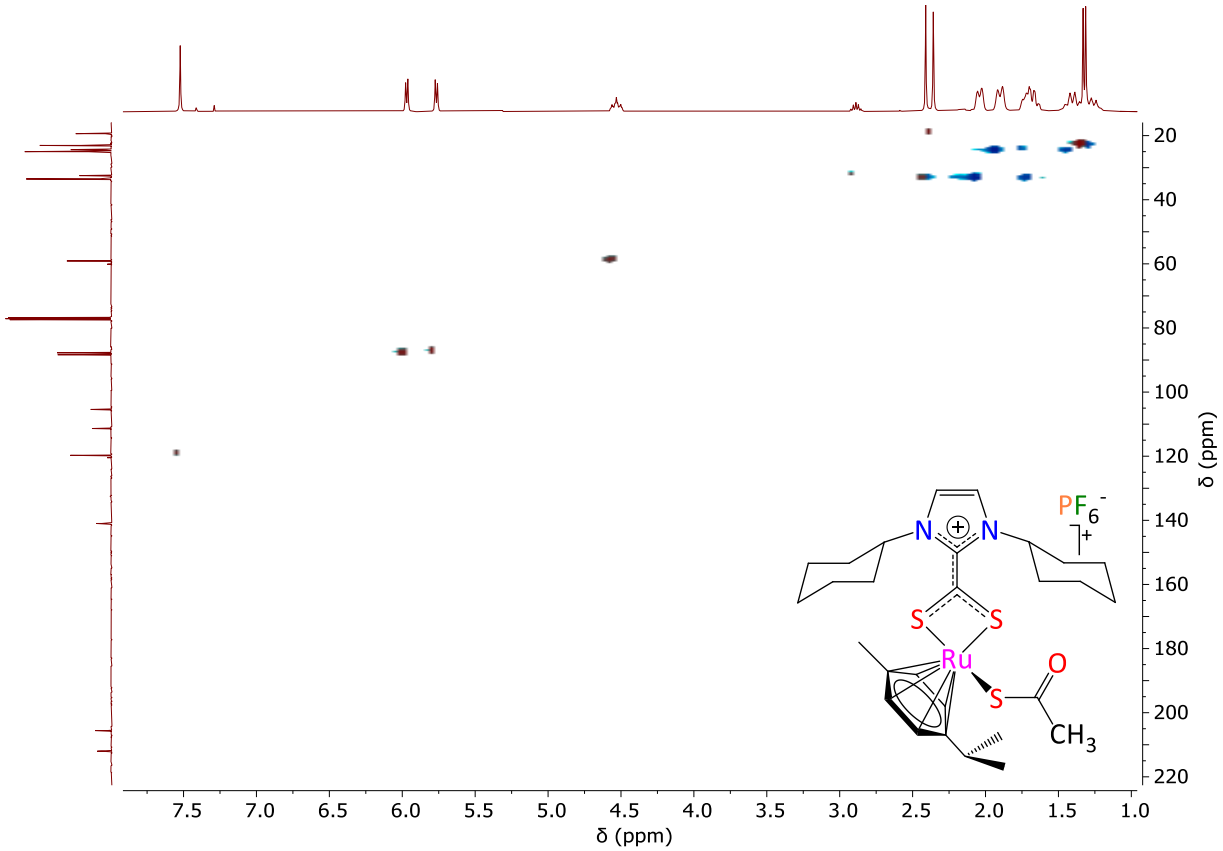

Fig. S15. HSQC spectrum of [Ru(κ^1-*S*-SAc)(κ^2-*S,S'*-S_2C·ICy)(*p*-cymene)](PF_6) (**5c**)

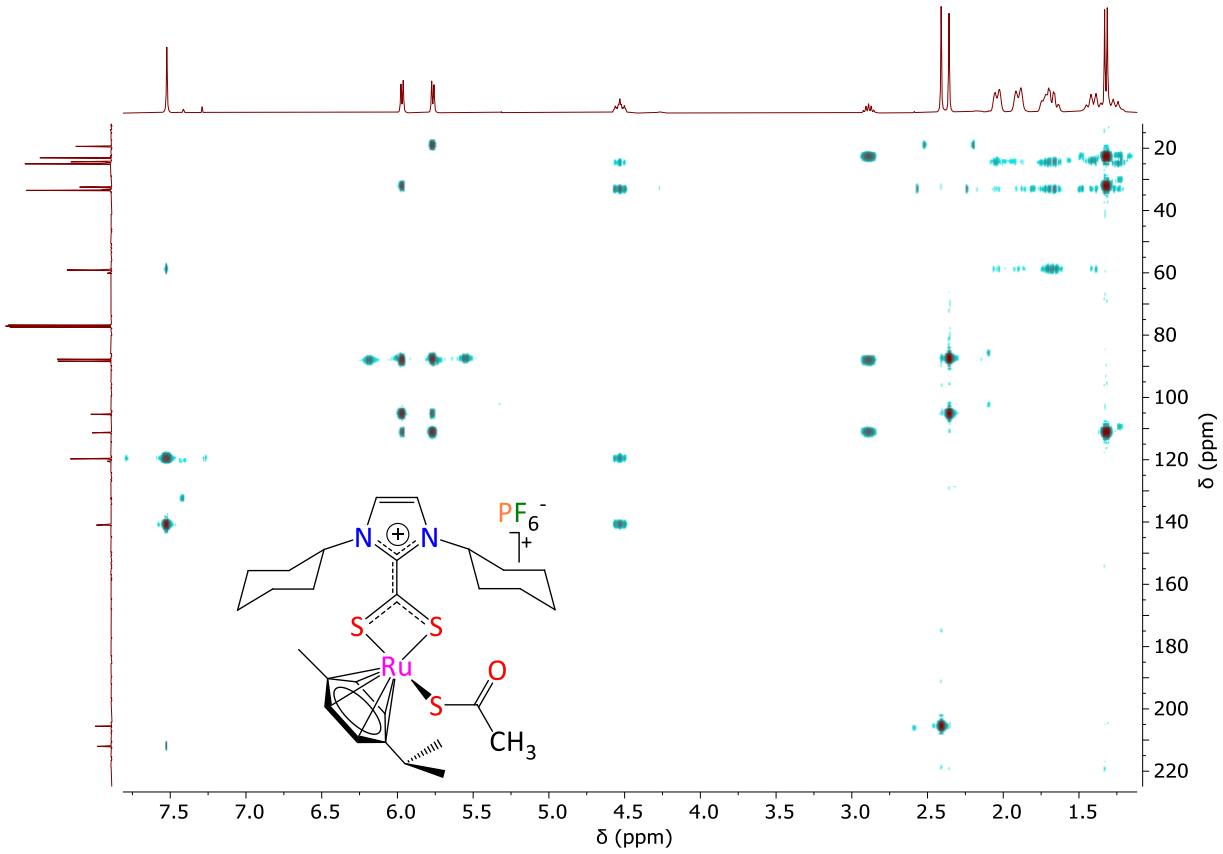

Fig. S16. HMBC spectrum of [Ru(κ^1-*S*-SAc)(κ^2-*S,S'*-S_2C·ICy)(*p*-cymene)](PF_6) (**5c**)

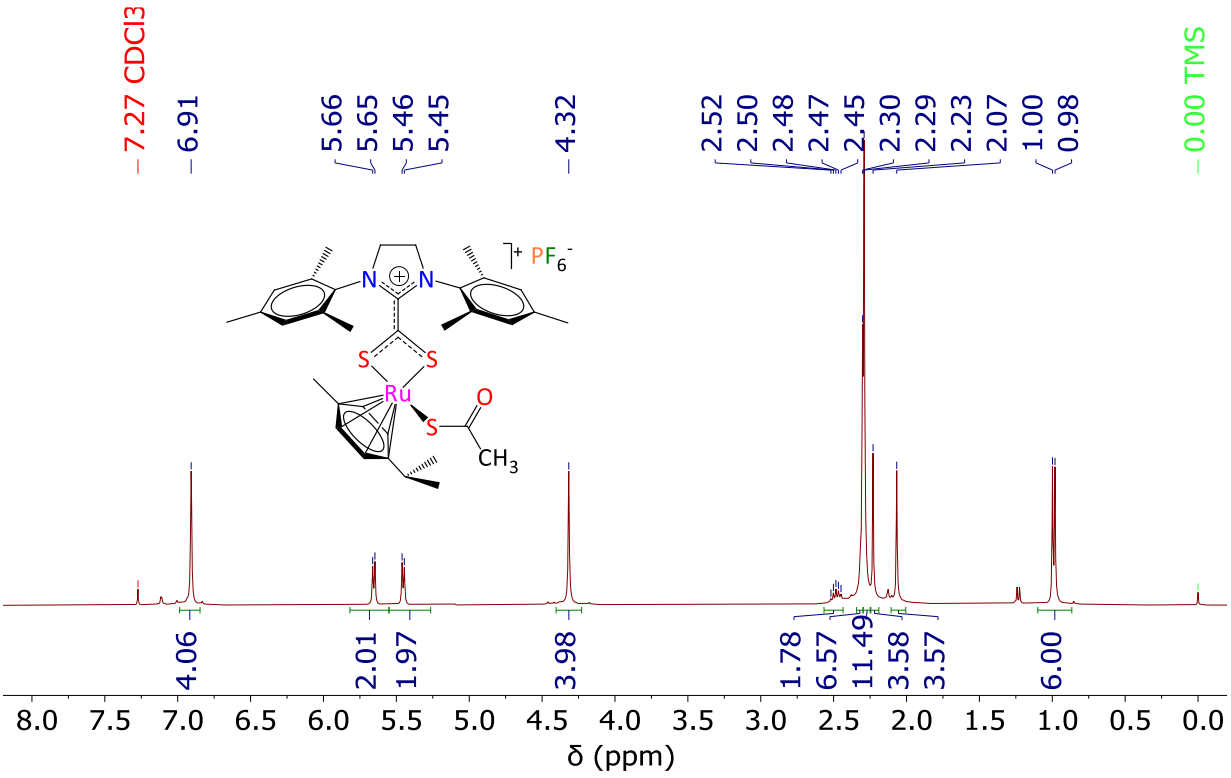

Fig. S17. ^{1}H NMR spectrum (400 MHz, $CDCl_3$, 298 K) of [Ru(κ^1-*S*-SAc)(κ^2-*S,S'*-S_2C·SIMes)(*p*-cymene)](PF_6) (**5d**)

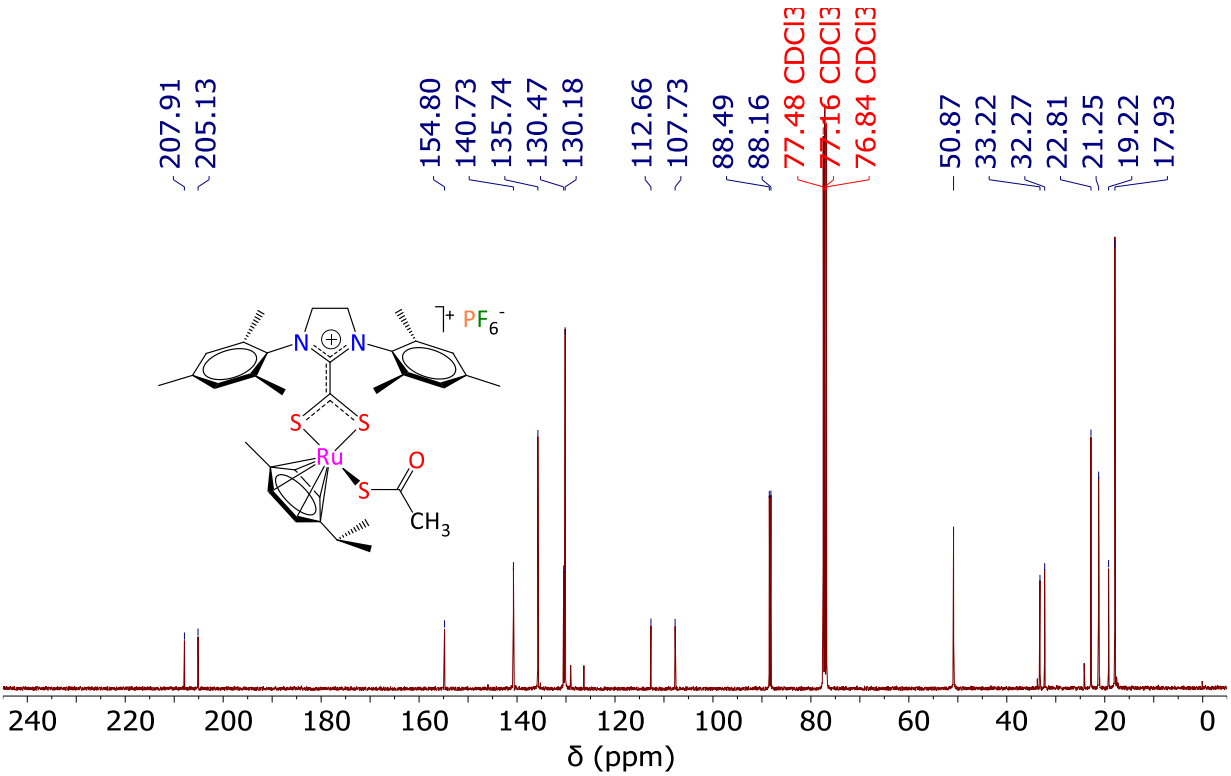

Fig. S18. ^{13}C{^{1}H} NMR spectrum (101 MHz, $CDCl_3$, 298 K) of [Ru(κ^1-*S*-SAc)(κ^2-*S,S'*-S_2C·SIMes)(*p*-cymene)](PF_6) (**5d**)

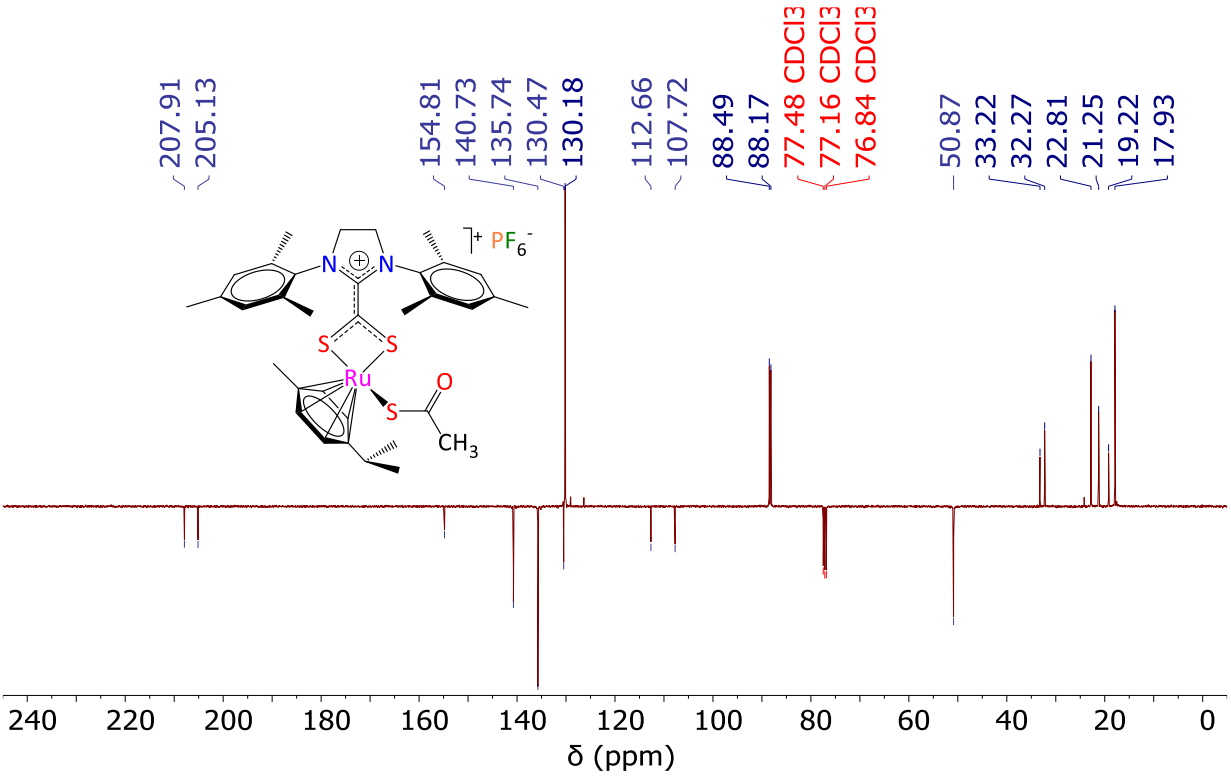

Fig. S19. APT NMR spectrum (101 MHz, $CDCl_3$, 298 K) of [Ru(κ^1-*S*-SAc)(κ^2-*S,S'*-S_2C·SIMes)(*p*-cymene)](PF_6) (**5d**)

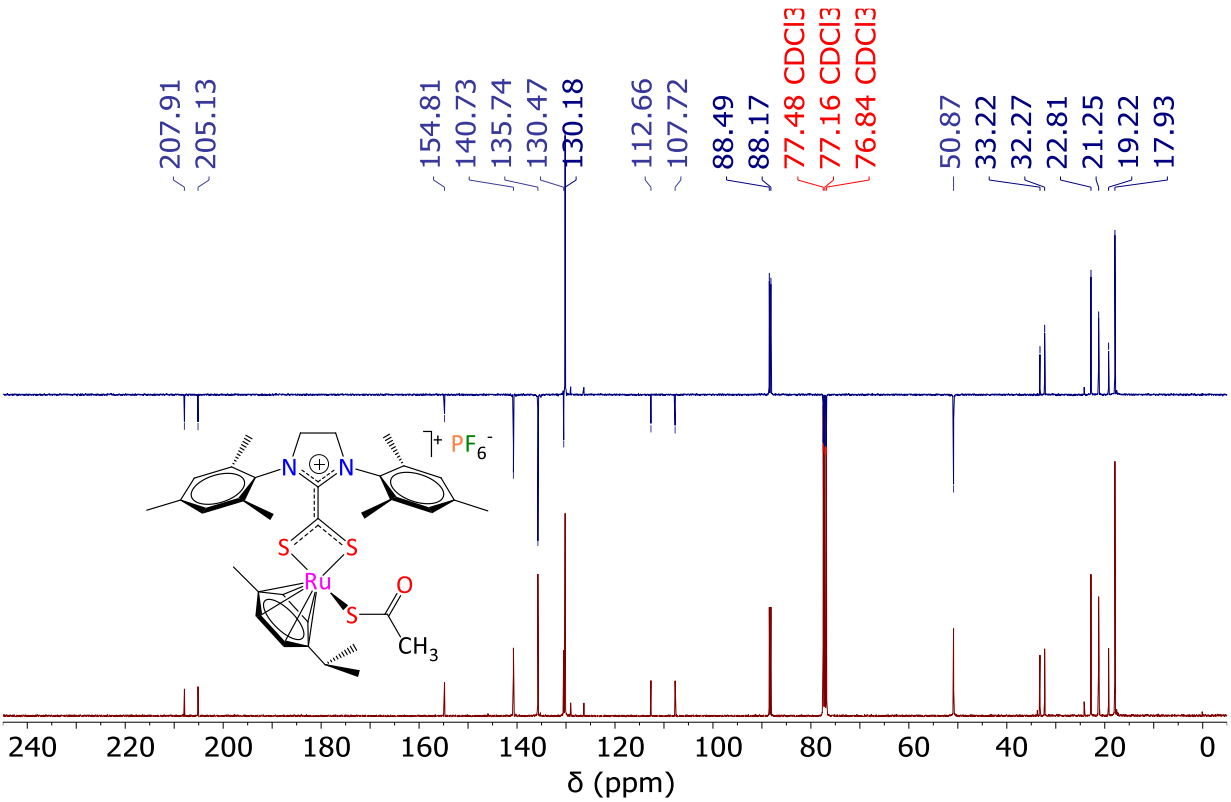

Fig. S20. ^{13}C and APT NMR spectrum (101 MHz, $CDCl_3$, 298 K) of [Ru(κ^1-*S*-SAc)(κ^2-*S,S'*-S_2C·SIMes)(*p*-cymene)](PF_6) (**5d**)

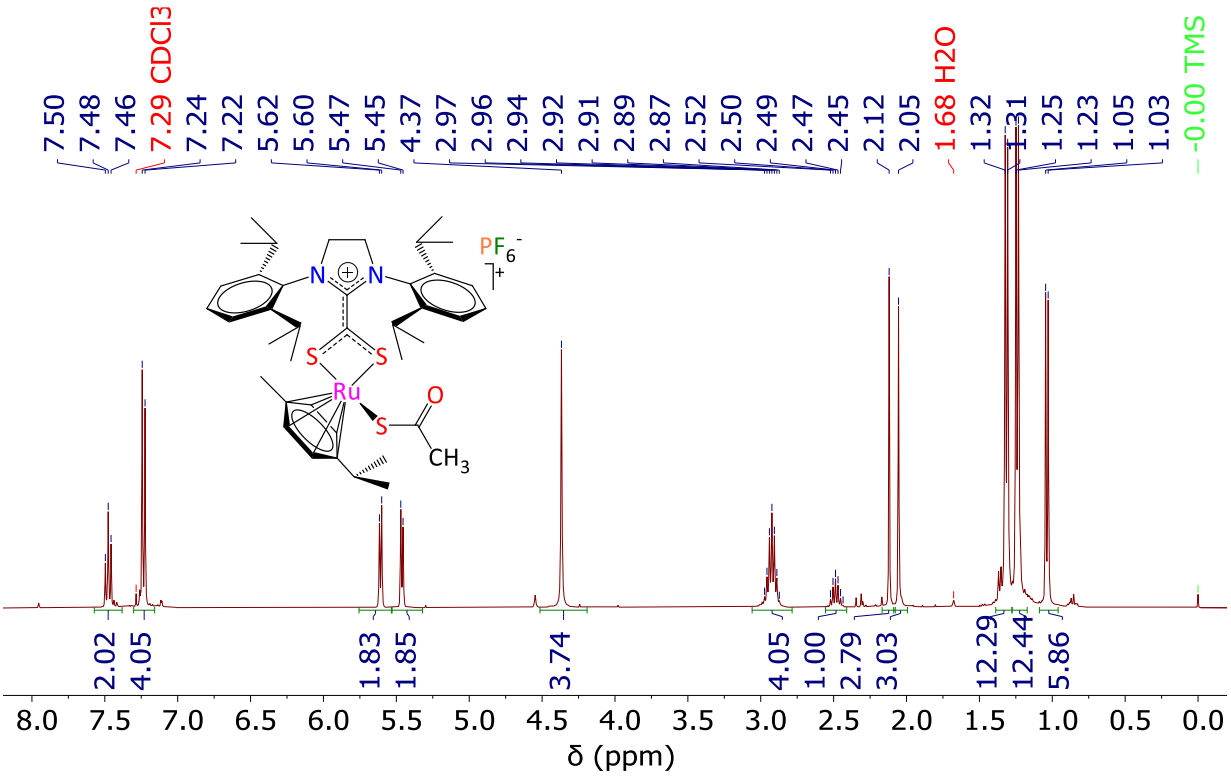

Fig. S21. ^{1}H NMR spectrum (400 MHz, $CDCl_3$, 298 K) of [Ru(κ^1-*S*-SAc)(κ^2-*S,S'*-S_2C·SIDip)-(*p*-cymene)](PF_6) (**5e**)

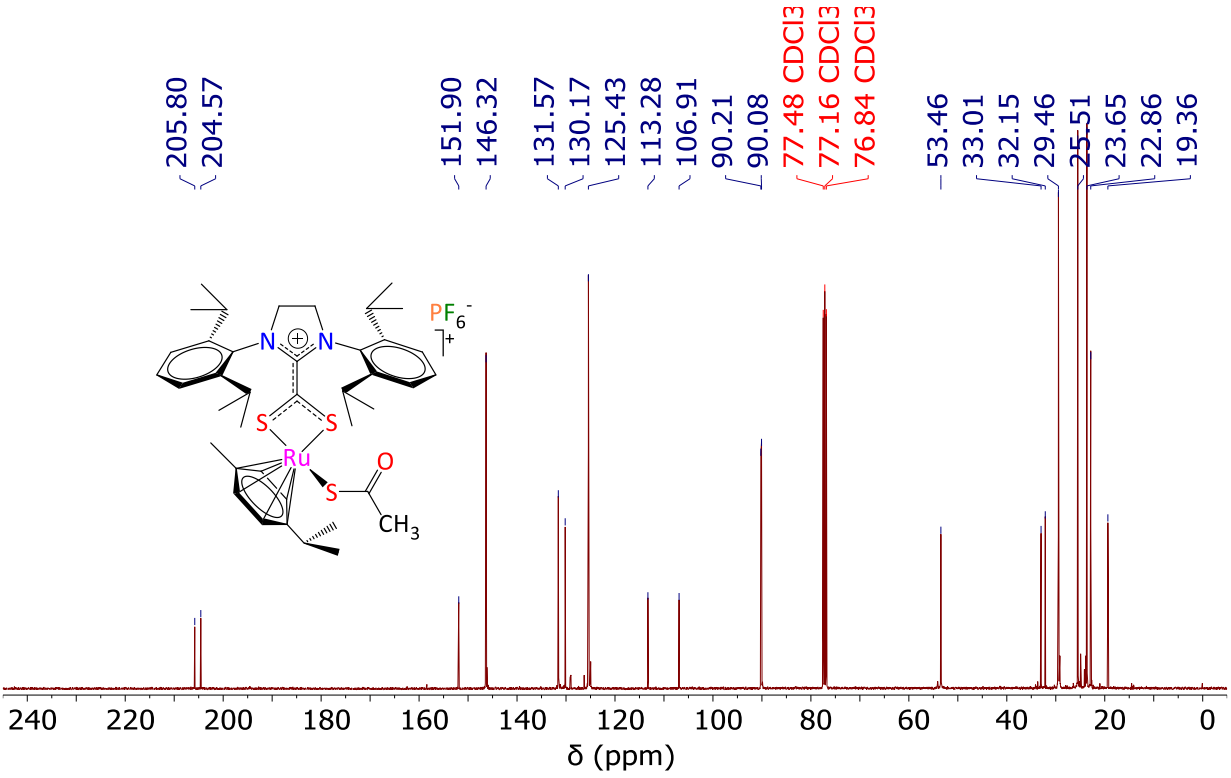

Fig. S22. ^{13}C{^{1}H} NMR spectrum (101 MHz, $CDCl_3$, 298 K) of [Ru(κ^1-*S*-SAc)(κ^2-*S,S'*-S_2C·SIDip)(*p*-cymene)](PF_6) (**5e**)

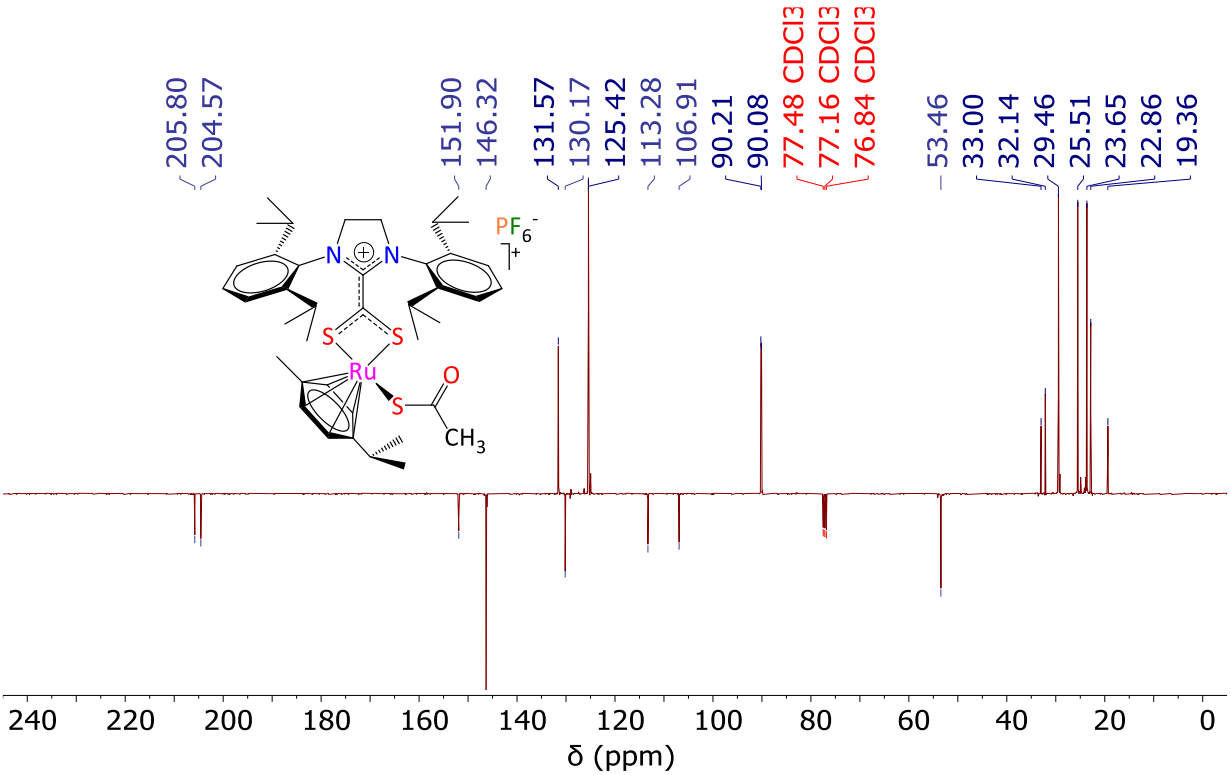

Fig. S23. APT NMR spectrum (101 MHz, $CDCl_3$, 298 K) of [Ru(κ^1-*S*-SAc)(κ^2-*S,S'*-S_2C·SIDip)(*p*-cymene)](PF_6) (**5e**)

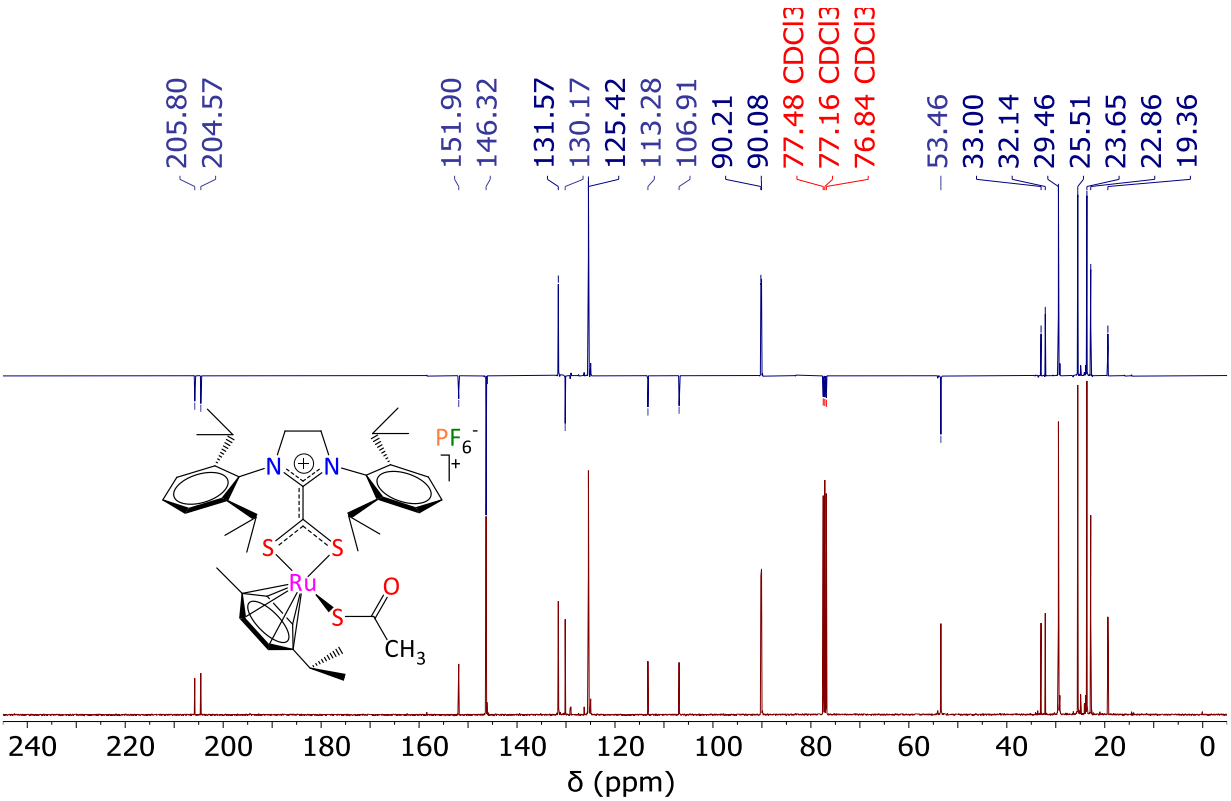

Fig. S24. ^{13}C and APT NMR spectrum (101 MHz, $CDCl_3$, 298 K) of [Ru(κ^1-*S*-SAc)(κ^2-*S,S'*-S_2C·SIDip)(*p*-cymene)](PF_6) (**5e**)

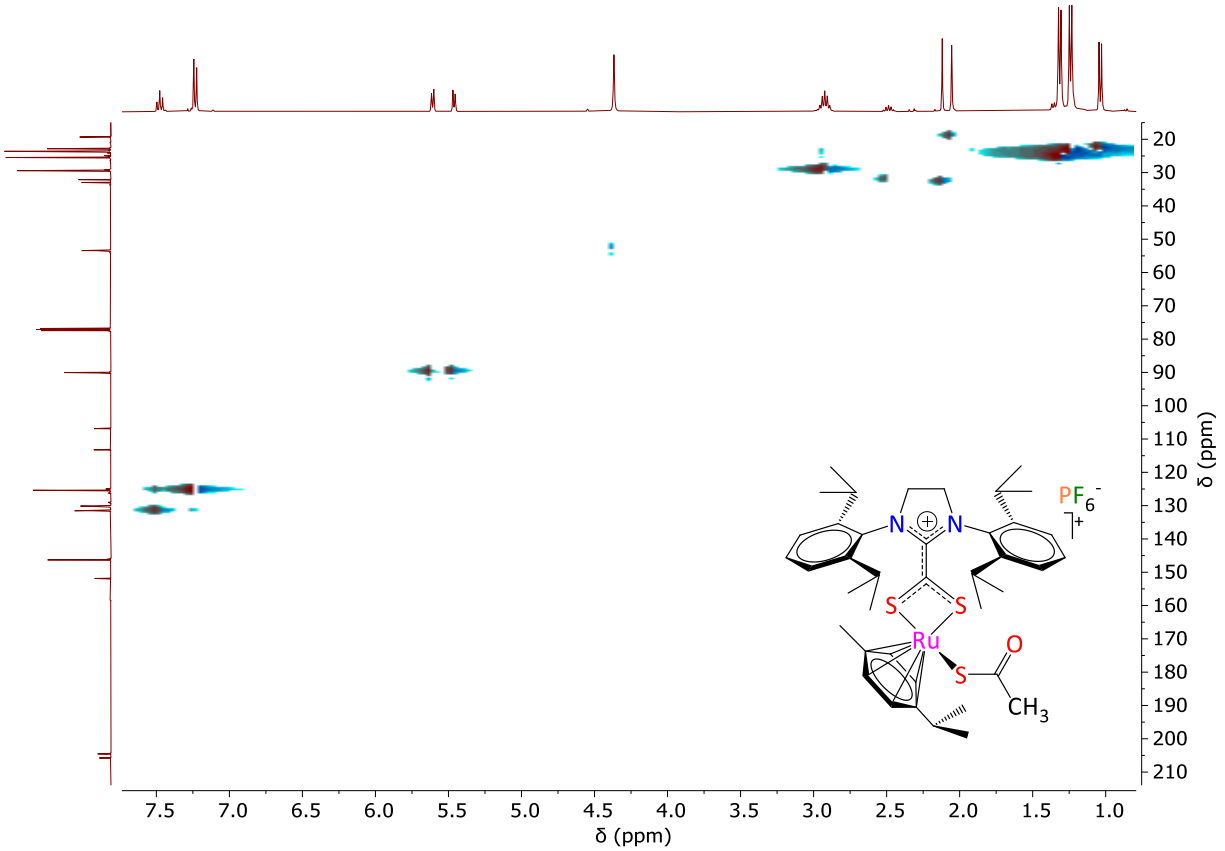

Fig. S25. HSQC spectrum of [Ru(κ^1-*S*-SAc)(κ^2-*S,S'*-S_2C·SIDip)(*p*-cymene)](PF_6) (**5e**)

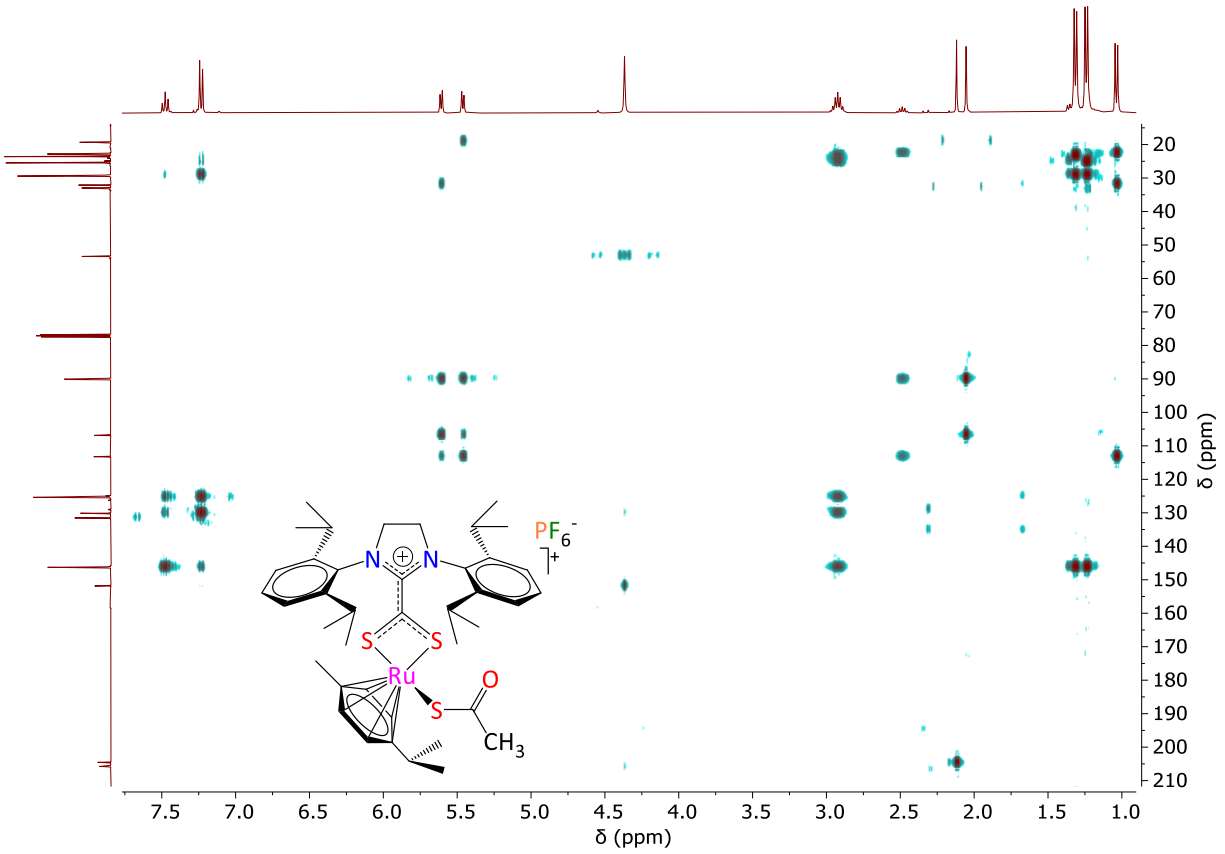

Fig. S26. HMBC spectrum of [Ru(κ^1-*S*-SAc)(κ^2-*S,S'*-S_2C·SIDip)(*p*-cymene)](PF_6) (**5e**)

Part 2 – IR spectra

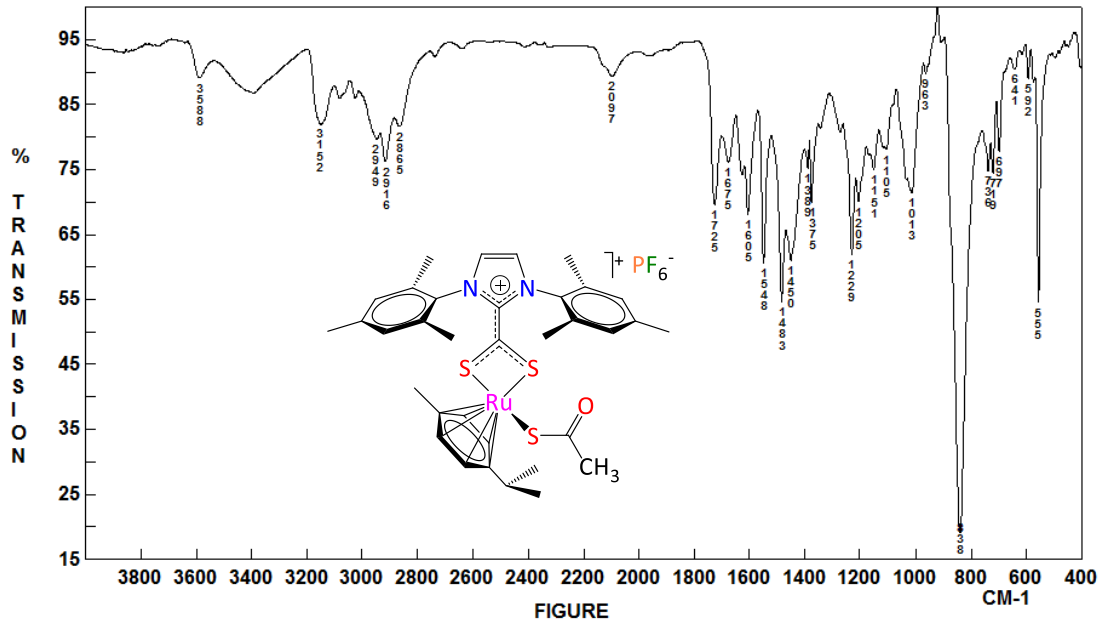

Fig. S27. FT-IR spectrum (KBr) of [Ru(κ^1-*S*-SAc)(κ^2-*S,S'*-S$_2$C·IMes)(*p*-cymene)](PF$_6$) (**5a**)

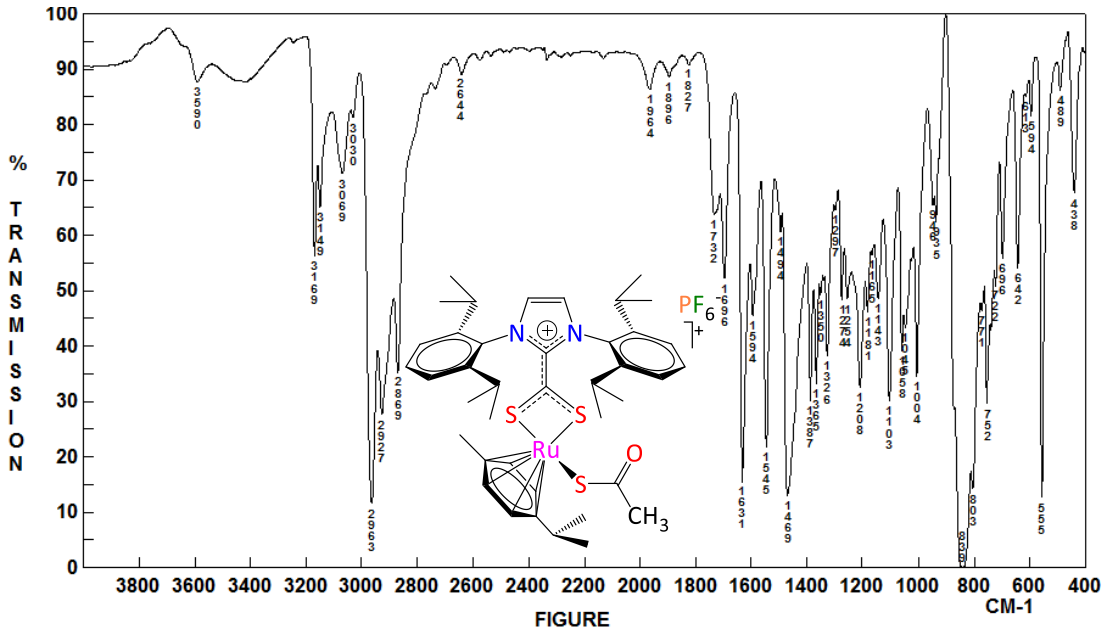

Fig. S28. FT-IR spectrum (KBr) of [Ru(κ^1-*S*-SAc)(κ^2-*S,S'*-S$_2$C·IDip)(*p*-cymene)](PF$_6$) (**5b**)

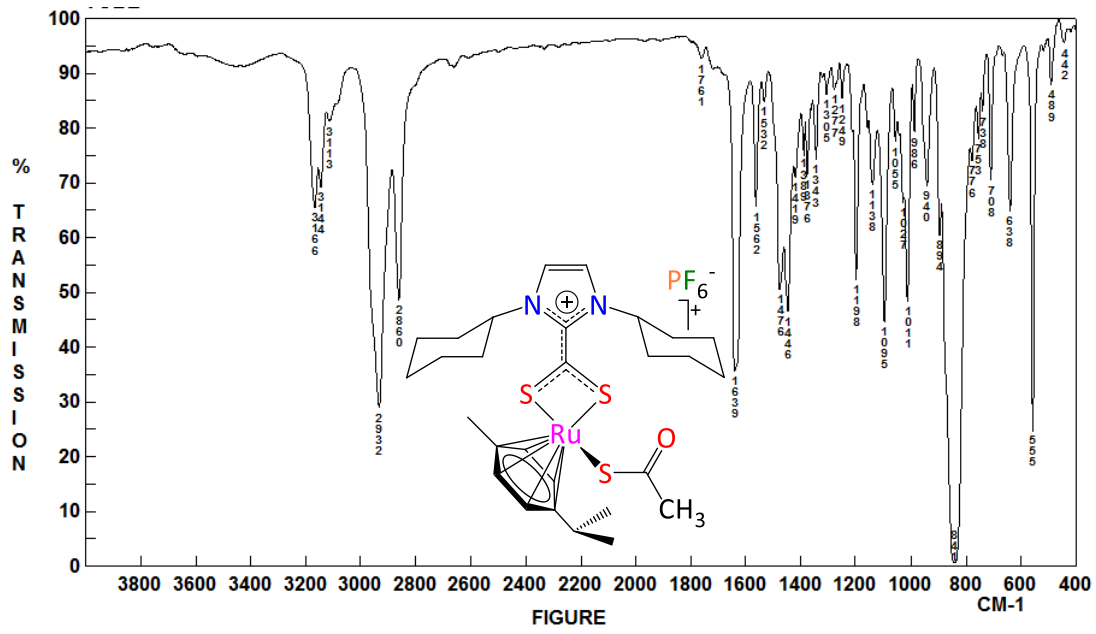

Fig. S29. FT-IR spectrum (KBr) of [Ru(κ^1-*S*-SAc)(κ^2-*S,S'*-S$_2$C·ICy)(*p*-cymene)](PF$_6$) (**5c**)

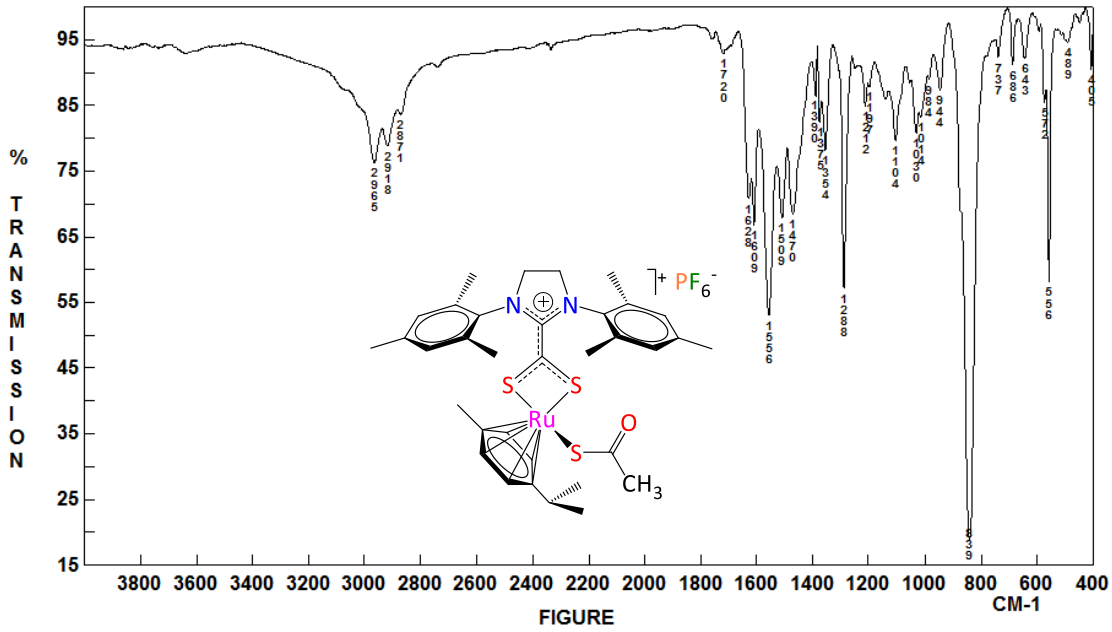

Fig. S30. FT-IR spectrum (KBr) of [Ru(κ^1-*S*-SAc)(κ^2-*S,S'*-S$_2$C·SIMes)(*p*-cymene)](PF$_6$) (**5d**)

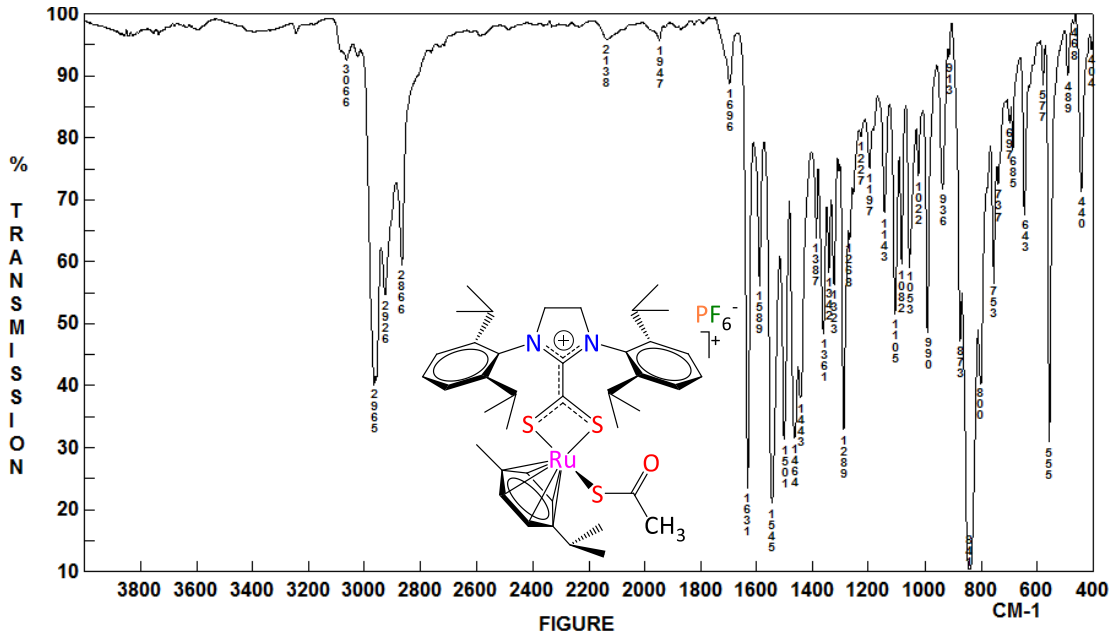

Fig. S31. FT-IR spectrum (KBr) of [Ru(κ^1-*S*-SAc)(κ^2-*S,S'*-S_2C·SIDip)(*p*-cymene)](PF_6) (**5e**)

Part 3 – Mass spectra

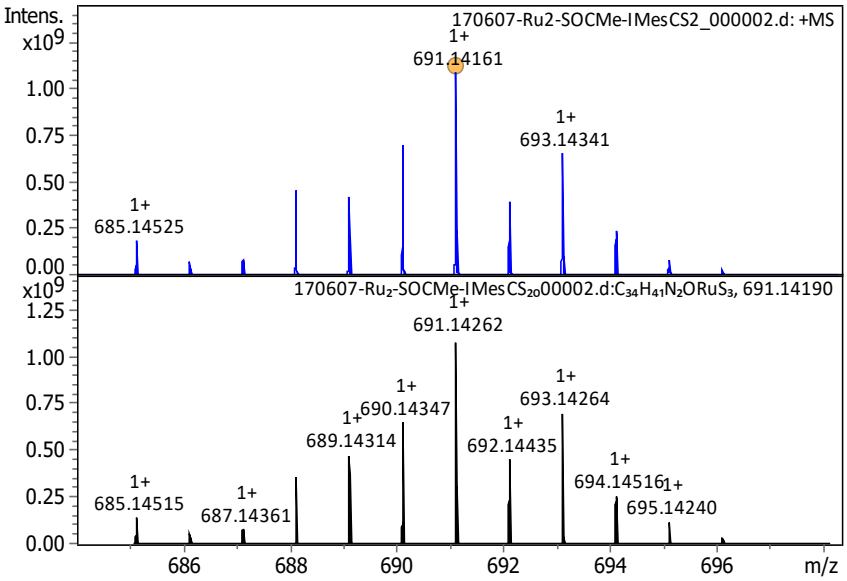

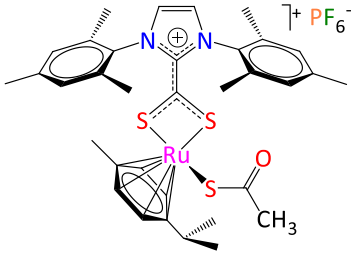

CF: $C_{34}H_{41}N_2ORuS_3^+$
Exact Mass: 691.14190

Fig. S32. HR-MS spectrum (CH_3CN, positive mode) of [Ru(κ^1-*S*-SAc)(κ^2-*S,S'*-S_2C·IMes)(*p*-cymene)](PF_6) (**5a**): isotope profile observed by ESI-MS for the [Ru(κ^1-*S*-SAc)(κ^2-*S,S'*-S_2C·IMes)(*p*-cymene)]$^+$ cation (top, blue) and simulated isotope pattern (bottom, black).

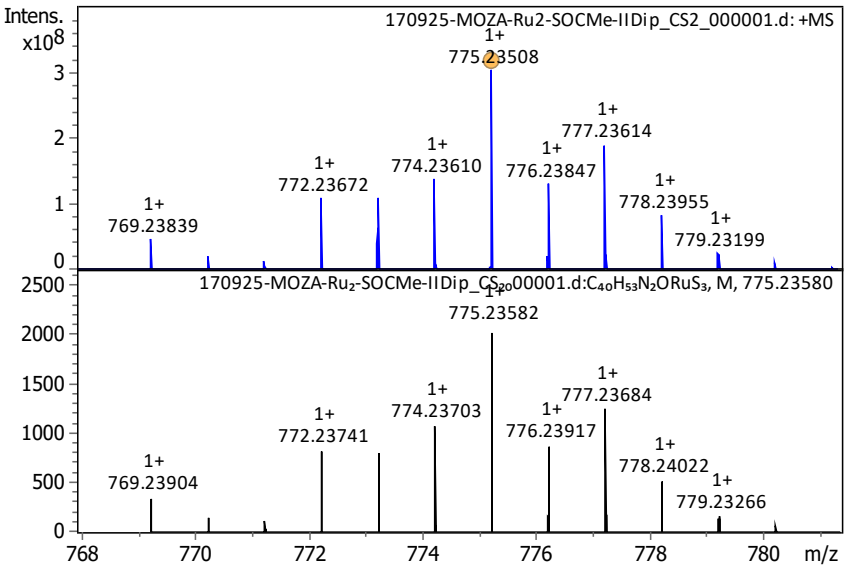

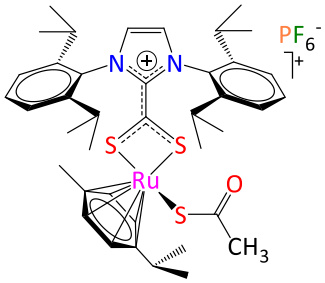

CF: $C_{40}H_{53}N_2ORuS_3^+$
Exact Mass: 775.23580

Fig. S33. HR-MS spectrum (CH_3CN, positive mode) of [Ru(κ^1-*S*-SAc)(κ^2-*S,S'*-S_2C·IDip)(*p*-cymene)](PF_6) (**5b**): isotope profile observed by ESI-MS for the [Ru(κ^1-*S*-SAc)(κ^2-*S,S'*-S_2C·IDip)(*p*-cymene)]$^+$ cation (top, blue) and simulated isotope pattern (bottom, black).

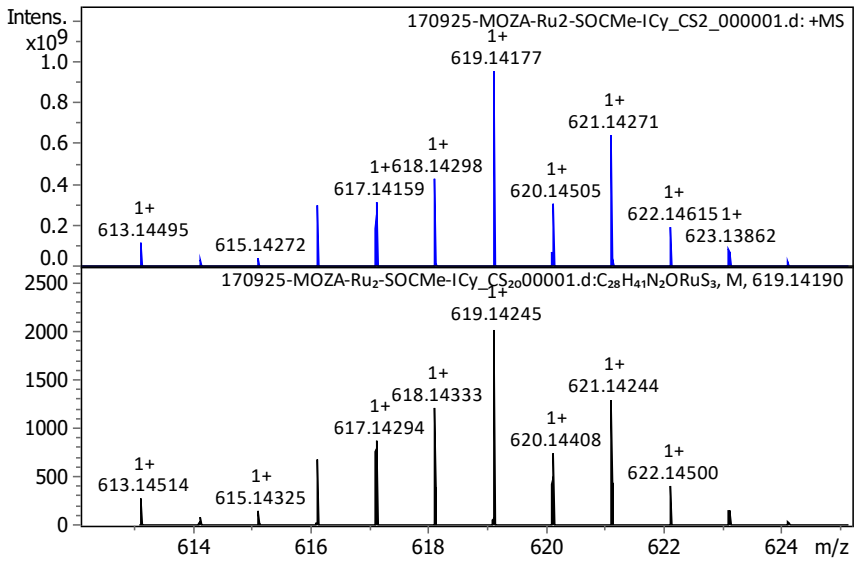

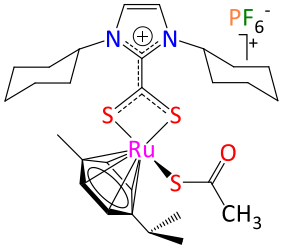

CF: $C_{28}H_{41}N_2ORuS_3^+$
Exact Mass: 619.14190

Fig. S34. HR-MS spectrum (CH_3CN, positive mode) of [Ru(κ^1-*S*-SAc)(κ^2-*S,S'*-S_2C·ICy)(*p*-cymene)](PF_6) (**5c**): isotope profile observed by ESI-MS for the [Ru(κ^1-*S*-SAc)(κ^2-*S,S'*-S_2C·ICy)(*p*-cymene)]$^+$ cation (top, blue) and simulated isotope pattern (bottom, black).

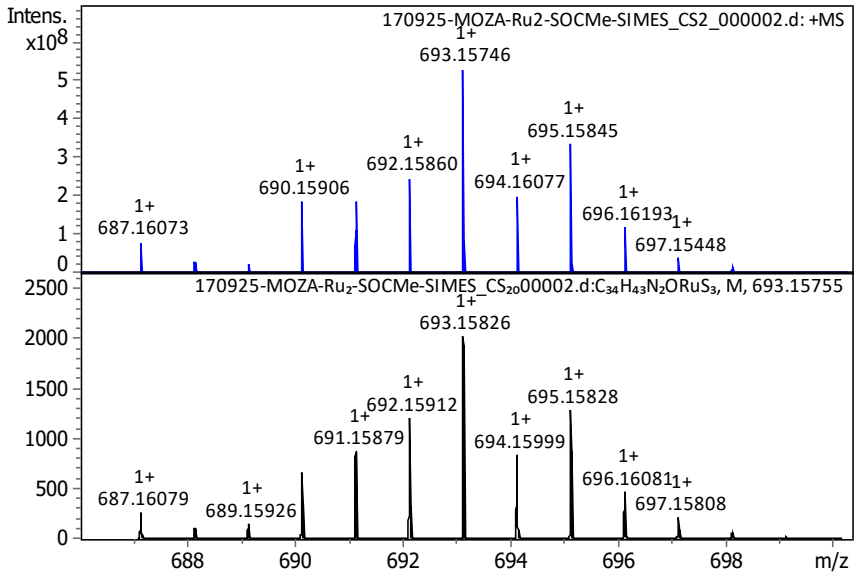

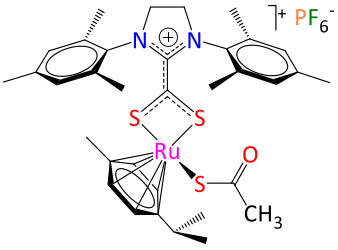

CF: $C_{34}H_{43}N_2ORuS_3^+$
Exact Mass: 693.15755

Fig. S35. HR-MS spectrum (CH_3CN, positive mode) of [Ru(κ^1-*S*-SAc)(κ^2-*S,S'*-S_2C·SIMes)(*p*-cymene)](PF_6) (**5d**): isotope profile observed by ESI-MS for the [Ru(κ^1-*S*-SAc)(κ^2-*S,S'*-S_2C·SIMes)(*p*-cymene)]$^+$ cation (top, blue) and simulated isotope pattern (bottom, black).

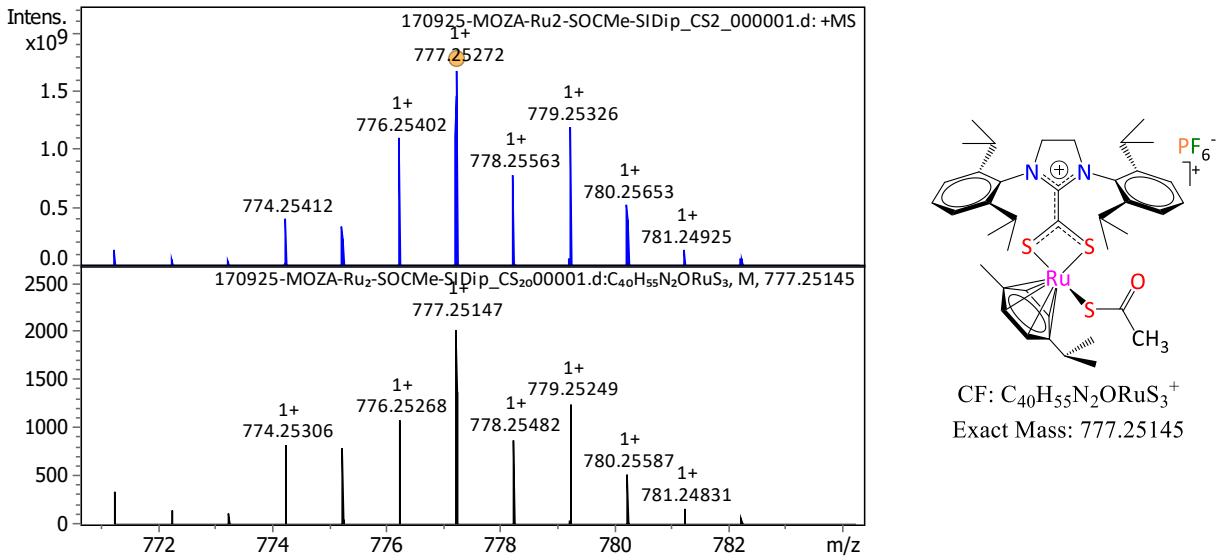

CF: $C_{40}H_{55}N_2ORuS_3^+$
Exact Mass: 777.25145

Fig. S36. HR-MS spectrum (CH_3CN, positive mode) of [Ru(κ^1-*S*-SAc)(κ^2-*S,S'*-S_2C·SIDip)(*p*-cymene)](PF_6) (**5e**): isotope profile observed by ESI-MS for the [Ru(κ^1-*S*-SAc)(κ^2-*S,S'*-S_2C·SIDip)(*p*-cymene)]$^+$ cation (top, blue) and simulated isotope pattern (bottom, black).

Part 4 – Stability in solution

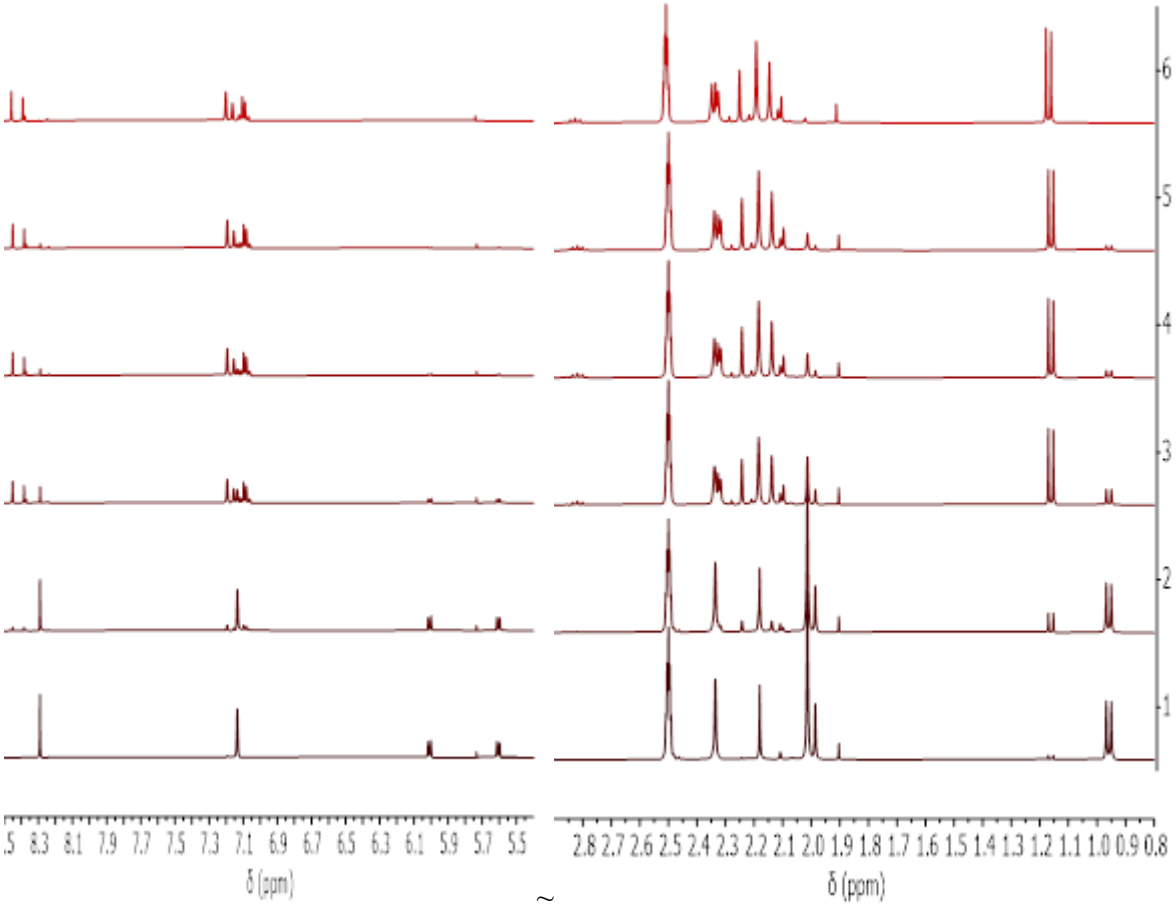

Fig. S37. Stacked ^{1}H NMR spectra (400 MHz, moist DMSO-d_6, 298 K) of [Ru(κ^1-*S*-SOCMe)-(κ^2-*S,S'*-S$_2$C·IMes)(*p*-cymene)](PF$_6$) (**5a**) after 0.04, 1.05, 7.45, 11.34, 13.44, and 22.43 days at room temperature.

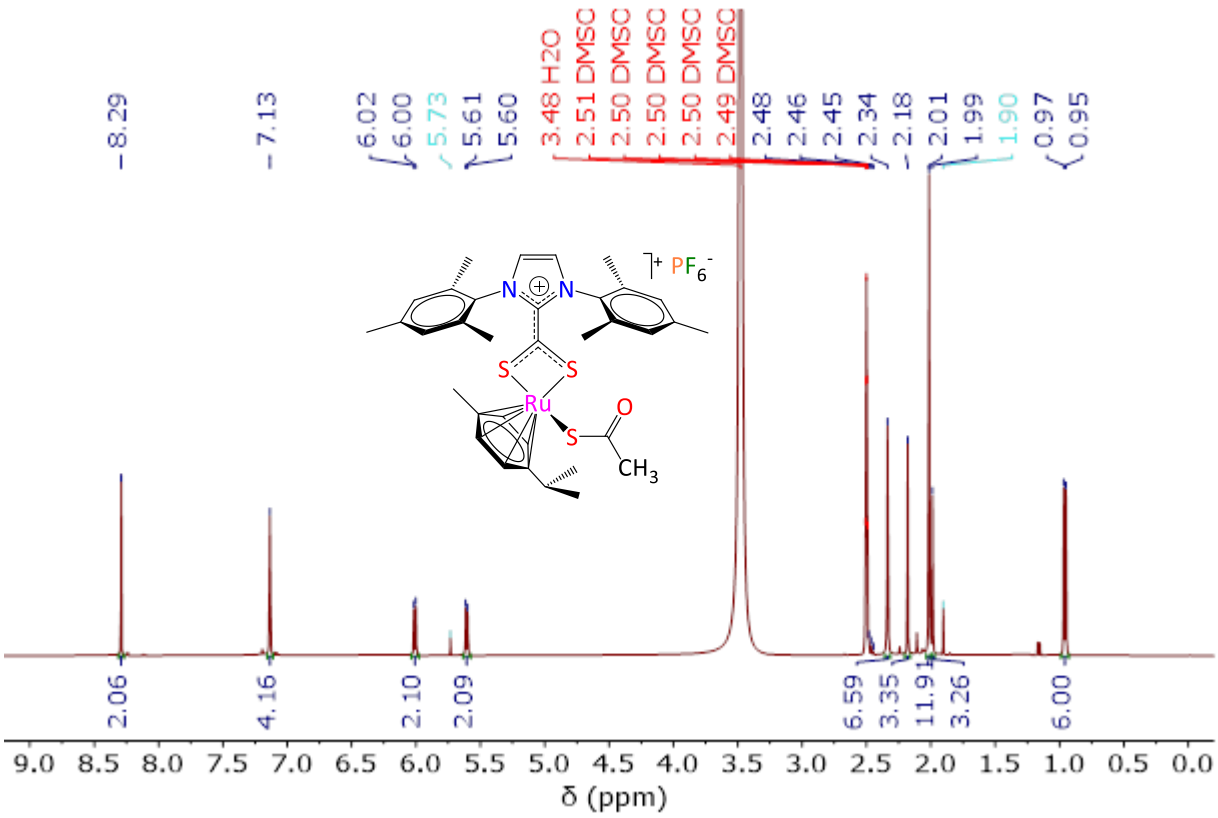

Fig. S38. ^{1}H NMR spectrum (400 MHz, moist DMSO-d_6, 298 K) of [Ru(κ^1-S-SOCMe)-(κ^2-*S,S′*-S$_2$C·IMes)(*p*-cymene)](PF$_6$) (**5a**) after 1 h in solution at room temperature.

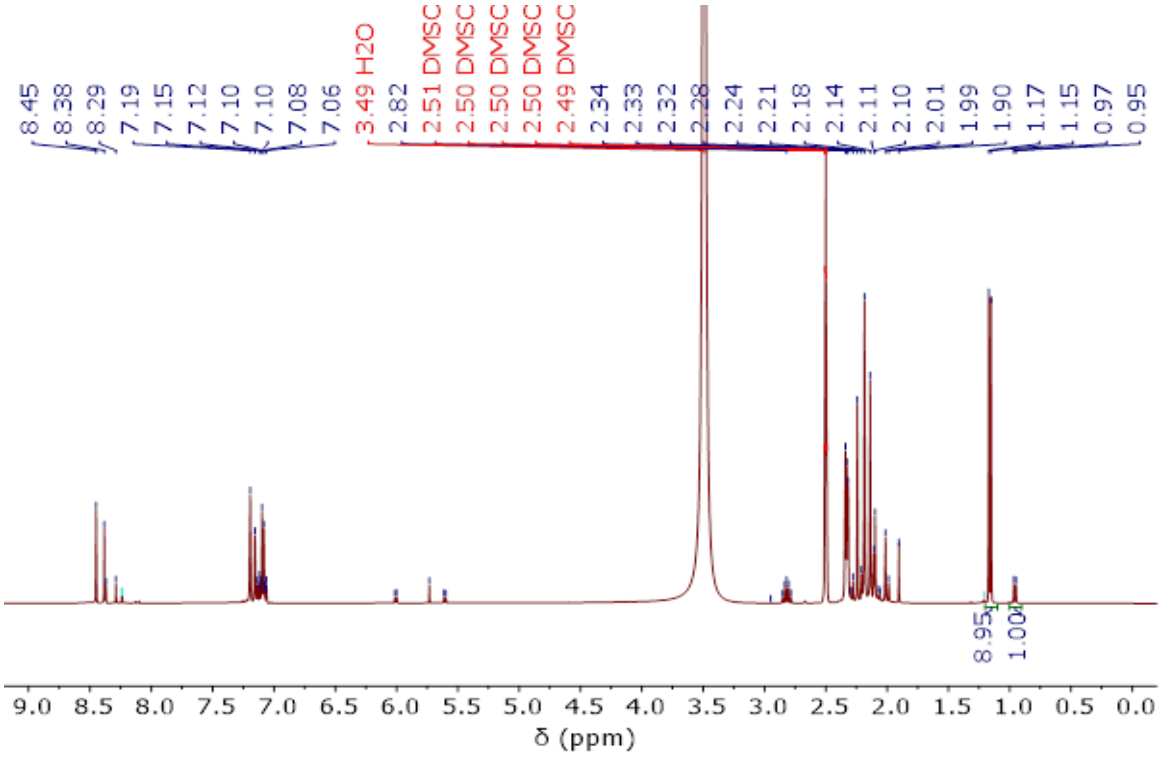

Fig. S39. ^{1}H NMR spectrum (400 MHz, moist DMSO-d_6, 298 K) of [Ru(*κ*^{1}-*S*-SOCMe)-(*κ*^{2}-*S,S′*-S$_2$C·IMes)(*p*-cymene)](PF$_6$) (**5a**) after 13.44 days in solution at room temperature.

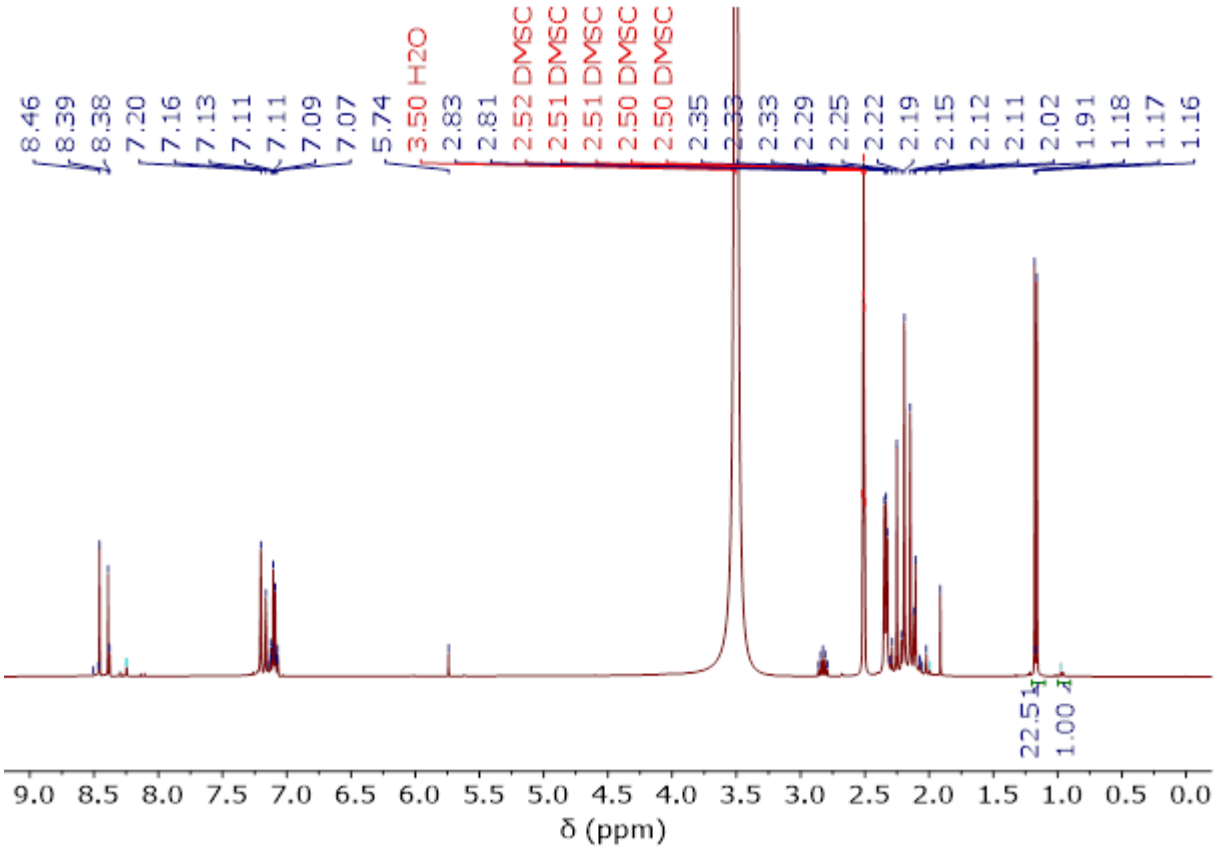

Fig. S40. ^{1}H NMR spectrum (400 MHz, moist DMSO-d_6, 298 K) of [Ru(κ^1-*S*-SOCMe)-(κ^2-*S,S'*-S$_2$C·IMes)(*p*-cymene)](PF$_6$) (**5a**) after 22.43 days in solution at room temperature.

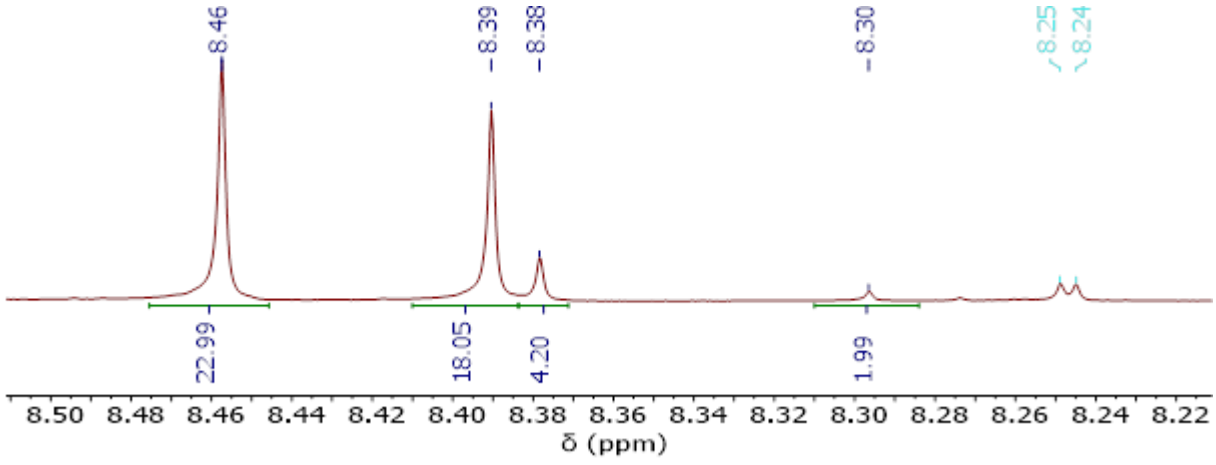

Fig. S41. Enlarged ^{1}H NMR spectrum (400 MHz, moist DMSO-d_6, 298 K) of [Ru(κ^1-*S*-SOCMe)(κ^2-*S,S'*-S$_2$C·IMes)(*p*-cymene)](PF$_6$) (**5a**) after 22.43 days in solution at room temperature showing the imidazolium protons.

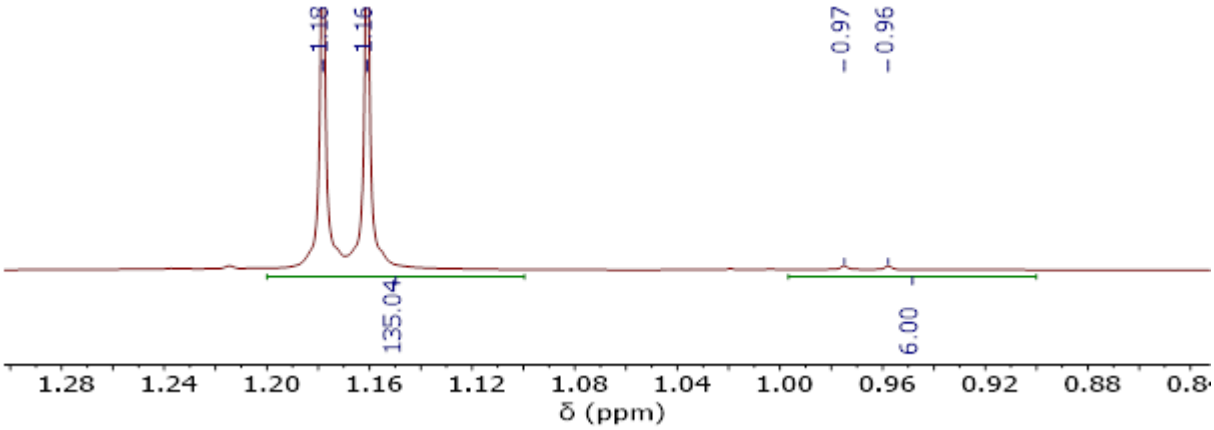

Fig. S42. Enlarged ^{1}H NMR spectrum (400 MHz, moist DMSO-d_6, 298 K) of [Ru(κ^1-*S*-SOCMe)(κ^2-*S,S'*-S$_2$C·IMes)(*p*-cymene)](PF$_6$) (**5a**) after 22.43 days in solution at room temperature showing the methyl protons of the isopropyl groups.

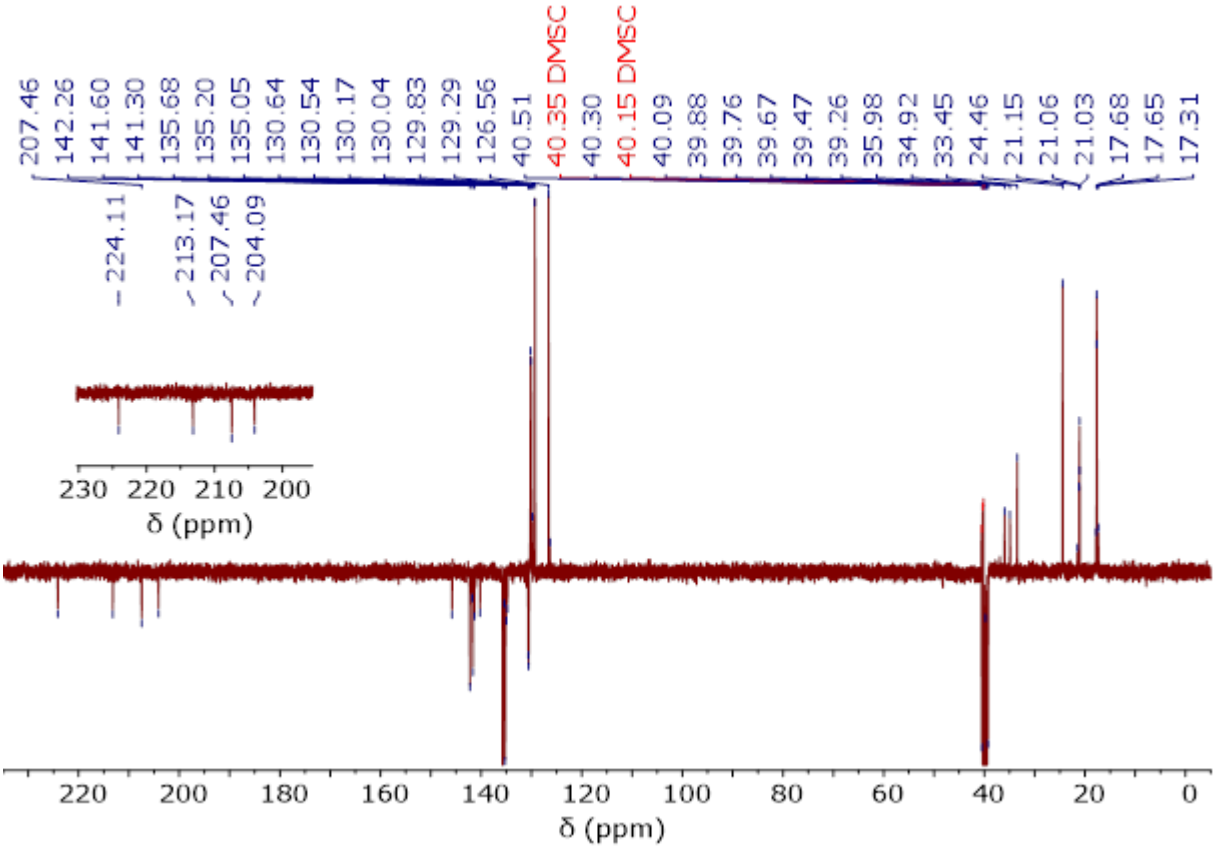

Fig. S43. APT NMR spectrum (101 MHz, moist DMSO-d_6, 298 K) of [Ruκ^1-*S*-SOCMe)-(κ^2-*S,S'*-S$_2$C·IMes)(*p*-cymene)](PF$_6$) (**5a**) after 22.43 days in solution at room temperature.

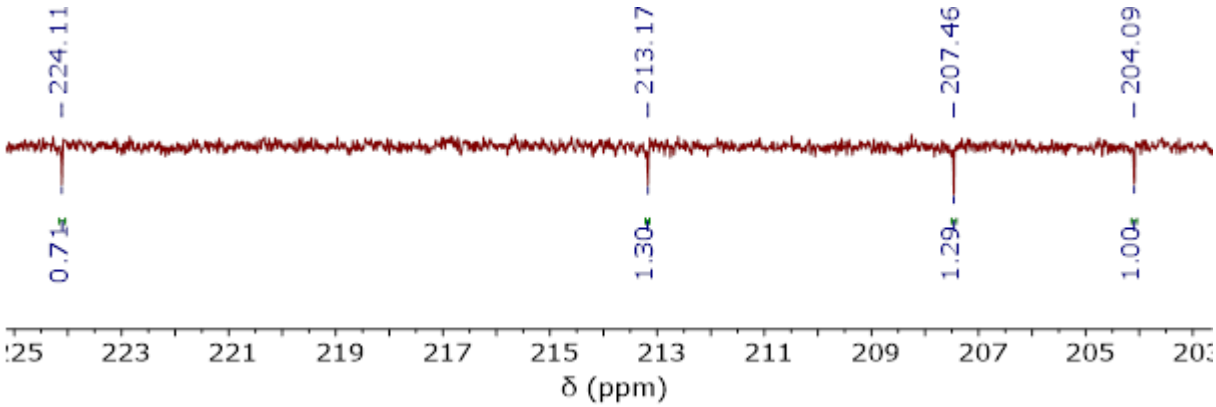

Fig. S44. Enlarged APT NMR spectrum (101 MHz, moist DMSO-d_6, 298 K) of [Ru(κ^1-*S*-SOCMe)(κ^2-*S,S'*-S$_2$C·IMes)(*p*-cymene)](PF$_6$) (**5a**) after 22.43 days in solution at room temperature showing the CS_2 and COS signals.

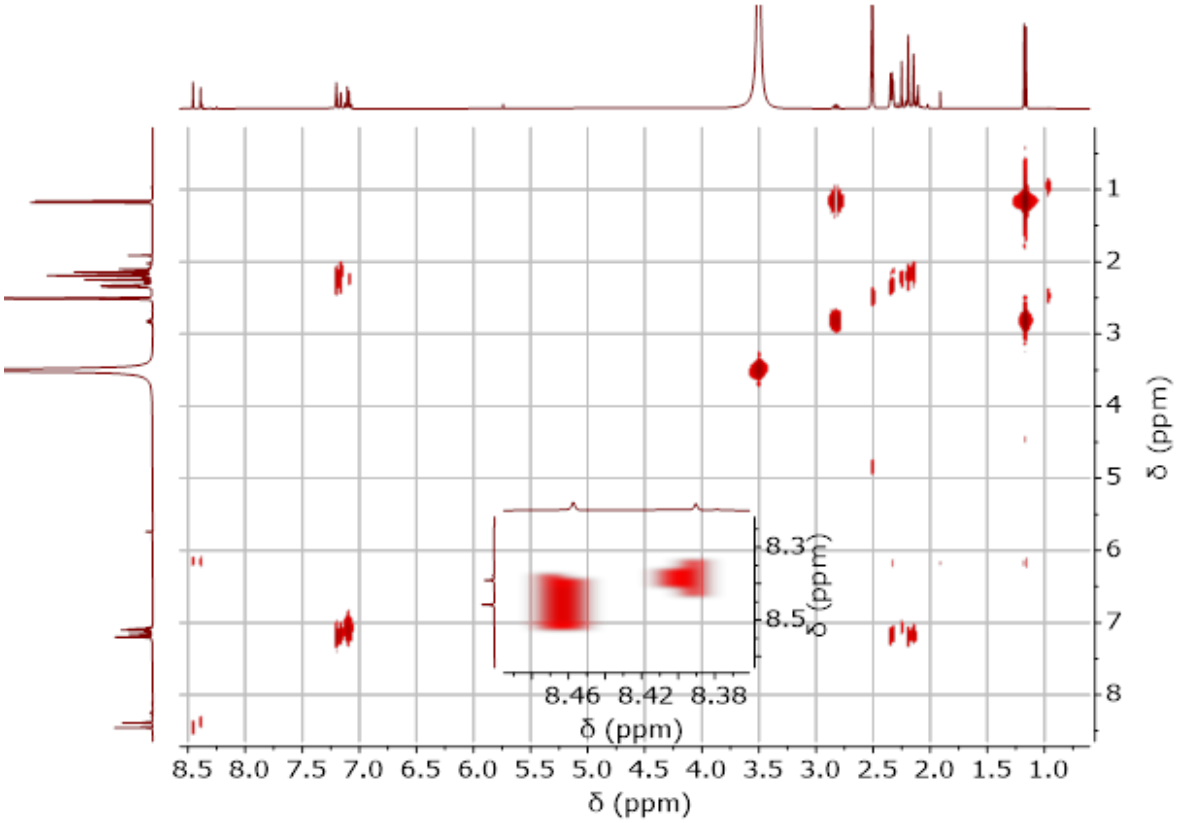

Fig. S45. COSY NMR spectrum (400 MHz, moist DMSO-d_6, 298 K) of Ru(κ^1-*S*-SOCMe)-(κ^2-*S,S'*-S$_2$C·IMes)(*p*-cymene)](PF$_6$) (**5a**) after 22.43 days in solution at room temperature.

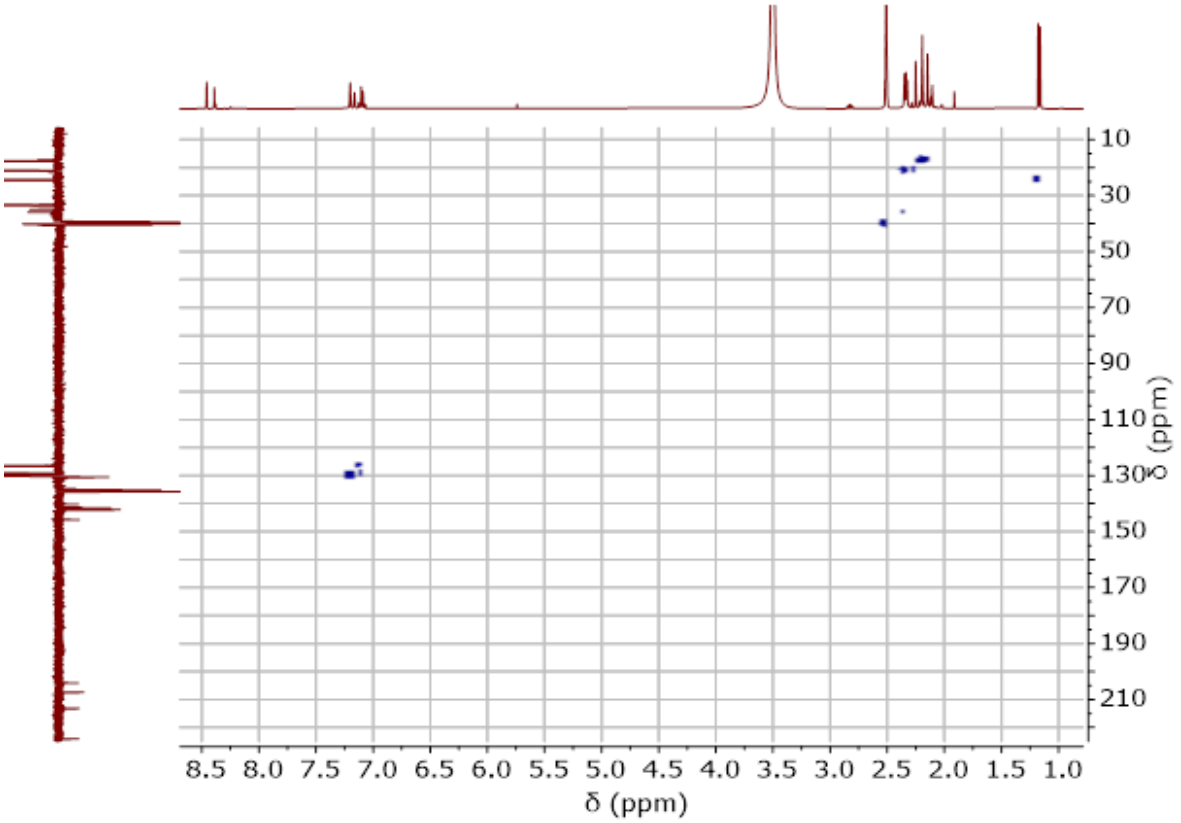

Fig. S46. HSQC NMR spectrum (400 MHz, moist DMSO-d_6, 298 K) of Ru(κ^1-*S*-SOCMe)-(κ^2-*S,S'*-S_2C·IMes)(*p*-cymene)](PF_6) (**5a**) after 22.43 days in solution at room temperature.

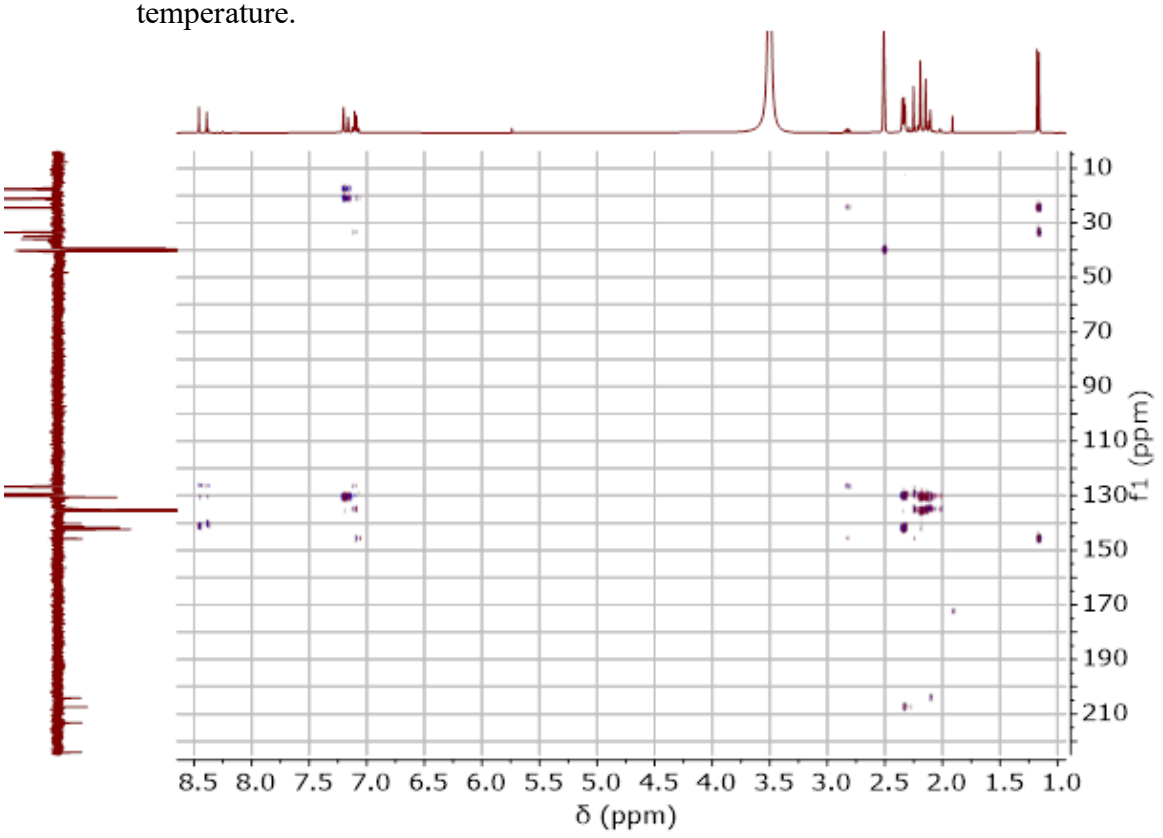

Fig. S47. HMBC NMR spectrum (400 MHz, moist DMSO-d_6, 298 K) of Ru(κ^1-*S*-SOCMe)-(κ^2-*S,S'*-S_2C·IMes)(*p*-cymene)](PF_6) (**5a**) after 22.43 days in solution at room temperature.

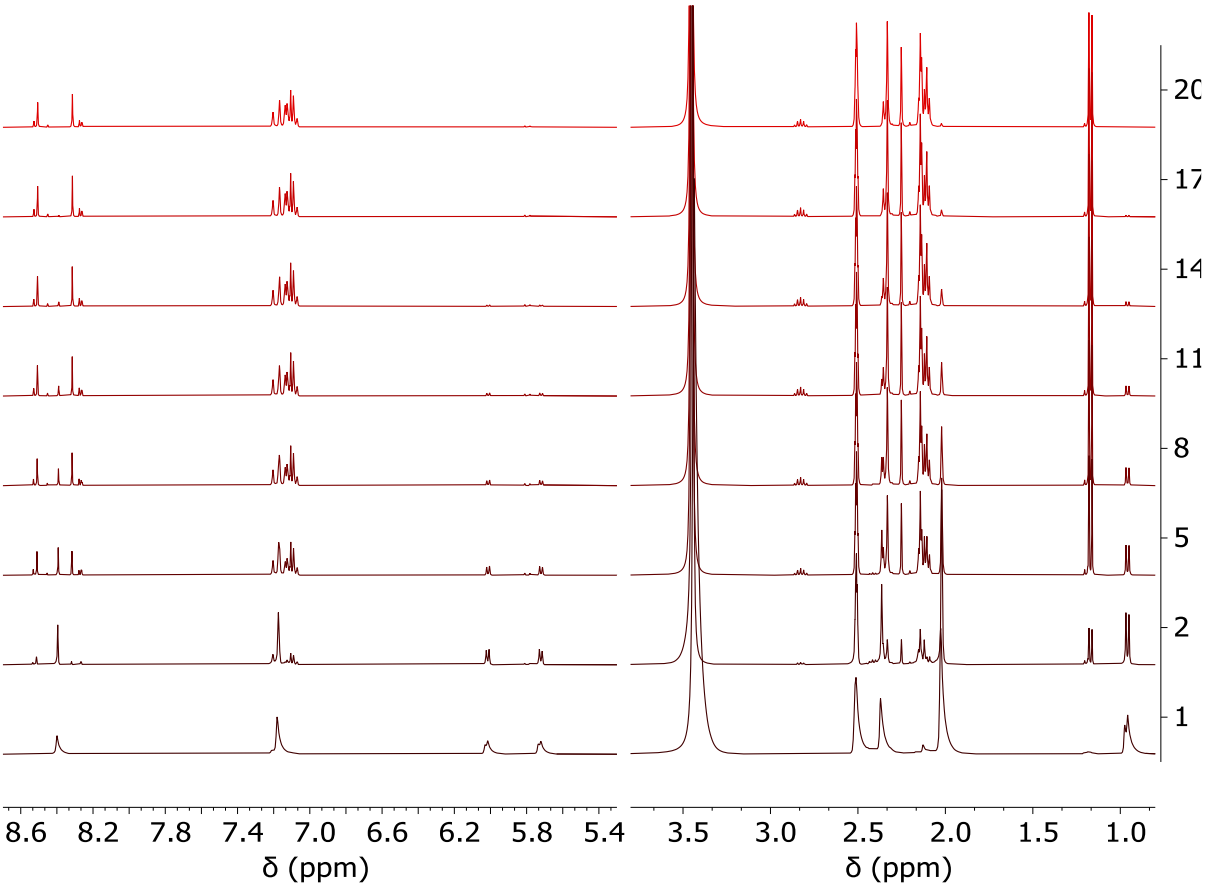

Fig. S48. Stacked ^{1}H NMR spectra (400 MHz, moist DMSO-d_6, 298 K) of [RuCl(κ^2-*S,S'*-S$_2$C·IMes)(*p*-cymene)](Cl) (**3a**) after 0.03, 1.49, 5.67, 8.33, 11.35, 14.76, 20.25 and 26.45 days at room temperature.

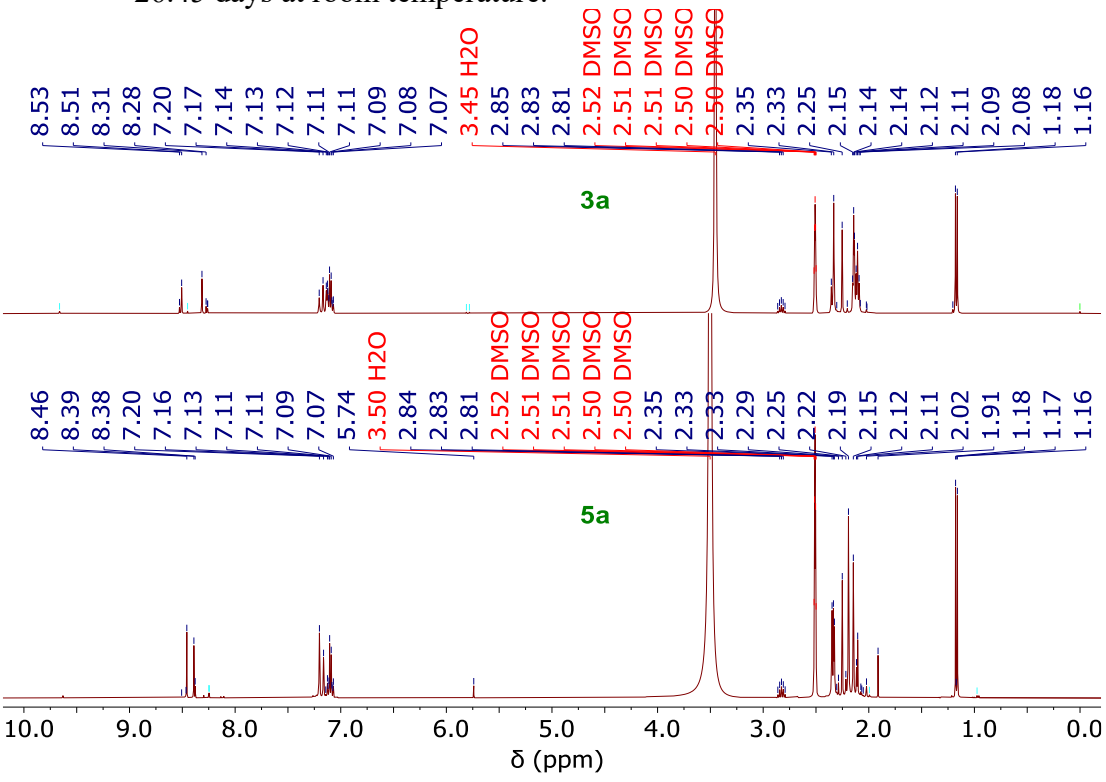

Fig. S49. Stacked ^{1}H NMR spectra (400 MHz, moist DMSO-d_6, 298 K) of [RuCl(κ^2-*S,S'*-S$_2$C·IMes)(*p*-cymene)](Cl) (**3a**) after 26.45 days and Ru(κ^1-*S*-SOCMe)(κ^2-*S,S'*-S$_2$C·IMes)(*p*-cymene)](PF$_6$) (**5a**) after 22.43 days at room temperature.

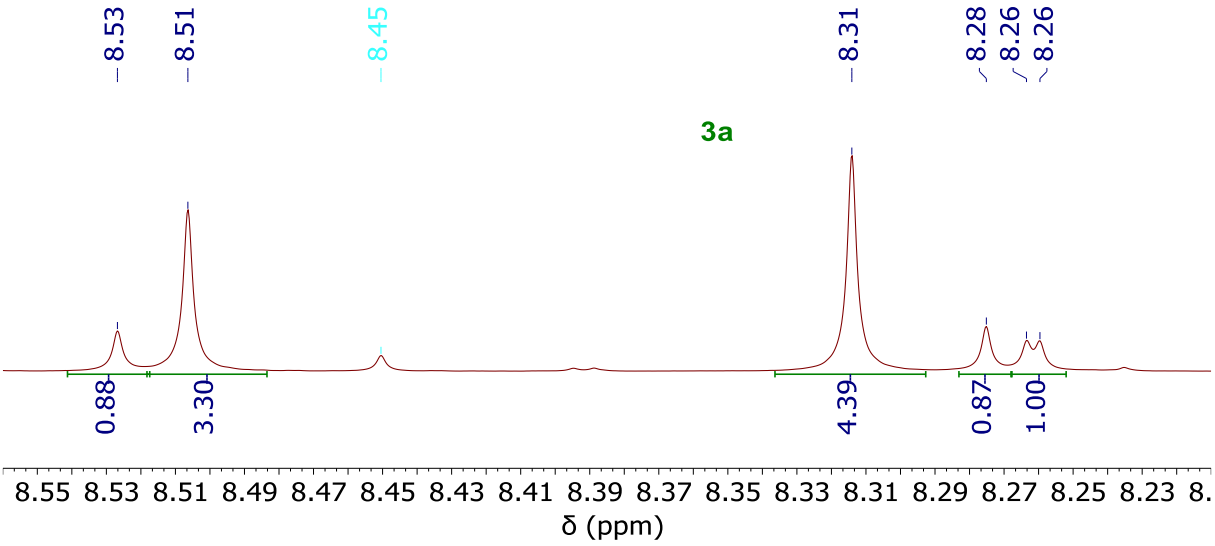

Fig. S50. Enlarged ^{1}H NMR spectrum (400 MHz, moist DMSO-d_6, 298 K) of [RuCl(κ^2-*S,S'*-S_2C·IMes)(*p*-cymene)](Cl) (**3a**) after 26.45 days in solution at room temperature showing the imidazolium protons.